Melt Pathways: Microstructure, Rheology, and history of melt-fluxing

Joyjit Dey

Submitted in accordance with the requirements for the degree of Doctor of Philosophy

The University of Leeds
School of Earth and Environment
January 2023

Declaration

The candidate confirms that the work submitted is his own and that appropriate credit has been given where reference has been made to the work of others.

This copy has been supplied on the understanding that it is copyright material and that no quotation from the thesis may be published without proper acknowledgement.

The right of **Joyjit Dey** to be identified as author of this work has been asserted by **Joyjit Dey** in accordance with the Copyright, Designs and Patents Act 1988.

Acknowledgements

First and foremost, I am incredibly grateful to my primary supervisor, Prof. Sandra Piazolo, for her invaluable advice, continuous support, and patience during my Ph.D. Sandra, thank you for recognizing my potential and allowing me to pursue my research interest. Thank you for your patience during the early stages of my project, when everything seemed a little overwhelming to me. I would also like to express my gratitude to Prof. Thomas Müller and Dr. Dan Morgan for their invaluable supervision and assistance throughout my research. Thank you very much, Thomas, for all your help in Göttingen. Prof. Nathan Daczko has been a constant source of support for me since my MRes days in Australia. Nathan, I am grateful for the time and effort you put into my project, as well as the friendship we formed over the last five years. This endeavor would not have been possible without the supervision of this incredible team. Their vast knowledge and extensive experience have inspired me throughout my academic studies and daily life.

A huge thanks to all the research staffs at SEE who helped me at various stages of this journey. Thank you, Richard, Lesley Neve, and Gary Keech for the training and assistance. Many thanks to John Wyn-Williams, who has been extremely helpful in resolving any sample-related issues. Eleanore, Thank you so much for your helpful advice and input on geochemical modelling. I would also like to thank Dr. Patrick Trimby Prof. John Wheeler, and Dr. Mohsen Bazargan for their contributions in my project.

I am grateful to the University of Göttingen, particularly the laboratory of correlative Light and Electron Microscopy (GoeLEM), for allowing me to carry on research during the pandemic. My deepest gratitude to Andreas Kronz, Dominik Sorger and Burkhard Schmidt for their assistance and training. A big thanks to Dominik for his guidance during my Ph.D. I am extremely grateful to Anthony for all our in-person and Skype conversations, which have yielded a wealth of ideas for resolving problems in my project. Anthony, you are a fantastic friend, I will cherish our academic and non-academic conversations. Thank you, Michelle, for responding to the endless document requests during Schengen visa applications and for your initial help in getting relocated to the UK.

I would like to acknowledge University of Leeds LIDS scholarship, IGT funding, and Geological Society of London Robert Scott Memorial Award for providing valuable

financial support for my field trip to Greenland, research, and travel to local and international conferences. Thank you, Julie, and the Greenland geological survey, for your help and support during and after the Greenland field trip.

I was fortunate to work with an extremely encouraging research team in both Leeds and Macquarie. At various stages during this journey, each of you has made my path easier. Many thanks to Anthony, Hindol, Robyn, Kim, Jack, Maeve, Mohsen, and Stefania. A special thank you to Hindol and Robyn for their unwavering support during this process.

The journey would have been much more difficult without the help of this incredible group of friends in the UK. I thank Supti and Ankit for all the incredible dinners, enjoyable conversations, and evening strolls. Supti, thank you for being an exceptional friend. I will always remember our political discussions (and arguments!) over lunch, followed by the sudden realization that it was time to return to work. Thank you so much to Sanchit for all your help throughout this journey. I will never forget the times we spent together on road trips, house hunting, and partying. Thank you, Sisir, for the enjoyable memories. Thanks for all the driving lessons, Soumyadeep.

Thank you to the 'Jadavpur' and 'IIT KGP' geology fraternities for your encouragement. Sincere gratitude to Profs. Manish Mamtani, Saibal Gupta, and Nibir Mandal for inspiring me to pursue structural geology. Many thanks to Prof. Abhijit Bhattacharya for all your guidance and inspiration. Thank you to the "Jodubongshio trio" of I, Avishek, and Bani for putting up with each other for more than a decade. And finally, I would like to thank my family for supporting my crazy dreams and doing everything within their power to help me achieve them. Thank you, Aditi, for celebrating my successes and consoling me during my failures; without you by my side, this endeavor would have been a lot harder. My aunt, who has been a pillar of support and inspiration. Thank you, Maa, and Baba, for believing me even when you didn’t understand what I was doing, let alone why. While I honestly do not think I will ever comprehend the true depth of your sacrifice. Thank you so much, Maa, for everything you endured so that I could get all the opportunities. I am dedicating this work to you.

Abstract

Melt migration transports heat, mass, and volatiles from depth to the surface and is critical in the formation of the Earth's layered structure. Furthermore, anatectic horizons are mechanically weaker areas of the crust where strain partitioning occurs, resulting in weak melt-bearing rocks. Therefore, understanding the chemical and rheological evolution of melt-bearing crust requires an understanding of melt migration mechanisms and their physicochemical signatures. This thesis employs a multidisciplinary approach, combining field, microstructural, and geochemical investigations to demonstrate the physio-chemical signatures of melt migration and their impact on the rheology of the middle-lower crust.

Selected granitoid and migmatite samples are examined for characterizing melt-crystallized grain microstructures. Localized internal crystal bending, subgrain boundaries with multiple slip systems, and a lack of CPO are distinct microstructures of melt-crystallized grains. Systematic lattice distortions are caused by crystal growth and do not show evidence of tectonic deformation. Minor crystal plastic deformation in framework minerals suggests that dislocation creep plays a minor role in syn-melt deformation. Field and microstructural data from granulite facies rocks in the Akia terrane, southwest Greenland, were collected to further investigate properties of syn-deformation melt-fluxing in natural environment. The field area contains abundance of reactive felsic veins within compositionally diverse protoliths. An alternative method is developed to measure local bulk chemistry from different compositional domains to constrain pressure-temperature conditions of heterogeneous rocks. The microstructures show evidence of melt forming an interconnected network and porous melt migration is identified based on i) field relationships, ii) 'frozen in' melt microstructures with high melt percentages, and iii) relatively constant major element chemistry during melt-fluxing. During syn-melt deformation, melt facilitates easy slip along grain boundaries, and amphibole grains align by rigid body rotation with their long axis parallel to the foliation. This thesis characterizes field, microstructural, and geochemical signature of rocks formed during syn-melt deformation.

Table of Contents

List of Figures and Tables

Abbreviations, acronyms, and symbols

a-x = activity-bulk composition relationship

BLG = Bulging recrystallization

CPO = Crystallographic preferred orientation

EBSD = Electron Backscatter Diffraction

EDS = Energy-dispersive spectrometer

EPMA = Electron Probe Micro Analyzer

GROD = Grain Relative Orientation Deviation

GBM = Grain boundary migration

GBS = Grain boundary sliding

IPF = Inverse pole figure

LDA = Low dihedral angle

LOI = Loss on ignition

MAD = Misorientation angle distribution

MA = Misorientation axis

M.U.D = Multiples of uniform distribution

OS = Orientation spread

PPL = Plane polarized light

P-T-d-t = Pressure-Temperature-Deformation-Time

RCMP = Rheologically critical melt percentage

SGB = Subgrain boundary

SGR = Subgrain rotation

SEM = Scanning Electron Microscope

Ti-in-bt = Ti in Biotite

Ti-in-amp = Ti in Amphibole

TTG = Tonalite-trondhjemite-Granodiorite

WBV = Weighted burgers vector

WDS = Wavelength-dispersive spectrometer

X = Bulk rock composition

XPL = Cross polarized light

XRF = X-ray fluorescence

µXRF = micro-X-ray fluorescence

Chapter 1

Introduction

1.1 Scientific Background

Comparison between primitive mantle derived volcanic rocks and Eu-depleted granitic rock in the upper crust, suggests formation of upper crust by intracrustal melting, involving extraction of granitic-granodioritic melts and its transfer through the crust (Brown, 2010). In addition, mantle derived melts must transfer through the lower crust (Ramberg and Smithson, 1975; Touret, 2009). Field investigations and geophysical studies suggest mid to lower crustal rocks are migmatitic, suggesting presence of melt at the base of active orogens (Brown, 2001a,b; Teyssier and Whitney, 2002; Unsworth, 2010). Migmatite terranes are polygenetic because they correspond to crustal levels where melting has occurred, drained, accumulated, and transferred (e.g., Brown, 2001b, 2008). In this thesis, I am particularly interested in understanding melt production, and the migration of melt from its source. Understanding of melt transport is crucial not only as it represents an effective mechanism of mass transfer but also heat from mantle and lower crust to the upper crust (Taylor and McLennan, 1995; Brown, 2006). Moreover, melt presence influences thermal and mechanical properties and can modify host rock chemistry or crustal responses to stresses (Brown and Solar, 1998). For example, anatectic horizons are mechanically weaker portions of the crust, and can affect orogenic development even when the melt fraction is very low (Schilling et al., 1997; Nelson et al., 1996; Beaumont et al., 2006). In the partially molten lower crust, stress-driven melt segregation may produce melt extraction pathways and localise deformation. Known theoretical feedbacks exist between melting, rheological weakening, shear zone development and transportation of melt (Brown, 2007 and references therein), however, comparatively little is known about strain partitioning in partially molten

rock volumes. Hence understanding melt pathways not only helps to discern mechanism of crustal differentiation but also is crucial to evaluate their effects on the rheology and physicochemical responses of a melt-bearing system. But *'how does melt migrate through the crust and what signatures it bears'* still needs to be understood properly as the mechanism of mass transfer through the mid-low crust is still debated (e.g., Petford, 1996; Brown, 2004, 2011). Furthermore, co-existence of molten rocks in conjunction with high-strain regions are observed frequently in active orogenic belts, but the mechanism and relative timing of their formation remain poorly understood (Rosenberg and Riller, 2000; Handy et al., 2001).

1.1.1 Melting of the continental crust and the nature of migmatites

Continental crust melts under different pressure–temperature (P–T) conditions depending on the rock composition (X) and availability of H_2O. Water-fluxed or wet melting occurs at low temperatures in the presence of an aqueous fluid, involving quartz, plagioclase, K-feldspar, and biotite. In the presence of aqueous fluid, common crustal protoliths like pelites, graywackes, and siliceous igneous rocks melt at 650–700 °C at crustal pressures (Sawyer, 2010). While in the absence of an aqueous fluid, melting is governed by the disintegration of H_2O-containing minerals (muscovite, biotite, amphibole, and typically hornblende) (Fig. 1.1a). These are known as dehydration melting reactions. Fluid undersaturated conditions predominate during high-grade metamorphism as there is little pore fluid just below the solidus. Thus, melts are typically H_2O-undersaturated and the rocks in the granulite facies are essentially "dry" (Yardley and Valley, 1997).

The term migmatite originates from the Greek word 'migma', which means mixture. The term was first coined by Sederholm (1907) who referred certain gneissic rocks as migmatites which looked like mixture of melts and solids. Sawyer (2008) defined migmatites as medium to high-grade metamorphic rocks, that are heterogeneous from microscopic to macroscopic scale, have undergone partial melting and produced two or more petrologically distinct parts. Migmatites commonly display two main components, referred to as paleosome and neosome. Paleosome is defined as a part of the migmatite that is non-fertile and do not take part in the melting process, it usually preserves pre-melting structures (bedding, layering, foliation, and folding). The neosome is the newly formed rock portions resulting from partial melting. Neosomes typically have two parts: a light-coloured part

(leucosome) that is predominantly quartzofeldspathic or feldspathic (e.g., enriched in silica, sodium, and potassium) and a residuum which is predominantly the solid fraction left after partial melting and extraction of some, or all, of the melt fraction. The darker-coloured residuum is called melanosome, which is enriched in ferromagnesian, aluminous, and/or calcic minerals (e.g., biotite, garnet, cordierite, orthopyroxene, and hornblende) (Sawyer, 2008; Brown, 2012; Pawley, 2013). High-temperature minerals are usually found within the quartzofeldspathic lenses, layers, or patches at the outcrop scale (i.e., the leucosome; Mehnert, 1968). The nature of the ferromagnesian minerals associated with leucosomes can be utilized to distinguish fluid-present melting from fluid-absent melting in migmatites and granulites. Leucosomes with anhydrous (peritectic) minerals like garnet or pyroxene are likely to have formed from fluid-absent melting (White et al., 2004). Mica- and hornblende-bearing leucosomes in mica- and hornblende-bearing hosts without anhydrous minerals such as orthopyroxene and garnet typically result from fluid-present melting (Milord et al., 2001). The mineralogy and microstructure of migmatites (at shallower level) and granulites (at deeper level) preserve a sequence of events that involve prograde melt-producing reaction, loss of melt, and retrograde reactions involving melt at grain boundaries (e.g., Brown et al., 1999; Sawyer, 1999; Brown, 2001a, 2001b; Marchildon and Brown, 2001, 2002; Holness and Sawyer, 2008).

Metamorphic segregation or differentiation in migmatites involves physical and chemical movement of minerals into layers that concentrates similar minerals and forms bands within an unbanded rock (Turner, 1941; Robin, 1979). Petrological, geochemical, and microstructural studies have shown that migmatites are also formed by some type of local mesoscopic differentiation (Mehnert, 1968; Brown, 1994a, 1995). The quartzo-feldspathic components are separated into discrete leucosomes during this process, as opposed to the ferromagnesian components, which are concentrated in melanosomes (Fig. 1.1b). For low-melt fraction migmatitic banding is present and the rock is called metatexite, whereas a high melt volume disrupts migmatite banding and the rock is known as diatexite (Brown, 1973). When leucosome and melanosome form bandings (with low ratio of thickness to length) parallel to the plane of schistosity, it is called stromatic migmatite.

Migmatites deform during anatexis and result in a rock with complex morphology (Brown, 2012). First order morphology in migmatite results from the partial melting whereas the second order morphology is a combined result of melt fraction and strain. Differences in strain rate across foliation planes create abundant dilatant structures where anatectic melt

migrates and, subsequently, crystallized to form the coarse-grained in situ, or in-source leucosomes (Fig. 1.1b). Since several granulites have geochemical and mineralogical characteristics consistent with an origin as restitic residues after segregation of melt (e.g., Clemens, 1989), it can be inferred that melt segregation in crustal rocks has sometimes been efficient. Many anatectic migmatites show that melt has segregated on a millimeter scale but not extracted from the system (McLellan, 1988). The forces that drive melt segregation range from grain-scale to surface-scale processes (Brown et al., 1995). Segregation of melt may relate to surface tension caused by interfacial energies, buoyancy caused by gravity, pressure gradients caused by applied differential stress, thermal effects, or volume changes during melting or crystallization. The process by which melt segregates from its residue are described by Sawyer (1991, 1994, 1998, 2001) and Brown (1994, 2010a) based on examples from the field. Separation velocity and segregation are weak at low melt fractions (<5% vol%), but as melting proceeds, segregation becomes apparent and migmatites may form (Brown et al., 1995). Melt, being less dense than its solid surroundings, is buoyant giving rise to a pressure gradient that drives it upwards in the crust. Pressure gradients caused by tectonic stresses acting on rocks of varying strengths are superimposed on buoyancy stresses and can lead to lateral or even downward melt migration.

1.1.2 Melt-rock interaction

The mechanisms of melt-rock interaction largely depend on the chemical difference between the host and melt and regulated by PT conditions at the time of reaction. In addition, the rate at which melt is segregated from pore spaces into larger melt pools determines whether the melt is in chemically and isotopically disequilibrium with the source. Melt extraction is anticipated shortly after the melt connectivity transitions at 7% of melt in a deforming system (Rosenberg and Handy, 2005). Thus, multiple melt accumulation and drainage cycles can be predicted along the prograde P-T evolution path and closed-system behaviour will not be retained at depth in the orogenic crust (Handy et al., 2001; Brown, 2007, 2010a). Melt extraction will probably alter the bulk composition of the source rock multiple times throughout the history of melt-rock interaction (Brown, 2004, 2006, 2007).

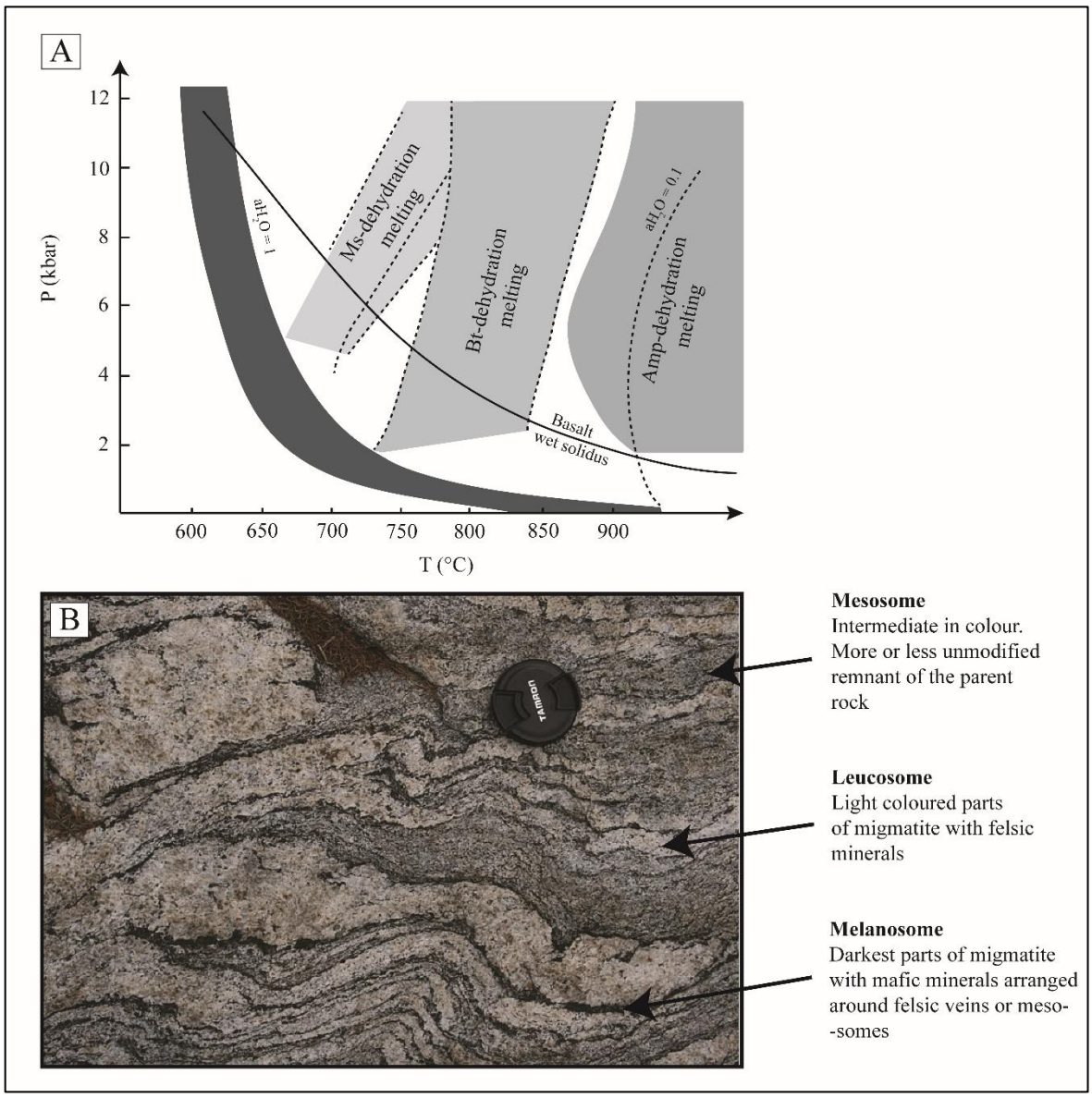

Figure 1.1 – Pressure (P)-Temperature (T) phase diagram of melting reactions and generic classifications of migmatite. (a) H_2O-present and -absent melting reactions with varying slopes and solidus temperatures (after Weinberg and Hasalová, 2015). Melting reactions with no added water and with 4% added water are represented by thick solid lines. (b) Migmatite indicating the leucosome, melanosome, and mesosome. Sinuous migmatite layers are seen. Photo courtesy of Etienne Médard. Definitions after Wimmenauer and Bryhni (2007).

Any reaction which involves re-equilibration of mineral assemblage accompanying any change in P-T condition also gets affected by presence of fluid (here melt) (Yardley, 2009). There are well documented examples where metamorphic reactions were only possible because of fluid presence (Austrheim, 1987; Jamtveit et al., 1990; Austrheim et al., 1997). As melt migrates relative to the solid residue during segregation and extraction, the major and trace-element composition of the liquid may change because of interaction with the

matrix (Jackson et al., 2003, 2005; Getsinger et al., 2009). Compatible elements, for instance, will be retained in the residue to be transported downward, whereas incompatible elements will preferentially enter the melt to be transported upward by compaction during melt extraction. Moreover, the dissolution of accessory minerals during melting and melt migration also control the rock and melt composition. Hence, melt presence may not only facilitate other reactions due to its kinetic effects but can also cause specific reactions due to its chemistry.

Hence, transport of melt relative to the solid matrix is a fundamental factor in the generation of temporal and spatial diversity in the major- and trace-element compositions of the parent rock (Brown, 2013), giving rise to a heterogeneous rock. The microstructural location of the minerals, the stability of the major rock-forming minerals (Watson et al., 1989; Bea et al., 2006), the kinetics of reaction (Bea, 1996; Watson, 1996), the extent of anatexis (Rubatto et al., 2001), the chemistry of the melt (Watson and Harrison, 1983), and the P-T path all play a role in the formation of heterogeneous rocks during melt-rock interaction. A strongly focused flow (like in a dyke) lead to a disequilibrium melt transport with few surfaces where reaction can occur which limits solid/liquid interaction (Kelemen et al., 1995; Jull et al., 2002). In contrast, diffuse porous flow in a chemically open system promotes vigorous melt/rock interaction and promotes formation of heterogeneous rocks even in the microscopic scale (Spigelman and Kenyon, 1992; Lundstorm, 2000). The influence of porous melt migration and the formation of compositionally different rock by melt-rock interaction has been studied in mantle rocks (Dick, 1989; Kelemen et al., 1997; Tartarotti et al., 2002), oceanic crust (Collier and Kelemen, 2010; Coogan et al., 2000; Rampone et al., 1997, 2009) and arc crust (Cashman et al., 2017; Daczko et al., 2016; Smith, 2014; Stuart et al., 2016, 2017; Zàvada et al., 2018), however, *to what extent the chemical heterogeneity produced by melt-rock interaction influences the original protolith composition and how this information can be used to better constrain the P-T condition of high-grade rocks is yet to be understood.*

1.1.3 Melt transport mechanisms and role of deformation

Local pressure fields generally control the first steps in melt migration. The change in volume and density, which is a function of the melting reaction, is a significant variable that controls the initial phase of melt migration (Weinberg and Hasalová, 2015).

Burg and Vanderhaeghe (1993) describe gravitational instability structures and propose that gravity is the driving force behind melt migration. A rise in volume causes buoyancy, which may result in the vertical ascent of the source region as a large diapiric mass. Volume change also has the potential to alter regional pressure gradients, resulting in fracturing within the source region. Many previous studies suggest that melt-bearing rocks deform at high temperatures and pressure, melt segregates, and organizes into melt-rich networks (Holtzman et al., 2003a, b; Parsons et al., 2008). Two end members of melt transport can be envisaged: channelized movement of melts and non-channelized flow (Fig. 1.1). Gravity driven diapiric flow in the ductile lower crust (Weinberg and Podladchikov, 1994; Weinberg, 1997), and dykes in the brittle upper continental crust fall under channelized melt transport (Marsh, 1982). The respective rate of melt ascent is suggested to be very different, 10^6 times faster in diking compared to diapiric rise (Clemens et al., 1997; Petford et al., 1993). Dikes produce discordant bodies of granite with very high aspect ratios and are variable in thickness. Diking was initially thought to be an efficient melt-transport mechanism in the upper crust but later it has been found that transporting felsic magmas to long distance is hampered by its stiffness and rapid heat loss (Weinberg, 1999). Scarcity of felsic dyke swarms in the upper crust also supports the same. Outcrop observations of many migmatite complexes exhibit melt transportation commonly occurs via a network of veins, structurally concordant channels of various shapes and sizes (Brown and Solar, 1998a, 1999).

However, an alternative mechanism of melt-transport as mesoscale porous flow is supported by various grain to outcrop scale structures (Brown, 1994; Collins and Sawyer, 1996). For example, melt can move through shear zones where an interconnected network forms by linking compaction bands, shear bands and dilation bands (Brown and Rushmer, 1997; Brown, 2004). *Diffuse porous melt flow* (Fig. 1.1) occurs when melt is distributed along grain boundaries and at triple junctions and flow localization occurs due to the 'reactive infiltration stabilities' (Scott and Stevenson, 1986; Turcotte and Ahern, 1978; Aharonov et al., 1997). A permeable grain boundary network within the solid framework can be achieved even for a low melt fraction of <5%). when the melt-solid dihedral angle is <60° (Faul, 2001; Zhu et al., 2011; Harte et al., 1993; McKenzie, 1984). Though most of the studies regarding porous melt flow concern mantle rocks (Fig. 1.1) (Aharonov et al, 1995; Dijkstra et al., 2003; Kelemen et al., 1992, 1995); it might be an effective melt-transport mechanism in the lower to middle continental crust (Scott and

Stevenson, 1986; Brown, 2007). The suprasolidus condition within the crust can be maintained by adiabatic heat transport (Brown, 2007; Weinberg, 1999) or by anatexis because of melt-rock interaction during porous flow (Stuart et al., 2017). Thus, subsequent batches of melt can reach shallower levels by heating the country rock (e.g., Jackson et al. 2003, 2018). Gravity-driven compaction of solids with Newtonian rheology and interstitial melt produces a melt layer above the compacted solid grains (McKenzie, 1984). It has been demonstrated that this procedure is too slow to account for melt migration (Brown et al., 1995), thus, porous melt flow in the crust is usually assisted by deformation. It has been characterized by the development of banded gneiss at higher strains by Hasalovà et al. (2008c). Melt tends to stay trapped within the pore network in the absence of external differential stresses, as observed in static, partially melted contact aureoles (Holness et al., 2011). and deformation is increasingly recognized as influencing melt segregation (e.g., McLellan, 1988, 1989b; Sawyer, 1991, 1994; Brown, 1994a). McLellan (1983) found that syntectonic migmatites display extensive melt segregation into leucosomes, leaving the residual melanosomes but post tectonic opthalmitic (patchy) migmatites show little or no melt-residue segregation.

The co-location of melt-zones and regional tectonics has been observed previously while studying close spatial and temporal relationship between migmatites, high temperature metamorphic rocks, crustal scale shear zones and plutons in active convergent margins (D'Lemos et al., 1992; Brown, 1995; Collins and Sawyer, 1996). Moreover, many granites are emplaced during active deformation (Brown and Solar, 1998) and partially molten rocks are localized in high strain zones (Davidson et al., 1992; Dijkstra et al., 2002). Partial melts infiltrate many shear zones and serve as the source of many large intrusive bodies (e.g., Brown, 1994; Vigneresse et al., 1996; Petford et al., 2000; Keay et al., 2001), with some areas displaying possible direct evidence of melt removal (e.g., Brown, 1994, Johannes et al., 2003, Stuart et al., 2016, Meek et al., 2019). Hence, differential stress on the crust in the presence of melt is likely the norm in most terranes during orogenesis (McLellan, 1984; Brown, 1994a). Melt migrates to specific structural sites, including fold axial surfaces (Mackenzie, 1957), boudin necks (Sawyer, 1991; Allibone and Norris, 1992), fractures (Clemens and Mawer, 1992), and shear zones and conjugate shear fractures (Clemens and Mawer, 1992). This may explain the common occurrence of leucosomes parallel to axial planar foliation of folds in migmatites (Weinberg et al., 2015). Stevenson (1989) also argues

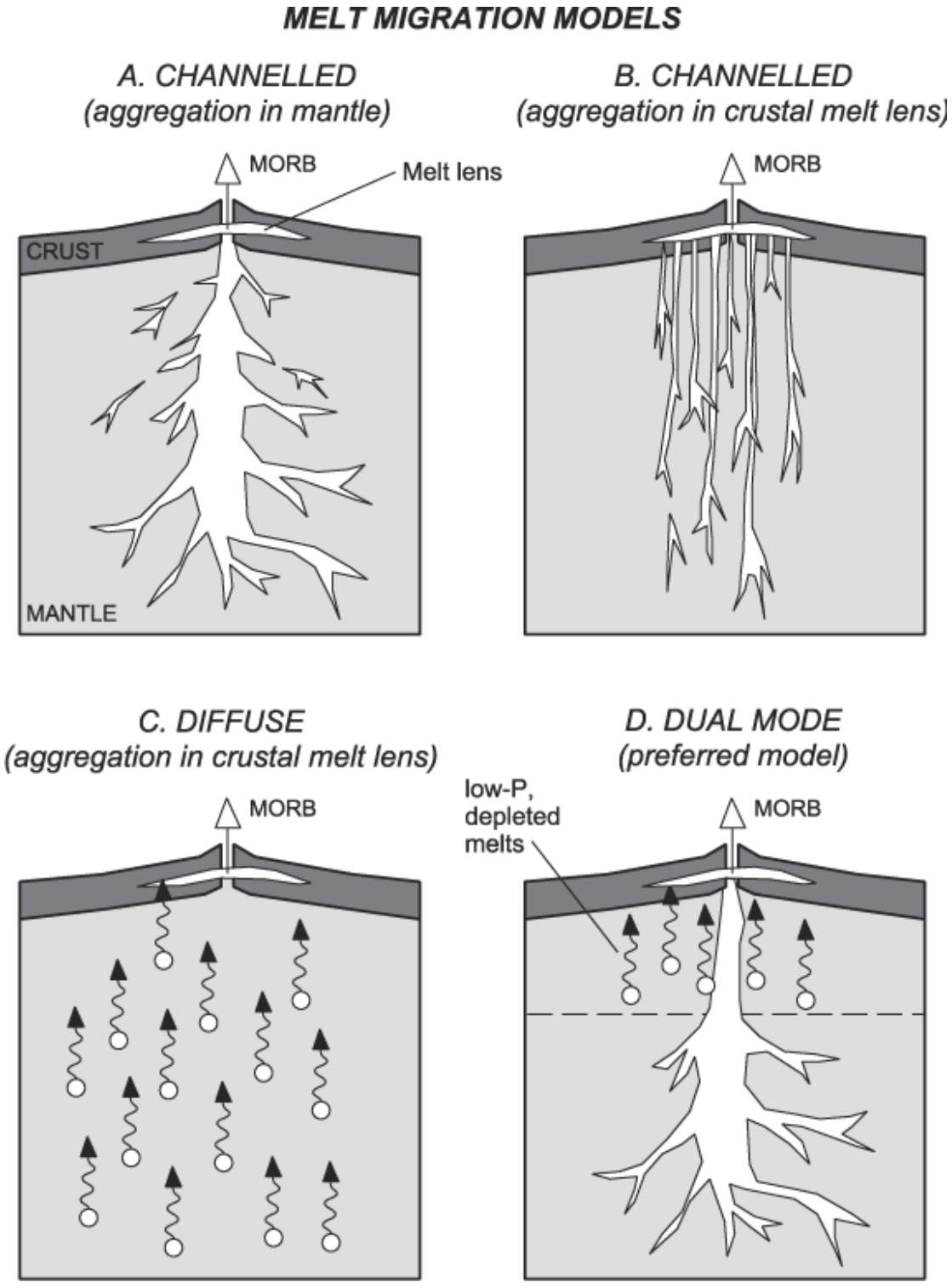

Figure 1.2 – Different models of melt migration and aggregation, shown for mantle (after Dijkstra et al., 2003), but it can also be an effective mechanism for continental crust. 'A' and 'B' shows channelized melt movement whereas 'C' shows diffuse porous flow. A) Melt migrating through dunnite channels and aggregating before reaching upper crustal melt lenses. B) The dunite channels, in this case, are separate and not interconnected. Melt aggregation occurs only in the upper melt lens. C) Melt migration occurs as diffuse porous flow and melt aggregates in the upper melt lens. D) Dual mode, where depleted melt moves as diffuse porous flow and deep met fractions migrate as isolated channels.

that melt migration occurs parallel to the axis of minimum compressive stress and accumulates melt in lenses or veins due to melt instability during the act of differential stress. During noncoaxial deformation of an anisotropic source region, any volume of melt above the threshold permeability in a ductiley deforming matrix will be squeezed out if it can migrate to nearby low-pressure sites, such as boudin necks, shear bands, or fractures (Sawyer, 1994). In the lower crust, deformation is the main mechanism that segregates and focuses melt flow (Brown et al., 1995; Brown and Rushmer, 1997; Vigneresse et al., 1996; McKenzie, 1984). Prescence of melt can also add to the original heterogeneous nature of the rocks and can affect the strain partitioning on all scales (Fossen and Cavalcante, 2017). Silicic melt may influence the rock strength to a large degree (Rosenberg and Handy, 2005), and can accommodate strain or localize deformation (Hollister and Crawford, 1986; Hollister, 1993; Brown, 1995; Davidson et al., 1992; Tommasi et al., 1994; Nelson et al., 1996). If melt volume exceeds a certain threshold, partial melt zones in orogenic systems can form a major zone of weakness that can mechanically detach the orogenic root from the overlying crust (Schott and Schmeling, 1998; Arnold et al., 2001). Závada et al. (2018) demonstrate occurrence of porous melt flow during deformation from deeper levels of the crust and evolution of banded orthogneiss to granofels. Štípská et al. (2019) identify grain scale modification during pervasive melt migration through the rock. The spatial distribution of melts and melt pocket morphology in a deforming environment is also controlled by deformation (at higher strain rate) (Groebner and Kohlstedt, 2006; Walte et al., 2011). Hence, the melt-pathways can get easily obliterated as a) the intergranular melt crystallizes with same optical features as adjacent grains and b) the progressive deformation might cause attenuation and closure of the magmatic conduits. The effects are more pronounced when the melt fraction is small, as in the case of diffuse porous flow (D'Lemos et al., 1992). Hence, identification of melt microstructures and understanding the feedback mechanism is essential to apprehend the spatial (porous vs channelized) and temporal (slow vs fast) characterization of melt fluxing and its relationship to deformation. A consensus related to the presence and efficiency of diffuse porous flow in transporting mass through the crust is, however, yet to be achieved. Hence, *detailed microstructural studies involving grain boundary melt flow and the physical and geochemical signatures of porous melt migration in the middle-lower continental crust are yet to be properly assessed* (Stuart et al., 2017; Meek et al., 2019; Dey et al., 2018; Lee et al. 2018). Moreover, even though the basic relationship is known, the *exact nature of melt migration during progressive deformation* and *feedback between deformation and melt transport*, is still poorly understood.

1.1.4 Microstructures indicative of former presence of melt

It is important to be able to identify the former presence of melt even in rocks that may have once contained only small melt percentages (e.g., 1-5% vol. melt) as it is predicted to weaken the rocks by at least one order of magnitude. Melt-pseudomorphs can be observed in at least three different scenarios: (i) crystallisation of granitoid rocks under no differential stress, (ii) static or dynamic migmatites, and (iii) high-strain melt-present shear zones. For granitic to granodioritic plutons a 'flow-channel network' results in a high abundance of low dihedral angles (LDA) expressed as euhedral/cuspate-shaped minerals of quartz, K-feldspar and/or plagioclase with sharply pointed extensions (Fig. 1.3a, b, f; Holness and Clemens, 1999; Clemens and Holness 2000; Sawyer, 2001). Furthermore, typical grain-scale features include a. retention of chemical zonation in feldspars (Vernon and Paterson, 2008; Holness et al., 2007), b. impingement of two grains (during solidification) (Vance, 1969; Holness et al., 2018), c. euhedral inclusions of plagioclase in K-feldspar, plagioclase in quartz, plagioclase in biotite, etc. (Fig. 1.3a; Holness et al., 2018), d. interstitial grains of quartz-K-feldspar (Fig. 1.3e), and d. other primary magmatic features involve granophyric microstructure and growth twins in K-feldspar, plagioclase, and hornblende (Vernon, 2010; Holness et al., 2018). In a statically partially melted rock (static migmatite), typical features include a. melt-wetted grain boundaries (Fig. 1.3b-c), and melt lenses (Walte et al., 2003), b. strongly distorted melt-filled triple junctions and multigrain-bounded melt pockets (Fig. 1.3d, g; Laporte 1994; Laporte and Watson, 1995) c. cuspate shaped minerals with pointed extension (Fig. 1.3f; Bons et al., 2004). On the microscopic scale, melts are observed as tiny droplets amidst reactant minerals. Even at very low melt fractions, these ponds remain isolated. As melt fractions increase, melt pools interconnect. The surface tension between melt and crystals, as reflected in their dihedral angles, determines how and when they connect. Since these angles for silicate melt and rocks are typically <60° (Fig. 1.3f), a stable network will form for melt fractions comprising a few percent of the rock (see Holness et al., 2011 for an extensive review). During slow cooling, melt films that are predominantly concentrated in thick films on grain boundaries can result in a "string of beads" texture. Field and experimental studies suggest deformation plays a critical role in melt segregation, extraction, and migration (see below), however, effect of deformation on grain scale melt distribution is also profound. Slow deformation during diffusion creep allows for textural equilibration, but as deformation rates increase, melt topologies become controlled by the deformation. (Marchildon and Brown, 2002). The grain-scale distribution of melt in

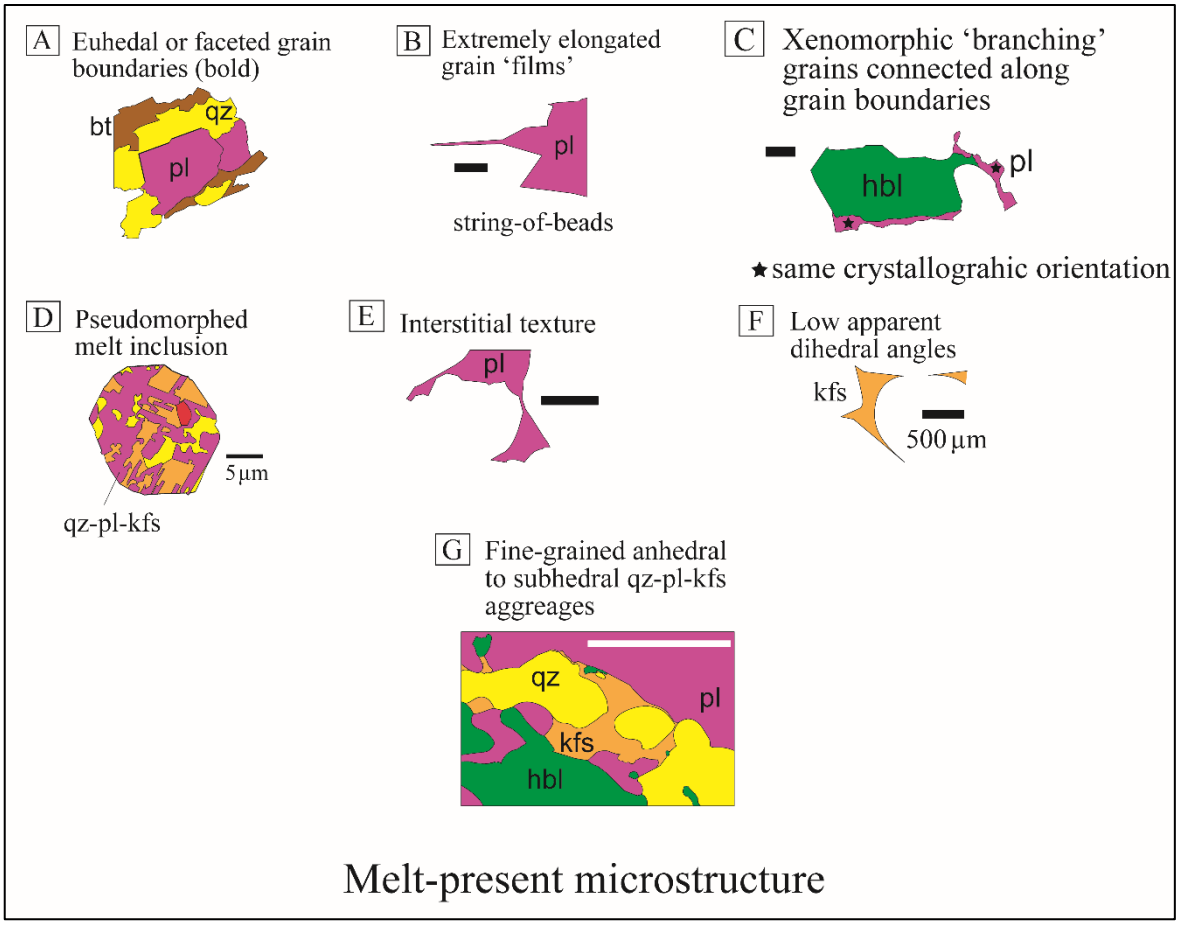

Figure 1.3 – Schematic diagram showing key microstructural features that formed in (I) high-strain melt migration pathways (i.e., zones of deformation-assisted migration of an externally derived melt), and (II) mylonite zones. Schematic diagram is modified after Daczko and Piazolo, 2022.

---

naturally deforming metamorphic rocks is of two types: melt either form aligned pockets parallel to foliation (e.g., Sawyer 2001; Marchildon and Brown 2002; Guernina and Sawyer 2003) or have elongated pockets on grain boundaries aligned at a sharp angle to the foliation (Rosenberg and Riller, 2000; Závada et al., 2007). In the latter scenario, melts may also fill intragranular fractures. These orientational differences depend on the magnitude of the stress and the amount of melt present. Typical characteristic features of melt crystallization under deviatoric stress field (high-strain zones) are very similar to those formed in static melt crystallization. Additional features may include a. dominantly unimodal grain size distribution, b. occasional intra- or inter-granular fractures, c. elongate melt pockets or shear bands, d. SPO formed by prismatic or flaky minerals (Rosenberg and Riller, 2000; Rosenberg, 2001; Stuart et al., 2018). All these demonstrate optical microstructures now

preserved as melt pseudomorphs. However, in all these studies the *internal grain-subgrain microstructures of the melt-crystallized grains and how they are related to the process of crystallization (accompanied with/without deformation)* have been up to now largely been neglected. However, such features may be another valuable indicator for former melt presence.

1.1.5 Deformation mechanisms in the presence and absence of melt

Melt present deformation: Even at small melt volumes, presence of melt in the grain boundary network is known to cause dramatic decreases in strength (e.g., Beaumont et al., 2001; Rosenberg and Handy, 2005; Jamieson and Beaumont, 2013; Levine et al., 2013). Melt segregation and transportation directly result from the relative motion between melt and the residue. Viscous grain boundary sliding, formation of pore space, and ductile fracturing influence the host-rock permeability and control the nature of melt migration. Thus, melt migration mechanisms and the rheology of a system have a direct relationship. Most rocks become heterogeneous because of melt-rock interaction (e.g., grain size, mineralogy, microstructure, etc.), and these heterogeneities influence strain partitioning (Fossen and Cavalcante, 2017). However, how the deforming matrix behaves in the presence of a melt has yet to be fully understood. The presence of melting during deformation may also lead to a change in deformation mechanism (Vigneresse, 2004; Rutter et al., 2006). Consequently, it is essential to consider the evolution of melt-present shear zones over time and the role that melt plays in the active deformation mechanisms during melt-free deformation to syn-melt and post-melt deformation.

Melt-bearing systems range from almost solid grain aggregates with minor melt between grains to almost fully liquid magma with suspended crystals. Deformation localises in rock weaknesses or fractures for melt volumes <7% (van der Molen and Paterson, 1979; Rutter and Neumann, 1995; Rosenberg and Handy, 2005). At this stage, the heterogeneity of the protolith (i.e., host rock anisotropies) and scale of melt movement are important factors. For planar and continuous anisotropies, leucosomes form parallel to anisotropic structures, such as banding or foliation during deformation (Sawyer, 1999). If strain incompatibilities are high between layers, then dilatant structures such as boudins, asymmetric foliation boudins, or shear bands form at an angle to the anisotropy. As melt

volume increases to 7%, grain-scale interconnected melt networks decrease rock strength and distribute deformation (Bruhn et al., 2000; Rosenberg and Handy, 2005). This is the "melt connectivity threshold" (MCT), where 90% of grain boundaries host a melt film (van der Molen and Paterson, 1979; Rosenberg and Handy, 2005). When melt volumes exceed 7%, intergranular films widen, and at high melt volumes of 40-60%, the solid framework breakdowns, and the rock passes through the "solid-to-liquid transition" (SLT) and "rheologically critical melt percentage" (RCMP) (van der Molen and Paterson, 1979; Rosenberg and Handy, 2005). The amount of melt is thus one of the primary parameters that determine the rheological behaviour. Three main types of behaviour can be distinguished:

1. At high melt fraction, crystals are suspended in the melt and the mechanical behaviour is controlled primarily by the liquid viscosity (Einstein, 1906; Ryerson et al., 1988)

2. At intermediate melt fraction, crystals form an aggregate and granular flow, and grain boundary sliding (GBS) predominate as the primary deformation mechanisms (Rutter, 1997; Petford and Koenders, 1998; Paterson, 2001). Mecklenburgh and Rutter (2003) observed linear viscosity during granular flow only at low strain rates, whereas a non-linear granular flow was characterized by the intermittent unsticking of sintered contacts between grains by a rate-dependent cracking and/or dislocation accommodation process.

3. At low melt fraction, grains form an interlocking load-bearing framework, and the deformation mechanics are governed by the rheology of the solid phases. Here, the (non-linear) viscosity of the solid controls diffusion or dislocation creep mechanisms (e.g., Hirth and Kohltstedt, 1995a, b; Gleason et al., 1999; Mei et al., 2002), or brittle deformation occurs due to intracrystalline fracturing (e.g., van der Molen and Paterson, 1979; Rutter, 1997; Renner et al., 2000; Holyoke and Rushmer, 2002). The grains recrystallize by very mobile grain boundaries that sweep highly strained areas of other crystals. Rotational recrystallization occurs with initial undulouse extinction concentrating into sub-grain boundaries, and finally the formation of new grains. These deformation structures are similar to high-temperature deformation regime 3 in Hirth and Tullis (1992) and grain boundary migration (GBM) regime of Stipp et al. (2002).

Walte et al. (2005) also classified liquid bearing systems into three deformation regimes: Regime I - deformation by compaction and distributed granular flow at a "high" liquid-fraction (~8–10 vol.% melt); Regime II - deformation by localised GBS with

compacting grain clusters at moderate liquid-fraction (<8–10 vol.% melt); and Regime III – dominated by an interlocking granular framework at a low liquid-fraction (<4-7 vol.% melt). GBS dominates deformation at high to moderate liquid fractions above 4–6 vol.%. Granular flow and grain boundary sliding of melt-bearing rocks is considered an important deformation mechanism (e.g., Rutter, 1997; Paterson, 2001; Rosenberg, 2001).

Melt absent deformation: Dislocation creep refers to the crystal plastic deformation in which dislocations move through the crystal lattice and minimize the internal strain energy of the grain (Poirier, 1985; Nicolas and Poirier, 1976). Dislocation creep is accompanied by dislocation glide or by dislocation climb. Distributed dislocations create undulose extinction, and as the material recovers, the dislocations concentrate in deformation bands, eventually forming subgrain boundaries. Grain boundary mobility reduces dislocation density in deformed crystals through recrystallization (Poirier, 1985; Jessell, 1987; Drury and Urai, 1990). Three main mechanisms of recrystallization, with increasing temperature and decreasing flow stress are: grain bulging (BLG), subgrain rotation (SGR), and grain boundary migration (GBM) recrystallisation (Hirth and Tullis, 1992; Stipp et al., 2002). Diffusion creep involves solid-state diffusion of atoms through a crystal lattice, or along grain boundaries, and are termed as Nabarro-Herring creep, and Coble creep, respectively (Poirier, 1985; Wheeler, 1992). During pressure solution materials are transported along grain boundaries in a liquid film rather than the movement of atoms and vacancies (Rutter, 1983). Dissolution-precipitation creep (DPC) refers to the process of material dissolving and precipitating. DPC may occur in a single phase or in conjunction with metamorphic reactions (Stünitz 1993; Okudaira et al. 2015). Diffusion creep and grain-boundary sliding occur together and are grain-size sensitive creep (Passchier and Trouw, 2005; and references therein). This is a predominant process in the lower crust where strain rate is high and the differential stress is low (Karato, 2010), *but is it a dominant mechanism when melt is present in the middle-lower crust*? *Understanding the overall deformation mechanisms of melt-bearing systems requires understanding the deformation of solid phases in the presence of melt, particularly the dominant amphibole-plagioclase minerals of the middle-lower crust.*

1.2 Main field area and geological background: Akia Terrane and Alanngua complex, Southwest Greenland

1.2.1 Rationale behind main field area chosen

Characterization and identification of melt pathways during partial melting and melt-flow require investigations of typical internal microstructures and chemical signatures of a melt-bearing system. Both these require not only evidence of obvious melt veins/fractures or melt reaction zones but also areas with very low melt fraction where porous melt migration can be envisaged. Microstructural characterization of cryptic melt pockets must incorporate a known field area where diffuse porous flow is likely (supported by the P-T condition) and allow comparison to other melt flow mechanisms. If melt is crystallized under differential stress environment, characterization of melt-present microstructures in connection with strain rate can also be made. In addition, a suitable field area must exhibit infiltration of chemically distinct melt into a single rock type or different compositional melts reacting with either a single or different protoliths to produce a spectrum of reactions, which helps to constrain the chemical and PT signatures during melt-rock interaction. In accordance with the above arguments Akia terrane from Southwest Greenland is chosen for study.

1.2.2 Akia terrane and Alanngua complex, SW Greenland

The North Atlantic Craton (NAC) (ca. 3.9 Ga) preserves a record of Neoarchean crust generation processes at a time when modern plate tectonic processes were becoming fully developed. The northern part of the Archean North Atlantic Craton (NAC) in the Akia terrane (Fig. 3.1 in Chapter 3) consists of well-exposed Eo-to-Neoarchean TTG (Tonalite–trondhjemite–granodiorite) orthogneiss intercalated with subordinate supracrustal associations of meta-sedimentary, meta-basaltic, ultramafic, and anorthositic plutonic rocks, all of which have been variously metamorphosed at amphibolite- to granulite facies (Friend and Nutman, 2005; Garde, 1990, 2007; Windley and Garde, 2009). The Akia terrane was first identified by Friend et al. (1988) as a separately evolved tectonic unit distinct from the previously mapped Amîtsoq gneisses (currently termed as a component of the Itsaq gneiss complex). Garde et al. (2000) modelled Akai terrane developed by inception of a ca. 3.1 Ga

magmatic arc over an older Mesoarchean crustal nucleus. The arc is exposed in Nuuk Fjord-the Qussuk peninsula and is inferred to have generated intermediate and subordinate felsic volcanic rocks (Garde, 2007; Garde et al., 2012a, Szilas et al., 2017). The juxtaposition of Akia terrane with an assemblage of Eo- to Mesoarchean terranes is hypothesized to have occurred along its southern boundary in a modern style horizontal tectonic setting during early Neoarchean (Friend et al., 1988, 1996). This hypothesis was later supported by Garde (1997), Nutman and Friend (2007), Kolb et al. (2012), Dziggel et al. (2014, 2017). Garde et al. (2000) suggested a diorite gneiss core in Nuuk region, around which arcs accreted, resulting in voluminous emplacement of diorite and tonalite sheets. However, Gardiner et al. (2019) defies earlier proposed singular terrane accretion and arc related magmatic processes and interpreted that the continental crust in the Akia terrane has derived from partial melting of a mafic precursor of Eoarchean age through deep infracrustal melting in a vertical tectonic setting (Johnson et al., 2017). Yakymchuk et al. (2020) suggested a stagnant lid tectonic regime in an oceanic plateau environment without subduction. An impact model, in which a giant bolide impact at >3Ga was responsible for the Mesoarchean thermal event in the Akia terrane, is also proposed by Garde et al. (2012, 2014) and Keulen et al. (2015). However, subsequent research has called the impact hypothesis into question (Kirkland et al., 2018a; Steenfelt, 2021).

All of these studies, however, show that the Akia terrane has a dioritic-amphibolitic core/root (age: 3.2-3.0 Ga) and an overlying Mesoarchean crust (Garde, 2007; Garde et al., 2012b; Nilsson et al., 2013). TTG gneisses intruded the core complex in 3.05-3.02 Ga (Garde, 1990, 1997; Garde et al., 2000), which was followed by low-P, high-T granulite facies metamorphism in 2.99-2.97 Ga (Friend and Nutman, 1994; Garde, 2007; Garde et al., 2000, 2012b). The supracrustals were partially molten and metamorphosed in high-P high-T granulite facies metamorphism at 820-850 °C and 0.8-1 GPa while D3 deformation occurred (age: 2.86-2.70 Ga; Kirkland et al., 2018a). Yakymchuk et al. (2020) reported orthopyroxene bearing metamorphic assemblages consistent with suprasolidus conditions at pressure of < 0.8 GPa and temperature > 750 °C. Gardiner et al. (2019) interpreted Finnefjeld and its surrounding pluton to represent melting at various depths, whereas Garde et al. (2012, 2014) interpreted a variety of melting and cataclastic structures in the Finnefjeld region because of the bolide impact. Alanngua complex had been (re)identified very recently. it is thought to have formed the basement of Akia-aged rocks that is tectonically intercalated with metasedimentary rocks (Steenfelt et al., 2021). Based on the compiled and new zircon

U-Pb dates, the authors describe that the history of the rocks within Alanngua complex spans over several hundred million years. The complex is interpreted as a Neoarchaean tectonic melange created by reworking during high-grade metamorphism, and it had taken part in the tectonic rearrangements identified in the Akia terrane during Neoarchean. Hence, even though there are contrasting models of crustal generation in this region, the chosen field area preserves a section of the lower crust and overlying supracrustal unit that were subjected to extensive melt-generation and melt-fluxing for an extended period. The two high-temperature granulite facies metamorphic events that occurred close to or at the solidus in large portions of the crust make it suitable for potential studies of physicochemical signature of melt flow.

1.3 Thesis aims

Based on the background provided above, it can be summarized that the melt pathways are crucial avenues within the crust through which melt moves from its source region to the sink. But the microstructural and geochemical signatures of melt flow are yet to be fully understood and recognized (Stuart et al. 2016; Meek et al., 2019). Additionally, even though *'Diffuse porous flow*' is an important melt-transport mechanism in the mantle (Scott and Stevenson, 1986; Turcotte and Ahern, 1978; Stuart et al. 2016) it has largely been unexplored in the crust (Brown, 2010; Sawyer, 1999; Weinberg, 1999)

The main aim of this Ph.D. is to *delineate and characterize melt pathways* in the crust by studying the general aspects of melt-bearing systems including signatures of melt-rock interaction, rheology of melt bearing rocks, internal microstructures of minerals crystallized from the melt.

An emphasis will be given to study: a) how important and effective is *diffuse porous melt flow* as a melt transporting mechanism in the crust? and b) how does it initiate, organize, and grade to other modes of melt transport? and lastly, c) how the cryptic signatures of diffuse porous flow can be recognized and utilized to understand its effect in the deforming mid-lower crust?

Aim 1: to identify heterogeneous domains and disequilibrium textures formed because of melt-rock interaction and develop an alternative method for using these

heterogeneous rocks to comprehend the pressure-temperature condition during melt fluxing/partial melting.

Aim 2: to identify existence of diffuse porous flow in mid- and lower-crustal rocks, and since it is largely controlled by deformation the feedback mechanism between melt-migration and deformation will be identified and discussed.

Aim 3: to characterize grain and sub-grain scale microstructures (apart from the conventional optical scale microstructures) of melt crystallized grains under different geo-tectonic settings having different melt amount.

Aim 4: to determine difference in deformation mechanisms of amphibole-rich lithologies during melt-present and melt-absent deformation.

1.4 Thesis set up

This thesis comprises eight chapters: this introductory chapter (Chapter 1), five related studies, a synthesis (Chapter 7), and conclusion section (Chapter 8), and an Appendix section. Chapter 1, Chapter 6, Chapter 7, and Chapter 8 are solely conducted by the PhD candidate while Chapter 2-5 are collaborative works. For the latter, each chapter begins with a preface outlining contribution of each author. Aside from the works presented in the thesis, the candidate was involved in two additional pieces of work (Bhattacharya et al., 2021; Ramirez-Salazar et al., 2022 [in preparation]), as well as two ongoing projects utilizing EBSD: (1) on crystal preferred orientations of mantle xenoliths with Prof. Balz Kamber, Queensland University of Technology, Australia, (data acquisition) and melt-present amphibolite from the Eastern Ghats with Prof. Prabhakar Naraga, IIT Bombay, India (project planning, data acquisition, and .processing)

In the following, the objectives of each chapter are provided along with links to the thesis Aims, connections between chapters and any other noteworthy aspects.

Chapter 1 is the introduction and provides a general overview of melting and migmatite formation, melt-rock interaction, different melt transport mechanisms, microstructures of former melt presence, role of deformation in melt migration, and deformation mechanism in the presence and absence of melt.

Chapters 2 and 3 (Aim 1) – Both chapters are dedicated to the study of macroscale and microscale heterogeneity in rock samples formed during melt-rock interaction. A collection of homogeneous and heterogeneous amphibolite samples from Akia terrane are utilized (Chapter 2). The melt-present samples are then used to calculate possible peak pressure-temperature conditions (Chapter 3), comparable to conventional studies with homogeneous rocks. Chapter 2 describes an alternative method for obtaining robust and representative local bulk rock compositions from locally equilibrated domains using micro XRF, spot EPMA chemical analysis, and the software package XMapTools (Lanari et al., 2014). This similar set of samples (along with one additional amphibolite) is used in Chapter 3 for phase equilibria modelling using locally derived bulk rock compositions from regions of interest. The larger implication of this study is understanding the P-T evolution of the Akia terrane and Alanngua complex. The P-T estimates for the granulitic facies metamorphism in the Akia terrane highlight the importance of studying melt-present rocks to delineate partial melting conditions. Both chapters are expected to be submitted in peer-reviewed journals shortly after the thesis submission.

Chapter 4 (Aim 2) – Based on a case study from lower crustal diorite gneiss in the Akia terrane, this chapter investigates the differences in microstructure, and geochemistry between melt-present low-strain and high-strain samples. Information retrieved from macroscopic, microscopic, and geochemical studies help in characterizing and discerning mechanism related to diffuse porous flow. Furthermore, the chapter conceptualizes the interplay between melt migration and deformation that assists the porous melt migration and proposes a mechanism for the formation of low and high-strain shear zones. The manuscript will be submitted to the journal 'Lithos' soon.

Chapter 5 (Aim 3) – This chapter documents and contrasts the microstructural features within grains of quartz crystallized from a silicate melt in different geotectonic scenarios. Representative rock samples from lower crustal sections of Pembroke granulite in New Zealand, Anmatjira-Reynolds Range in the Arunta Block of Central Australia, and Wongwibinda Metamorphic Complex in Australia are used to determine the microscopic grain scale structures of melt crystalized grains and their relationships with deformation utilizing in-depth electron backscattered diffraction (EBSD) orientation analyses. This will aid in identifying and contrasting microstructures in melt-present versus melt-absent shear zones. The manuscript will be submitted to the ‘Journal of Structural Geology’ in the very near future.

This is to mention that an initial work investigating characters of crystallized quartz grains was done during my Master of Research at the Macquarie University, Australia in 2018. A set of already known samples with grains crystallizing from melt and aqueous fluid was studied using HKL Channel 5 EBSD processing software and weighted burgers vector analysis – WBVs (details can be found in MQ online library: Dey et al., 2018). However, no quantitative CPO analyses, quantification of lattice distortion, dislocation orientation and density maps were investigated. During the PhD, in addition to quantifying CPO, several grain orientation deviation analyses, brand new dislocation density and slip system activation analyses are performed using the advanced AZTEC Crystal software. Reason for lattice distortion is also probed using COMSOL Multiphysics software.

Chapter 6 (Aim 4) – explains microstructural and geochemical differences between melt-present and melt-absent amphibolite samples. Representative samples are studied with foliation and lineation formed by amphibole-rich lithologies. The grain scale microstructures of the host minerals (amphibole-plagioclase) are investigated to document and compare deformation mechanisms during melt-present vs. melt-absent deformation. This has far-reaching ramifications for the rheology of the lower crust. The manuscript will be submitted to the 'Journal of Structural Geology' the near future.

Chapter 7 - focuses on overall discussion of the main findings presented in the thesis and their implications for studying various aspects of melt-bearing systems in the mid- to lower-crustal conditions.

Chapter 8 – the main conclusions of the studies, open questions and future research directions are presented.

Chapter 2

Testing the robustness of MapComp: A tool to derive local chemistry for heterogeneous rock samples using a combination of µXRF, EPMA and XMapTools

This chapter represents a manuscript draft that focuses on defining an alternative method for determining local bulk chemistry for heterogeneous rocks. This study uses 'melt-present' heterogeneous rocks formed due to melt-rock interactions and identify bulk composition from different domains. This chapter will be submitted to the journal Computers and Geoscience. I will be the first author of this contribution with Dominik Sorger, Anthony Ramirez Salazar, Thomas Müller, and Sandra Piazolo as co-authors. I am responsible for writing the original manuscript draft, conceptualization, most of the data collection (apart from where it is indicated below), data processing, figures, and data analyses. Dominik Sorger obtained a high-resolution EPMA map of one of the studied samples and helped in conceptualization. Anthony Ramirez Salazar assisted me in the whole rock XRF analyses and during post-processing of the data. Sandra Piazolo and Thomas Müller oversaw the conceptualization and reviewed the draft manuscript.

Abstract

Thermodynamically consistent isochemical phase diagrams are widely used by the geological community to characterize absolute or relative changes in P-T-X conditions during orogenesis. For this purpose, in recent years, isochemical phase diagrams have been

explored extensively. The latter assumes a specific fixed bulk rock chemistry in which the phases are in chemical equilibrium. Hence, defining the equilibrated volume and measuring its chemical composition becomes imperative for quantitative petrographic investigations. However, if a rock is heterogeneous at the hand specimen scale, e.g., layering or banding, then the local chemistry cannot be easily obtained by classic XRF analysis from crushed and powdered hand specimen samples. An alternative approach is using quantitative element maps on regions of interest derived at the thin section scale. Such quantitative composition maps can be acquired directly using EPMA, or semi-qualitative maps (EDS or µXRF Xray maps) in combination with EPMA spot analyses. While EPMA analysis directly produces a large volume of quatitative mineral data, the method is costly, time-intensive, and often limited by instrument availability. Micro-XRF instruments provide a time-efficient alternative to acquiring large-scale element maps limiting the required EPMA time to a series of point analyses on each phase required to quantify and calibrate the pixel intensities. Here, a systematic study is presented to test the feasibility of using a combination of X-ray intensities maps from micro XRF, spot EPMA chemical analysis, and the software package XMapTools (Lanari et al., 2014) to obtain robust and representative local bulk rock compositions from locally equilibrated domains.

We systematically investigate samples with different scales of heterogeneity to test the reliability of this technique relative to classic whole-hand specimen sample whole-rock XRF analyses. Results show that the presented method is a viable alternative, allowing sufficiently precise local bulk chemistry determination. However, the presented method is limited by the spatial resolution (spot size of 15 µm) and element detection limit (10 ppm) of micro XRF data. Our tests suggest that analysis of grain sizes and element compositions that are about one order of magnitude larger than the equipment limits produce reasonable results.

2.1 Introduction

Thermodynamic phase equilibrium models are widely used by the geological community to characterize absolute or relative changes in P-T-X conditions during tectono-metamorphic events (Vance and Mahar, 1998). Standard phase diagrams are graphical representation of equilibrium phase assemblage as a function of intensive and extensive variables (Powell et al., 2005). Constructing phase diagrams require knowledge of the phase rule and of equilibrium thermodynamics (Powell, 1978; Spear et al., 1995). Phase diagrams

for a chemical system are termed as ‘petrogenetic grids’ where mineral or mineral-assemblage stability ranges are plotted as reaction boundaries in a pressure-temperature space (Bowen, 1940; Albee, 1965). The topology of these univariant reactions can be constrained by Schreinemaker’s rule (Zen, 1966). Over the years a wide variety of these diagrams have been investigated for low- to high-grade rocks (e.g., Kelsey and Hand, 2015) and for a range of chemical systems (e.g., White et al., 2008). However, petrogenetic grids pose two important limitations as a specific rock will only experience a subset of the total number of reactions, and secondly metamorphic reactions are multivariant but are not displayed on petrogenetic grids. Isochemical phase diagrams are equilibrium phase diagrams in which fields of equilibrium phase assemblage are calculated as a function of bulk rock composition (X) for the assumed equilibration volume and the pressure-temperature (P-T) condition at the time of phase crystallization (Powell et al., 1998, Palin et al., 2012, 2013a). Isochemical phase diagrams are powerful than petrogenetic grids as they can be used for a particular rock and can be contoured for phase proportions and compositions. Isochemical phase diagrams utilize internally consistent thermodynamic datasets (e.g., Powell et al., 1998) and activity-composition (e.g., Evans et al., 2010; White et al., 2014a) models that relate end member proportions to end member activities. As relationships between phases/minerals heavily rely on the bulk composition, it is pivotal for any isochemical phase diagrams (also called ‘pseudosections’ in metamorphic literature) to identify and determine the petrologically appropriate local bulk composition (Bowen, 1913).

The community uses freely available computer software like Thermocalc (Powell et al., 1998), Theriak-Domino (De Capitani and Petrakakis, 2010), and Perple_X (Connolly, 1990) for obtaining isochemical phase diagrams. It is known that there are several systematic and random errors associated with phase equilibria modeling. Systematic errors stem from the uncertainties on the physical properties of the end members and are associated with the a-x relations of solid solution mixing (Evans and Bickle, 2005) whereas random errors include those associated with compositional analyses based on analytical or machine error and geological errors involved in petrological investigations (e.g., bias in sampling techniques, petrographic descriptions, etc.) (Palin et al., 2016). If different portions of a single hand specimen are chemically distinct, i.e., heterogeneous, rock-wide chemical equilibrium may not be achieved. In such situations, local domains of equilibration need to be defined for petrological investigations as the mineralogical information of calculated phase diagrams is related to the local chemistry used (Palin et al. 2016). Chemical heterogeneity at the cm, i.e.,

thin section scale is very common in metamorphic rocks as spatial heterogeneity is caused by the physical segregation of material, for example, by mass transfer during interaction with a reactive fluid, by metamorphic differentiation, solid-state transformations, deformation, or by partial melting (Milord et al., 2001; Mahan et al., 2006; Brouwer and Engi, 2005; Lanari et al., 2013). Consequently, the traditional way of deriving bulk rock composition by crushing a hand specimen and performing a chemical analysis of its fused, homogenized powder may not always be appropriate. Determining local bulk rock composition is not only crucial for metamorphic studies focused on major phases but also for analyzing accessory mineral stability and melt production (Stevens et al. 1997; Pickering-Witter and Johnston 2000; Tinkham et al. 2001; Evans and Bickle 2005).

The importance of obtaining a thermodynamically appropriate bulk composition has been recognized within the community and several methods are currently in use. Three main methods of bulk composition determination (Yakymchuk, 2017) utilize either i) XRF-derived whole-rock analyses of crushed and milled rock samples, ii) major element compositional maps of thin sections using EPMA or scanning electron microscope (e.g., Indares et al., 2008), and iii) a combination of point-counting or automated mineral mode analysis (QEMSCAN and MIL) with quantitative mineral compositions obtained using electron microprobe. XRF provides proportions of oxide components for major, minor, and trace elements. For the second method, quantitative compositional maps are generated using an electron microprobe with the diffracting crystal in each wavelength-dispersive spectrometer (WDS) set to one wavelength to record X-ray intensity as the beam scans through a chosen area. Hence, bulk rock compositions can be extracted for specifically defined areas in texturally complex domains, which would be otherwise impossible to obtain (Clarke et al., 2001). Previous studies have also proposed other means to construct quantitative X-ray maps within a reasonable time frame (Tinkham and Ghent, 2005; Lanari et al., 2014a, 2019). Unfortunately, this technique is still expensive in terms of analysis time and costs. The third method employs a weighted calculation involving minerals present in the thin section and their representative compositions. The other common method to determine bulk chemistry of chemically distinct domains at thin section scale utilizes qualitative image analysis in combination with quantitative chemical spot analysis (Carson et al., 1999, Indares et al., 2008). For example, Brouwer and Engi (2005) determined the chemistry of distinct domains within a thin section by combining backscatter electron images with electron microprobe spot analyses. Here the geologists are free to decide which

minerals to include based on their petrographic observations and the total bulk composition can be reduced to a 'model-ready' bulk composition (Palin et al., 2016). This method is helpful for rocks exhibiting mosaic equilibrium (Powell, 1978) or having textural evidence of polymetamorphism (Argles et al., 1999). Tinkham and Ghent (2005) used 'analytical standardization' (using Bence-Albee algorithm to convert raw X-ray counts at each map pixel to wt% oxide) in the program XRMapAnal. Recently, an advanced numerical tool, XMapTools has been introduced for data processing, calibration, and visualization via single or multi-channel maps. XMapTools incorporates internal analytical standardization with raw X-ray data (in photons count per pixel) for extracting high accuracy quantitative petrological information (Lanari et al., 2014c). Here, the local "bulk" composition for the desired area is first mapped spatially integrated (using the oxide wt%), and a density correction is applied for each mineral phase. This allows extracting composition of any domain from the compositional maps. In the following, this method is termed MapComp.

To date there has been no systematic evaluation of the validity and robustness of semi-quantitative microXRF elemental maps in determining local bulk rock chemical data from various domains within a thin section, even though the techniques described above have been used extensively. In the past, high-resolution electron probe microanalysis (EPMA) with wavelength dispersive spectrometers (WDS) elemental maps have been used for this purpose. Indares et al. (2008) used maps acquired by energy dispersive X-ray (EDX) analytical system, but preferred bulk compositions measured with EPMA for isochemical phase diagram. In this study systematic investigations are made on how reliable microXRF elemental maps are for robust bulk composition determination, despite their low count rates and limited spatial resolution. For this purpose, samples with variable heterogeneity at the thin section scale are systematically investigated. The results of micro XRF X-ray compositional maps are derived from a chemically distinct region in the thin section, and how they differ from conventional whole rock XRF results are assesed. Additionally, a similar comparison is made between bulk compositions obtained using X-ray maps from electron probe microanalysis (EPMA) vs. low intensity microXRF compositional map for the same region. It is observed that microXRF maps with lower count rates of 10ppm and a spatial resolution of 15µm represent a reliable input for determining local bulk rock chemistry.

2.2 Methodology

2.2.1 General methodology and samples selection

Four metamorphic samples were selected exhibiting a different range of heterogeneity at the hand specimen and thin section scale. The samples were collected from the Paleo to Mesoarchean Akia terrane with TTG orthogneiss, amphibolite, metasedimentary and ultramafic rocks metamorphosed at amphibolite to granulite facies conditions (Kirkland et al., 2018a). For each sample, specific domains with chemical heterogeneity are determined at the hand specimen and subsequently at the thin section scale. Samples were cut and powdered to allow conventional XRF bulk composition analyses, while MapComp is applied on microXRF X-ray maps of the representative thin section areas. First, a homogeneous mafic gneiss (SPI1399A) and a compositionally layered gneiss (SPI1382) are used to establish the reliability of MapComp technique. XRF bulk rock chemistry from the whole/mechanically separated thin section blocks is determined and compared with MapComp results for this purpose. Next, bulk chemistry is measured from different domains in compositionally heterogeneous Amphibolite (SPI1338) and Diorite gneiss (SPI1321) using the proposed technique. The term “Domain” is used for denoting a specific portion of a rock that is distinct in modal% of phases and grain size of constituent minerals from other portions within the same sample. These can be identified at hand specimen, thin section block, and thin section scale. An “Area” is defined as a particular 2D area within a thin section. Whole rock data using XRF is obtained from the whole sample block when individual domains cannot be mechanically separated with confidence or from a particular ‘Domain’, where it can be deciphered and mechanically separated for the XRF analyses. ‘Areas’ are used for MapComp calculations and assumed to represent a particular ‘Domain’. The robustness of this technique is also tested by selecting ‘Areas’ of specific sizes within a single ‘Domain’ and comparing the coherency of local bulk rock composition within these areas. One area is also chosen for bulk chemistry determination using elemental map obtained by electron probe microanalyzer (EPMA).

2.2.2 XRF Whole rock chemistry

Powders for bulk rock chemistry were obtained from twin chips of the studied thin sections. Care was taken that the minimum amount of powder was 8 gram representing approximately a volume of 2.8 cm^3 of the whole thin section area. Samples were first crushed into a fine powder (particle size < 70 µm) with a jaw crusher and milled in a tungsten-carbide Zibb mill prior to preparation of fused discs for major element analyses. The jaw crusher and mill were cleaned between two samples to avoid cross-contamination. The weight difference of powders before and after overnight heating at 1025 °C was obtained to determine the loss of ignition (LOI). Fused glass beads for X-ray fluorescence (XRF) analyses were prepared with a mix of 0.4 g dried sample, 4.0 g of 66% Li tetraborate: 34% metaborate flux, and 1-2 drops of lithium Iodide solution in a $Pt_{95}Au_5$ crucible. Mixtures were fused in the furnace at 1150 °C for a total of 40 minutes, gently swirling the samples at 20-, 30-, and 35-min intervals to intervals to ensure proper mixing before cooling. Major elements bulk rock chemistry was acquired from the fused beads by XRF spectrometry using a Rigaku ZSX Primus II spectrometer at the University of Leeds. Accuracy in major elements for the certify standard STSD4 was ±≤1 % relative for SiO_2, ≤ 2.5 % relative for Al_2O_3, ≈3.5% relative for FeO_{tot}, 1 to 5% relative for MgO, 4 to 6 % relative for MnO, ≈6% relative for TiO_2 and 2 to 12% relative for P_2O_5 and Na_2O.

2.2.3 Major element spot analyses and elemental mapping by electron microprobe microanalyzer (EPMA)

Point analysis of major mineral phases and X-ray compositional maps are performed using a JEOL JXA-8900RL electron probe microanalyzer (EPMA) at the Göttingen Laboratory for correlative light and electron microscopy (GoeLEM) at the Geoscience Centre, University of Göttingen equipped with an energy-dispersive (ED) and five wavelength-dispersive (WD) spectrometers. Measurement conditions for point analysis were 15 kV acceleration voltage, 20 nA beam current and a beam diameter of 5 µm. A total of 12 elements (Si, Al, Fe, Mg, Ca, Mn, K, Na, Ti, Cr, Ba, and Cl) were measured in three serial WDS cycles. To obtain representative compositions, a total of 10 individual measurements are made for each major mineral phase (5 from the core and 5 from the rim area). The analyzed points are carefully marked on the thin section overlays and/or zoomed

in BSE images for later correlation. Fe-oxide and ilmenite are only found to be a major phase in one of the studied samples, hence EPMA analyses for those grains are not performed. Additionally, qualitative X-ray intensity map (Mg, Na, K, Ti, Mn: measured with WDS, and Al, Si, Fe, Ca, P: measured with EDS) is obtained using EPMA for one sample (*Heterogeneous rock III: Diorite Gneiss* SPI1321 - 'Area I_2') at 20 kV acceleration voltage and 80 nA beam current, with a step-size of 6 µm and a dwell-time of 50 ms per pixel. Both X-ray maps in µXRF and EPMA rely on the detection and investigation of the characteristic X-rays produced by the primary electrons, but they differ on how the X-ray is detected. WDS provides much better spectral resolution (~5 eV) than that of microXRF (~ 100eV). Another advantage of using EPMA X-ray maps over EDS images are its capability of detecting lighter elements measured with WDS. Count rates for Na, and K are 300 and 800 counts per pixel, respectively.

2.2.4 Micro X-ray fluorescence (µ-XRF) compositional mapping

Whole thin section X-ray composition maps for all the studied samples were obtained using a Bruker M4 Tornado micro-XRF at the Geoscience Centre, University of Göttingen, Germany. Element mapping is done using small spot micro-X-ray fluorescence employing Bruker XFlash® silicon drift detectors (SSD) which offers the highest resolution of <15µm with a detection limit of 10 ppm. A step size of 20 µm is used with a speed of 8 mm/sec. Maximum X-ray signals are found for Al, Fe, Mn, Si, Ti, and Ca (e.g., in the weakly heterogeneous sample-1382 micro-XRF map) with 40, 1500, 62, 150, 65 and 400 counts per pixel, respectively. However, count rates for lighter elements like K, Mg, and Na are substantially lower around 15, 8 and 8 counts per pixel, respectively. However, µXRF can gather spectrum of all elements in the sample simultaneously. In comparison, the data collection is usually much slower in EPMA.

2.2.5 XMapTools

XMapTools (Lanari et al., 2014) is a MATLAB© based GUI software for processing compositional maps (e.g., X-ray intensity maps from EPMA or element concentration maps from LA-ICP-MS analyses). The intensity maps are used to: classify minerals and convert X-ray intensities into calibrated weight percentages. Detailed procedures of map calibration

and internal standardization for determining accurate compositional maps using XMapTools is outlined in Lanari et al. (2014).

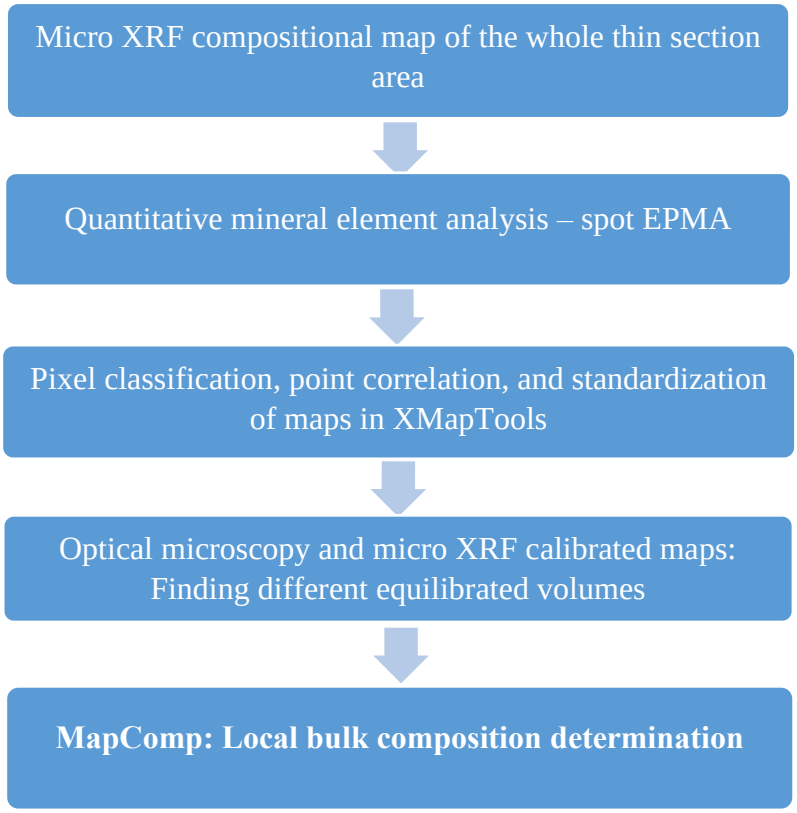

Figure 2.1 – A workflow model for calculating of local bulk chemistry for heterogeneous rock specimens using MapComp method which combines micro XRF compositional maps and quantitative EPMA spot analyses.

2.2.6 MapComp: combining micro XRF composition maps-EPMA spot analyses and XMapTools

We define 'MapComp' as a method that can be used to derive bulk rock geochemical data from the thin sections. MapComp combines 'semi quantitative' X-ray composition maps with high precision EPMA spot analyses integrated in the software package of XMapTools (Fig. 2.1). For the purpose of this study, micro XRF compositional maps are obtained as first step. Acquired composition maps are exported in ASCII format text files (*.txt files) where photon counts per pixel are represented as matrices with the number of collected photons per analyzed element per pixel. In Step 2, EPMA point analyses are

obtained for subsequent quantification of the element maps. The points are selected from both the rim and core of each mineral phase (at least 10 points per each mineral phase). In Step 3, The X-ray maps are loaded into the XMapTools. Based on statistical analyses of their compositions, pixels are grouped as mineral phases, fractures, or voids and corresponding masks are created. EPMA data are used for quantificationby assigning oxide weight percentage to each pixel. Thereafter, local bulk compositions are determined from different equilibrated domains. For a domain, the local bulk composition equates to the summation of composition of mineral phases multiplied by its mass fraction if the surface covered by a particular phase can be extrapolated to a volume fraction (Lanari and Engi, 2017). This assumption is valid as long as: (i) the sample is cut perpendicular to the foliation, (ii) the compositional map is acquired on an unaltered surface, (iii) the size of the map is sufficient for a good sampling, and (iv) the area covered is large enough to ensure 20-30 grains per phase (Lanari and Engi, 2017). A build-in density correction was applied, and local bulk composition values were extracted directly from compositional maps by user defined polygon boundaries. Suggestion from Lanari and Engi (2017) are followed, and domains are defined by polygons with sides at least 10-30x of the average grain size.

2.3 Results

2.3.1 Petrography and micro XRF phase maps

Homogeneous rock: hornblende-orthopyroxene-clinopyroxene bearing mafic gneiss (SPI1399A)

This sample is compositionally homogeneous in hand specimen and at thin section scale (Fig. 2.2a, b). It is a medium grained rock with a weakly developed foliation defined by the alignment of amphibole and biotite grains (Fig. 2.2b). It comprises 64% amphibole, 0.5% plagioclase, 8.5% biotite, 3% clinopyroxene and 24% orthopyroxene (Fig. 2.2b). Average grain size of amphibole, biotite, plagioclase, clinopyroxene and orthopyroxene grains are 0.5-0.9 mm, 0.15-0.3 mm, 0.05-0.4 mm, 0.4-0.8 mm, and 0.5-1 mm, respectively. The largest grain size observed for amphibole and biotite grains is 0.9 mm and 0.7 mm, respectively. Amphibole grains are subhedral and elongated with their long axis parallel to the foliation. Orthopyroxene and clinopyroxene grains are subhedral to anhedral (Fig. 2.2c),

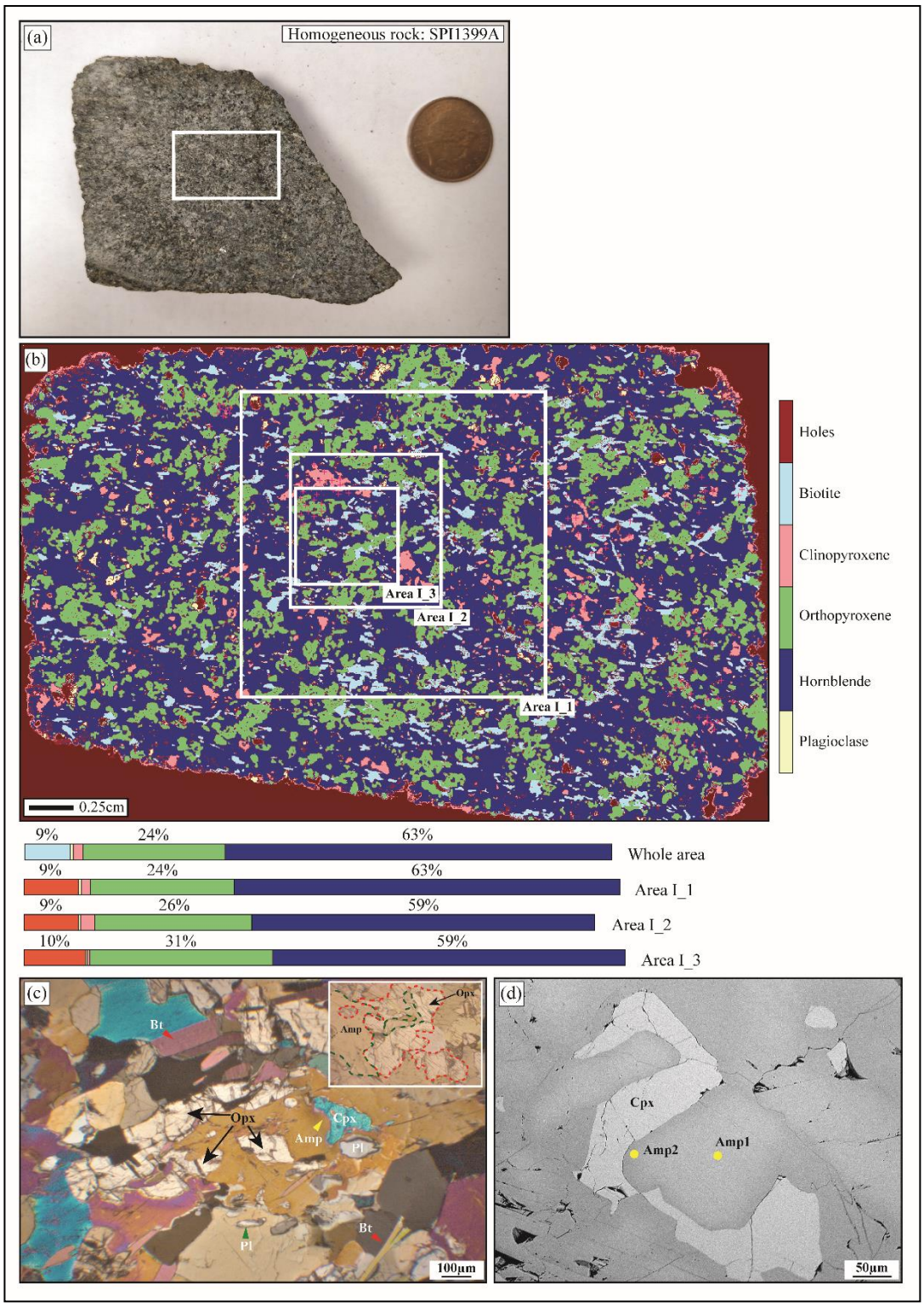

Figure 2.2 – A homogeneous mafic gneiss (SPI1399A) with sample-scale and thin section homogeneity. (a) The rock specimen lacks any visible compositional domain in centimeter-scale. The white rectangle area represents studied thin section block. The same block is used for whole rock XRF analyses. (b) Micro XRF phase map with different areas marked for MapComp analyses. Locations of EPMA spot analyses are shown with '+'. (c) Photomicrograph displaying elongated orthopyroxene-clinopyroxene grains engulfing the large amphibole grain along its boundary (also see inset). (d) Clinopyroxene grains occur at the amphibole grain boundary. Zonation is denoted by change in the greyscale colour. Both 'Amp1' and 'Amp2' are chosen for EPMA spot analyses (Tab. 2.3).

ranging from irregular, elongated laths to equiaxed grain shapes. Orthopyroxene and clinopyroxene grains are seen to be occurring along the amphibole grain boundaries (see inset of Fig. 2.2c). Zonation in the amphibole grains adjacent to these grains is also observed (Fig. 2.2d). These textures are homogeneously distributed throughout the thin section. Plagioclase grains are subhedral to anhedral. 'Area I_1' (Fig. 2.2c), with sides ~30x maximum gran size, is chosen for acquiring major oxide weight percentage using MapComp. 'Area I_2', and 'Area I_3' (within 'Area I_1'), with sides ~15x and ~10x maximum grain size, respectively, are also selected for observing the robustness of this approach.

Compositionally layered rock I: Amphibolite with a foliation parallel, thick 3mm domain (SPI1382)

The sample is compositionally heterogeneous in hand specimen and thin section scale (Fig. 2.3a, and its twin block in Fig. 2.3b). Overall, it is a medium grained rock with 28% amphibole, 45% plagioclase, 17% clinopyroxene, 8% orthopyroxene, 1.5% Fe-Oxide, and 0.5% Ilmenite (Fig. 2.3c). The average grain size of amphibole, clinopyroxene, plagioclase, and orthopyroxene grains are 0.15-0.5 mm, 0.15-0.4 mm, 0.3-0.7 mm, and 0.1-0.5 mm, respectively (Fig. 2.3c). Amphibole grains are equigranular, subhedral with elongated to platy grain shapes (Fig. 2.3d). Amphiboles form a strong alignment with their long axes parallel to the foliation. Orthopyroxene and clinopyroxene grains occur as fingers and engulf amphibole grains along their boundaries (Fig. 2.3d). The plagioclase grains are clean with characteristic polysynthetic twinning (yellow arrow in Fig. 2.3d).

On the thin section scale, a notable increase in grain size and a difference in mineral modal percentage demarcate a compositionally different layer ('Domain II' in Fig. 2.3b, c). Here 7.5% amphibole, 52% plagioclase, 20% clinopyroxene, 17.5% orthopyroxene, 2% Fe-oxide and 1% Fe-oxide are observed (Fig. 2.3c). The average grain sizes of amphibole, clinopyroxene, plagioclase, and orthopyroxene grains vary between 0.15-0.5 mm, 0.5-0.7 mm, 0.4-0.9 mm, and 0.3-0.7 mm, respectively. However, the maximum grain size in this domain (i.e., 'Domain II') for plagioclase, orthopyroxene and clinopyroxene reaches up to 0.9-1 mm (Fig. 2.3e). The overall mineral texture in this layer is very similar to that of the

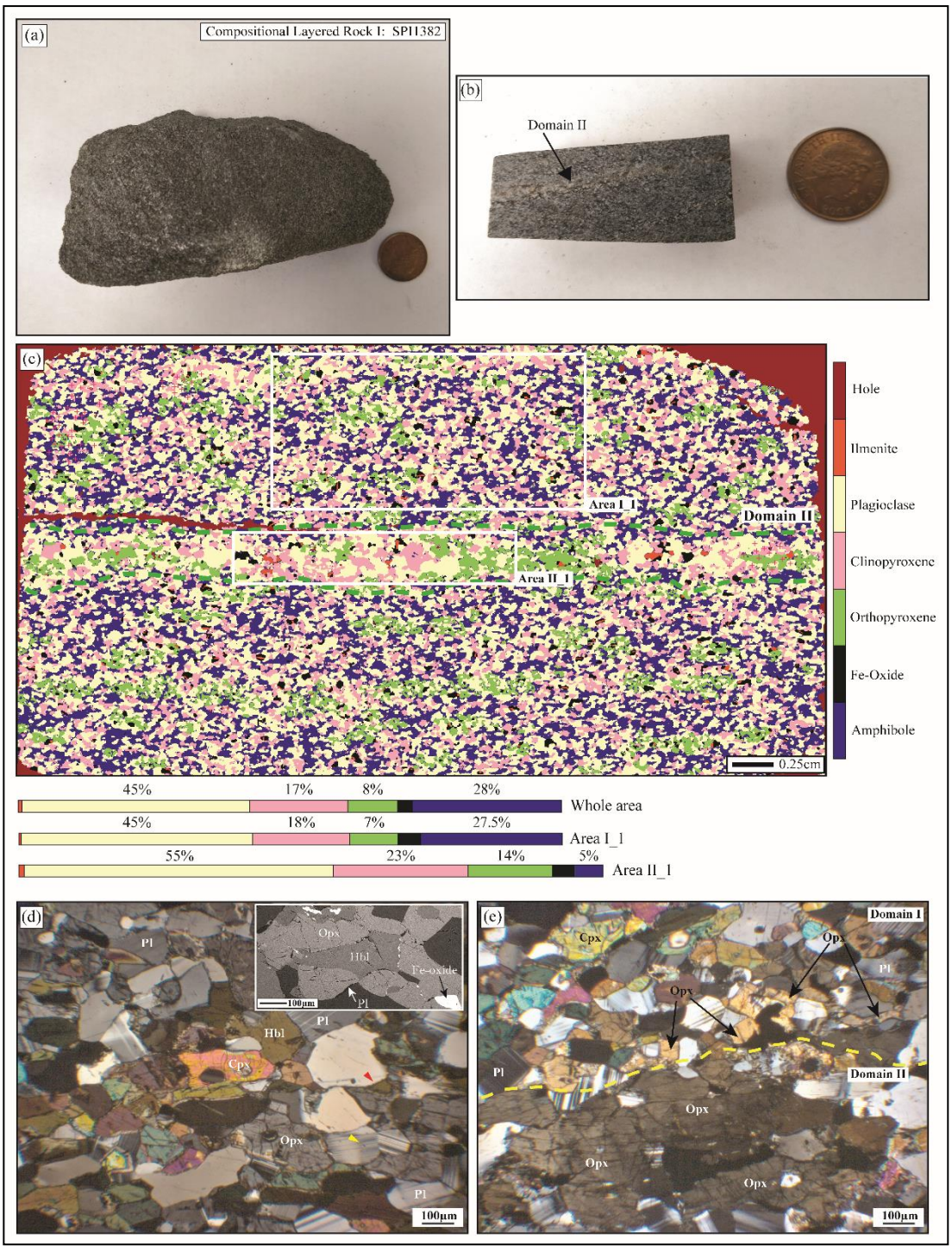

Figure 2.3 – Compositionally layered rock I: amphibolite (SPI1382) represents sample-scale and thin section heterogeneity. (a-b) Field specimen lacks any visible composition domain. Representative thin section block exhibits a felsic, elongated, and coarse-grained domain (i.e., 'Domain II'). Surrounding homogeneous area is termed 'Domain I'. The entire block is used for the whole rock XRF analyses. (c) Large orthopyroxene-clinopyroxene-plagioclase with a relative scarcity of amphibole grains differentiate 'Domain II' from 'Domain I'. Representative areas ('Area I_1' within 'Domain I' and 'Area II_1' within 'Domain II', marked with white boxes) are chosen for major oxide MapComp analysis. Different areas have varying mineral modal abundance. Locations of EPMA spot analyses are marked with '+'. (d) Orthopyroxene-clinopyroxene grains replace amphiboles along grain boundaries (red arrows; also see inset). Plagioclase grains show polysynthetic twins (yellow arrow). Minerals in 'Domain I' are equigranular with a polygonal mosaic texture. (e) Photomicrograph reveals a difference in microstructures between the two domains. Note the difference in orthopyroxene grain size in the two domains.

surrounding ‘Domain I’. ‘Area I_1’ (Fig. 2.3c), with width ~30x and height ~10x the maximum grain size, is chosen to determine major oxides concentration of ‘Domain I’ using MapComp.

Compositionally heterogeneous rock II: Amphibolite with crosscutting, 6mm garnet bearing domain (SPI1338)

The sample is compositionally inhomogeneous in hand specimen and at thin section scale (Fig. 2.4a, and its twin block in Fig. 2.4b). Parallel mafic and felsic layers denote the heterogeneous nature (Fig. 2.4a). Overall, it is a medium-grained rock with 47% amphibole, 24% plagioclase, 25% quartz, 2% garnet, 1% biotite, and 0.5% clinopyroxene (Fig. 2.4c). Fe-oxide and ilmenite grains comprise 0.5 modal% and are avoided for this study. The average grain sizes of amphibole, plagioclase, quartz, biotite, clinopyroxene and garnet grains are 0.2-0.8 mm, 0.5-0.7 mm, 0.25-0.4 mm, 0.05-0.1 mm, 0.2-0.5 mm, and 0.3-0.5 mm, respectively. Amphibole grains are not equigranular, subhedral to anhedral, elongated forming the foliation. The grain boundaries are highly irregular and often contain embayment (Fig. 2.4d). Individual biotite grains are elongated parallel to the host foliation. Plagioclase grains are fresh with characteristic polysynthetic twins. The clinopyroxene grains are intensely replaced by the amphibole grains. The abundance of clinopyroxene is very localized (i.e., only five to six grains in the bottom of the studied thin section) and hence they are avoided during this study for the sake of simplicity. Quartz grains are bimodal with subhedral to anhedral grain shape (Fig. 2.4d). Small grains are 0.06-0.15 mm, whereas large grains have a grain size population of 0.5-0.8 mm. Though the quartz grains are evenly distributed in the matrix, their high population and large grain sizes are observed in two elongated patches: a. with the plagioclase grains and b. with garnet grains along their grain boundaries. This denotes an inhomogeneity in the modal% and grain size of the quartz grains (Fig. 2.4c). Garnet grains are only concentrated at a specific domain in the thin section with quartz grains along their sides (marked as ‘Domain II’ in Fig. 2.4c). The garnet grain sizes are variable where the smallest grain size is 0.2 mm, largest grain reaches up to 2 mm. They also have variable grain shapes ranging from extensively elongated grains with irregular grain boundaries to semi-rounded grains with regular boundaries (Fig. 2.4e). ‘Domain III’ shows a large population of elongated quartz and plagioclase grains. The maximum grain size of quartz reaches up to 0.9 mm. Hence, the sample exhibits different domains with

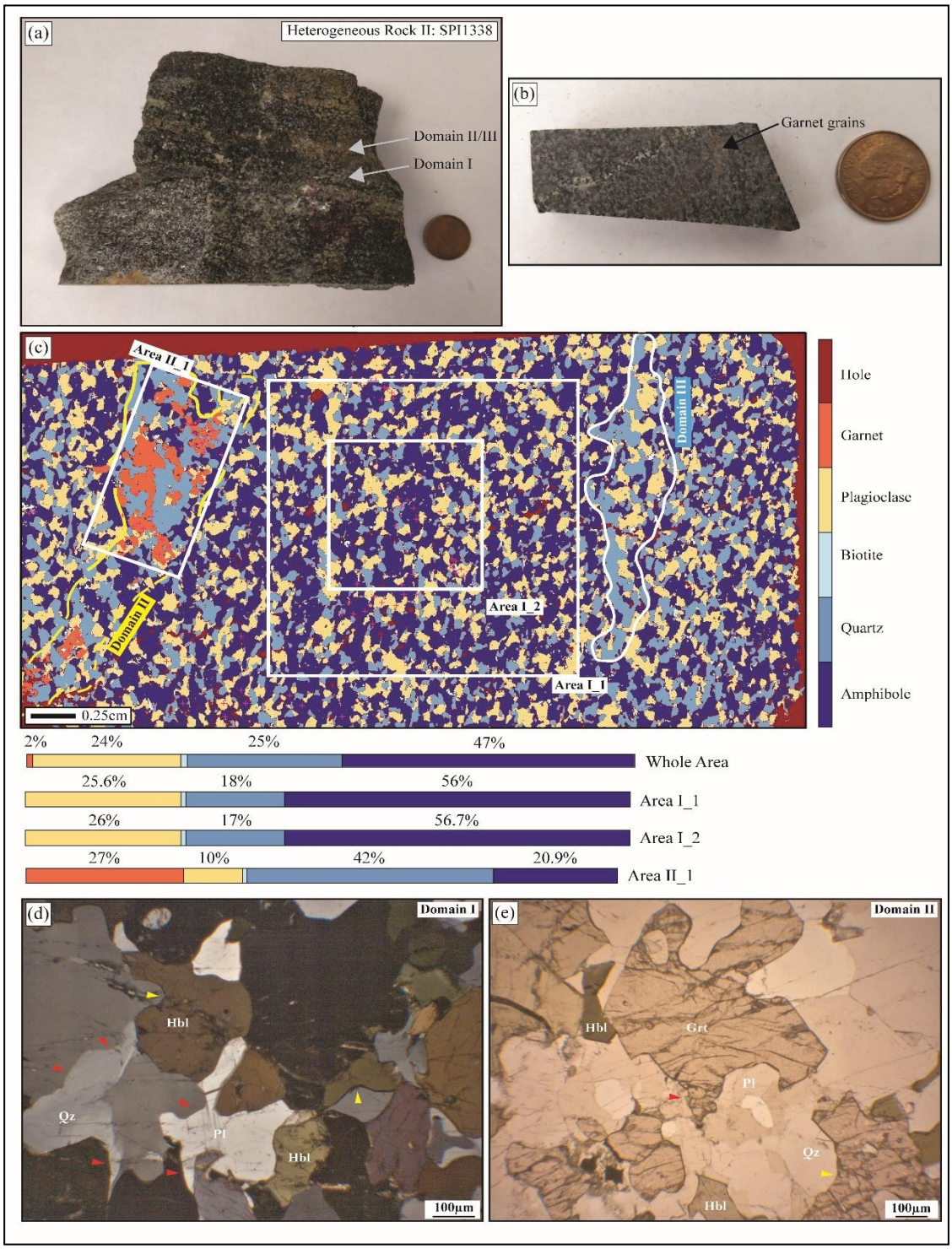

Figure 2.4 – Heterogeneous rock II: Amphibolite (SPI1338) with characteristic sample-scale and thin section-heterogeneity. (a-b) Representative sample with parallel mafic and felsic layers seperating 'Domain I' and 'Domain II'. Thin section block characterzing 'Domain II' with clustered garnets. The same block is used for the whole rock XRF analyses. (c) 'Domain II' (marked with yellow lines) with large garnet grains confirms sample scale observation. 'Domain III' (marked with white line) has larger grains and a higher modal abundance of plagioclase + quartz. 'Domain I' represents the homogeneous matrix. Representative areas ('Area I_1','Area I_2' within 'Domain I' and 'Area II_1' within 'Domain II') are chosen for major oxide MapComp analyses. Locations of EPMA spot analyses are marked by '+'. Difference in phase distribution amongst different areas is found. (d) Photomicrograph from 'Domain I' shows interlocking texture with hornblende (yellow arrows) and irregular quartz (qz) grains (red arrows). (e) 'Domain II' exhibits garnet porphyroblasts with varying sizes and a high proportion of quartz + plagioclase. A large garnet grain with irregular boundary (red arrow) and a small garnet with regular grain boundary (yellow arrow) are marked.

differences in mineral phases and mineral modal abundances (Fig. 2.4c). Domains with high modal abundance of large quartz grains (with or without garnet grains) may indicate modification in the later phase of rock history. For example, 'Domain II' has 15% garnet, 15% plagioclase, abundances. Textural heterogeneity also implies that certain textural sites diverge from the average bulk rock composition. 'Domain I' has 25.5% plagioclase, 0.5% biotite, 18% quartz, 0.2% biotite, 36% quartz, and 33.8% amphibole grains (Fig. 2.4c). 'Area I_1', with sides 40x maximum gran size, within 'Domain I', and 'Area II_1', within Domain II' (Fig. 2.4c) were chosen to evaluate the major oxide weight percentage and the compositional difference between these two domains using the MapComp technique. 'Area I_2' comprises a remarkably similar mineral abundance, with sides 20x maximum grain size, and is used for testing the robustness of this technique.

Heterogeneous rock III: Diorite Gneiss with 2cm thick felsic domain (SPI1321)

The sample is compositionally inhomogeneous in hand specimen and thin section scale (Fig. 2.5a, and its twin block in Fig. 2.5b) with distinct compositional banding demarcating two characteristic domains (Fig. 2.5a, b) marked by- i) parallel dark streaks formed by oriented mafic minerals ('Domain I' in Fig. 2.5c) and ii) pale felsic domain ('Domain II' in Fig. 2.5c). Overall, amphibole-biotite-plagioclase-quartz-K-feldspar and apatite are the dominant mineral phases (Fig. 2.5c) with modal abundances of 19%, 5%, 50%, 22%, 3.5%, and 0.5%, respectively. Elongated amphibole and biotite grains form the foliation. Amphibole grains are subhedral with irregular grain boundaries (yellow arrow in Fig. 2.5d). Biotite grains are subhedral and observed along amphibole grain boundaries. Plagioclase grains are fresh with polysynthetic twins and show granoblastic texture. The grain sizes of amphibole, biotite, K-feldspar, quartz, and plagioclase grains are 0.6-1.2 mm, 0.3-0.5 mm, 0.2-0.4 mm, 0.6-1.5 mm, 0.8-1.5 mm respectively. 'Domain I' exhibits modal abundances of 32%, 0.5%, 44%, 18.5%, 4% and 1% for amphibole-biotite-plagioclase-quartz-K-feldspar and apatite grains, respectively. 'Domain II' has qtz-plag-kfs-biotite grains with modal abundances of 28%, 57%, 2.5% and 12%, respectively, very little amphibole (0.3 modal%) and apatite (0.2 modal%) grains are also found. Hence, modal abundance of the mineral phases in 'Domain II' is strikingly different to that of 'Domain I'. An average grain size of 0.8 mm, 1.2 mm, and 0.6 mm for qtz-plag-kfs grains with a large population of elongated, euhedral to subhedral biotite grains (maximum 0.1-1 mm grain

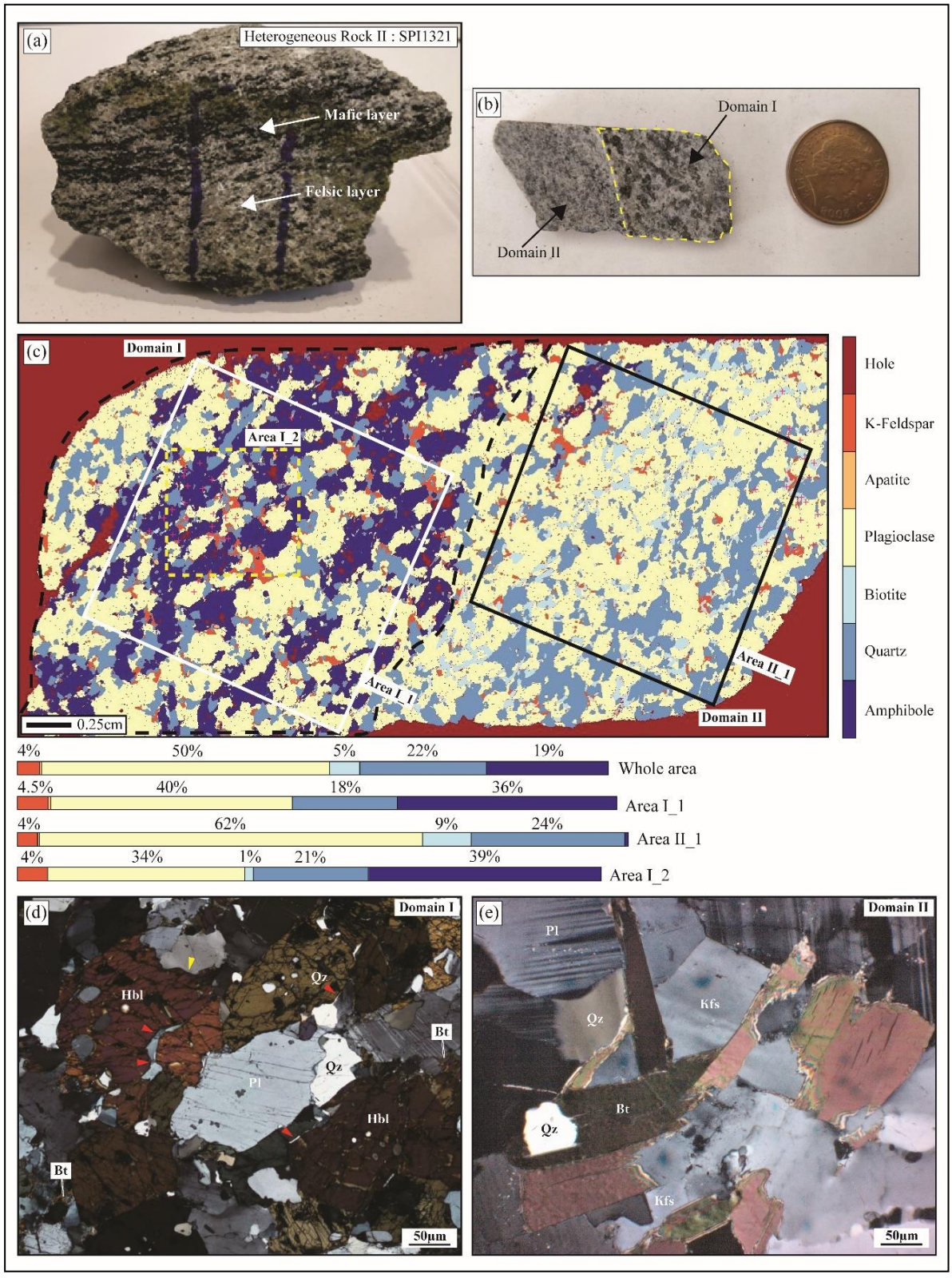

Figure 2.5 – Heterogeneous rock III: Diorite gneiss (SPI1321) exhibiting sample-scale and thin-section scale heterogeneity. (a-b) Field specimens with parallel mafic (Domain I) and felsic mineral (Domain II) rich domains. For the whole rock XRF analysis, only 'Domain I' (yellow dotted area) is used. (c) Micro XRF map displaying distribution of phases and difference in mineral modal abundance between the domains. 'Area I_1' (in 'Domain I') and 'Area II_1' (in 'Domain II') (marked with white and black squares) are chosen for MapComp analyses. Locations of EPMA spot analyses are marked with '+'. 'Area I_2' in Domain I (square with yellow dotted sides) is used for EPMA XRF mapping and subsequent major oxide analyses. (d) Domain I shows large, elongated amphibole grains with tiny biotite grains. Red arrows mark the elongated quartz grains. (e) Large plagioclase, K-feldspar with elongated biotite grains characterizing textural difference of Domain II.

size) parallel to the foliation are found (Fig. 2.5c). The biotite grains have irregular boundaries (Fig. 2.5e). Quartz and K-feldspar grains display interstitial nature, with quartz grains being highly elongated (red arrows in Fig. 2.5e). 'Area I_1' (Fig. 2.5c), ~15x the maximum grain size, within 'Domain I' is chosen to evaluate the major oxide weight percentage using the MapComp technique. 'Area II_1' (Fig. 2.5c), with ~10x the maximum within Domain II' is selected for determining how local bulk composition of the 'Domain II' deviates from the 'Domain I'. Another representative area (with ~ 5% K-feldspar, 34.5% plagioclase, 1% biotite, 19% quartz, and 40.5% amphibole) within the 'Domain I' ('Area I_1') is chosen for quantitative EPMA major element XRF mapping. The same area is also used to determine local bulk rock major oxide composition using MapComp.

2.3.2 Major element EPMA spot analysis

Homogeneous rock: hornblende-orthopyroxene-clinopyroxene bearing mafic gneiss (SPI1399A)

EPMA spot analyses show Mg# of 0.69-0.74, 0.82-0.87, and 0.81-0.93 for orthopyroxene, clinopyroxene and amphibole respectively without any compositional in-grain zonation (Tab. 2.1). However, the amphibole grains adjacent to the orthopyroxene-clinopyroxene show $Al^{(IV)}$ of 0.05-0.7 and a value of 0.8-1.1 is observed away from it. End member plots show the amphibole grains adjacent to the orthopyroxene-clinopyroxene grains are 'actinolites' (Fig. 2.2e, Fig. 2.6a: dotted area; Tab. 2.1). Amphiboles away from the replacement zones are of 'magnesiohornblende' composition (Fig. 2.6a; Tab. 2.1). Anorthite grains are chemically homogeneous with an An% of 25-29% (Fig. 2.6b; Tab. 2.1). Average composition of the clinopyroxene grain is 'diopside' (with Wo 46% En 47% Fe 7%) and the orthopyroxene grains have an average composition of 'enstatite' (with Wo 0.7% En 69.3% Fs 30%) (Fig. 2.6c; Tab. 2.1). Biotite grains have Mg# of 0.80-0.83 (Tab. 2.1) and end member plot shows its chemical homogeneity (Fig. 2.6e).

Compositionally layered rock I: Amphibolite with a foliation parallel, thick 3mm domain (SPI1382)

EPMA spot analyses in the 'Domain I' indicate Mg# of 0.59-0.67, 0.56-0.58, and 0.67-0.74 in amphibole, orthopyroxene and clinopyroxene grains respectively without any

	Homogeneous Mafic Gneiss (1399A)						Compositionally Layered Rock I (SPI1382)			
Mineral	Opx	Cpx	Plag	Bt	Amp1	Amp2	Opx	Cpx	Plag	Hbl
	DOMAIN 1						DOMAIN 1+2			
SiO_2	53.91	53.75	60.6	38.31	48.75	55.3	52.49	52.44	55.77	43.75
TiO_2	0	0	0	1.99	0.66	0.12	0	0	0	1.16
Al_2O_3	0.5	0.8	24.4	14.24	6.71	1.9	1.1	1.52	28.35	11.66
Cr_2O_3	0.04	0.23	0	0.5	0.6	0.1	0	0.05	0	0.04
FeO(tot)	18.11	4.88	0	8.63	7.71	5.46	25.33	8.57	0.14	14.18
MnO	0.44	0.13	0	0	0.16	0.14	0.85	0.29	0	0.13
MgO	25.79	15.61	0	19.71	17.72	21.1	20.14	13.49	0	11.91
CaO	0.32	23.71	5.6	0	11.49	12.1	0.37	23.01	10.37	11.98
Na_2O	0.03	0.54	8.6	0.3	1.41	0.4	0	0.41	5.56	1.22
K_2O	0	0	0.19	9.53	0.45	0.07	0	0	0.16	1.17
Total	99.14	99.65	99.4	93.21	95.66	96.6	100.28	99.77	100.4	97.2
No of O	6	6	8	22	24	24	6	6	8	24
Si	1.98	1.98	2.71	5.65	7.04	7.74	1.98	1.96	2.5	6.48
Ti	0	0	0	0.22	0.07	0.01	0	0	0	0.13
Al	0.02	0.03	1.29	2.48	1.14	0.31	0.05	0.07	1.5	2.04
Cr	0	0.01	0	0.06	0.07	0.01	0	0	0	0.01
Fe(tot)	0.56	0.15	0	1.07	0.93	0.64	0.8	0.27	0.01	1.76
Mn	0.01	0	0	0	0.02	0.02	0.03	0.01	0	0.02
Mg	1.41	0.86	0	4.34	3.82	4.4	1.13	0.75	0	2.36
Ca	0.01	0.93	0.27	0	1.78	1.81	0.01	0.92	0.5	1.9
Na	0	0.04	0.75	0.09	0.4	0.11	0	0.03	0.48	0.35
K	0	0	0.01	1.79	0.08	0.01	0	0	0.01	0.22
Total	4	4	5.02	15.69	15.35	15.1	4	4	5	15.25
Mg#	0.72	0.85	NA	0.8	0.8	0.87	0.59	0.74	NA	0.57
An%	NA	NA	26.2	NA	NA	NA	NA	NA	50.29	NA

	Compositionally Heterogenous Rock II (SPI1338)				Compositionally Heterogenous Rock III (SPI1321)			
Mineral	Grt	Plag	Bt	Hbl	Kfs	Plag	Bt	Hbl
	DOMAIN 2	DOMAIN 1+2+3			DOMAIN 1+2			
SiO_2	37.75	55.35	35.4	40.43	64.06	61.08	37.19	44.84
TiO_2	0	0	4.13	1.96	0	0	3.32	0.78
Al_2O_3	20.64	28.01	15.3	12.84	18.97	24.39	15.55	9.24
FeO(tot)	27.18	0	20	19.45	0.06	0.02	15.18	13.96
MnO	2.47	0	0.1	0.23	0	0	0.15	0.32
MgO	3.05	0	10.7	7.92	0	0	13.32	12.82
CaO	8.7	10.05	0	11.5	0	5.75	0	11.87
Na_2O	0	5.96	0	1.5	0.78	8.27	0.01	1.22
K_2O	0	0.12	9.74	1.69	15.37	0.42	9.87	1.01
Total	99.79	99.49	95.35	97.52	99.24	99.93	94.63	96.15
No of O	6	8	22	24	8	8	22	24
Si	3	2.5	5.38	6.19	2.97	2.72	5.55	6.69
Ti	0	0	0.47	0.23	0	0	0.37	0.09
Al	1.93	1.49	2.74	2.32	1.04	1.28	2.74	1.31
Fe(tot)	1.8	0	2.54	2.49	0	0	1.9	1.74
Mn	0.17	0	0.01	0.03	0	0	0.02	0
Mg	0.36	0	2.42	1.81	0	0	2.97	2.85
Ca	0.74	0.49	0	1.89	0	0.27	0	1.9
Na	0	0.52	0	0.45	0.07	0.71	0	0.3
K	0	0.01	1.89	0.33	0.91	0.02	1.88	0.19
Total	8	5.01	15.5	15.71	5.01	5.01	15.43	15.06
Mg#	0.17	NA	0.49	0.42	NA	NA	0.61	0.62
An%	NA	47.9	NA	NA	NA	27.08	NA	NA
Or%	NA	NA	NA	NA	92.85	NA	NA	NA

Table 2.1 – Representative compositions of minerals in the studied samples. Note the location of 'Amp1' and 'Amp2' for the Homogeneous Mafic Gneiss (SPI1399A) are marked in Fig. 2.2d. Compositions shown here are highlighted in Tab. AP3.1-AP3.6 and AP4.1-AP4.4.

compositional zonation of the constituent mineral phases (Tab. 2.1). Amphibole grains are 'magnesiohornblende' in composition whereas the orthopyroxene grains are of 'enstatite' composition (with En56.3% Wo0.9% Fs42.8%) (Fig. 2.6a, c; Tab. 2.1). Average composition of the clinopyroxene grain is 'diopside' (with Wo 45.6% Di 37.9% Hd 16.5%; Tab. 2.1) (Fig. 2.6c). Plagioclase grains are devoid of any zonation with an Anorthite component of 49-51% in the constituent plagioclase grains (Fig. 2.6b; Tab. 2.1). In Domain II, amphibole, plagioclase, orthopyroxene and clinopyroxene grains have same chemical composition as in Domain I (Fig. 2.6a-d; Tab. 2.1).

Compositionally heterogeneous rock II: Amphibolite with crosscutting, 6mm garnet bearing domain (SPI1338)

EPMA spot analyses show Mg# of 0.40-0.47 and 0.49-0.58 for amphibole and biotite grains respectively in 'Domain I' (Tab. 2.1). Amphibole grains are 'ferrotschermakite' and the biotite grains are 'magnesio biotite' in composition (Fig. 2.6a, d). An anorthite component of 46-53% is observed in the constituent plagioclase grains in the 'Domain I' (Fig. 2.6b; Tab. 2.1). In the 'Domain II' (Fig. 2.4c), the garnet grains are without any major compositional zonation with Mg# of 0.012-0.016 (with almandine 59.5%) (Fig. 2.6d; Tab. 2.1). The amphibole, plagioclase and biotite grains in 'Domain II' are compositionally similar (Fig. 2.6a-b, e; Tab. 2.1) to that of 'Domain I'.

Heterogeneous rock III: Diorite Gneiss with 2cm thick felsic domain (SPI1321)

In 'Domain I', EPMA spot analyses show Mg# of 0.56-0.69, and 0.59-0.69 for amphibole, and biotite grains (Tab. 2.1). Amphibole grains are 'magnesio hornblende' and the biotite grains are 'magnesio biotite' in composition (Fig. 2.6a, e). An% and Or% of 26.5-30% and 90.2-96.1% is observed in the constituent plagioclase and orthoclase grains (Fig. 2.6b; Tab. 2.1). In 'Domain II', amphibole, plagioclase, orthoclase, and biotite grains are of similar chemistry with respect to the 'Domain I' (Fig. 2.6a-b, e; Tab. 2.1).

2.3.3 Conventional XRF bulk rock compositional analyses using rock blocks

Whole rock XRF for the whole thin section area in *homogeneous mafic gneiss* (SPI1399A) show major oxide weight percentage of 5.47% Al_2O_3, 9.05% CaO, 9.57% FeO, 0.92% K_2O, 20.37% MgO, 0.19% MnO, 0.91% Na_2O, 51.23% SiO_2, 0.4% TiO_2 and a LOI value of 0.26% (Tab. 2.2). For the *Compositionally layered rock I: amphibolite* (SPI1382), the concentrations are 14.74% Al_2O_3, 11.64% CaO, 12.13% FeO, 0.31% K_2O, 7.71% MgO, 0.19% MnO, 2.71% Na_2O, 48.75% SiO_2, and 0.95% TiO_2 (Tab. 2.2) for the whole thin section block (Fig. 2.4b). Similarly, *compositionally heterogeneous rock II: Amphibolite* (SPI1338) yields 13.30% Al_2O_3, 8.45% CaO, 11.08% FeO, 0.89% K_2O, 4.25% MgO, 0.15% MnO, 2.03% Na_2O, 57.75% SiO_2, 1% TiO_2 and a LOI value of 0.38% (Tab. 2.2) from the representative whole thin section block. For both these heterogeneous samples no mechanical separation can be made between 'Domain I' and 'Domain II' and hence XRF compositional analyses was done from the whole thin section area. For *Heterogeneous rock III: Diorite Gneiss* (SPI1321), physical separation between distinctly placed 'Domain I' and 'Domain II' was made with confidence and compositional XRF analysis is obtained from the 'Domain I' (Fig. 2.4c). Major oxide weight percentage obtained from 'Domain I' is 15.14% Al_2O_3, 6.27% CaO, 5.1% FeO, 1.09% K_2O, 4.69% MgO, 0.12% MnO, 4.07% Na_2O, 62.32% SiO_2, 0.3% TiO_2 and 0.67% MgO (Tab. 2.2). This is to be noted that the conventional whole rock XRF utilizes 3D thin section blocks, in comparison, any image analyses only yield results from the exposed 2D surface of a thin section from that representative block.

2.3.4 MapComp results

For the *homogeneous mafic gneiss* (SPI1399A) major oxide weight percentage calculated using MapComp from the whole thin section area is 5.21% Al_2O_3, 9.18% CaO, 9.80% FeO, 1.12% K_2O, 20.71% MgO, 0.20% MnO, 0.35% Na_2O, 51.10% SiO_2, and 0.47% TiO_2 (Tab. 2.2). Hence, whole rock XRF and MapComp derived major oxide values show a perfect correlation for the whole thin section area (Fig. 2.7a; Tab. 2.2). Weight% derived from MapComp is subtracted from its corresponding whole rock XRF weight% value to find out absolute deviation in calculated weight% between these two methods. For SPI1399A, this difference is found minimal, with only ~ 0.1-0.3% change between the conventional

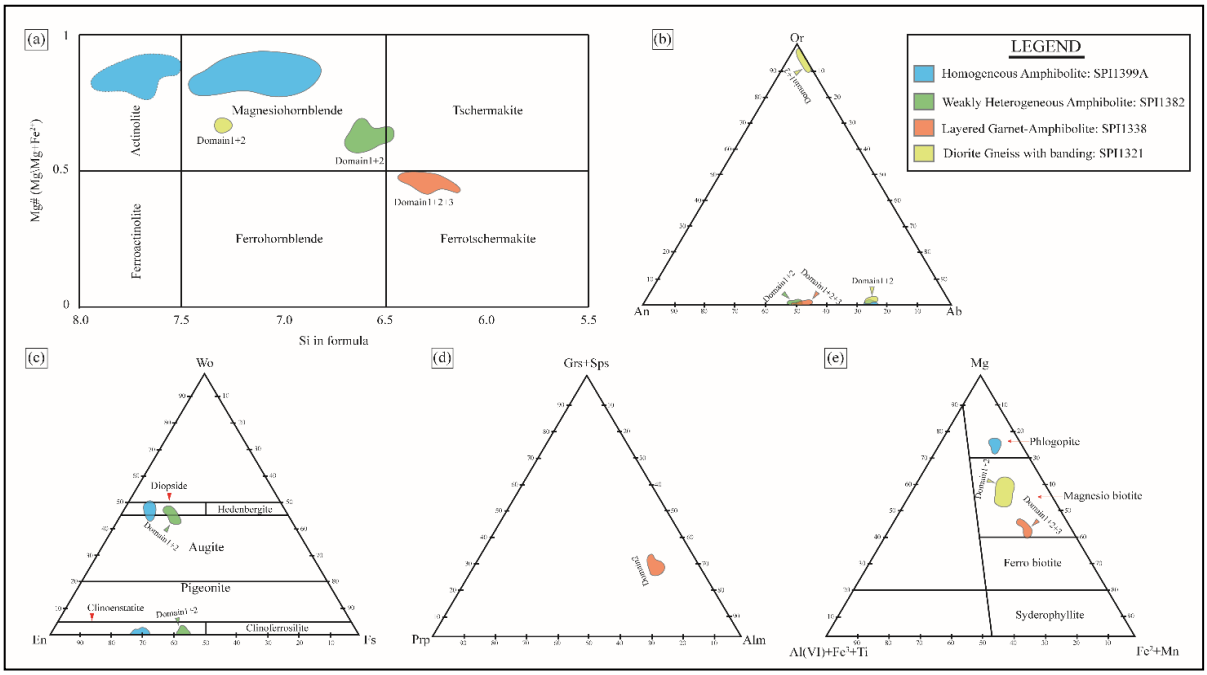

Figure 2.6 – Mineral composition in the investigated samples for various 'Domains' of consideration. (a) Mg# versus Si (in formula unit) classification diagram of calcic amphiboles (Leake, 1977). Analysed amphibole grains in all the heterogeneous samples (SPI1382, SPI1338, SPI1321) exhibit chemical homogeneity across different domains. Actinolite amphiboles surround orthopyroxene and clinopyroxene grains in the homogeneous mafic gneiss SPI1399A. (b-e) Other minerals (plotted in ternary diagrams) have similar compositions in all the studied samples.

XRF and MapComp analyses (Fig. 2.7b). A slightly larger variation of ~ 0.6 weight% is observed for the Na_2O (Fig. 2.7b). Next, the absolute difference is normalized with respect to its corresponding whole rock XRF weight% value to determine a relative change in MapComp derived value (Tab. 2.3). For most of the elemental oxides this deviation is <5% (Fig. 2.8a; Tab. 2.3). However, K_2O and TiO_2 show a large deviation of ~ 20% and Na_2O yields a maximum relative change of ~ 60% even though the absolute change of Na_2O was only ~ 0.6% (Fig. 2.8a; Tab. 2.3). To characterize the robustness of the MapComp technique, major oxide values from 'AreaI_1', 'Area I_2' and 'Area I_3' are determined (Fig. 2.2b). 'Area I_1', with sides ~30x the maximum grain size, consists of a very similar modal% of constituent mineral phases compared to the whole thin section area (Fig. 2.2b; Tab. 2.4). 'Area I_2' (with sides ~15x the maximum grain size) yields a little higher modal% of orthopyroxene and clinopyroxene grains while hornblende modal% is 4% less than observed for whole thin section area or in 'Area I_1' (Fig. 2.2b; Tab. 2.4). Area I_3', with sides ~10x the maximum grain size, have higher modal% of orthopyroxene and biotite grains whereas modal% of hornblende and clinopyroxene is less than observed in the whole thin section

area (Fig. 2.2b; Tab. 2.4). The degree of change in mineral modal abundance is the highest for 'Area I_3'. Major oxide values for 'Area I_1' are very similar to the whole rock XRF derived oxide values for the whole thin section area/block (Tab. 2.2, 2.4). The absolute deviations in major oxide values between these two methods are only ~ 0.2 weight%. Relative deviations are also within <10% for most of the oxides, while large deviations are associated with Na_2O, K_2O, and TiO (Fig. 2.8b; Tab. 2.4). Na_2O yields a maximum relative change of ~ 65%, very similar to the relative deviations observed for the whole thin section area. For 'Area I_2', the absolute deviations are in the range of 0.01-0.9 weight%. The relative deviations for most of the oxides increase, and higher degree changes are associated with FeO and MnO (Fig. 2.8b; Tab. 2.4). Maximum relative changes are observed

	Homogeneous Mafic Gneiss SPI1399A		Compositionally Layered Rock I: SPI1382	
	MapComp – Whole Area	Whole rock	MapComp – Whole Area	Whole rock
Al_2O_3	5.21	5.47	15.36	14.74
CaO	9.18	9.05	11.46	11.64
FeO	9.80	9.57	10.61	12.13
K_2O	1.12	0.92	0.31	0.31
MgO	20.71	20.37	7.35	7.71
MnO	0.20	0.19	0.19	0.19
Na_2O	0.35	0.91	2.39	2.71
SiO_2	51.10	51.23	49.57	48.75
TiO_2	0.47	0.40	0.79	0.95
L.O.I		0.26		
SUM	98.14	98.62	98.03	99.13

	Compositionally Heterogeneous Rock II: SPI1338		Compositionally Heterogeneous Rock III: SPI1321	
	MapComp – Whole Area	Whole rock	MapComp – Area I_1	Whole rock – Area I_1
Al_2O_3	13.36	13.30	14.73	15.14
CaO	7.73	8.45	6.52	6.27
FeO	9.20	11.08	5.29	5.10
K_2O	0.79	0.89	1.07	1.09
MgO	3.92	4.25	4.46	4.69
MnO	0.16	0.15	0.14	0.12
Na_2O	1.69	2.03	4.11	4.07
SiO_2	56.19	57.75	61.02	62.32
TiO_2	1.04	1.00	0.28	0.30
L.O.I		0.38		0.67
SUM	94.08	99.29	97.62	99.77

Table 2.2 – Comparison between major oxide weight percentages obtained using MapComp and whole rock XRF in the studied samples. The measurements are done for the whole thin section areas/blocks except in Compositionally Heterogeneous Rock III (SPI1321).

for Na_2O, and K_2O. For 'Area I_3', the relative deviations are either similar or increases from 'Area I_2'. However, relative changes in SiO_2 values are minimal in all three areas. In 'Area I_3', K_2O, MnO, and Na_2O record the highest degree deviations amongst the three studied areas (Fig. 2.8b; Tab. 2.4).

In *Compositionally layered rock I: amphibolite* (SPI1382), MapComp derived major oxide weight percentage for the whole thin section area is 14.74% Al_2O_3, 11.64% CaO, 12.128% FeO, 0.31% K_2O, 7.71% MgO, 0.19% MnO, 2.71% Na_2O, 48.75% SiO_2, and 0.95% TiO_2 (Tab. 2.2). Major oxide values from whole rock XRF and MapComp, indicate similar weight percentages for Al_2O_3, CaO, K_2O, MgO, MnO, Na_2O, and TiO_2 for the same area (Fig. 2.7c), with a little absolute variation of ~ 0.01-0.3% between these two methods (Fig. 2.7d; Tab. 2.2). A relatively large variation of ~ 0.8% and ~ 1.5% are seen in the absolute values for SiO_2 and FeO, respectively between these two methods (Fig. 2.7d; Tab.

	Homogeneous Mafic Gneiss SPI1399A		Compositionally Layered Rock I: SPI1382	
	Whole rock	Relative change in oxide weight%	Whole rock	Relative change in oxide weight%
Al_2O_3	5.47	5	14.74	4
CaO	9.05	1	11.64	2
FeO	9.57	2	12.13	13
K_2O	0.92	22	0.31	0
MgO	20.37	2	7.71	5
MnO	0.19	5	0.19	0
Na_2O	0.91	62	2.71	12
SiO_2	51.23	0.3	48.75	2
TiO_2	0.4	18	0.95	17
SUM	98.62	0.49	99.13	1.11

Table 2.3 – Relative change in MapComp derived oxide weight percentage values normalized to the whole rock XRF major oxide values for the whole thin section area in homogeneous mafic gneiss SPI1399A and compositionally layered gneiss SPI1382.

2.2). Similar to homogeneous mafic gneiss SPI1399A, relative changes in MapComp calculated and XRF derived values are measured. For most of the oxides this deviation is <5% (Fig. 2.8c; Tab. 2.3). A large relative deviation of ~ 15% is observed for Na_2O, FeO, and TiO_2 (Fig. 2.8c; Tab. 2.3). Note, even though a comparatively large change is observed in absolute values of SiO_2, the relative deviation is very little (Tab. 2.2, 2.3). 'Area I_1' in 'Domain I' shows a very similar modal% of constituent minerals to the whole thin section area except a relatively high modal abundance of Fe-oxides (Fig. 2.3b). The major oxide

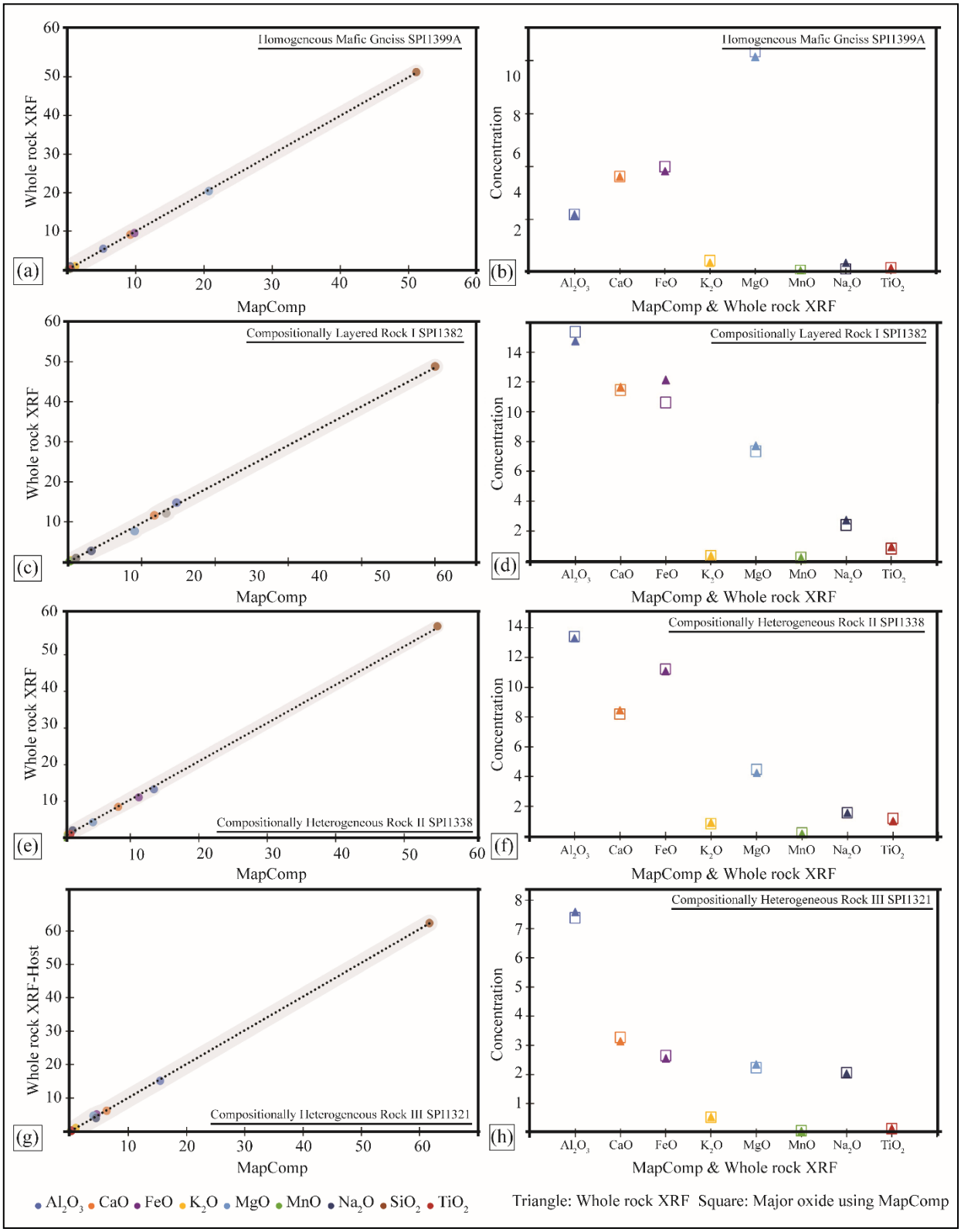

Figure 2.7 – Comparison of major oxide weight percentage calculated from the thin section areas using whole rock XRF and MapComp. For the four studied rocks, left panel shows a good correlation in oxide weight percentage obtained using these two methods (a, c, e, g). The right panel exhibits a nearly perfect correlation between whole rock XRF and MapComp derived major oxide values measured for entire thin section areas (b, d, f, h).

deviation between two measured values. Comparatively high relative changes are associated with Na_2O and TiO_2, where Na_2O shows maximum deviation of ~40%. Compared to the whole thin section area or 'Area I_1', 'Area II_1' in 'Domain II' shows high modal abundance of orthopyroxene, clinopyroxene and plagioclase with very little amphibole values show a relatively large difference of ~ 1.5% and ~ 2.5% for Al_2O_3 and SiO_2, respectively, when compared to the XRF derived oxide values for the whole thin section block (Tab. 2.2, 2.5). For other oxides, this difference is very small and vary in the range of ~ 0.01-1 weight% (Tab. 2.2, 2.5). The relative changes are also very little with <10% grains (Fig. 2.3b). MapComp derived major oxide values show a relatively large difference of ~ 1.6%, 1.7% and ~ 2.2% for Al_2O_3, SiO_2, and FeO, respectively, when compared to the XRF measured oxide values (Tab. 2.2, 2.5). Na_2O yields an absolute change of ~1 weight%. Even though the measured absolute changes are comparatively higher for Al_2O_3, SiO_2, and FeO, but high relative deviations of ~70% and 40% are found for K_2O and Na_2O. A high relative deviation of ~20% is also observed for FeO. Hence, relatively high deviations are associated with Na_2O, K_2O and TiO_2, very similar to the observations made in SPI1399A. In SPI1382, absolute and relative changes for FeO are also higher (>10%) for the whole thin section area, and Area II_1.

Compositionally heterogeneous rock II: amphibolite (SPI1338) shows 13.36% Al_2O_3, 7.73% CaO, 9.20% FeO, 0.79% K_2O, 3.99% MgO, 0.16% MnO, 1.69% Na_2O, 56.19% SiO_2 and 1.10% TiO_2 calculated using MapComp for the whole thin section area (Tab. 2.2). Hence, this correlates well with major oxide weight percentage values measured using whole rock XRF for the same area (Fig. 2.7e; Tab. 2.2) with a slight variation of ~ 0.01-0.7% for Al_2O_3, CaO, K_2O, MgO, MnO, Na_2O and TiO_2 (Fig. 2.7f; Tab. 2.2). For SiO_2, this variation is relatively large ~ 1.5 weight%, and for FeO an absolute difference of ~ 1.8 weight% is found (Fig. 2.9a; Tab. 2.2). The relative deviations are found to be large with ~16% for Na_2O and FeO (Fig. 2.9b). Using MapComp, major oxide weight percentage values are also determined for 'Area I_1', 'Area I_2' in 'Domain I' and 'Area II_1' in 'Domain II' (Tab. 2.5), and they show major deviations in the calculated values compared to the results obtained from whole rock XRF. 'Area I_1' has no garnet grains, and modal abundance of quartz decreases while amphibole grains are more compared to the whole thin section area (Fig. 2.4b). For 'Area I_1', compared to the XRF derived SiO_2 weight percentage, a maximum difference of ~ 6 wt% in SiO_2 is observed (Tab. 2.2, 2.5; Fig. 2.9a). And for the other oxides, this range is very small ~ 0.002-1% (Fig. 2.9a). Even though, a

large absolute variation is observed for SiO_2, the relative deviation is only 10% when compared to XRF derived values for the whole thin section block (Fig. 2.9b). However, a large relative deviation of ~36% is observed for TiO_2. MapComp calculated major oxide values in 'Area I_2' are found very similar to the results obtained for larger 'Area I_1' in

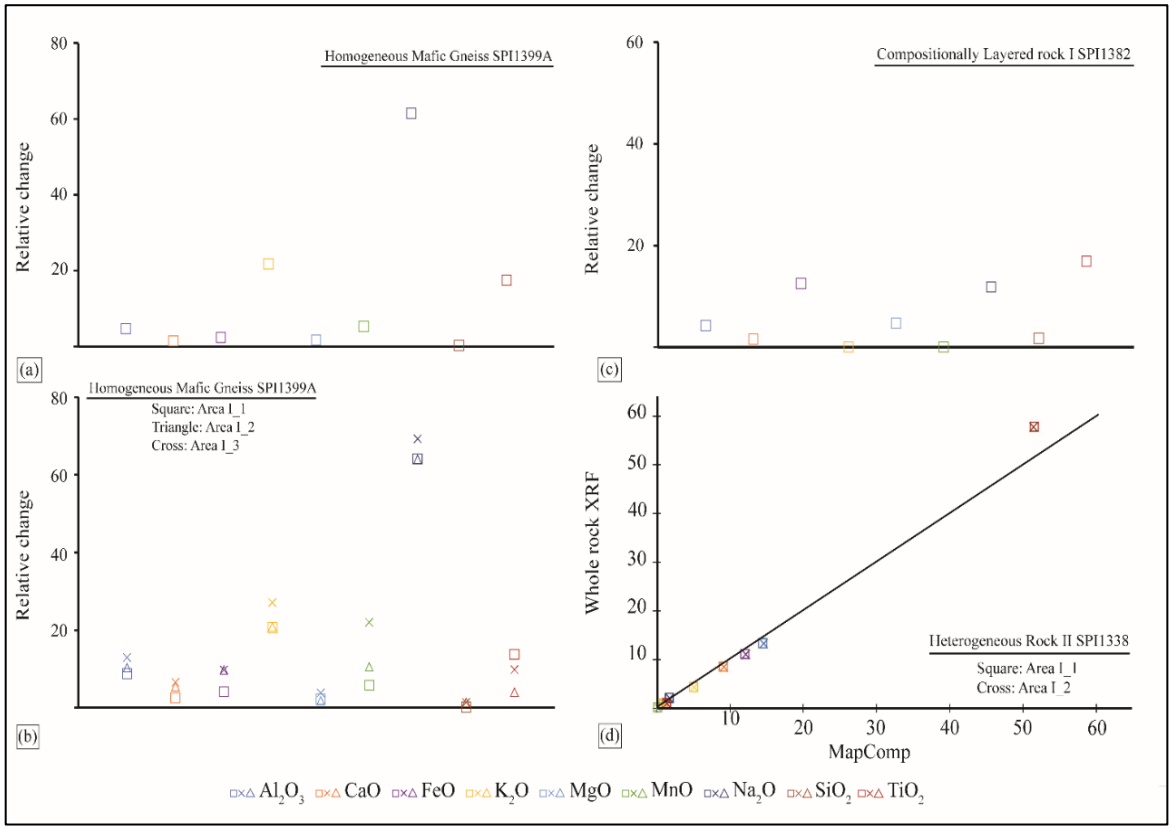

Figure 2.8 – Relative deviations in MapComp derived oxide weight percentage (normalized to whole rock XRF oxide weight%) in the studied samples. (a) Homogeneous mafic gneiss (SPI1399A) exhibiting large relative deviations for K_2O, Na_2O and TiO_2. (b) Relative deviation in MapComp major oxide weight percentage with respect to whole rock XRF values between 'Area I_1', 'Area I_2', and 'Area I_3' in Homogeneous mafic gneiss (SPI1399A). (c) Relative changes in measured oxide weight percentage for compositionally Layered rock I (SPI1382). (d) Major oxide values obtained using MapComp from 'Area I_1' and 'Area I_2' (within 'Domain I') in compositionally Heterogeneous rock II: Amphibolite (SPI13338). MapComp major oxide weight percentage from both the areas are plotted against the whole rock XRF values obtained from the entire thin section area. Both the areas have similar values, but their divergence from the identity line (black line) indicates deviation from whole rock XRF.

'Domain I' (Fig. 2.8d; Tab. 2.5). The absolute deviation in major oxide weight percentage between these two areas are in the range of ~ 0.1 weight%. 'Area I_2' also shows similar modal abundance of constituent phases compared to 'Area I_1' (Fig. 2.4b). MapComp calculated major oxide values for 'Area II_1' (in 'Domain II', Fig. 2.4c) yields deviation in

bulk rock composition compared to the whole thin section area and 'Area I_1' (Fig. 2.9a-b; Tab. 2.5). A maximum variation of ~ 2 weight% for CaO, ~ 3 weight% for FeO, and ~ 4 weight% for SiO_2 is found when compared to XRF derived whole rock major oxide values. For the other oxides, these values vary between 0.2-1.5 wt% (Fig. 2.9a; Tab. 2.2, 2.5). Relative deviations, calculated with respect to XRF derived values, are substantially high with ~25% variation observed in CaO and FeO, and ~52% and ~72% change for K_2O and MnO. Na_2O shows a massive relative deviation of 263% (Fig. 2.9b). Similarly, an absolute difference of ~ 3% Cao, ~ 2% FeO, and ~ 10% SiO_2, is observed between MapComp derived values for 'Area I_1' and 'Area II_1'. For the other oxides, this range is 0.3-1.5 wt% (Tab. 2.5).

For *Heterogeneous rock III: Diorite Gneiss* (SPI1321), XRF derived bulk composition for thin section block of 'Domain I' yields similar major oxide weight percentage values compared to MapComp calculated values for 'Area I_1' (Fig. 2.7g-h; Tab. 2.2). However, an absolute difference of ~ 2 weight% is observed for SiO_2 between these two methods. Other oxide values vary in the range of ~ 0.02-1 wt% (Tab. 2.2). Relative deviations are very little with highest change of 15% observed for MnO. Compared to the whole area and 'Area I _1', 'Area II_1' in 'Domain II' shows higher modal abundance of biotite, quartz, and plagioclase, whereas the amphibole grains are scarce (Fig. 2.5b). MapComp derived values for 'Area II_1' shows a large difference in bulk rock composition (i.e., oxide weight percentage values) compared to 'Area I_1' in 'Domain I'. A maximum difference of ~ 3 wt% is observed for Al_2O_3, CaO, FeO and MgO (Fig. 2.9c-d; Tab. 2.5). A large deviation of ~ 6 wt% is also observed for SiO_2 (Fig. 2.9c; Tab. 2.5). For other oxides, this range is in the order of ~ 0.1-1.5 wt%. Relative deviations are found substantially higher in the order of ~70% for FeO, MnO, and MgO. Except SiO_2, all the oxides show a large relative deviation of >20%. Hence, 'Area II_1' yields a large difference in bulk rock composition compared to both XRF and MapComp derived bulk chemistry of 'Domain I'. MapComp derived major oxide weight percentage from 'Area I_2' within 'Domain I' in *Heterogeneous rock III: Diorite Gneiss* (SPI1321), shows very similar results to the bulk composition obtained using EPMA XRF map (Fig. 2.10a; Tab. 2.6). Major oxide weight percentages from MapComp are: 13.16% Al_2O_3, 6.74% CaO, 6.34% FeO, 1.26% K_2O, 5.24% MgO, 0.16% MnO, 3.32% Na_2O, 60.15% SiO_2, and 0.35% TiO_2 (Tab. 2.6). The same set of EPMA composition analyses are used in both these methods. The major oxide values show a maximum absolute deviation of only ~ 0.5 wt% between these two methods (Tab.

2.6). Relative change in the calculated weight percentage for most of the oxides only yield values <5% (Fig. 2.10b; Tab. 2.6). However, a large difference is observed for MgO and MnO where relative changes reach up to ~10% (Fig. 2.10b; Tab. 2.6).

Homogeneous mafic gneiss SPI1399A			
MapComp- Area I_1			
Modal%	MapComp major oxides		
		Absolute Values	Relative change
Plagioclase (0.5%)	Al_2O_3	4.99	9
Clinopyroxene (3%)	CaO	9.28	3
Hornblende (63.5%)	FeO	9.97	4
Orthopyroxene (24%)	K_2O	1.11	21
Biotite (9%)	MgO	20.83	2
	MnO	0.20	6
	Na_2O	0.33	64
	SiO_2	51.30	0
	TiO_2	0.46	14
	SUM	98.46	
MapComp- Area I_2			
Modal%	MapComp major oxides		
		Absolute Values	Relative change
Plagioclase (0.3%)	Al_2O_3	4.91	10
Clinopyroxene (5.5%)	CaO	9.54	5
Hornblende (59%)	FeO	10.49	10
Orthopyroxene (26%)	K2O	1.11	21
Biotite (9.2%)	MgO	20.75	2
	MnO	0.21	11
	Na_2O	0.33	64
	SiO_2	51.93	1
	TiO_2	0.42	4
	SUM	99.68	
MapComp- Area I_3			
Modal%	MapComp major oxides		
		Absolute Values	Relative change
Plagioclase (0.1%)	Al_2O_3	4.76	13
Clinopyroxene (0.3%)	CaO	8.46	7
Hornblende (58.6%)	FeO	10.50	10
Orthopyroxene (31%)	K_2O	1.17	27
Biotite (10%)	MgO	21.15	4
	MnO	0.23	22
	Na_2O	0.28	69
	SiO_2	51.90	1
	TiO_2	0.44	10
	SUM	98.76	

Table 2.4 – Modal abundance and major oxide weight percentage calculated for 'Area I_2', 'Area I_2, and 'Area I_3' in the studied Homogeneous mafic gneiss (SPI1399A). The relative changes are calculated with respect to major oxide values obtained by whole rock XRF.

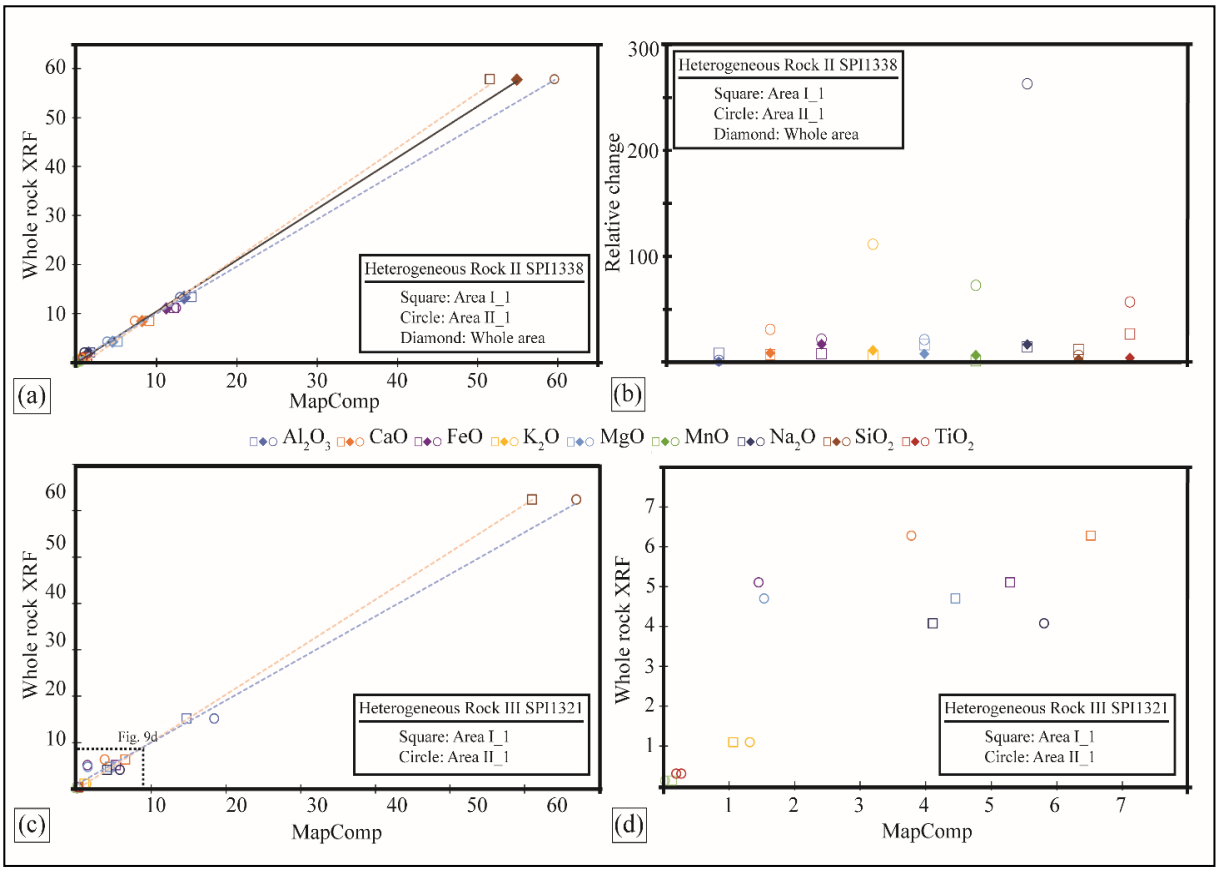

Figure 2.9 – Major oxide weight percentage obtained using MapComp for different 'Areas' within the 'Domains' of compositionally Heterogeneous rock II: Amphibolite (SPI1338) and Heterogeneous rock III: Diorite gneiss (SPI1321). Major oxide weight percentage for the whole thin section area is determined using both whole rock XRF and MapComp. Only MapComp is used to derive major oxide weight percentage from different areas. For SPI1338, (a) XRF-derived major oxides values are plotted against MapComp values for the entire thin section area (plotted as a straight line). Oxide values from 'Area I_1' in 'Domain I', and 'Area II_1' in 'Domain II' (plotted with dotted lines) deviate from the whole rock major oxide values. (b) Relative deviations in MapComp derived oxide weight percentage for 'whole thin section area', 'Area I_1' and 'Area II_1' normalized to XRF-calculated oxide weight%. For Heterogeneous rock III: Diorite gneiss (SPI1321), (c) major oxide whole rock XRF values for the entire thin section area are plotted against MapComp values for 'Area I_1' in 'Domain I' and 'Area II_1' in 'Domain II'. The absolute values of SiO_2 and Al_2O_3 differ significantly between the two areas. (d) A zoomed in portion of 'Fig. 9C' depicts the difference in MapComp calculated oxide values between the two areas.

2.3.5 Bulk rock composition analysis using EPMA major element map

Bulk composition for an area ('Area I_2' within 'Domain I') in *Heterogeneous rock III: Diorite Gneiss* (SPI1321), is calculated using major element X-ray map (Fig. AP2 – 1) obtained using electron probe microanalyzer (EPMA) with wavelength dispersive spectrometers (WDS). Quantitative X-ray maps are constructed for bulk rock analyses with referential spot analyses within the mapped area using XMapTools (Lanari et al., 2014). The results show 12.94% Al_2O_3, 6.43% CaO, 6.25% FeO, 1.24% K_2O, 5.79% MgO, 0.15% MnO, 3.19% Na_2O, 60.00% SiO_2, and 0.36% TiO_2 (Tab. 2.5).

2.4 Discussion

MapComp is a technique to create quantitative chemical maps by combining low intensity µXRF X-ray maps with EPMA referential spot analyses within the mapped area. Conventionally, bulk rock compositions are determined using bulk rock XRF or by combining high intensity EPMA X-ray maps and spot analyses. In this study, a different approach is suggested that allows for the use of low intensity microXRF X-ray maps. It is demonstrated that for the same thin section block, bulk compositions measured using MapComp and whole rock XRF produce remarkably similar results. The major oxide weight% calculated using EPMA X-ray maps also show very similar results. MapComp is also applied for quantitative evaluation of inhomogeneities within heterogeneous rocks. In the following these results will be discussed in detail and recommendations will be made as to where MapComp can be applied with great confidence.

2.4.1 Comparison of XRF and MapComp derived compositions

MapComp calculated major oxide values with the results obtained by two conventional approaches, i.e., direct measurement from bulk rock XRF and using EPMA X-ray elemental map are compared to investigate the robustness of MapComp in determining reliable local bulk composition from domains within heterogeneous rocks. The comparisons are carried out at various scales, from entire thin sections to user defined domains. The MapComp derived major oxide weight percentage for the entire thin section area correlates very well with bulk rock XRF in homogeneous mafic gneiss (SPI1399A), with only a very slight difference of 1 weight% (Fig. 2.7a-b; Tab. 2.2). For majority of oxides, the relative

differences between these two methods are also negligible (5%), with a higher relative deviation observed for elements with very low concentrations like K_2O, Na_2O, and TiO_2 (Fig. 2.8a; Tab. 2.3). Quantitative spot analyses reveal variations of amphibole composition near orthopyroxene-clinopyroxene grains, but no change in the mineral chemistry from the rim to core of other constituent minerals is found (Fig. 2.6a-e; Tab. 2.1). Thus, during bulk

	Compositionally Layered Rock I: SPI1382	
	DOMAIN I	DOMAIN II
	MapComp- Area I_1	MapComp- Area II_1
Al_2O_3	16.26	16.31
CaO	12.07	12.14
FeO	11.39	9.92
K_2O	0.34	0.10
MgO	6.92	7.17
MnO	0.18	0.23
Na_2O	1.58	1.64
SiO_2	46.17	47.06
TiO_2	0.80	0.94
SUM	95.71	95.50

	Compositionally Heterogeneous Rock II: SPI1338		
	DOMAIN I		DOMAIN II
	MapComp- Area I_1	MapComp- Area I_2	MapComp- Area II_1
Al_2O_3	14.49	14.61	13.09
CaO	9.12	9.16	6.45
FeO	12.06	12.14	14.14
K_2O	0.95	0.97	0.42
MgO	5.09	5.09	3.50
MnO	0.15	0.15	0.55
Na_2O	1.78	1.77	0.56
SiO_2	51.56	51.44	61.75
TiO_2	1.37	1.38	0.64
SUM	96.55	96.69	101.10

	Compositionally Heterogeneous Rock III: SPI1321		
	DOMAIN I		DOMAIN II
	MapComp- Area I_1	MapComp- Area I_2	MapComp- Area II_1
Al_2O_3	14.73	13.16	18.44
CaO	6.52	6.75	3.79
FeO	5.29	6.34	1.46
K_2O	1.07	1.27	1.32
MgO	4.46	5.24	1.54
MnO	0.14	0.17	0.03
Na_2O	4.11	3.32	5.81
SiO_2	61.02	60.15	66.94
TiO_2	0.28	0.35	0.20
SUM	97.61	96.73	99.52

Table 2.5 – Major oxide weight percentage calculated using MapComp for different areas within ‘Domain I’ and ‘Domain II’ in the studied samples.

chemistry determination, the observed chemical variation in amphibolite is adequately represented, and the referential spots used for quantitative X-ray mapping effectively reflect compositional variability within the mineral grain. 'Area I_1' within SPI1399A has very similar mineral modal abundance and yields very little change in major oxide values when compared to the whole rock XRF or MapComp values for the entire thin section area (Fig. 2.8b; Tab. 2.4). The relative deviations are also very similar and maximum deviations are associated with Na_2O, K_2O, and TiO_2 similar to the whole thin section area (Fig. 2.8a-b; Tab. 2.4). This perhaps suggests that the higher degree changes in K_2O, Na_2O, and TiO_2 are not directly related to the scale of observation. Instead, a small variation in the major oxide values can result in a significant relative deviation for these oxides. When compared to 'Area I_1', 'Area I_2' with slightly different phase proportion exhibits a relatively larger deviation for most of the oxides (Fig. 2.2b, 8b; Tab. 2.4). However, relative changes in K_2O and Na_2O are found to be similar since modal abundances of biotite and plagioclase are nearly identical between 'Area I_1' and 'Area I_2' (Fig. 2.2b; Tab. 2.4). In comparison to 'Area I_1' and 'Area I_2', 'Area I_3', with the highest change in mineral modal abundance, also exhibits largest relative deviations for most of the oxides (Fig. 2.8b; Tab. 2.4). The highest deviation in Na_2O is caused by the decreased modal abundance of plagioclase in 'Area I_3' (Tab. 2.4). Hence, MapComp derived major oxide values are mainly controlled by change in mineral modal abundances. The larger the difference in mineral phase% in the areas of observations, the more relative changes in major oxide values are observed. For K_2O, Na_2O, MnO, and TiO_2, an absolute change of only 0.02 weight% results in relative deviation of 10%. However, for SiO_2, FeO, and MgO, the relative deviations are little even when the absolute values change by 1-4 weight%. Hence, this method is very sensitive to the presence of oxides in low concentrations, and the error accentuates further the phase% deviates from that of the average modal abundance. Mapping areas with mineral modal abundances similar to the entire thin section area is necessary to ensure the least amount of error. Here 'Area I_1' with sides greater than 30x the largest grain size ensures a similar mineral modal abundance in SPI1399A. Thus, areas with sides between 20 to 30 times the largest grain size most likely represent optimal areas for attaining most accurate average bulk composition of the whole thin section area using MapComp. In the *Compositionally layered rock I: amphibolite* (SPI1382), bulk rock chemistry measured using whole rock XRF also correlates well with the MapComp derived values with only a small absolute difference of <1 weight% (Fig. 2.7c-d; Tab. 2.2). A significant absolute change of ~1.5 weight% and a higher relative

change are seen for FeO (Fig. 2.8c; Tab. 2.5). This is perhaps due to the exclusion of Fe-Oxides (due to the lack in EPMA compositional measurements) during the MapComp analyses. For most of the oxides, the relative changes are minimal, but oxides with low concentration (e.g., Na_2O and TiO_2) exhibit relatively large deviations (Fig. 2.8c; Tab. 2.5). 'Area I_1' shows large absolute changes for Al_2O_3 and SiO_2 even though the relative

	Compositionally Heterogeneous Rock III: SPI1321		
	EPMA XRF - AreaI_2	MapComp - AreaI_2	Relative changes in oxide wt%
Al_2O_3	12.94	13.16	1.68
CaO	6.43	6.74	4.90
FeO	6.25	6.34	1.44
K_2O	1.24	1.26	2.02
MgO	5.79	5.24	9.54
MnO	0.15	0.16	9.17
Na_2O	3.19	3.32	4.00
SiO_2	60.00	60.15	0.25
TiO_2	0.36	0.35	1.93
SUM	96.35	96.73	0.39

Table 2.6 – Major oxide weight percentage calculated for 'Area I_2' in Compositionally Heterogeneous Rock III (SPI1321) using both the EPMA XRF map and MapComp. Relative changes are calculated using MapComp derived oxide weight percentage normalized to oxide weight% calculated using EPMA major element map for the same area.

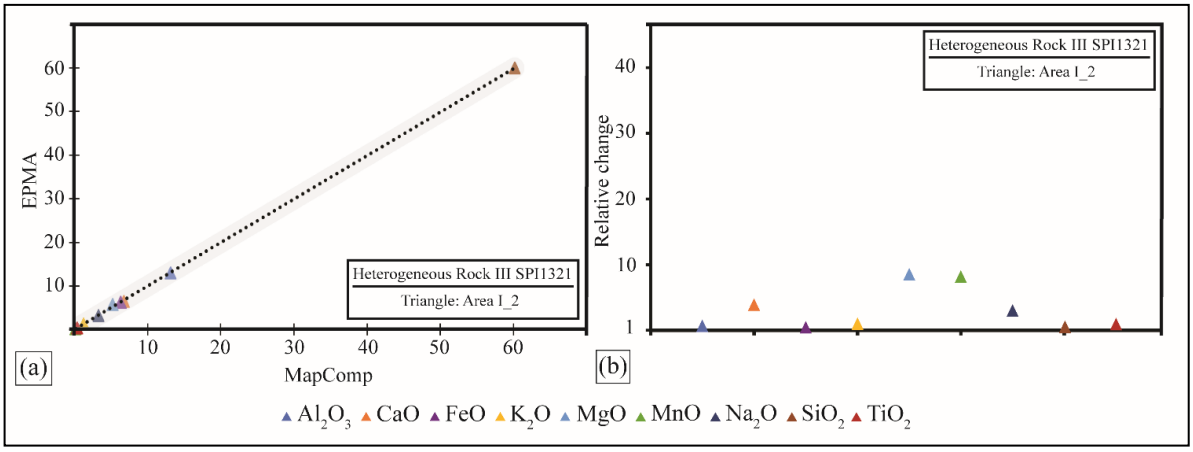

Figure 2.10 – Comparison between major oxide weight percentage calculated using MapComp and EPMA major element map for 'Area I_2' in the Heterogeneous Rock III: Diorite gneiss (SPI1321). (a-b) Absolute and relative deviations in MapComp derived oxide weight percentage. To derive the relative changes MapComp major oxide values are normalized to oxide weight% calculated using EPMA major element map.

deviations are very little (Fig. 2.3b; Tab. 2.5). However, higher degree deviations are again observed for Na_2O and TiO_2. This is also true for 'Area II_1' in 'Domain II', where the differences are highlighted by a shift in the mineral modal abundance in comparison to 'Domain I' or the whole thin section area (Fig. 2.3b; Tab. 2.5). For isochemical phase diagrams, mineral proportions and compositions are typically obtained via electron microprobe analysis (EPMA) of a 2D thin section; however, it is unlikely that the observed mineral proportions will match those present in a 3D volume, even if the thin section is cut from the same block used for XRF analysis. Hence, the conventional XRF analyses are also subjected to errors. However, a small overall variation in bulk composition can be predicted not to cause any major change in the isochemical phase diagrams. Thus, results from these two rocks indicate MapComp can be used as a suitable alternative to the traditional whole rock XRF for homogeneous and weakly heterogeneous rocks as long as the mineral modal abundances are similar.

For the *Compositionally heterogeneous rock II: amphibolite* (SPI1338) and *Heterogeneous rock III: Diorite Gneiss* (SPI1321), all the constituent minerals show the same chemical composition in both the compositional domains (Fig. 2.6a-e), however, the modal abundance of minerals vary between 'Domain I' and 'Domain II' (Fig. 2.4c, 2.5c). In both these rocks, MapComp provides very similar bulk composition for the same area/block used in conventional whole-rock XRF (Fig. 2.7e-h; Tab. 2.2). It is possible that the exclusion of Fe-Oxides during MapComp analyses in SPI1338 is the cause of a relatively large relative deviation in FeO. Different domains render differences in calculated local bulk rock composition (Tab. 2.5). In SPI1338, 'Area I_1', with slight variation in mineral modal abundance (than observed for the whole area), exhibits a maximum variation of ~ 6 weight% in SiO2 compared to the whole rock XRF (Fig. 2.9a; Tab. 2.5). Even though the relative deviation is found only ~10% (Fig. 2.9b), it can become crucial when obtaining isochemical phase diagrams. Similar to SPI1399A and SPI1382, Na_2O, and TiO_2 exhibit smaller absolute changes but more significant relative deviations when compared to SiO_2 (Fig. 2.9b). MapComp derived major oxide values from 'Area II_1', with very different mineral modal abundances, show the highest degree deviations in both absolute and relative major oxide values. For Na_2O and K_2O in 'Area II_1', relative deviations reach as high as 263% and 110%, respectively (Fig. 2.9b; Tab. 2.5). This can be correlated to the greatest degree change in modal abundance of plagioclase and hornblende. Thus, it can be confirmed that a change in phase proportions influence local bulk composition. Relative deviations for MnO and

TiO_2 are also higher compared to their corresponding values for whole area and 'Area I_1'. Thus, while there is little difference in MapComp bulk composition between the whole area and 'Area I_1', 'Area II_1' has remarkably different local bulk composition due to a large change in mineral modal abundance. Calculating local bulk chemistry from different domains is impossible with a conventional whole rock XRF, especially when domains are indistinguishable with the naked eye and/or mechanical separation cannot be performed with confidence, as in compositionally *Layered rock I: amphibolite (SPI1382)* and compositionally *Heterogeneous rock II: amphibolite (SPI1338)*. A smaller area ('Area I_2' in Fig. 2.4c) in 'Domain I' with very similar mineral modal abundance (compared to 'Area I_1') and similar local bulk chemistry (Fig. 2.8d; Tab. 2.5) supports our previous observation that areas with sides ~20 times the maximum grain size is favorable for MapComp analyses. MapComp derived major oxide values in 'Domain I' differ from those in 'Domain II' for *Heterogeneous rock III: Diorite Gneiss* (SPI1321). Due to higher modal abundance of quartz and plagioclase (Fig. 2.5c), 'Area II_1' in 'Domain II' has a ~6.5% increase in SiO_2 weight percentage (Fig. 2.9c-d; Tab. 2.4). Relative deviations are also significantly higher where all oxides (except SiO_2) have a large relative deviation of more than 20%. Hence different 'Domains' within the thin section can cause major changes in the local bulk chemistry, which can only be detected using MapComp. Local bulk chemistry measured using EPMA X-ray map from 'Area I_2' within 'Domain I' in the *Heterogeneous rock III: Diorite Gneiss* (SPI1321) also yields very similar results when compared to the MapComp calculated values for the same area (Fig. 2.10a; Tab. 2.6). The relative deviation in measured oxide weight percentage between these two methods is very small (<10%) (Fig. 2.10b; Tab. 2.5). This is also true for elements with low concentration (e.g., Na_2O and TiO_2) (Fig. 2.10d; Tab. 2.6). This suggests that the low intensity µXRF X-ray maps can be used in place of high intensity EPMA X-ray maps for local bulk chemistry determination, even though EPMA X-ray maps have much better spectral resolution. This is also true for oxides of lighter elements (e.g., Na_2O, K_2O), for which EPMA X-ray maps with high count rates are typically preferred.

2.4.2. Determination of local chemical composition using a MapComp approach: Opportunities and Recommendations

MapComp is a combination of qualitative microXRF X-ray elemental map and quantitative EMPA spot analyses using a software package of XMapTools (Fig. 2.1). The measured oxide values (obtained using the same thin section block) for the entire thin section area agree well with the whole rock XRF values. Equilibrated volume is often considered based on petrographic observations for heterogeneous rocks with variable mineral modal abundances. X-ray fluorescence (XRF) is a conventional technique for bulk chemistry determination; however, it cannot be easily applied to millimeter-scale compositional domains within rocks. In contrast, MapComp preserves textural information, making it an effective tool not only for very small domains but also when domains are transitioning or have complex shapes. In contrast to X-ray fluorescence (XRF), MapComp is a non-destructive and highly scalable technique to create quantitative chemical maps. Here case studies are provided on how this method can be used to quickly determine the local bulk chemistry of individual domains in rocks with textural heterogeneity. As a result, it is possible to study various equilibrated domains within heterogeneous rock samples directly from the thin sections. The formation process of small-scale inhomogeneities may record a key metamorphic event and can be retrieved by combining textural information and local bulk chemistry from quantitative µXRF maps using this technique. Additionally, this gives the user the freedom to change an estimated equilibrated volume at a later time and makes it very simple to calculate the local bulk rock chemistry for any new domain. Similar major oxide weight percentage values are estimated for the same studied area using MapComp and EPMA X-ray map for *Heterogeneous rock III: Diorite Gneiss* (SPI1321). Even though the X-ray counts of lighter elements in EPMA map are roughly 20-30x higher than in microXRF X-ray maps, the major oxide values of lighter elements are similar. Hence this method can reliably substitute the necessity of obtaining qualitative and/or quantitative EPMA maps for local bulk chemistry calculation.

Here, minerals with intense chemical zoning (except the amphiboles in *homogeneous mafic gneiss* SPI1399A) are not seen. However, this requires careful consideration, and a large number of EPMA spot analyses must be performed to cover the whole range of textural and compositional heterogeneity. In this study, the standard points are taken from the rim and core of each mineral phase for this particular purpose. For

producing a trustworthy result, this is highly advised. A detailed investigation on this is beyond the limit of this study and may provide a future scope of investigation. To classify pixels, both the 'normalized' and 'classical' approaches must be followed, and different masks should be derived. The ones that best represent the observed mineral associations from the petrographic observation must be selected for further analyses. The composition of the pixels at the contact between two phases are not always accurate, and hence are avoided during classification. To ensure that the photon values are accurately transferred to the weight percentage, the method of map calibration and standardization also needs to be meticulously examined. This process requires time. Internal standards that correlate poorly must be excluded without drastically reducing the total number of standards for a specific mineral phase, as doing so will decrease the overall quality of the standardization. Additionally, the composition of each mineral phase must be examined (either by choosing an area within a specific mineral grain or a group of related grains), and any discrepancy in the major oxide values must be corrected. Here minor phases (such as apatite, ilmenite, and Fe-oxides) are avoided, but when present widely, they must be included in the mineral list. When the oxide sum in MapComp is close to 96-99%, it has been found that the calculated major oxide weight percentage corresponds well with the bulk rock XRF measurements. However, LOI (loss of ignition) values cannot be measured using the MapComp approach. Low count rates for Na_2O, MgO, and K_2O can pose serious issues that need to be verified in future research. It has been observed that for lighter elements (Na_2O and K_2O) and for oxides with low concentration (TiO_2), the relative differences in oxide weight percentage between these two methods are much higher (Fig. 2.8a-b). This is due to a low count rate of lighter elements during µXRF X-ray mapping. Therefore, minerals that are extremely sensitive to minor change in Na_2O, K_2O, and TiO_2 weight percentage must be dealt with caution. The difference between MapComp and traditional XRF-derived values for Na_2O in all the studied samples is notably higher than observed in the other oxides, necessitating careful consideration. This difference applies to elements with low count rates. To prevent any overestimation or underestimation in the measured values, it was ensured that the standards were uniformly distributed and covered both the low and high counts of sodium (Na) in the plagioclase grains. As Na_2O is only concentrated in the plagioclase grains in all the studied samples, it did not pose a significant threat. However, introduction of other Na-rich minerals, such as Na-rich amphibole, can be problematic and needs further research. MicroXRF has a detection limit of 10ppm, and hence the concentration of minor oxides/ trace elements cannot be assessed with this method. The other limiting factor is the grain size range to

which this method can be applied. The highest resolution of microXRF X-ray map is 15µm; thus, if the spatial resolution of the X-ray map is sufficient to separate mineral phases, this technique can be applied to coarse-grained rocks. It is possible that fine-grained schists with extensive recrystallization or areas with symplectite will not produce viable results.

2.5 Conclusion

- MapComp shows a remarkably similar major oxide weight percentage compared to the conventional whole rock XRF when measured for the same area in both the homogeneous and heterogeneous samples.
- The advantage of using MapComp over conventional whole rock XRF is its flexibility in choosing an area and determining local bulk chemistry of that specific domain very quickly.
- The advantage of MapComp over EPMA X-ray maps for bulk chemistry determination is its cost effectiveness. X-ray maps obtained using SEM (Scanning Electron Microscopy) with EDS (Energy Dispersive X-ray Spectrometry) and Electron probe micro analyzers are expensive, with high running costs. Once the sample is prepared, SEM-EDS can take a day to measure more than a couple of square centimeters. While creating a quantitative X-ray map by collecting quantitative point analyses requires an unrealistically extended period. A typical point analysis requires ~ 1 min for 10 elements (e.g., Si, Cr, Fe, Ti, Al, Mg, Mn, Ca, Na, and K), and approximately one week would be needed to create a 100 × 100-pixel map (Yasumoto et al., 2018). Since EPMA provides a better count rate, the intensity maps are still extremely useful for detailed quantitative and qualitative chemical characterization and particularly for elements with incredibly low concentrations.
- The presented method is limited by the spatial resolution and trace element detection limit of micro XRF data, commonly in the order of 15 µm and 10 ppm.

Chapter 3

Testing the proposed terrane boundary between the Mesoarchean Akia terrane and the Alanngua complex, West Greenland: Insights from P-T estimates derived from amphibolites

The following chapter is currently planned to be submitted as a Greenland Geological Survey Report after the thesis defense. As such, it is written for the most part as an independent work, resulting in some repetition with respect to other chapters of this thesis. The authors and their contributions to this chapter are as following: Joyjit Dey (sample collection, petrographic, SEM, whole rock geochemical and EPMA data collection, conceptualization, data analysis, original draft, figures, review, and editing), Dominik Sorger (conceptualization, supervision, thermodynamic modelling), Thomas Müller (supervision, review, and editing), and Sandra Piazolo (sample collection, conceptualization, review, and editing).

Abstract

The Meso-Neoarchaean (3.3–2.9 Ga) Akia terrane lies adjacent to the 2.9–2.5 Ga Tuno terrane in West Greenland. Recent work suggests that between these two terranes the Allanngua complex represents a terrane boundary complex, which amalgamated with the Akia terrane during Neoarchean terrane assemblage. It is suggested that the Kangerluarsuk

Supracrustal Belt, which underwent prolonged high-temperature metamorphism reaching ~820–850 °C and 0.8–1 GPa during regional ductile deformation. To characterize peak metamorphic conditions and to contrast and compare the metamorphic evolution of the Allangua Complex to that of the Akia terrane, we study amphibolites exhibiting melt microstructures from these two areas. Our results confirm the general medium to high pressure, syn-melt conditions at 760-812 °C and 0.61-0.76 GPa for the Alanngua complex, whereas P-T conditions are less well constrained for the Akia terrane at >760 °C and 0.8 GPa. Accordingly, the proposed boundary complex and the Akia terrane underwent similar peak conditions suggesting amalgamation at the time of peak metamorphism.

3.1 Introduction

It is believed that the Archean cratons developed by the juxtaposition of heterogeneous crustal blocks or 'terranes' that formed at distinct times and possibly in distinct geodynamic settings (Bleeker, 2003; Friend et al., 1988b). The North Atlantic Craton (NAC) of West Greenland in the Nuuk region comprises a series of Eo-Neoarchean crustal gneissic terranes accreted during the late Neoarchean (Friend and Nutman, 1994, 2005; Friend et al., 1996). Based on combined geochronological, metamorphic, and structural studies, Friend and Nutman (2019) demonstrated that the Archean gneiss complex in this region exhibits repeated cycles of crust production with magma formation in a convergent setting and repeated amalgamation of crustal blocks resulting in collisional orogeny. However, the details of crustal amalgamation and metamorphic conditions are still hotly debated (e.g., Gardiner et al., 2019; Yakymchuk et al., 2020; Steenfelt, 2021).

The Akia terrane is one of the northernmost crustal blocks in the NAC and is located north of capital Nuuk (Figure 3.1). (Friend et al., 1988; McGregor et al., 1991). The Akia terrane is bounded to its north by the Meso-Neoarchean Tuno terrane (Yi et al., 2014) and to its south by several Eo-Mesoarchean terranes of the Nuuk region, which amalgamated in the early Neoarchean (Friend et al., 1996; Friend and Nutman, 2005). The Akia terrane hosts a significant proportion of diorite gneiss in addition to tonalitic-trondhjemitic-granodioritic (TTG) gneisses and late-tectonic diorite, tonalite, and granitic rocks. The terrane experienced at least two major phases of crustal growth: a diorite phase – the Nordlandet diorite with magmatic ages of 3.22-3.18 Ga exposed in the southern Akia terrane (Garde et al., 2000), and a massive tonalite body dated between 3.05 and 3.02 Ga exposed in the

Finnefjeld region (Garde et al., 2000, 2012b). Akia terrane experienced at least three metamorphic events. A rapid high-T, low-P, granulite facies metamorphism occurred during or after the emplacement of the nascent tonalite crust at 2.99-2.97 Ga. (Friend and Nutman, 1994; Garde et al., 2000). The tonalite components are currently exposed as orthogneisses and are tectonically intercalated with supracrustal rocks (such as the Kangerluarsuk supracrustal belt in the north and the Storø supracrustal belt in the south) along with mafic-ultramafic intrusive complexes. The supracrustal rocks are interpreted as remnants of arc-related oceanic crust, whereas the precursor of orthogneiss intruded within a convergent plate tectonic regime (Garde 1990, 1997; Szilas et al., 2017). Based on phase equilibria modelling, Kirkland et al. (2018a) interpret the Kangerluarsuk rocks within Akia terrane to have been deposited onto a basement of 3.0 Ga tonalite (with rare c. 3.2 Ga diorite) and buried to > 30 km depth where they experienced peak P-T conditions of 820-850 °C and 0.8-1 GPa. Yakymchuk et al. (2020) reported orthopyroxene-bearing metamorphic assemblages consistent with suprasolidus conditions at pressure 0.8 GPa and temperature > 750 °C for the high T, high P metamorphic event. This second metamorphic event was followed by a 2.63 Ga metamorphism with loosely constrained conditions between > 450°C and <850 °C, which produced volumetrically minor cross-cutting granitic magmatism. This occurrence also indicates terrane accretion (Nutman and Friend, 2007).

Steenfelt et al. (2021) introduced a new subdivision of the Akia terrane, based on the existence of a 'distinct crustal segment' in the northern portion of the Akia terrane, which is comprised of folded orthogneiss and a higher population of metasedimentary rocks called the Alanngua Complex (Fig. 3.1). The Alanngua Complex appears on their revised terrane map between the Tuno and Akia terranes to the north and south, respectively. However, it is currently unknown how the Alanngua Complex is related to the Akia terrane and whether it shares the same metamorphic evolution as the Akia terrane or forms a separate terrane. One way to gain insight is to characterize and compare the metamorphic history of supracrustal sequences associated with the Alanngua complex to potential supracrustal portions of the Akia terrane. Most metamorphic studies in the Akia terrane have so far concentrated on TTG rocks, with an emphasis on the timing and nature of granulite facies metamorphism (Garde et al., 2000; Garde, 2007; Yakymchuk et al., 2020), but little work has been done on the nature of metamorphism of the metasedimentary unit (Dyck et al., 2015; Kirkland et al., 2018a).

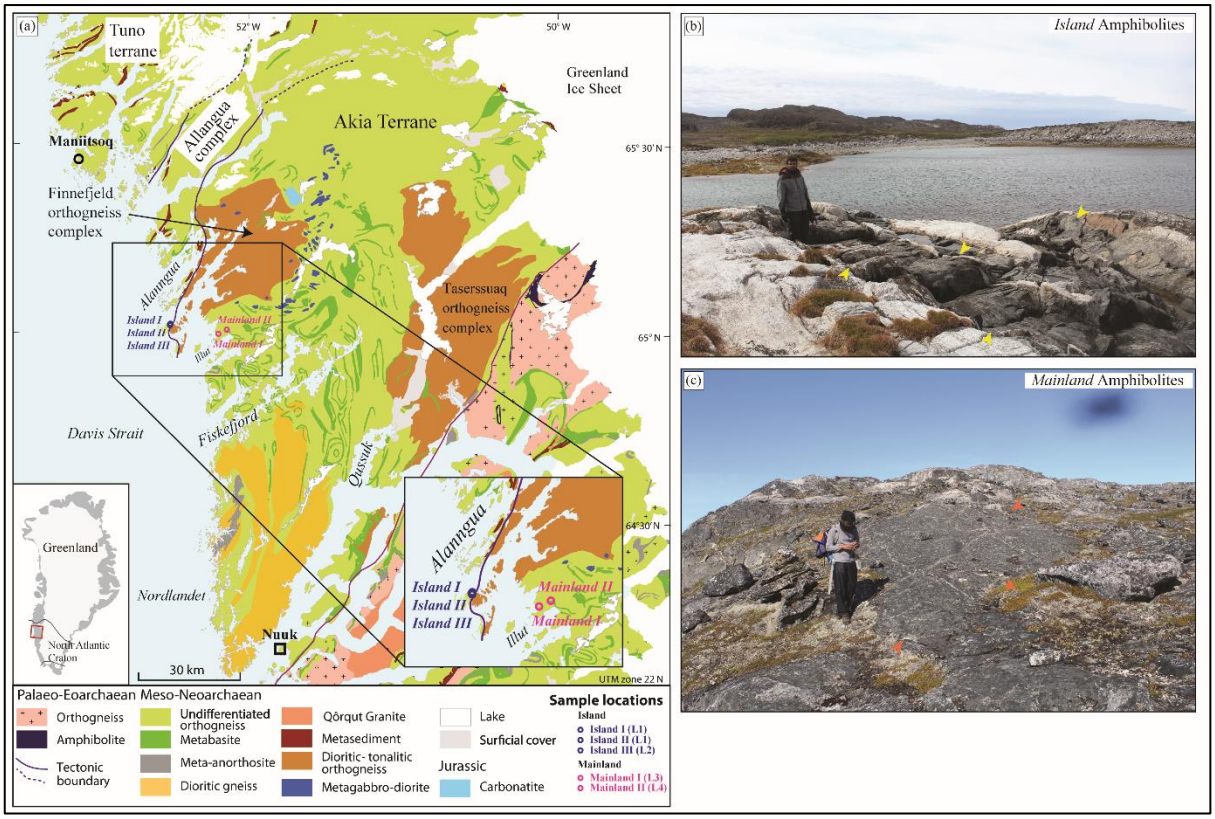

Figure 3.1 – Simplified geological map and field photographs of the studied samples. (a) Geological map of the Nuuk region, with major terranes, lithological units marked and samples for this study identified. Amphibolite samples from the *Island* within the Alanngua melange zone are in blue text, and those from the *Mainland* within the Akia terrane are in red text. Geology based on geological maps published by Geological Survey of Greenland with modified after Gardiner et al. (2019). Location of Alanngua complex and its tectonic boundaries are marked following Steenfelt et al. (2021). (b-c) Island amphibolites are elongated bodies (yellow arrows) associated with parallelly oriented metapelitic and metapsammite rocks. Mainland amphibolites occur as massive bodies (red arrows).

Here, we present field, microstructural, and phase equilibria data from two different amphibolite sample sets: The first set is from the supracrustal sequence of the Alanngua complex near the island of Napasoq, and the second set is from the mainland, well within the Akia terrane (Fig. 3.1). The primary objective is to characterize and compare the peak pressure-temperature conditions of these two regions to evaluate their geotectonic setting.

3.2 Sample selection

We chose representative samples for each of the distinct terranes proposed. The three "island samples" are collected from representative amphibolites from the supracrustal belts of Alanngua complex at two locations (Sample localities- L1: N65° 02' 15.9", W052° 27'

31.0" and L2: N65° 02' 16.0", W052° 27'; Fig. 3.1). Another two representative amphibolite samples are also obtained from amphibolite bands in the TTG gneisses south of the Finnefjeld complex in the Akia terrane (Sample localities- L3: N65° 00' 26.8", W052° 09' 06.2", L4: N65° 01' 02.3", W052° 06' 56.0").

3.3 Field relationships

On the island of Napasoq, amphibolites are found as elongated bodies associated with parallelly oriented (SE-NW trending) interlayered sequence of supracrustal rocks each 30-80 metres in width. They include biotite gneisses, pyroxene-hornblende gneisses, garnet-, and biotite bearing schists, migmatites and a thin sliver of ultramafics at the north-western side of the island (refer to Fig. 4.1 in Chapter 4). Two garnet-bearing samples *Island I* (SPI1338), and *Island II* (SPI1340) are collected from the same elongated amphibolite body (Fig. 3.1b). Samples are medium to coarse grained with a well-developed foliation (118-125°/80-85° SW). At the outcrop scale, the rock is dark green to black exhibiting discontinuous leucocratic, quartzo-feldspathic bands with variable width subparallel to the foliation formed by the alternation of felsic layers (Fig. 3.2a) and oriented amphibole grains which form a lineation (70° → 190°). While *Island I* represents the host to a few quartzo-feldspathic bands (5-10 vol.%) and small garnet grains visible only adjacent to the felsic veins (Fig. 3.2a), *Island II* has ~10cm continuous veins and segregated patchy felsic fractions (Fig. 3.2b). In this sample, garnet grains are evenly distributed throughout the whole rock, with more abundant garnet grains parallel to foliation (Fig. 3.2b). In other areas (see arrow in Fig. 3.2b) garnet grains are smaller and are characterized by higher population of amphibole + biotite. Aside from these zones of occurrence and relative proportion of garnet grains, there is no discernible difference in the overall appearance of *Island I* and *II*. Approximately 150 meters away from the sample locality of L1, at L2, a clinopyroxene bearing amphibolite occurs as a sandwich between thick two-pyroxene gneiss, *Island III*, SPI1341B. The rock is medium to coarse grained with its foliation defined by alternating felsic and amphibole/clinopyroxene rich layers (Fig. 3.2c), while the lineation is defined by the elongated amphibole grains. The rock is overall homogeneous with large, visible clinopyroxene grains occurring in some undeformed, elongated felsic zones (Fig. 3.2c).

In the mainland, within the Akia terrane sensu stricto, two pyroxene amphibolites (*Mainland I* SPI1399A from L3 and *Mainland II* SPI1382 from L4; near Illut in Fig. 3.1a)

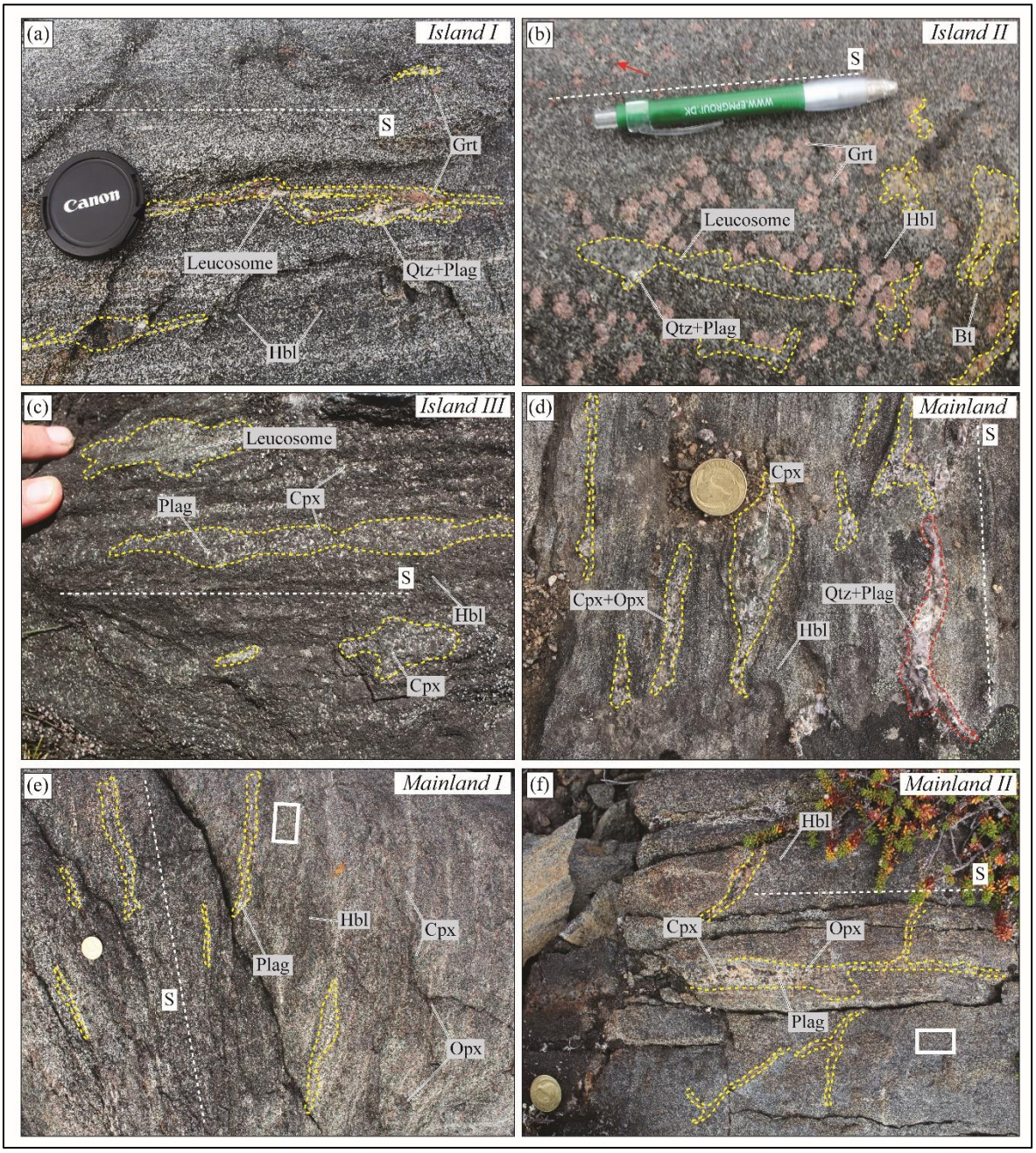

Figure 3.2 – Field photographs of *Island* and *Mainland* amphibolites with felsic veins parallel to the host foliations. All the felsic veins are marked with yellow dotted lines. (a) *Island I* with thin, elongated felsic veins parallel to the host foliation (S1). Observe the garnet (Grt) grains in the felsic veins, but the host is nearly devoid of any garnet. (b) *Island II* contains quartzofeldspathic fractions as elongated veins or random patches. Compared to *Island I*, a relatively higher population of garnet grains is observed. The garnet grains are evenly dispersed throughout the host, but the grain sizes vary between layers (red arrow). (c) *Island III* with elongated pale felsic veins parallel to the host foliation (S). Felsic veins exhibit clinopyroxene (Cpx) grains with larger grain sizes than the host. (d) The foliations (S1) in *Mainland* amphibolites are defined by elongated amphibole (Amp) grains. Large clinopyroxene (Cpx)-orthopyroxene (Opx) grains are observed in foliation parallel elongated veins. Quartzofeldspathic pegmatitic veins (depicted by red dashed lines) occur parallel to or occasionally transverse to the host foliation. (e-f) *Mainland I* has leucocratic veins that are elongated. The veins in *Mainland II* are disorganised and of variable thickness. White boxes indicate locations for thin sections (not in scale).

were collected from two large, thick, elongated (100-400 metre in width and a few kilometres in length) amphibolite bodies which in this area are intercalated with the dominant TTG gneiss (Fig. 3.1c). The rocks are dark brown in appearance with characteristic foliation (210-220°/70-75° SE) parallel to the general trend (225°) of these bodies and consist mainly of amphibole + plagioclase + clinopyroxene + orthopyroxene. A compositional change, in the centimetre scale, from amphibole + plagioclase to amphibole + plagioclase + clinopyroxene ± orthopyroxene is observed in association with clinopyroxene + plagioclase ± orthopyroxene bearing, subparallel to foliation veinlets. These occur either as 1x5 cm lenses, with 0.5 cm large clinopyroxene grains, or as continuous veinlets of 2-5 mm width (Fig. 3.2d). Amphibolites are variably intruded by cross-cutting, non-reactive, undeformed fine-grained homogeneous plagioclase ± quartz felsic veins (Fig. 3.2d-f). *Mainland I* (SPI1399A) stems from a homogeneous rock without any visible felsic vein (Fig. 3.2e). *Mainland II* (SPI1382) is collected from a relatively homogeneous block, nearly 2 kilometers away from SPI1382, and have no noticeable leucocratic vein in its vicinity (Fig. 3.2f). It is part of a different amphibolite layer than *Mainland I*.

Melt present peak conditions

Garnet grains in *Island I and II* are spatially associated with the leucocratic veins (Fig. 3.2a-b). In Island III large clinopyroxene grains are also observed within the felsic vein (Fig. 3.2c). Mainland amphibolites are transected by undeformed elongated felsic veins parallel to the host foliation (Fig. 3.2). These associations of quartzofeldspathic veins within the *Island* and *Mainland* samples are consistent with incongruent melting of hydrous Fe-Mg minerals (e.g., biotite and amphibole) and generation of anhydrous peritectic minerals (e.g., garnet, clinopyroxene and orthopyroxene) and melt (Brown, 2013). Reactants (amphibole, plagioclase, biotite, and quartz) are usually found as inclusions inside garnet, clinopyroxene and orthopyroxene grains, which is compatible with incongruent melting reactions and imply a partial melting process (Sawyer, 2001). Pressure-temperature estimates from previous studies also confirm granulite facies condition with features of incipient partial melting within metasedimentary and metabasic rocks (e.g., Kirkland et al., 2018a; Palin et al., 2016a). Thus, macroscopic features of island amphibolites suggest the peak metamorphic assemblages were in equilibrium with a melt phase.

3.4 Petrography including determination of distinct compositional zones

3.4.1 Island Amphibolites

Island I (SPI1338): Garnet bearing amphibolite

Island I (SPI1338) is a heterogeneous sample with a 0.5 cm wide garnet bearing vein. The felsic veins (with and without garnet grains) are referred to as 'Zone 2', while the matrix grains are referred to as 'Zone 1'. The thin section contains a ‘Zone 2’ felsic vein with garnet grains to the left, and another ‘Zone 2’ felsic vein is demarcated by a high population of quartz-plagioclase to the centre (Fig. 3.3a). The composition of 'Zone 1' is 47% amphibole, 24% plagioclase, 25% quartz, 1% biotite, 2% garnet, 0.5% clinopyroxene, and 0.5% ilmenite (Fig. 3.3a). The grain sizes of amphibole, plagioclase, quartz, biotite, garnet and clinopyroxene grains vary between 0.2-0.8 mm, 0.5-0.7 mm, 0.25-0.4 mm, 0.05-0.1 mm, 0.3-0.5 mm, and 0.2-0.5 mm, respectively. The grains of amphibole are inequigranular, subhedral to anhedral, and elongated, forming the foliation (Fig. 3.3a). The grain boundaries are irregular and contain embayments (green arrows, Fig. 3.4a). Biotite is long, elongated and is intergrown with amphibole grains. Clinopyroxene grains are subhedral and are intensely replaced by amphibole grains (Fig. AP3 – 1). Plagioclase grains are subhedral and have characteristic polysynthetic twins (Fig. 3.4b). Quartz grains are bimodal in grain size (Fig. 3.4b). Small grains are found as anhedral, interstitial grains along the grain boundaries of other minerals (orange arrow in Fig. 3.4b), as well as large anhedral grains (0.5-0.8mm) with cuspate and straight grain boundaries (green arrows and blue arrows respectively in Fig. 3.4b). Low dihedral angles are also observed in quartz grains (Fig. 3.4b). These characteristics indicate that quartz crystallized from melt. Large quartz grains (up to 1 mm) account for 35-40% of the area in the garnet-bearing ‘Zone 2’ (Fig. 3.3a). Within that felsic vein, garnet grains are visible as large porphyroblasts with anhedral quartz grains and subhedral plagioclase grains along their sides (Fig. 3.3a, 3.4c). Garnet grains have irregular to straight faceted grain boundaries and amphibole, plagioclase, and biotite inclusions (blue arrows, Fig. 3.4c). Thus, phase relationships indicate that the interpreted peak metamorphic assemblage in ‘Zone 1’ includes amphibole, plagioclase, quartz, biotite, and ilmenite.

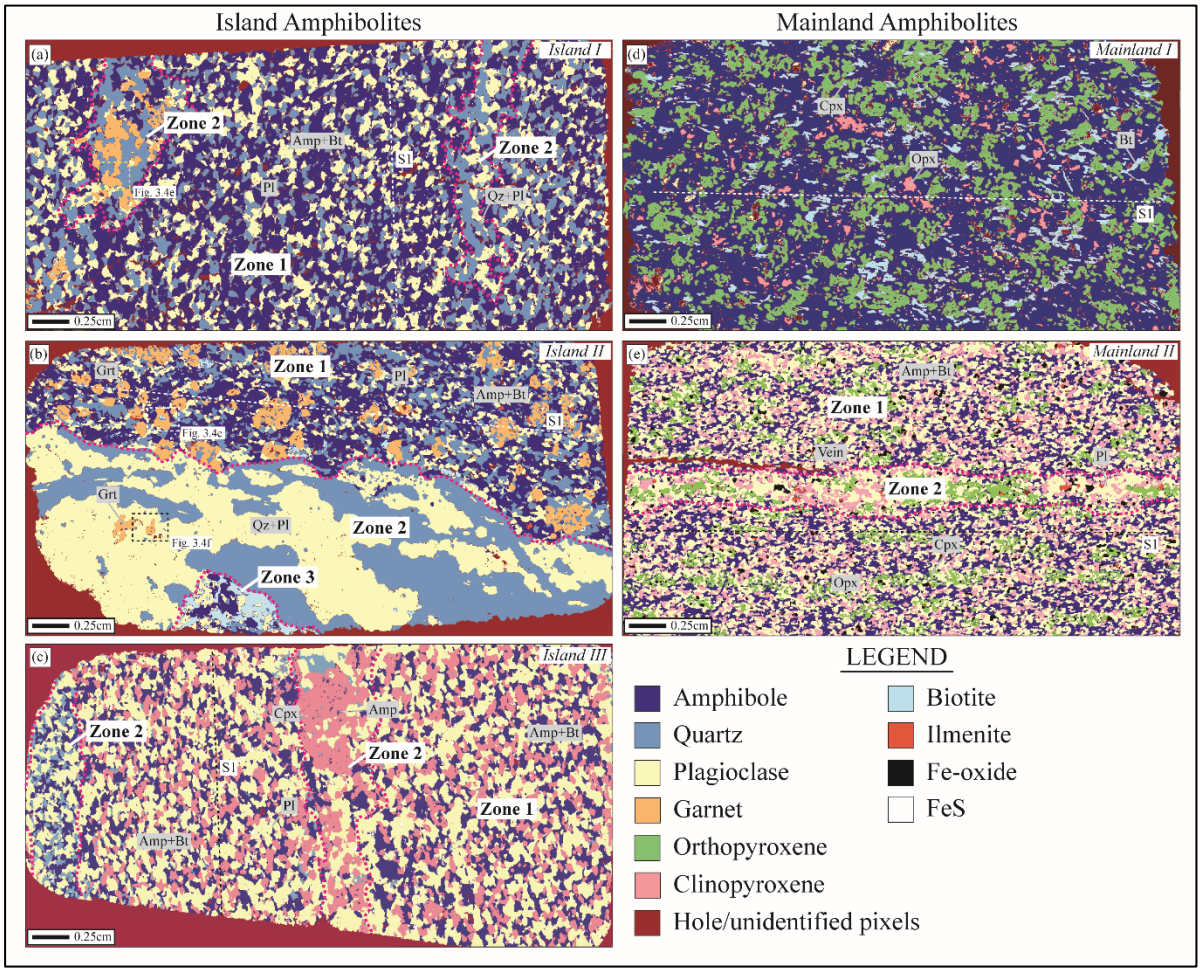

Figure 3.3 – Micro-XRF phase maps of the amphibolite samples studied. 'Zone 2' leucocratic veins are marked with red stippled lines. (a) In *Island I*, 'Zone 2' is made up of leucocratic veins with varying proportions of quartz, plagioclase, and garnet grains parallel to host-foliation (S1). (b) In *Island II*, 'Zone2' represents felsic vein parallel to the host foliation. (c) In *Island III*, central 'Zone 2' leucocratic vein has large clinopyroxene grains and 'Zone 2' felsic vein with high population of quartz is visible in the left corner. Both 'Zone 2' veins are elongated parallel to host foliation (S1). (d-e) *Mainland I* and *Mainland II* have uniform distribution of clinopyroxene-orthopyroxene grains, with elongated amphibole grains forming the foliation (S1). 'Zone 2' with large population of plagioclase grains is observed in *Mainland II*. The MapComp local bulk rock geochemical analysis disregards regions corresponding to compositional veins in 'Zone 2'.

Island II (SPI1340): Garnet bearing amphibolite

Island II is compositionally heterogenous with a foliation-parallel large felsic vein (Fig. 3.3b). The host of this rock is identified as 'Zone 1' while the felsic vein is termed as 'Zone 2' (Fig. 3.3b). 'Zone 3' refers to a small region near the base of the sample (marked with a yellow rectangle in Fig. 3.3b). The 'Zone 1' comprises 44.5% amphibole, 16% plagioclase, 23% quartz, 2% biotite, 14% garnet, and 0.5% ilmenite (Fig. 3.3b). 'Zone 2' is

1 cm wide with 44% quartz, 55% plagioclase, 1% garnet. Amphibole, plagioclase, quartz, biotite, and garnet grains in 'Zone 1' are 0.3-0.7 mm, 0.1-0.6 mm, 0.1-0.5 mm, 0.05-1 mm, and 0.3-1.2 mm in size, respectively. Amphibole grains are subhedral and elongated, with predominantly straight grain boundaries. Some grains have irregular cuspate boundaries against plagioclase and quartz grains (green arrows, Fig. 3.4d). Small biotite grains are found along amphibole grain boundaries, whereas large grains are euhedral and have straight boundaries (Fig. 3.4d). Garnet grains occur as porphyroblasts in 'Zone 1' and are subhedral to euhedral in shape, with amphibole and biotite grains along their grain boundaries (Fig. 3.4e). Some anhedral elongated garnet grains are also observed. As small inclusions within the garnet, biotite, amphibole, quartz, and plagioclase grains can be found (Fig. 3.4e). Plagioclase grains are subhedral with regular grain boundaries in 'Zone 1', whereas quartz grains are polymodal and have different shapes. Quartz grains have xenomorphic grain shape (red arrows, Fig. 3.4e), occur as small, elongated films along grain boundaries with low dihedral angles (Fig. 3.4e), and show well developed facets (blue arrows, Fig. 3.4e) or cuspate grain boundaries (green arrows, Fig. 3.4e). These characteristics indicate that quartz crystallized from melt. Large plagioclase and quartz grains (up to 2 mm) are seen parallel to the foliation of the host amphibolite (Fig. 3.4f). Thus, the felsic vein likely pre-dates or is synchronous to the deformation that produced the foliation in the host amphibolite. . Elongated tabular garnet grains are found adjacent to plagioclase grains, with minor biotite and plagioclase grains as inclusions (Fig. 3.4f). 'Zone 3' comprises large, elongated biotite (termed as 'Bt2') and medium sized amphibole grains (termed as 'Amp2') with elongated quartz trails along their boundaries (Fig. 3.4g). Intergrowth of quartz and plagioclase grains is also seen (Fig. 3.4g). From the microstructural relationships, 'Zone 2' is interpreted to be in disequilibrium with 'Zone 1'. Thus, based on phase relationship the interpreted peak metamorphic assemblage includes garnet, amphibole, plagioclase, quartz, biotite, and ilmenite of 'Zone 1'.

Island III (SPI1341B): Clinopyroxene bearing amphibolite

Island III is a heterogeneous rock with large clinopyroxene and quartz grains in the leucocratic veins (designated as 'Zone 2'), while the host, termed as 'Zone 1', contains 25% amphibole, 41% plagioclase, 1% ilmenite, 9% quartz, and 24% clinopyroxene (Fig. 3.3c).

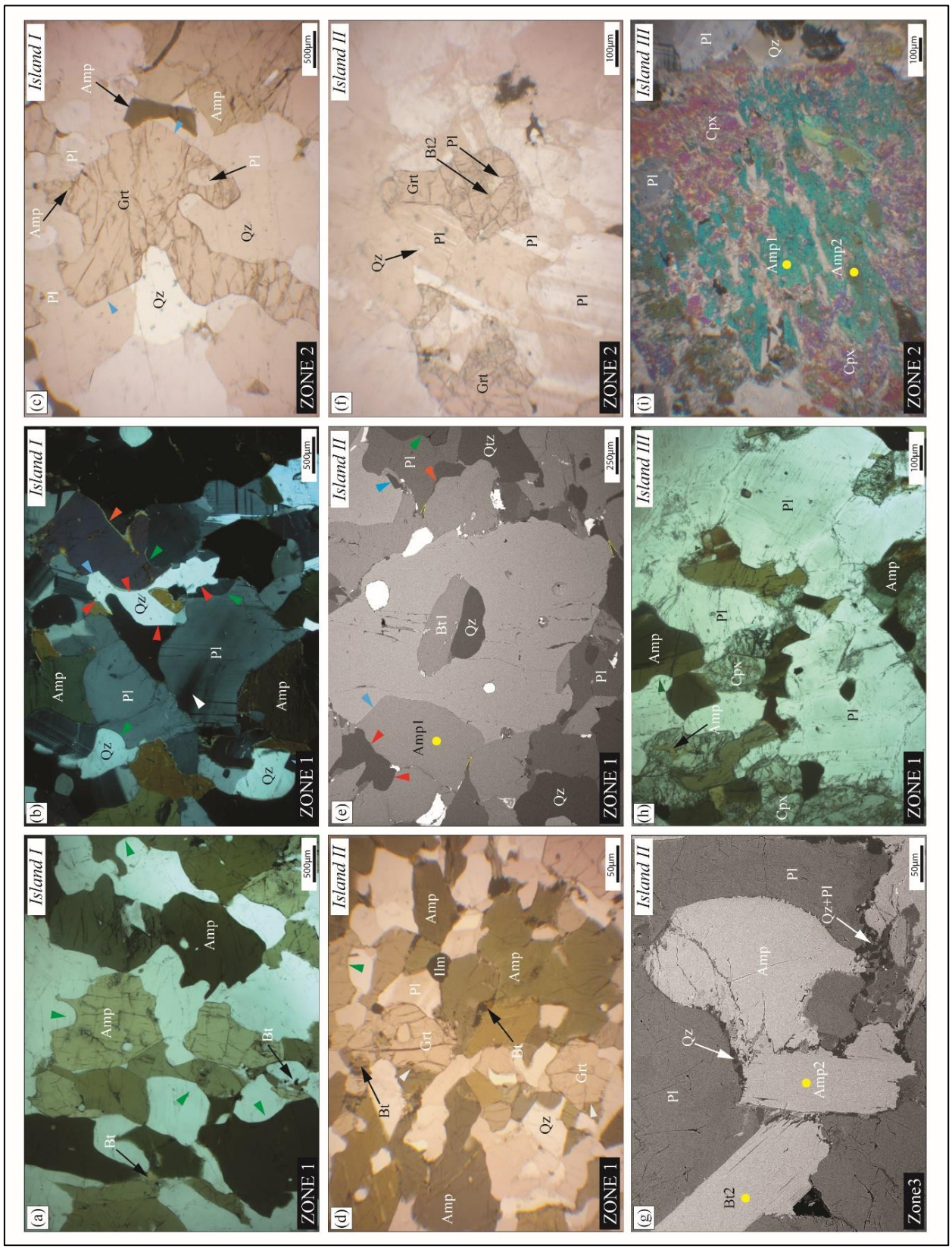
(a)
Island I
ZONE 1
500µm
Amp
Bt
(b)
Island I
ZONE 1
500µm
Amp
Pl
Qz
(c)
Island I
ZONE 2
500µm
Amp
Pl
Grt
Qz
(d)
Island II
ZONE 1
50µm
Amp
Bt
Ilm
Pl
Grt
Qz
(e)
Island II
ZONE 1
250µm
Amp1
Bt1
Qz
Pl
Qtz
(f)
Island II
ZONE 2
100µm
Grt
Bt2
Pl
Qz
(g)
Island II
Zone3
50µm
Bt2
Pl
Qz
Amp2
Amp
Qz+Pl
(h)
Island III
ZONE 1
100µm
Amp
Cpx
Pl
(i)
Island III
ZONE 2
100µm
Pl
Cpx
Qz
Amp1
Amp2

Figure 3.4 – Photomicrographs showing peak mineralogy and microstructures of island amphibolites (*Island I*, *Island II*, and *Island III* samples). (a-c) In *Island I*, (a) amphibole grains are elongated, irregular and contain embayments or have cuspate grain boundaries (green arrows). Biotite grains are spatially associated with amphiboles, (b) quartz grains are large xenomorphic (red arrows) and exhibit elongated grains as pseudomorphed 'melt films' (orange arrow), straight facets (blue arrows), and cuspate grain boundaries (green arrows) interpreted as former presence of melt. Plagioclase grains display undulose extinction (white arrows), (c) 'Zone 2' garnet grains are large, elongated, and anhedral, with minor surrounding amphibole grains. Plagioclase in 'Zone 2' are larger in size than in 'Zone 1'. Small plagioclase grains occur as garnet inclusions. (d-g) In *Island II*, (d) peak assemblage is defined by garnet + amphibole + biotite + quartz + ilmenite + plagioclase. Amphibole grains have cuspate grain boundaries (green arrow), (e) quartz grains with anhedral grain shape (red arrows), low dihedral angles (yellow dotted lines), and elongated grains along grain boundaries (orange arrow) indicate pseudomorphed melt films. Both quartz and plagioclase grains have cuspate grain boundaries. Garnet grains show straight facets (blue arrow) and have plagioclase-biotite-quartz inclusions, (f) garnet grains are subhedral, highly fractured and show irregular grain boundaries in 'Zone 2', (g) large, elongated biotite grains are seen in 'Zone3'. Quartz and plagioclase grains have intergrown texture, and elongated quartz grains along amphibole grain boundaries indicate former melt presence. Amphibole and biotite in 'Zone3' are compositionally different and termed as 'Amp2' and 'Bt2', respectively. (h-i) In *Island III*, peak mineral assemblage is defined by clinopyroxene + amphibole + quartz + plagioclase. Amphibole grains have cuspate grain boundaries (green arrow in 'h'). In 'Zone 2', large clinopyroxene grains have two types of amphibole inclusions (termed as 'Amp1' and 'Amp2').

In 'Zone 1', amphibole, plagioclase, quartz, and clinopyroxene grains are 0.3-0.6 mm, 0.4-1.5 mm, 0.5-0.7 mm, and 0.1-0.5 mm in size, respectively. Amphibole is subhedral with regular and/or cuspate grain boundaries (green arrow in Fig. 3.4h). Biotite grains are subhedral to euhedral and occur along amphibole grain boundaries (Fig. 3.4h). Plagioclase grains are subhedral with characteristic polysynthetic twins. Small quartz grains have cuspate grain boundaries or are found as long, elongated films indicating a former presence of melt. Large quartz grains with irregular grain boundaries are xenomorphic and mostly visible in 'Zone 2' felsic veins. Clinopyroxene grains are subhedral to euhedral with regular grain boundaries. They replace the amphibole grains and have small subhedral amphibole-biotite grains as inclusions (Fig. 3.4h). 'Zone 2' (the middle vein in Fig. 3.3c) constitutes 17% amphibole, 40% plagioclase, 38% clinopyroxene, and 5% quartz, where large, patchy clinopyroxene grains (0.6-1.2 mm) have amphibole grains as inclusions (Fig. 3.3c, 3.4i). Based on the difference in interference colour, two types of amphibole grains (labelled 'Amp1' and 'Amp2') are identified (Fig. 3.4i). The other vein is composed of 32% amphibole, 45% plagioclase, 5% clinopyroxene, and 18% quartz. It has an abundance of

irregular xenomorphic quartz grains characterizing former melt presence. From the microstructural relationships, the veins of 'Zone 2' are interpreted to be in disequilibrium with 'Zone 1'. Hence, the interpreted peak metamorphic assemblage within the 'Zone 1' includes clinopyroxene, ilmenite, amphibole, plagioclase, and quartz.

3.4.2 Mainland Amphibolites

Mainland I (SPI1399A): Orthopyroxene-clinopyroxene bearing amphibolite

Mainland I is compositionally homogeneous with a weakly developed foliation defined by the aligned amphibole and biotite grains (Fig. 3.3d). The rock comprises 64% amphibole, 0.5% plagioclase, 8.5% biotite, 3% clinopyroxene and 24% orthopyroxene (Fig. 3.3d). Grain size of amphibole, biotite, plagioclase, clinopyroxene and orthopyroxene grains are 0.5-0.9 mm, 0.15-0.7 mm, 0.05-0.4 mm, 0.4-0.8 mm, and 0.5-1 mm, respectively. Orthopyroxene-clinopyroxene grains have a medium to coarse grain size and are subhedral to anhedral in shape. They partially replace amphibole grains, causing zonation along the replacement boundaries (shown in Fig. 3.5b as 'Amp1' and 'Amp2'). These replacement textures are homogeneously distributed throughout the thin section. Plagioclase grains are subhedral to anhedral in shape, with xenomorphic grain boundaries indicating crystallization from melt (Fig. AP3 – 2). The interpreted peak metamorphic assemblage includes clinopyroxene, orthopyroxene, amphibole, plagioclase, and biotite.

Mainland II (SPI1382): Orthopyroxene-clinopyroxene bearing heterogeneous amphibolite

Mainland II is a heterogeneous rock with a compositionally different layer (termed as 'Zone 2') demarcated by a notable increase in grain size and difference in mineral modal abundance (Fig. 3.3e). The host rock (termed as 'Zone 1') comprises 28% amphibole, 45% plagioclase, 17% clinopyroxene, 8% orthopyroxene, 1.8% Fe-Oxide, and 0.2% Ilmenite (Fig. 3.3e). Grain size of amphibole, clinopyroxene, plagioclase, and orthopyroxene grains vary between 0.15-0.5 mm, 0.15-0.4 mm, 0.3-0.7 mm, and 0.1-0.5 mm, respectively. Amphibole grains are equigranular, subhedral, and have elongated to platy grain shapes with

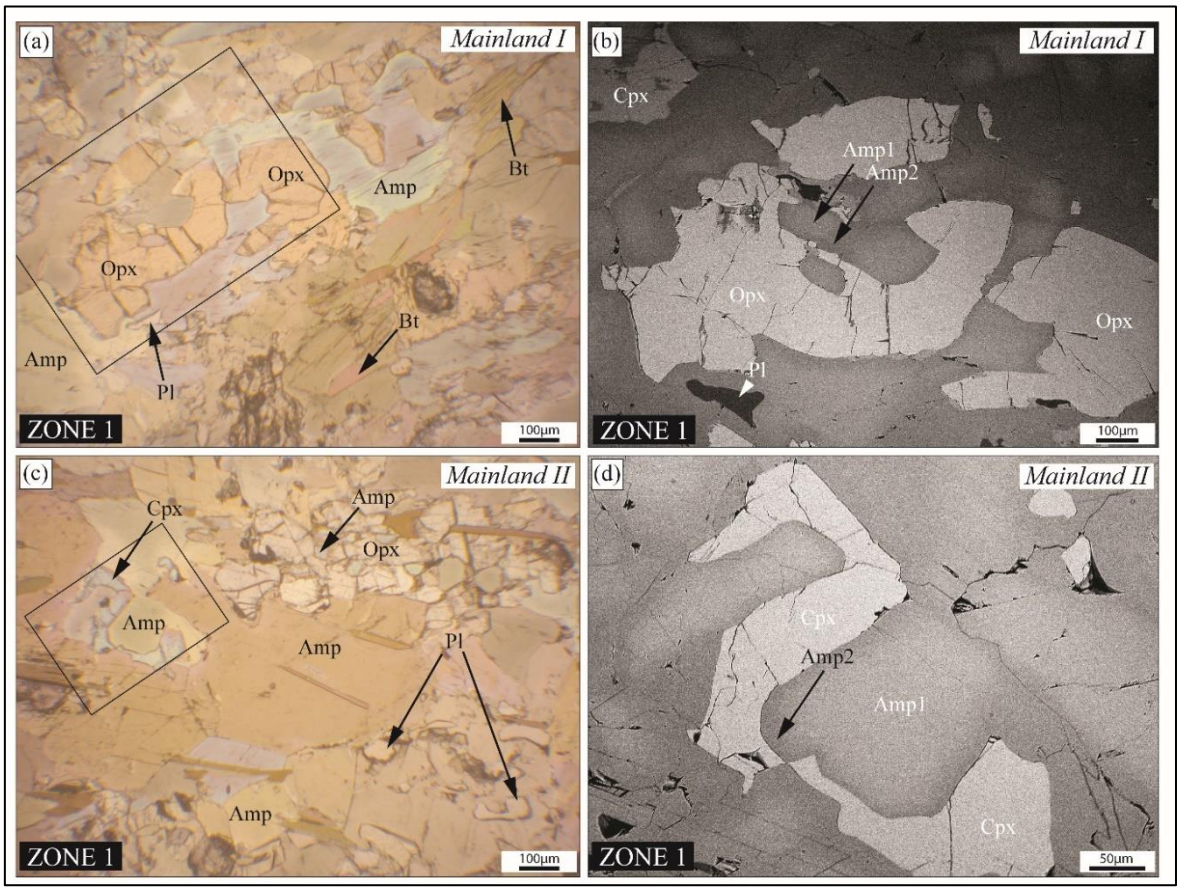

Figure 3.5 – Photomicrographs showing peak mineralogy and microstructures of mainland amphibolite samples (*Mainland I* and *Mainland II*). (a-b) In *Mainland I*, peak metamorphic assemblage is represented by amphibole + orthopyroxene + clinopyroxene + biotite + plagioclase. Inset shows location of 'b'. In the BSE image, amphibole shows compositional differences with varying shades of grey. The dark grey zones surrounding the orthopyroxene-clinopyroxene grains are labelled 'Amp2,' while the central pale grey zones are labelled 'Amp1'. Plagioclase grains are subhedral in shape. (c-d) In *Mainland II*, peak metamorphic assemblage is represented by amphibole + orthopyroxene + clinopyroxene + quartz + plagioclase + magnetite + ilmenite. Orthopyroxene-clinopyroxene grains are subhedral and often contain inclusions of amphibole and plagioclase.

---

a strong alignment (Fig. 3.3e). Orthopyroxene and clinopyroxene grains occur as fingers and replace amphibole along their grain boundaries (Fig. 3.5c) or have small amphibole grains as inclusions (Fig. 3.5d). The plagioclase grains are fresh, subhedral with characteristic polysynthetic twins. Some grains are anhedral with irregular grain boundaries, while others are interstitial with cuspate grain boundaries (Fig. AP3 - 2), indicating melt-pseudomorphs. In 'Zone 2', the modal abundance of clinopyroxene and orthopyroxene grains increases (Fig. 3.3e) and the maximum grain size of orthopyroxene, clinopyroxene and plagioclase grains reach up to 1mm. The interpreted peak metamorphic assemblage includes clinopyroxene, orthopyroxene, amphibole, plagioclase, quartz, biotite, and ilmenite.

3.5 Analytical techniques and methodology

3.5.1 Whole rock major oxides using X-ray Fluorescence and MapComp

For all the samples, bulk rock chemistry was obtained using the MapComp approach (see Chapter 2 for details). The equilibrium texture of heterogeneous *Island I* (SPI1338) amphibolite is shown by amphibole + plagioclase + quartz + clinopyroxene + biotite assemblage of 'Zone 1'. Hence, for P-T estimation, MapComp local bulk chemistry from 'Zone 1' must be used. However, this results in a broad P-T range for *Island I*, so the bulk composition of the entire thin section area is used, as the narrow stability field of garnet will help constrain a reasonable peak P-T condition. For *Island II* (SPI1340), MapComp derived local bulk chemistry from 'Zone1' is used for phase equilibria modelling. For the other samples (clinopyroxene and orthopyroxene bearing amphibolites: *Island III* SPI1341B, *Mainland I* SPI1399A, and *Mainland II* SPI1382) MapComp compositional data are also determined avoiding the felsic veins of 'Zone 2'. MapComp analyses can be used with confidence because all of the samples are coarse-grained, and plagioclase is the only dominant Na-bearing phase. The reader is directed to Chapter 2 for more information on the technique used, while Fig. 3.3 shows the zones used for calculations. Bulk rock geochemistry (in oxide weight%) obtained from the investigated rocks are listed in Tab. 3.1.

3.5.2 Electron microscopy

In the studied sections point analysis of major mineral phases were performed using a JEOL JXA-8900RL electron probe microanalyzer (EPMA) at the Göttingen Laboratory for correlative light and electron microscopy (GoeLEM) at the Geoscience Centre, University of Göttingen equipped with an energy-dispersive (ED) and five wavelength-dispersive (WD) spectrometers. Measurement conditions for point analysis were 15 kV acceleration voltage, 20 nA beam current and a beam diameter of 5 µm. A total of 12 elements (Si, Al, Fe, Mg, Ca, Mn, K, Na, Ti, Cr, Ba, and Cl) were obtained in three serial WDS passes. A range of natural and synthetic mineral standards was used for element calibration, namely albite (Na), sanidine (K), wollastonite (Si, Ca), rutile (Ti), rhodonite (Mn), hematite (Fe), NaCl (Cl), olivine (Mg), anorthite (Al), celsian (Ba) and Cr_2O_3 (Cr) were used. Representative composition of minerals in the analyzed samples are given in Tab. 3.3-3.6.

3.5.3 Conventional Geobarometry

To constrain peak metamorphic condition, we combine classical geothermobarometry utilizing mineral pairs. We apply Ti-in-amphibole geothermometer from Liao et al. (2021), Ti-in-biotite geothermometer from Henry et al. (2005), and amphibole-plagioclase geothermobarometer using Holland and Blundy (1994) geothermometer along with Molina et al. (2015) geobarometer. Ti-in-amphibole thermometer is reasonable for rocks that have experienced granulite-facies (> 800-900 °C) condition due to relatively sluggish diffusion of Ti even in high temperature rocks. The temperature is estimated by calculating T from the expression: T = ([2400/1.52-log(Ti)]-273), where T is temperature and log (Ti) is the Ti content of amphibole in atom per formula unit (a.p.f.u) expressed in the logarithm to base 10. The uncertainty is in the range of ±35 °C. Note that application of the thermometer is only valid in the presence of Ti-phases (rutile, ilmenite or titanite) and under low oxygen fugacities. All the *Island* amphibolites contain Ti-rich phase ilmenite. The chosen Ti-in-biotite geothermometer is developed for metapelite samples containing ilmenite or rutile and graphite at low to medium pressures, where temperatures can be determined by calculating T from the expression: $T = ([\ln(Ti) - a - c(X_{Mg})^3]/b)^{0.333}$, where T is temperature in °C, Ti is the a.p.f.u normalized to 22 oxygen, X_{Mg} is Mg/(Mg + Fe), and a, b and c parameters are -2.3594, $4.6482e^{-9}$ and -1.7283, respectively. The uncertainty is in the range of ±12-24 °C. This thermometer is valid in the calibrated range of X_{Mg} = 0.275-1.000, Ti = 0.04-0.60 pfu, and T = 480-800 °C (Henry et al., 2005). These requirements are met by the analyzed samples. Holland and Blundy (1994) geothermometer is used to calculate peak temperature for amphibole + plagioclase assemblage with an uncertainty of ±40 °C. This calculation is based on the reaction edenite + albite = richterite + anorthite – where exchange of the plagioclase vector component $(NaSi)(CaAl)_{-1}$ between amphibole and plagioclase forming the basis of the thermometer. This thermometer is suitable for medium to high temperatures (500-900 °C) and for rocks with appreciable X_{An} content (0.1-0.9). Amphiboles must have X_{Na}^{M4} > 0.03, Al^{VI} < 1.8 pfu, and Si in the range of 6-7.7 pfu. Furthermore, the geobarometer of Molina et al. (2015) is used for the same data set as the geothermometer of Holland and Blundy (1994). The barometer is limited to amphibole compositions with > 0.05 pfu Al^{VI}, and > 0.02 pfu Ti, equilibrated at > 650 °C with an uncertainty of ± 0.15 to 0.23 GPa (Molina et al., 2015). Advantage of using this barometer is its suitability for medium to high temperature systems

(650-1050 °C) and for quartz and/or garnet-free assemblages as compared to other barometers involving amphibole + plagioclase (Kohn and Spear, 1989, Bhadra and Bhattacharya, 2007).

3.5.4 Isochemical phase diagram

To constrain peak metamorphic conditions, isochemical phase diagrams i.e., pseudosection are calculated using the software Perple_X version 6.9.1 (Connolly, 2005).

	Weight % measured using MapComp approach									
	Al_2O_3	CaO	Fe_2O_3(T)	K_2O	MgO	MnO	Na_2O	SiO_2	TiO_2	Total
Island I	13.36	7.73	10.22	0.79	3.92	0.16	1.69	56.19	1.04	95.11
Island II	15.98	14.52	9.51	0.47	6.80	0.14	1.13	49.81	0.58	98.94
Island III	14.22	13.88	9.56	0.59	5.34	0.24	2.42	53.91	0.65	100.81
Mainland I	5.21	9.18	10.89	1.12	20.71	0.20	0.35	51.10	0.47	99.23
Mainland II	14.74	11.64	13.49	0.31	7.71	0.19	2.71	48.75	0.95	100.49

Table 3.1 – Compositions used for phase diagrams. Fe_2O_3(T) : Total Fe as Fe_2O_3.

Calculations were performed in the MnNCKFMASHTO (MnO-Na_2O-CaO-K_2O-FeO-MnO-MgO-Al_2O_3-SiO_2-H_2O-TiO_2-O_2) model system using an updated version of the internally consistent Holland and Powell (2011) data set (ds63, 2015 update). The used solution models were those of White et al. (2014a) for garnet, biotite, cordierite, orthopyroxene, and mica with updates for Mn bearing phases of White et al. (2014b), the ternary feldspar model of Holland and Powell (2003), and that of White et al. (2000) for ilmenite and the models of Green et al. (2016) for augitic clinopyroxene, clinoamphibole, and tonalitic melt. MnO values for bulk composition were corrected according to the measured contents in amphibole in each sample, since the used clinoamphibole model does not account for MnO. The aluminosilicates, quartz, rutile, titanite and aqueous fluid (H_2O) are assumed as pure phases. The amount of H_2O used for modelling was set to approximate the modes of hydrous phases in the inferred peak assemblage field. The amount of O_2 was set to transform 15-25 % of FeO to Fe_2O_3.

3.6 Results

3.6.1 Mineral major and minor element chemistry

Amphibole

Island samples: Within the 'Zone 1' of two-garnet bearing amphibolites (*Island I and II*) amphiboles are pargasite to ferropargasite in composition without any compositional zoning (Fig. 3.6a). Ti content is very similar between 0.17 to 0.24 (Tab. 3.2). For *Island I* and *II*, Na+K are similar with 0.61-0.76 pfu and 0.58-0.65 pfu, while X_{Mg} values vary between 0.43-0.48 and 0.46-57, respectively (Tab. 3.2). Amphibole in 'Zone 3' of *Island II* ('Amp2' in Fig. 3.4g) is magnesiohornblende in composition and has a slightly higher Mg content (X_{Mg} values of 0.64-0.68) than amphibole in 'Zone 1' ('Amp2' in Tab. 3.2). Ti content is noticeably low (0.06-0.07 pfu), whereas Na+K content is comparable to amphiboles in 'Zone 1', with values ranging between 0.41-0.45 pfu (Tab. 3.2). In *Island III* (including both 'Zone 1' and 'Zone 2'), two groups of calcic amphiboles are detected (Fig. 3.4i). The dominant group is very similar to pargasite-ferropargasite amphiboles observed in 'Zone 1' of *Island I* and *II*, with X_{Mg} values of 0.47-0.54 (Fig. 3.6a) and similar Ti and Na+K content of 0.17-0.21 and 0.58-0.69 pfu, respectively ('Amp1' in Tab. 3.2). The second, subordinate group (found as inclusions inside clinopyroxene grains) is magnesiohornblende with slightly higher X_{Mg} values (X_{Mg} = 0.65-0.67, 'Amp2' in Tab. 3.2). Ti and Na+K content are lower with 0.02-0.05 and 0.21-0.32 pfu, respectively (Tab. 3.2). Amphibole in *Island I-III* have Al^{VI} values varying between 0.3-0.7 pfu.

Mainland samples: Mainland amphiboles are distinct from those of the island having in general higher X_{Mg} values. *Mainland I* has two groups of amphiboles. The dominated group is magnesiohornblende (Fig. 3.6b) with X_{Mg} values of 0.83-0.87. Ti and Na+K content varies between 0.05-0.08 and 0.18-0.24 pfu, respectively (Tab. 3.2). Subordinate group around the orthopyroxene-clinopyroxene grains ('Amp2' in Fig. 3.5b; Tab. 3.2) has relatively higher X_{Mg} value of 0.88-0.92 whereas Ti and Na+K have a range of 0.01-0.02 and 0.04-0.09 pfu, respectively (Tab. 3.2). The amphiboles are actinolite in composition (Fig. 3.6b). In *Mainland II* (including both 'Zone 1' and 'Zone 2'), calcic amphibole shows X_{Mg} values of 0.60-0.64 without any compositional zonation (Fig. 3.6b; Tab. 3.2). Ti and Na+K content ranges between 0.13-0.20 and 0.21-0.27 pfu (Tab. 3.2), respectively.

Amphiboles are magnesiohornblende in composition (Fig. 3.6b). In *Mainland I*, amphibole-core (magnesio hornblende in composition; Fig. 3.6a) has Al^{VI} values ranging between 0.17 to 0.33 pfu, whereas the actinolites have a range of 0.01 to 0.1 pfu. Amphibole in *Mainland II* have Al^{VI} values varying between 0.3-0.8 pfu.

Plagioclase

Plagioclase in 'Zone 1' of *Island I* (including both 'Zone 1' and 'Zone 2') is intermediate in composition (An_{45-52}; andesine) with minor (~1.5 mol%) orthoclase content (Fig. 3.6c; Tab. 3). Plagioclase in *Island II* has varied composition with plagioclase in 'Zone 1' are anorthite-rich (An_{77-82}; bytownite) (Fig. 3.6c; Tab. 3.3), plagioclase inclusions inside garnet are more albitic (An_{34-42}; andesine), and plagioclase in 'Zone 2' have an intermediate composition (An_{55-70}; labradorite). Plagioclase inclusions inside amphibole grains in 'Zone3' is also intermediate (An_{54-58}; labradorite) in composition (Fig. 3.6c; Tab. 3.3). In *Island III* (including both 'Zone 1' and 'Zone 2'), plagioclase grains are albite-rich (An_{40-46}; andesine) with minor orthoclase content (Fig. 3.6c; Tab. 3.3).

Plagioclase in *Mainland I* is distinct with albite rich composition (An_{26-29}; oligoclase) (Fig. 3.6c; Tab. 3.3). In *Mainland II* (including both 'Zone 1' and 'Zone 2'), plagioclase grains are homogenous with an intermediate composition (An_{49-51}; labradorite) and have minor (~1 mol%) orthoclase content (Fig. 3.6c; Tab. 3.3).

Garnet

The garnet porpyhroblasts in *Island I* show distinct chemical zoning with an increase in mole% of almandine and spessartine from 56 to 61 and 4 to 7, respectively, and a decrease in the mole% of pyrope and grossular from 16 to 12 and 25 to 18, respectively, from core to the rim (Fig. 3.6d; Tab. 3.4). Garnet in 'Zone 1' of *Island II* is relatively homogeneous with mole% of almandine, pyrope, and spessartine varying between 57-61, 16-20, and 4-6 from core to rim, respectively (Fig. 3.6d; Tab. 3.4). While grossular displays a large change from 24 mol% in the core to 16 mol% in the rim (Fig. 3.6d; Tab. 3.4). Garnet in 'Zone 2' show distinct compositional zoning from core (Alm_{54-59} Pyr_{22-36} Grs_{13-16} Sps_{4-6}) to rim (Alm_{60-65} Pyr_{14-18} Grs_{13-17} Sps_{6-8}).

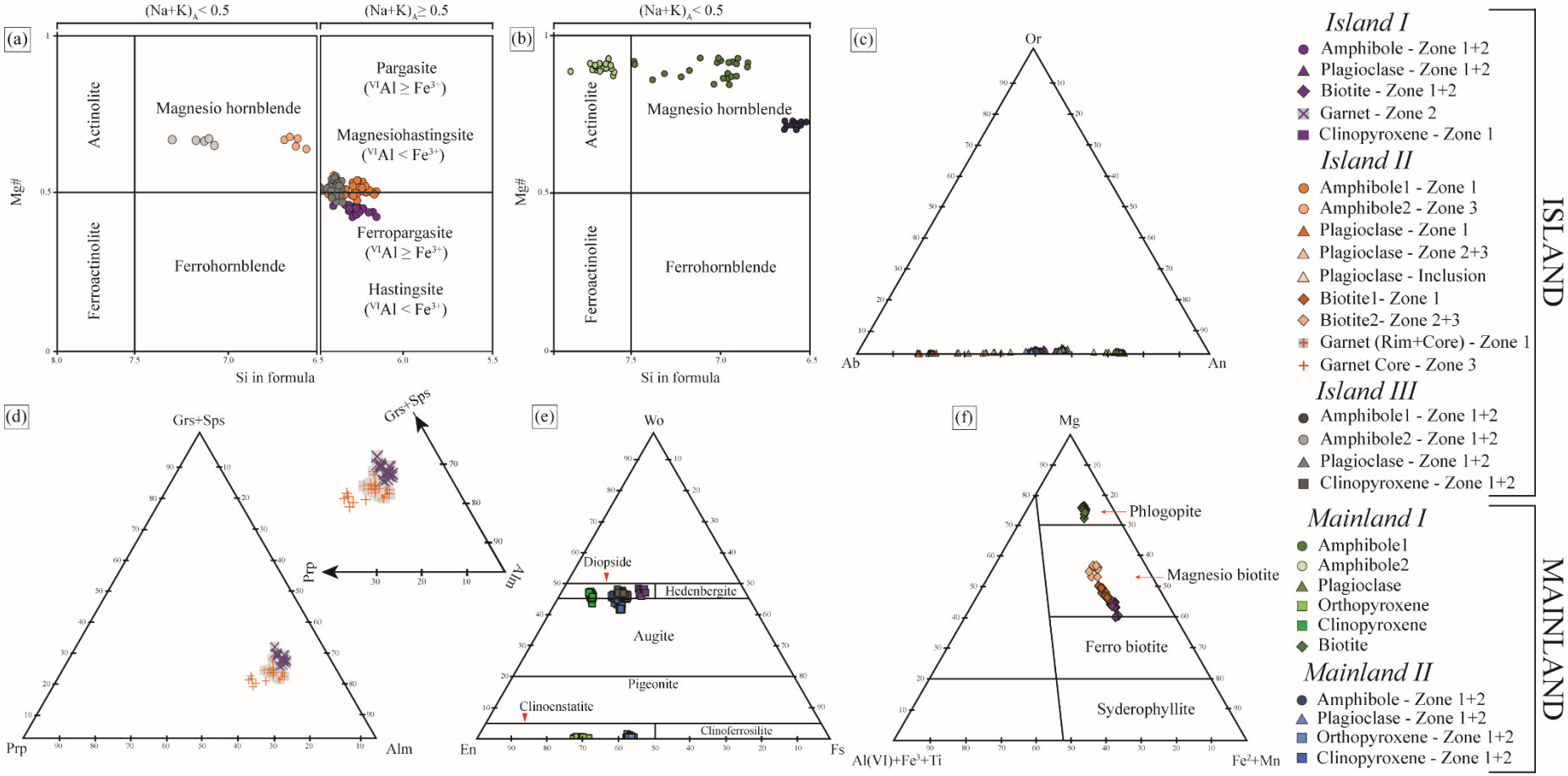

Figure 3.6 – Mineral major element compositions in the studied samples. (a-b) Mg# vs. Si in amphibole (plotted following Leake et al., 1997). *Island II*, *Island III*, and *Mainland I* exhibit a change in chemical compositions of amphibole. (c) Ternary diagram of plagioclase (An – anorthite; Ab – albite; Or – orthoclase) displays a homogeneous composition, except for *Island II*, where plagioclase in 'Zone 1' have higher Ab% than plagioclase in 'Zone 2', and plagioclase inclusions in amphibole-garnet grains. (d) Ternary diagram of garnet (Py – pyrope; Al – almandine; Grs+Sps – grossular- spessartine) in *Island I* and *Island II* samples. 'Zone 1' garnet in *Island II* have similar core-rim composition, but 'Zone 2' garnet grains have pyrope-rich core. (e) Ternary diagram of pyroxene (Wo – wollastonite; En – enstatite; Fs – Ferrosilite) reveals that orthopyroxene-clinopyroxene grains are homogeneous in *Mainland I*, *Mainland II*, and *Island III*. (f) Biotite end member plot (following Foster, 1960 and Sepidbar et al., 2017) show homogeneous biotite composition in *Island I* and *Mainland I*. In *Island II*, biotite in 'Zone 3' and biotite inclusions within garnet in 'Zone 2' have a higher Mg# than biotite in 'Zone 1'.

Calcic-Amphibole								
	Island I	*Island II*		*Island III*		*Mainland I*		*Mainland II*
	SPI1338	SPI1340		SPI1341B		SPI1399A		SPI1382
	Zone1+2	Zone1	Zone3	Zone1+2				Zone1+2
		Amp1	Amp2	Amp1	Amp2	Amp1	Amp2	
SiO_2	40.43	41.13	44.9	41.82	48.5	48.75	55.25	43.75
TiO_2	1.96	1.68	0.6	1.64	0.35	0.66	0.12	1.16
Al_2O_3	12.84	13.2	10.47	11.46	7.19	6.71	1.9	11.66
Cr2O3	0		0.09	0.2	0.07	0.6	0.1	0.04
FeO(tot)	19.45	17.89	15.48	18.48	14.39	7.71	5.46	14.18
MnO	0.23	0.19	0.28	0.32	0.31	0.16	0.14	0.13
MgO	7.92	8.81	12.1	8.57	13.1	17.72	21.06	11.91
CaO	11.5	11.38	11.15	11.79	12.29	11.49	12.08	11.98
Na_2O	1.5	1.28	1	1.02	0.78	1.41	0.4	1.22
K_2O	1.69	1.22	0.76	1.57	0.57	0.45	0.07	1.17
BaO								
Total	97.52	96.77	96.84	96.87	97.56	95.66	96.58	97.2
No of O	24	24	24	24	24	24	24	24
Si	6.19	6.24	6.62	6.4	7.09	7.04	7.74	6.48
Ti	0.23	0.19	0.07	0.19	0.04	0.07	0.01	0.13
Al	2.32	2.36	1.82	2.07	1.24	1.14	0.31	2.04
Cr			0.01	0.02	0.01	0.07	0.01	0.01
Fe(tot)	2.49	2.27	1.91	2.36	1.76	0.93	0.64	1.76
Mn	0.03	0.02	0.04	0.04	0.04	0.02	0.02	0.02
Mg	1.81	1.99	2.66	1.95	2.86	3.82	4.4	2.36
Ca	1.89	1.85	1.76	1.93	1.93	1.78	1.81	1.9
Na	0.45	0.38	0.29	0.3	0.18	0.4	0.11	0.35
K	0.33	0.24	0.14	0.31	0.11	0.08	0.01	0.22
Ba								
Total	15.71	15.53	15.3	15.57	15.25	15.35	15.07	15.25
Mg#	0.42	0.51	0.68	0.48	0.65	0.8	0.87	0.57
Na+K	0.78	0.61	0.43	0.61	0.29	0.48	0.12	0.57
Ti	0.23	0.19	0.07	0.19	0.04	0.07	0.01	0.13

Table 3.2 – Microprobe data of amphibole (Hbl) in the studied samples. Modal proportions are shown. Analyses were rejected for totals below 94%. Mg# denotes $Mg^{2+}/Mg^{2+} + Fe^{2+}$. 'Amp1' and 'Amp2' represent two different types of amphiboles, explained in the text. Compositions shown here are highlighted in Tab. AP3.1.

Plagioclase									
	Island I SPI1338		*Island II* SPI1340				*Island III* SPI1341B	*Mainland I* SPI1399A	*Mainland II* SPI1382
	Zone1 Core+Rim	Garnet inclusion	Zone1 Core	Garnet inclusion	Zone2	Amphibole inclusion	Zone1+2 Core+Rim	Core+Rim	Zone1+2 Core+Rim
SiO_2	55.82	58.8	46.56	58.82	52.91	54.36	57.66	60.63	55.77
TiO_2									
Al_2O_3	27.79	25.52	33.94	25.81	29.85	28.91	26.56	24.38	28.35
Cr_2O_3			0.03	0.04	0.03	0.03			
FeO(tot)									
MnO									
MgO									
CaO	9.78	6.93	17.12	7.26	12.37	11.24	8.6	5.6	10.37
Na_2O	6.06	7.83	2.01	7.6	4.71	5.27	6.76	8.6	5.56
K_2O	0.26	0.11	0.03	0.08	0.07	0.07	0.24	0.19	0.16
BaO			0.06	0.05	0.05	0.05	0.05		0.05
Total	99.71	99.19	99.74	99.65	99.99	99.93	99.87	99.4	100.26
No of O	8	8	8	8	8	8	8	8	8
Si	2.52	2.65	2.15	2.64	2.4	2.46	2.59	2.71	2.5
Ti									
Al	1.48	1.35	1.84	1.36	1.59	1.54	1.41	1.29	1.5
Cr									
Fe(tot)									
Mn									
Mg									
Ca	0.47	0.33	0.85	0.35	0.6	0.54	0.41	0.27	0.5
Na	0.53	0.68	0.18	0.66	0.41	0.46	0.59	0.75	0.48
K	0.02	0.01	0	0	0	0	0.01	0.01	0.01
Ba			0	0	0	0	0		0
Total	5.01	5.02	5.02	5.02	5.01	5.01	5.01	5.02	4.99
An*	46.4	32.7	82.4	34.4	59	53.9	40.7	26.2	50.3
Ab*	52.1	66.8	17.5	65.2	40.6	45.7	57.9	72.8	48.8
Or*	1.5	0.6	0.1	0.4	0.4	0.4	1.4	1	0.9

Table 3.3 - Microprobe data of plagioclase (Plag) in the *Island* and *Mainland* amphibolites. Modal proportions are shown. Analyses were rejected for totals outside of 99.0-101.0% for feldspars. An* = Anorthite, Ab* = Albite, and Or* = Orthoclase. Compositions shown here are highlighted in Tab. AP3.6.

	Garnet						Orthopyroxene		Clinopyroxene			
	Island I		*Island II*				*Mainland I*	*Mainland II*	*Island I*	*Island III*	*Mainland I*	*Mainland II*
	Zone2		Zone1		Zone2							
	Core	Rim	Core	Rim	Core	Rim		Zone1+2	Zone1	Zone1+2		Zone1+2
SiO_2	37.69	37.72	37.78	37.89	38.71	38.25	53.91	52.49	51.16	52.2	53.75	52.44
TiO_2									0.17	0.15		
Al_2O_3	21.01	20.87	21.27	21.18	21.98	21.7	0.5	1.1	2.05	1.97	0.8	1.52
Cr_2O_3		0.04			0.05		0.04			0.07	0.23	0.05
FeO	25.47	27.57	27.1	28.63	25.12	27.45	18.11	25.33	12.66	10.17	4.88	8.57
MnO	2.04	2.55	1.67	2.28	1.93	2.71	0.44	0.85	0.41	0.43	0.13	0.29
MgO	3.38	3.35	4.43	4.02	6.41	4.58	25.79	20.14	10.67	12.2	15.61	13.49
CaO	9.86	7.83	7.78	6.39	6.54	6.07	0.32	0.37	22.25	22.25	23.71	23.01
Na_2O							0.03		0.39	0.47	0.54	0.41
K_2O												
BaO												
Total	99.45	99.93	100.03	100.4	100.7	100.8	99.14	100.28	99.76	99.91	99.65	99.77
No of O	6	6	6	6	6	6	6	6	6	6	6	6
Si	2.98	2.99	2.97	2.98	2.98	2.99	1.98	1.98	1.95	1.96	1.98	1.96
Ti												
Al	1.96	1.95	1.97	1.97	2	2	0.02	0.05	0.09	0.09	0.03	0.07
Cr											0.01	
Fe	1.69	1.83	1.78	1.89	1.62	1.79	0.56	0.8	0.4	0.32	0.15	0.27
Mn	0.14	0.17	0.11	0.15	0.13	0.18	0.01	0.03	0.01	0.01	0	0.01
Mg	0.4	0.4	0.52	0.47	0.74	0.53	1.41	1.13	0.61	0.68	0.86	0.75
Ca	0.84	0.66	0.65	0.54	0.54	0.51	0.01	0.01	0.91	0.9	0.93	0.92
Na									0.03	0.03	0.04	0.03
K												
Ba												
Total	8	8	8	8	8	8	4	4	4	4	4	4
Pyr*	13.85	13.73	18.36	16.32	25.2	18.08						
Grs+Sps*	30.09	25.28	22.08	20.67	20.72	22						
Alm*	56.06	60.99	59.56	63.02	54.09	59.92						
Mg#	0.19	0.18	0.23	0.2	0.31	0.23	0.72	0.59	0.6	0.68	0.85	0.74

Table 3.4 – Microprobe data of garnet (Grt), orthopyroxene (Opx), and clinopyroxene (Cpx) in the studied samples. Modal proportions are shown. For *Mainland II* amphibolite orthopyroxene and clinopyroxene grains are from both 'Zone 1' and 'Zone 2'. Analyses were rejected for totals outside of 99.0-101.0% for the minerals. Here for garnet grains, Pyr* = Pyrope, Grs+Sps* = Grossularia+Spessartina and Alm* = Almandine. Mg# denotes $Mg^{2+}/(Mg^{2+} + Fe^{2+})$. Compositions shown here are highlighted in Tab. AP3.3-AP3.5

Orthopyroxene

Orthopyroxene grains in *Mainland I* display X_{Mg} of 0.70-0.73 with Al of 0.01-0.03 pfu (Tab. 3.4). The grains are enstatite-rich (En_{69-72}) with minor (0.3-0.9 mol%) wollastonite

(Fig. 3.6d; Tab. 3.4). Orthopyroxene in *Mainland II (*including both 'Zone 1' and 'Zone 2') has slightly lower X_{Mg} values of 0.56-0.58 with Al of 0.04-0.06 pfu (Tab. 3.4). Orthopyroxene in *Mainland II* are poorer in enstatite (En_{55-57}) with slightly increased wollastonite (0.6-1.5 mol%) compared to *Mainland I* (Fig. 3.6d; Tab. 3.4).

Clinopyroxene

Clinopyroxene In *Island I* are diopside in composition (Fig. 3.6d) with X_{Mg} of 0.58-0.61, Ca content ranging between 0.89-0.91 pfu, and Na content of 0.03-0.04 pfu (Tab. 3.4). In *Island III* (including both 'Zone 1' and 'Zone 2'), clinopyroxene is diopside with slightly higher X_{Mg} of 0.65-0.70 (Fig. 3.6d; Tab. 3.4), and similar Ca, Na content of 0.89-0.95 pfu, and 0.02-0.05 pfu, respectively, compared to *Island I* (Fig. 3.6d; Tab. 3.4).

In *Mainland I*, clinopyroxene grains have the highest X_{Mg} value of 0.83-0.86 with Ca and Na content ranging from 0.88-0.94 pfu and 0.03-0.05 pfu, respectively (Tab. 3.4). In *Mainland II* (including both 'Zone 1' and 'Zone 2'), clinopyroxene has lower X_{Mg} content of 0.67-0.73, with similar Ca and Na content of 0.82-0.91 pfu, 0.03-0.04 pfu, respectively, compared to *Mainland I* (Tab. 3.4). In both the samples, clinopyroxene grains are diopside in composition (Fig. 3.6d).

Biotite

Biotite grains in *Island I* (including both 'Zone 1' and 'Zone 2') have X_{Mg} values of 0.51-0.54 with Ti content of 0.41-0.53 pfu (Tab. 3.5). 'Zone 1' in *Island II* has very similar biotite with X_{Mg} of 0.55-0.60 and Ti content varying between 0.42-0.49 pfu, compared to *Island I* (Tab. 3.5). Biotite in 'Zone 3' of *Island II* ('Bt2' in Fig. 3.4f), have slightly higher X_{Mg} of 0.64-0.73 and lower Ti content ranging between 0.22-0.31 pfu (Fig. 3.6e; 'Bt2' in Tab. 3.5). Biotite inclusions inside the garnet grains in 'Zone 2' has similar composition. Biotite grains in both the studied samples are magnesiobiotite (Fig. 3.6e).

Biotite in *Mainland I* is phlogopite in composition with the highest X_{Mg} values of 0.81-0.83 with Ti content of 0.21-0.27 pfu (Tab. 3.5).

Biotite				
	Island I SPI1338	*Island II* SPI1340		*Mainland I* SPI1399A
	Zone1+2	Zone1	Zone3	
		Bt1*	Bt2*	
SiO_2	35.42	35.55	36.67	38.31
TiO_2	4.13	3.76	2.19	1.99
Al_2O_3	15.31	15.72	16.70	14.24
Cr_2O_3			0.09	0.50
FeO(tot)	19.97	18.29	15.51	8.63
MnO	0.10			
MgO	10.68	11.33	13.50	19.71
CaO				
Na_2O		0.05	0.07	0.30
K_2O	9.74	9.61	9.61	9.53
BaO				
Total	95.35	94.31	94.34	93.21
No of O	22	22	22	22
Si	5.38	5.41	5.49	5.65
Ti	0.47	0.43	0.25	0.22
Al	2.74	2.82	2.95	2.48
Cr		0.00	0.01	0.06
Fe(tot)	2.54	2.33	1.94	1.07
Mn	0.01	0.00		
Mg	2.42	2.57	3.02	4.34
Ca		0.00		
Na		0.01	0.02	0.09
K	1.89	1.87	1.84	1.79
Ba				
Total	15.45	15.45	15.51	15.69
Mg#	0.51	0.55	0.63	0.82
Ti	0.47	0.43	0.25	0.22

Table 3.5 – Microprobe data of biotite (Bt) from *Island* and *Mainland* amphiboloites. Modal proportions are shown. Analyses were rejected for totals below 94% for biotites. Mg# denotes $Mg^{2+}/(Mg^{2+} + Fe^{2+})$. *Two different types of biotites, explained in the text. Compositions shown here are highlighted in Tab. AP3.2.

3.6.2 Temperature and Pressure constraints using geothermobarometer

Island samples

Ti-in-amphibole thermometry using the 'Zone 1' amphiboles yields temperature values of 821±18 °C, and 813±15 °C for *Island I-II*, respectively. In 'Zone3' of *Island II* temperature estimates are significantly lower at 614±4°C (Fig. 3.7c; Tab. 3.6). Ti-in-biotite thermometers yield slightly lower temperatures of 725±8 °C, and 734±9 °C for 'Zone 1' biotite of *Island I-II*, respectively (Fig. 3.7d; Tab. 3.6). 'Zone3' of *Island II* gives temperature estimates of 686±16 °C (Fig. 3.7d; Tab. 3.6). All studied samples have the required chemical range of amphibole-plagioclase grains for the application of Holland and Blundy (1994) geothermometer (cf. section 3.6.1). Temperature values are estimated at arbitrary 0.2 GPa and 0.9 GPa pressures (based on previous estimates, Kirkland et al., 2018a). The geothermometer estimates temperatures of 747-763 °C at 0.2 GPa and 795-819°C at 0.9 GPa, 886 °C at 0.2 GPa and 939 °C at 0.9 GPa, for 'Zone 1' in *Island I-II*, respectively (Fig. 3.7a; Tab. 3.6). 'Zone 3' in *Island II* estimates a comparatively lower temperature of 693 °C and 752 °C, at 0.2 GPa and 0.9 GPa, respectively (Fig. 3.7a; Tab. 3.6). *Island III* has temperatures of 769-781 °C at 0.2 GPa and 812-822 °C at 0.9 GPa (Fig. 3.7a; Tab. 3.6). Next Molina et al. (2015) geobarometer is used to estimate pressure values at temperature conditions for the same amphibole-plagioclase pairs for a temperature window of 650-950 °C. All *Island* amphibolite samples have the required chemical range for the application of Molina et al. (2015) geobarometer. Using this barometer, the estimated pressure ranges at 650 °C for *Island I-III* are 0.34-0.45 GPa, 0.36-0.59 GPa, and 0.44-0.49 GPa, respectively (Fig. 3.7a). At 950 °C, these values are 0.8-0.9 GPa, 0.54-0.8 GPa, and 0.91-1 GPa, respectively (Fig. 3.7a; Tab. 3.6). *Island II* displays a wide pressure range, with 'Zone 1' amphibole having low pressure values (0.36 GPa at 650 °C and 0.54 GPa at 950 °C; Tab. 3.6) and 'Zone 3' magnesio hornblende exhibiting relatively higher-pressure estimates (0.59 GPa at 650 °C and 0.8 GPa at 950 °C; Tab. 3.6). Next calculated pressure and temperature estimates are used to find intersections in the P-T space to determine the precise P-T range (Fig. 3.7a). Using these intersections, temperature and pressure estimate for *Islands I-II* are 775-792 °C at 0.61-0.67 GPa and 910 °C at 0.51 GPa, respectively (Fig. 3.7a). 'Zone 3' in *Island II* indicates pressure of 0.66 GPa and a relatively low temperature of 730°C. The pressure-temperature range for *Island III* is 0.68-0.74 GPa and 800-810°C (Fig. 3.7a).

	Geothermobarometry			
	T(L) (in °C)	T(H) (in °C)	T(HB) (in °C)	P(M) (in GPa)
Island I SPI1338	821±18	725±8	795-819	0.8-0.9
Island II SPI1340-Host	813±15	734±9	939	0.54
Island II SPI1340-Zone3	614±4	686±16	752	0.8
Island III SPI1341B	NA	NA	812-822	0.9-1
Mainland I SPI1399A (with 'Amp1')	NA	NA	681-684	0.3-0.35
Mainland I SPI1399A (with 'Amp2')	NA	NA	650-680	NA
Mainland II SPI1382	748±17	NA	791-793	0.87-0.92

Table 3.6 – P-T values of the investigated samples calculated using conventional geothermobarometers. T(L): temperature estimates using Ti-in-amphibole thermometer following Liao et al. (2021); T(H): temperature estimates using Ti-in-biotite thermometer following Henry et al. (2005); T(HB): temperature estimates at 0.9 GPa using amphibole-plagioclase thermometer following Holland and Blundy (1994); P(M): pressure estimates at 950 °C using amphibole-plagioclase barometer following Molina et al. (2015). NA: not applicable. Average deviations for T(L) and T(H) are represented in Tab. AP3.7 and Tab. AP3.8, respectively. T(L) and T(H) cannot be applied to *Island III* and *Mainland I* as there are no biotite and/or Ti-rich phases like ilmenite and/or rutile. No biotite grains are found in *Mainland II*.

Mainland samples

Ti-in-amphibole thermometer for *Mainland II* sample yield temperature conditions of 748±17 °C. All studied samples have the required chemical range of amphibole-plagioclase grains for the application of Holland and Blundy (1994) geothermometer (cf. section 3.6.1). The calculated results for *Mainland I*, assuming plagioclase equilibrated with actinolite, give temperature estimates of 600-633 °C at 0.2 GPa and 650-680 °C at 0.9 GPa (Fig. 3.7b; Tab. 3.6). Temperature ranges of 650-660 °C at 0.2 GPa and 681-684 °C at 0.9 GPa are observed while assuming equilibration between plagioclase and magnesio hornblende (i.e., before clinopyroxene-orthopyroxene replacement) (Fig. 3.7b; Tab. 3.6). *Mainland II* shows temperature values of 744-748 °C at 0.2 GPa and 791-793 °C at 0.9 GPa (Fig. 3.7b; Tab. 3.6). All studied samples excluding actinolite amphibole of *Mainland I* have the required chemical range for the application of Molina et al. (2015) geobarometer. Using this barometer, pressure ranges estimated at 650 °C for *Mainland I-II* yield values of 0.18-0.19 GPa and 0.55-0.60 GPa, respectively (Fig. 3.7b). These values are 0.31-0.35 GPa and 0.87-0.92 GPa at 950 °C, respectively (Fig. 3.7b; Tab. 3.6). In *Mainland I*, dominant magnesio hornblende has abnormally low estimation of pressure for both 650 °C and 950

°C. Intersections of pressure-temperature estimates in the P-T space result in very low peak pressure-temperature condition for *Mainland I*, while *Mainland II* produces temperature and pressure estimates of 780-785 °C and 0.69-0.75 GPa, respectively (Fig. 3.7b). A summary of the calculated pressures (at 950 °C) and temperatures (at 0.8 GPa) using the conventional thermobarometer are presented in Tab. 3.6.

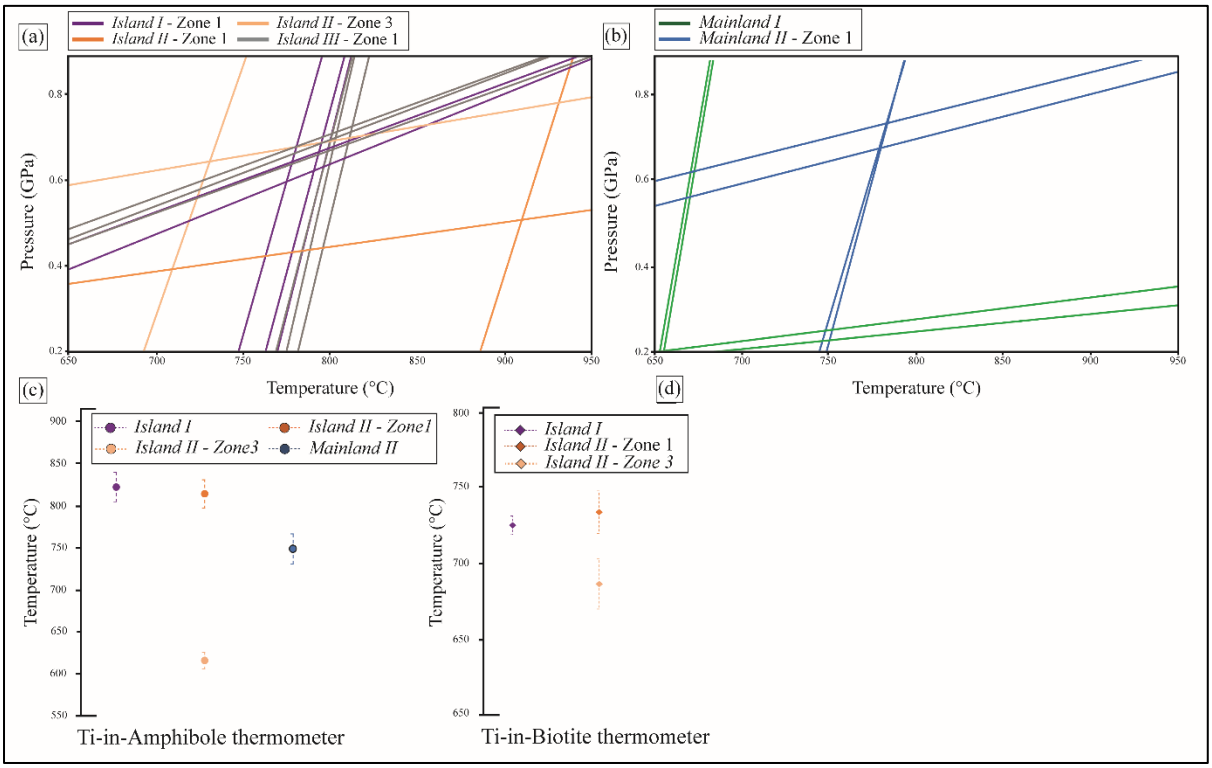

Figure 3.7 – Results from classical geothermobarometers for all the studied samples. (a-b) The pressure-temperature conditions of the studied samples are constrained by the intersections of amphibole-plagioclase thermometric and barometric plots in the P-T space. The pressure values are estimated for a window of 650-950 °C, while the temperature values are measured for a pressure range of 0.2-0.9 GPa. (c) Average temperature values (with error bars) returned from Ti-in-amphibole and (d) Ti-in-biotite thermometers.

3.6.3 Isochemical phase diagrams

<u>Island Amphibolites</u>

Island I: Garnet-amphibolite SPI1338

Peak metamorphic assemblage includes amphibole, biotite, plagioclase, quartz, clinopyroxene, garnet, melt, and ilmenite. The absence of orthopyroxene limits temperature

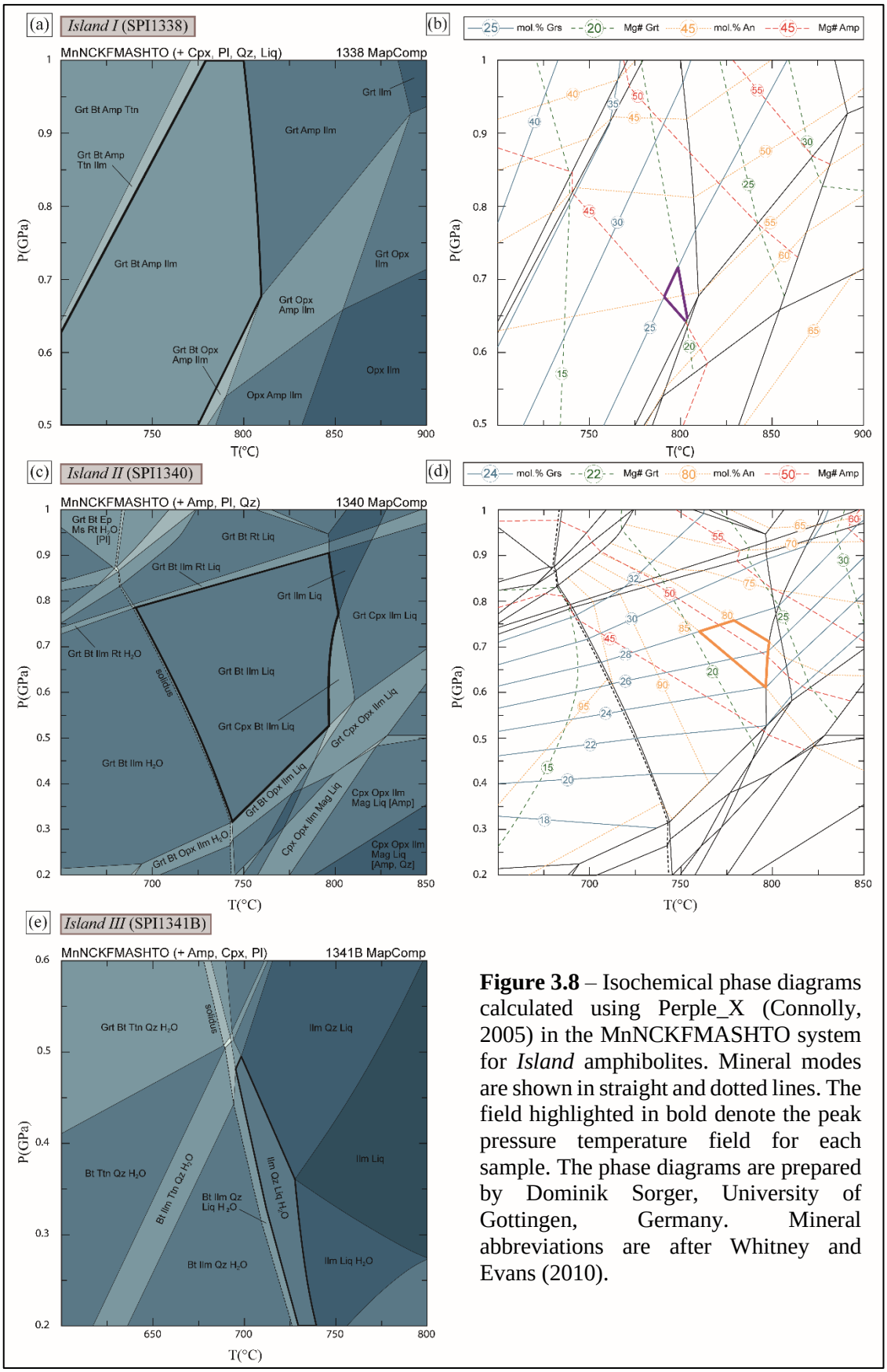

Figure 3.8 – Isochemical phase diagrams calculated using Perple_X (Connolly, 2005) in the MnNCKFMASHTO system for *Island* amphibolites. Mineral modes are shown in straight and dotted lines. The field highlighted in bold denote the peak pressure temperature field for each sample. The phase diagrams are prepared by Dominik Sorger, University of Gottingen, Germany. Mineral abbreviations are after Whitney and Evans (2010).

to 810 °C and pressure to > 0.68 GPa (Fig. 3.8a). The mole% of grossular towards the core of the garnet is 25 and the mole% of anorthite in plagioclase is 45 (cf. section 3.6.1).

Isopleths are calculated using these values, and isopleths with garnet and amphibole X_{Mg} values are plotted (Fig. 3.8b). Pressure 0.77 GPa is restricted by the isopleth of 25 mole% grossular, which also corresponds to X_{Mg} value of 20 in garnet (Fig. 3.8b). However, 45 mole% anorthite isopleth suggests a slightly higher-pressure value of > 0.82 GPa. Within the peak assemblage field, X_{Mg} of amphibole indicates a pressure-temperature range ranging from ~740 °C at 0.81 GPa to ~810 °C at 0.64 GPa. Peak metamorphic condition for *Island I* is estimated 785-810 °C and 0.64-0.72 GPa based on convergence of garnet X_{Mg}, mole% grossular, and amphibole X_{Mg} isopleths (Fig. 3.8b).

Island II: Garnet-amphibolite SPI1340

Peak metamorphic assemblage is garnet, amphibole, biotite, plagioclase, quartz, and ilmenite in the presence of melt. The field containing this assemblage on the pseudosection is bound by orthopyroxene at lower pressure, and clinopyroxene at higher temperature (Fig. 3.8c). The lower temperature boundary of the peak assemblage field is defined by the solidus, which ranges from ~ 680 °C at > 0.8 GPa to ~ 740 °C at 0.3 GPa (Fig. 3.8c). The high-pressure range is restricted by appearance of rutile beyond > 0.75 GPa. Isopleths corresponding to the mole% grossular, X_{Mg} in garnet and amphibole, and mole% of anorthite are drawn (Fig. 3.8d). The host (in 'Zone 1') garnet, amphibole and anorthite compositions are used for this calculation. Amphibole from 'Zone 3' with X_{Mg} of 0.66 does not fall within the peak assemblage field and hence is disregarded. The 80 mole% anorthite isopleth defines peak temperature to ~ 800 °C for the peak assemblage field. Peak metamorphic condition for *Island II* is estimated 765-800 °C at 0.61-0.75 GPa based on the convergence of all the isopleths (Fig. 3.8d).

Island III: Clinopyroxene bearing amphibolite SPI1341B

Peak metamorphic assemblage is amphibole, plagioclase, quartz, ilmenite, clinopyroxene in the presence of melt. The stability field of this peak assemblage is bounded at high temperature by the quartz-out field boundary (Fig. 3.8e). This sample does not contain biotite which restricts the lowest temperature to ~ 725 °C and highest pressure < 0.5

GPa. However, no compositional isopleths are calculated for *Island III* because the observed compositional ranges of amphibole, clinopyroxene, and plagioclase are stable over a wide P-T range and thus are ineffective for constraining specific P-T conditions. Therefore, the estimated condition of peak metamorphism for *Island III* is ~ 725-740 °C and < 0.5 GPa (Fig. 3.8e).

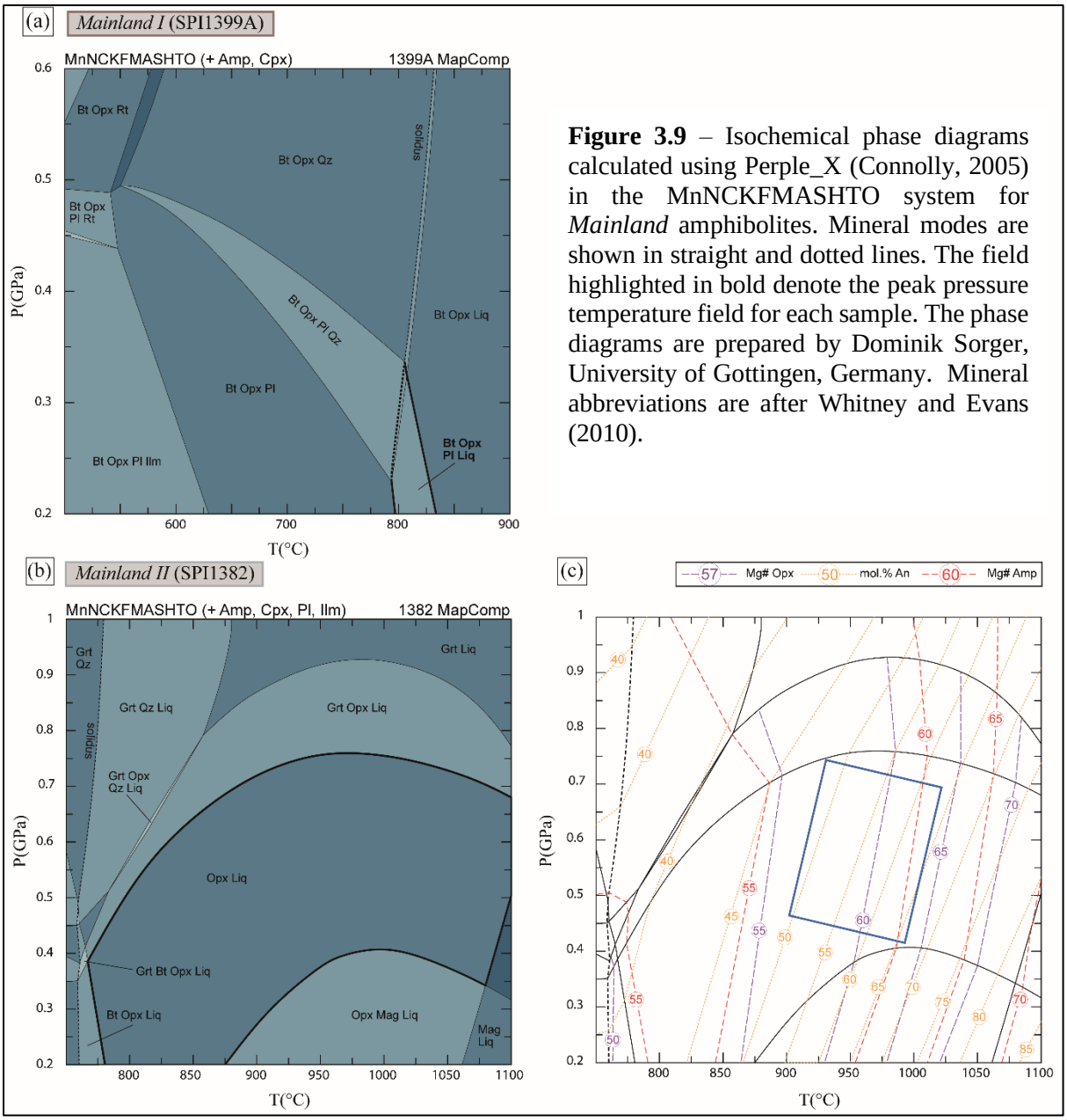

Figure 3.9 – Isochemical phase diagrams calculated using Perple_X (Connolly, 2005) in the MnNCKFMASHTO system for *Mainland* amphibolites. Mineral modes are shown in straight and dotted lines. The field highlighted in bold denote the peak pressure temperature field for each sample. The phase diagrams are prepared by Dominik Sorger, University of Gottingen, Germany. Mineral abbreviations are after Whitney and Evans (2010).

Mainland Amphibolites

Mainland I: Orthopyroxene-clinopyroxene bearing amphibolite SPI1399A

Peak metamorphic assemblage is amphibole, plagioclase, biotite, orthopyroxene, clinopyroxene in the presence of melt. The stability field of this phase assemblage (Fig. 3.9a) is bounded by the plagioclase-out field boundary at high temperature and pressure. The lower temperature boundary of this peak assemblage field is defined by the solidus (Fig. 3.9a). The estimated conditions of peak metamorphism are ~ 800-825 °C and < 0.35 GPa (Fig. 3.9a).

Mainland II: Orthopyroxene-clinopyroxene bearing amphibolite sample SPI1382

Peak metamorphic assemblage is amphibole, plagioclase, ilmenite, orthopyroxene, and clinopyroxene. These minerals are only in equilibrium above the solidus with the

presence of melt (Fig. 3.9b). The stability field of the assemblages is bound by appearance of garnet at higher pressure and the magnetite-in field boundary at lower pressure. The lower temperature boundary is constrained by the presence of biotite (Fig. 3.9b). Isopleths correspond to mole% anorthite, X_{Mg} in orthopyroxene and amphibole are drawn (Fig. 3.9c). The 50 mole% anorthite isopleth, amphibole isopleth of X_{Mg} = 60, and orthopyroxene isopleth of X_{Mg} = 57 identify temperature > 860 °C. The estimated condition of peak metamorphism is ~ 900-1000 °C and < 0.75 GPa (Fig. 3.9c).

3.7 Discussion

3.7.1 Conditions of peak metamorphism

The studied samples exhibit field observations suggesting melt present deformation where oriented felsic veins are arranged parallel to the foliation (Fig. 3.2). Microstructural observations also suggest former melt presence where quartz-plagioclase grains occur as elongated, anhedral grains with low dihedral angles along grain boundaries of surrounding minerals. Interstitials, partial faceted grains are also observed indicating direct crystallization from the melt (Fig. 3.4-3.5). We suggest that extraction and segregation of the melt phases may have formed the felsic veins at a relatively local scale (‘Zone 2’ in Fig.

3.3). For *Island I*, peak temperature is well constrained to a temperature range of 770-821 °C based on conventional Ti-in-amphibole, amphibole-plagioclase geothermometers, and P-T pseudosection (Fig. 3.7a, 3.10; Tab. 3.6). In comparison, Ti-in-biotite temperature estimate of 725±8 °C is relatively low (Fig. 3.7d; Tab. 3.6). Pressure estimates of 0.52-0.69 GPa using amphibole-plagioclase barometer correspond well with the 0.64-0.72 GPa estimates from the isochemical phase diagram (Fig. 3.10). Similarly, *Island II* gauges temperature range of 765-813 °C using Ti-in-amphibole and P-T pseudosection considering 'Zone 1' mineral composition and peak mineral assemblages (Fig. 3.10, 3.7c). In comparison, temperature estimate of 734±9 °C using Ti-in-biotite thermometer indicates low-temperature value (Fig. 3.7d; Tab. 3.6), and amphibole-plagioclase thermometer yields a relatively higher temperature of 910 °C (Fig. 3.7a, 3.10). Pressure estimates of 0.52 GPa from amphibole-plagioclase barometer is slightly lower than the values of 0.61-0.75 GPa, measured using isochemical phase diagram (Fig. 3.7a, 3.10). Hence, in all the *Island* samples, Ti-in-biotite represents a slightly lower temperature value than estimated using Ti-in-amphibole geothermometer or measured using phase equilibria modelling (Fig. 3.7c-d, 3.10). The low temperature values may be due to absence of any graphite grain in the studied samples and the rocks being non metapelite in composition for which the calibration was performed. Ti-in-biotite temperatures for metaplectic rocks with Ti-saturating minerals, but without graphite, are observed to produce reasonable results but an underestimation of temperature by 20±12 °C (Henry et al., 2005). Amphibole-plagioclase thermobarometers considering magnesiohornblende gains in 'Zone 3' of *Island II* yield peak metamorphic conditions of 730 °C at 0.65 GPa. The temperature estimates also indicate a lower range than measured in 'Zone 1' of *Island II* using conventional geothermobarometers or phase equilibria modelling (Fig. 3.7a, c-d; Tab. 3.6). Hence, it is suggested that 'Zone 3' in the studied *Island II* does not record peak metamorphic condition. Furthermore, the amphibole-plagioclase thermobarometer of Island II estimates a lower pressure and higher temperature range than Ti-in-amphibole, Ti-in-biotite, or pseudosection analysis (Fig. 3.7, 3.8, 3.10; Tab. 3.6); this may be due to the varying composition of amphibole in the studied sample (Fig. 3.6; Tab. 3.2) and is thus ignored for this discussion. Amphibole-plagioclase geothermobarometer in *Island III* estimates pressure values ranging between 0.68-0.74 GPa at 800-805 °C (Fig. 3.7a), while phase diagram recognizes slightly lower peak metamorphic conditions of 725-740 °C at < 0.5 GPa (Fig. 3.8e). To summarize, *Island I* records an estimated peak P-T condition that is compatible with the P-T range of *Island II*, while the

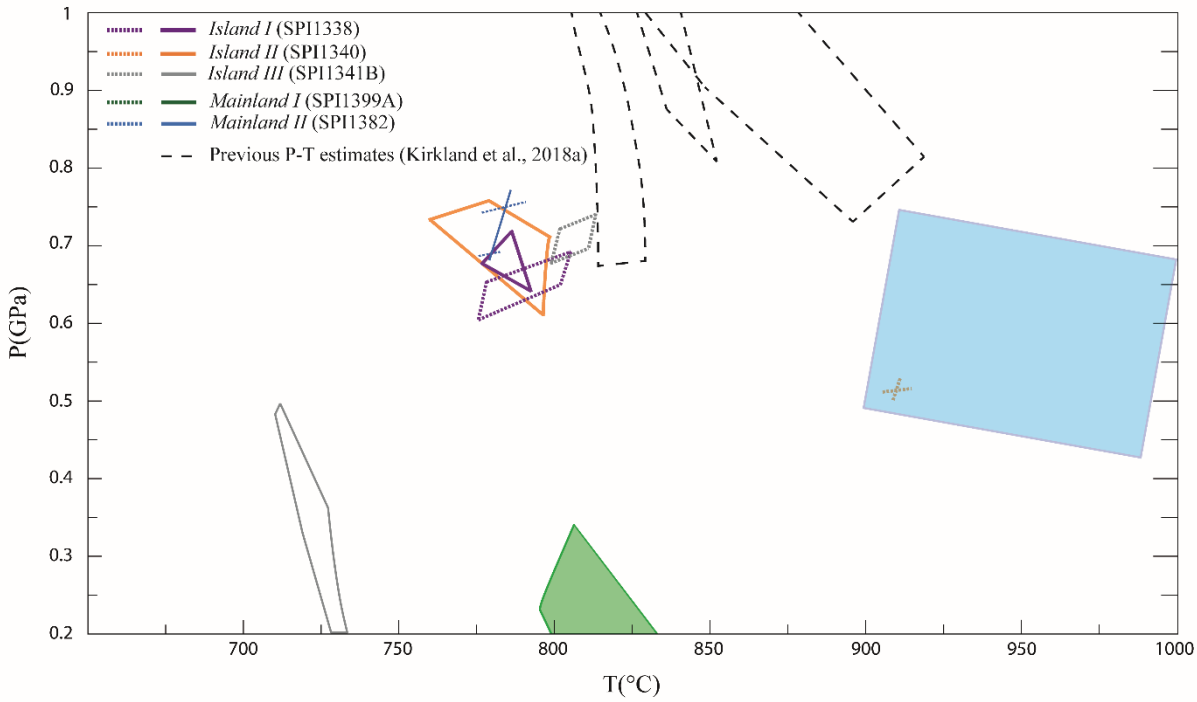

Figure 3.10 – Compilation of peak P-T conditions derived from conventional geothermobarometers and isochemical phase diagrams for all the studied samples. P-T ranges obtained from amphibole-plagioclase geothermobarometer (from Figure 3.7a-b) are also plotted (stippled lines). Fields with stippled black outlines are P-T ranges calculated for Kangerluarsuk supracrustal belt, close to the island samples, from Kirkland et al. (2018a).

isochemical phase diagram of *Island III* records lower pressure, temperature values (Fig. 3.10). These differences in phase equilibria modelling results could be attributed to a variety of uncertainties, including effective bulk rock composition, activity-composition models, and the thermodynamic data set (Palin et al., 2016). Because the *Island I-II* exhibit very similar P-T conditions to the pressure-temperature estimates for *Island III*, it is assumed that the metamorphic conditions of *Island I-III* are fairly similar . Therefore, the modelled *Island* amphibolites record well constrained peak P-T conditions of 0.61-0.76 GPa and ~ 760-812 °C (Fig. 3.10). The peak P-T estimates record conditions above the solidus (Fig. 3.8a-e) and are consistent with the field and microstructural observations (Fig. 3.2a-c, 3.4b, e-g). This peak P-T condition is also compatible with an apparent thermal gradient of 1000-1330 °C/GPa, consistent with Neoarchean terranes worldwide (Johnson et al., 2017).

Mainland amphibolites differ in composition but exhibit a similar outcrop pattern with oriented felsic veins in the field (Fig. 3.2). *Mainland I* reveals temperature, pressure estimates of ~ 800-825 °C and < 0.35 GPa from the phase diagram (Fig. 3.9a). Amphibole-

plagioclase geothermobarometer shows unreliably low pressure of <0.1 GPa (Fig. 3.7b) even though the calibrated temperature range and amphibole-plagioclase compositions are justified. This can arise due to an error in calculating ferrous/ferric ratio in the amphibole grains. The actinolite zoning on magnesio-hornblende must have taken place in a typical greenschist-facies condition indicating retrogression. For *Mainland II* peak pressure temperature conditions using amphibole-plagioclase geothermobarometer yield 780 °C at 0.69-0.75 GPa (Fig. 3.7b), while Ti-in-amphibole exhibits temperature values slightly lower at 748±17 °C (Fig. 3.7c; Tab. 3.6). Isochemical phase diagram records a higher temperature range of 900-1000 °C and a slightly lower pressure of < 0.7 GPa (Fig. 3.9b-c). Hence, the estimated pressure and temperature values for both *Mainland* samples differ significantly. Nonetheless, for the *Mainland* samples, a general not as well constrained window of > 750 °C and pressure 0.8 GPa (Fig. 3.10) can be deduced. It should be noted that this value fall within the pressure range of Island amphibolites (Fig. 3.10). Peak P-T estimates (Fig. 3.9a-c) record conditions above the solidus and are consistent with field and microstructural observations (Fig. 3.2d-f, 3.5b, AP3 – 2). Due to the uncertainty in the estimated pressure and temperature values of *Mainland* amphibolites a clear distinction in metamorphic condition between the *Island* (Alanngua complex) and *Mainland* (Akia terrane) cannot be assessed reliably. However, in principle, in the range of error, they record very similar PT conditions.

3.7.2 MapComp whole rock geochemical data for phase equilibria modelling

For heterogeneous samples (*Island II-III* and *Mainland II*) areas defined by felsic veins (‘Zone 2’ in all the samples along with ‘Zone 3’ in Island II) are ignored for obtaining MapComp derived local bulk composition required for the isochemical phase diagrams. For *Island I*, we choose the bulk composition of the whole thin section area so that garnet compositional isopleths can be used to better constrain the P-T range. In summary, it can be stated that even though compositional veins do have an influence on the determined bulk composition in *Island I*, their effects depend very much on the ratio of "host" to "vein". Individual smaller veins have little influence on bulk rock composition and thus on phase equilibria modeling (e.g., *Island I*), but if they exceed a certain volume fraction in the sample/thin section, they can have a significant impact on composition and P-T determination (e.g., *Island II* or Heterogeneous rock III: SPI1321 in Chapter 2).

3.7.3 Implications for the metamorphic conditions in the Akia terrane-Alanngua complex

The continental crust in the Akia terrane formed during two metamorphic events: a diorite component at 3.2 Ga and a tonalite event at c. 3.0 Ga (Garde, 1997; Garde et al., 2000; Gardiner et al., 2019). Although the geodynamic setting of the 3.2 Ga metamorphic event is uncertain, Re-Os isotope data suggest that an extremely high degree of partial melting occurred during this period, possibly within a mantle plume setting (Szilas et al., 2016). These authors conclude that the genesis of the continental crust in Akia terrane happened through deep melting of the old, thick mafic crust in a vertical type tectonic setting. Gardiner et al. (2019) suggested that the two magmatic events in Akia terrane incorporated older mafic crust and deep melting in the presence of garnet. Kirkland et al. (2018a) identified a subsequent metamorphic event based on observations from garnet bearing leucosomes in amphibolite-metabasite units and garnet-sillimanite bearing metapsammite units from the Kangerluarsuk supracrustal belt in the Akia terrane. A thermal event at ~ 820-850 °C and 0.8-1 GPa during latest Mesoarchean to early Neoarchean (2.85-2.75 Ga) is characterized (Fig. 6 from Kirkland et al., 2018a). In the *Island* amphibolites, we find similar garnet-bearing leucosomes. The *Island* amphibolites also exhibit a similar metamorphic condition of 760-812 °C at 0.61-0.76 GPa in this study. The high temperature event can be linked to syn-deformation partial melting/melt fluxing as evidenced by garnet bearing felsic veins in parallel to the host foliation. A metapsammite sample in the same vicinity from Kirkland et al. (2018a) shows P-T condition of < 920 °C at > 0.75 GPa. Hence, a similar high pressure and high temperature granulitic facies metamorphism can be concluded from the samples belonging to the Alanngua complex in the West Greenland. Steenfelt et al. (2021) identify a part of the Akia terrane as Alanngua complex that separates the Akia terrane and Tuno terranes and hosts most of the Neoarchean magmatic, metamorphic, and tectonic activity. The boundary is defined based on an aeromagnetic study, and it is interpreted that this complex is distinct from its surrounding terranes. In this study, the pressure-temperature conditions of *Mainland* amphibolites from the Akia terrane are not well constrained, but conditions of high temperature metamorphism at > 750 °C and < 0.8 GPa can be postulated. Orthopyroxene bearing gneisses and leucosomes in the Maniitsoq region and across a broad region of the Akia terrane are identified by Friend and Nutman (1994), Garde (1990, 1997), and Garde et al. (2000). In the field, the *Mainland* amphibolites also provide evidence of clinopyroxene-orthopyroxene bearing veins.

Yakymchuk et al. (2020) observed similar undeformed two-pyroxene leucosomes in metamafic migmatites and argued a high temperature low pressure metamorphism in the Akia terrane. Though existence of the Alanngua melange zone and its tectonic nature with the surrounding Akia terrane are beyond the scope of this study; the high-grade metamorphism (0.61-0.76 GPa and ~ 760-812 °C) observed in the *Island* amphibolite of the Alanngua complex indicate very similar metamorphic condition (> 750 °C at < 0.8 GPa) to that of the *Mainland* amphibolites from Akia terrane. Furthermore, the similar granulite facies metamorphism observed in both regions, as well as that observed by Kirkland et al. (2018a), may indicate tectonic communication between the Akia terrane and Alanngua complex even in the late Mesoarchean, prior to the widespread granulite facies metamorphism observed in this study.

3.8 Conclusion

- Whole rock geochemical data obtained by MapComp can be utilized for phase equilibria modelling which can produce very reliable results. Here, different domains within the thin sections are used to calculate whole rock geochemistry for the isochemical phase diagrams. However, care must be taken in selecting the equilibrium mineral assemblage and domain for this modelling.

- *Island* amphibolites (at the boundary of Alanngua complex) show evidence of high-pressure high temperature metamorphism (~ 760-812 °C at 0.61-0.76 GPa). The results substantiate observation made by Kirkland et al. (2018a) from the Kangerluarsuk supracrustals in the nearby region (granulite facies metamorphism at ~820-850 °C and 0.8-1 GPa). This also suggests a high temperature thermal event with an apparent geothermal gradient of 1000-1330 °C/Gpa.

- The *Mainland* amphibolites within the Akia terrane and to the south of the Finnefjeld gneiss also exhibit similar high pressure and high temperature metamorphism (> 750 °C at < 0.8 GPa). This demonstrates that there is tectonic communication between the Alanngua complex and Akia terrane.

Chapter 4

Multi-scale porous melt flow facilitates melt migration, accumulation, and rheological weakening: an example from the Archean Akia terrane, West Greenland

This chapter is a manuscript draft that provides a case study on the interplay between deformation and melt migration. The chapter will be submitted to the journal *Lithos* soon after the thesis submission. I will be the first author of this contribution with Sandra Piazolo, Nathan Daczko, and Eleanore Blereau as co-authors. I was responsible for conceptualization, manuscript writing, data collection, data processing, figures, and data analysis. Sandra Piazolo and Nathan Daczko supervised and were involved in the conceptualization. Nathan Daczko obtained the high-resolution SEM scans of the thin sections and Eleanore Blereau conducted thermodynamic modelling. Dominik Sorger obtained EPMA geochemical spot analyses of two samples while Thomas Müller discussed the project at the very beginning with me. Both Dominik Sorger and Thomas are to be acknowledged in the acknowledgements.

Abstract

Presence of melt weakens the crust and, thus, plays an important role in orogenic deformation and exhumation styles, the mechanism of melt migration and its relationship with deformation is still poorly understood. Here, we report field, microstructural, and geochemical evidence of syn-deformation melt flow in dioritic gneiss, which exhibits an

abundance of straight to folded felsic veins within high and low strain domains, respectively. In the studied outcrops, low- and high-strain domains correlate with low and high abundance of felsic veins, respectively. Interestingly, the grain-scale microstructure, crystallographic orientation, and geochemical signatures are similar in both the domains. Frozen-in melt microstructures such as anhedral quartz-plagioclase and K-feldspar grains with cuspate grain boundaries, euhedral grains with straight crystal facets, elongated grains at grain interstices, low dihedral angles (LDA), and polymineralic quartz-plagioclase intergrowth (e.g., 'nanogranitoid') reveal 'igneous-like' microstructure within the host and in the veins of studied samples. Pseudosection modelling suggests peak metamorphic temperatures of 690–705°C, consistent with incipient biotite melting. At the microscale, however, the observed proportion of melt far exceeds the melt percentage generated by in-situ biotite melting. Our findings indicate that externally derived melt entered the rock via diffusive porous melt flow. We propose a melt migration mechanism involving pervasive melt movement along grain boundaries during heterogeneous deformation in an open system, resulting in the formation of low and high-strain domains. The presence of melt-fluxing is also supported by consistent major element chemistry in the constituent minerals, an increase in SiO_2 content in the host and X_{Ab} in plagioclase from the low to the high-strain domain. This also suggests that the high-strain rocks are more evolved and have experienced a higher degree of melt-rock interaction during pronounced melt influxing. Deformation was accommodated within the solid phases, by rigid body rotation accompanied by grain boundary sliding, resulting in the observed strong fabric. Minor internal crystal plastic deformation observed in the framework minerals suggests that dislocation creep has a negligible contribution to deformation. The relationship between high melt % and macroscopic high strain suggests significant rheological weakening during external melt influx, whereas the presence of a high percentage frozen-in melt indicates that the driving force for melt escape was minimal. Our findings show that porous melt flow is a significant process within the mid to lower crust, playing a larger role in melt transfer and melt accumulation than previously thought.

4.1 Introduction

Partial melt extraction from lower crustal rocks and its transport to higher crustal levels are fundamental processes responsible for the differentiation of the crust (Taylor and

McLennan, 1995; Brown and Rushmer, 2006). However, the exact nature of melt transport within the lower and middle crust are still debatable (Brown, 2004; Petford, 1996). Melt is a viscous phase, and its migration is primarily controlled by pressure gradients along with properties of the crust such as porosity, elasticity, and yield strength, as well as fluid properties such as viscosity and buoyancy (Sleep, 1988; Spence et al., 1987). Two main mechanisms of channelized melt transport within the crust are proposed: dykes within the brittle regime or through flow in shear zones within the ductile regime (Sleep, 1988; Weinberg, 1996; Beach and Fyfe, 1972; Cartwight and Barnicoat, 2003). Melt is concentrated at triple junctions, grain boundaries or along microfractures, and drains into low pressure sites along the shear zones or through a network of melt filled dykes (Lister and Kerr, 1991; Petford et al., 1994). Another model involves pervasive melt flow through a porous space that is strongly influenced by the permeability of the system (McKenzie, 1984; Weinberg, 1999). Here, melt is distributed along grain boundaries and at triple junctions within a solid framework forming a melt filled network (Turcotte and Ahern, 1978). Crucial prerequisites for such diffuse porous melt flow are deformation (because the viscosity contrast between the host rock and migrating melt are not enough) and lower solidus temperature of the country rock compared to that of the penetrating melt (Haslová et al., 2008a, 2008b). Though this melt transport mechanism has been well documented in the mantle (Dijkstra et al., 2003; Godard et al., 1995), and a few numerical studies have been conducted to prove its viability in the crust (Jackson et al., 2003, 2005), natural crustal examples of large-scale diffuse porous melt flow are scarce (e.g., Stuart et al., 2016, 2018a-b; Meek et al., 2019). Solano et al. (2012) suggest diffuse porous flow is an effective process of melt extraction if porosity is in the order of 20%. Haslová et al. (2008a) describes pervasive infiltration of an external melt which reacts with an orthogneiss producing a migmatitic texture along with an open system reaction causing chemical and microstructural changes (Haslová et al., 2008b). Stuart et al. (2016) discovers partial replacement microstructures in the Pembroke Granulite because of pervasive (kilometre scale), externally derived, reactive melt transport via diffuse porous flow. Active deformation in the source region can also improve melt extraction, both in terms of rate and minimum melt required for extraction (McKenzie, 1984). Melt presence may cause dramatic change to the rocks' strength, even for small melt volumes, and may aid strain localization (Beaumont et al., 2001; Rosenberg and Handy, 2005; Lee et al. 2018; Daczko et al. 2016). Hence, strong feedback exists between melted zones and deformation, which can influence the style of melt extraction, migration, strain partitioning, and shear zone nucleation (Brown, 2007, and

references therein). Despite knowing these fundamental relationships, deducing the behaviour of partially molten crust and the true nature of strain accumulation and partitioning is difficult (Lee et al., 2017, 2018). For example, even though the migmatites are commonly associated with one or several shear zones, it is unclear what causes strain partitioning or in-situ accumulation of melt (Labrousse et al., 2004; Lee et al., 2018).

To investigate the melt transport mechanism and nature of melt present deformation, we chose a study area in the lower crustal diorite gneiss of Akia terrane, SW Greenland. The field site presents an exceptional opportunity to study the mechanism and signature of melt transport because it is located within the deep amphibolite – to granulite facies domain in an arc environment (Garde, 1997) where high melt production and/or melt transfer are anticipated (e.g., Milan et al., 2017). Our study documents ubiquitous evidence of multi-scale syntectonic melt migration through the lower crust. Deformation plays a vital role in forming multiple low- and high-strain domains with varying numbers of felsic veins and their arrangements. A series of representative rocks are chosen from these two structural domains. High-strain domains have high melt percentages, resulting in significant differences in effective rheology compared to low strain domains. We show that the evolution of these two domains is a response to multiscale porous melt flow by combining microstructures, melt volume calculations, REE patterns, and quantitative orientation analyses.

4.2.1 Geological setting

The studied area is an island (between 65.0° and 65.5°N) situated near to the Alanngua fjord, approximately 10 km from the mainland, in the western coastal region of the Akia terrane in South-West Greenland (Fig. 4.1a). The island itself is made up of supracrustal rocks, dioritic orthogneiss and Tonalite–trondhjemite–granodiorite (TTG) gneisses (Fig. 4.1b-c). The Paleo- to Mesoarchean Akia terrane shows TTG orthogneiss, amphibolite, metasedimentary and ultramafic rocks metamorphosed at amphibolite to granulite facies conditions (Kirkland et al., 2018a). It is postulated that the precursor to the orthogneiss was produced by slab melting of the subducted oceanic crust whereas other models highlighted the role of protracted deep infracrustal melting of older thickened mafic crust in a vertical tectonic type setting (Gardiner et al., 2019). The supracrustals were originally interpreted as remnants of arc-related oceanic crust, formed at ca. 3.07 Ga, into

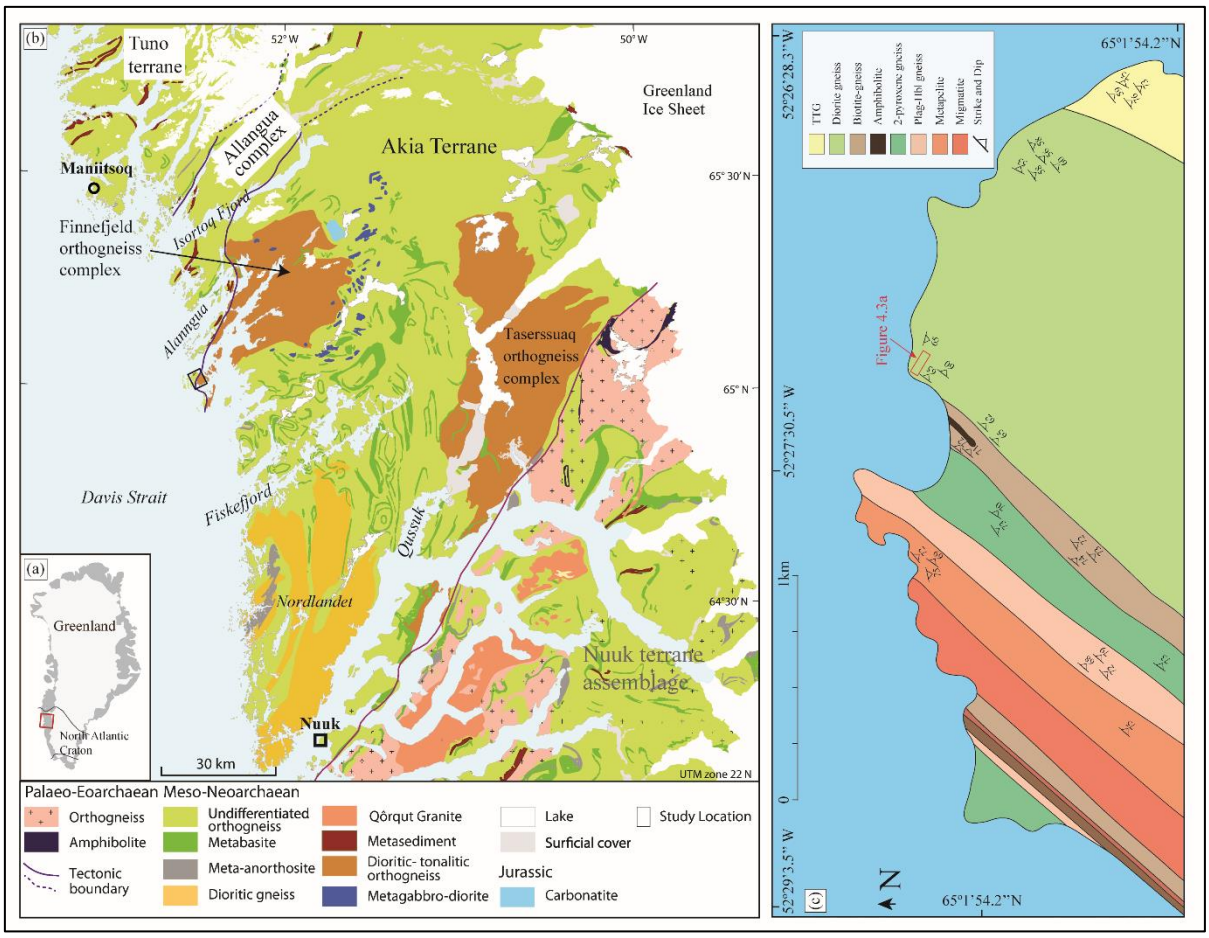

Figure 4.1 – (a-b) Simplified geological map of Nuuk region, SW Greenland, modified from Gardiner et al. (2019b), with study region labelled. Main lithological units and location of tectonic terranes within the Nuuk-Maniitsoq region are labelled. (c) Enlarged map of the study area with different lithological units (i.e., TTG, Diorite gneiss, Biotite gneiss, Two pyroxene gneiss, and metasediments oriented along the strike). Red rectangle box (not in scale) shows the studied section in Figure 4.3a.

---

which precursors of orthogneiss were intruded in the period of ca. 3.05-3.01 Ga (Garde, 1997; Garde et al., 2000; Garde, 2007). Metamorphism in the northern Akia terrane is associated with widespread granulite facies under suprasolidus condition at pressure < 9 kbar and temperature > 750°C (started at ca. 2.97 Ga), which affected the nascent tonalitic crust (Garde et al., 2000; Yakymchuk et al., 2020). The temperature exceeded 900°C locally during this first metamorphic event causing widespread partial melting (Friend and Nutman, 1994; Garde et al., 2000). This period was synchronous with the emplacement of Late-tectonic tonalitic intrusions, including the Taserssuaq Tonalite and Finnefjeld Gneiss (Fig. 4.1b; Gardiner et al., 2019). A second metamorphic event occurred between 2.85 and 2.7 Ga, causing widespread metamorphism, deformation, and partial melting (Friend et al.,

1996). Kirkland et al. (2018a) interpreted the peak metamorphic condition at 820-850°C and 8-10 kbar from Kangerluarsuk supracrustal rocks in the nearby region, which also characterize our study area (Chapter 3). The phase equilibrium modelling of the Kangerluarsuk metapelites suggests burial depth of >30 km and substantial partial melting(Kirkland et al., 2018a). Hence, the Akia terrane of South-West Greenland had a prolonged Mesoarchean-Neoarchean thermal history, with high temperatures reoccurring at least three times in ca. 3.0-2.5 Ga. (Garde, 1997; Kirkland et al., 2018a; Gardiner et al., 2019; Yakymchuk et al., 2020; Kirkland et al., 2020) and thus makes a perfect candidate for studying melt flow mechanisms and signature of melt migration in the lower crust.

A 1.5-kilometer-wide section of the diorite gneiss studied here occurs along a discontinuous belt with laterally extensive supracrustal rocks (approximately 5 kilometres north of the supracrustal belt studied by Kirkland et al., 2018a) extended over several kilometres. Amphibole- and biotite-bearing diorite gneisses coexist with metapelitic and metapsammitic units in the supracrustal rocks (Fig. 4.1c).

4.2.2 Field observations and Sampling strategy

A diversely deformed mafic rock with differently arranged leucocratic veins is observed in the field. Overall, the rock has a 'migmatitic' appearance. The host is a homogeneous dark mafic diorite gneiss with foliation (S) formed by oriented amphibole (amp) grains (Fig. 4.2a; foliation: 95-120°/60-65° SW and lineation: 40-50° → 165-170°) related to the first phase of deformation (D1). Internally (plastically) undeformed felsic veins are composed of fine-grained plagioclase (pl), quartz (qz), and K-feldspar. The veins have mostly diffuse boundaries to the host gneiss. They cut across or run parallel to the host foliation in places (Fig. 4.2a-b; AP4 – 1 in Appendix) or exhibit open (S or Z-type) and/or tight (M-type) folds associated with a second phase of deformation (D2). Shear bands formed by felsic veins are in response to a dextral sense of shear.

Low and high strain domains with different vein types

We mapped a 300-meter section of the diorite gneiss (Fig. 4.1c; 4.3a) to determine the distribution of high and low strain areas. The terms low- and high-strain are used in the rest of the chapter in a relative sense The felsic veins in the low-strain rocks also exhibit

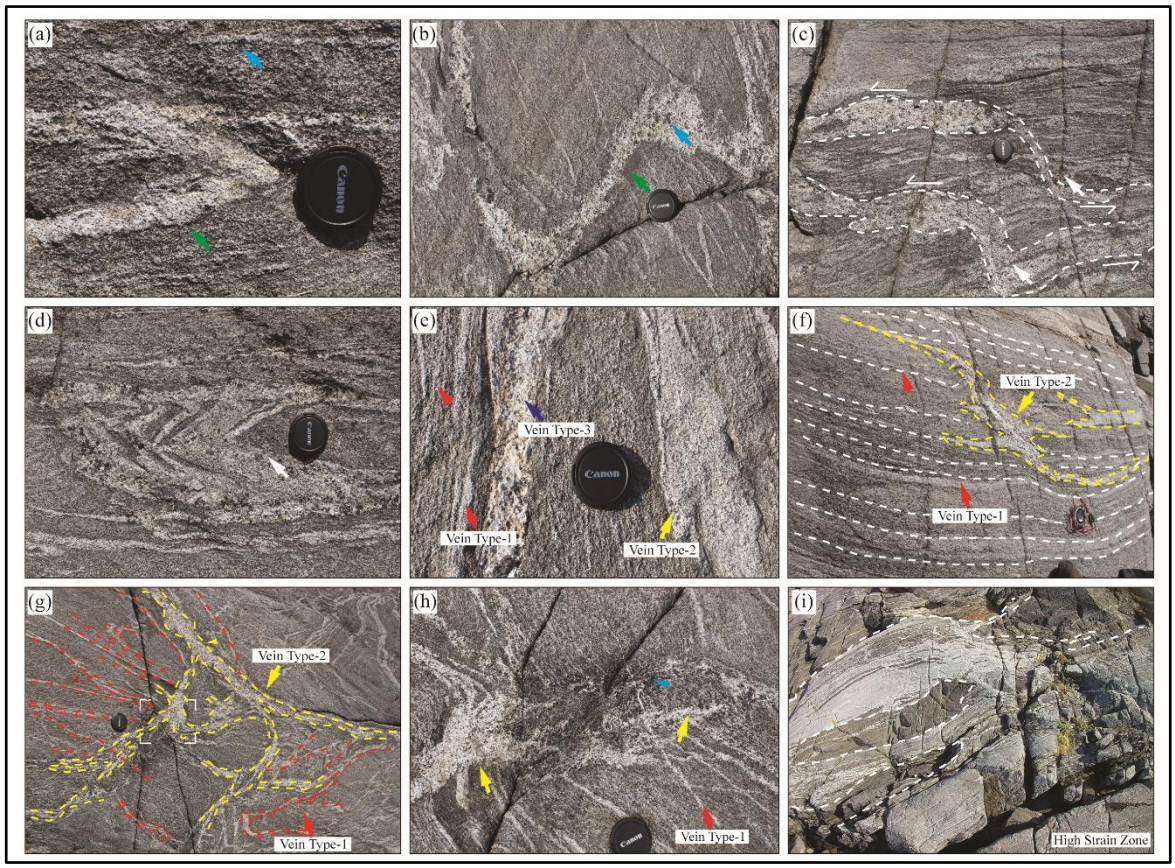

Figure 4.2 – Diorite gneiss with differently arranged plastically undeformed felsic veins closely resembling migmatites. (a) Tightly folded felsic vein with diffuse boundaries against the mafic host (green arrow). Large, elongated amphibole and biotite (blue arrow) grains are parallel to the felsic vein and host foliation. (b) Felsic veins with large open folds demarcate a low strain domain. Observe the dark mafic layer around the felsic zone in contact with its immediate host (green arrow). (c-d) Conjugate sheared tension gashes in 'c' and formation of shear bands in 'd' indicating syn-melt deformation. A dextral sense of shear is observed. (e) Three vein types: Type1 is thin, elongated, and has a fine-grained texture (red arrows), type2 is medium-grained (yellow arrow), and type3 is pegmatitic with large K-feldspar and plagioclase grains (purple arrow). (f) Type1 veins (white dashed lines) are parallel to host foliation. Type2 veins (yellow dotted line) crosscut but also run-in parallelism with type1 veins. (g) In the low strain zone, the interaction of two vein types (type1: red and type2: yellow) is observed. One vein type often grades to the other. Inset shows the location of 'h'. (h) Dark mafic patch indicating a zone of 'melt-loss'. Red and yellow arrow(s) denote felsic vein type1 and type2, respectively. (i) Large thick felsic veins (marked with white dashed lines) parallel to the foliation demarcate the 'high strain' domain.

---

evidence of folding (Fig. 4.2b; details below), whereas the veins in the high-strain rocks are mostly subparallel to the host-rock fabric (Fig. 4.2a, i). The boundaries between these areas are gradual, ranging from 0.5 to 1 meter. The variation in fold tightness and felsic vein abundance reveals strain variability. Folds are tighter and veins are commonly subparallel to the main fabric of the rock in areas with a high vein abundance. These domains are

interpreted to be high strain, as opposed to low strain domains with low vein abundance and open type folding. Mostly the veins are fine grained with pl>qz>kfs, termed as vein Type 1. Two additional felsic vein types are also observed: Type 2 is medium to coarse grained with qz-pl-kfs (pl>qz>kfs) and large euhedral plagioclase grains (Fig. 4.2e). They have diffused boundaries to the host rock, crosscut the low-strain domains, but mostly become parallel to the main fabric of the high-strain domain (Fig. 4.2f). Type 3 pegmatitic veins with coarse-grained qz-pl-kfs (kfs>qtz>plag) that crosscut the other two vein types (Fig. 4.2c, e) and exhibit very sharp boundaries against both the other vein types and host rock. Sometimes collapse structures can also be observed associated with vein type 1 and vein type 2 (Fig. 4.2g-h). Vein Type 2/3 crosscut the low-strain domains but is commonly transposed into the high-strain domains.

Character of low-strain domains

The low-strain domain has a general dark appearance and is characterized by 15-20veins/metre^2 and open asymmetric folding (S or Z-type) of vein Type 1 (Fig. 4.2b, felsic veins in Fig. 4.3a). The 3-5 cm wide felsic veinlets are mostly at an angle between 10-30° to the overall foliation (S) (Fig. 4.3b). The representative samples from the low-strain domain include the lowest strain SPI1317, devoid of any felsic vein, and low strain SPI1314 with both the host and vein material (Fig. 4.3a-b).

Character of high-strain domains

The high-strain domain, in contrast, has a more felsic-like overall appearance and is distinguished by having significantly more felsic veins (30-35 veins/metre^2) than the low-strain domain. Veins range from 3 to 5 cm in thickness. Vein Type 1 exhibits some symmetric tight isoclinal folding (Fig. 4.2a). While some felsic veins reveal diffuse boundaries with the mafic host, others record clear, sharp boundaries. Felsic veinlets are transposed, parallel to the host foliation (S), resembling a stromatitic migmatite (Fig. 4.2i). Representative high strain SPI1315 is collected adjacent to a characteristic felsic vein which display diffuse boundaries to the host. Heterogeneous strain distribution with high strain parts occurring between lower strain parts is commonly interpreted as progressive localization of deformation causing narrowing of shear zones (Means, 1995).

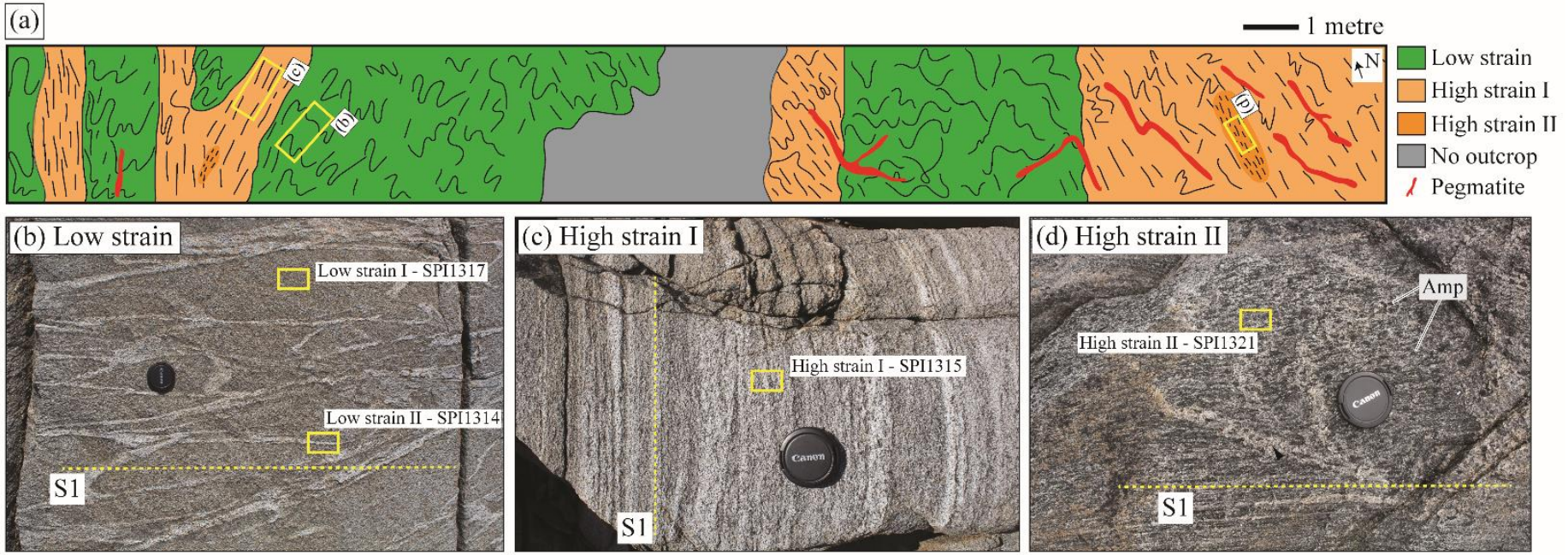

Figure 4.3 – Surface features observed in a 25-meter section of the diorite gneiss. (a) Repetitive low-high strain domains display a difference in the folding patterns of felsic veins (black lines; not in scale). Insets show the location of the field photographs. (b) In the low strain domain, 'low strain I - SPI1317' without any characteristic vein and 'low strain II - SPI1314' with a felsic vein sample are selected. Observe the 'S' and 'Z' type folds oriented at an angle to the main foliation (S1). (c) 'High strain I' domain with closely oriented felsic veins parallel to host foliation S1. Sample location of 'high strain I - SPI1315' (with a characteristic felsic vein) is shown. (d) 'High strain II' domain is identified with strongly oriented large mafic grains (amphibole ± biotite) parallel to type1 and type2 felsic veins. The foliation S1 direction is shown. Notice a relatively darker appearance of this zone compared to 'High strain I' domain. These zones occur sporadically within the 'High strain I' domain (observe in 'a'). Sample location of 'High strain II - SPI1321' with a felsic vein is shown.

Mafic pods and discontinuous layers (60-80 centimetres wide) occur throughout the outcrop, typically associated with the high strain domain and vein Type 1 (Fig. 4.3c). These are distinguished by large amphibole (>1 cm) and/or biotite (>1 cm) grains oriented parallel to the general foliation observed elsewhere. SPI1321 from the highest strain domain is collected, along with its characteristic vein representing a more mafic layer within the high strain domain.

4.3 Methods

4.3.1 Whole rock chemistry

Major and trace element whole-rock compositions were obtained from four representative samples, characterized by low vs. high-strain domains. Fresh samples only of the hosts were powdered using a TEMA tungsten carbide mill, and then analyzed using X-Ray Fluorescence (XRF) spectroscopy. Both major and trace elements of the four samples were analyzed at the Central Analytical Facilities (CAF) at the Stellenbosch University, Western Cape, South Africa, using a PANalytical PW2400 Sequential WDXRF Spectrometer. Trace elements were obtained using an Agilent 7700 Q ICP-MS. Fusion disks were prepared by an automatic Claisse M4 Gas Fusion instrument and ultrapure Claisse Flux, using a ratio of 1:10 sample: flux. The mount was mapped and then polished for analysis. Data processing was done using the LA-ICP-MS data reduction software package LADR from Norris Scientific (Norris et al., 2018). To correct for variations in ablation yield between standards and samples, an internal standard element of known concentration is used (Longerich et al 1996). Bulk rock geochemistry (in oxide weight%), concentration of trace elements (in ppm) and REEs (in chondrite normalised values of Anders and Grevesse, 1989) for rocks is listed in Tab. 4.2. Chondrite normalised REE profiles for average continental crust and lower continental crust are calculated using values from Rudnick and Gao (2003).

Major element whole-rock chemistry of two representative samples were verified using Rigaku ZSX Primus II, wavelength dispersive XRF with a Rhodium tube Spectrometer, calibrated with 70 international standards for major elements calibration at the School of Earth and Environment, University of Leeds, UK.

4.3.2 Petrography and Backscatter Electron Images

Polished thin sections were made from blocks cut perpendicular to the foliation (S) orientation and parallel to lineation (i.e., XZ section). Petrographic descriptions of the polished thin sections are made using a petrographic microscope combined with the Virtual Petrographic Microscope (Tetley and Daczko, 2014) and Image J v1.52 (Rasband, 1997-2015). Analyses include quantifying modal differences between rock types and measurements of the grain size. Backscatter electron (BSE) images are obtained to characterize differences between the studied samples and identify features discerning the former presence of melt, mineral reactions (if present) using FEG-SEM at the Leeds Electron and Mass Spectrometry unit (LEMAS), School of Earth and Environment, University of Leeds, UK. The SEM was run using an accelerating voltage of 20-30 kV, a beam current of 5-10 nA, and working distances of 11-13 mm.

4.3.3 Melt volume calculation

Paleo-melt volume calculation is done to understand the rheology and effect of strain localization and how it may have evolved in the low- and high-strain shear zones. Mesoscale leucosome content is determined at the outcrop scale using ImageJ (Schneider et al., 2012) of digitized outcrop photos. Photographs were simplified, redrawn, and corrected for shadows, cracks, vegetation at the outcrop scale. We also use BSE micrographs of the representative samples for qualitative microscale melt determination. It is assumed that the vein minerals crystallized from 100% melt. Next, microstructures indicative of the former presence of melt are distinguished within the host gneisses. Schematic diagrams are drawn mimicking these melt pseudomorphs grains. ImageJ software is used to calculate the total area% representing those grains, which is equivalent to the total melt area% of the host. Fe-oxides and holes are ignored for this calculation. Plane polarized (PPL), cross-polarised (XPL), and whole section BSE scans are used to determine the melt-solid interpretation.

4.3.4 Major element mineral chemistry

Mineral chemistry was analyzed using a JEOL JXA-8900RL electron probe microanalyzer (EPMA) at the Göttingen Laboratory for correlative light and electron

microscopy (GoeLEM) at the Geoscience Centre, University of Göttingen equipped with an energy-dispersive (ED) and five wavelength-dispersive (WD) spectrometers to characterize mineralogical changes and chemical environment during melt-rock interactions. The EMP analyses a spot size of 5 µm with an accelerating voltage of 15 kV and a beam current of 20 nA. Representative composition of minerals in the analyzed samples are given in Tab. 4.3. Additional spot analyses for plagioclase (Pl), K-feldspar (kfs), biotite (bt), and amphibole (amp) grains were performed using the University of Leeds, JEOL JXA8230 electron microprobe operated at 15kV and 15 nA with a defocused beam (all the measurements are recorded in Tab. AP4.1-4.4 in Appendix).

Raw data from the EMP are recalculated to cations per formula unit for each mineral. The amphibole classification spreadsheet of Locock (2014) and classification diagrams and nomenclature following Leake et al. (1997) are used. Mineral abbreviations are after Whitney and Evans (2010). Similarly, the plagioclase, K-Feldspar, and Biotite grains are analyzed. For amphibole-biotite, X_{Mg} (Mg_2/Mg_2+Fe_2) and similarly for plagioclase and K-Feldspar, X_{Ab} (Na_2/Na_2+Ca_2+K) and X_{Or} (K/Na_2+Ca_2+K) are represented, respectively.

4.3.5 Thermodynamic Modelling and geothermobarometry

To constrain the *P–T* conditions at which melting started, thermodynamic modelling in the NCKFMASHTO (Na_2O-CaO-K_2O-FE_2O_3-MgO-Al_2O_3-SiO_2-H_2O-TiO_2) system was undertaken. The whole-rock composition of low strain I - SPI1317 (Tab. 4.2), characterized by the absence of any felsic veins, is used on the basis that nearly the entire volume was in equilibrium as no mass was lost due to melt transport. Moreover, no major element chemical zonation was seen in the constituent minerals during melt-rock interaction. X-ray fluorescence data were recalculated into mole proportions for THERMOCALC (Tab. 4.2).

Modelling was undertaken using THERMOCALC 3.40 (Powell and Holland, 1998) and the internally consistent data set, tc-ds62 (produced 6/2/2012), of Holland and Powell (2011) and the activity models of Green et al., (2016). Minerals considered in the pseudosection are amphibole (hornblende) (Hbl), biotite (Bt), quartz (Qz), K-feldspar (Kfs), plagioclase (Plag), ilmenite (Ilm), magnetite (Mag), sphene/titanite (Sph/Ttn), rutile (Rt), epidote (Ep), garnet (Grt), chlorite (Chl), orthopyroxene (Opx), albite (Ab) and silicate melt (Liq). Mineral abbreviations are after Whitney and Evans (2010).

Initial investigations of low strain I - SPI1317 showed stability of orthopyroxene, which is not observed when using the measured LOI as H_2O. To constrain the amount of H_2O at $T–X_{H2O}$ from the measured LOI value to 2 wt% an X value of 0.1 (2.54 mol%) was chosen to reduce the stability of orthopyroxene. Using this composition, magnetite was not stabilised within the peak assemblage, however, so the amount of O (as O = FeO/2 * %) was progressively increased to ~50% of FeO/2 (1.40 mol%) to stabilise the recorded assemblage in the final modelled $P–T$ pseudosection.

To consolidate the estimated P-T condition independently Ti-in-Amphibole (following Liao et al., 2021), Ti-in-Biotite (following Henry et al., 2005) thermometers and amphibole-plagioclase thermobarometers (Holland and Blundy, 1994 for geothermometer and Molina et al., 2015 for geobarometer) are used.

4.3.6 Quantitative orientation analysis: Electron backscatter diffraction analysis

Microstructural-crystallographic characterization of the studied samples was performed using an FEI Quanta 650 FEG-Scanning Electron Microscope (SEM) with an Oxford/HKL Nordlys EBSD system at the Leeds Electron and Mass Spectrometry unit (LEMAS), University of Leeds, UK. Electron backscatter diffraction (EBSD) mapping was performed on a quarter micron polished thin section (with an additional 8-minute polishing using the colloidal silica-water solution) covering large areas of the sample. The sample was coated with ~3 nm of carbon. Conditions were set at 30 kV accelerating voltage, 80nA beam current, working distance of 12 mm, specimen tilt of 70º, and step size of 10 µm for large map scans and 3 µm for small maps. Post-processing is performed using AZTEC CRYSTAL analysis software (Oxford Instruments) and the procedure of Prior et al. (2002) and Piazolo et al. (2006) are used for noise reduction and removal of zero solutions. The data has been used to construct phase maps, orientation maps, GROD maps (in colour) and equal area pole figures plotted in the upper hemisphere. Grain boundaries are identified with misorientation >10°. Subgrain boundaries are defined as having misorientations larger than 2° and less than 10°. Phase and orientation maps are used to decipher grain orientations and associations. Orientation maps are presented with inverse pole figure (IPF) colour scheme which produces a colour for each orientation according to the crystallographic axis aligned with the sample direction (chosen by the X, Y, or Z). Here IPF maps parallel to the ‘Z’

direction are presented. GROD maps show spatial variation of the grain reference orientation distribution (GROD) within constituent mineral grains. GROD angle maps utilize average orientation of each grain and plot the angular deviation from this mean orientation for each pixel. This allows any substructures within the grains to be visualized, even the smallest misorientation angle pixel by pixel. Misorientation profiles are drawn to show cumulative change in crystal orientation relative to its starting point. For all the pole figures, X denotes the direction of the lineation and foliation is normal to the Y axis. One point per grain is used (>10° threshold angle for grain boundaries) to eliminate the possibility of large grains distorting the interpretation by causing single-crystal maxima. Pole figures are contoured using 15° half-width contouring and multiples of uniform density (MUD) values are calculated. A constant MUD value is chosen to show difference in pole figure strength between samples. Mineral mode% are also calculated using the phase maps (Fig. AP4 - 1 in Appendix).

4.4 Results

4.4.1 Mineral assemblage and microstructure

General characteristics of the Dioritic Gneiss

Even though the samples were collected from distinct structural domains (Fig. 4.3) within the low- and high-strain shear zones, several similar grain scale microstructures are found, such as : A) amp-bt-plag-qtz-kfs-ttn are the dominant minerals (Fig. 4.4a, e, i; Fig. 4.6a), B) elongated amp-bt grains give rise to the characteristic foliation S (Fig. 4.4a, e, i; Fig. 4.6a), C) amphibole grains show embayment microstructures along their boundaries (Fig. 4.5a), D) biotite grains show disequilibrium textures indicated by irregular grain boundaries (Fig. 4.4b-c, g; Fig. 4.6d), E) plagioclase grains form the solid framework and often show unfilled microcracks (Fig. 4.4-4.6), and F) no noticeable increase in the degree of recrystallization of the constituent quartz-plagioclase grains with increasing strain (Fig. 4.4, 4.6). The vein-present samples (i.e., SPI1314-SPI1315-SPI1321) show felsic veins parallel to host foliation S (Fig. 4.4e, i; Fig. 4.6a). In mafic host of all the studied samples modal% of plagioclase is the highest (~59-60%) (Tab. 4.1; Fig. AP4 - 1 in Appendix). This is followed by 17-18 modal% of quartz. The host of low strain I - SPI1314 exhibits a

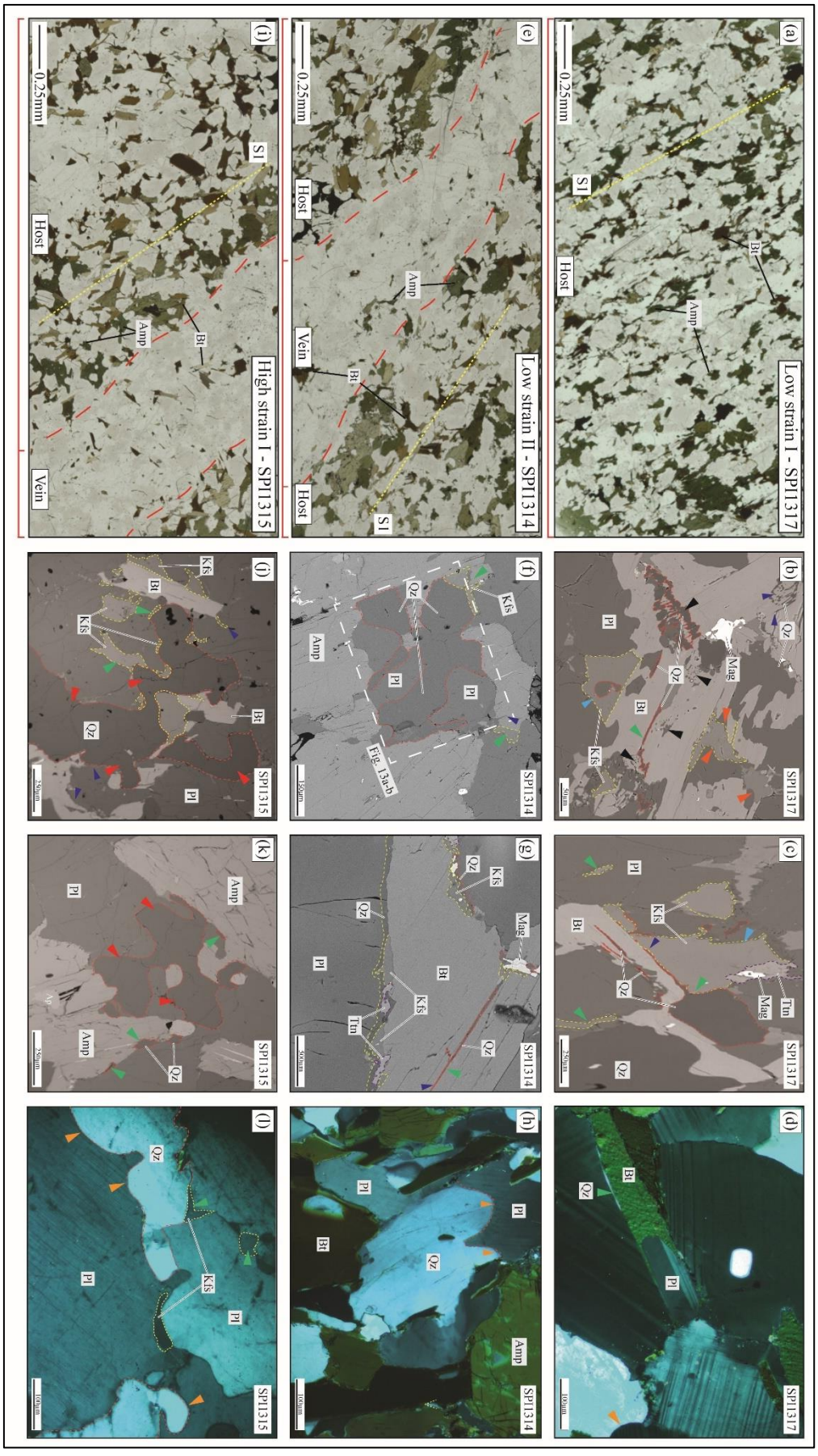
(a)
Low strain I - SPI1317
0.25mm
S1
Host
Bt
Amp
(b)
SPI1317
Qz
Mag
Qz
Pl
Bt
Kfs
(c)
SPI1317
Pl
Kfs
Bt
Mag
Ttn
Qz
Qz
(d)
SPI1317
Bt
Qz
Pl
(e)
Low strain II - SPI1314
0.25mm
Host
Amp
Vein
Bt
S1
Host
(f)
SPI1314
Kfs
Qz
Amp
Pl
Pl
Fig. 13a-b
(g)
SPI1314
Qz
Kfs
Mag
Qz
Pl
Bt
Kfs
Ttn
Qz
(h)
SPI1314
Pl
Pl
Bt
Qz
Amp
(i)
High strain I - SPI1315
0.25mm
S1
Host
Amp
Bt
Vein
(j)
SPI1315
Kfs
Bt
Kfs
Qz
Bt
Pl
(k)
SPI1315
Amp
Pl
Amp
Qz
(l)
SPI1315
Qz
Pl
Kfs
Pl

Figure 4.4 – Photomicrographs display similar grain structures (grain size, mineral associations, microstructures, and alignment of grains) in low strain I - SPI1317, and hosts of low strain II - SPI1314, and high strain I - SPI1315 samples. (a) Overview PPL photomicrograph of low strain I - SPI1317 shows oriented amphibole-biotite grains forming foliation (S). Dark and light bandings demarcate the segregation of mafic-felsic layers. (b-d) Close up BSE images and XPL photomicrograph of low strain I - SPI1317 exhibit K-feldspar with partial facets (blue arrows), elongated quartz and K-feldspar extending along grain boundaries of adjacent biotite-amphibole (green arrows), cuspate grain boundaries of K-feldspar and quartz (orange arrows), and fine-grained quartz corroding biotite grains (black arrows) indicative of former presence of melt. A biotite grain partially corroded by plagioclase is observed in 'd'. Interstitial quartz grains with low-dihedral angles (LDA) and 'string of beads' texture. Purple arrows indicate LDA as low as <10°. Grain outlines of quartz, K-feldspar, and titanite grains are shown with red, yellow, and purple stippled lines. (e) Overview PPL image of low strain I - SPI1314 exhibits a felsic vein parallel to S. Large quartz + plagioclase + K-feldspar with little biotite + hornblende constitute the vein. Close up BSE and XPL images from low strain II - SPI1314 display (f) multiphase aggregates of quartz-plagioclase implying small pockets of crystallized melt. Note: large plagioclase-quartz are irregularly shaped while K-feldspar grains occur as anhedral interstitials. LDA of quartz is as low as <10° (purple arrow). EBSD area is marked, (g) thin films of fine-grained quartz + K-feldspar + titanite along irregular grain boundary of biotite suggest biotite melting, (h) regular cuspate grain boundaries between plagioclase and quartz grains (orange arrow) where quartz grain appears to corrode the plagioclase. (i) Overview PPL photomicrograph of high strain I - SPI1315 indicates a felsic vein parallel to S. Close up BSE and XPL photomicrographs exhibit (j-l) quartz and K-feldspar as small interstitials or extending along grain boundaries of adjacent grains (green arrows). Large xenomorphic quartz grains (red arrows), and cuspate grain boundaries (orange arrows) indicate former melt presence. Purple arrows indicate LDA as low as <10°. Mineral abbreviations are after Whitney and Evans (2010).

		Low strain Domain		**High strain Domain**	
		Low strain I - SPI1317	Low strain II - SPI1314: Host	High strain I - SPI1315: Host	High strain II - SPI1321: Host
Amphibole		Mode: 17%	Mode: 29%	Mode: 8%	Mode: 31%
Grain size	Avg.	0.4-0.9 mm	0.4-1 mm	0.4-0.9 mm	0.4-0.8 mm
	Max.	1.5-1.7 mm	1.5-2 mm	1-1.5 mm	2-2.2 mm
Aspect ratio	Avg.	2	2	2-2.5	2
	Max.	3-5	3-4	4-6	5-5.3
Biotite		Mode: 3%	Mode: 4%	Mode: 12%	Mode: 0.5%
Grain size	Avg.	0.3-0.6 mm	0.2-0.5 mm	0.2-0.6 mm	0.3-0.5 mm
	Max.	0.8-1 mm	0.6-1 mm	1-1.5 mm	0.6-0.8 mm
Aspect ratio	Avg.	2	2-2.2	2-3	2-3
	Max.	4-6	4-5	6-7	7-8
Plagioclase		Mode: 59%	Mode: 60%	Mode: 60%	Mode: 48.5%
Grain size	Avg.	0.8-1.2 mm	0.4-1 mm	0.4-0.8 mm	0.4-0.6 mm
	Max.	1.5-2 mm	1.3-1.8 mm	1.3-1.8 mm	3-3.5 mm
Aspect ratio	Avg.	1.8	1.8	2-2.5	1.8-2
	Max.	2-4	2-3.5	3.5-5	5-6.2
Quartz		Mode: 18%	Mode: 6%	Mode: 16%	Mode: 17%
Grain size	Avg.	0.3-0.8 mm	0.5-1 mm	0.4-1 mm	0.3-0.7 mm
	Max.	1.3-1.5 mm	1.2-1.7 mm	1.5-1.9 mm	2-2.5 mm
Aspect ratio	Avg.	1.8	1.8-2	1.8-2	1.8-2
	Max.	3-4	2.5-3.5	4.5-7	6-7.2
K-feldspar		Mode: 2%	Mode: 1%	Mode: 3%	Mode: 3%
Grain size	Avg.	0.1-0.3 mm	0.1-0.3 mm	0.15-0.3 mm	0.1-0.3 mm
	Max.	0.5 mm	0.4-0.6 mm	0.4-0.6 mm	0.5-0.7 mm
Aspect ratio	Avg.	1.8	1.8-2	2-4	2
	Max.	3-4	2.3-3.5	4-6	3.3-5

Table 4.1 - Properties for constituent amphibole, plagioclase, and quartz grains in each rock sample derived from the EBSD data set (Fig. AP3 - 1). Only the host portions are used for low strain II - SPI1314, high strain I - SPI1315, and high strain II - SPI1321. For each mineral, modal proportions are shown.

---

relatively low quartz grain population (~6 modal%). Amphibole displays variable modal% in the host of all studied samples. In low strain I - SPI1317, it constitutes 17 modal% but its population increases to 29 modal% in low strain II - SPI1314 (Tab. 4.1; Fig. AP4 - 1 in Appendix). A decrease in amphibole modal abundance (~8 modal%) is observed in high strain I - SPI1315 but high strain II - SPI1321 again exhibits an increase in the amphibole grain population (17 modal%) (Tab. 4.1; Fig. AP4 - 1 in Appendix). Biotite grains constitute only 3-4 modal% in low strain samples, a high population of 12 modal% is observed in the high strain I - SPI1315 whereas the host of high strain II - SPI1321 displays only 0.3 modal% of biotite. K-feldspar grains have uniform abundance of 2-3 modal% in the host; whereas modal% of Fe-oxides (magnetite and ilmenite) are the lowest (0.5-1%) (Tab. 4.1; Fig. AP4 - 1 in Appendix). In SPI1321, additional epidote grains are observed, but no magnetite/ilmenite grains are found.

Amphibole in the host of all studied samples exhibit bimodal grain size where small grains of 0.2-0.6 mm and large grains of 1-2.3 mm are found (Tab. 4.1). Aspect ratio of amphibole varies between 1 to 5, with an arithmetic mean of 2.2. Similarly, biotite grains have a small grain size of 0.2-0.5 mm and a large grain size of 0.6-1.5 mm. The grain aspect ratio averages between 2.5 and 3. In the mafic host of high strain II - SPI1321 biotite grains are smaller (with a maximum gain size of 0.80 mm), and amphibole grains are larger (1.3-2 mm in size) than in other samples (Tab. 4.1). Small amphibole grains (0.4-0.8 mm in diameter) are also present in the host. Plagioclase-quartz grains in the host of all studied samples show bimodality in grain size, where average grain size ranges between 0.5 to 1 mm. The average grain size of plagioclase grains decreases slightly from low strain I – SPI1317 to high strain II – SPI1321 (Tab. 4.1). However, high strain I – SPI1315 and high strain II – SPI1321 also record the maximum grain size of plagioclase, with grain sizes of up to 2.2 mm and 3.5 mm, respectively. Hence, some plagioclase grains are coarser in the high strain samples, though the population of fine-grained plagioclase increases. In contrast, from low strain I -SPI1317 to high strain II – SPI1321, average grain size of quartz increases (Tab. 4.1). In high strain I - SPI1315 and high strain II - SPI1321, similarly, largest quartz

grains are up to 1.9 mm and 2.5 mm, respectively (Tab. 4.1). Therefore, quartz grain size is coarser in the high strain samples. K-feldspar grains have unimodal grain size distribution of 0.1-0.3 mm, with a maximum grain size of 0.6-0.7 mm (Tab. 4.1). Plagioclase in all the studied samples show an average aspect ratio of 1.8-2 (Tab. 4.1). Occasionally, large quartz grains are elongated with an aspect ratio of 2-3. In low strain I - SPI1317, aspect ratio of large quartz grains can reach 3-4, whereas the average aspect ratio of small and medium sized grains is 1.8. The aspect ratio of quartz and plagioclase increases from low strain I - SPI1317 to high strain II – SPI1321 (Tab. 4.1).

The veins have variable composition where plagioclase dominates (60-67 modal% in SPI1314 and SPI1321 veins, and 50 modal% in SPI1315: vein) followed by quartz (29 modal% in SPI1314: vein, SPI1321: vein and 47 modal% in SPI1315: vein) (Fig. AP4 - 1 in Appendix). The abundance of K-feldspar grains is uniform with 1-2 modal%. Biotite grains are sparse (1-2 modal%) in SPI1314 and SPI1315 veins but have an increased population of 9 modal% in SPI1321: vein (Fig. AP4 - 1 in Appendix). Amphibole grains are also limited with 0.5 modal% in SPI1314 and SPI1315 veins, whereas vein of SPI1321 has no amphibole grains (Fig. AP4 - 1 in Appendix). Hence, felsic veins have a relatively higher population of quartz-plagioclase and K-feldspar (97-98% in total) with minor amphibole-biotite grains (1-3%; Fig. 4.4e, i; Fig. AP4 - 1 in Appendix), except for SPI1321-vein, which has large, elongated biotite grains (up to 9 modal%; Fig. 4.6a, AP4 - 1 in Appendix). Quartz grains in the vein have a relatively larger grain size than those found in the host. Large quartz grains in the SPI1314 and SPI1315 veins range in size from 2.8 to 3.9 mm in size. Similarly, in SPI1321, the plagioclase and quartz grain sizes in the vein can reach 3.7 mm and 2.6 mm, respectively.

Rose diagrams (Fig. AP4 - 2 in Appendix) for low strain I - SPI1317 show that the long axes of plagioclase, biotite, amphibole, and quartz in XZ sections have a preferred orientation of 15-20° inclined to the foliation direction. K-feldspar, on the other hand, has a bimodal distribution, with one maximum subparallel to the main foliation and a second at an acute angle (50°) to it. Low strain II - SPI1314 exhibits strong plagioclase SPO sub-parallel to the main foliation. Amphibole and biotite exhibit a slightly inclined SPO oriented at a 25° angle. Quartz has a SPO that is subparallel to the aggregate elongation direction (at 10° angle to the foliation). K-feldspar distribution is bimodal again, with one maximum inclined to the main foliation and a second almost perpendicular to it. Thus, SPO strength increases as strain increases. High strain I - SPI1315 has a very weak SPO for plagioclase

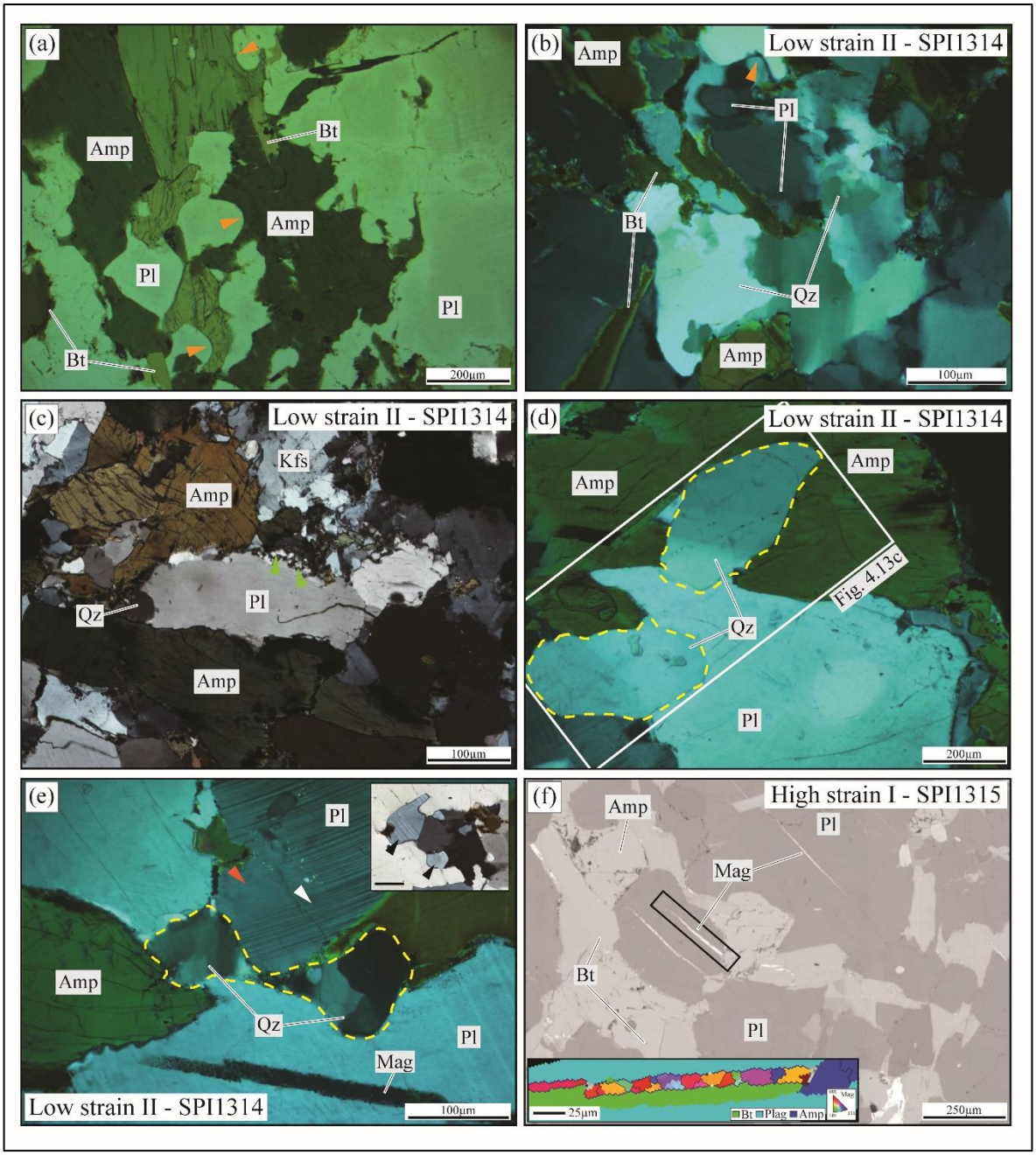

Figure 4.5 – Close up PPL, XPL and BSE images indicate minor plastic and brittle deformation in low strain I - SPI1317, low strain II - SPI1314, and high strain I - SPI1315. (a) Irregular grain boundaries of amphibole represent grain embayment (orange arrows). Matrix of low strain II - SPI1314 display (b) a fine-grained region with dynamic recrystallization in quartz. Recrystallization is concentrated at the grain boundaries of undeformed plagioclase grains and (c) large plagioclase with small, recrystallized grains (green arrows) along its grain boundary. The other boundaries are regular and show a cuspate grain shape. (d) Large subhedral quartz grains representing pre-melting metamorphic history. EBSD area is marked. (e) Anhedral quartz grain (grain shapes indicate a crystallized 'melt pocket') reveals strong undulose extinction. Large plagioclase with minor bending in twins towards the grain-center (white arrow), the outer rims lack any bending and are sometimes devoid of any deformation twins (orange arrow). Small plagioclase grains (inset) are fresh, show cuspate grains, and lack any deformation twin (black arrows; scale bar = 100mm). (f) Straight microcracks filled with biotite + magnetite inside a plagioclase grain in high strain I - SPI1315: matrix. Inset shows EBSD crystallographic orientation map of a multiphase mineral filled crack

(location marked with black rectangle) with numerous magnetite grains crystallized in different crystallographic orientations (inset shows colour coded key). Similar cracks are also observed in low strain I - SPI1314 (observe magnetite grains along a crack marked in 'e').

---

and a near random orientation for biotite. Amphibole and K-feldspar have a bimodal distribution with inclined SPO (at 25° angle to the foliation direction). Quartz grains are strongly inclined, with one orientation nearly parallel to the foliation. This suggests that SPO weakens from low strain II - SPI1314 to high strain I - SPI1315, and grains, except for amphibole, become more randomly arranged. High strain II - SPI1321 has the highest SPO, and all the minerals are almost parallel to the foliation direction.

Macro- and Microstructural evidence for melt

It is often assumed that at outcrop scale former melt presence is evident when there are quartzo-feldspathic layers interpreted as leucosomes (Mehnert, 1968). In the field, we observe low- and high-strain domains with different proportions of such quartzofeldspatic veins. Fig. 4.2-4.3 shows characteristic outcrop scale variation with differently arranged leucocratic veins. They are of different types (type1 to type 3) based on their mode of occurrence and microscale grain structures. High strain domains have the highest melt content, and variation in migmatite structure and melt fractions reflect rheological variation. However, no high-temperature mineral assemblage (i.e., orthopyroxene and/or garnet and/or cordierite) indicative of dehydration melting of micas is observed, and hence it becomes imperative to study any microscopic evidence of melt.

Melt pseudomorphs of mainly quartz and K-feldspar within a solid framework of plagioclase in both host and veins of studied samples are found. Typical melt microstructures include (A) cuspate grain boundaries of qtz-plag-kfs grains (orange arrows in Fig. 4.4b-d, h, l; Fig. 4.6b-c, f), (B) fine grained, elongated qtz-kfs grains (with very high aspect ratios > 10) along grain boundaries between two grains of contrasting mineral phases. Elongated grains also occur along grain boundaries of large, faceted amphibole grains. The elongated grains may represent isolated single grains or it may form as an overgrowth (green arrows in Fig. 4.4c-d, f-g, j-l; Fig. 4.6b, e-f), (C) large xenomorphic qtz grains corroding grain boundaries of surrounding plag-hbl (red arrows in Fig. 4.4j-k; Fig. 4.6b-c, e-f), (D) partial straight faceted qtz-kfs grains (Fig. 4.4b-c; Fig. 4.6c, e-f), (E) some qtz-plag grains

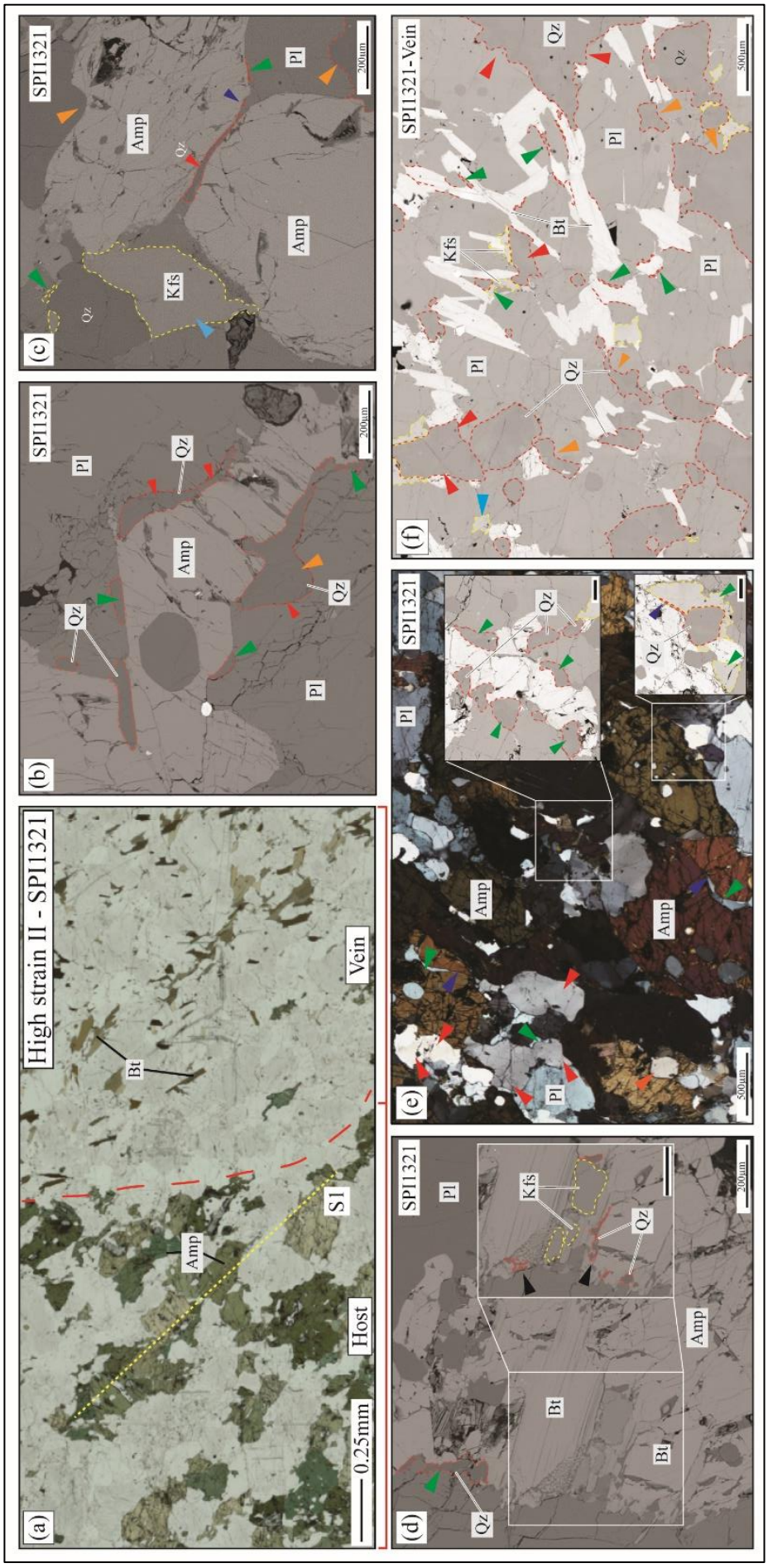
(a)
High strain II - SPI1321
Bt
Amp
S1
Host
Vein
0.25mm
(b)
SPI1321
Pl
Qz
Amp
Qz
Qz
Pl
200um
(c)
SPI1321
Amp
Qz
Qz
Kfs
Amp
Pl
200um
(d)
SPI1321
Pl
Kfs
Qz
Amp
Bt
Bt
Qz
200um
(e)
SPI1321
Pl
Amp
Amp
Pl
Qz
Qz
500um
(f)
SPI1321-Vein
Qz
Pl
Kfs
Bt
Pl
Qz
Qz
500um

Figure 4.6 – Photomicrographs display distinct microstructural features of former melt presence in high strain II - SPI1321. (a) Overview PPL photomicrograph shows the host is primarily devoid of large biotite grains/grain-clusters but is prevalent in the adjacent felsic vein. Amphibole grains are oriented parallel to host foliation (S). Observe the larger grain size of amphibole compared to previously studied samples. Grain outlines of quartz and K-feldspar are shown in red and yellow dotted lines, respectively. (b-c) Close up BSE images exhibit elongated interstitial quartz along amphibole grain boundaries (green arrows). Anhedral grains (red arrows), partially faceted K-feldspar grain (blue arrow), or cuspate grain boundaries of quartz (orange arrows) indicate quartz-K-feldspar grains as last crystallizing phases. Notice amphibole and plagioclase grains are fractured. (d) In the host, fine-grained K-feldspar, and quartz grains partially corrode biotite along its boundary (black arrows) (see inset; scale bar = 150µm). (e) XPL and BSE photomicrographs exhibit interstitial quartz-K-feldspar (green arrows) and xenomorphic quartz grains (red arrows). Purple arrows indicate low dihedral angle as low as <10° (insets show interstitial grains and LDA of quartz; scale bar = 50µm). (f) BSE image from high strain II - SPI1321: vein displays similar 'melt-microstructures' such as interstitial quartz grains along biotite grain boundaries as 'melt films' (green arrows), large xenomorphic grains (red arrows), quartz and K-feldspar with cuspate grain boundaries (orange arrows), and K-feldspar with partial straight facets (blue arrow). Note the elongated quartz grains in 'f' also parallel biotite alignment. Quartz grains often corrode plagioclase grain boundaries giving the cuspate appearance. Mineral abbreviations are after Whitney and Evans (2010).

---

exhibiting low apparent dihedral angles from <10° to up to <60° (Fig. 4.4b-c, g, j-l; Fig. 4.6b-c, e) giving them an interstitial appearance. Small dihedral angles occur as terminations of elongated grains or as cuspate boundaries at triple junctions, (E) disequilibrium texture of biotite with laterally continuous, fine-grained, elongated qtz-kfs-ttn commonly coating entire irregular grain boundaries of biotite (Fig. 4.4b, d, g; Fig. 4.6d), (F) multiphase aggregate with qtz-plag grains (Fig. 4.4f). Polycrystalline aggregates are typically 100-250 µm with either large anhedral grains (50-100 µm) or fine grained (20-40 µm) subhedral aggregates. Plagioclase and quartz are always present and may include K-feldspar grains. These are often observed at triple junctions, and (G) strings of rounded bleb-shaped minerals ('string of beads' texture; Holness et al., 2011) (Fig. 4.6e). It is to be noted that qtz-kfs within the host and vein form much larger individual grains compared to when they are observed along the irregular boundaries of biotite in all the studied samples. Quartz and K-feldspar are sometimes elongated parallel to the foliation (Fig. 4.6f). Other microstructural features include amphibole grains with irregular grain embayments surrounding qtz-plag in all the studied samples (Fig. 4.5a). Small quartz-plagioclase grains occur as inclusions inside the amphibole. Fractures in amphibole are filled with small, elongated quartz grains whereas microcracks in plagioclase grains are generally unfilled. In some areas, especially in low-strain II - SPI1314, patches with recrystallized quartz grains (Fig. 4.5b) or plagioclase grains with small, recrystallized fractions along their irregular grain boundaries (Fig. 4.5c) are found. Subrounded quartz grains with regular grain boundaries, devoid of any typical melt

microstructures (Fig. 4.5d) are observed. Anhedral interstitial quartz grain (resembling a melt pocket) exhibits mild to strong undulatory extinction (Fig. 4.5e). Hence, the transitional rock from low strain to high strain domain show some evidence of localized sub-solidus deformation. In both the low strain II - SPI1314 and high strain I - SPI1315 some plagioclase grains are found to host straight long fractures. EBSD orientation analysis on one such fracture records biotite and long trails of magnetite with differently oriented grains (identified from varying in IPF colour coded images of magnetite). Elongated, anhedral, interstitial magnetite grains with low dihedral angle (sometimes <10°) are also observed denoting crystallization from an external fluid (Fig. AP4 - 3 in Appendix). Within the veins (in SPI1314, SPI1315, and SPI1321), similar microstructures of qtz-plag-kfs occurring as anhedral interstitials, elongated films along grain boundaries of other minerals, fine grained aggregates corroding grain boundaries of biotite, grains with curved cuspate boundaries, and quartz- K-feldspar grains with low dihedral angles (LDA) are observed (Fig. AP4 - 4 in Appendix).

Melt volume

Fig. 4.7 shows an example of the quantification of the melt via field photographs and photomicrographs where melt is denoted as white, and black represents solid host (Fig. 4.7). The low strain domain shows a maximum felsic proportion (preserved as felsic veins) of 30% (Fig. 4.7a) whereas in the high strain domain this amount increases to a maximum 48-49% (Fig. 4.7d). However, this does not mean up to 30-50% of the crust was melt, as the leucosome content only indicates maximum melt proportion left in-situ. Felsic content of the low strain domain is used for low strain samples SPI1317-SPI1314, and the high melt% of the high strain domain is used for high strain samples SPI1315-SPI1321.

Melt% preserved in the host of low strain I - SPI1317, low strain II - SPI1314, high strain I - SPI1315, and high strain II - SPI1321, from the representative XPL photomicrographs and BSE scans, comes around 19% (Fig. 4.7b), 9% (Fig. 4.7c), 17% (Fig. 4.7e), and 25% (Fig. 4.7f) respectively. Since precursor quartz-plagioclase grains also recrystallize in the presence of melt, we roughly consider that 50% of the melt pseudomorphed grains were originally solid. Thus melt% in the host is estimated 9.5%, 4.5%, 8.5% and 12.5% respectively for low strain I - SPI1317, low strain II - SPI1314, high strain I - SPI1315, and high strain II - SPI1321. Hence considering both leucocratic veins

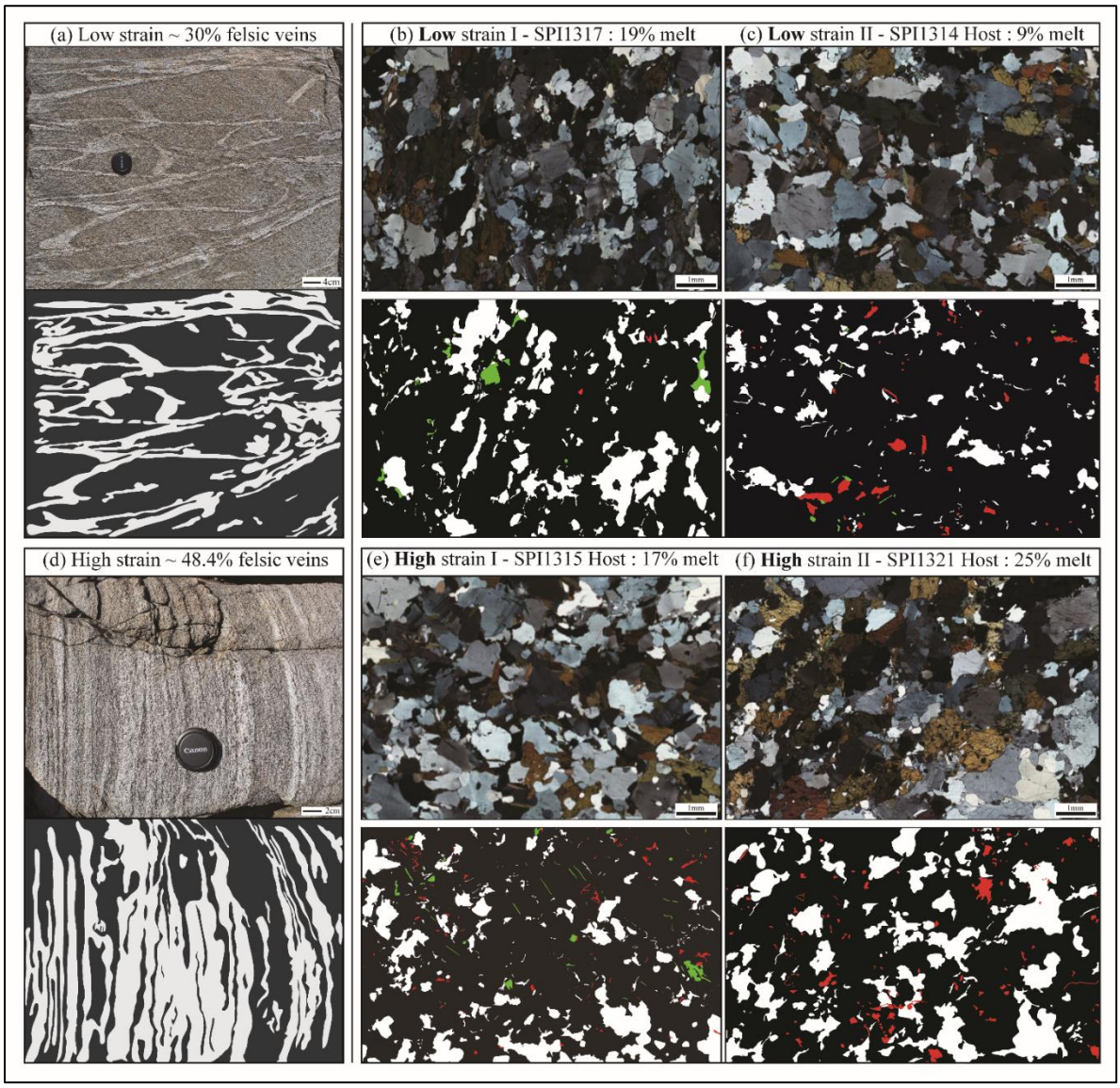

Figure 4.7 – Leucosome and melt volume observed in the diorite gneiss. Image analyses of field photographs from both the low and high-strain domains ('a' and 'd') are used to calculate macroscale leucosome volume at the outcrop scale. Microscale melt volume from the host is calculated via image analysis of thin section images (‘b-c’ for low strain - host and ‘e-f’ for high strain - host). Melt pseudomorph grains: white, solid precursor grains: grey/black, holes: red, and oxides: green.

---

and microscale melt% from the host, total melt% in the representative samples reach up to ~ 9.5%, 33.2%, 56% and 58% . In this calculation, it is assumed that all the melt was liquid at the same time, which is unlikely. Hence, they best represent a time integrated melt%. The melt% estimation from the BSE micrographs can also be skewed depending on the observation scale, e.g., an area with many melt microstructures may not represent the whole thin section. Nevertheless, the leucosome and the interpreted time-integrated melt percentages are systematically higher as the strain increases in the shear zone.

4.4.2 Geochemistry

Whole-rock compositions

Hosts of the studied samples show an intermediate subalkaline/tholeiitic composition (according to the TAS classification: Cox et al., 1979; Fig. AP4 - 5 in Appendix). Low strain I - SPI1317, low strain II - SPI1314, and the high strain I - SPI1315 have quartz monzodioritic composition whereas the highest strain II - SPI1321 grades to a tonalite (Fig. AP4 - 5 in Appendix). Hosts of the studied samples show an increasing trend in SiO_2 content from 59-60 wt% in low strain I - SPI1317 and low strain II - SPI1314 to 62 wt% in high strain I - SPI1315 and high strain II - SPI1321 (Fig. 4.8a-c). A decreasing trend in TiO_2 from 0.9 wt% in low strain SPI1317, SPI1314 to 0.7 wt% in high strain I - SPI1315 and a further decrease to 0.3 wt% in high strain II - SPI1321 is observed (Tab. 4.2). There is also a systematic decrease in MgO content from 3 wt% in low strain I - SPI1317 to 2.6 wt% in high strain II - SPI1315 (Fig. 4.8a). However, high strain II - SPI1321 shows an abruptly high value of MgO (~ 4.7 wt%, Fig. 4.8a; Tab. 4.2). Na_2O also shows a systematic increase from 4.3 wt% in low strain I - SPI1317 to 4.9 wt% in high strain I - SPI1315 (Fig. 4.8b; Tab. 4.2). However, SPI1321 shows a relatively low value of 4.07 wt% (Fig. 4.8b; Tab. 4.2). The low strain I - SPII317, has the highest loss of ignition value of 0.54 wt% (Tab. 4.2), indicative of the higher water content in the initial sample. All the studied samples show <1 Rb/Sr ratio where both the low- and high-strain samples (SPI1314 and SPI1315) have values greater than the low strain I - SPI1317 (Fig. 4.8c). However, high strain II - SPI1321 does not follow this trend and has the lowest ratio (Fig. 4.8c). REE patterns, shown relative to the REE chondrite values, shows an enrichment for La-Lu in all the studied samples. The REE patterns conform to the average continental crust. LREEs are observed to have higher values compared to the lower continental crust in all the studied samples.

Mineral Compositions

Calcic amphiboles in low strain I - SPI1317, low strain II - SPI1314, and high strain I - SPI1315 are similar and have a magnesiohastingsite composition (after Leake et al., 1997; Fig. 4.9a). In contrast, amphiboles in SPI1321 are ferroedenitic (Fig. 4.9a). Amphiboles in low strain I - SPI1317, low strain II - SPI1314, and high strain I - SPI1315 have X_{Mg} = 0.53-0.57 with Ti content within 0.17-0.2 per formula unit (pfu) (Fig. 4.9a, AP4 - 6 in Appendix;

Tab. 4.3). The vein amphiboles (in SPI1314 and SPI1315) is comparable to that of the host (Tab. AP4.3 in Appendix). In SPI1321, amphiboles show higher X_{Mg} values ranging from 0.62 to 0.7 and Ti content decreases to 0.09 pfu (Fig. 4.9a, Fig. AP4 - 6 in Appendix; Tab.

Sample	**SPI1317**	**SPI1314: Host**	**SPI1315: Host**	**SPI1321: Host**
Structural Domain	Low strain I	Low strain II	High strain I	High strain II
Major elements (wt% oxide; XRF)				
Al_2O_3	16.83	17.4	17.23	15.14
CaO	5.97	4.19	4.67	6.27
$FeO^{(tot)}$	7.06	6.45	5.42	5.73
K_2O	1.54	2.18	1.77	1.09
MgO	3.08	2.7	2.58	4.69
MnO	0.1	0.08	0.08	0.12
Na_2O	4.33	4.77	4.9	4.07
P_2O_5	0.29	0.33	0.22	0.07
SiO_2	59.46	60.8	62.32	62.32
TiO_2	0.89	0.88	0.68	0.3
L.O.I.	0.58	0.26	0.34	0.37
Total	100.13	100.04	100.21	100.19
Trace elements (ppm; XRF)				
Rb	50.88	84.04	60.6	15.09
Sr	442.34	392.36	395.57	352.67
REE data (chondrite normalised values of Anders and Grevesse, 1989)				
La	130.04	133.87	88.22	75.21
Ce	101.27	99.9	73.09	69.67
Pr	82.08	68.59	58.65	62.79
Nd	64.58	50.09	43.02	48.92
Sm	34.94	24.1	23.49	33.81
Eu	22.68	18.36	20.52	19.93
Gd	21.95	14.58	13.62	17.95
Tb	16.33	10.83	10.78	16.87
Dy	13.54	7.76	8.81	11.32
Ho	12.33	7.14	7.55	11.13
Er	11.17	5.94	7.21	9.24
Yb	9.94	6.24	6.26	10.82
Lu	9.76	5.6	5.62	10.63

Table 4.2 - Representative bulk compositions of the studied samples from different structural domains

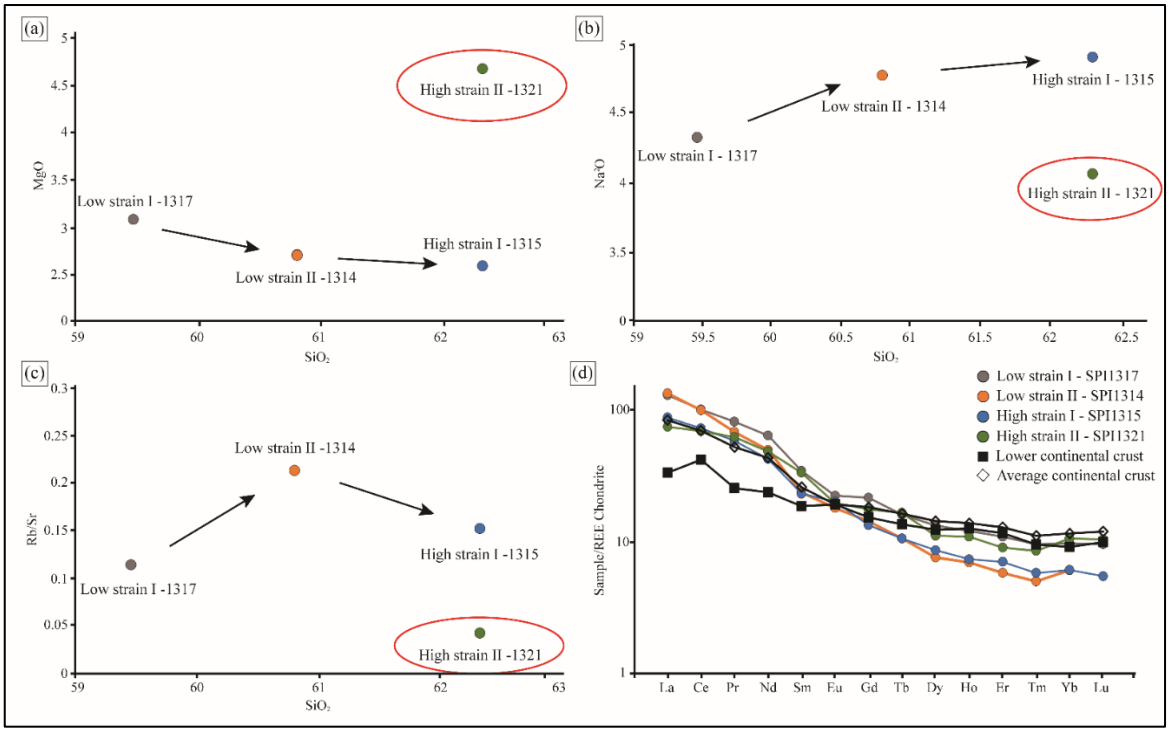

Figure 4.8 – Difference in geochemistry from low strain to high strain samples. In low strain II - SPI1314, high strain I - SPI1315, and high strain II - SPI1321 whole rock values are measured from mechanically separated hosts. (a-b) Harker diagrams of MgO-SiO_2 and Na_2O-SiO_2 show a decreasing and increasing trend, respectively, from low-strain to high-strain samples (except in the high strain II - SPI1321). (c) SiO_2 plotted against Rb/Sr reveals higher values for low strain II - SPI1314 and high strain I - SPI1315 w.r.t low strain I - SPI1317. High strain II - SPI1321 exhibits very low value. (d) Chondrite normalized REE patterns plotted for all studied samples, lower continental crust, and average continental crust. Values from Rudnick and Gao (2003) are used for REE compositions of the crust.

4.3). Cl content (in wt% Cl) of amphibole in SPI1321 is also markedly different (Fig. AP4 - 6 in Appendix). Amphibole grains in the host or vein lack any major element compositional zonation (Fig. 4.9a). Like amphiboles, biotite in low strain I - SPI1317, low strain II - SPI1314, and high strain I - SPI1315 show uniform composition with X_{Mg} values ranging from 0.57 to 0.60, and Ti content fall within 0.37-0.44 pfu (Tab. 4.3). Biotite grains in the veins also show very similar composition (Tab. AP4.4 in Appendix). Hence, amphibole and biotite grains in the low strain I - SPI1317, low strain II - SPI1314, high strain I - SPI1315 show a remarkably homogeneous X_{Mg} values and Ti content. In high strain II - SPI1321, small biotite grains in the host have X_{Mg} = 0.67 and Ti = 0.15 pfu while biotite in the vein show X_{Mg} = 0.65 and Ti = 0.29 pfu (Fig. 4.9b; Tab. 4.3, AP4.4 in Appendix). Hence, not only biotite in SPI1321 shows significant chemical variation in comparison to the other three samples, but the host and vein biotite grains are also chemically different (Fig. 4.9b).

Chlorine content (in wt% Cl) of biotite in high strain II - SPI1321 have higher values than observed in the other samples (Fig. AP4 - 6 in Appendix). In low strain I - SPI1317, plagioclase is albite rich (Ab_{67-71}; andesine in composition) and minor K-feldspar content (~0.6-1.4 mol%) (Fig. 4.9c). Plagioclase in the matrix of low strain II - SPI1314, high strain I - SPI1315, and high strain II – SPI1321 are compositionally homogeneous but more albitic (Ab_{71-74}; oligoclase in composition) with minor K-feldspar (~0.6-1.6 mol%) (Fig. 4.9c). Plagioclase in the veins of low strain II - SPI1314, high strain I - SPI1315, and high strain II – SPI1321 show a minor compositional difference and a wide compositional range than observed in their host counterparts (Fig. 4.9c). Plagioclase in veins of low strain II - SPI1314, high strain I - SPI1315, and high strain II – SPI1321 have Ab_{70-75}, Ab_{71-74}, and Ab_{69-73}, respectively (Fig. 4.9c). K-feldspar in the studied samples do not show significant compositional variation and are Or_{92-96} in composition (Fig. 4.9d). Though the high strain samples (i.e., SPI1315 and SPI1321) show a large compositional range compared to the low strain samples. No compositional zonation from core to rim is observed in both the plagioclase and K-feldspar grains. Hence, major element composition of constituent minerals is homogeneous, except for amphibole and biotite in high strain II - SPI1321.

4.4.3 Metamorphic P-T conditions

P-T pseudosection for the low strain I - SPI1317 is shown in Fig. 4.10 along with temperature estimates using classical Ti-in-biotite and Ti-in-amphibole geothermometers from the four studied samples. P-T estimates using amphibole-plagioclase geothermobarometers is also used (Fig. AP4 – 6 in Appendix). The interpreted peak metamorphic assemblage in low strain I - SPI1317 includes plagioclase, amphibole, quartz, K-feldspar, biotite, ilmenite, and magnetite. Macroscopic and microscopic features of low strain I - SPI1317 clearly suggest that the peak metamorphic assemblages formed in equilibrium with the melt. Fine grained quartz and K-feldspar are often spatially associated with biotite corroding its grain boundary. The stability field of the phase assemblage (Fig. 4.10a) in low strain I - SPI1317 is bounded at high temperature by the orthopyroxene-in boundary and the magnetite/ilmenite-out field boundary at low temperature; this results in an estimated temperature of 705-810°C. The estimated peak pressure is restricted to <5.3 kbar as pressure above this will cause the disappearance of magnetite. The amount of biotite in the thin section does not exceed 5 vol%. Calculated isopleths of biotite modes (green dotted lines) are shown in Fig. 4.10a. The 5 vol% biotite isopleth identifies peak

metamorphic temperature > 790°C. Hence the estimated peak P-T conditions for this whole rock composition are 790-805°C, and <5.5 kbar. The solidus temperature is > 630°C. Hence, at the peak metamorphic conditions, partial melting will produce melt proportions of 3-4% (Fig. 4.10a).

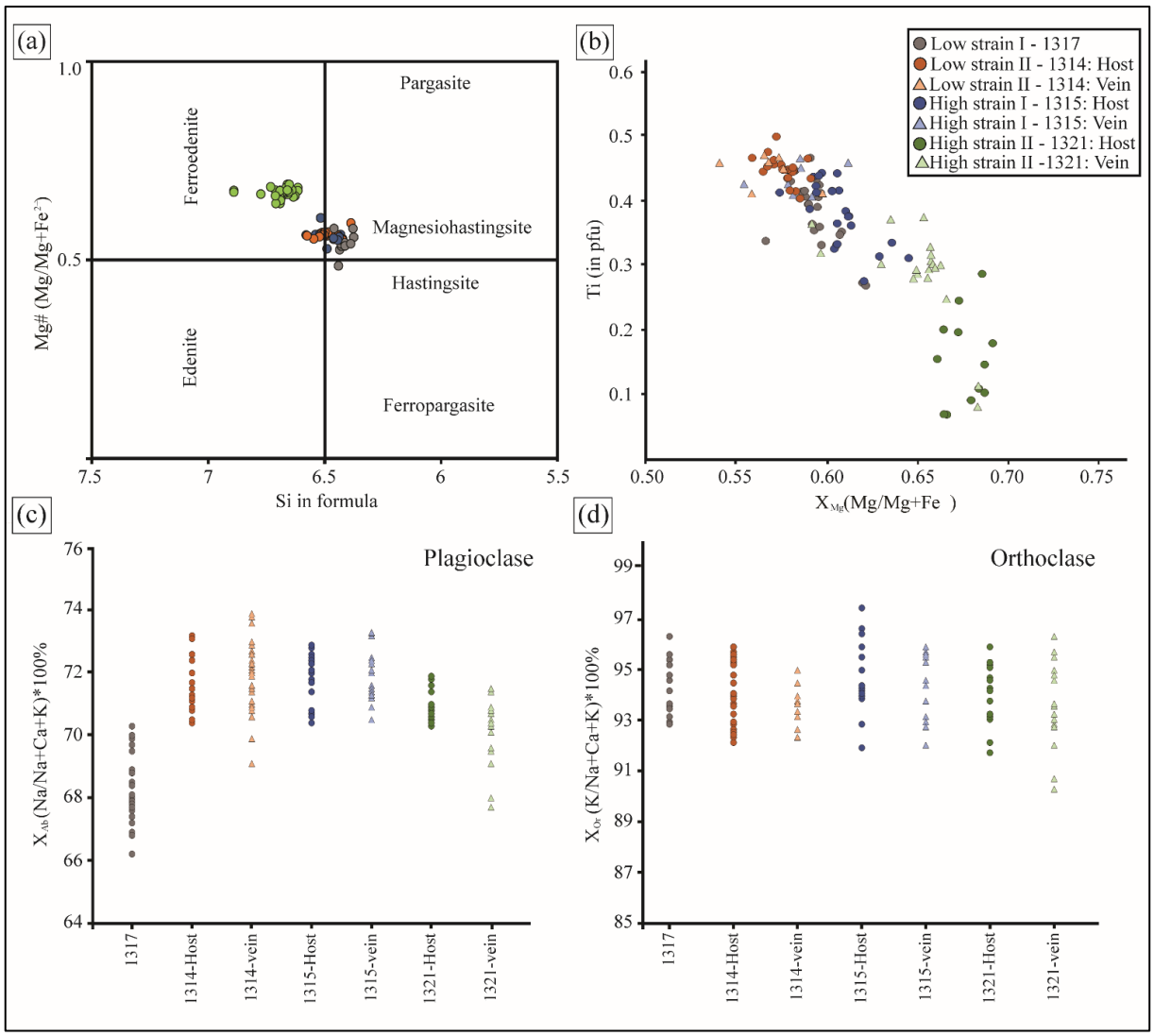

Figure 4.9 – Mineral major element compositions in the studied samples. (a) Mg# vs. Si in amphibole exhibits a similar composition in low strain I - SPI1317, low strain II - SPI1314, and high strain I - SPI1315. In contrast, high strain II - SPI1321 shows a very different composition. (b) Ti (pfu) is plotted against the X_{Mg} in biotite for all studied samples. High strain II - SPI1321 displays different biotite compositions. (c) Albite content in plagioclase and (d) orthoclase content in K-feldspar in all the studied samples. X_{Ab} in plagioclase increases from low strain I - SPI1317 to the rest of the high strain samples. Plagioclase grains in the veins reveal a sizeable compositional range. Orthoclase in the studied samples exhibits a similar compositional range where high strain I - SPI1315 and high strain II - SPI1321 show a higher degree spread in X_{Or} values.

To better constrain peak metamorphic condition, we combine classical geothermobarometers along with P-T pseudosection modelling. The Ti-in-Amphibole thermometer is reasonable for rocks metamorphosed at granulite-facies (>800-900 °C) conditions and the thermometer is only temperature dependent with the presence of Ti-phases (rutile, ilmenite or titanite). The Ti-in-amphibole thermometer applied for calcic amphiboles with Ti content of 0.17-0.2 pfu in low strain I - SPI1317, low strain II - SPI1314, and high strain I - SPI1315 yield temperature conditions of 803±16°C, 771±22°C and 775±12°C, respectively (Fig. 4.10b; Tab. AP4.5 in Appendix). Thus, there is a slight decrease in the estimated temperatures from low strain I - SPI1317 to high strain I - SPI1315. Temperature estimated by the Ti-in-amphibole thermometer in SPI1317 is found similar to the pseudosection modelling. Based on natural biotite, Henry et al. (2005) proposed the Ti-in-Biotite geothermometer for metapelite samples at low to medium pressures containing ilmenite or rutile. Application of this thermometer agrees for rocks metamorphosed in upper-Amphibolite to granulite facies conditions. In low strain I - SPI1317, low strain II - SPI1314, and high strain I - SPI1315, Ti-in-biotite geothermometer yields temperature estimates of 712±20°C, 717±15°C and 736±4°C, respectively (Fig. 4.10b; Tab. AP4.6 in Appendix). Thus, Ti-in-biotite do not show significant changes in estimated temperature between samples. For high strain II - SPI1321, Ti-in-biotite and Ti-in-amphibole thermometers cannot be utilized due to the unavailability of any Ti-rich phase such as ilmenite and/or rutile. Overall estimated temperatures using the Ti-in-Biotite geothermometer exhibit lower temperature values than the Ti-in-Amphibole thermometer for the same sample.

Additionally, the Holland and Blundy (1994) geothermometer is used to calculate peak temperature from amphibole-plagioclase assemblages in the studied samples. Next Molina et al. (2015) geobarometer is also utilized to determine peak pressure conditions based on Al-Si partitioning between amphibole and plagioclase for the same amphibole-plagioclase pairs. Temperature values are estimated at arbitrary 3 kbar and 11 kbar pressures. A broad pressure range is chosen to incorporate pressure values estimated by P-T modelling (this study and previous studies by Kirkland et al., 2018a and Yakymchuk et al., 2020). Pressure conditions are measured at temperature conditions estimated using Ti-in amphibole geothermometer. Hence, a temperature window of 650-850°C is used for this calculation. Next calculated pressure values are used in conjunction to the temperature estimates to obtain intersections in the P-T space (Fig. AP4 – 6 in Appendix). Low strain I - SPI1317, low strain II - SPI1314, and high strain I - SPI131, and high strain II - SPI1321 yield pressure

	Low strain I - SPI1317				Low strain II - SPI1314: Host			
Mineral	Kfs	Plag	Bt	Amp	Kfs	Plag	Bt	Amp
N	17	28	15	20	31	26	19	25
SiO_2	65.18	60.43	36.26	42.14	63.79	61.39	36.38	42.62
TiO_2	0.04	0	3.64	1.88	0	0	3.23	1.56
$Al2O_3$	18.55	24.53	15.89	10.99	18.83	24.35	15.35	10.17
$Cr2O_3$	0	0	0.06		0	0	0.07	0.02
FeO(tot)	0.043	0.24	16.19	17.85	0.02	0.14	16.61	16.84
MnO	0.02	0	0.23	0.38	0	0	0.24	0.42
MgO	0	0	12.06	9.12	0	0	12.85	10.38
CaO	0.08	5.84	0	11.7	0.01	5.59	0	11.5
Na_2O	0.71	8.3	0	1.44	0.6	8.34	0.02	1.38
K_2O	15.3	0.25	9.94	1.44	15.49	0.15	9.88	1.28
BaO	0.86	0			1.27	0.04		
Total	100.78	99.59	94.27	96.94	100.01	100	94.63	96.17
No of O	8	8	22	24	8	8	22	24
Si	2.99	2.7	5.48	6.44	2.97	2.73	5.49	6.49
Ti	0	0	0.41	0.22	0	0	0.37	0.18
Al	1.01	1.29	2.83	1.56	1.03	1.28	2.73	1.51
Cr	0	0	0.01		0	0	0.01	
Fe(tot)	0	0.01	2.05	2.28	0	0.01	2.1	2.14
Mn	0	0	0.03	0.01	0	0	0.03	
Mg	0	0	2.72	2.08	0	0	2.89	2.36
Ca	0	0.28	0	1.92	0	0.27	0	1.88
Na	0.06	0.72	0	0.39	0.06	0.72	0.01	0.34
K	0.9	0.01	1.92	0.28	0.92	0.01	1.9	0.25
Ba	0.02	0			0.02	0		
Total	4.96	5.01	15.45	15.18	5	5.02	15.53	15.15

	High strain I - SPI1315: Host				High strain II - SPI1321: Host		
Mineral	Kfs	Plag	Bt	Amp	Plag	Bt	Amp
N	17	22	23	25	30	21	20
SiO_2	64.14	61.6	36.19	42.64	61.08	37.19	44.84
TiO_2	0	0	3.96	1.63	0	3.32	0.78
Al_2O_3	18.71	24.12	14.87	10.08	24.39	15.55	9.24
Cr_2O_3	0	0	0.01	0	0	0.04	0.09
FeO(tot)	0.06	0.05	17.63	17.14	0.02	15.18	13.96
MnO	0	0	0.19	0.37	0	0.15	0.32
MgO	0	0	12.18	10.5	0	13.32	12.82
CaO	0.04	5.35	0.02	11.34	5.75	0	11.87
Na_2O	0.62	8.6	0.04	1.49	8.27	0.01	1.22
K_2O	15.51	0.26	9.79	1.3	0.42	9.87	1.01
BaO	0.82						
Total	99.9	99.98	94.88	96.49	99.93	94.63	96.15
No of O	8	8	22	24	8	22	24
Si	2.98	2.74	5.47	6.48	2.72	5.55	6.69
Ti	0	0	0.45	0.19	0	0.37	0.09
Al	1.03	1.26	2.65	1.52	1.28	2.74	1.31
Cr	0	0	0		0	0	
Fe(tot)	0	0	2.23	2.15	0	1.9	1.74
Mn	0	0	0.03		0	0.02	
Mg	0	0	2.75	2.38	0	2.97	2.85
Ca	0	0.26	0	1.85	0.27	0	1.9
Na	0.06	0.74	0.01	0.36	0.71	0	0.3
K	0.92	0.02	1.89	0.25	0.02	1.88	0.19
Ba	0.02						
Total	4.99	5.02	15.48	15.18	5	15.43	15.07

Table 4.3 - Mineral chemistry data of plagioclase (Plag), Orthoclase/K-feldspar (Kfs), biotite (Bt) and amphibole (Amp) for four studied samples. N is the number of spot analyses per mineral, analyses were rejected for totals outside of 99.0-101.0% for feldspars and below 94% for hornblende and biotite. Compositions shown here are highlighted in Tab. AP4.1-AP4.4. Mineral abbreviations are after Whitney and Evans (2010).

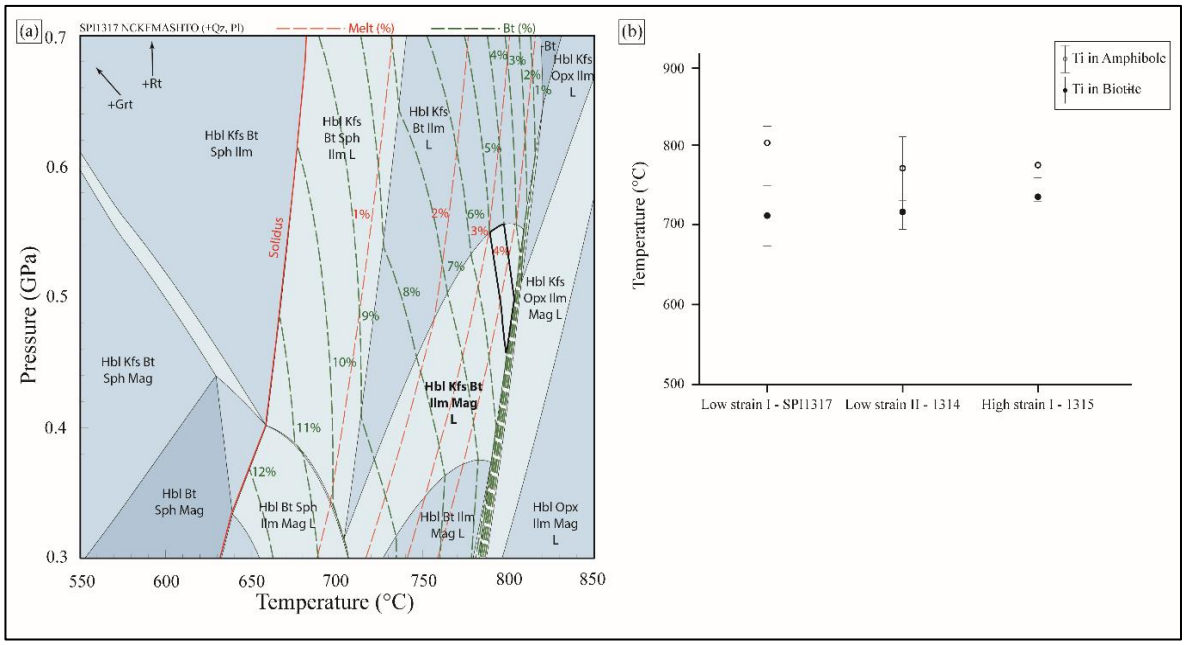

Figure 4.10 – (a) Isochemical phase diagram determined using THERMOCALC in NCKFMASHTO system. The phase diagram is calculated assuming H_2O saturated condition and Fe_2O_3 = 7.84% (Table 4.1). All fields contain quartz and plagioclase. Mineral abbreviations are after Whitney and Evans (2010). The field highlighted in bold denotes the peak pressure-temperature field. (b) Ti-in-Biotite (following Henry et al., 2005) for the studied samples show temperature estimations of 712 °C, 717 °C and 736 °C whereas the Ti-in-amphibole (following Liao et al., 2021) thermometer yields temperature values of 803 °C, 771 °C, 771 °C, respectively for low strain I - SPI1317, low strain II - SPI1314 and high strain I - SPI1315. Average deviations for Ti-in-amphibole and Ti-in-biotite are represented in Tab. AP4.5 and Tab. AP4.6, respectively. High strain II - SPI1321 lacks any Ti-rich phase and hence the thermometers are not applied. Mineral abbreviations are after Whitney and Evans (2010).

-temperature conditions of 690-728°C at 5.7-7.8 kbar, 670-715°C at 5.8-7.5kbar, 682-705°C at 5.5-7kbar, and 670-682°C at 5kbar, respectively (Fig. AP4 – 6 in Appendix). Low strain I - SPI1317 shows relatively higher temperature values than the rest of the samples.

4.4.4 Quantitative orientation analysis

Figures 4.11-4.12 show the pole figures of amphibole, biotite, plagioclase, quartz, and K-feldspar for the samples studied. Only the host grains are considered for low strain II - SPI1314 and high strain I - SPI1315. For high strain II - SPI1321, biotite grains from the

vein is considered in addition to the host, as the host alone lacks an appreciable number of biotite grains to calculate a crystallographically relevant CPO.

Low strain I – SPI1317 and low strain II – SPI1314

Amphibole orientation data from low strain I - SPI1317 and low strain II - SPI1314 (Fig. 4.11a) show a weak CPO with (100) poles in a single point distribution normal to the (S) foliation (XY-pole figure section), (010) poles are aligned in a very weak girdle subnormal to the foliation, and [001] axes form a girdle at high angle to the lineation (X-direction). The maximum multiples of the uniform distribution (MUD) values of pole figures for amphibole grains are 4-5 with M-index values of 0.1-0.2, indicating weak CPO strength (Fig. 4.11a). It is to be noted that the (010) poles in low strain II - SPI1314 have no discernible point clusters or girdle. In low strain I - SPI1317, a biotite CPO pattern is evidenced by weak girdles of (100) and (010) poles subparallel to the lineation with some points parallel to the foliation plane, and a strong maximum of [001] axes normal to the foliation (Fig. 4.11b). The weak girdle of (100) poles is also subparallel to the lineation in low strain II - SPI1314, but (010) poles are parallel to the XZ-pole figure section (Fig. 4.11b). The [001] axes form a strong girdle parallel to the foliation plane (Fig. 4.11b). Biotite CPOs are stronger than amphibole grains, with the low strain II - SPI1314 having the highest M-index value of 0.7. In both low strain I - SPI1317 and low strain II - SPI1314, plagioclase (anorthite) and quartz are randomly oriented and lack a CPO (Fig. 4.11c-d). Low M-index values of 0.05-0.06 in plagioclase and 0.1-0.2 in quartz support this. Poles to (100) and (010) in K-feldspar are random, exhibiting a very weak CPO, though [001] axes in both samples show a very weak girdle at an angle to the foliation (Fig. 4.11e). Some clusters associated with specific grain orientation are also observed, resulting in high M-index values, but they are not indicative of any CPO pattern. In-depth EBSD crystallographic orientation characterization (Fig. 4.13) is carried out in a low strain II - SPI1314 quartz-plagioclase aggregate (location shown in Fig. 4.4f). The pole figure shows that quartz grains have the same crystallographic orientation (Fig. 4.13a-b). Two plagioclase grains in this aggregate also have the same 3D crystal orientations but are not in contact with each other (Fig. 4.13a-b). Therefore, the quartz-plagioclase in this polycrystalline aggregate represents single xenomorphic grains that are connected along grain boundaries in three dimensions, even if they are not connected in 2D. Subparallel subgrain (black arrows in Fig. 4.13c) and dauphiné twin boundaries are observed in two subhedral quartz grains (from low strain II - SPI1314,

as shown in Fig. 4.5d). The GROD EBSD map also shows parallel deformation bands (white arrows in Fig. 4.13c), which are sometimes crosscut by dauphiné twin boundaries (orange arrow in Fig. 4.13c). Quartz grains exhibit a higher degree distortion of ~12°, compared to

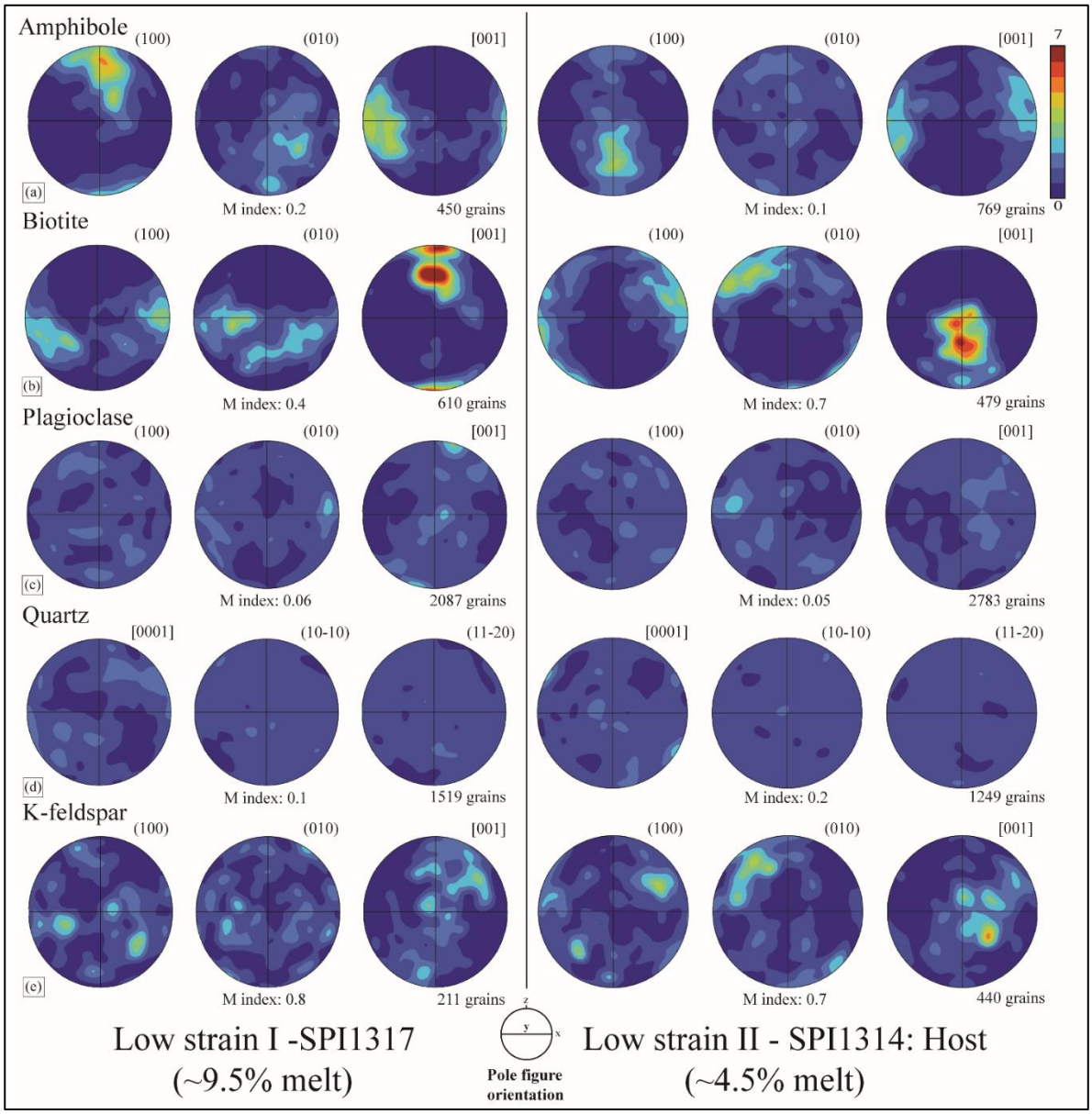

Figure 4.11 – Contoured pole figures of crystallographic orientation (one point per grain) of (a) amphibole (hornblende), (b) biotite, (c) plagioclase, (d) quartz and (e) K-feldspar from low strain I - SPI1317 and host of low strain II - SPI1314. Reference frame for all the pole figures is shown at the bottom. Note the scale bar (in multiples of uniform density) for each mineral across the studied samples are kept constant.

other mineral grains. EBSD phase map of a low strain II - SPI1314 type-area with multiphase grains shows bimodal grain size distribution of plagioclase, K-feldspar and quartz grains (Fig. 4.13d). An intergrowth texture is distinguished by small plagioclase and quartz grains. Subhedral plagioclase grains have regular twin boundaries parallel to the grain sides. Large K-feldspar grains are seen with cuspate boundaries and partial straight facets, whereas large quartz grains are anhedral with irregular grain boundaries. Small quartz grains are devoid of any dauphiné twin and frequently display low dihedral angles of <10° (Fig. 4.13d). The crystal lattices of coarse quartz and K-feldspar grains are bent (i.e., the orientation of the crystal lattice changes within an individual grain) with ~8° lattice distortion (Fig. 4.13e). The misorientation profiles also exhibit a gradual but significant change in grain orientation. The GROD angle values can reach 13° in large quartz grains and 16° in large K-feldspar grains. However, subgrain boundaries (shown in Fig. 4.13f with white arrows) are random, and parallel deformation bands are absent. The crystal orientation of plagioclase and amphibole grains changes very little (2°) (Fig. 4.13e). Also, small quartz and K-feldspar grains have no significant internal deformation (Fig. 4.13f). Small plagioclase grains, like large plagioclase grains, also lack any deformation twin (Fig. 4.13d). Low GROD angle values (max 6° in plagioclase and 2.9° in amphibole, Fig. 4.13f) support this, indicating minimal intragranular deformation. Hence, most of the multiphase aggregates are composed of an intergrowth of undeformed grains, with large changes in crystal orientation observed only in the coarse quartz and K-feldspar grains, even though their finer sized fractions lack any significant internal distortion.

<u>High strain I – SPI1315 and high strain II – SPI1321</u>

Amphibole in high strain I - SPI1315 and high strain II - SPI1321 exhibit a strong CPO with (100) poles in a single point distribution normal to the foliation (Fig. 4.12a). The amphibole CPO is slightly stronger with M-index of 0.2-0.3, and poles to (010) display crystallogrphically distinct patterns in the high strain samples compared to their low strain counterparts. In high strain I - SPI1315, (010) poles align in a girdle subparallel to the foliation, whereas the clusters in high strain II - SPI1321, are parallel to the lineation direction. [001] axes in high strain I - SPI1315 are subparallel to the foliation but form a cluster near the Y-axis in high strain II - SPI1321 (Fig. 4.12a). Thus, despite the similar distribution of amphibole (100) poles, [001] axes exhibit a distinct fabric in high strain II – SPI1321 compared to the rest of the samples. Biotite CPO patterns are identical in both high

strain and low strain samples, with (100) and (010) poles subparallel to the foliation and [001] axes exhibiting a girdle at high angle to the lineation (Fig. 4.12b). Similar to low strain samples, Plagioclase and quartz grains are randomly oriented and lack a CPO pattern (Fig. 4.12c, d). The low M-index values of 0.04-0.08 in plagioclase and 0.1 in quartz support

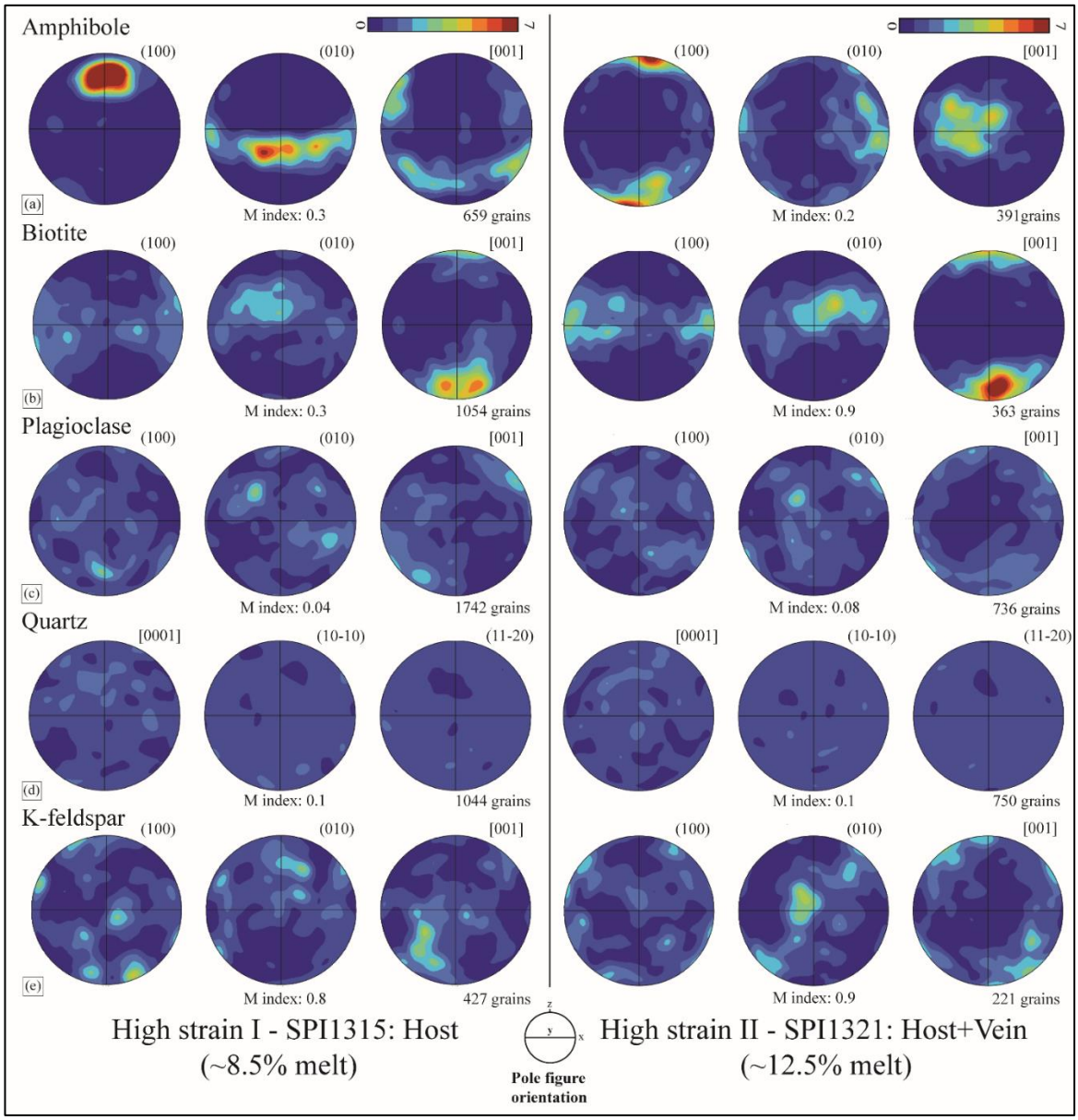

Figure 4.12 – Contoured pole figures of crystallographic orientation (one point per grain) of (a) amphibole (hornblende), (b) biotite, (c) plagioclase, (d) quartz, and (e) K-feldspar from the host of high strain I - SPI1315 and high strain II - SPI1321. For high strain II - SPI1321, only the biotite grains from the vein are considered here. Reference frame for all the pole figures is shown at the bottom.

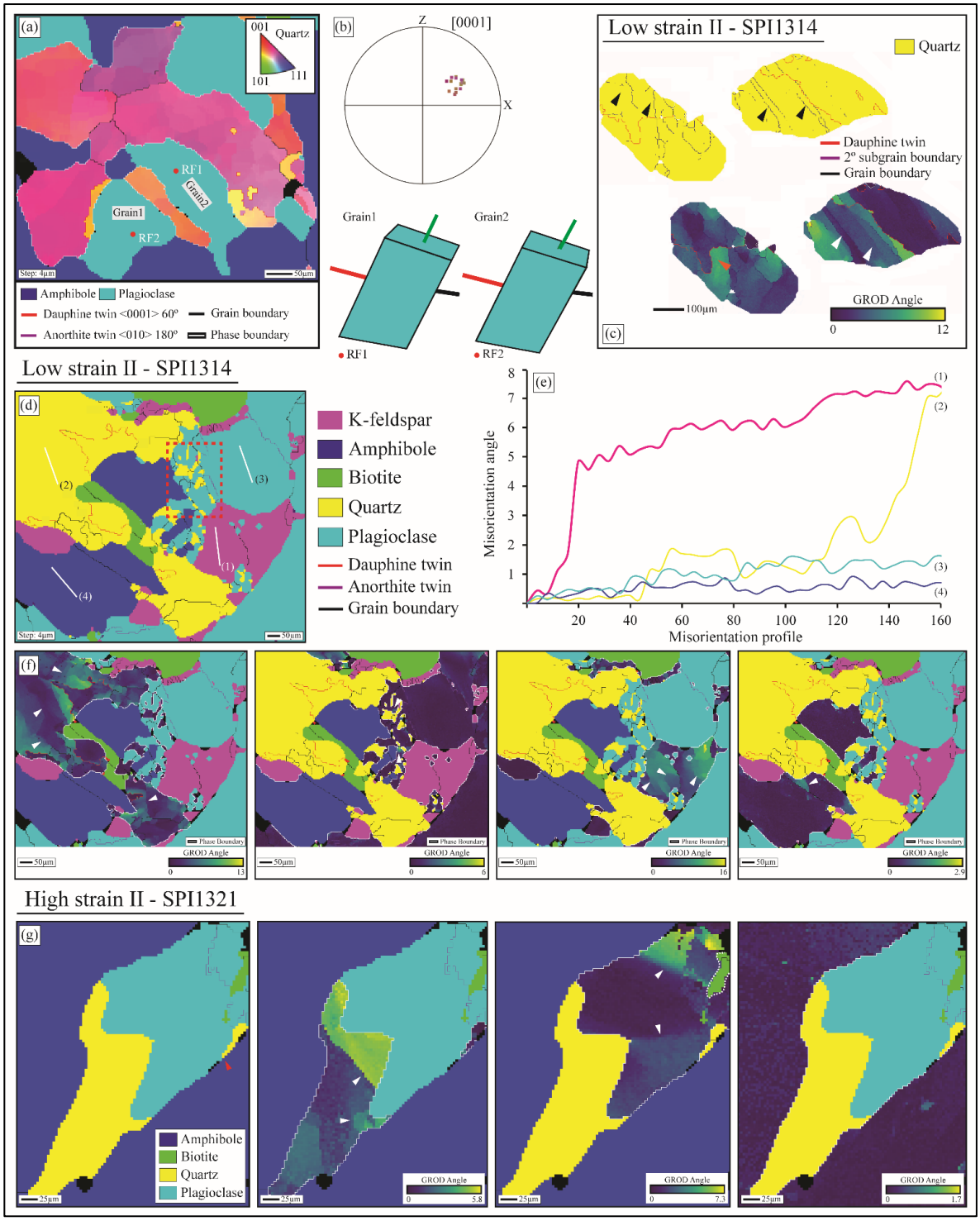

Figure. 4.13 – EBSD microstructural characteristics of constituent minerals in low strain II - SPI1314 and high strain II – SPI1321. All the maps are with 3µm step size. (a-b) EBSD phase map of multiphase aggregate from low strain I - SPI1314. Quartz orientation colouring (in 'a') and pole figure (in 'b') show consistent orientation of quartz grains in the map area. 'Grain1' and 'Grain2' plagioclase grains, not connected in 2D, but also exhibit same 3D crystal orientation (measured at reference points 'RF1' and 'RF2' in 'Grain1' and 'Grain2', respectively. Quartz grains are shown with IPF colouring whereas plagioclase and amphibole are shown in phase colours. (c) EBSD map of two quartz grains (from Fig. 4.5d) lack typical melt microstructures. Colour coded grain relative orientation deviation (GROD) map shows sub parallel deformation bands and subgrain boundaries (arrowed). (d) Low strain II - SPI1314 EBSD phase map with quartz and K-feldspar grains exhibiting typical melt microstructures. Inside the rectangle, quartz grains with low dihedral angle of <10° are

found. (e) Misorientation profiles of equal length (along lines ‘1’, ‘2’, ‘3’ and ‘4’) exhibit highest cumulative change in crystal orientation (up to ~8°) in quartz and K-feldspar. Plagioclase and amphibole show minimal change (<2°). (f) GROD EBSD map of melt pseudomorphed quartz and K-feldspar grains record maximum change in crystal orientation while plagioclase and amphibole exhibit very minimal change in orientation. White arrows indicate the locations of potential subgrain boundaries. Notice quartz and K-feldspar subgrain boundary orientations are random and in plagioclase, subgrain boundaries are only associated close to the quartz inclusions. (g) Melt pseudomoprhed grains in high strain II - SPI1321. Quartz grain with low dihedral angle of <10° is marked with red arrow. GROD EBSD map shows similar change in crystal orientation in plagioclase and quartz grain. Subgrain boundary orientations are random (marked with white arrows). Amphibole is devoid of any subgrain boundary.

---

this. In high strain I - SPI1315, K-feldspar grains exhibit a very weak CPO, where poles to (100) and (010) are random, but [001] axes display a very weak girdle at an angle to the foliation (Fig. 4.12e). CPO pattern in veins of high strain samples (SPI1315 and SPI1321) also reveals extremely similar fabric where quartz, plagioclase, and K-feldspar lack any sample scale CPO (Fig. AP4 – 7 in Appendix). In low strain II - SPI1314, vein CPO measurements cannot be performed due to insufficient data points. The point clusters in the pole figures are the result of single-grain orientations and lack any known CPO pattern. We also suspect that the strong CPO observed in K-feldspar in SPI1321-vein is due to the fewer grains (Fig. AP4 – 7 in Appendix). Quartz-plagioclase aggregates in high strain II - SPI1321 exhibit comparable internal deformation to low strain II - SPI1314, with GROD angles as low as 7°. (Fig. 4.13g). The intragranular deformation in amphibole grain is minimal (GROD angle ~1.7°), and subgrain boundaries are randomly oriented (white arrows, Fig. 4.13g). Thus, the EBSD orientation analyses yield very similar results for both low- and high-strain samples, where large plagioclase and amphibole grains exhibit very little internal deformation and minor subgrain boundaries. Small quartz-plagioclase aggregates exhibit minimal intragranular deformation. Large quartz and K-feldspar grains with melt microstructures have bent crystal lattices and randomly oriented subgrain boundaries (Fig. 4.13d-g). In contrast, subhedral quartz grains devoid of melt microstructures display parallel deformation bands and average GROD angle values (Fig. 4.13c).

4.5 Discussion

4.5.1 Melting occurs at mid-crustal conditions with a typical hot Archean geothermal gradient

Previous studies in and around the Nuuk region discovered two granulite facies metamorphic events. The first granulite facies metamorphism occurred at temperatures >750°C and pressure <7 kbar in the period of 2.97 Ga, while the second event took place at c. 820-850°C and 8-10 kbar during 2.85-2.7 Ga (Garde et al., 2012; Kirkland et al., 2018a; Yakymchuk et al., 2020; Gardiner et al., 2019). Kirkland et al. (2018a) observed Akia terrane experiencing partial melting associated with regional ductile deformation during the Neoarchean high P, high T metamorphism. Hence, previous research works indicate to a protracted high thermal event. In our study, we also discovered variously arranged abundant leucocratic veins with igneous like features (Fig. 4.2-4.3). P-T conditions of 790-805°C, and <5.5 kbar is suggested from isochemical phase diagram for low strain I - SPI1317 (Fig. 4.10a). Similar temperature estimates are found using Ti-in-Amphibole thermometer for low strain I - SPI1317, low strain II - SPI1314 and high strain I - SPI1315 which yield temperature values ~770 °C. Temperature estimates using Ti-in-Biotite thermometers in these three samples also exhibit values >700 °C (Fig. 4.10b). The lower temperature estimates obtained with Ti-in-biotite thermometers could be attributed to a lack of graphite grains and the initial bulk composition not being a metapelite for which the thermometer has been calibrated. Temperatures of 670-730 °C and pressures of 5.7 to 7.8 kbar are suggested by amphibole-plagioclase thermobarometers (Fig. AP4 – 6 in Appendix). Therefore, overall, a high temperature metamorphic condition with maximum apparent thermal gradient of 850-1300 °C/GPa can be suggested from mineral phase equilibria modelling in SPI1317. Dyck et al. (2015) reported that high grade metamorphism in this region developed under an apparent thermal gradient of ~ 660 °C/GPa while Kirkland et al. (2018a) conclude an apparent thermal gradient of 750-1000 °C/GPa. Dziggel et al. (2012) propose a medium pressure granulite facies metamorphism of ~ 850 °C, at ~ 7.5 kbar, indicating a Mesoarchaean thermal gradient of ~ 1100 °C/GPa. Archaean rock records are frequently distinguished by low to moderate pressure (P) and moderate to high temperature (T) metamorphic conditions with apparent thermal gradients of ~ 750–1000 °C/GPa, whereas ultra-high temperature terranes preserve thermal gradients of 850-1250 °C/GPa (Brown,

2007; Diener et al., 2005; Lowe, 1994). High dT/dP rocks with thermal gradients >775 °C/GPa (mean 1100 °C/GPa) are registered widely in the rock records dating back to ca. 2.8 Ga (Brown and Johnson, 2018). All these values are very similar to our estimation of the peak P-T condition. A slight overestimation of thermal gradient may have resulted from a possible underestimation of pressure values. The pressure-temperature conditions reported here and from previous studies are sufficient for partial melting of metabasic rocks (Palin et al., 2016a).

Previous experiments together with phase equilibrium modelling indicate that dehydration melting of biotite occurs via a reaction: Biotite + Plagioclase + Quartz = Orthopyroxene + Garnet/Cordierite + K-feldspar + Melt (Johnson et al., 2008). At the calculated P-T conditions, biotite must begin to melt. The microscopic observation of biotite disequilibrium textures, in which biotite grain boundaries are corroded by plagioclase and surrounded by fine grained quartz, K-feldspar, and titanite (sphene), supports this (Fig. 4.4, 4.6). Breakdown of hydrous ferromagnesian phases (e.g., biotite, amphibole) to generate peritectic products and melt are examples of incongruent melting reactions (Brown, 2013). Even though biotite shows evidence of partial melting, no peritectic mineral phases (garnet and/or orthopyroxene) are found. Some examples suggest amphibole bearing felsic igneous rock can be a product of anatexis of biotite + plagioclase + quartz gneisses. Kenah and Hollister (1984) described formation of amphibole + plagioclase ± quartz bearing leucocratic melt as the product of incongruent melting of biotite-plagioclase-quartz (BPQ) and concomitant crystallization of amphibole. Büsh et al. (1974) showed granodiorite-tonalite melts formed during the low P high T condition in a near isochemical conditions involving biotite and plagioclase according to the reaction:

Bio + Plag + Qtz =Hbl + Sph + An-rich Plg + $(Kfs+An\text{-}poor\ Plg + H_2O + Qtz)_{melt}$.

Brown (2010) suggests leucosomes carrying mica and amphibole are more likely to be a product of fluid-saturated melting. Similarly, Mogk (1992) suggests that the formation of migmatites is the result of incongruent melting of biotite-bearing gneisses in the presence of a fluid at 680-735°C and pressure of ≥ 8 kbar, producing amphibole-quartz bearing granitic lenses, according to the generalized reaction:

$Bio+Plg(I)+Qtz+Epi+(H2O)_{fluid}$ = Hbl+Plg (II)+Kfs-rich granitic melt.

Fluid present melting of biotite can also occur at temperatures at least 100°C lower than those obtained from fluid-absent (dehydration) melting reaction experiments. If a free

aqueous fluid phase is present crustal rocks can melt even at 700°C (Brown, 2010). The bulk composition is not the most important factor in producing hornblende from a BPQ assemblage, but the addition of H2O is required at any pressure to stabilize the amphibole. In this case, a water content of 2% is assumed to produce the suitable mineral assemblage seen in the thin section (Fig. 4.10a). However, the microstructures and grain associations do not indicate that amphibole is a melt product. Even if some amphiboles are formed because of the melt forming reaction, they cannot be identified. Overall, it is proposed that a fluid present melting of mid-crustal dioritic gneiss at this peak P-T condition produced 3-4 wt% of melt (Fig. 4.10a).

4.5.2 Host rocks exhibit signatures of former melt presence during progressive deformation

Field observations reveal a high proportion of macroscopic, internally undeformed leucocratic materials arranged as felsic veins in the diorite mafic host (Fig. 4.2-4.3). The felsic material is patchy in some places (Fig. 4.2h), indicating surreitic or ophthalmic migmatite texture (Lee et al., 2018). It can be assumed, at least in part, that the classic migmatitic appearance and high proportion of leucocratic materials (>30 area% in Fig. 4.7) represent the crystallization of former melt (as observed in Brown and Solar, 1998a; Carvalho et al., 2016, 2017; Piazolo et al., 2020). Between the low-strain and high-strain domains, there are differences in the population and arrangement of the thin, elongated type 1 felsic veins. Veins show large, undeformed, euhedral plagioclase grains resembling igneous microstructure (Fig. 4.2). They also exhibit open or close folding and shear bands just like in a stromatic migmatite. The cross-cutting relationships of different vein types in the low strain domain indicate that type1 veins came first followed by type2 and type3. Their local interaction and parallel relationships in the high-strain domain imply that they are concomitant with progressive deformation. The highly layered morphology of these rocks can be attributed to transposition of leucosomes during melt-present deformation (Park, 1983). Transposition can occur in areas of crystal-melt mixtures that are now visible as veins. Even if there is some residual melt in the host rock, it will remain segregated from the vein material. Furthermore, the high strain domain exhibits a change in colour, deflections of leucocratic veins from low strain rocks into the high strain domain, and a change in foliation intensity with strongly banded layers, all of which are similar to the characteristics observed in high strain melt transfer zones described by Daczko and Piazolo

(2022). However, segregation of quartzofeldspathic domains can also be caused by solid-state deformation and recrystallization processes. Moore et al. (2020) find that locally enhanced dissolution can lead to metamorphic differentiation of rock in a shear zone. Hence it is critical to determine whether felsic-mafic domains are formed by dissolution-precipitation or by local melt extraction or accumulation. The studied samples contain quartz and K-feldspar with microstructural features typical of the former presence of melt (Vernon, 2011 and references therein). The main features include (Fig. 4.4-4.6): (i) anhedral, elongated, monomineralic quartz-K-feldspar extending into the surrounding grains as interstitial minerals, interpreted as pseudomorphs of grain boundary melt films wetting grain boundaries of other minerals (e.g., Rosenberg and Riller, 2000; Sawyer, 2000), (ii) cuspate grain boundaries of quartz-plagioclase-K-feldspar grains inferred to have grown from the melt (Sawyer, 2001), (iii) partial straight faceted euhedral grains (Holness, 2005) indicating neoblasts growing into indentations (embayments), (iv) low dihedral angles (LDA) of crystals of a single phase between two other grains of a different phase representing melt pseudomorphs, (v) elongated melt pockets at triple junctions, and (vi) polycrystalline multiphase aggregates of quartz-plagioclase (Sawyer, 1999, 2001; Holness et al., 2005, 2011). On their own, these features are not unequivocal indicators of the former melt presence but when found together significantly strengthen the interpretation (Vernon, 2011). Embayed amphibole-plagioclase grains suggest partial replacement of the non-melt phases by melt crystallized grains (quartz and K-feldspar) (Fig. 4.5).

The shape preferred orientations of amphibole and biotite grains (Fig. AP4 – 2 in Appendix) may imply submagmatic flow caused by parallel or subparallel alignment of elongate euhedral crystals to the maximum elongation direction. The minerals are not internally (plastically) deformed and the strain is accommodated by the melt phase (Vernon, 2000; Vernon and Paterson, 2006). Melt-filled pseudomorphs are indicative of the presence of melt in high-grade metamorphic rocks (Holness et al., 2011). Here we use the term melt pseudomorph to represent single or multiple minerals crystallized from melt that filled microscopic porosity (Sawyer, 2001; Stuart et al., 2018). A string of beads (Fig. 4.4, 4.6) with round blebs of pseudomorphed former melt (e.g., quartz) along grain boundaries indicates a slow crystallisation rate that allows individual grains to form from the melt (Holness, 2008; Holness et al., 2011). Grain boundary melt films form where dihedral angles are less than 60°. Very low dihedral angles also indicate melt flow from triple point junctions along grain boundaries to form an interconnected melt network (Von and Waff, 1986). The

apparent dihedral angles in this study are as low as 10°, but they range evenly from 10° to 60° (Fig. 4.4, 4.6). When dihedral angles approach zero, elongated grains pseudomorph grain boundary melt films. Hence, elongated quartz and/or K-feldspar grains along grain boundaries of amphibole-plagioclase-biotite (Fig. 4.4, 4.6) are interpreted to indicate former melt situated at grain boundary pores. Pore spaces are typically pseudomorphed by single grains when bounded by fewer than four surrounding grains; however, as pore size increases, polymineralic aggregates can crystallize (Hasalová et al., 2008). Multiphase crystal aggregates (Fig. 4.4f) indicate late-stage crystallization of melt filled pores during cooling (Holness and Sawyer, 2008). The quartz-plagioclase aggregates found in the studied samples are mostly pseudomorphs of pores with four or more bounding grains where anhedral quartz-plagioclase grains display cuspate boundaries. Even when not connected in 2D, interstitial plagioclase grains are shown to be connected in 3D (due to their identical 3D crystal orientation) (Fig. 4.13a-b). Similarly, quartz grains in this melt pocket also show the same crystallographic orientation (Fig. 4.13a-b). These results are interpreted as the formation of a plagioclase/quartz grain pseudomorphing interconnected melt-filled pores in which both quartz and plagioclase grains crystallize with crystallographic continuity (Holness and Sawyer, 2008). Stuart et al. (2018) and Meek et al. (2019) have observed discontinuous plagioclase grains with a constant, single orientation, which is consistent with growth from melt filling an interconnected network. Small dihedral angles of interstitial grains, elongated grains, xenomorphic plagioclase connected in three dimensions, and fine-grained multiphase aggregates were the characteristics Stuart et al., 2018 identified for melt present deformation. All these features are also present in the studied samples. If melt-crystallization had occurred under static condition (absence of any deformation), the crystallized grains would reach textural equilibrium with uniform grain size and interfacial angles (103°-115° for quartz, plagioclase, and K-feldspar; Vernon, 1968). This is very different to a rock deforming in the solid state. In a paleo shear zone, one would expect microstructural variations with strain (e.g., straight grain boundaries, 120° triple junctions, deformation twinning in plagioclase, fracturing, recrystallization – reduction in grain size, undulatory extinction in quartz). In contrast to their macroscale appearance, representative samples from the low- and highstrain domains do not show significant changes in the microscale, indicating microstructural homogenization.

Even though there is a strong alignment of biotite-amphibole grains in all the samples (Fig. 4.4-4.6), most quartz-plagioclase-K-feldspar grains do not show significant

recrystallization, deformation twinning and subgrain formation. However, in the low strain II - SPI1314, some large quartz grains with intense dynamic recrystallization or plagioclase grains with small, recrystallized grains along their boundary are inferred to be relict porphyroclasts (Fig. 4.5b-c; Daczko and Piazolo, 2022). Quartz grains with no discernible melt microstructures (Fig. 4.5d) exhibit subparallel subgrain boundaries, deformation bands and large, continuous dauphiné twins, which may have formed due to outside tectonic stress during deformation (Fig. 4.13c). Because the low melt% in the host may have necessitated some strain to be accommodated by solid precursor grains, these features are only observed in low strain II - SPI1314. However, even though the delicate melt microstructure is preserved, local melt crystallized quartz grains exhibit substantial undulatory extinction (Fig. 4.5e). EBSD orientation analyses of melt pseudomorphed quartz and K-feldspar grains show significant bend in the crystal lattice (Fig. 4.13d-e). The large grains have lattice distortions of up to 7°, and GROD angle analysis reveals a large variation in crystal orientation with the formation of distinct subgrain boundaries (Fig. 4.13e-f). This is thought to have formed during the crystallization of a grain from a nucleus, rather than through deformation (Frondel, 1945; Spruzeniece et al., 2017; Chapter 5). Similar lattice distortions in migmatites characterized by melt fluxing and subsequent crystallization from the melt are also described by Haslová et al. (2008). Plagioclase, amphibole grains show very little change in orientation and are devoid of subgrain boundaries (Fig. 4.13e-f). They are interpreted to form the framework grains (along with biotite), with most of the strain absorbed by the melt occurring as thin melt films along grain boundaries, inhibiting solid-state crystal plastic deformation of host mineral grains. Small quartz-plagioclase aggregates in high strain II - SPI1321 show a low degree of internal deformation in quartz (Fig. 4.13g), which is very similar to the plagioclase, indicating that constituent grains likely crystallized under static conditions after the cessation of deformation. This is also seen in the small quartz-plagioclase aggregates (in Fig. 4.13d). The lack of deformation microstructure in the framework grains also suggests that deformation was brief following the crystallization of melt. The presence of these delicate disequilibrium textures precludes any significant annealing after deformation. Small plagioclase grains without any deformation twinning (Fig. 4.5e), connected 3D grains (Fig. 4.13a) or large plagioclase with undeformed rims (Fig. 4.5e) indicate crystallization of plagioclase from the melt. Because xenomorphic quartz, K-feldspar grains pseudomorph the melt-filled network, some grains pseudomorph melt by forming an overgrowth on an existing framework grain and are thus cryptic in nature. Hence, although their local association varies, crystallization of quartz-plagioclase and K-feldspar

account for the migration of a former granitic melt through this rock and crystallizing near or at solidus (Vernon, 2011).

In summary, we interpret the diorite gneiss to have formed during melt-present deformation based on the following observations. The studied rocks I) have high fraction (>30%) of undeformed leucocratic materials in the macroscale and felsic veins with large undeformed grains showing igneous like textures in the microscale, II) exhibit a combination of microstructural features indicating the former presence of melt and are thought to be associated with the crystallization of the final fractions of the melt (as quartz, plagioclase and K-feldspar grains) in the pore spaces, III) do not fully record the strain observed in outcrop because the solid frameworks lack any substantial intracrystalline deformation, IV) lack dislocation creep or microstructures common to mylonite, and V) show microstructural homogenization in both the low- and high-strain domains, indicating melt-rock interaction. We believe the rock has interacted with a melt of broadly granitic composition during deformation, where xenomorphic quartz-K-feldspar grains pseudomorph interconnected pores between solid grains and the final fraction of melt crystallized in melt pockets under nearly static conditions. Brittle fractures in ductile high strain zones form because of ductile fracturing caused by hardening of the rock as the rock approaches/crosses the solidus or by volume changes during melt-rock interaction, which may increase melt fluid pressure inducing fracturing (Jamtveit et al., 2009; Weinberg and Regenauer-Lieb, 2010). Melting reactions can also result in melt overpressure, which causes microcracking (Etheridge et al., 2021). Melt overpressure causes small scale microcracking in the plagioclase grains, followed by the crystallization of biotite and magnetite grains in those cracks (Fig. 4.5f).

4.5.3 Combined partial melting and melt fluxing indicated by mineral microstructure and geochemistry

Haslová et al. (2008a) described the injection of externally derived melt into a porous rock and argued that large scale pervasive flow does not require channelized movement but can also occur penetratively, along grain boundaries. Stuart et al. (2016) proposed that silicate melt is transported along grain boundaries (i.e., diffuse porous flow) in an open chemical system, forming microstructures produced by the reaction of hydrous silicate melt and anhydrous high-grade assemblage of the host rock in a shear zone. The inferred geochemical signatures of external melt influx are proposed as a) formation of new mineral

assemblages, b) melt-driven metasomatism and asymmetric corona microstructures, c) homogeneous mineral compositions at an outcrop scale, and d) igneous like REE pattern in the new minerals (Stuart et al., 2016, 2018).

The veins within the diorite gneiss exhibit diffuse, irregular boundaries (except Type 3 veins) and a similar mineral assemblage to the rest of the diorite gneiss, except for a greater abundance of melt pseudomorphed grains (Fig. 4.4, 4.6). This implies that the veins are all part of the same body and are most likely the accumulation and final precipitation of melt. Zones corresponding to melanosome and leucosome must be present in a typical migmatite. Here in the studied thin sections, we do not observe any dark, melanocratic layer or reaction microstructures around the felsic veins. External melt and its interaction with the host rock may be indicated by reaction rims around some veins in the field (Fig. 4.2) (e.g., Daczko et al., 2016; Meek et al., 2019). Although the microstructures described above can be used to infer the former presence of melt, they cannot rule out in-situ partial melting or infiltration of melt from an external source as a potential origin. Here, in all the samples, the host appears to be mesocratic, with abundant evidence of former melt crystallizing along grain boundaries and pseudomorphing interconnected melt filled pores (Fig. 4.4, 4.6). Biotite exhibits highly localized partial melting, with continuous, fine grained qtz-kfs-ttn rimming its corroded grain boundary (Fig. 4.4, 4.6). However, large, anhedral quartz, plagioclase, and K-feldspar account for most of the melt-pseudomorphed grains and are largely away from biotite in all the studied samples (Fig. 4.4, 4.6). The melt crystallized grains in the veins of low strain II - SPI1314 and high strain I - SPI1315 are even larger and occur almost without any biotite grain in their vicinity (Fig. 4.4a, e, i). Thus, if the melt pseudomorphs observed in the studied thin sections were all the result of in situ partial melting, a local grain scale melt migration from the site of production to the site of accumulation must have occurred. This necessitates melt connectivity and effective melt extraction from grain boundaries, both of which occur at a minimum melt fraction of 7 vol% under dynamic conditions (melt connectivity transition; Rosenberg and Handy, 2005). However, in low strain I - SPI137, the maximum partial melt amount suggested is 4-5 vol.% (from isochemical phase diagram in Fig. 4.10), which is insufficient for melt extraction and formation of the large volume of leucocratic veins. Furthermore, the observed melt volume produced at the peak P-T condition does not agree with the observed high melt percentage in the studied rocks (Fig. 4.7). The host of all studied samples shows melt volume preservation of > 4%, and the total melt is ~9% in low strain I - SPI1317, ~30% in low strain

II - SPI1314, and ~50% in high strain SPI1315, and SPI1321. Because this quantification only considers the melt pseudomorphed grains preserved in the microstructure, it may underestimate if significant melt loss has occurred or overestimate if melt crystallized in the shear zone for an extended period. The collapse structures observed in the field provide evidence of melt loss (Fig. 4.2h). Furthermore, high strain rocks must lose a greater amount of melt due to increased melt extraction caused by strain. In contrast, the high strain domains in this study have a higher percentage of preserved melt (melt vol. of 56-58%) than their low strain counterparts (melt vol. of 10-33%).

Therefore, in situ biotite melting cannot account for the high melt% observed in the studied samples. Furthermore, the amount of melt does not always correlate with the biotite modal% in the rock. The biotite mode in high strain SPI1315 is higher (12 modal%) than in low strain SPI1317-SPI1314 (3-4 modal%), as shown in Fig. 4.4 and Tab. 4.1, but the preserved melt amount is higher in high strain SPI1315 (Fig. 4.7). The high melt percentage observed in the high strain rocks would imply a higher degree of partial melting (if in situ) and, as a result, a lower modal abundance of biotite. In this case, the increase in observed melt% from SPI1317 to SPI1321 is more closely related to strain (Fig. 4.7). A high melt% in high strain domains also indicates an increasing degree of melt-rock interaction. As a result, low strain II - SPI1314, high strain I - SPI1315, and high strain II - SPI1321 are more evolved than low strain I - SPI1317. This is paradoxical because a decreasing equilibration temperature is observed from low strain SPI1317 to higher strain SPI1314, SPI1315 (Fig. 4.10b). The grain size does not vary much from SPI1317 to SPI1314, despite the progressive development of regular distribution of all felsic phases. High strain I - SPI1315 and high strain II - SPI1321 contain some coarse quartz and plagioclase grains, but there is an overall increase in small sized grains with characteristic melt microstructures from low strain to the high strain domain. Furthermore, while K-feldspar grains are equant in all the samples, partial melting should result in grain size increase of individual felsic minerals (Dallain et al., 1999; Haslová et al., 2008a).

Hence the disparities between our observations and the generally accepted trend for anatectic terranes necessitates an explanation. We propose *melt fluxing* from an external source as a possible explanation, where melt flows pervasively along the grain boundaries through the whole rock volume. Local incipient partial melting creates a permeable, interconnected network throughout the existing framework of the rock (Stuart et al., 2016). Even with a low melt%, melting wets residual grains and causes the crust to become porous

(Brown, 2010). The porosity required for a melt network is created due to the combined effects of biotite melting, and grain scale microcracking caused by melt overpressure (Etheridge et al., 2021). External melt infiltrates along the permeable grain boundaries during melt-present deformation, forming an interconnected, highly permeable network of melt movement (Scott and Stevenson, 1986). Due to the small viscosity difference between the inflowing felsic melt and the host, melt migration must be aided by deformation. The high strain domain has gradually attracted more melt, as evidenced by the high melt% in high strain I - SPI1315 and high strain II - SPI1321.

Geochemical signatures must also be indicative of diffuse porous flow. Because of melt-rock interaction, the studied samples contain a large volume of crystallized melt, resulting in a difference in bulk rock composition. Nearly consistent melt-rock interaction in low strain I - SPI1317, low strain II - SPI1314, and high strain I - SPI1315 is indicated by the overall homogeneous bulk rock composition (Fig. AP4 - 5 in Appendix). During melt fluxing, melt passes through the rock when the temperature of the rock and the melt is similar. As the rock approaches the solidus (i.e., decrease in P-T condition during exhumation), melt begins to crystallize. Here, individual rock types represent different stages and degrees of melt migration through the host rock. A different bulk rock chemistry in high strain II - SPI1321 (Fig. AP4 - 5 in Appendix) results from either a chemically different protolith or extensive metasomatic alteration during melt-rock interaction with a compositionally different melt. This interaction may have occurred at a lower temperature (Fig. AP4 – 6 in Appendix). However, a gradual increase in the SiO_2 content from low strain SPI1317: host to high strain SPI1321: host is consistent with the calculated melt% (Fig. 4.7). Thus, during melt infiltration and accumulation, more melt is drawn towards the high strain zone, resulting in an increase in SiO_2 (Fig. 4.8a, b). The hosts record a slight decrease in MgO content and an increase in Na_2O from low strain SPI1317 to high strain SPI1315 (Fig. 4.8a-b). The decreasing MgO trend may be due to a change in the amphibole-biotite modal percentage in the studied samples, whereas the increasing Na_2O trend may be due to increased interaction of the host rocks with incoming melt as strain increases. The decrease in MgO and TiO_2 content from low to high strain samples could also be attributed to increased felsic proportions in high strain samples due to higher degrees of melt-rock interaction. Melt-driven metasomatic alterations are common during melt rock interactions. Increased Rb/Sr values from low strain I - SPI1317 to high strain II - SPI1315 could be attributed to a shift in the K-feldspar to plagioclase ratio. The systematic modification of

mineral chemical composition across the studied samples is also incompatible with the model of in situ partial melting. Stuart et al. (2017) discovered semi-regularly spaced, distinct elongated zones caused by instabilities developing in the reaction front, altering mineral assemblage and mineral chemistry. The presence of enriched REE pattern in all the studied samples also suggests interaction with silicate melt in an open chemical system (Tab. 4.2). This also precludes the possibility that the inflowing melt is a product of incipient biotite melting. Instead, the melt must have formed in the deeper crust, migrated upward, and interacted with the diorite gneiss (Fig. 4.8d). The chemistry of high strain II - SPI1321 is anomalous in all these plots, indicating a different bulk composition and/or extensive metasomatic origin for this sample. Though the increased SiO_2 content in the host is consistent with a higher degree of external melt migration and subsequent melt crystallization in the high strain zones. For each of four melt fluxing types, Stuart et al. (2018a) described distinct mineral assemblages and compositions. Small ranges in mineral composition/less pronounced zoning are often associated with higher time integrated external melt influx and better equilibration during melt-rock interaction (Fig. 5, 6 in Stuart et al., 2018). We see a similar pattern here, where low strain I - SPI1317, low strain II - SPI1314, and high strain I - SPI1315 have overlapping mineral compositions of amphibole, biotite, K-feldspar, and plagioclase grains despite having experienced varying degrees of melt-rock interaction (Fig. 4.9). The compositions are similar in veins, implying that all mineral compositions were buffered by melt (Fig. 4.9). The compositions are found similar also in the veins, suggesting that melt buffered all the mineral compositions. In high strain II - SPI1321, plagioclase and K-feldspar show similar chemistry for both host and the vein compared to other samples (Fig. 4.9). A lack in compositional difference in the melt-crystallizing minerals also indicate a large equilibration volume. In, high strain II - SPI1321 different bulk rock composition may be responsible for a change in amphibole and biotite compositions (Fig. 4.9a, b; AP4 – 6 in Appendix). Many experimental and field studies suggest that during in situ partial melting process, the composition of plagioclase would shift towards higher anorthite content, and the X_{Fe} of biotite would decrease (Gardien et al., 1995; Greenfield et al., 1998; Dallain et al., 1999). This contradicts the high albite content observed in the more evolved high strained rocks versus low strain I - SPI1317. There is no zoning in plagioclase and amphibole grains (Fig. 4.4-4.6). This also suggests that grain scale homogenization happened during melt fluxing. Due to the lack of any precursor host it is impossible to comment on the existence of any metasomatic changes associated with the initial phase of melting/melt-fluxing.

4.5.4 Low and high-strain domains exhibit little grain scale variations: Implications for deformation mechanisms

Walte et al. (2005) investigated the deformation behaviour of melt-bearing rocks and described framework dominated to liquid dominated behaviour that is compatible with the melt connectivity transition of Rosenberg and Handy (2005). In the case of low melt (i.e., <7 vol.%), the grains form solid framework, and the deformation mechanics are controlled by the solid phases. Solid grains deform by diffusion or grain boundary migration accommodated dislocation creep (e.g., Hirth and Kohlstedt, 1995a, b; Gleason et al., 1999; Mei et al., 2002). During intermediate melt volume (~7 vol.%), granular flow and grain boundary sliding control the rheological behaviour (e.g., Rutter, 1997; Petford and Koenders, 1998; Paterson, 2001), whereas in high melt volume (>7 vol.%), crystals are suspended in the melt and the rheology is controlled by liquid viscosity (e.g., Ryerson et al., 1988). The solid framework begins to breakdown, at high melt volume of 40-60% melt, and the rock goes through the 'solid-to-liquid transition' (SLT) (Rosenberg and Handy, 2005). If the shear zones did not undergo melting and/or melt-fluxing, they should have preserved a record of pre-, syn- and post-melt deformation. This means that the absence of any evidence of former melt presence will indicate that the crystal microstructures have not been 'reset', and thus an observable crystal preferred orientation of the constituent mineral grains is expected (Lee et al., 2018). In contrast, if the shear zone has experienced syn- and/or post-melting/melt-fluxing, the microstructures will be reset with crystallization of the melt.

Recent experimental studies (Ko and Jung, 2015; Kim and Jung, 2019) differentiate between four different types of amphibole CPO patterns based on differential stress and temperature at a pressure range of 5-10 kbar. Type-1 CPO has (100) poles subnormal to the shear plane and [001] axes aligned parallel to the shear direction. In contrast, a type-2 pattern is formed by a cluster of (100) poles subnormal to the shear plane and (010) poles aligned subparallel to the shear direction. Type-3 pattern is a hybrid of type-1 and type-2, with (010) poles and [001] axes forming a girdle subparallel to the lineation (X). Unlike in other patterns, type-4 shows a girdle of (100) poles and [001] subparallel to the lineation (X). Kim and Jung (2019) observed type-2 and a mix of type-1 and 2 develop under low shear strain (γ <3) and at low to intermediate temperature (at ~500-600°C), whereas type-4 pattern is found at higher strain ($\gamma \geq 3$) across 500-700°C. All 4 types of CPO patterns are seen here. Amphibole CPO corresponds to type-I pattern in low strain I - SPI1317, whereas amphibole

CPO coincides with type-IV pattern in low strain II - SPI1314 (Fig. 4.11a). High strain I - SPI1315, on the other hand, has a type-III CPO, whereas high strain II - SPI1321 has a type-II CPO pattern (Fig. 4.12a). A strong amphibole SPO is observed in all samples, subparallel or inclined to the foliation plane (Fig. AP4 – 7 in Appendix). Previous research has found type-IV CPO in natural rocks deformed under high-strain conditions and/or in mylonitized shear zones in the middle crust (Imon et al., 2004; Lamarque et al., 2016; Tatham et al., 2008). Thus, the type-4 pattern observed in low strain I - SPI1314 could have been caused by high strain. This is supported by dynamic recrystallization of quartz and the formation of subgrains in plagioclase in low strain I - SPI1314. The lower melt% observed in SPI1314-host would imply that the solid grains accommodated majority of the deformation. The melt proportions observed in the host of all the other samples is >7%, indicating that the nature of deformation is controlled by the melt. The presence of CPO is normally attributed to dislocation creep (Wenk and Christie, 1991). However, in the studied samples, amphibole lacks microstructures indicating crystal plastic deformation (Fig. 4.13). Hence, CPO patterns of amphibole observed in the samples suggest growth during deformation or rigid body rotation with [100] poles subnormal to the shear direction (Stokes et al., 2012; Kim and Jung, 2019). Elongated shape of the amphibole grains also supports a CPO of the long axes parallel to the fabric attractor (Passchier, 1997). When the solid framework does not record the strain observed in the outcrop (Fig. 4.13), a melt present deformation scenario can be proposed. The strain is achieved through GBS accommodated by the melt movement along grain boundaries (Rosenberg, 2001; Walte et al., 2005). In the high strain samples, a stronger CPO intensity in amphibole is formed due to easy rotation of grains with a high amount of melt at grain boundaries (Fig. 4.12a). Stuart et al. (2018) observed similar CPO patterns during melt present high strain deformation. During rigid body rotation, biotite also exhibits preferential orientation of its long axes [001] subnormal to the shear direction. In all the samples, plagioclase exhibit a very weak CPO (Fig. 4.11c, 4.12c) which may indicate diffusion creep that must be accommodated by grain-boundary sliding to prevent the formation of internal cavities, resulting in a weak CPO (Bestmann and Prior, 2003; Svahnberg and Piazolo, 2010). Hence, a model of deformation by melt present GBS can be predicted for both the initial and melt-crystallizing phases (Jiang et al., 2000; Piazolo and Jaconelli, 2014; Dutta et al., 2021). Melt pseudomoprhs along grain boundaries and at interstices between larger grains also support this model. Individual quartz and K-feldspar grains exhibit significant crystal bending, but their CPO patterns are random. This suggests that the deformation observed in these grains is local and related to growth (Fig. 4.13e-f;

Chapter 5). This is also supported by the randomly oriented sub structures observed in these grains (Fig. 4.13f-g). A non-systematic, weak grain scale CPO of qtz-Kfs (Fig. 4.11d-e; Fig. 4.12d-e) also imply absence of dislocation creep. However, (001) poles of K-feldspar show a weak pattern, oblique to the lineation (Fig. 4.11e, 4.12e). If deformation structures observed in the field formed pre- or post-melt, we would expect a strong CPO of quartz and K-feldspar. Thus, deformation forming the low- and high-strain shear domains occurred prior to or after melt fluxing. Similar observations are made by Prakash et al. (2018) and Lee et al. (2018).

4.5.5 Dynamics of a long-lived melt transfer zone during progressive deformation: A model of heterogeneous, multiscale porous melt flow

The co-location of partially molten rock and high strain regions has been long recognized and studied, particularly in regional geological studies. Feedback between melting, rheological weakening, and shear zone nucleation as a mechanism of melt transport at a regional scale has been documented in many studies (Hollister and Crawford, 1986; Brown and Solar, 1998a; Rosenberg and Handy, 2005; Brown, 2007, and the references therein; Stuart et al. 2016, 2018a; Daczko et al. 2016; Meek et al. 2019). Levine et al. (2013) identify concentrated deformation along melt producing reactions zones at the sub-millimeter to millimeter scale. Searle (2013) addresses the chicken-egg problem of whether ‘shear zone controls the generation and ascend of magmas or magmas trigger nucleation of shear zones?’.

We propose a model that depicts the dynamics of syn-deformation in situ melting and melt fluxing, strain localization, and the formation of a series of low- and high-strain domains (Fig. 4.14). We advocate that met migration is facilitated by pervasive melt movement along grain boundaries during heterogeneous deformation in an open system, resulting in the formation of low- and high-strain zones. We choose to discuss the model as consecutive stages; however, it should be noted that this is a simplification. Each stage was most likely active at different times in different parts of the rock. We propose the existence of spatial and temporal heterogeneity. To develop the high strain domain exemplified by high strain II - SPI1321 with the highest cumulative melt flux, all three stages were required. In other locations, only stage I or only stage I followed by stage II would have occurred. In other areas, only stage I or stage I followed by stage II would have been observed.

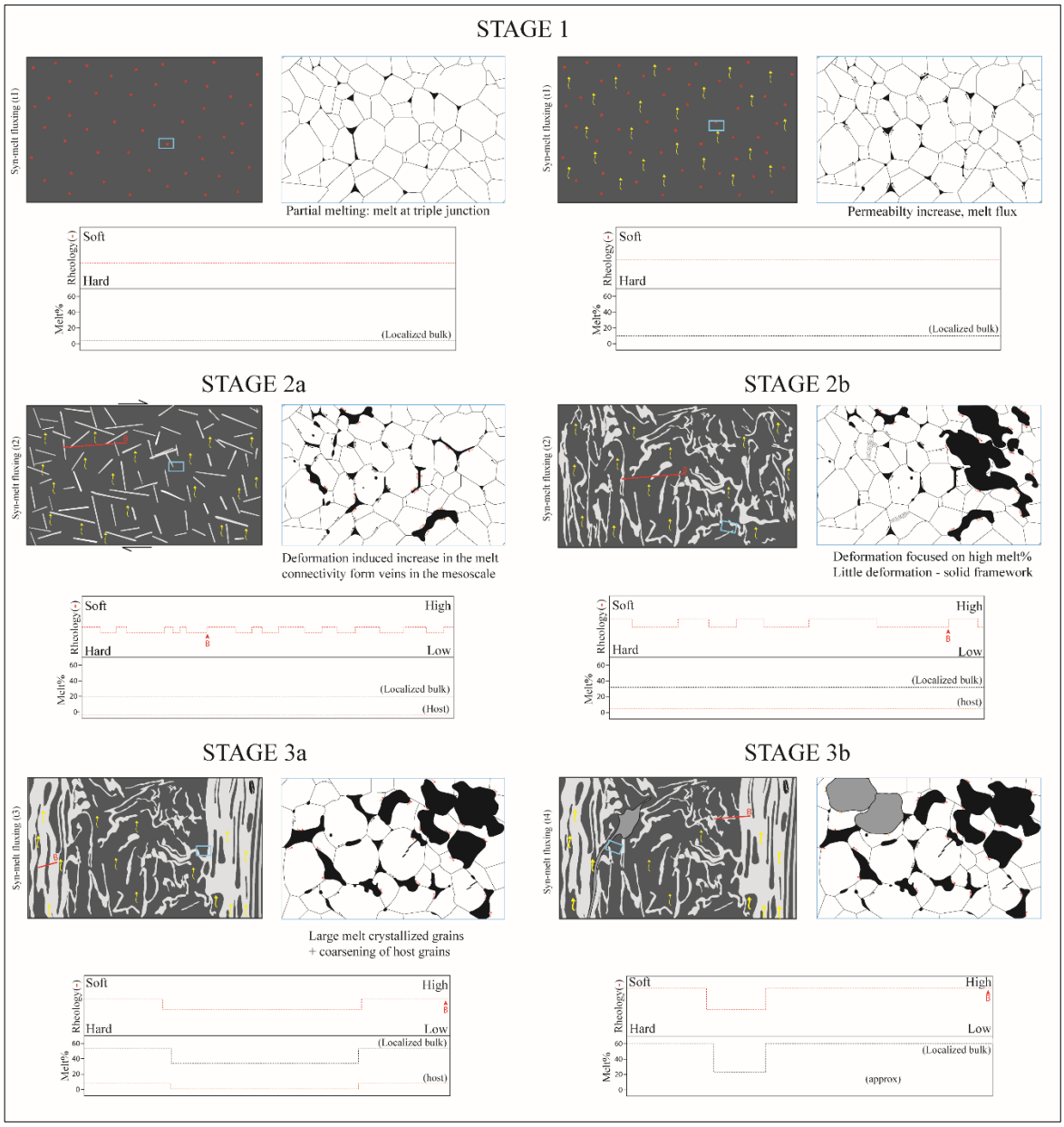

Figure 4.14 – Schematic diagram depicting the formation of low- and high-strain zones at the outcrop scale (from stage 1 to stage 3) and the associated microscale grain structures. Rheology is schematically shown across profiles (marked with 'B' profiles; not in scale) for each stage to illustrate the progressive evolution through space and time; red and yellow arrows represent in-situ partial melting and externally derived melt, respectively. Melt% in each stage is also shown for the localized bulk. Three stages are depicted, each with two snapshots (left snaps representing outcrop scale and right snaps showing microscale structures) to demonstrate the system's evolution. Location of thin sections are shown with blue rectangles. *Stage 1*: (a) homogeneous solid gneiss experiences partial melting of biotite at time t1 (see text for details). Melting occurs only at the triple junctions, and melt percentages are low (cf. Fig. 4.10a), when LDA <10° interconnected melt filled pores form a permeable network. (b) External melt influx (yellow arrows) through the permeable network causes porous melt flow, an increase in melt percentage, and melt connectivity (higher number of arrows in the microscale). In areas with a high melt percentage, the rock is rheologically softer. At time t2, (c) *Stage 2a*: deformation induced melt segregation and extraction forming melt (felsic) veins at time t2. Many melt-disequilibrium features are observed at the microscale (distinguished as large anhedral grains, and elongated melt films at grain boundaries). (d) *Stage 2b*: rheological difference causes flow perturbation folding, resulting in randomly oriented melt veins. Rheologically, felsic melt zones

are softer than their solid surroundings. Because of deformation enhanced melt extraction, the host has a relatively low melt%. This leads to local grain scale deformation features at solid-solid grain interface. At the time t3, (e) *Stage 3a*: strain localization due to rheological difference in zones of high melt connectivity. Increased intensity of melt fluxing due to local strain localization resulting in the formation of 'high melt zones'. An increase in host melt% indicative of high melt influx. Surrounding areas with low melt% and open felsic folds form the 'low strain' zones. Local entrainment of surrounding veins into high strain zones describes synchronicity of the 'low and high-strain' domains and a relative increase in the strain component along high melt zones. Take note of the grain scale features and observe an increase in overall grain size of melt pseudomorphed grains in the host, and evidence of grain fractures caused by melt overpressure. (f) Late-stage pegmatite veins crosscut the 'low-strain' domain but run-in parallelism with the 'high-strain' domains, indicating that they outlast their low-strain counterparts. Large K-feldspar grains (grey) form on the microscale because of this pegmatitic intrusion. The presence of varying melt% and relative timing of melt-crystallization causes differences in rheology.

At *Stage1* of the model, partial melting of a solid gneiss and in situ biotite melting, at time t1, occur at PT peak conditions of 690-705°C and <5.3kbar. This incipient melting generates grain scale permeability and an interconnected network throughout the solid framework. At the peak pressure-temperature condition, biotite melting is supported by the isochemical phase diagram, and a small melt fraction of 3-4% melt is observed (Fig. 4.10). The porosity and interconnected network created by the onset of melting produce a melt filled grain boundary network with a high permeability. High permeability can also be caused by small microcracks or may have formed during the melting reaction. Later, externally derived melt utilizes this high permeable grain boundaries and infiltrate the rock, resulting in a diffuse porous melt flow (Stuart et al., 2016) (Fig. 4.14a). The external melt flow is intermittently related to deformation (Haslová et al., 2008c) because the viscosity difference between the host and melt in the crust is not significant. The overall orientation of melt pseudomorphed grains parallel to the foliation also demonstrates this (Fig. 4.6, AP4 – 2 in Appendix). The grain scale characteristics reveal both equilibrium (melt at triple junctions with dihedral angle <60°) and disequilibrium textures (e.g., large, elongated melt films fully wetting grain boundaries of other minerals, trapped interstitial melt pseudomorphed grains along grain boundaries, distorted triple junctions etc.). Once established, this interconnected network can be reused (if the rock remains above the solidus) and the permeable grain boundaries are utilized to infiltrate the rock with ever-increasing amounts of external melt (Fig. 4.14b). A preserved melt amount of 9% is observed in the rock microstructure (Fig. 4.7b). However, it is anticipated that the melt network present at any given time will be relatively heterogeneously distributed (e.g., Stuart

et al. 2016). Locally, melt percentages may exceed several percent, causing localized rheological softening (Rosenberg and Handy, 2005). Local melt segregation will occur concurrently with the rheological softening.

At *Stage 2* (time t2), deformation induced melt segregation cause local channelized melt migration. Melt is extracted locally into interconnected melt veins due to increased melt amount and melt connectivity (Stage 2a, Fig. 4.14c). As a result, the amount of melt in the host may decrease significantly (4.5%; e.g., low strain SPI1314-host, Fig. 4.7c). Melt is first localized into melt pockets, which coalesce into veins from which melt can be extracted and fluxed at a faster rate. It should be noted that melt extracted in one location will then flux in another location. Melt is extracted from the host as well as infiltrated and fluxed, resulting in melt flow at two scales - grain boundary network and vein network. As a result, the bulk rock (host and vein) would have a high melt presence, as demonstrated by the measured melt amount of 33% in low strain II - SPI1314. Flow perturbation folding is caused by the rheological difference between softer melt veins that are melt-crystal composites and relatively harder host (mostly with amphibole-plagioclase-biotite and relict quartz grains) (Stage 2b, Fig. 4.14d). Field observations of small-scale folds (primarily 'S' and 'Z'-types), shearing of melt veins, shear bands, and curved fold hinges all point to syn-melting deformation.

At *Stage* 3 (time t3), with continued progressive melt fluxing, certain zones of higher melt connectivity (due to local heterogeneity caused by either change in local composition or melt vein organization) would experience a reduction in the effective viscosity. Presence of melt is known to make a rock weak and can result in high-strain localization for the same shear stress (Rosenberg and Handy, 2005; Holyoke and Tullis, 2006) (Stage 3a, Fig. 4.14e). Because viscosity changes exponentially with melt percentage, viscosity reductions can be extreme (Rosenberg and Handy, 2005, inset Fig. 4.14). This phenomenon is supported by local entertainment of veins from low-strain domains into high-strain zones (Stage 3b, Fig. 4.14f). Increased strain localization is aided by high melt fluxing and stress driven organization of melt (e.g., Brown and Solar, 1998; Rosenberg and Handy, 2005; Vanderhaeghe, 2009; Lee et al., 2018). The preferential melt organization is comparable to the foliation-parallel melt flow observed by Weinberg and Searle (1998) and Sawyer (2001). These channels continue to focus melt at advanced stages of melt fluxing, and the rock experiences a greater degree of melt inflow. High melt fluxing is also evidenced in high strain rock samples (~56% in high strain I - SPI1315 and 58% in high strain II - SPI1321).

Melt disequilibrium features are discovered to be widespread and melt overpressure results in the formation of small microcracks. Some large host grains are visible here, indicating grain growth at high temperatures during melt transport. Later, high-strain zones are actively transporting melt, whereas low-strain zones may have started to cease, possibly due to melt crystallization. This is indicated by the cross-cutting relationship of the coarse-grained Type 3 veins in the low-strain domain (Fig. 4.2), but they run in parallelism with the high-strain zones (Fig. 4.2, as observed in Stage 3b). These veins of varying composition imply melt migration through a vein network on a larger scale than the outcrop studied. In contrast to the diffuse boundaries observed here, the intrusion of such a vein into a solid host rock would result in a sharp boundary. Thus, even when these veins were present, there was still enough melt in the host rock, indicating melt migration at the grain boundary network scale with concurrent large scale melt fluxing in a vein network.

As the CPOs of amphibole and biotite grains coincide with their SPOs, pervasive flow can be deduced as a deformation driven process associated with mechanical rotation of amphibole-biotite grains (Fig. 4.11-4.12). Only a few large quartz, K-feldspar and plagioclase grains exhibit crystal plastic deformation (e.g., undulose extinction in qtz, plag with deformation twinning, and local recrystallization of qtz-plag grains; Fig. 4.5, 4.13), indicating that the melt network was not pervasive resulting in dislocation creep in low strain II - SPI1314 (melt% in the host is the lowest in this sample). Alternatively, the solid-state deformation may have happened during the late active phase of the high-strain domains, when the low-strain domains already began to solidify (stage 3b). Elsewhere, the framework plagioclase, amphibole, and biotite crystals show little crystal bending, indicating that much of the strain is absorbed by the melt (Lee et al., 2018). The absence of microscopic evidence of metasomatism suggests that melt-rock interaction was nearly isochemical. This also implies that the influxing melt was derived externally as a partial melt of the dioritic gneiss or a similar rock and was thus only slightly out of equilibrium with the dioritic gneiss at low pressure. Therefore, the in situ partial melt in the dioritic gneiss did not differ significantly from the influxing melt upwelling from below. The high temperature (higher than the solidus of the overlying unit) enables the melt to migrate upwards without crystallizing. This can potentially lead to injection complexes observed in hot terrains (Weinberg, 1999). The open system nature of melt migration precludes an accurate estimation of the time integrated melt influx. Presence of melt makes a rock weak evidenced by the zones of high melt influx localizing more strain. Hence upon complete crystallization this rock becomes rheologically

hard, and the deformation shifts elsewhere. If deformation had continued below the solidus (as observed by Lee et al., 2020 in the shear zone flanks) melt microstructures could have been overprinted during solid-state deformation. Moreover, delicate grain and subgrain scale microstructures observed in the studied samples (e.g., LDA, interstitial grains, xenomorphic grains in Fig. 4.4-4.6) are transitory disequilibrium features that return to equilibrium geometry during recrystallization and annealing (Walte et al., 2003). Hence the timing, duration and intensity of the deformation are inextricably linked to the history of melt fluxing, which governs the difference in melt% and its distribution. This results in a series of low- and high-strain zones where high melt percentage preservation invokes a model of melt stagnation and crystallization in the observed lower crust.

4.6 Conclusion

Based on detailed field, microstructural and geochemical investigations, diorite gneiss in the Akia Terrane is identified to have experienced both in-situ and external melt fluxing during progressive deformation. Though the rock unit exhibits different domains of low-high strain due to the varying arrangements of felsic veins in the field, there are no progressive changes in mineral assemblage, microstructure, and mineral chemistry. Melt infiltration is thought to occur primarily in an open system, with changes in the frozen-in whole rock chemistry being directly related to melt crystallization in situ.

The field microstructural evidence and melt percentage indicate that an external melt infiltrated the dioritic gneiss via porous flow along an interconnected grain boundary network as well as a melt vein network, aided by deformation. This network was initially formed because of in-situ partial melting of pre-existing biotite, which created pathways for multiscale, external melt infiltration. Depending on effective rheology, melt extraction, melt influx and in situ melt crystallization, heterogeneous deformation and melt fluxing result in the formation of low vs. high strain domains.

The proposed model of external melt fluxing may explain the origin of some felsic migmatites in other high-grade metamorphic terranes that can influence rheology of larger crustal domains. If proven widespread, it has wider implication for mechanism of melt transport in crustal units overlying anatectic crustal segments, as well as its feedback with deformation mechanisms.

Chapter 5

Characteristics of quartz grains pseudomorphing former melt under static and dynamic condition

This chapter represents a manuscript draft that provides in-depth microstructural characterization of melt pseudomorphed quartz grains in various geotectonic settings. This draft will be submitted to the *Journal or Structural Geology* soon after the thesis submission. The authors and their contributions to this chapter are as following: Joyjit Dey (petrography, SEM-EBSD data collection, conceptualization, data analysis, original draft, figures, review, and editing), Sandra Piazolo (conceptualization, supervision, review, and editing), Nathan Daczko (review and editing), John Wheeler (provided access to the WBV-analyses software, review, and editing), and Mohsen Bazargan (COMSOL numerical modelling and editing).

Abstract

While microstructures such as systematic crystal distortions within individual grains are commonly interpreted as signs of post-growth deformation, it is unclear what microstructures are typical in minerals pseudomorphing former melt. Here, we document and contrast the microstructural features within grains of quartz crystallized from a silicate melt in various geotectonic environments to identify features typical of melt present situations. We investigate in detail microstructures developed in a) slowly cooled granite,

b) low-strain statically heated and cooled migmatite, and c) melt-fluxed high-strain shear zone using electron backscattered diffraction (EBSD) and weighted burgers vector (WBV) analysis. Aside from the typical petrographical melt-microstructures, quartz formed during the final stages of melt crystallization differs significantly from those formed in response to solid-state crystal plastic deformation in their nature of distortion and identified slip system. Within all geotectonic scenarios studied, quartz grains pseudomorphing former melt exhibit internal lattice distortions such as gradual lattice bending, the presence of subgrain boundaries, and dauphiné twins near grain edges, as well as a lack of sample scale crystallographic preferred orientation (CPO). ESBD orientation analysis of subgrain boundaries suggest crystal bending was accommodated by edge and screw dislocations on both basal (<c> slip) and/or non-basal (<a> slip) planes. Individual grains record activity of slip systems that are commonly interpreted to be activated across a broad temperature range. We interpret that the observed internal deformation features develop during crystal growth from melt in a confined space. In-depth microstructural findings show that systematic lattice distortions can result from crystal growth alone and do not have to be a sign of tectonic deformation.

5.1 Introduction

Many thermal and mechanical properties of high-temperature systems containing melt are affected by its grain scale distribution (Walte et al., 2003). Anatectic horizons are thought to be mechanically weaker portions of the crust, and even when the melt fraction is only a few percent, it can still have a significant impact on orogenic development (Schilling et al., 1997; Nelson et al., 1996; Beaumont et al., 2006). Accordingly, it is important to recognize rocks that contained small proportions of ‘frozen in’ melt. Despite its significance, the characterization of internal microstructures of crystallized melt, with or without active tectonic stress, has only been discussed in a few sample-scale melt-rock interaction studies, primarily as one of many aspects of their studies (e.g., Stuart et al., 2016, 2017; Haslovà et al., 2008a-b). This contrasts the plethora of work concentrating on the in-depth analysis of the grain- and sub-grain scale features related to solid-state deformation (e.g., Hobbs, 1968; Tullis, 1977; Blumenfeld et al., 1986; Schmid and Casey,1986; Dell’Angelo and Tullis, 1989; Gleason et al., 1993; Stipp et al., 2002; Lloyd, 2004; Menegon et al., 2008; Stipp and Kunze, 2008). Particularly, it is unexplored how to recognize and differentiate grain internal

microstructures pertaining to solid-state crystal-plastic deformation versus those formed in melt pseudomorphs when crystallization occurs with/without a deviatoric stress field.

Melt pseudomorphs may occur in at least three different scenarios: (i) slow crystallization of plutonic granitoid rocks without external differential stress, (ii) static or dynamic migmatites, where static and dynamic refers to the absence and presence of differential stress during melt crystallization, respectively, and (iii) high-strain melt-present shear zones, interpreted to be the products of coeval melting or melt fluxing and strain localization (e.g. Weinberg et al., 2009, 2015; Brown and Solar, 1998b, Daczko and Piazolo, 2022).

Silicate melt has a relatively low viscosity and will therefore develop a 'flow-channel network' along the grain boundary network (Smith, 1957) where the melt topology is mainly controlled by differential stress, confining pressure, and the amount of melt in the system (Rosenberg, 2001). In statically crystallizing granite/granitoids, this melt network is readily identifiable due to the presence of quartz, K-feldspar and/or plagioclase grains crystallized from the melt late in the crystallization sequence. During partial melting within migmatites, the reactant phases become unstable at higher temperature and give rise to melting at triple junctions (Laporte and Watson, 1995; Haslová et al., 2008; Holness & Sawyer, 2008). Under hydrostatic stress, when the melt fraction is sufficiently low (e.g., ~20%), the melt does not leave the solid matrix and the system behaves as a closed system (Sawyer, 1999). In a static environment, melt-crystallized grains show a set of grain-scale features i) low dihedral angles (LDA) of <60° forming a cuspate-shaped mineral with sharp, pointed extension (Holness and Clemens, 1999; Clemens and Holness 2000; Sawyer, 2001). If dihedral angles are very small, grain may become tabular (Holness, 2006), ii) retention of chemical zoning in feldspars (Vernon and Paterson, 2008; Holness et al., 2007), iii) impingement of two grains (during solidification) with grain boundaries oriented at high angles to the crystal growth faces, sometimes with small inclusions (Vance, 1969; Graeter et al., 2018; Holness et al., 2018), iv) euhedral inclusions of plagioclase in K-feldspar, plagioclase in quartz, plagioclase in biotite, etc. (Holness et al., 2018), v) presence of primary growth twins in K-feldspar, plagioclase & hornblende, and vi) fine grained polymineralic intergrowths having granophyric microstructure (Vernon, 2010; Holness et al., 2018). In a static melt bearing rock, the silicate melt is interconnected by a stable network of channels along three grain junctions (Laporte and Provost, 2000; Haslovà et al., 2008; Holness et al., 2011) resulting in pseudomorphs of fully wetted grain boundaries, and melt lenses trapped between grains (Walte et al., 2003).

In rocks deforming in the presence of melt, depending on the magnitude of the deviatoric stress and the melt fraction in a rock, the grain scale melt distribution can localize along a foliation plane or form elongate melt pockets or veinlets at a high angle to the foliation plane (Rosenberg and Riller, 2000; Sawyer, 2001; Marchildon and Brown, 2002; Zàvada et al., 2007; Stuart et al. 2016). The effect of deformation on the development of grain-scale microstructure is governed by the rate of deformation relative to the interfacial energy between melt and solid phases acting to achieve textural equilibrium (Marchildon and Brown, 2002). In such cases, if the melt fraction is >7%, deformation improves melt connectivity and promotes the formation of shear bands along which melt is further segregated (Rosenberg and Handy, 2000, 2001). A study by Haslová et al. (2008a) suggests deformation-enhanced melt-infiltration leads to a regular distribution of individual minerals and a reduction in the overall shape-preferred orientation. Typical characteristic features of melt-crystallization in a deviatoric stress field and in high-strain zones resemble those formed under static conditions. These characteristics include interstitial melt pockets, quartz/feldspar melt 'fingers' protruding into other grains, cuspate boundaries of reactant grains or mineral inclusions, LDA relationships of interstitial minerals, irregular xenomorphic grains along grain boundaries, melt films along grains forming elongated string-of-beads texture, euhedral faceted grains at small pores and polymineralic intergrowth at large pores: nanogranitoids (Mehnert et al., 1973; Laporte, 1994; Vernon, 2011; Holness and Sawyer, 2008; Cesare et al., 2009; Stuart et al., 2018; Lee et al., 2018). Additional features exclusive to the dynamic deformation environment may include a) dominantly unimodal grain size distribution of constituent mineral phases, b) occasional intra- or inter-granular fractures, c) elongated melt pockets or shear bands, d) SPO formed by prismatic or flaky minerals (Rosenberg and Riller, 2000; Stuart et al., 2018, Shao et al. 2021). However, until now no study has particularly focused on in-depth intercrystallite microstructures of melt-crystallized grains.

In contrast, extensive research has been conducted on the grain, subgrain, and sample-scale microstructural characteristics of solid-state deformation in quartz. Two main end-member regimes are identified, namely diffusion creep and dislocation creep which is often referred to as crystal plasticity (e.g., Hobbs 1968; Vernon 2000; Paterson et al., 1989). Solid state deformation by diffusion creep is facilitated by stress induced diffusion of vacancies. In contrast, during dislocation glide and/or creep, stress induced movement of dislocations through the crystal lattice results in plastic deformation (Poirier 1985; White, 1977; Ranalli and Fischer, 1984; Hirth and Tullis, 1992). While diffusion creep is not

expected to result in sample-scale crystallographic preferred orientation (CPO), crystal plasticity does (e.g., Law 1990). Typically, CPO patterns are interpreted in terms of the relative activation of slip systems, the activity of which is governed by temperature, strain rate, differential stress, and fluid content (e.g., Hobbs, 1968; Hirth and Tullis, 1992; Poirier and Guillope, 1979; Stipp et al., 2002). Deformation by dissolution-precipitatin creep may theoretically result in a CPO if dissolution and precipitation rates are anisotropic woth respect to the crystallographic orientations (Bons and den Brok, 2000). Here, no dislocation movement is involved, and hence no lattice bending is expected.

In contrast to the knowledge of microstructural features resulting from solid-state deformation, characteristics such as 3D crystal orientations, nature and degree of lattice alignments, and nature and characteristics of internal grain structures have yet to be evaluated for melt-crystallized grains. This study sheds new light on the microstructures formed in melt-crystallized quartz grains within confined spaces in an effort to close the knowledge gap concerning the detailed crystallographic orientation characteristics of melt-crystallized minerals. We focus on cases where low melt fractions are present or the mineral in question has crystallized from melt. Recognition of former melt presence is most difficult in this scenario because no outcrop scale melt segregation with easily discernible composition differences is expected. In this study, rocks of known geological history are investigated systematically. Under the optical microscope, quartz microstructures indicating the former presence of melt are identified using the criteria outlined above and highlighted by Daczko and Piazolo (2022). These carefully chosen grains were then subjected to detailed quantitative orientation analyses to identify the intra-grain microstructural features typical of minerals pseudomorphing former melt. As such, these features serve as an additional tool for determining former presence of melt. The link between the identified characteristic microstructural features and the processes that occur during melt crystallization in confined space is then discussed.

5.2 Analytical methods

To gain in-depth understanding on microstructural features of melt crystallized grains, first we must identify quartz grains which retain microscopic features of former melt using standard petrographic microscope and scanning electron microscope from the three studied samples. Next, to obtain crystallographic orientation data for studying grain

orientation deviation, crystal preferred orientation of a group of grains, and change in crystal orientation along profiles or with respect to certain crystallographic axes, the identified grains are mapped with SEM-based electron backscatter diffraction (EBSD). For characterizing low-angle boundary geometry and its 3D orientation, subgrain boundaries are studied with boundary trace analyses and weighted burgers vector (WBV) analysis.

5.2.1 Sample preparation

Samples were cut parallel to the lineation (X-direction) and perpendicular to foliation (XY plane of finite strain) to obtain desired XZ sections for general petrographic and EBSD analysis. If no structural features were present, such as in granite and static migmatite samples, thin sections were cut randomly. Petrographic thin sections were prepared by polishing samples to ~30 µm thickness. Thin sections were again polished down a further 1 µm and colloidal silicate mechano-chemical polishing (syton polishing) was performed for 3min on each sample (Fynn and Powell, 1979; Prior et al. 1996). Samples were then carbon coated (with 3nm of carbon) before analysis. Mineral abbreviations used follow those proposed by Whitney and Evans (2010).

5.2.2 Back-scatter electron imaging

Backscatter electron (BSE) images were used to characterize fine-grained microstructures indicative of the former presence of melt that are easy to miss during classical optical microscopic studies. Thin sections were coated with ~10 nm of carbon and analysed in a Field Emission Gun Scanning Electron Microscope (FEG-SEM) at the Microscopy unit of University of Leeds, UK. The SEM was operated at high vacuum with an accelerating voltage of 15–20 kV and a beam current of 5.0–10.0 nA, with working distances of 11–13 mm.

5.2.3 Quantitative orientation analysis (Electron backscatter diffraction: EBSD analysis)

Crystallographic orientation data were obtained from automatically indexed EBSD patterns using Symmetry S2 detector on the FEI Quanta 650 FEG-SEM with Oxford X-max 80 SDD EDS at the University of Leeds, UK. Conventional working conditions were followed i.e 25kV accelerating voltage, ~0.8 nA beam current, working distance of 20mm,

and 70° sample tilt in low vacuum mode (0.3-0.4 torr). EBSD patterns were automatically indexed using AZTEC Crystal analytical software. The overall indexing was between 70-90% for trigonal quartz of Laue group-3m. Post processing were also performed using AZTEC Crystal analytical software following the procedure of Prior et al. (2002) and Piazolo et al. (2006) were used for noise reduction and removal of zero solutions. EBSD orientation data (presented as maps) with 1.5, 5, 8 and 10µm step sizes were obtained from the studied samples, where the low resolution (8 and 10µm step size) maps were used to identify grain association and crystallographic preferred orientation (CPO), while the higher spatial resolution maps (1.5 and 5µm steps size) were used for detailed crystallographic investigations in quartz and its surrounding grains.

We present data in the following formats: (a) greyscale band contrast maps (BC) to display variety in pattern quality, where darker pixels are normally attributed to the grain or subgrain boundaries, (b) orientation maps of melt-crystallized quartz grains to display crystal orientation at each point. Crystal orientations are plotted according to a colour coded inverse pole figure (IPF) parallel to any of the sample coordinate directions (X/Y or Z). The BC and IPF map layers are used for identifying pattern qualities during data cleaning. We define grains as areas fully enclosed by boundaries with misorientation > 10°; while subgrain boundaries exhibit misorientation angles between 2-10°. Dauphiné twins are defined by a rotation of 60° around the quartz c-axis. For plagioclase grains, polysynthetic twins are plotted (rotation of 180° with respect to the 'b' axis following 'albite twin law'). The twins are identified to represent non-random localized boundaries with special orientation relationships. Dauphiné twin density in quartz is studied to understand possible relationships between twinning and deformation condition (e.g., Lloyd, 2004, Menegon et al. 2011). To quantify dauphiné twin density, the total area covered by dauphiné boundaries is measured and then divided by the whole grain area, (c) 'GROD Angle' EBSD maps are presented for highlighting distortion levels inside grains. Average orientation for each grain is calculated and the change in crystal orientation with respect to its average orientation is plotted for each pixel with a colour coded map. GROD maps are independent of grain size and hence can be used for comparing differently sized grains within/across samples. We manually define upper and lower limit of GROD angle range (0-3°, 0-5° or 0-10°) for better characterizing where distortion is concentrated.

Pole figures, for individual quartz grains, are plotted as upper-hemisphere, equal-angle stereographic projections. For all pole figures, X denotes the direction of the lineation. The following directions and planes are plotted: [0001] (c-axis), <11-20>, <2-1-10> <-12-

10> as different a-axes, {10-10} prism {m}. To decipher any dominant slip system activated in quartz an inverse pole figure (IPF), with a large data set of misorientation axis of low-angle boundaries is plotted. Misorientation is defined here as the minimum angle of orientation change between two orientations. For comparison purposes, (c) <a>, {m/r/z} <a>, and {m} [c] will be termed as 'Type1', 'Type2' and 'Type3' slip systems, respectively.

To assess the strength of the sample scale crystal preferred orientation (CPO), quartz and feldspar grains are shown with one point per grain. The fabric strength is also quantified using 'M-index', a dimensionless characterization, measured based on misorientation angle distribution. This value varies from zero for a random fabric to one for a well-developed alignment of minerals/foliation (Skemer et al., 2005). Misorientation analysis is used to quantify the overall distribution of crystal orientations and is utilised herein to investigate the degree of deformation in each studied sample (Wheeler et al., 2001). Mean misorientation illustrates overall change in orientation inside a grain, whereas mean misorientation/ area is calculated for comparing relative distortions inside quartz grains across studied samples (values of more than 50 quartz grains are taken into consideration). Change in crystallographic orientation within a grain is documented along profiles (misorientation profiles) either on a point-to-point basis or w.r.t the first point (cumulative). Change in crystal orientation/µm along misorientation profiles identify maximum orientation deviation within individual grains across different samples. Misorientation angle distribution (MA) can be measured for neighbouring (grains sharing a boundary) or random (randomly picked grains) pairs (Wheeler et al., 2001). The random-pairs (orange bars) indicate misorientations between randomly selected points in the data set, and the neighbour-pair misorientation distributions (blue bars) display data between neighbouring points. The relative frequency of MAs is plotted in a diagram for a selected range along with the reference theoretical misorientation angle distribution for a random distribution of high-trigonal crystals. The statistical mismatch between neighbour pair and random pair distribution is studied to gauge boundary processes active in the rock (Wheeler et al., 2001).

5.2.4 Boundary trace analysis

During deformation, intracrystalline dislocations can form subgrain boundary where rotation of subgrains along this boundary create misorientation between two associated crystallites with misorientation axis corresponding to the rotation axis (e.g., Borthwick & Piazolo, 2010; Neumann, 2000; Llyod et al., 1997). Boundary trace analysis is a method

which provides crystallographically meaningful boundary geometry of a low-angle boundary when its 3D orientation is not known. This method is utilized for determining active slip system(s) from EBSD data (e.g., Prior et al., 2002; Piazolo et al., 2008; Menegon et al., 2011). Here we sample areas (termed as 'Domains') around 2D traces of subgrain boundaries (SGB) and the dispersion of the orientation data around a rotation axis is plotted on a pole figure. The rotation axis is identified as a direction with no or little dispersion (Lloyd and Freeman, 1994). To verify this, misorientation axis for low-angle rotation (2-5° or 5-10°) is also plotted in an inverse pole figure. The data is displayed in terms of multiples of uniform density (MUD). In case of a tilt boundary, boundary plane contains both the 2D boundary trace and rotation axis, and a plane oriented at 90° (or at a high angle) represents the most likely active slip plane with a particular slip direction. Conversely a twist boundary has the rotation axis orthogonal to the boundary plane. In our study, this method is applied to characterize nature of low-angle boundaries by selecting different domains surrounding 2°/5° subgrain boundaries within a single quartz grain. Several schematic diagrams are made where misorientation/ rotational axis is shown by 'R.A.' and the bold lines extending outwards from the primitive circle denote subgrain boundary trace orientation. Two great circles are shown (with blue and green colours) for the reconstructed boundary plane orientation, following a tilt and twist wall model. Slip plane and slip directions are also determined using all the above-mentioned information.

5.2.5 Weighted Burger Vector (WBV) analysis

To characterize subgrain walls in terms of vector field, dislocation type, and to constrain dislocation densities, the Weighted Burger Vector analysis (WBV) is used (following Wheeler et al., 2009 and using AZtecCrystal). The principle of this technique is based on sum, over all type of dislocations, of [(density of intersections of dislocation lines with map) × (Burgers vector)] using estimates of orientation gradients of a 2D EBSD map. The results are weighted because of the 2D nature of EBSD data set. AZtecCrystal calculates WBV values at any point in the map by integrating orientation changes around the perimeter of a defined loop using a sliding loop method. The output of WBV analyses is presented as: (1) maps with magnitude of weighted Burger vectors for quartz grains at each point. These are converted to geometrically necessary dislocation density (GND density) maps using a dominant burger vector length of 4.6Å (considering basal slip with burgers vector 0.5 <11-20>) for quartz, and (2) maps with arrows showing

orientation of WBV at each point along any dislocation substructure (here along a subgrain boundary). The orientations are also presented in pole figures plotted with respect to the sample coordinates or in inverse pole figures plotted in crystal reference frame. The WBV orientations are also displayed on colour coded maps. Information of WBV directions can be used to provide information about the slip system and dislocation types. They are also compared to the results obtained from EBSD 'boundary trace analyses'. WBV magnitude calculated over selected areas in the given samples and decomposed into three a-axis and one c-axis of the quartz crystallographic structure (expressed as K_{a1}, K_{a2}, K_{a3} and K_c). The average GND densities are measured for numerous quartz grains presented in an area or by creating interactive loops for different domains within a single grain. However, it is to be noted that the GND densities are only minimum estimations and true GND density is likely to be higher. Here, we have used EBSD maps with fixed step sizes of 1.5µm and loop size of 5×5 pixels for effective comparisons between different data sets. Short WBVs are more prone to error propagation, and hence the presented analysis is only restricted to WBVs of length > 0.01 μm^{-1} (Wheeler et al., 2009). WBV data for each domain is represented in a colour coded map with WBV magnitude.

5.3 Sample selection and sample geological background

Three different samples are selected to a) characterize the nature of microstructures in grains pseudomorphing former melt and b) to assess if microstructures are influenced by rate of crystallization and presence/absence of differential stress during melt crystallization (Tab. 5.1).

Sample 'W0809A' represents slow melt crystallization without influence of external tectonic stresses. It stems from the Rockvale pluton (Fig. 5.1a) which is a coarse grained, statically cooled monzogranite intruding into the Wongwibinda Metamorphic Complex (WMC) at low pressure after deformation and regional metamorphism (Danis et al., 2010; Craven et al., 2012; Jessop et al., 2019). In the following text, this sample will be referred to as the "slowly crystallizing static granitoid".

Sample 'ST1108B' (Fig. 5.1b; Tab. 5.1) represents an in-situ melted and statically crystallized migmatite. It stems from the regional contact aureole at Mt. Stafford situated within the Anmatjira-Reynolds Range in the Arunta Block of Central Australia (Wang et

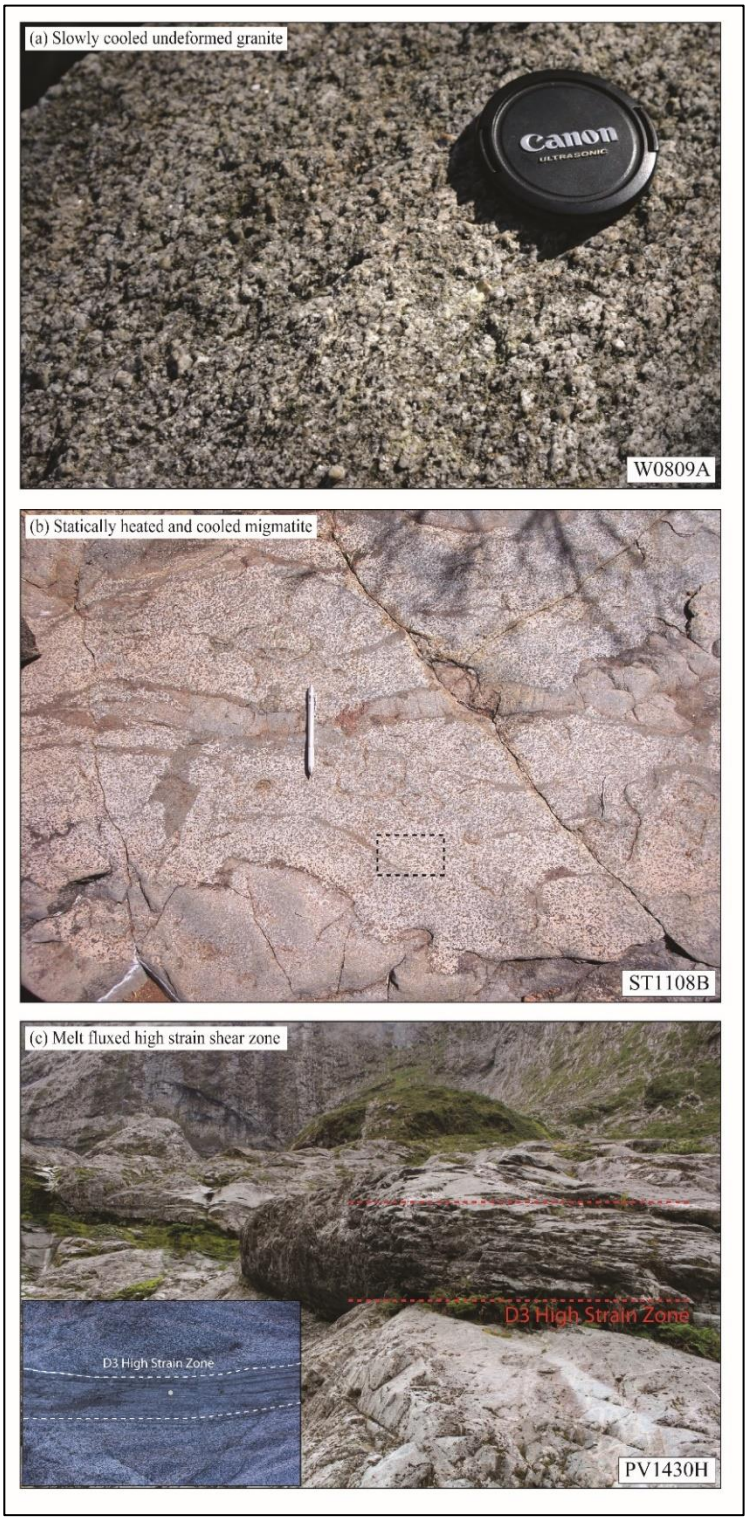

Figure 5.1 - Field photographs of the studied samples: (a) slowly crystallizing static granitoid (W0809A) from Hillgrove Plutonic suite of Wongwibinda metamorphic complex (WMC), (b) statically heated and cooled migmatite (ST1108B) from Mt. Stafford. The grey dikes are ignored, and the dashed box depicts the sampling area, (c) melt-fluxed high-strain shear zone in the Pembroke Granulite. Inset shows the location of the sample.

al., 2014). Here, a turbidite sequence is metamorphosed at a confining pressure of 2.8–4 kbar under no to low-strain condition (Greenfield et al., 1995; Wang et al., 2014). In the following this sample is referred to as the "statically heated and cooled migmatite".

Within the third sample (PV1430H) quartz crystallized from melt syntectonically. It stems from a high-strain shear zone in which deformation occurred in the presence of melt (D3 zone; Stuart et al., 2018a, b). This high strain zone is developed within the Pembroke Granulite, Fiordland, New Zealand (Fig. 5.1c). Here, a gabbroic protolith with an igneous assemblage of enstatite, diopside, pargasite, plagioclase and ilmenite partially recrystallized during syntectonic granulite facies condition at ~850°C and <11kbar. Subsequently, this granulitic gneiss was deformed in narrow D3 high-strain zones at 676 ± 34 °C and 14 ± 1.26 kbar (Daczko et al., 2001a, b). Stuart et al. (2018a) demonstrated that the D3 high strain zones formed because of externally derived melt migrating during deformation assisted diffuse porous melt flow and that deformation ceased when the melt crystallised completely. In the following, this sample will be referred to as the "melt-fluxed high-strain shear zone".

Sample	**Approximate melt percentage**	**Geological setting (Process of crystallization)**
Slowly crystallizing static granitoid (Monzogranite) (W0809A)	100—0%	Arc setting (statically cooled felsic melt)
Statically heated and cooled migmatite (ST1108B)	< 10%	Regional/contact aureole (static partial melting and cooling)
Melt fluxed high strain shear zone (PV1430H)	<5%	Arc setting (Porous melt flow in high strain domain)

Table 5.1 - Analysed samples, their geological history and field relationships.

5.4 Results

5.4.1 General Petrography

The **slowly crystallizing static granitoid (**Sample W0809A) is a coarse-grained rock with K-feldspar, quartz, plagioclase, biotite, and minor amounts of Fe-oxides as the constituent mineral phases. There is a lack of any characteristic foliation or shape preferred orientation (Fig. 5.2a-b). The rock has a unimodal grain size distribution of plagioclase and K-feldspar phenocrysts. Plagioclase grains are 0.5-1 mm in size and have concentric chemical zoning (red arrow, Fig. 5.2c); K-feldspar grains are large (up to 2 mm in size) with well-developed crystal faces (white arrow, Fig. 5.2f). Small xenomorphic interstitial quartz

grains are up to 0.1-0.8 mm in size (blue arrows, Fig. 5.2c-d), whereas large quartz grains (1.2-2.5 mm) show well developed crystal faces (green arrow, Fig. 5.2d). Interstitial quartz is often extended along grain boundaries of other grains and exhibit low-dihedral angles (LDA) (yellow arrows, Fig. 5.2e-f). Elongated plagioclase grains have planer growth surfaces, and form clusters or impinge against each other (yellow arrows, Fig. 5.2c-d, f). Some plagioclase grains also display resorbed irregular grain boundaries (green arrow, Fig. 5.2f). A group of spatially distant quartz grains are connected in 3D as shown by their similar interference colour upon insertion of an accessory plate (a set of blue and purple arrows, Fig. 5.2d-f). Similar orientation is also suggested by the fact that these grains, under the normal cross-polarised light, go to extinction at the same time (Fig. 5.2d-f). Though the sample lacks recrystallized quartz-plagioclase grains, or deformation twins in plagioclase, minor evidence of undulose extinction are found in quartz (green arrow, Fig. 5.2c). However, lack of sample scale foliation and/or lineation, presence of large well-faceted phenocrysts of quartz/feldspars grains along with interstitial, xenomorphic quartz grains confirm this rock to be a typical igneous rock crystallized under static conditions (Vernon, 2010).

The **statically heated and cooled migmatite** *(sample ST1108B)* contains biotite-K-feldspar-quartz-cordierite-plagioclase-sillimanite-andalusite-ilmenite grains and have a bimodal grain size distribution (Fig. 5.3a-b). Coarse (close to 1mm across) euhedral K-feldspar dominate the overall assemblage (~55 vol. %). Quartz grains are also bimodal where both the small (0.08-0.2 mm in size) and the large grains (0.3-0.9 mm in size) are anhedral and sometimes show low dihedral angle (LDA) relationships with surrounding grains (red and blue arrows, Fig. 5.3c-f). Quartz grains with partial straight facets are also seen (yellow arrows, Fig. 5.3c-f). With insertion of accessory plate, some quartz grains show similar interference colour and are inferred to be connected in 3D (green arrows in Fig. 5.3c; red arrows in Fig. 5.3f). K-feldspar grains have both irregular (sometimes cuspate; purple arrows in Fig. 5.3d, f) and straight (white arrows in Fig. 5.3d-f) boundaries. In summary, the rock exhibits abundant microstructures indicative of the former presence of melt and is described by Wang et al., 2014, 2019. Quartz with well-developed crystal facets (yellow arrows, Fig. 5.3c-f) and those with very high aspect ratios along grain boundaries of adjacent minerals (red arrows, Fig. 5.3c-f) are interpreted to represent grains crystallized from melt.

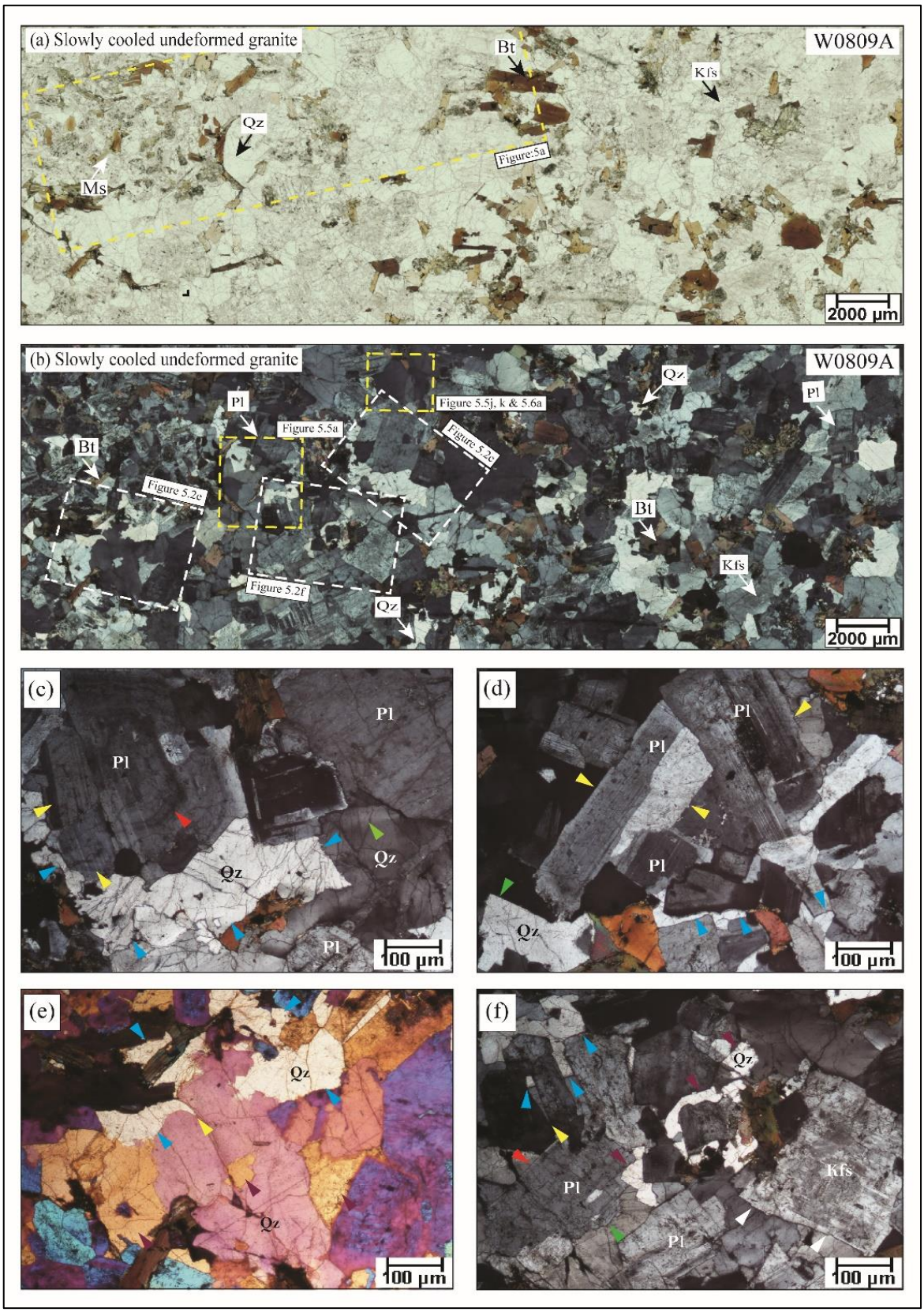

Figure 5.2 - Petrographic characteristics of slowly cooled undeformed granite (W0809A). (a-b) Thin section PPL and XPL overview images. Locations of subsequent photomicrographs (white boxes) and EBSD analyses (yellow boxes) are shown. Lack of foliation and a unimodal grain size distribution of quartz-plagioclase-Kfs is observed. (c) Plagioclase feldspar with concentric oscillatory zoning (red and yellow arrows) surrounded by irregular quartz grain (blue arrows).

Undulose extinction in quartz is observed (green arrow), (d) Elongated plagioclase grains with interstitial quartz grains (blue arrows). Note the grain boundaries in plagioclase clusters are planer and parallel to the growth faces (yellow arrows). Quartz grain displays straight facets (green arrow), and lack of undulose extinction, subgrain formation. (e) Photomicrograph (with accessory plate of λ= 150nm) identifies two groups of quartz grains with same interference colour (purple and blue arrows denoting the two groups). Quartz grain with cuspate grain boundary and sharp pointed edge forming LDA (yellow arrow). (f) Irregular Quartz grains connected in 3D and go to extinction together (blue and purple arrows). Quartz grain with LDA (yellow arrow). Elongated large plagioclase grain (at the lower left corner) with planer (red arrow) and irregular grain boundaries (green arrow) at two sides. Note the euhedral shape K-feldspar at the lower right corner (white arrows).

All these attributes indicate partial melting and subsequent crystallization in a low stress environment.

The **melt-fluxed high-strain shear zone** sample (PV1430H) has coarse grained hornblende, biotite, and quartz grains forming the main foliation whereas clinozoisite and plagioclase grains represent the fine-grained matrix (Fig. 5.4a-b). At the resolution of the optical microscope, features commonly indicative of former presence of melt cannot be readily identified. However, quartz (0.06-0.2 mm) and plagioclase grains (0.08-0.3 mm) are generally devoid of undulose extinction and deformation twins, respectively (yellow arrows, Fig. 5.4c). High resolution BSE images show elongated xenomorphic quartz grains along the grain boundaries of plagioclase-hornblende grains (green arrow, Fig. 5.4d, e) and irregular plagioclase grains along the grain boundaries of quartz-hornblende grains (dark blue arrows, Fig. 5.4e-f). Quartz and plagioclase grains at grain triple junctions show cuspate boundaries (purple arrows, Fig. 5.4d-f), and sometimes show low dihedral angle relationships (LDA) with surrounding grains (red arrows, Fig. 5.4d-f). Euhedral quartz-plagioclase grains with partial straight facets (sky blue arrows, Fig. 5.4e-f) and polycrystalline aggregates of quartz-plagioclase at grain triple junctions (white dashed box in Fig. 5.4f) are observed. In summary, the rock displays a shape-preferred orientation of flaky/prismatic minerals at the optical scale (Fig. 5.4 a-b), but at a higher resolution, melt pseudomorphed quartz-plagioclase grains are observed as thin, elongated melt films, polymineralic aggregates, and exhibit low dihedral angles between grains.

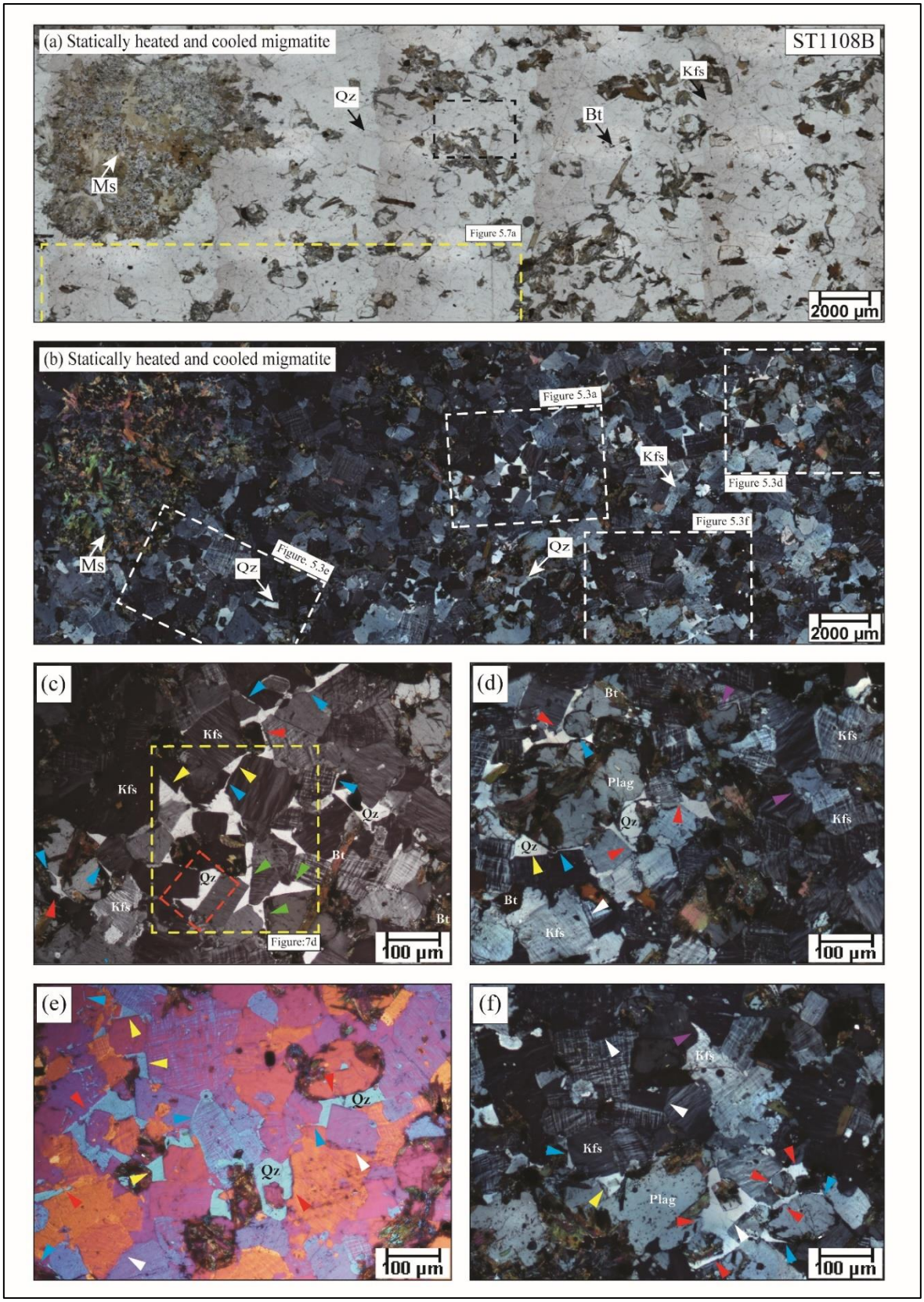

Figure 5.3 - Petrographic characteristics of statically heated and cooled migmatite (ST1108B). (a-b) Thin section PPL and XPL overview images. Locations of subsequent photomicrographs (white boxes) and EBSD analyses (yellow boxes) are shown. Large clots of Biotite-Muscovite and aluminosilicates are observed. (c) Quartz grains have straight facets (yellow arrows), and irregular xenomorphic shapes (red arrows). Note the interconnected nature of the quartz grains (green arrows).

Elongated quartz grains with LDA against the surrounding feldspar grains (blue arrows) are observed. Quartz and feldspar grains are devoid of any undulose extinction and subgrain formation. Inset shows areas for subsequent EBSD (yellow dashed box) analysis. The red box indicates a region with quartz-plagioclase melt-pseudomorphs, modelled in the numerical simulation (Fig. AP5.3-5.6). Yellow dashed box shows area for EBSD analysis. (d) Elongated xenomorphic quartz grains wetting grain boundaries of orthoclase (red arrows). Protruding ends of elongated quartz forming LDA with surrounding orthoclase grains (blue arrows). Orthoclase grains display both cuspate (purple arrows) and straight facets (white arrow). (e) Photomicrograph with accessory plate of λ= 150nm identifies irregular, xenomorphic quartz grains wetting grain boundaries of surrounding feldspar grains (red arrows). (f) Photomicrograph shows large (0.1-0.2 mm) K-feldspar grains with elongated cuspate (violet arrow) and straight boundaries (white arrows). A large xenomorphic quartz grain is seen to be well connected (red arrows) and have LDA at grain triple junctions (blue arrows).

5.4.2. Detailed microstructure and quantitative orientation analysis

Slowly crystallizing static granitoid (W0809A)

Both quartz and feldspar lack a sample-scale CPO and their M-index is close to zero (Fig. 5.5b-c). For quartz grains, some orientation clusters are also observed (marked with red arrows for c-axis pole figure, Fig. 5.5b). Quartz grain size ranges between 0.01-1.6x10^4 μm^2 (Fig: 5a, d; Tab. 5.2); grain aspect ratio ranges from 1 to 4, and grains display predominantly straight crystal boundaries. Within quartz grains, dauphiné twin boundaries occur in patches while subgrain boundaries with 2-5° misorientation dominate (Fig. 5.5a, d). Low-angle grain boundaries occur preferentially close to grain edges and are parallel or perpendicular to it (Fig. 5.5d). Dauphiné twins are also abundant near the grain boundaries (Fig. 5.5a, d) and occasionally exhibit a rosette-like shape (marked with black arrows in Fig. 5.5d). Grains not connected in 2D, show same 3D crystal orientation, and are interpreted to be connected in 3D (e.g., 'Grain1-Grain2' and 'Grain3-Grain4' in Fig. 5.5d). A representative misorientation profile across a grain shows a cumulative change in crystal orientation up to 7° over 200μm (profile 'A-B' in Fig. 5.5e). Point to point analysis shows a jagged profile where regions of high internal misorientation (4°) are separated by regions with very low misorientation (<1°) (Fig. 5.5e). The maximum value of mean misorientation

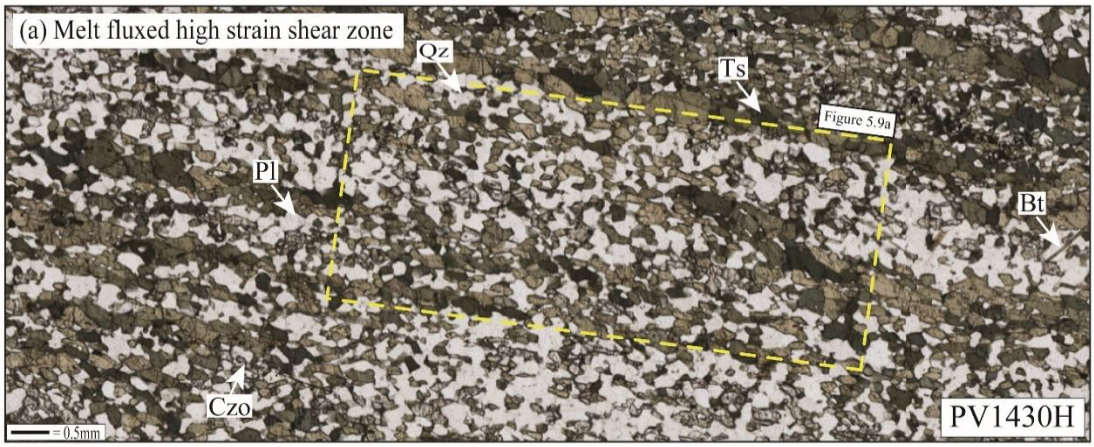
(a) Melt fluxed high strain shear zone
Qz
Ts
Figure 5.9a
Pl
Bt
Czo
= 0.5mm
PV1430H

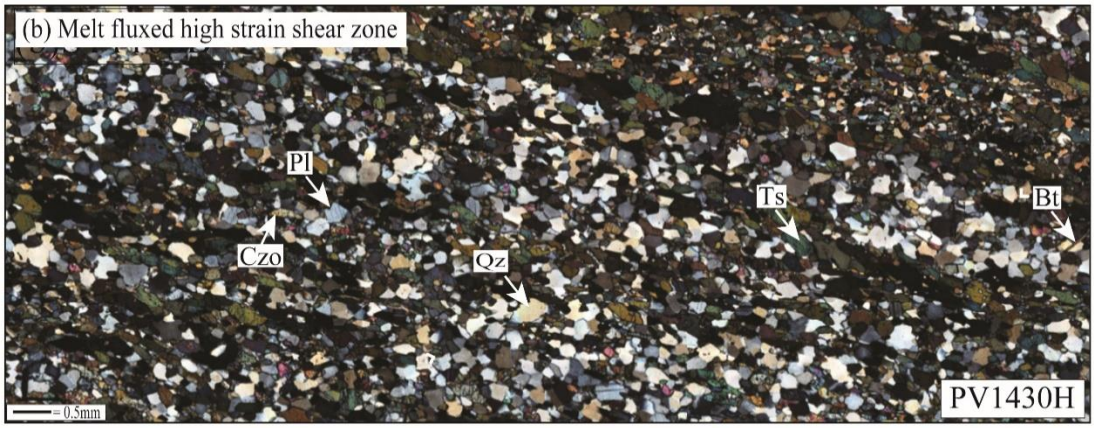
(b) Melt fluxed high strain shear zone
Pl
Ts
Bt
Czo
Qz
= 0.5mm
PV1430H


(c)
S3
Czo
Qz
Qz
Pl
Ts
Ts

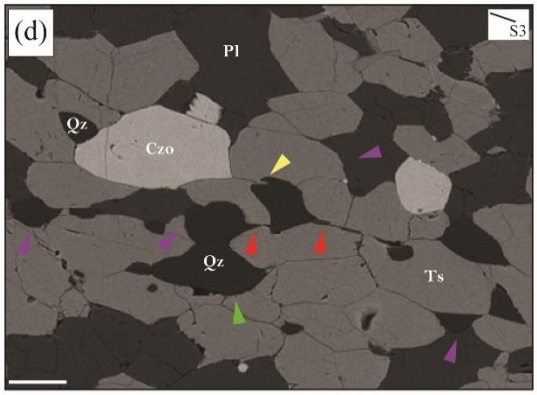
(d)
S3
Pl
Qz
Czo
Qz
Ts

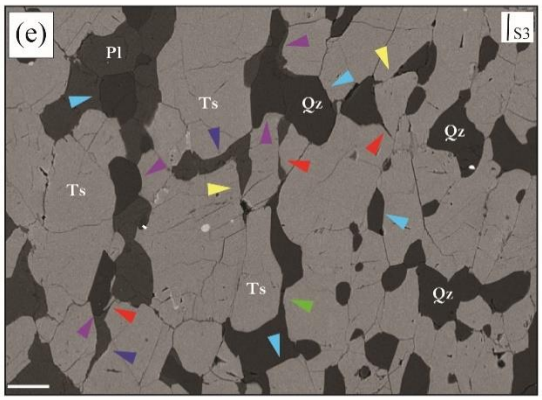
(e)
S3
Pl
Ts
Qz
Qz
Ts
Ts
Qz

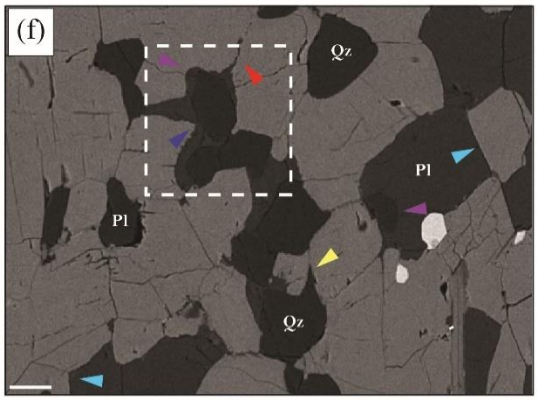
(f)
Qz
Pl
Pl
Qz

Figure 5.4 - Petrographic characteristics of melt fluxed high strain shear zone (PV1430H). (a-b) Thin section PPL and XPL overview images. A bimodal grain size distribution is observed where the hornblende-biotite-quartz grains form the foliation inside a fine-grained clinozoisite-plagioclase matrix. Rectangle area for subsequent EBSD analysis. (c) Unimodal grain size distribution with a general lack of undulose extinction, deformation twins, and subgrain formation in quartz and plagioclase. No melt microstructures can be identified. Foliation direction (S3) is marked. (d-f) Quartz and plagioclase grains show cuspate grain boundaries (purple arrows), low dihedral angle at grain triple junctions (red arrows), elongated xenomorphic quartz grains (green arrows), euhedral quartz and plagioclase grains with straight boundaries (sky blue arrows), elongated plagioclase along grain boundaries of hornblende (sky blue arrows). Polycrystalline aggregates of quartz-plagioclase grains are also seen (white dashed box in 'f'). Later stage solid state re-equilibration changes the low dihedral angles slightly (yellow arrows). All scale bars are 50µm.

spread for quartz grains is 4.5° (Tab. 5.2 and 'Domains' in Tab. 5.3, see later) whereas mean misorientation for most of the quartz grains varies between 0.2-0.8°. The mean misorientation spread for quartz grains varies from 0.02° to 28°, with nearly 70% of grains showing an average range of 15.6° (both calculated for 10^2 mm^2 grain area). The disparity between neighbour- and random-pairs misorientation angle distribution (MAD) and a high frequency of neighbour pair MAD at low degree MAs indicating non-random angle distribution of the subgrain boundaries whereas high angle MAD (~55–60°) corresponds to quartz dauphiné twins (both are arrowed in Fig. 5.5f). The density of dauphiné twins is highly variable; for example, 'Grain1' is 2.7x larger than 'Grain3' (Fig. 5.5d), but their relative dauphiné densities vary a little (from 0.25 in 'Grain1' to 0.22 in 'Grain3'). The average misorientation in 'Grain1' and 'Grain3' is also very similar and only varies from 3.6° to 4.2°, respectively. However, the composition and relative abundances of surrounding minerals have no influence on it (Tab. 5.2). GROD angle EBSD map (with a misorientation range of 0-5°) for both quartz-feldspar grains displays internal misorientations close to the crystal edges (Fig. 5.5g-j; marked with white arrows). The GROD angle map in quartz also highlights the substructures, developed within the grain, as well as the dauphiné twins that crosscut them (Fig. 5.5i; marked with black arrows). Plagioclase grains have internal misorientation that runs parallel to plagioclase twins (Fig. 5.5h, j; marked with black arrows). For the majority of grains, one or two way small circle dispersions (for both <a> and [c] axes; denoted by '1' and '2') ranging from 5-23° are observed (Fig. 5.5k-m; Tab. 5.2). For instance, 'Grain1' and 'Grain2' with one-way dispersion of quartz <a> axes (in the pole figures) and a clustering around [c] axis (in the IPF) indicate that it is the dominant misorientation axis for low-angle grain boundaries (Fig. 5.5k-l). For 'Grain5', however, a

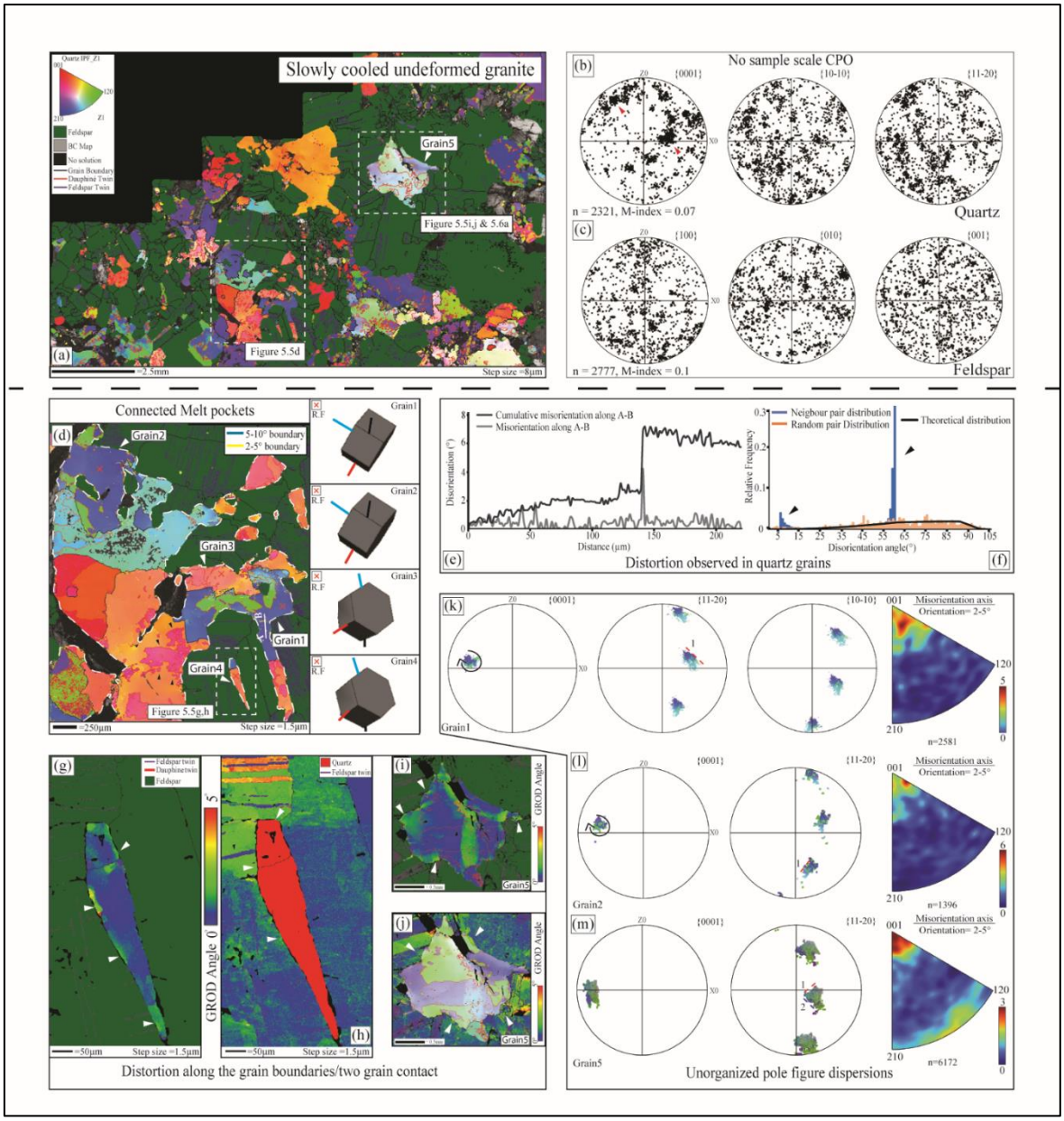

Figure 5.5 - Detailed microstructures and quantitative orientation analysis for slowly crystallizing static granitoid (W0809A). (a) Sample scale EBSD analysis (step size 12μm). Quartz fraction is represented with IPF colour coding and feldspar grains are assigned a particular phase colour (green). Note the elongated xenomorphic grains of quartz. Quartz grains with different crystal orientation show different colours. 10° boundaries are shown (black lines). Red and purple lines display dauphiné twins of quartz and plagioclase grains respectively. Rectangle areas for further EBSD analysis. (b-c) Quartz and plagioclase crystallographic preferred orientation (CPO) data. All plotted in the XZ plane of kinematic reference frame. Local clusters are marked with red arrows in 'b'. (d-m) In-depth EBSD analyses (maps with step size 1.5μm). (d) Quartz grains (Grain1 to Grain4) with IPF colour scheme, subgrain boundaries (2-5° and 5-10°), quartz-feldspar twins, trace of the misorientation profile, 3D crystal orientations, and look up table for IPF colouring are provided. Note subgrain boundaries and dauphiné twins are populated close to the grain edges. Grain edge is marked by fine black line (>10° boundaries). 'Grain1' and 'Grain2' show similar crystal orientation while 'Grain3' and 'Grain4' have identical 3D crystal orientation (all measured at a reference point 'x'). White box shows area for subsequent analyses (in 'g-h'). (e) Misorientation profile ('A-B' in 'd') show maximum change in crystal orientation of ~ 4° (point to point) and cumulative change in orientation of ~7°. (f) Misorientation angle distribution (MAD) with disparity b/w correlated and

uncorrelated data set at two places (marked with arrows). High frequency of neighbour pair MAD is observed at low MAs of <10°. (g-h) GROD angle (with 0-5° misorientation) EBSD map with distortion along the shared grain boundaries of quartz and plagioclase (white arrows). Undeformed regions are shown in blue, whereas increasing misorientation is highlighted by a progression of greens through yellow to red. (i-j) Similar analyses for another grain (location of 'Grain5' shown in 'a') with concentration of misorientations along quartz-plagioclase grain boundaries. Note: this grain is used for boundary trace analyses in Fig. 5.6. (k-l) Pole figures show grain in colour of orientation maps 'a', and 'd'. 'Grain1' and 'Grain2' record one way dispersion (marked with '1'). Misorientation axis-angle pair for these two grains exhibit clustering around [0001]. (m) 'Grain5' with two-way dispersion (marked with '1' and '2') and IPF showing two misorientation axes orientations.

Sample	Grain area ($x10^4$ µm²)	Average misorientation	Mean OS/area (°/ 10^2mm²)	Systematic dispersion in pole figure	Surrounding phases (rough estimation)
W0809A	3.01	0.98°	0.32	NO	Pl (100%)
	3.37	1.90°	0.56	NO	Bt (50%), Qz (50%)
	6.30	2.00°	0.32	18.00°	Bt (17%), Qz (49%),Kfs(34%)
	4.25	2.80°	0.66	15.35°	Bt (13%), Qz (48%), Pl (39%)
	3.70	2.60°	0.70	17.09°	Qz (40%), Pl (60%)
	0.61	3.40°	5.57	9.00°	Qz (50%), Pl (50%)
	7.73	1.12°	0.15	12.53°	Qz (30%), Pl (70%)
	0.0384	0.59°	15.36	4.11°	Qz (20%), Kfs (70%), Pl (10%)
ST1108B	3.74	1.17°	0.31	8°	Qz (33%), Pl (67%)
	4.34	2.51°	0.58	10.7°	Bt (13%), Qz (62%), Pl (38%)
	0.423	1.58°	3.73	7.00°	Qz (40%), Pl (60%)
	8.57	2.29°	0.27	11.52°	Pl (85%), Bt (15%)
	5.06	1.45°	0.29	7.08°	Pl (80%), Bt (20%)
	4.69	2.48°	0.53	11°	Pl (85%), Bt (15%)
PV1430H	0.40	1.3°	3.25	7°	Qz (20%), Hbl (80%)
	0.46	1.83°	3.98	14.01°	Qz (3%), Hbl (97%)
	0.22	1.24°	5.64	9.94°	Hbl (100%)
	0.47	2.02°	4.3	11.86°	Qz (28%), Hbl (72%)
	0.13	0.94°	7.24	4.5°	Qz (14%), Hbl (86%)
	0.44	1.98°	4.5	7.72°	Qz (35%), Hbl (65%)

Table 5.2 - Properties, derived from EBSD data set in Fig. 5.5-5.10, for quartz grains randomly selected from each rock sample. To quantify crystal bending and change in crystal orientation, average misorientation for an individual quartz grain is measured. The result is then divided by the grain area to determine the area control on crystal bending. Spread of <a> and/or <c> axes of a single quartz grain are measured from pole figure dispersions. To evaluate the effect of neighboring phase composition on the crystal bending of quartz, the phases that surround the grains under study are provided (in percentage).

two-way pole figure dispersion in the pole figures and misorientation axis with clustering around both the <a> and [c] axes (Fig. 5.5m) fails to identify a single dominant slip system and indicates that at least two systems are active.

In order to understand the nature of subgrain walls in more detail (i.e., slip system associated with the low-angle boundary and dislocation types), 'Grain5' is analyzed using boundary trace and WBV analysis (step size: 1.5µm, Fig. 5.6). Individual subgrain

boundaries (SGB) from two domains are selected (Fig. 5.6a). GND density map shows concentartion of high dislocations around the grain edges, though sub-parallel continuous fine lines with high dislocation denisty are also extended vertically inside the grain and also cross cut dauphine twins (arrows in Fig. 5.6b). Lines with high dislocation density are coincident with the subgrain boundaries (Fig. 5.6a-b). The maximum GND density is $0.4x10^{14}/m^2$ for a maximum WBV magnitude of $0.02\mu m^{-1}$ (Fig. 5.6b). The WBV orientation shows a strong clustering close to the <c> axis, consistent with significant activation of non-basal slip (WBV magnitude of >15% of the maximum WBV value are plotted in Fig. 5.6b). Misorientation axis for low-angle grain boundaries (plotted with an inverse pole figure in crystal coordinate system) are conventionally used for identifying particular slip system and is described in Fig. 5.6c (modified from Neumann, 2000). Demarcated domains with WBV values associated with <a> and [c] axes are presented in Fig. AP5 – 1 in Appendix. The diagonal subgrain boundary trace (inclined at ~55° to the horizontal) in 'Domain1' (Fig. 5.6a) shows significant small-scale dispersion for all the axes except for [c] (Fig. 5.6d), and it is identified as the rotation axis (R.A). Misorientation axis-angle pair further confirms this (Fig. 5.6e). The WBV analysis shows a maximum 2.27° misorientation, and the maximum WBV is parallel to the a-axis (Fig. AP5 – 1 in Appendix; Tab. 5.3). WBV magnitude map of 'Domain1' (Fig. 5.6b) picks out a linear feature where all the WBVs are oriented along a particular direction (WBVs with magnitude ranging between 0.01-0.016 μm^{-1} are shown with arrows). WBV orientation analyses for this domain also shows a near single point clustering in the pole figure while the IPF shows an array of edge dislocations parallel to the basal plane, close to the <a> direction (Fig. 5.6g). The dislocation density corresponds to this subgrain wall is found $0.43 \times 10^{14}/m^2$ (Tab. 5.3). A schematic diagram (Fig. 5.6i) shows the orientation of different axes (as shown in Fig. 5.6d) with reconstructed boundary plane following a tilt model (rotation axis is marked as 'R.A'). The subgrain boundary cannot be a twist wall as then it will not conform to the boundary trace geometry observed in Fig. 5.6a, f. Thus, the boundary plane is parallel to {11-20} and defines a burger vector orientation (B.G.) parallel to <11-20> direction (Fig. 5.6i), as observed in Fig. 5.6h. This can only be explained by the activation of {10-10} <11-20> slip system. A similar conclusion can be made by comparing the observed misorientation axis for this subgrain boundary (in Fig. 5.6e) with the reference slip system in Fig. 5.6c. Hence, 'Type2' slip system (basal slip: {m} <a>) describes the nature of this low-angle grain boundary even though the whole grain showed an unorganized pole figure dispersion (Fig. 5.5m) and WBV IPF identified the development of non-basal slip (Fig. 5.6b). A similar analysis in 'Domain2', on a vertical

subgrain boundary trace (Fig. 5.6j), confirms the misorientation/rotation axis as one of the <11-20> axis (Fig. 5.6j-k; Tab. 5.3). The misorientation reaches up to 2.60° with a maximum value of WBV parallel to the c-axis (K_c) (Fig. AP5 – 1 in Appendix). From WBV magnitude map, this boundary trace can be identified (WBVs ranging between 0.01-0.017 μm^{-1} are plotted) with arrows oriented along a particular direction (Fig. 5.6l). The pole figure (Fig. 5.6m) confirms this uniformity in direction as near to a single point clustering and the WBV IPF shows an array of basal edge dislocations (Fig. 5.6n). A schematic diagram (Fig. 5.6o), and a similar tilt wall approach is found to be consistent with this subgrain boundary geometry. In this case, a subgrain boundary plane coincides with a prism plane {10-10} (Fig. 5.6o), and the geometry can only be explained by activation of {10-10} [0001] slip system (Tab. 5.3). This is also conclusive from the reference slip observed in Fig. 5.6c. We term it as 'Type3' slip system (with [c] slip on the prism plane). For this boundary plane, Boundary trace analysis defines burgers vector (B.G.) parallel to the <0001> direction (Fig. 5.6o), similar to the observation made from WBV orientation analysis (Fig. 5.6n). Dislocation density associated with this subgrain boundary is 0.45 x $10^{14}/m^2$ (Tab. 5.3). WBV orientation map for this grain is also plotted (in Fig. AP5 – 2 in Appendix) in a crystallographic reference frame for WBV magnitudes >15 % of the maximum WBV value. The colour scheme in the legend reflects the crystal structure of quartz and it is found that the low angle boundaries have two major populations – those in blue and green (WBV parallel to <10-10> and <11-20>), and those in red (WBV parallel to <001>). This is clear evidence for the operation of at least two separate slip systems with these different Burgers vector directions. It is also to be noted that the WBV orientations parallel to <a> direction are mostly populated along the grain edges while WBVs parallel to <c> direction crosscut the grain and are oriented perpendicular to the grain edges.

Statically heated and cooled migmatite (ST1108B)

Both quartz and feldspar grains (in Fig. 5.7a) do not exhibit a sample-scale CPO (Fig. 5.7b, c) and low M-index values (close to zero). Small local clusters may correspond to the 3D connected grains and hence have similar orientation. A high spatial resolution map

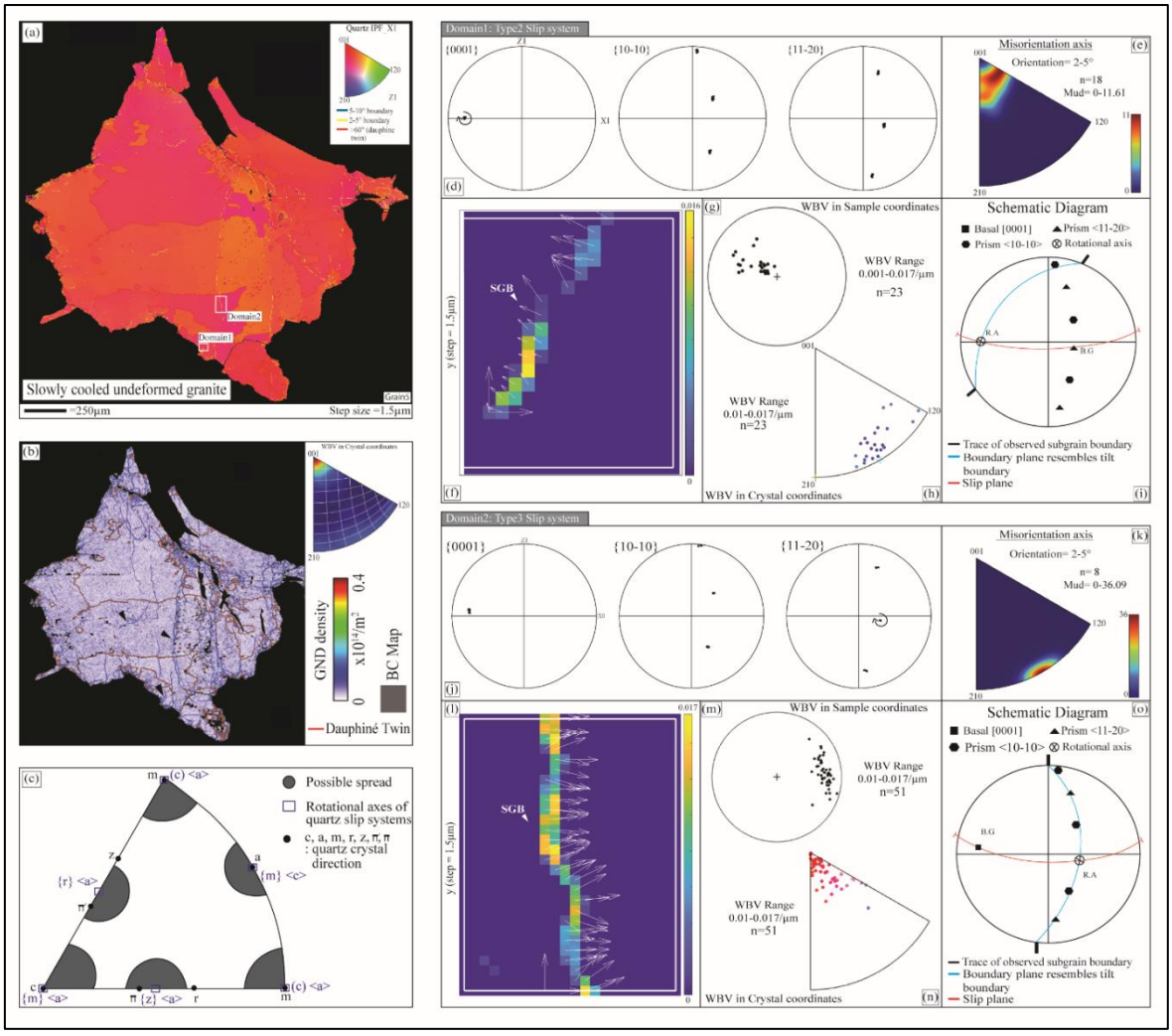

Figure 5.6 - Subgrain boundary trace analyses for slowly crystallizing static granitoid (W0809A). (a) EBSD orientation image of 'Grain5' with IPF colour coding. Note dauphiné twins, and 2-5° subgrain boundaries are along grain edges (subgrain boundaries, quartz-plagioclase twins, and lookup table for IPF colouring are provided in the inset). Two domains are selected for the boundary trace analysis. (b) Quartz GND density map considering basal slip with burgers vector 0.5 <11-20>. High GND densities are along fine lines coincident with low-angle grain boundaries observed in 'a'. WBV orientations are dominantly parallel to [c]. (c) Misorientation axes for low-angle grain boundaries and associated quartz slip systems (modified after Neumann, 2000). (d-h) Boundary trace analyses of 'Domain1' as shown on the EBSD orientation map (in 'a'). (d) Pole figure display misorientation/rotational axis where data do not show significant dispersion (arrowed). (e) Misorientation axis-angle pair for the same data set (as in 'd'). (f) WBV magnitude map of 'Domain1' shows trace of subgrain boundary (SGB) with consistently oriented WBVs along a particular direction (WBVs ranging from 0.01-0.016 μm^{-1} are plotted with arrows). (g-h) WBV orientations are plotted in sample coordinates (as pole figure) and in crystal coordinates (as inverse pole figure - IPF). Note the clustering of WBVs on the basal plane consistent with <a> slip. (i) A schematic pole figure showing the orientation of different axes and pole to planes, as shown in 'd'. The dispersion is not shown. Interpreted rotational axis (R.A) and Burgers vector (B.G) orientations are marked (see text for details). The slip system for this SGB is{m}<a> (Tab. 5.3) with the subgrain boundary representing a tilt wall. The rotation axis (R.A), burgers vector (B.G), and the trace of subgrain wall are plotted on the pole diagram. (j-n) Analysis for 'Domain2' as shown on the EBSD orientation map (in 'a'). (j) Pole figure of 'Domain 2' (shown in 'a') with rotational axis marked by an arrow. (k) Contoured IPF for the same data set (as in 'j'). (l) The WBV magnitude map of 'Domain 2' with the SGB trace as observed in 'a'. WBVs (values ranging between 0.01-0.017 μm^{-1} are plotted

with arrows) are oriented along a particular direction. (m-n) WBV pole figure and inverse pole figure (IPF) show clustering of points. WBV IPF denotes <c> slip. (o) Similar schematic diagram as shown in 'i'. 'Domain 2' identifies{m}[c] slip system (Tab. 5.3). The subgrain boundary represents a tilt wall. The rotation axis (R.A), burgers vector (B.G), and the trace of the subgrain wall are plotted on the pole diagram.

Sample Number	**Step size (µm)**	***Domain***	***Avg. Misorie-ntation***	K_{a1}	K_{a2}	K_{a3}	K_c	***Dislocation density***	***Slip system***	***Dislocation type***
W0809A	1.5	1	2.27°	-1.92	-0.09	2.01	0.32	0.43	Type2: {10-10} <11-20>	Edge, <a>
		2	2.60°	-0.38	0.16	0.22	-3.62	0.45	Type3: {10-10} [0001]	Edge, [c]
ST1108B	1.5	1	3.48°	3.77	0.32	-4.1	-0.27	0.08	Type1: (0001) <10-10>	Edge, <a>
		2	2.82°	0.18	0.44	0.62	-3.25	0.45	Type3: {10-10} [0001]	Screw, [c]
PV1430H	1.5	1	4°	-3.12	-7.19	10.31	-2.38	0.23	Type2: {10-10} <11-20>	Edge, <a>
		2	6.20°	-9.59	-4.78	14.37	-41.09	0.7	Type3: {11-20} [0001]	Screw, [c]

Table 5.3 - WBV characteristics for the 'Domains' in all the studied samples. Corresponding step sizes and misorientation for the same data set are shown. The WBVs are decomposed parallel to the main four crystallographic axes and represented as K_{a1}, K_{a2}, K_{a3}, & K_c (following Wheeler et al., 2009). The inferred slip systems and dislocation types for each domain are provided.

(Fig. 5.7d; step size 5µm) displays several quartz grains with low angle (<5°) subgrain boundaries and continuous dauphiné twins close to grain edges (Fig. 5.7d), like in W0809A (Fig. 5.5). Quartz grain size ranges between 0.05-1.6x10^4 µm^2 (Tab. 5.2). Grains also display crystal facets ('Grain1' to 'Grain4' in Fig. 5.7d). 'Grain1' to 'Grain4' show similar crystal orientation suggesting a connection in 3D (Fig. 5.7d). Maximum value of mean misorientation is 4.5° (Tab. 5.2 and 'Domains' in Tab. 5.3, see later) but mean misorientation spread for most of the quartz grains (>70%) lies between 0.07–1°. A representative misorientation profile ('A–B' in Fig. 5.7d) displays orientation change up to 7° (Fig. 5.7e). Point-to-point analysis exhibits an average change of 3–4° (Fig. 5.7e). Disparity between the correlated and uncorrelated data sets (arrowed in Fig. 5.7f) are observed, where neighbour pair MAD at low angle (<10°) describes non-random distribution of the grain boundaries. The density of dauphiné twins is highly variable, for

example, ‘Grain1’ is 2.7x larger than ‘Grain4’ (Fig. 5.7d), but their relative dauphiné densities vary by 10x, from 0.31 to 0.03, even though the average misorientation for these two grains are very similar, 2.25° and 2.45°, respectively. The mean misorientation spread varies from 0.08-8.5° (calculated for 10^2 mm^2 grain area) (Tab. 5.2). Nearly 70% of the measured quartz grains show a misorientation range of 0.08-5.7° (calculated for 10^2 mm^2 grain area). However, the composition and relative abundances of surrounding minerals have no influence on it (Tab. 5.2). The GROD angle EBSD map (with a misorientation range of 0-10°) highlights internal misorientations near the quartz grain edges and at two-grain contacts (Fig. 5.7g, arrowed). Similar analysis for the neighbouring plagioclase grains also confirms this (Fig. 5.7h, arrowed). Pole figures (Fig. 5.7i-k) show notable one-way dispersion for all the grains (ranging from 3-10°, Tab. 5.2), however, misorientation axis-angle pair for ‘Grain1’ and ‘Grain 3’ fail to recognize development of any misorientation axis (Fig. 5.7i, k). For ‘Grain4’, one-way dispersion is observed in <11-20>, but the misorientation axis suggests <11-20> as the rotation axis (Fig. 5.7j).

In 'Grain4' (Fig. 5.8a, step size: 1.5µm), two distinct domains with two distinct subgrain boundaries are marked for subsequent boundary trace analyses (Fig. 5.8). The GND density map (Fig. 5.8b) displays linear features with high dislocation densities that correspond exceptionally well to the subgrain boundaries (Fig. 5.8a). High dislocation densities are observed at grain contacts, but they are also found to be extended inside the quartz grains. The maximum GND density for quartz grains is $0.7x10^{14}/m^2$ for a maximum WBV magnitude of 0.02 μm^{-1} (Fig. 5.8b). WBV orientations show strong clustering on the basal plane, but also WBVs parallel to <c> and <r> directions are noticed, suggesting development of all possible slip systems found in a deformed quartz grain (Fig. 5.8b). WBV magnitude map with values associated with <a> and [c] axes for these two domains (as in Fig. 5.8a) are shown in Fig. AP5 – 1 in Appendix. Misorientation values vary from 2.8-3.5° (Tab. 5.3). WBV orientation map exhibit very consistent preferred orientation parallel to <a> direction in ‘Domain1’ while in ‘Domain2’ WBVs are consistently parallel to <c> axis (Fig. 5.8c). WBV orientation parallel to <c+a> direction is also found. The traces of subgrain boundaries in Fig. 5.8c also mimics low-angle boundary traces (Fig. 5.8a). In ‘Domain 1’ pole figure dispersions (Fig. 5.8d) and misorientation axis-angle pair (Fig. 5.8e) indicate one of the a-axes <11-20> as the misorientation/rotational axis (R.A). WBV magnitude map of ‘Domain 1’ (Fig. 5.8f) identifies this boundary as a linear feature having a similar morphology with WBVs oriented along a particular direction (for WBV magnitude ranging between 0.012-0.026 μm^{-1}) (Fig. 5.8c). The pole figure, for the same data set, shows a near

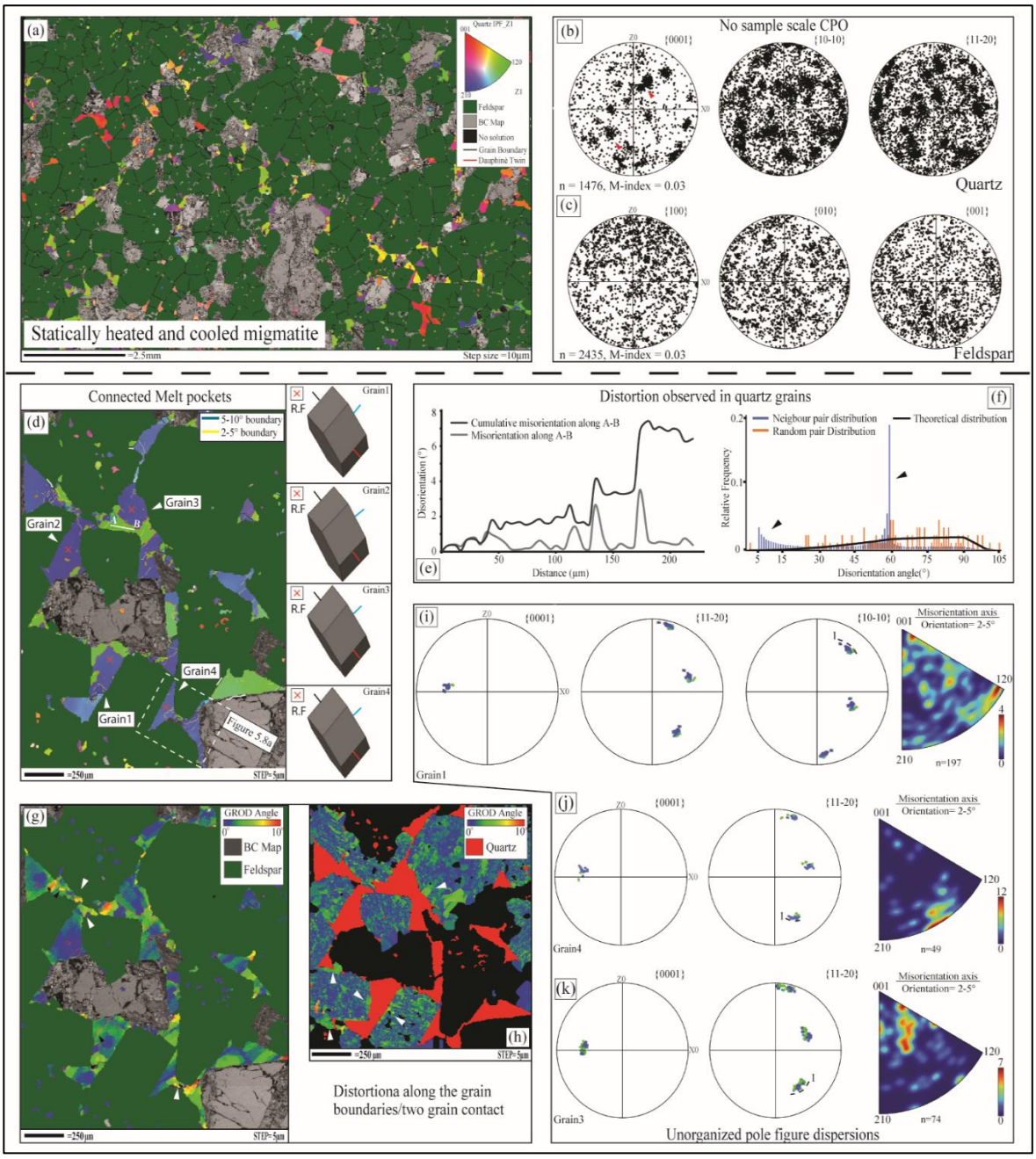

Figure 5.7 - Detailed microstructure and quantitative orientation analysis of static heated and cooled migmatite (ST1108B) (a) Sample scale EBSD analysis, step size 12 μm. Quartz fraction is represented with IPF colour coding and feldspar grains with a phase colour (green). All the other minerals are displayed as band contrast image. Note the proximal quartz grains display similar colours (i.e., similar crystal orientation). Black, red, and purple lines represent 10° grain boundaries, quartz, and plagioclase twins, respectively. (b-c) Quartz and plagioclase crystallographic orientation (CPO) (on the map of 'a'). Local clusters are marked with red arrows in 'b'. (d-k) In-depth EBSD analyses of quartz and surrounding feldspar grains (maps with step size 5μm). (d) Quartz grains ('Grain1' to 'Grain4', shown with IPF colour scheme) show similar crystal orientation (all measured at a reference point 'x') suggesting 3D connectivity. Low angle boundaries, trace of the misorientation profile (for 'e'), and 3D crystal orientations are provided. Note >2°, >5° grain boundaries and dauphiné twins are populated close to the grain edges. White box shows area for subsequent boundary trace analysis in Fig. 5.8. (e) Misorientation profile ('A-B' in 'd') display change in crystal orientation of 3-4° (when measured point to point) with a cumulative change of 7°

(see text). (f) Disparity in misorientation angle distribution (MAD) b/w correlated and uncorrelated data set at two places (marked with arrows) where low-angle disparity is seen near to ~5°. (g-h) GROD angle (with 0-10° misorientation) EBSD map shows distortion along the shared grain boundaries and at two grain contacts (marked with white arrows). Relation of internal misorientation with twins are marked with black arrows. (i-k) Pole figures of 'Grain1' and 'Grain3' show similar one-way dispersion (marked by '1'). The misorientation axis angle pair do not recognize a particular rotation axis. 'Grain4' shows one-way dispersion with <11-20> as the rotation axis.

---

point clustering (Fig. 5.8g), and WBV IPF also describes concentration of an array of edge dislocation on the basal plane, specifically around <01-10> (Fig. 5.8h). This is also supported by the higher value of K_{a3} for 'Domain1' (Tab. 5.3; Fig. AP5 – 1 in Appendix). Dislocation density corresponds to this subgrain boundary is 1.1 x $10^{14}/m^2$ (Tab. 5.3). A schematic pole figure diagram shows orientation of different axes (Fig. 5.8i), where the subgrain boundary plane is found to be consistent with a tilt boundary model. The estimated burger vector (B.G.) is parallel to <10-10> direction (similar to Fig. 5.8c, g), and the observed slip system is (0001) <10-10> or 'Type1' slip system (with <a> slip on the basal plane). Another domain is similarly analysed. Pole figure dispersions and the misorientation axis-angle pair (Fig. 5.8j-k) for the inclined subgrain wall in 'Domain 2' (as shown in Fig. 5.8a, c) decipher one of the <11-20> axes as the rotation axis (R.A). WBV magnitude map observes this subgrain wall (Fig. 5.8l) with high magnitude WBVs uniquely oriented along a particular direction (Fig. 5.8m with WBVs ranging from 0.009-0.014 μm^{-1} are plotted). IPF shows WBVs clustering close to the [c] direction (Fig. 5.8n), as expected from the higher value of K_c for 'Domain2' (Tab. 5.3; Fig. AP5 – 1 in Appendix). This is consistent with the observation made in Fig. 5.8c. A schematic diagram (Fig. 5.8o) suggests a tilt boundary model cannot explain this. A twist boundary geometry with screw dislocations on the basal plane and burgers vectors (B.G) parallel to the [0001] axis is found consistent with the observed subgrain boundary trace which leads to the activation of {10-10} [0001] slip ('Type3' slip system, i.e <c> slip on prism plane) (Tab. 5.3). The dislocation density associated with the subgrain boundary is 0.45 x $10^{14}/m^2$ (Tab. 5.3). WBV analyses for another grain reveal high dislocation density substructures with subgrain boundaries oriented perpendicular to the grain wall having WBVs parallel to the [c] direction and subgrain boundaries parallel to the grain boundary having WBVs parallel to the <a> direction (similar to observations made in W0809A) (Fig. AP5 – 2 in Appendix). The misorientation axes depict the activation of various rotation axes. This clearly indicates the operation of at least two distinct slip systems with these two distinct Burgers vector directions (Fig. AP5 – 2 in Appendix).

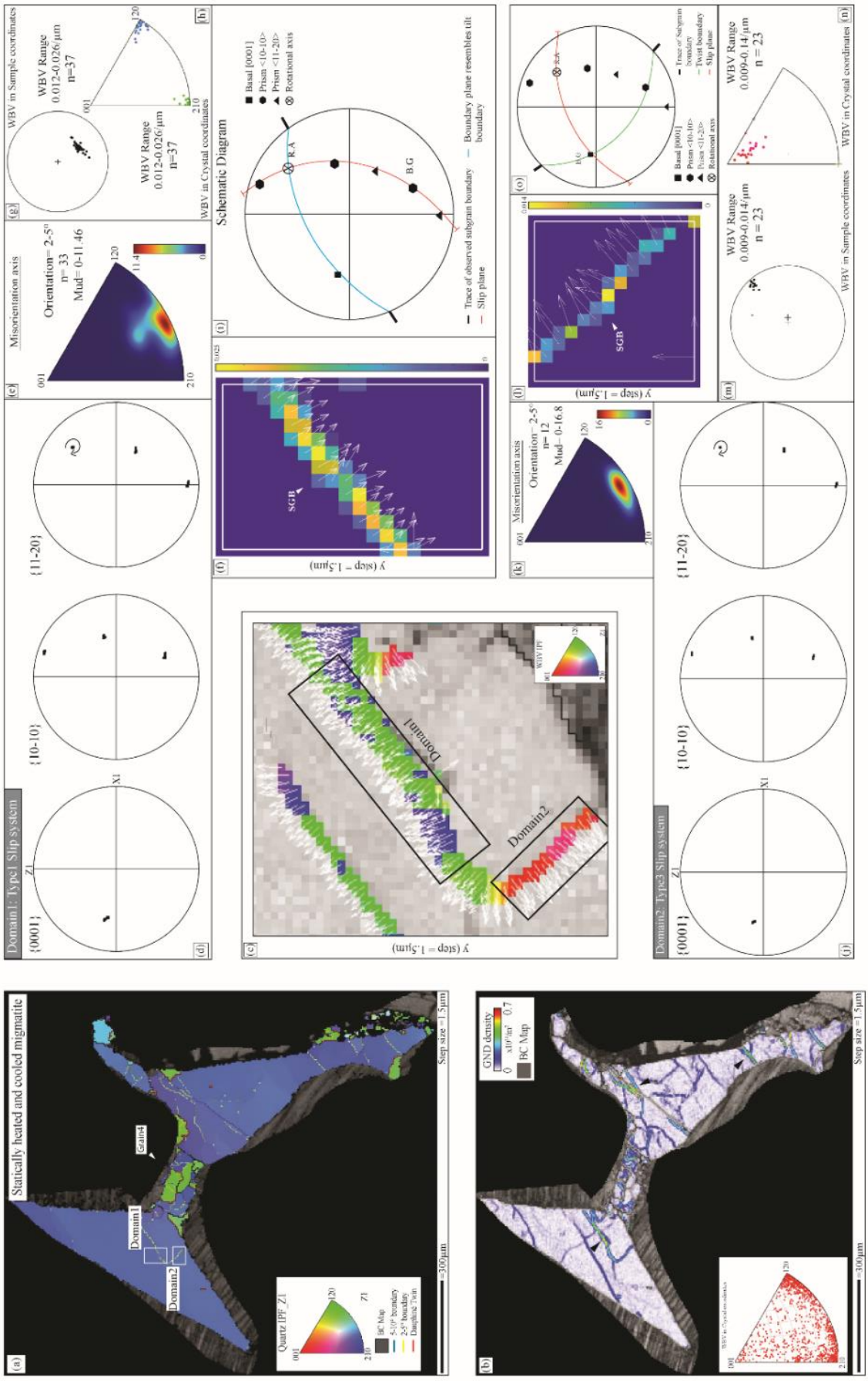
Statically heated and cooled migmatite
Grain4
Domain1
Domain2
Quartz IPF: Z1
BC Map
5-10° boundary
2-5° boundary
Daughter Twin
Step size = 1.5μm
300μm
GND density
BC Map
Step size = 1.5μm
300μm
Domain1: Type1 Slip system
{0001}
{10-10}
{11-20}
Misorientation axis
Orientation= 2-5°
n= 33
Mud= 0-11.46
WBV in Sample coordinates
WBV Range
0.012-0.026/μm
n=37
WBV in Crystal coordinates
Schematic Diagram
Basal [0001]
Prism <10-10>
Prism <11-20>
Rotational axis
Trace of observed subgrain boundary
Slip plane
Boundary plane resembles tilt boundary
R A
B G
SGB
y (step = 1.5μm)
Misorientation axis
Orientation= 2-5°
n= 12
Mud= 0-16.8
Trace of Subgrain boundary
Twist boundary
Slip plane
WBV Range
0.009-0.014/μm
n = 23
Domain2: Type3 Slip system

Figure 5.8 - Subgrain boundary trace analyses for statically heated and cooled migmatite (ST1108B). (a) 'Grain4' with IPF colour coding. Two domains are selected with 2° subgrain boundaries (SGB) for boundary trace analysis. (b) GND density map of the quartz grains measured considering basal slip with burgers vector 0.5 <11-20>. High GND densities are along fine lines coincident with the low-angle grain boundaries of 'a'.WBV orientations are parallel to the [c] axis and are concentrated on the basal plane. (c) WBV IPF map for an area around the studied domains exhibit the SGB traces observed in 'a'. WBV orientations (for WBV magnitudes >15 % of the maximum WBV value) distinguish two distinct orientations for the subgrain boundaries labelled as 'Domain1' and 'Domain2'. The colour scheme in the legend reflects the crystal structure of quartz. (d-h) Boundary trace analysis of 'Domain1'. (d-e) Pole figure and misorientation axis-angle pair deciphers <11-20> as misorientation axis. (f) WBV magnitude map display WBVs oriented along a particular direction (magnitude ranging between 0.012-0.026 μm^{-1} are shown with arrows). (g-h) WBV orientations plotted in pole figure and inverse pole figure (IPF), for the same data set (as in 'b'), identify a consistent direction. WBVs are oriented on the basal plane (similar to orientation in 'c') consistent with <a> slip. (i) A schematic pole figure with the position of different axes (as shown in 'd'), rotational axis (R.A), and Burgers vector (B.G) orientation. The slip system for this SGB is found (c) <a> (Tab. 5.3). Here the subgrain boundary represents a tilt wall. (j-n) Analysis for 'Domain 2'. (j) Pole figure with misorientation axis (arrowed). (k) Contoured IPF for the same data set confirms the rotation axis. (l) WBV magnitude map shows trace of SGB with consistently oriented WBVs along a particular direction (WBVs ranging from 0.009-0.014 μm^{-1} are plotted as arrows). (m-n) WBV pole figure shows clustering and the IPF displays existence of <c> slip, as observed in 'c'. (o) A schematic pole figure with the position of different axes (as shown 'j'), interpreted rotational axis (R.A), and Burgers vector direction (B.G) (see text for details). A {10-10} [0001] slip system is observed (Tab. 5.3) where the subgrain boundary represents a twist wall.

Melt-fluxed high-strain zone (PV1430H)

Both quartz and feldspar grains (Fig. 5.9a) in PV1430H lack a sample-scale CPO (Fig. 5.9b, c), as evidenced by low M-index values (close to zero) for both these minerals. A high-resolution map (Fig. 5.9d; step size 1.5µm) shows several quartz grains with low angle grain boundaries and Dauphiné twins along quartz grain edges (the grains are marked in Fig. 5.9d). However, this is less obvious than observed in W0809A or ST1108B. Quartz grain size ranges between 0.006-0.7x10^4 μm^2 (Tab. 5.2). The grains are elongated (aspect ratio of 1.3-5.6) and have cuspate grain boundaries (Fig. 5.9d). The maximum value of mean misorientation is 6-7° (Tab. 5.2; and 'Domains' in Tab. 5.3, see later), and the mean misorientation spread for most of the quartz grains (>70%) varies from 0.4 to 1.9°. The average misorientation ranges between 0.7-10.25°, where nearly 70% of grains show a range of 0.7-6.6° (both calculated for 10^2 mm^2 grain area). However, the composition and relative abundances of surrounding minerals do not influence on it (Tab. 5.2). The misorientation profile (profile 'A–B' in Fig. 5.9d) displays cumulative changes in crystal orientation up to 10°, and point-to-point analysis indicates maximum changes in orientation up to 9° (Fig. 5.9e). This is significantly higher than observed in W0809A and ST1108B (Tab. 5.3).

Misorientation angle distribution (MAD) with the disparity between the correlated and uncorrelated data set at a high angle (55–60°) corresponds to dauphiné twins and at a low angle (<10°) orientation describes non-random angle distribution of the grain boundaries (Fig. 5.9f). Dauphiné twins are highly variable, for example, 'Grain2' is 2.3x larger than 'Grain1', but their relative dauphiné twin density varies by 7x, from 0.22 to 0.03, even though the average misorientation of these two grains is nearly identical, 1.83° and 2.02°. This is comparable to the previously studied W0809A and ST1108B. The GROD angle EBSD map (with a misorientation range of 0-5°) highlights internal misorientation near to the quartz grain edges and at two grain contacts (Fig. 5.9g, arrowed), comparable to the previous observations. Similar analysis for the neighbouring amphibole grains also confirms this (Fig. 5.9h-i, arrowed). GROD angle EBSD map also displays very similar grain distortion (Fig. 5.9k). Misorientation profile (Fig. 5.9i) shows change in orientation up to 1.4° (Fig. 5.9j). All the quartz grains in Fig. 5.9d show the development of multiple misorientation axes where the dominant rotation axis is parallel to the [c] direction (Fig. 5.9l). Grains display notable pole figure dispersions ranging between 4°-15° (Tab. 5.2). 'Grain 2' shows a two-way dispersion (marked by '1' and '2') for the <a> axis, while misorientation axis-angle pair finds [0001] as the rotation axis (Fig. 5.9m). 'Grain3' also exhibits two-way dispersion for the [0001] axis, but the misorientation axis is difficult to identify (Fig. 5.9n).

Two different domains are selected (in 'Grain2' and 'Grain3', Fig. 5.10a) for subsequent subgrain boundary trace analysis (Fig. 5.10). The WBV magnitude map for the same data set (as in Fig. 5.10a) highlights the values parallel to <a> and [c] axes for these two domains (Fig. AP5 – 1 in Appendix; Tab. 5.3). The maximum GND density for the quartz grains is $0.3x10^{14}/m^2$ for a maximum WBV magnitude of $0.01\mu m^{-1}$ (Fig. 5.10b). High GND densities are along linear features, which correlate well with the observed subgrain boundaries in Fig. 5.10a. The subgrain boundaries are along grain edges, sometimes extending inside the grains, and even cut across the dauphiné twins. This is similar to the observations made in the previous samples. The WBV orientations show a strong clustering on the basal plane, close to the <a> direction (Fig. 5.10b), which is consistent with dominant slip on the <11-20> [0001] or <11-20> {10-10} slip systems. Domain1' and 'Domain2' record 4° and 6.2° misorientation, respectively (Tab. 5.3). In 'Domain 1' pole figure dispersions (Fig. 5.10c) and misorientation axis-angle pair (Fig. 5.10d) indicate [0001] as the rotational axis (R.A). This boundary is identified by a WBV magnitude map (Fig. 5.10e) as having a similar morphology with uniquely oriented high concentration of WBVs ranging

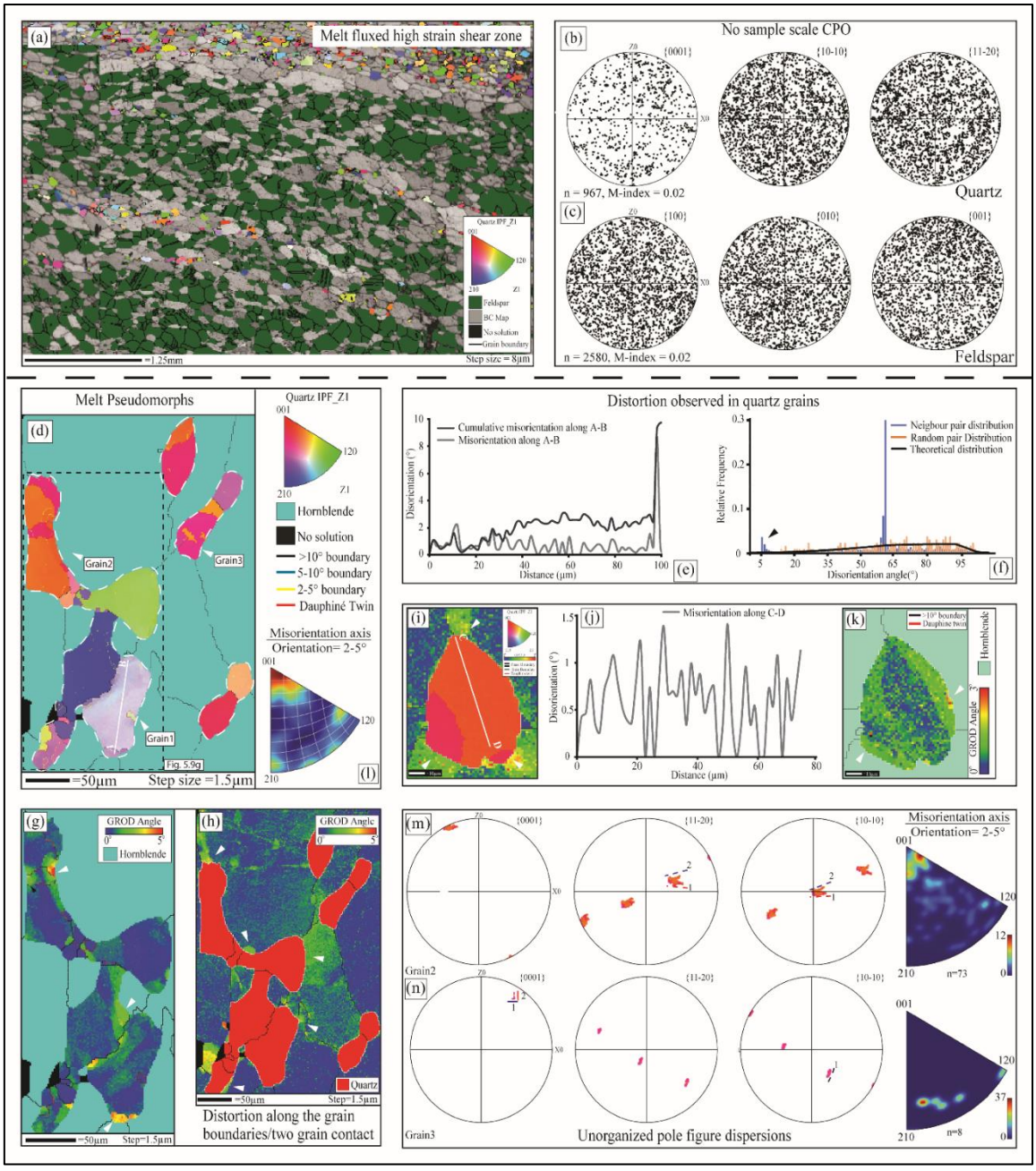

Figure 5.9 - Detailed microstructure and quantitative orientation analysis of melt-fluxed high-strain shear zone (PV1430H). (a) Quartz fraction (mostly observed in the upper half) is represented with IPF colour coding and feldspar grains are assigned a phase colour (green). All the other minerals are presented as band contrast map. (b-c) Quartz and plagioclase CPO (on the map of 'a'). (d-m) In-depth EBSD analyses of quartz and surrounding hornblende grains (with step size 1.5µm). (d) Quartz grains ('Grain1'-'Grain3') with low-angle grain boundaries and trace of misorientation profile. Low angle subgrain boundaries and dauphiné twins are populated close to the quartz edges. The grains are elongated and have cuspate grain boundary. (e) Misorientation profile ('A-B' in 'd') showing change in crystal orientation of 8° (measured point to point) and a cumulative change of 10° (see text). (f) Disparity in misorientation angle distribution (MAD) b/w correlated and uncorrelated data set (marked with arrows). (g-h) GROD angle (with 0-5° angle range) EBSD map identifies distortion along the shared grain boundaries of quartz and hornblende (arrowed). Relation of internal misorientation with quartz twins is marked with black arrow. (i, k) Another quartz grain (shown in IPF colour coding) exhibits distortion in hornblende along the grain edges (arrowed), and a GROD angle EBSD map shows misorientation distribution of 3.09° concentrated along the

grain edges (arrowed). (j) Misorientation profile ('C-D' in 'i') shows a change in crystal orientation (point to point) of up to 1.5°. (l) Quartz grains show activation of different rotation axis. (m-n) Pole figure of 'Grain2' and Grain3 show two-way dispersion (marked by '1' and/or '2') but the misorientation axis-angle pair for 'Grain2' develops only one rotation axis and fails to recognize any misorientation axis for 'Grain3'.

---

between 0.016-0.025 μm^{-1}. The pole figure (Fig. 5.10f), for the same data set, shows a near point clustering, and WBV IPF shows concentration of an array of edge dislocation on the basal plane (Fig. 5.10g). Dislocation density corresponds to this subgrain boundary is 0.23 x $10^{14}/m^2$ (Tab. 5.3). A schematic pole figure diagram (Fig. 5.10h) shows that the subgrain boundary geometry is consistent with a tilt boundary model having burger vectors (B.G.) parallel to <11-20> direction. Following the tilt model, the necessary slip system to describe this boundary wall is {10-10} <11-20> ('Type2' slip system, i.e., <a> slip on prism plane). 'Domain2' (with low angle 5-10° boundary) is similarly analysed (Fig. 5.10i-n), where orientation of different crystal-axes (Fig. 5.10i) and the misorientation axis-angle pair (Fig. 5.10j) confirms <10-10> as the rotation axis (R.A) for the analysed subgrain wall (45° to the horizontal axis, Fig. 5.10a). WBV magnitude map picks a portion of this subgrain wall (Fig. 5.10k) with high concentration of oriented WBVs ranging between 0.01-0.045 μm^{-1}. WBV orientation in the sample reference frame shows a single point clustering in Fig. 5.10k, and the IPF shows evidence of WBVs oriented parallel to the [c] direction (Fig. 5.10m), as expected from the higher value of K_c in 'Domain2' (Fig. AP5 – 1 in Appendix; Tab. 5.3). Thus, while the WBVs are predominantly oriented parallel to <a>, they are also parallel to the [c] direction for some substructures. A schematic diagram (Fig. 5.10n) suggests that the observed subgrain wall geometry is consistent with a twist boundary model with screw dislocations on the basal plane. The analysed subgrain wall is parallel to {10-10} and activation of {11-20} [0001] slip ('Type3' slip system, i.e., <c> slip on prism plane) is inferred (Tab. 5.3). The geometrically necessary dislocation density for this subgrain wall is 0.7 x $10^{14}/m^2$ (Tab. 5.3).

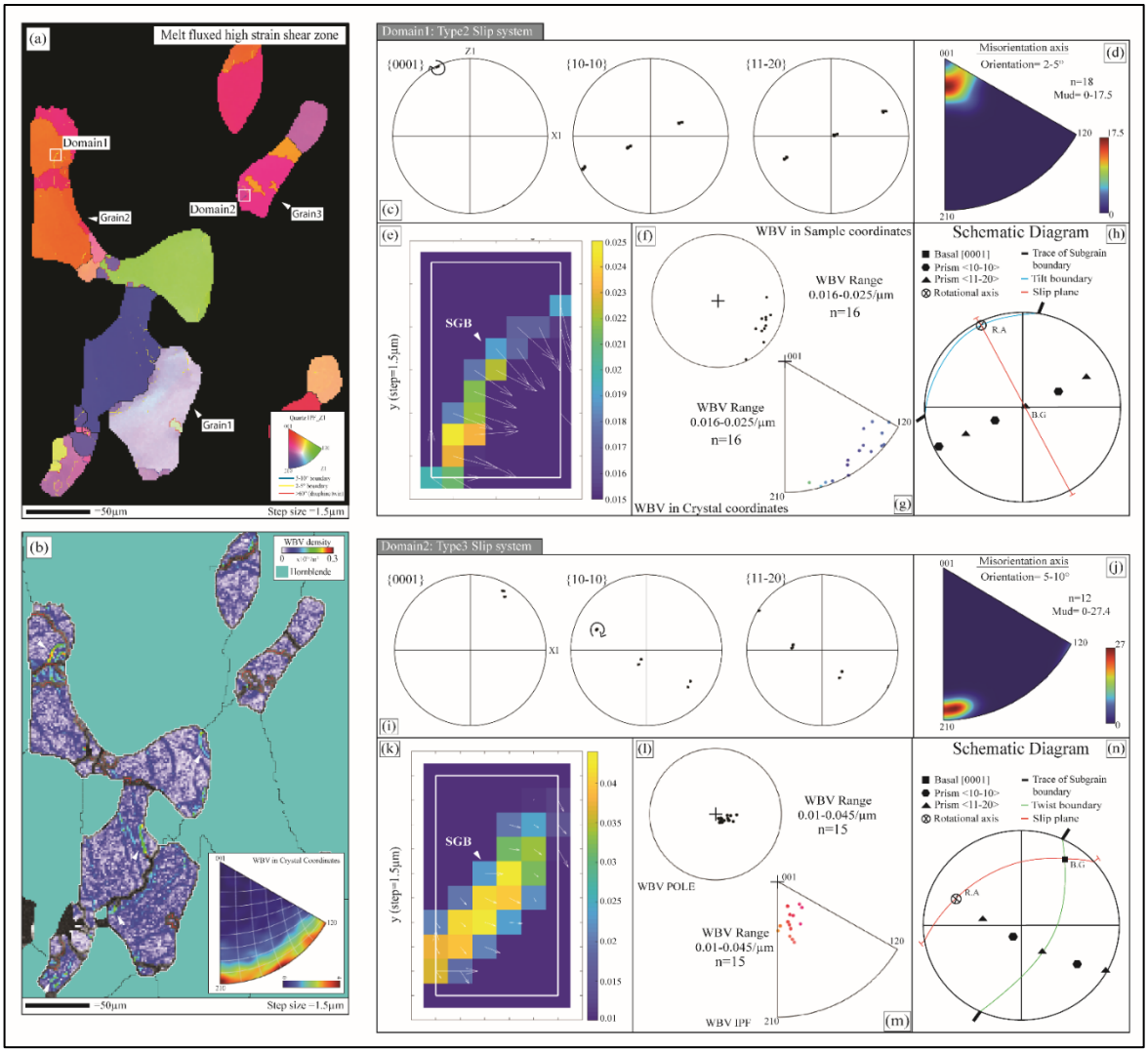

Figure 5.10 - Subgrain boundary trace analyses for melt-fluxed high-strain shear zone (PV1430H). (a) EBSD orientation imaging (step size 1.5µm) of quartz grains ('Grain1' to 'Grain3') with IPF colour coding, as shown in 'd'. Inset with low angle boundaries (yellow and blue lines), dauphiné twins (red lines), and lookup table for IPF colour coding. Two domains in 'Grain2' and 'Grain3' are selected with 2° and 5° subgrain boundaries for boundary trace analysis. (b) GND density map of the quartz grains measured considering basal slip with burgers vector 0.5 <11-20>. High GND densities are along fine lines coincident with the low-angle grain boundaries of 'a'. WBV orientations are parallel to <a> axis. (c-g) 'Domain1' boundary trace analysis (as shown in 'a'). (c) Pole figure for 'Domain1' shows [0001] as the rotation axis (arrowed). (d) Misorientation axis-angle pair for low-angle rotation for the same dataset confirms this. (f) WBV magnitude map (values ranging from 0.016-0.025 μm^{-1} are plotted as arrows) of 'Domain 1' identifies trace of the subgrain boundary (SGB) as observed in 'a'. (f-g) Pole figure and inverse pole figure (IPF) identify clustering of the WBVs. IPF shows <a> slip. (h) A schematic pole figure for 'Domain 1' with the position of different axes (as shown in 'c'), Rotational axis (R.A), and Burgers vector (B.G) orientation (see text for details). The slip system for this SGB is {m} <a> (Tab. 5.3). Here the subgrain boundary represents a tilt wall. (i-n) Boundary trace analysis for 'Domain 2'. (j-k) Pole figure and misorientation axis-angle pair confirms the <10-10> as rotation axis. (k) WBV magnitude map identifies trace of SGB with high concentration of WBVs oriented along a particular direction (values ranging from 0.01-0.045 μm^{-1} are plotted as arrows). (l-m) Pole figure shows clustering of the WBV and the IPF displays existence of <c> slip. (n) A schematic pole figure with the position of different axes (as shown in 'i'), interpreted rotational axis (R.A), and

Burgers vector orientation (B.G) (see text for details). A {11-20} [0001] slip system is identified (Tab. 5.3) where the subgrain boundary represents a twist wall.

5.5 Discussion

5.5.1 Optical and internal microstructures of quartz grains pseudomorphing former melt pockets: General similarities and sample dependent differences

All samples have retained several optical characteristics that are typical of the former presence of melt. The main features are (A) xenomorphic quartz grains with cuspate grain boundaries or grains having sharply pointed extensions (Fig. 5.2e-f, 5.3c-f, 5.4d-f), (B) low dihedral angle (LDA) between grains of a single phase and grains of a different phase (Fig. 5.2e-f, 5.3c, 5.4d-f), (C) straight faceted grain boundaries of the phase that pseudomorphs the former melt pockets (Fig. 5.2d, f, 5.3c-e, 5.4c-f). Here, parallel growth twining is observed at the quartz-plagioclase interface, making it simple to identify facets (Fig. 5.2d), (D) polyphase intergrowths (Fig. 5.4f), (E) spatially isolated grains with similar grain orientation depicting a single grain connected in 3D (Fig. 5.2e-f, 5.3c, e), and (F) The absence of intense dynamic recrystallization and formation of strain-free finer grain fractions (Fig. 5.2c, f, 5.3b-c, 5.4c). However, minor crystal lattice bending is also observed (Fig. 5.2c).

Some additional characteristics are unique to the dynamic environment (exemplified by the melt-fluxed high-strain zone), including (I) pervasive foliation defined by elongated phase(s) (Fig. 5.4a-b), (II) smaller grain size of melt-pseudomorphed quartz grains than found in the static cases (specially for the static granitoid), (III) rare typical interstitial microstructures under a petrographic microscope; their scale is smaller; therefore, they can only be observed with a scanning electron microscope (Fig. 5.4a-b), (IV) shape preferred orientation of grains parallel to the shear plane that pseudomorphed former melt along grain boundaries of foliation-defining minerals (Fig. 5.4d-e) (see also Stuart et al. 2018; Fig. 5.5d, 5.6g). Such shape-preferred orientation of melt pseudomorphs along the foliation plane has been observed in mantle peridotites as well as during melt-present deformation experiments (Zimmerman et al., 1999; Sawyer, 2001; Holtzman et al., 2003). However, Rosenberg and Handy (2000) also showed development of melt-bearing shear bands at an angle to the foliation.

In terms of sample scale features, all the samples exhibit (A) lack of sample scale CPO (Fig. 5.5b-c, 5.7b-c, 5.9b-c), despite the presence of a significant change in crystal orientation within the quartz grains (Fig. 5.5e, 5.7e, 5.9e, j; Tab. 5.2), (B) pronounced crystal lattice bending occurring primarily at grain edges or at two grain contacts (Fig. 5.5g, i, 5.7g, 5.9g, k) with low angle subgrain boundaries and abundant dauphiné twins (Fig. 5.5d, 5.7d, 5.9d). The subgrain boundaries may also extend inside the grains and sometimes crosscut the dauphiné twins (Fig. 5.5d, 5.6a, 5.7d, 5.9d), (C) distinct substructure, with subgrain boundaries exhibiting high GND densities and WBVs aligned in a particular direction (Fig. 5.6b, 5.8b, 5.10b), (D) a maximum value of mean misorientation in quartz of up to 4-5° (Fig. 5.11b). Notably, the amount and character of crystal lattice bending is not influenced by the composition of various surrounding phases (Tab. 5.2), (E) highly variable dauphiné twin density that is independent of grain size and grain orientation. Additionally, phases surrounding quartz exhibit localized lattice distortions along their shared boundaries (Fig. 5.5h, j, 5.7h, 5.9h-i), and (F) a high frequency of low angle neighbour pairs MADs (Fig. 5.5f, 5.7f, 5.9f) due to the high population of low angle grain boundaries (Wheeler et al. 2001). Additionally, for an individual quartz grain, three types of pole figure appearances can be seen: (i) a disorganized clouded pattern, (ii) one-way and/or (iii) two-way dispersion of the crystallographic axes (Fig. 5.5, 5.7, 5.9, 5.11c). For a single quartz grain, misorientation axis-angle pairs for low angle rotation exhibit clustering either parallel to one or two directions, or it is extremely difficult to distinguish (Fig. 5.11c). Consequently, individual quartz grains lack organized lattice dispersion and the formation of a prominent single rotational axis (Fig. 5.5k-m, 5.7i-k, 5.9m-n, 5.11c). Within the same sample, different grains develop different misorientation axes, and also a single grain exhibit more than one misorientation axis (Fig. 5.9l).

Even though the above-mentioned features are present in all the three analysed samples, there are systematic differences in the extent of internal deformation between the statically cooled interstitial melt grains (i.e., slowly crystallizing static granitoid W0809A and static migmatite ST1108B) vs. a crystallizing quartz grain in the dynamic environment (i.e., melt-fluxed high strain zone PV1430H). In the dynamic environment, a single grain of quartz exhibits a relatively large change in grain orientation (6-7°, Fig. 5.11b, d). Almost 70% of the quartz grains in the statically crystallized samples have a mean misorientation range of 0.08-1°, whereas the dynamically crystallized sample has a mean misorientation range of 0.4-1.9°. (Fig. 5.11b). Misorientation/profile is also higher for quartz grains

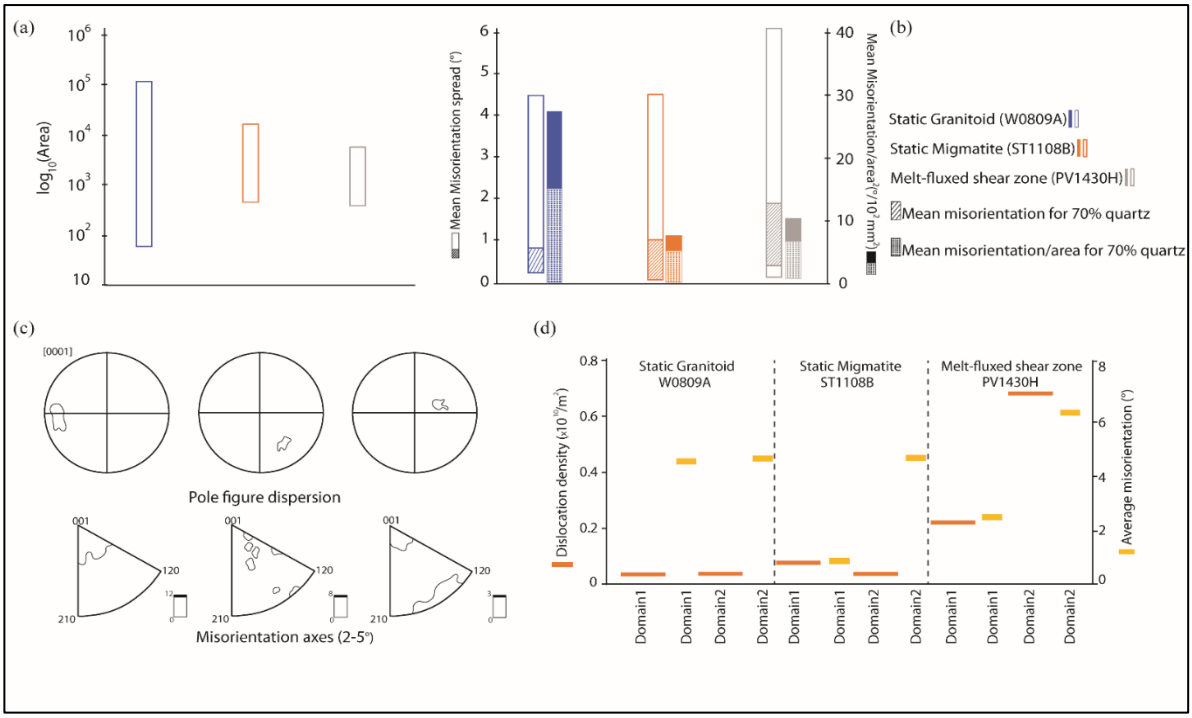

Figure 5.11 - Comparison of microstructural features in the studied samples. (a) Quartz grain size of the studied samples. The static granitoid (W0809A) has a large variation when compared to the other two samples. (b) Mean misorientation (cross-hatched bars) and mean misorientation/area (solid bars with circles). The cross-hatched area represents the mean misorientation value for >70% quartz grains, whereas the areas with circles represent misorientation/area for 70% quartz grains. (c) Types of pole figure dispersions for [0001] and misorientation axes for low angle rotation in the studied samples. From left to right, the pole figures show an unorganized to one-way to two-way dispersion of crystallographic axes (upper panel). The lower panel shows the evolution of a crystal rotation axis from a single point clustering to multiple clusters from left to right. (d) Misorientation (in °) and dislocation density (in $10^{14}/m^2$) measured for different domains (Tab. 5.3). Note the melt-fluxed high-strain shear zone sample shows higher dislocation density and high degree of average misorientation.

---

crystallized in a dynamic environment, at 0.08°/µm, than for statically crystallized samples, at 0.02°/µm. However, nearly 70% of the quartz grains in the static granitoid exhibit a large mean misorientation/area (up to 15.6° per 10^2 mm^2) when compared to the dynamically crystallized sample (up to 6.6° per 10^2 mm^2), whereas the static migmatite exhibits a relatively small change of 5.7° per 10^2 mm^2 (Fig. 5.11b). The large variation in grain size explains the large change in misorientation per area in the static granitoid (Fig. 5.11a). It is not affected by the mean misorientation, which is much lower in this sample than in the others (Fig. 5.11b). The GND density values (calculated using WBV from the EBSD maps with the same step size) are similar with a value of 0.4-0.7x$10^{14}/m^2$ in the statically crystallized ST1108B (Fig. 5.8b, AP5 – 2) and values ranging between 0.3-0.4 x$10^{14}/m^2$ in the melt-flux high strain sample PV1430H or static granitoid W0809A (Fig. 5.6b, 5.8b,

5.10b). In general, the GND density values for subgrain boundaries in quartz grains crystallizing in the high-strain zone are an order of magnitude higher (varies from 0.2–0.7x10^{14}/m^2), whereas this variation is from 0.08-0.45x10^{14}/m^2 in the statically cooled granitoid and migmatite (Fig. 5.11d; Tab. 5.3).

5.5.2 Internal microstructure of quartz grains pseudomorphing former melt: Are they distinct from structures developed during solid-state deformation caused by tectonic stresses?

Deformation features within the quartz grains crystallized from the melt are distinctly different from rocks that experienced solid-state deformation by dislocation creep induced by large-scale tectonic stresses. In the latter case, microstructures show systematic lattice reorientation/grain rotation. A dominant external, tectonic differential stress field creates simple pole figure patterns both for individual grains and at the sample scale (Drury and Urai, 1990; Hirth and Tullis, 1992).

If grain reorientations are related to crystal plasticity, CPO patterns are typically interpreted in terms of activation of a dominant intracrystalline slip system essentially controlled by the temperature of deformation (Kruhl, 1996; Stipp et al., 2002). Because there is a direct relationship between grain shape and grain reorientation, CPO is frequently accompanied by a shape-preferred orientation (SPO) (Mainprice and Nicolas, 1989). In general, at low to moderate temperatures (300-400°C), basal <a> slip dominates, whereas at higher temperatures (~400-500°C), a transition from basal <a> to rhomb <a> slip is seen (Tab. 5.4; Kruhl, 1996; Stipp et al., 2002). The transition temperature of rhomb <a> to prism <a> or prism [c] slip is ~500–650°C or >650°C (Tab. 5.4; Kruhl, 1998; Stipp et al., 2002). At temperatures >750°C, numerous other slip systems, including slip on prism planes and second-order pyramidal planes {2111}, have been documented (Bäeta and Ashbee, 1969; Tab. 5.4). Previous research, however, suggested that other factors, such as water weakening, can control this transition (see Law, 2014 for a review), such as prism [c] slip at lower temperatures (550-600°C) (Garbutt & Teyssier, 1991; Okudaira et al., 1995) or a low strain rate can reduce the temperature required for prism [c] slip transition (Blacic, 1975; Kruhl, 1996). Dauphiné deformation twins are traditionally described to form during grain growth (Piazolo et al., 2005), high to low-quartz phase transition (Putnis, 1992), or as a response to the local stress concentration (Lloyd, 1987; Menegon et al., 2011).

The absence of CPO (Figs. 5.5b-c, 5.7b-c, 5.9b-c) in the studied samples, even when differential stress was present (as in the PV1430H), suggests that the quartz/feldspar grains do not take up 'tectonic stress induced strain' during crystallization and instead represent a 'frozen-in microstructure' as the melt crystallizes. If deformation exists beyond melt crystallization the melt microstructures would have been lost. It should be noted that the absence of CPO in a deforming environment can also be a sign of deformation by diffusion creep (e.g., Law, 1990, Prior et al., 1999, Bestmann and Prior, 2002, Svahnberg and Piazolo, 2010). The retention of melt-present features at the optical scale in our samples (e.g., low dihedral angle of quartz-plagioclase grains, cuspate grain boundaries, xenomorphic grains, etc.) rules out diffusion creep (Fig. 5.2-5.4). A lack of post-crystallization solid-state overprinting features such as recrystallized grains, grain bulging, or migrating grain boundaries indicates that the rocks were not subjected to subsequent tectonic stresses after solidification. This also implies that once the melt crystallized, these rocks became rheologically hard (Stuart et al., 2018; Lee et al., 2018; Prakash et al., 2018).

The presence of well-developed subgrain walls (Fig. 5.6, 5.8, 5.10) is commonly attributed to dislocation generation and rearrangement during crystal plastic deformation (Wilsdorf and Hansen, 1991; Hirth and Tullis, 1992; Borthwick and Piazolo, 2010). However, it is only recently discovered that subgrain walls can form during fluid-mediated replacement reactions. Though, these are less well defined in terms of common dislocation types (Spruzeniece et al. 2016). The systematic generation of dislocations in our study is demonstrated by systematic small circle lattice dispersions in the observed pole figures (e.g., Fig. 5.5k-m, 5.7i-k, 5.9l-m; Tab. 5.2) (e.g., Reddy et al. 2007, Piazolo and Jaconelli, 2014). In the analysed samples, the dispersion path for any individual grain is readily identifiable (e.g., Fig. 5.5k-m, 5.7i-k, 5.9m-n, 5.11c). However, unlike in tectonic differential stress induced crystal-plastic deformation, defining the rotational axis is difficult here because either the dispersion has affected more than one axis (e.g., Fig. 5.5m, 5.7i, k, and second panel in Fig. 5.11c), or it is hard to identify a particular orientation (Fig. 5.9m, and third panel in Fig. 5.11c). Furthermore, because the exact slip systems from the CPO figures cannot be translated, the samples provide no evidence for the activation of any preferential sample-scale slip system. It means either i) a non-systematic dislocation generation (as in replacement reactions), or ii) a mixture of slip systems (corresponding to different subgrain boundaries within a single grain) has resulted in non-distinct dispersion for all crystallographic axes.

Conventional slip systems for solid-state deformation at various strain rate and temperature					
Rocks	Slip system(s)	Slip plane(s)	Slip direction	Strain rate	Temperature
Subsolidus sheared rock	Type1: (0001)<11-20>	Basal (c)	<a>	High ($10^{-13}s^{-1}$)	300-400°C*
	Type2: {10-10<11-20> {1101}<11-20>	Prism {m} or Rhomb {r/z}	<a>	Lower ($<10^{-13}s^{-1}$)	400-650°C*
	Type3: {10-10} [0001]	Prism {m}	[c]	Lower ($<10^{-13}s^{-1}$)	>650°C*
Observed slip systems for the array of melt bearing rocks					
Granite	{10-10} [0001]	On all planes	In all possible	Zero	~650-900°C
Static migmatite	(0001) <10-10>	Basal (c)	directions:	Zero	~800°C
Melt fluxed shear zone	{11-20} [0001] {10-10}<11-20> (0001) <10-10>	Prism {m} Rhomb {r/z}	<a>, [c]	High* in bulk rock	~850°C
*Wilson, 1975; Bouchez and Pêcher, 1981; Bouchez et al., 1984; Blumenfeld et al., 1986; Okudaira et al., 1995; Kruz et al., 2002; Law et al., 2014; Paschier and Trouw, 2005; Toy et al., 2008.					

Table 5.4 - Comparison of conventional quartz slip systems observed for a mylonitic rock deformed under subsolidus condition (from Law, 2014 and references therein) vs. slip systems observed in the melt pseudomorph quartz grains crystallized under static and dynamic condition.

The activation of a unique slip system normally occurs at a specific deformation temperature, which distinguishes low temperature (200-400°C), transitional (400-600°C), and high temperature (700°C) crystal plastic deformation (Tab. 5.4). Even a single melt pseudomorphed quartz grain in our samples exhibits an array of slip systems corresponding to different temperatures (Fig. 5.6, 5.8; Tab. 5.4). Individual subgrain walls within a single grain exhibit (0001) <10-10> slip (Fig. 5.8d-i showing 'Type1' slip system), indicating a low temperature-high strain rate response, as well as {10-10} <11-20> slip (Fig. 5.6d-i, 5.10c-h showing 'Type2' slip system), indicating a relatively higher temperature-lower strain rate feedback (Tab. 5.3, 5.4). Also, activation of {10-10} [0001] / {11-20} [0001] slip (Fig. 5.6j-o, 5.10i-n showing 'Type3' slip systems) is discovered, which detects temperatures >650°C (Tab. 5.4).The findings are consistent with the observed WBV orientations in the studied samples (Fig. 5.6b, 5.8b, 5.10b), as well as WBV IPF maps that show subgrain boundaries with WBVs oriented parallel to the a>, [c], and <a+c> directions (Fig. AP5 – 1, AP5 – 2 in Appendix). The simultaneous activation of all these slip systems, which correspond to a range of deformation temperatures (300-650°C), has never been reported before from sub-solidus deformation of a single rock (Tab. 5.4). The static granitoid exhibits the formation of subgrain walls parallel to both the basal plane (Fig. 5.6o) and the prism plane (Fig. 5.6i), conventionally known as high temperature 'chessboard extinction' (Blumenfeld et al., 1986; Okudaira et al., 1995; Kruhl, 1996). The subgrain boundaries are

identified as twist walls with oriented screw dislocations in both static migmatite and dynamic melt fluxed samples (Fig. 5.8o, 5.10n; Tab. 5.3). Dislocation densities in the studied rocks range from 10^{12}–10^{13}/m^2 (Tab. 5.3), whereas in the deformed granites, and in naturally or synthetically deformed quartz, dislocation densities record a range of 10^{12}–10^{15}/m^2 (Wenk et al., 2008). All of these represent a distinct mode of slip system genesis because they a) disagree with the inferred temperature ranges, though b. show similar GND density values with preferentially oriented WBVs, and c. are not induced by external tectonic stress (evidenced by lack of sample-scale CPO). These microstructural patterns are distinct from those observed in crystal-plastic solid-state deformation caused by large-scale tectonic stresses.

In conclusion, quartz grains crystallizing from melt exhibit consistent microstructural responses such as (A) lack of sample-scale CPO, (B) for a single quartz grain, a disorganized pole figure pattern or crystallographically controlled two-way pole figure dispersions without activation of any clear rotation axis (three types in Fig. 5.11c). Those grains in static granitoid with a clear rotation axis (from the IPF) but no recognizable crystallographically controlled pole figure dispersion (Fig. 5.5k-l), resulting in a discrepancy between pole figure dispersion and IPF, (C) activation of several slip systems associated with a single subgrain boundary ('Type1', 'Type2', and 'Type3') (Tab. 5.4), (D) development of tilt and twist walls associated with subgrain boundaries parallel to the basal and prism planes, and (E) similar dislocation density values comparable to natural mylonites. The above characteristics (A-C) will result in the absence of sample-scale CPO but induce pole figure dispersion with the activation of one or two different rotation axes (Fig. 5.11; Tab. 5.3) during a whole grain analysis. For some grains, pole figure dispersion and misorientation axis are difficult to determine (Fig. 5.11c). A specific slip system can be identified only when a specific subgrain wall is investigated (Tab. 5.3), and they are crystallographically well organized, with oriented dislocations (Fig. 5.6f, l; Fig. 5.8c, f, l; Fig. 5.10e, k) indicating a particular set of burgers vectors (Fig. 5.6g-h, m-n; Fig. 5.10f-g, l-m). The results above point to a similar textural paragenesis of a melt-present rock. This is possible only if deviatoric stress affects a quartz grain on a very local scale and induces dislocation glide/climb while forming different subgrain walls at different temperatures. The high density of subgrain boundaries and pronounced crystal lattice bending along the grain edges also demonstrate the ultra-local nature of stress concentration. Based on the preceding discussion, we propose that quartz grains pseuodmorphing former melt pockets are

subjected to local stresses throughout a decreasing temperature window associated with cooling and crystallization of melt.

5.5.3 Effective differential stress values derived from grain pseudomorphing former melt using dislocation density values from WBV analyses

To calculate the amount of differential stress a quartz grain has been subjected to, we use the local geometrically necessary dislocation (GND) density values calculated from different domains and the quantitative relationship between differential stress and grain-substructure (Bird et al., 1969; Twiss, 1986; Ross et al., 1980). Under steady-state conditions, the dislocations density varies monotonically with differential stress and is affected by temperature and pressure via the shear modulus constant (White, 1980). However, it is independent of strain/strain-rate values and can be used as a 'paleopiezometer' (Bird et al., 1969; Twiss, 1986; White, 1980).

The relation between dislocation density and flow stress (based on the 'back stress' model by Cooper et al., 1978 and Weathers et al., 1979) is found:

$\sigma_1 - \sigma_3 = a\mu b N^{0.5}$ .....(eqn.1)

McCormick (1977) determined experimentally the following stress-dislocation density relationship using synthetic quartz grains:

$\sigma_1 - \sigma_3 = 1.64 \times 10^{-4} N^{0.66}$.....(eqn.2)

$\sigma_1 - \sigma_3$ is the differential stress (in MPa), N the dislocation density (in cm^{-2}), a is a dimensionless material constant, μ the shear modulus (in N/m^2), and b the burgers vector (in cm). However, because only a fraction of the applied stress is stored as internal stress, and some dislocations are lost during cooling, the calculated differential stress is a minimum estimate using these equations (Nicolas and Poirier, 1976; White, 1979). Furthermore, at low flow stress, the interdependence of dislocation density and differential stress decreases, and grain size can influence the density value (Twiss, 1986). The dislocation density values for the statically cooled and crystallized samples (W0809A and ST1108B) range from 4.3-8.5 x $10^8/cm^2$ (Fig. 5.11d; Tab. 5.3). Using the back-stress model, the corresponding stress value is 131-184 MPa (eqn.1) (where a = 3.0, μ = 42×10^9 N/m^2 and b = 0.5 nm; Cooper et al., 1978; Christie and Ord, 1980; Passchier and Trouw, 2005). Equation 2 (McCormick, 1977) yields slightly lower values of 81-128 MPa. The dislocation density values for the dynamically crystallized shear zone sample, range from 20-70 x $10^8/cm^2$. The corresponding stress values are 281-527 MPa (using eqn. 1) and 225-516 MPa (using eqn. 2) (Fig. 5.11d).

5.5.4 Origin of lattice distortions internal to quartz pseudomorphing former melt

To understand the origin of the observed lattice distortions in quartz pseudomorphing former melt, the boundary conditions during crystallization must be examined. Here we consider quartz grains that form when only isolated pore spaces remain filled with liquid while much of the rock is solid. Mineral growth in confined environments occurs in a variety of geological settings, including but not limited to vein initiation and growth (Fletcher and Merino, 2001), salt growth in pore spaces (Wellman and Wilson, 1965; Scherer 2004, etc.), and mineral growth due to CO_2 sequestration (Muller et al., 2009). Both the static and dynamic cooling conditions are thought to be similar. However, the dynamic system has a higher dislocation density, average crystal misorientations, and crystal bending (measured as mean misorientation in Fig. 5.11), implying that it was subjected to higher effective stresses than the statically cooled melt-crystallized grains. Three distinct scenarios emerge when the processes and stress conditions of melt crystallization in a confined space are considered (Fig. 5.12):

Scenario 1. Force of crystallization: When a pore fluid is supersaturated in confinement, a mineral will nucleate and grow against the normal stress (Scherer, 2000, 2002; Noiriel et al., 2010). Stresses develop at the crystal faces due to the mineral crystallization in confinement and can be described as (Correns, 1949; Flatt et al., 2006; Fig. 5.12a):

$$\Delta P = \sigma - P = \frac{RT}{V_s} \ln(S) \dots\dots (eqn. 3)$$

where R is the molar gas constant (R= 8.32 m^3 Pa K^{-1} mol^{-1}), V_s is the molar volume of the solid phase, T is the temperature in K, and S denotes degree of supersaturation. σ refers to the nonhydrostatic stress acting on the grain boundary and P is the hydrostatic pressure. $'\Delta P'$ is often referred to as 'Force of Crystallization (FOC)' (Wellman and Wilson, 1965; Scherer 2004). This is the maximum nonhydrostatic stress exerted by the growing grain (Maliva and Siever, 1988). Several authors reported development of stress during grain growth at pore spaces (Maliva and Siever, 1988; Ostapenko and Yaroshenko, 1975). Existence of FOC is also found in the laboratory experiments (e.g., Becker and Day 1916; Correns, 1949; Noiriel et al., 2010). In geology, FOC can lead to the upliftment of the overlying rock during travertine growth (Gratier et al., 2012) or during authigenic grain growth (Folk, 1964).

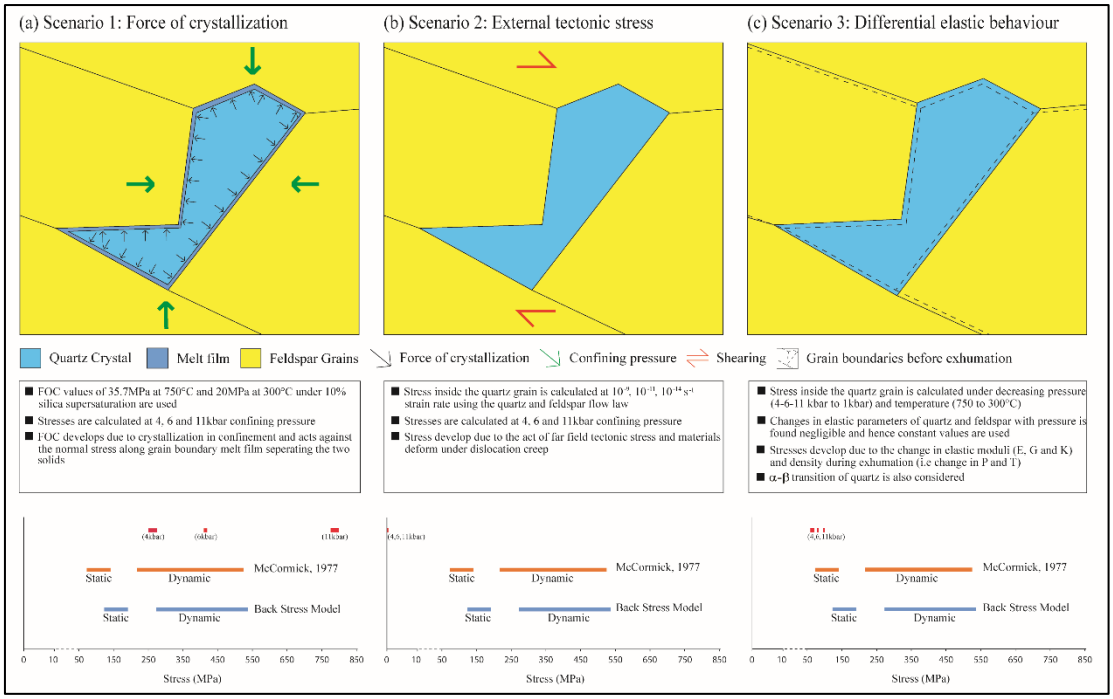

Figure 5.12 - Schematic diagrams, descriptions, and inferred stress magnitudes based on the three possible scenarios that lead to observed lattice distortion in crystallizing quartz in a confined space; (top panel) schematic diagrams, blue: quartz, yellow- surrounding plagioclase (see Appendix for more details); (middle panel) descriptions of the main features of each scenario, used as inputs for numerical modelling; (bottom panel) stress values from: numerical models (calculated at 4, 6 and 11 kbar and displayed in red bars), and empirical calculations (using equations of McCormick, 1977 and Back stress models, in orange and blue bars respectively). (a) force of crystallization (FOC) in confined space, (b) forces due to differential tectonic stress, (c) forces exerted due to change in quartz-plagioclase elastic parameters with temperature. Note the numerical stress value from the force of crystallization corresponds well with the empirical calculations.

Similarly, growth of calcite may produce fracturing or can cause permanent damage during vein initiation and growth (Fletcher and Merino, 2001). The halite supersaturation can produce a pressure in the range of 20.5-41Mpa under 10% supersaturation (Flatt, 2002; Noiriel et al., 2010). Noiriel et al. (2010) observed FOC in the range of 0.2-10Mpa for 2‰ to 11‰ supersaturation of NaCl within a porous rock. Considering a felsic silicate melt system, the force of crystallization (σ) will be same in both the static and dynamic conditions. Here, the stress values inside the quartz grain are modelled for felsic melt 10% supersaturated with silica as an order magnitude approximation. Considering FOC value of 20MPa (refer to AP.5.1 in Appendix for details), accumulated stress inside the crystallizing grain varies from 270MPa to 800 MPa (Fig. 5.12a; Tab. AP5.2 in Appendix) at 4kbar and 11kbar confining pressure, respectively. For a higher FOC value of 35.77 MPa, calculated at 750°C, the accumulated stress inside the quartz grain is found 255MPa, 410MPa and 780MPa at 4, 6, and 11 kbar confining pressure, respectively. The systematic difference in the accumulated

stress is found to be regulated only by the confining pressures of the melt bearing systems. Melt that has crystallized at a greater depth displays higher concentration of stress inside the crystallizing grain (Fig. 5.12a). This value is very close to the observation from empirical calculations utilizing dislocation density, which ranges from 131 MPa to 527 MPa (from the back stress model) and 81-516 MPa (using McCormick, 1970) for static and dynamic samples, respectively (Fig. 5.12a, section 5.5.3 for details).

Scenario 2. External tectonic stress: Dislocation creep in naturally deformed quartz (Fig. 5.12b) leads to the development of crystallographic preferred orientation (CPO) (Law, 1986; Stipp et al., 2002; Bouchez 1978). Lack of a sample scale CPO is therefore interpreted as either the absence of significant far-field stress or a different deformation mechanism such as grain boundary sliding or diffusion creep (e.g., Svahnberg & Piazolo, 2010, Bestmann & Prior, 2002). In the latter case, no grain scale deformation is expected. However, local grain scale lattice distortions without a sample scale CPO may be related to minute small tectonic stress. However, in this case, local grain boundary modification from facets to non-facets is to be expected. GPS and global slip rate data indicate that the strain rate for natural mylonites ranges between 10^{-11} to 10^{-13} s^{-1} (Fagereng and Biggs, 2018). From geodetic measurements along major fault systems this value comes out to be 10^{-14} s^{-1} (Kreemer et al., 2014). Under this normal geological strain rate (modelled at 10^{-9} s^{-1} to 10^{-14} s^{-1}), the stress values range from 10^{-12} MPa to 10^{-17} MPa, respectively (Fig. 5.12b; refer to AP.5.2 and Tab. AP5.2 in Appendix for details). These values are minute because shape change of the grains are assumed to be minimal. Natural samples also show little to no systematic change in the shape of the melt-pseudomorphed pockets (Section 5.4). These values are insignificant in comparison to the stress induced by dislocation densities (Section: 5.5.3, Fig. 5.12b). Moreover, a creep $>10^{-11}$ s^{-1} will cause distortion of the melt pseudomorphed grains, as suggested by the white contour lines.

Scenario 3. Stress as the result of differential elastic behaviour of quartz and feldspar during cooling (Fig. 5.12c): The elastic properties of both quartz and feldspar have a certain pressure-temperature dependence. During exhumation contrast in compressibility and density between minerals can lead to an internal stress concentration. Change in pressure is reported to have negligible effects on elastic constants (C_{ij}) and bulk modulus (K) of quartz (0.74% and 1% change respectively for 1 kbar change in pressure) (Kimizuka et al., 2007). Similarly, the bulk modulus of plagioclase (for An_{100}) shows only 0.4% change with 1 kbar

change in pressure (Angel, 2004). Additionally, we observe very little change in confining pressure during exhumation in our studied samples (i.e., from 4-10 kbar to the surface, Tab. 5.1), implying that pressure has little to no influence on elastic parameters of both quartz and feldspar. The elastic properties of quartz are dependent of temperature and strongly influenced by the α-β transition at 573°C (Ohno et al., 2006, see AP5 – 6). Heating experiments on α-quartz shows 15% softening, with the Young's modulus (E) changing linearly from 97 GPa at room temperature to 81 GPa at 500°C (Gregorová et al., 2015), and a steep decrease to 43GPa while passing through the phase transition (Peng and Redfern, 2013). A numerical model that accurately models these changes shows that the accumulated stress inside the crystallizing grain is expected to be in the order of ~80MPa for a temperature change from 750°C to 0°C at 4kbar pressure, and ~100MPa for a temperature change from 750°C to 0°C at 11kbar (Fig. 5.12c; refer to AP.5.3 and Tab. AP5.2 in Appendix for details). These values are lower than the empirically calculated stress levels in natural samples (Section: 5.5.3, Fig. 5.12c).

Based on the preceding discussion, the stress accumulated in the crystallizing grain is a result of the interaction between the force of crystallization and confining pressure during melt crystallization and it provides a plausible explanation for the observed lattice distortions in the quartz grains in both the static and dynamic environments. The observed higher mean misorientation and dislocation density in the melt fluxed shear zone sample can be explained by its greater crystallization depth alone (Fig. 5.12a), with no contribution from subsolidus shearing required.

5.6 Conclusion

An identification scheme that allows us to characterize melt-crystallized grains is critical, especially in rocks with a low melt fraction and/or high strain zones with cryptic melt signatures. It is essential to distinguish melt pseudomorphed grains from those crystallizing in a solid environment (Daczko and Piazolo, 2022). With new techniques it is possible to go beyond optical characteristics.

At the optical scale, quartz grains are observed with euhedral facets or with cuspate boundaries, low dihedral angles (LDA) where a grain extends to meet two other grains, or as elongated xenomorphic grains connected in 3D, melt-pseudomorphs of thin grain boundary melt films, and a general lack in SPO of quartz, presence of porphyroclasts, grains

with serrated or lobate boundaries or recrystallized fractions. These observations are very similar to those made by other authors (e.g., Vernon, 2011; Holness, 2008; Holness and Sawyer, 2008; Holness and Vernon, 2015; Daczko and Piazolo, 2022).

In addition, interstitial quartz grains grown from a melt exhibits (A) lack of sample scale CPO, but (B) bending in grains and formation of subgrain boundaries, (C) localized disorientation and highly populated dauphiné twins along the grain edges, (D) disorganized pole figure patterns or two-way pole figure dispersions in the absence of any discernible rotation axis, (E) activation of a mixture of slip systems within a single quartz grain, (F) distinct substructure, with high GND densities at subgrain boundaries and WBVs aligned in a specific direction, and (G) development of tilt and twist walls parallel to quartz basal and prism planes. These features are observed to be consistent regardless of geodynamic environment or melt percentage. The presence of CPO (or SPO) and the activation of multiple slip systems distinguish melt pseudomorph quartz grains from quartz deformed under sub-solidus conditions. This provides us with a toolbox to identify quartz deformation microstructures that formed during the final stages of silicate melt crystallization. However, there are very subtle differences in the general responses of crystallizing quartz under static vs. dynamic conditions. The dynamically crystallized quartz grain has a relatively high degree of mean misorientation and dislocation density.

The reasons behind this localized stress development could be attributed to differences in surface energy between solid and melt, force of crystallization (FOC), and volumetric changes during melt-crystallization. The force of crystallization is discovered to be capable of producing stress levels comparable to those observed from dislocation densities in these naturally studied samples.

Chapter 6

Similar amphibole crystallographic preferred orientation produced by different deformation mechanisms: melt-present versus melt-absent deformation in the middle to lower crust

This chapter represents a manuscript draft that focuses on how different deformation mechanisms can produce similar crystallographic preferred orientations of amphibole grains. The chapter is written in a way that refers to methods described, and features shown in previous chapters. The plan for this chapter is for me to be the first author, with Sandra Piazolo as the co-author. I am in charge of writing the first draft of the manuscript, as well as conceptualization, sample preparation, EBSD and EPMA data analysis. Sandra Piazolo provided the melt-free samples from her collection, oversaw the conceptualization, and reviewed the first draft. The manuscript will be submitted to the *Journal of Structural Geology* soon after the thesis submission.

Abstract

Crystallographic preferred orientations are commonly used to derive deformation conditions and infer deformation mechanisms. In this study, we investigate four samples with amphibole revealing very similar crystallographic preferred orientations, even

though they crystallized under melt present and melt absent deformation condition. The samples are foliated amphibolites and diorite gneiss from the Akia terrane, Faeiringehavn terrane in SW Greenland and Northern Nagssugtoqidian Orogen of West Greenland. The crystallographic and shape preferred orientations of amphibole-plagioclase grains in both the melt-present and melt-absent samples are nearly identical, with only minor differences. Microstructures and crystallographic preferred orientation (CPO) data suggest that the amphibole grains are arranged with their long axis and [001] crystallographic direction oriented at a small angle to the foliation, accounting for the strong linear fabric observed for amphibole. Melt facilitates easy slip along grain boundaries and amphibole grains align by rigid body rotation. The characteristics of the melt-absent samples are consistent with amphibole CPO formation in response to dissolution precipitation creep as the main deformation mechanism. Support of this interpretation is provided by the presence of cuspate grain boundaries, a slight difference in mineral chemistry between the rim and core of amphibole grains and for amphibole little in-grain lattice distortions. Plagioclase and quartz grains lack significant sample scale CPO, implying that dislocation creep is limited, even though the phases show higher in-grain lattice distortion due to localized dislocation generation and movement. Hence, amphibole grains with strong alignment parallel to the foliation and similar CPO responses may suggest different deformation mechanism due to the presence or absence of melt and presence of aqueous fluid.

6.1 Introduction

Lower continental crust is, on average, more mafic in composition compared to the quartozofeldspathic upper continental crust. It is primarily comprised of plagioclase, amphibole, and pyroxene (Berger and Stünitz, 1996). Hence, understanding the deformation mechanism of these individual minerals may help to understand kinematics and dynamics of deformed lower crustal rocks (e.g., Cao et al., 2010; Imon et al., 2004). Lattice preferred orientation of anisotropic minerals, with amphibole being the most important phase in the lower crust, also contribute significantly to the seismic stratification and seismic anisotropy across the entire range of crustal depths (e.g., Mainprice et al., 2000; Tatham et al. 2010; Cao et al., 2010; Ji et al., 2015).

Depending on the temperature and strain rate, amphiboles can accommodate deformation by cataclastic flow, rigid body rotation, dislocation creep and diffusion creep

(e.g., Getsinger et al., 2013; Imon et al., 2004). At temperatures of greenschist facies, amphibole is deformed by brittle processes often in combination with metamorphic breakdown reactions (e.g., Brodie and Rutter, 1985; Stünitz 1993) whereas at higher pressure-temperature conditions crystal plastic deformation causes dislocation glide and subgrain formation in amphiboles (Hacker and Christie, 1990). Crystal plasticity of plagioclase is relatively well studied, where at high stresses and high temperature (>700 °C) it may significantly contribute to strain localization in the lower crust (e.g., Olsen and Kohlstedt, 1984; Svahnberg and Piazolo, 2010). In some cases, grain size reduction is significant enough to allow grain boundary sliding to occur (e.g., Svahnberg and Piazolo, 2010 and references therein). The presence of CPO is commonly interpreted as evidence of crystal plasticity, along with other microstructural indicators such as significant lattice distortion within grains identified by development of undulose extinction, and dynamic recrystalization (e.g., Hobbs et al., 1976; Wenk, 1985). Dislocation creep involving intracrystalline deformation and dislocation glide in the amphibole grains is only observed at high stresses and strain rates at temperatures from 450 to >650 °C (Rooney et al., 1970, 1975; Morrison-Smith 1976; Aspiroz et al., 2007; Pearce et al., 2011). In the case of dislocation creep the flow of the rock is characterized by a non-linear relationship between stress and strain rate (e.g., Ashby, 1985). Another significant deformation mechanism that may lead to CPO development is dissolution-precipitation creep (DPC), where in the presence of a fluid differential stress induces dissolution at high stress sites and precipitation at low stress sites leading to a change of shape of a rock volume (Rutter, 1976). Equant grain shape, grain indentions and truncations, grain flattening, strain shadows, and a lack of CPO are commonly cited signatures of DPC. Bons and Brok (2000) showed that the crystallographically controlled anisotropy in the rates of dissolution and precipitation during DPC can produce a CPO. Orientation dependent dissolution and/or growth is also observed in experimentally deformed albite aggregates by Heidelbach et al. (2000). CPOs are also reported in naturally deformed quartz rocks in which some form of DPC was the dominant deformation mechanism (Hippertt, 1994; Stallard and Shelley, 1995). In this case the associated flow law is characterized by a grain size sensitivity and a linear relationship between stress and strain rate (e.g., Rutter and Brodie, 1985).

Connectivity of melt network can also influence deformation mechanisms of the constituent mineral grains, and thus influence the inherent strength of the lower crust (e.g., Holyoke and Tullis, 2006). Rosenberg and Handy (2005) discovered a dramatic decrease in

strength of up to two orders of magnitude when transitioning from 'melt-free' rock to a rock with highly connected melt-filled channels. At low melt fractions (1-4 vol%), grain boundary migration and dislocation creep dominate whereas at slightly higher melt volume (<8 vol%) deformation grain boundary sliding (GBS) dominates (Dell'Angelo and Tullis, 1988; Sawyer, 1994, 1996; Walte et al., 2005). As a result, melt volume and connectivity can influence the deformation mechanisms of amphibole-plagioclase grains in the presence of melt. In naturally and experimentally deformed rocks, amphibole crystallographic preferred orientations (CPOs) typically have poles to the (100) plane forming a girdle parallel to foliation, whereas [001] is observed parallel to lineation. This CPO character is often attributed to dislocation creep (e.g., Svahnbert and Piazolo, 2010; Cao et al., 2010). However, it has been recognized that strong alignment in amphibole grains can produce by rigid body rotation within a weaker plagioclase matrix aided by an interconnected weak layer structure and high phase strength-contrast between amphibole and plagioclase (e.g., Baratoux et al., 2005; Aspiroz et al., 2007).

The short summary above shows that a strong amphibole CPO can be caused by various deformation mechanisms, resulting in different flow laws as well as microstructural characteristics. In this study, we examine and compare the microstructure, SPO, and internal deformation fabrics of four amphibole bearing samples with very similar CPO fabric patterns. A melt-present set from the Mesoarchean Akia terrane in SW Greenland is studied, as are melt-absent amphibolite samples from the Northern Nagssugtoqidian Orogen and Faeiringehavn terrane in Greenland. While it is clear that dislocation creep played only a minor role in accommodating strain in both sets, the mechanisms by which amphiboles achieved the observed high CPO are quite different. In melt-present samples, rigid body rotation enabled by slip along melt-present boundaries is the dominant deformation mechanism, whereas in melt-absent samples, dissolution precipitation creep is responsible for the strong amphibole alignment. For melt absent versus melt present samples, the resulting flow laws are expected to be close to Newtonian with and without grain size sensitivity creep.

6.2 Geological Setting

6.2.1 Melt present samples

The sample locations of amphibolite (SPI1338) and diorite-gneiss (SPI1311) are in an island (between 65.0° and 65.5°N) near to the Alanngua fjord, approximately 10 km from the mainland, in the western coastal region of the Akia terrane. The reader is referred to section 3.3, Chapter 3 for details on the geotectonic setting and previous work. The island itself shows supracrustal rocks dominated by amphibole and biotite-bearing gneisses, metapelitic-metapsammitic units, elongated bodies of amphibolite, alongside thick zones of diorite orthogneiss and TTG gneisses. The rock units outcropped as interlayered sequence parallel to each other for several kilometres (Fig. 4.1c in Chapter 4). Both SPI1338 and SPI1311 are medium to coarse grained rocks. The rocks are dark in colour, indurated, with leucocratic quartzo-feldspathic materials broadly concordant to the foliation. Amphibolite SPI1338 is collected from an isolated elongated body towards the western side of the island (Fig. 3.1a in Chapter 3). The outcrop of SPI1338 displays very few distinct quartzo-feldspathic domains (5-10 vol.%). In diorite gneiss SPI1311, highly elongated parallel thin aggregates of quartz grains (~12-15 vol.%) are observed denoting a higher degree of felsic-mafic segregation in response to the strain. Diorite gneiss sample SPI1311 is gathered near to the eastern boundary of the diorite gneiss (Fig. 4.1c in Chapter 4). In both the samples, elongated undeformed leucocratic materials parallel to the foliation imply melt present deformation.

6.2.2 Melt absent samples

Amphibolite sample (430643) is collected (location: 68°12’53’’N, 53°17’38’’ W) from a ~50 metre wide amphibolite dominated layer intercalated with quartzofeldspatic metasediments within the amphibolite/granulite facies transition zone in the Northern Nagssugtoqidian Orogen (map presented in Kangaatsiaq map sheet in the Fig. 2 of Piazolo et al., 2004). The region is part of the Palaeoproterozoic Nagssugtoqidian orogen, which formed as a result of a continent-continent collision between the North Atlantic Craton to the south and a continental mass to the north (Kalsbeek et al. 1987; Connolly et al. 2000; Van Gool et al. 2002a). The transitional zone occurs over a distance of 10 to 12 km where

mineral assemblages suggest P - T conditions of 650 ± 30 °C at 4-5 kbar in the amphibolite zone (Piazolo, 2002). Diorite gneiss (475768) is collected (location: 63°59’46’’N, 51° 22' 57" W) from an amphibole bearing gneiss covering large areas intercalated with bands of heterogeneous amphibolite typical for the area in Fæiringehavn terrane (~25-kilometre south-east to the Nuuk, map presented in Fig. 1 of Friend and Nutman, 2007). Multiple metamorphic events occurred in the Eoarchean Fæiringehavn terrane, resulting in granulite facies (Griffin et al., 1980; Friend and Nutman, 2005c). The supracrustal unit is composed of amphibolites that have relict early high-pressure assemblages of clinopyroxene + garnet + plagioclase + quartz ± hornblende that are commonly replaced by lower pressure assemblages (7-5 kbar) such as hornblende + plagioclase + quartz ± garnet (Friend and Nutman, 2007).

6.3 Methods of study

Samples are cut in the X-Z section of the kinematic reference frame where X-axis parallels the stretching direction and Z-axis denote pole to the foliation. The mineral abbreviations follow those suggested by Whitney and Evans (2010). For more information on petrography and BSE imaging (Fig. 6.1-6.4), see Section 4.3.2 in Chapter 4. Pressure temperature condition of the studied samples is determined from the chemical analyses of amphibole, plagioclase, and biotite grains using the following geothermobarometric expressions: a. Ti-in-amphibole geothermometer by Liao et. al. (2021) (uncertainty: ± 35 °C); b. Ti-in-biotite geothermometer by Henry et al. (2005); and c. amphibole-plagioclase geothermobarometers (Holland and Blundy, 1994 geothermometer with an uncertainty of ±40 °C, and Molina et al., 2015 geobarometer with an uncertainty of ±1.5 to 2.3 kbar). For amphibole-plagioclase thermobaromtery, amphibole-plagioclase pairs are chosen based on equilibrium textural evidence and analyses are made immediately adjacent to their straight grain boundaries. Holland and Blundy (1994) thermometer is used for a pressure range of 0.2-1 GPa, whereas Molina et al. (2015) geobarometer is used for a temperature window of 500-950°C. For more information on electron microprobe analysis and empirical thermobarometry, the reader is advised to refer to 3.5.2 and 3.5.3 sections in Chapter 3. EBSD orientation analyses are carried out using the methods described in Section 5.2.4 of Chapter 5. Furthermore, grain orientation for amphibole and plagioclase grains is calculated using a fitted ellipse and its long axis orientation. The maximum orientation spread, which

represents values of maximum misorientation, is used to depict the overall change in orientation in the grain (values of more than 50 quartz grains are taken into consideration). Mean orientation spread represents the average degree of orientation change in the grain. For comparing relative distortions inside the constituent mineral grains across studied samples, average maximum orientation spread/area and mean orientation spread/area are calculated. EBSD orientation data (presented as maps) with step sizes of 1µm and 10µm were used. The low resolution (10µm step size; Fig. AP6 – 2 in Appendix) maps were utilized to identify grain shape, size parameters and crystallographic preferred orientation (CPO) data. Targeted maps with high spatial resolution (1µm steps size) characterized detailed crystallographic investigations in plagioclase, quartz, and amphibole grains.

6.3.1 Signatures interpreted to indicated melt presence during deformation

Field evidence for former melt presence during deformation include – (i) continuous or discontinuous dyke and hydrofractures in the outcrop (Holness et al., 2005), (ii) magmatic foliations and shape preferred orientation of elongated crystals, and mafic schlieren (Vernon, 1986, 1987), (iii) strongly foliated and flattened enclaves, (iv) stromatic migmatite with strongly layered morphology involving coarse grained felsic materials (i.e, leucosome) (Park, 1983), (v) felsic minerals in shear bands and elongated cm-scale pockets, and (vi) shear zones with leucocratic material in the outcrop without sub-solidus deformation microstructures. The microstructural features of melt-present rocks include – (i) minerals with euhedral crystal faces (Platten, 1982), (ii) cuspate grain boundaries with low dihedral angles representing melt-pseudomorphs, (iii) string of beads texture denoting melt pseudomorphed grains (Holness, 2008), (iv) grains pseudomorphing melt films along grain boundaries or fractures (Walte, 2005; Holness, 2008; Vernon, 2011), (v) reaction rims and symplectites in response to melt-rock interaction (Daczko et al., 2016; Stuart et al., 2016, 2017), (vi) xenomorphic grains with similar crystallographic orientations suggesting a single grain branches in 3D (Daczko and Piazolo, 2022), and (vii) fine-grained, intergrown of multiphase aggregates having a concave shaped and occurring at grain triple junctions (Holness et al., 2011).

6.3.2 Signatures interpreted to indicate melt-absence during deformation

Common field features of melt-absent deformation include – (i) strongly developed regularly spaced planer foliation, (ii) a mylonitic rock with finer grain size relative to the adjacent rocks with compositional bandings (Hobbs et al., 1986; Passchier and Trouw, 2005), (iii) formation of new-fabric such as fold, lineation, and shear bands (Carreras et al., 2005) or deflection of planer elements into the high-strain zone, and (iv) microfolding and some asymmetric structures. Microstructural evidence of ductile deformation with the high-strain shear zones are – (i) bimodal grain size distribution with small grains forming the matrix of elongated grains which exhibit deformation lamellae or twins, (ii) undulose extinction and development of subgrains, (iii) deformation twins, micro-folding, core-mantle structures or mantles porphyroclasts where large grains are surrounded by small dynamically recrystallized grains, (iv) curved to highly irregular grain boundaries forming window and pinning structures (Jessel, 1987), (v) strong shape preferred or crystal preferred orientation (SPO and CPO) (Law, 1990), (vi) strongly distorted grains due to crystal plastic deformation or stronger minerals deforming in a brittle manner forming clasts in a ductile matrix (Hobbs et al., 1986; Tullis et al., 1982), and (vii) highly elongated quartz grains with very high aspect ratios (i.e., quartz ribbons).

6.4 Results

6.4.1 Melt present samples – general description

Amphibolite (SPI1338) consists of 47% amphibole, 24% plagioclase, 25% quartz, 1% biotite, 2% garnet, 0.5% clinopyroxene and 0.5% ilmenite (Fig. 6.1a-b; Tab. 6.1). Garnet grains occur as large porphyroblasts and are only visible along a felsic vein with large anhedral quartz grains and subhedral plagioclase grains along their sides (Fig. 6.1a-b). In contrast, the dioritic gneiss (SPI1311) has less amphibole and more plagioclase and a lack of garnet (Fig. 6.1c-d; Tab. 6.1). For the amphibolite (SPI13338) the general grain sizes of amphibole, biotite, plagioclase, quartz, garnet and clinopyroxene ranges between 0.2-0.8 mm, 0.05-0.1 mm, 0.5-0.8 mm, 0.25-0.4 mm, 0.3-0.5 mm, and 0.2-0.5 mm, respectively. Large plagioclase and quartz grains are up to 1.6-1.7 mm, and 3-4 mm, respectively. The dioritic gneiss (SPI1311) shows an overall range of slightly smaller grain sizes with grain

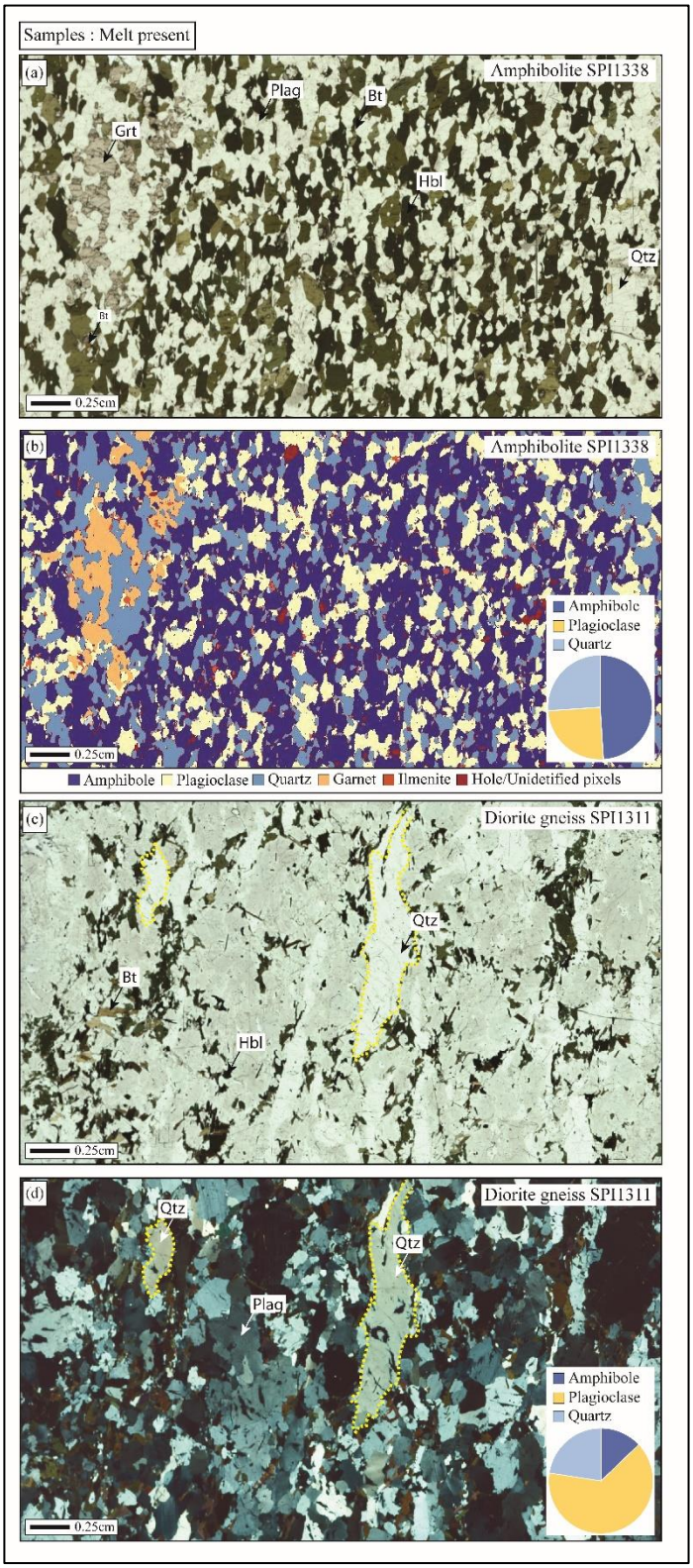

Figure 6.1 – Studied melt-present amphibolite and dioritic gneiss showing oriented amphibole-biotite grains forming well defined foliations; (a), (c) overview plane-polarized light (PPL), (c) phase distribution based on XMapTools using MicroXRF data; (d) cross polarized light (XPL).The modal percentages are presented in pi-charts.

		Melt-present samples		Melt-absent samples	
		Amphibolite (SPI1338)	Diorite gneiss (SPI1311)	Amphibolite (430643)	Amphibolite (475768)
Amphibole		Mode: 47%	Mode: 12%	Mode: 35%	Mode: 16%
Grain size	Avg.	0.2-0.8 mm	0.1-0.5 mm	0.3-1.2 mm	0.3-1 mm
	Max	2-2.5 mm	1.5-1.7 mm	2-2.3 mm	2.5-3 mm
Aspect ratio	Avg.	2-2.5	2-2.6	1.8-2.1	1.9
	Max	5-7	6-7	4-5	4.5-5
Avg. Grain OS*	MeanOS /Area	0.003°	0.01°	0.04°	0.03°
	MaxOS /Area	0.008°	0.04°	0.09°	0.07°
Plagioclase		Mode: 24%	Mode: 60%	Mode: 44%	Mode: 20%
Grain size	Avg.	0.5-0.8 mm	0.1-0.4 mm	0.1-0.7 mm	0.1-0.5 mm
	Max	1.2-1.4 mm	4-4.5 mm	1.5-1.7 mm	1-1.2 mm
Aspect ratio	Avg.	1.5-2	1.5-2	1-2	1.5-2
	Max	6-7	6-7	4-5	3-4
Avg. Grain OS*	MeanOS /Area	0.003°	0.02°	0.07°	0.03°
	MaxOS /Area	0.009°	0.05°	0.12°	0.07°
Quartz		Mode: 25%	Mode: 21%	Mode: 10%	Mode: 45%
Grain size	Avg.	0.2-0.4 mm	0.2-0.4mm	0.1-0.4 mm	0.2-0.6 mm
	Max	4-6 mm	6.5-7 mm	1-1.5 mm	1.2-1.5 mm
Aspect ratio	Avg.	1-2	1-2	1.9-2.2	1.5-2
	Max	3.5-4	6-7	2-3	3.5-4
Avg. Grain OS*	MeanOS /Area	0.007°	0.05°	0.06°	0.03°
	MaxOS /Area	0.01°	0.12°	0.15°	0.07°

Table 6.1 – Properties, derived from EBSD data set for constituent amphibole, plagioclase, and quartz grains in each rock sample. To quantify crystal bending, average grain orientation spread for any individual grain with a grain area of 100 μm^2 is measured. OS* = Orientation spread

sizes of amphibole, biotite, plagioclase, quartz, ilmenite, apatite, and magnetite ranging between 0.1-0.5 mm, 0.2-0.4 mm, 0.1-0.4 mm, 0.2-0.4 mm, 0.1-0.2 mm, 0.09-0.1mm, 0.05-0.4 mm, and 0.1-0.3 mm, respectively). Large plagioclase and quartz grains are up to 1.2-1.4 mm, and 4-6 mm, respectively. Texture and aspect ratio of quartz grains are slightly different in these two samples. In amphibolite SPI1338, large quartz grains (up to 1 mm) with high modal abundance are observed in two elongated felsic veins along with plagioclase and garnet (Fig. 6.1b). Medium to large quartz grains have aspect ratios ranging between 1-2. In comparison, large quartz grains with maximum aspect ratio of 3.5-4 are found in the diorite gneiss SPI1311 (Tab. 6.1). The large quartz grains in SPI1311 occur as extremely elongated, anhedral grains oriented parallel to the foliation (grains outlined in Fig. 6.1c-d and Fig. 6.3f, h) whereas large quartz grains in SPI1338 are subhedral to anhedral but lack highly elongated grain shape (Fig. 6.1a-b).

In both the samples, elongated amphibole-biotite grains are parallel to the foliation (Fig. 6.1a-d). Amphibole grains are inequigranular, subhedral to anhedral (Fig. 6.3a, e-f), with an average aspect ratio of 2-2.6. Grain boundaries of amphibole are irregular and often contain embayment (concave inward; green arrows in Fig. 6.3a, e-f). Large amphibole grains exhibit straight grain boundaries against quartz and plagioclase grains (orange arrows in Fig. 6.3a, f). Small amphibole grains with subhedral to anhedral grain shape are also found. In diorite gneiss (SPI1311), amphibole grains are robust but sometimes occur as fingers (Fig. 6.3e-f). Extremely elongated amphibole grains with aspect ratio varying between 5-7 are found. In both the samples amphibole grains show fractures but disintegrations of grains or dynamic recrystallization are not observed. Biotite grains are elongated intergrown with amphibole grains. Clinopyroxene grains are subhedral and are intensely replaced by the amphibole grains in the amphibolite SPI1338. Large plagioclase grains have characteristic polysynthetic twins and often display cuspate (embayed) grain boundaries. Minor bending of plagioclase twin lamellae and undulose extinction of quartz grains are also seen indicating crystal plastic deformation (black arrows in Fig. 6.3f). However, intense recrystallization of the plagioclase-quartz grains did not take place. Small and medium sized plagioclase grains are subhedral to anhedral (blue arrows, Fig. 6.3b-c). Aspect ratio of plagioclase grains in both the samples range between 1.5-2. In both the amphibolite (SPI1338) and diorite gneiss (SPI1311), Quartz grains are bimodal with subhedral to anhedral grain shape. Additionally, quartz grains also exhibit ubiquitous evidence of former melt presence. This is characterized by: A) large anhedral quartz grains with irregular grin boundaries (white arrows in Fig. 6.3c, f, h), B) Small interstitial quartz grains occurring along grain boundaries of other minerals (yellow arrows in Fig. 6.3b-d, f-h) representing ‘melt films’ (Sawyer, 1999; Rosenberg and Riller, 2000; Haslová et al., 2008a). The small elongated ‘melt films’ yield a higher aspect ratio of 3-3.5, C) large, elongated xenomorphic quartz grains with cuspate (concave outward; green arrows in Fig. 6.3a-c) and straight grain boundaries. Straight faceted grain boundaries are inferred to be due to crystal growth from melt (Vernon et al., 1990; Marchildon and Brown, 2003; Vernon, 2011), D) Fingers of quartz grains extending along plagioclase, biotite, and amphibole grain boundaries, with finely tapered ends, suggesting low dihedral angles of ~60° or less (red arrows in Fig. 6.3d, f) (Holness and Clemens, 1999; Rosenberg and Riller, 2000), and E) biotite grains projecting into other grains (Fig. 6.3a, h) indicating partial melting. The rounded grain shapes of plagioclase and amphibole grains against quartz grains may also form due to corrosion during partial melting or representing low-energy solid-liquid crystal shapes. Cuspate grain boundaries of quartz can be inferred

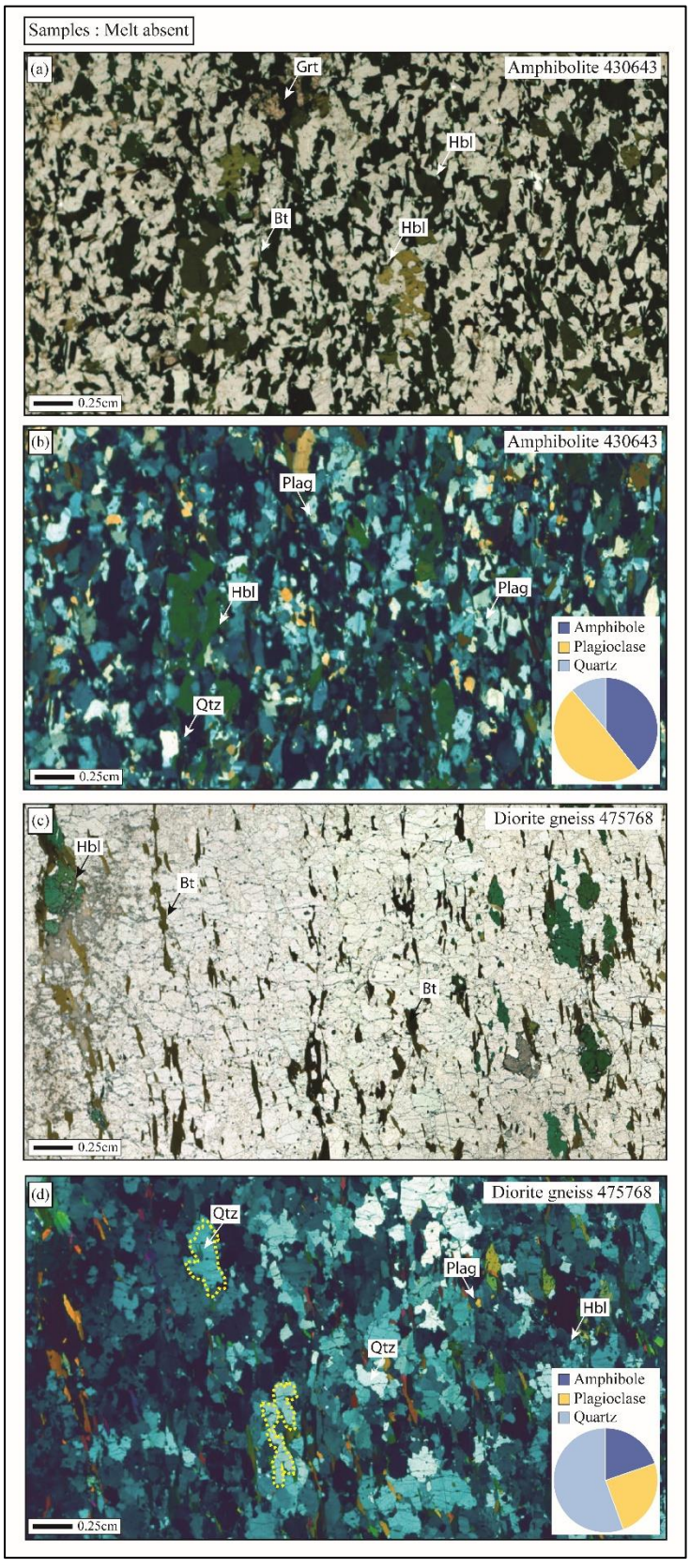

Figure 6.2 – Studied melt-absent amphibolite and dioritic gneiss showing oriented amphibole-biotite grains forming well defined foliations; (a), (c) overview plane-polarized light (PPL), and (b), (d) overview PPL images. The modal percentages are presented in pi-charts.

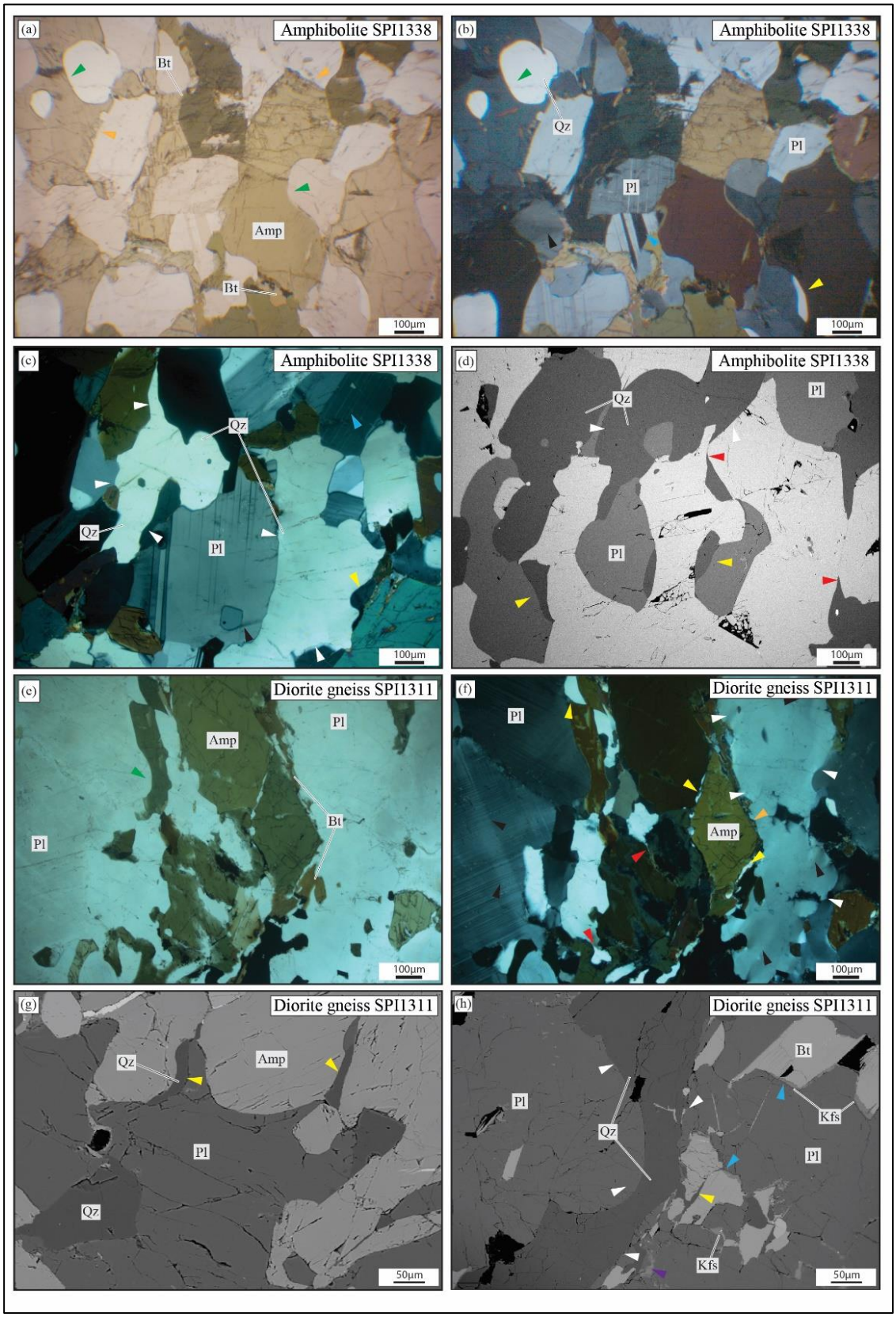

Figure 6.3 – Photomicrographs of amphibolite (SPI1338) and diorite gneiss (SPI1311) show microstructural features indicative of former presence of melt. (a-d) Close up PPL, XPL

photomicrographs and BSE images of SPI1338 exhibit cuspate grain boundaries of constituent minerals (green arrows), elongated quartz and plagioclase grains extending along grain boundaries of adjacent biotite-amphibole grains (yellow arrows), irregular quartz grains (white arrows), low dihedral angle (LDA) (red arrows) indicating last crystallizing phases. Amphibole grains have straight facets (orange arrows in 'a'). (e-h) Close up PPL, XPL photomicrographs and BSE images of SPI1311 reveal similar microstructures: elongated amphibole grains having cuspate (green arrow) or partial straight faceted boundaries (orange arrow), small xenomorphic, elongated interstitial quartz grains are along grain boundaries of amphibole and biotite (yellow arrows). Some grains are extended into other grains with low dihedral angle as low as <10° (red arrows). Large, elongated quartz grains with high aspect ratios and regular, curvy grain boundaries are parallel to the foliation (white arrows). K-feldspar grains are interstitial (purple arrow) along the biotite grain boundaries (blue arrows) with elongated quartz grains.

---

to represent former melt that has partly penetrated along grain boundaries and are surrounded by "embayed" amphibole and plagioclase grains inferred to have been partly melted (Marchildon and Brown, 2001; Holness, 2008; Sawyer, 1999). Diorite gneiss SPI1311, displays small interstitial K-feldspar grains at triple junctions (purple arrow, Fig. 6.3h) indicative of crystallization from melt. They often pseudomorph outer grain boundaries of biotite (blue arrows in Fig. 6.3h) and indicate partial melting. These observations point towards the existence of a grain boundary melt network in both the studied samples. In the diorite gneiss SPI1311, very small, recrystallized quartz grains occur locally as bulges along the grain boundaries of elongated quartz grains indicating minor dislocation creep (Fig. AP6 – 1a-b in Appendix). The recrystallized grains are identified as small grains with very little GROD angle (suggesting recrystallization) and are formed surrounding the parent grain (Grain A). Elongated precursor quartz gains also show a higher degree of grain reference orientation deviation (GROD), Grain B also develops dauphiné twins adjacent to its grain boundary (Fig. AP6 – 1c-d in Appendix). This also indicates that this rock has undergone minor solid-state deformation syn- or post melt crystallization. These features in the melt crystallized quartz grains of SPI1338 are not seen. Thus, along with highly elongated quartz grains parallel to foliation and existence of minor solid-state deformation features suggest that the diorite gneiss SPI1311 represents melt crystallization under relatively higher strain rate than observed for SPI1338. However, the groundmass is devoid of any intense recrystallization of quartz and plagioclase grains in both these samples (Fig. 6.3).

6.4.2 Melt-absent samples – general descriptions

Amphibole, plagioclase, biotite, and quartz are the primary phases in both the amphibolite (430643) and diorite gneiss (475768) samples. Amphibolite 430643 is a coarse-grained rock with 35% amphibole, 44% plagioclase, 10% quartz, 5% biotite, 2% garnet, 1.5% apatite, 1.5% magnetite, and 1% ilmenite (Fig. 6.2a-b; Tab. 6.1). Amphibole, plagioclase, quartz, biotite, and garnet grains have grain sies ranging from 0.3-1.2 mm, 0.1-0.7 mm, 0.1-0.4 mm, 0.25-0.4 mm, 0.3-0.7 mm, and 0.2-0.5 mm respectively. Large amphibole grains are 2-2.3 mm, while large plagioclase and quartz grains are up to 1.5-1.7 mm, and 1-1.5 mm, respectively. In comparison, diorite gneiss 475768 lacks garnet grains and has a lower modal abundance of amphibole and plagioclase grains (16% amphibole and 20% plagioclase) but a higher modal abundance of quartz and K-feldspar grains (45% quartz and 15% orthoclase) (Fig. 6.2c-d; Tab. 6.1). In contrast to high-strain amphibolite (475768), which exhibits alternate strong bandings of mafic and felsic layers, amphibolite (430643) exhibits alternate semi-parallel narrow bands predominantly with dark amphibole + biotite and light plagioclase. Mineral grains in diorite gneiss 475768 have unimodal grain size distributions, with average grain sizes that are very similar to amphibolite 430643 (grain sizes ranging between 0.3-1 mm, 0.1-0.5 mm, 0.2-0.6 mm, 0.3-0.7 mm, and 0.1-0.6 mm, for amphibole, plagioclase, quartz, biotite, and K-feldspar respectively). Large plagioclase and quartz grains are up to 1.2 mm, and 1.5 mm in size, respectively, while amphibole grains are as large as 2.5-3 mm. In both the samples, small amphibole, plagioclase, and quartz grains range in grain size from 0.02 to 0.08 mm. Similarly, to the melt-present sample set, only small quartz grains (0.3-0.4 mm) in amphibolite (430643) exhibit high aspect ratio, whereas large quartz grains (1.5-2 mm in size) in diorite gneiss (475768) exhibit very high aspect ratio (the grains are marked in Fig. 6.2d, and Fig. 6.4d).

In both samples, elongated amphibole-biotite grains are arranged parallel to the foliation (Fig. 6.2a-d). Amphibole grains are inequigranular and subhedral, with aspect ratios of 1.6-2 (Tab. 6.1). For highly elongated grains, the maximum aspect ratio of amphibole grains can reach 4-5 (Tab. 6.1). Amphibole grains in both the samples are prismatic with straight boundaries (Fig. 6.4a, c), they also display embayments against surrounding plagioclase-quartz grains (green arrows, Fig. 6.4a-c). Plagioclase and quartz inclusions are also found in amphibole grains. Biotite grains are large (up to 3 mm in size) and are typically found with amphibole grains (Fig. 6.4a, c). They have straight grain

boundaries and frequently extend into the minerals around them. Biotite grains projecting into the orthoclase and quartz grains are interpreted as partial inclusions (Fig. 6.4b, d). Amphibolite (430643) has quartz + plagioclase K-feldspar grains and a granoblastic polygon texture, whereas diorite gneiss (475768) has a granoblastic interlobate texture. Plagioclase grains are subhedral, and mostly occur in patches with regular grain boundaries. Plagioclase

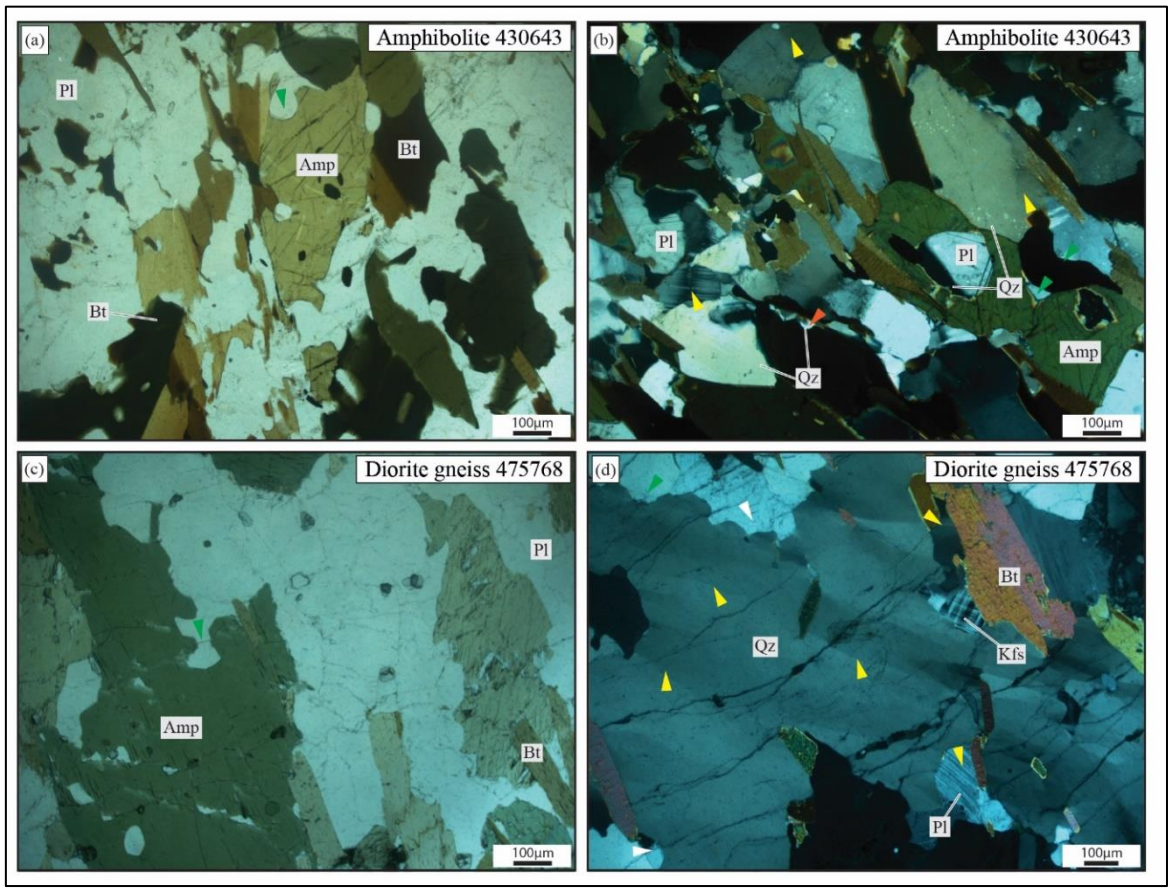

Figure 6.4 – Photomicrographs of amphibolite (430643) and diorite gneiss (475768) lack microstructural features indicative of former melt. (a-b) Close up PPL and XPL images in 430643 exhibit elongated amphibole grains with straight and cuspate grain boundaries (green arrows), and minor deformation in plagioclase and quartz (yellow arrows). Small quartz grains at the interstices lack elongated grain shapes and low dihedral angles (LDA). (c-d) PPL and XPL images in 475768 display elongated amphibole grains with irregular grain boundaries, and plagioclase-quartz grains with cuspate grain boundaries (green arrows). Plagioclase-quartz grains are subhedral and reveal intracrystalline deformation (yellow arrows). Highly irregular, elongated quartz grains with serrated grain boundaries (white arrows) parallel to the foliation indicate grain boundary migration (GBM).

---

grains with lobate boundaries are also found (green arrows in Fig. 6.4b, d). Minor bending is also observed in twin lamellae (yellow arrows in Fig. 6.4b, d). Plagioclase has an average aspect ratio of 1.7-2 (Tab. 6.1), with highly elongated grains having an aspect ratio of 3-4. The quartz-plagioclase grain boundaries range from smooth to broadly indented. Straight facets to irregular lobate shaped grain boundaries are also found in the inequigranular quartz

grains (Fig. 6.4b). Small quartz grains are also discovered in the interstitial spaces between grains in amphibolite sample 430643 (red arrow in Fig. 6.4b). They lack the elongated xenomorphic grain shape and low dihedral angles seen in melt-present samples. Furthermore, the quartz grains have an ameboid grain shape with extremely irregular grain boundaries (white arrows in Fig. 6.4d). Quartz grains exhibit strong undulose extinction (yellow arrows in Fig. 6.4b, d), but there is no evidence of recrystallization. Despite the presence of cuspate grain boundaries in quartz-plagioclase grains, the indentations are interpreted to be the result of partial inclusion of one mineral in another during simultaneous solid-state metamorphic growth of primary grains. This is also supported by the absence of any low-dihedral angle in grains exhibiting cuspate grain boundaries, as would be expected in the case of partial melting. Interstitial quartz grains can form in metamorphic rocks as a result of nucleation rate, growth rate, and mineral proportions that are independent of melting. In the presence of melt, crystallisation would have formed interstitial grains with euhedral grain shapes or elongated grains along grain boundaries, which were not identified here. Furthermore, no partial melting of amphibole-biotite grains is observed. Hence, neither of these rocks has undergone any partial melting after crystallization. Undulose extinction in quartz, minor bending in plagioclase twin lamellae, and microscopically visible microcline twinning indicate minor deformation and solid-state readjustments (Fig. 6.4b, d).

6.4.3 Shape preferred orientation

The SPO types of all the samples are very similar. In the melt-present samples, the preferred orientation of the long axes of all amphibole grains in XZ sections show a strong maximum ~10° inclined to the foliation (Fig. 6.4a, c). Plagioclase grains exhibit a relatively strong SPO pattern, but it is less intense than that of amphibole grains (Fig. 6.4b, d). Plagioclase grains in diorite gneiss (SPI1311) also exhibit a strong maximum ~20° inclined to the foliation as well as less pronounced differently orientated peaks (Fig. 6.4d), whereas plagioclase grains in amphibolite (SPI1338) are comparatively well aligned. Long axes of the amphibole grains show strong maximum oriented parallel to the lineation with an inclination of ~5° in amphibolite 430643 (Fig. 6.5e). Amphibole in diorite gneiss (457786) exhibit highest SPO of amphibole grains with an offset of ~10-15° (Fig. 6.5g). Plagioclase grains also record a similar shape preferred orientation and exhibit a similar intensity as observed in the melt-present samples (Fig. 6.5f, h).

6.4.4 Mineral chemistry

All the samples have in general similar amphibole and biotite composition (Fig. 6.6); however, some differences are highlighted here. $(Na+K)_A$ in amphibole shows a continuous decrease from 0.68-0.71 pfu in the core to 0.62-0.65 pfu in the rim in melt-present

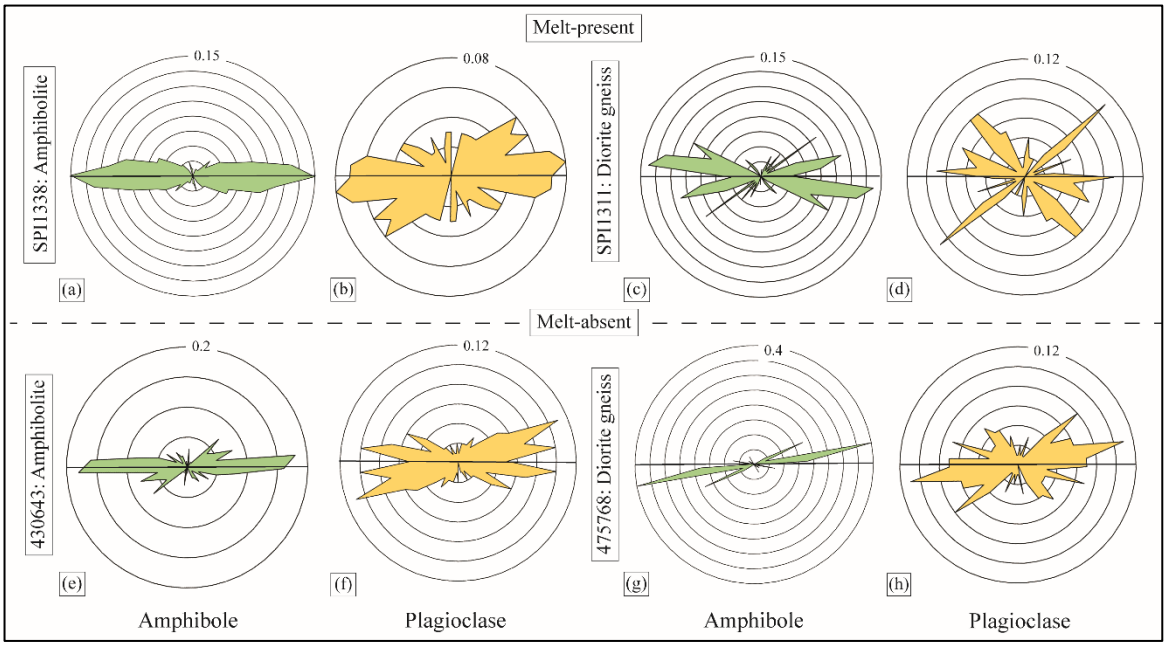

Figure 6.5 – (a-h) Plot of grain shape preferred orientation (SPO) of minerals in rose diagrams for individual rock types. Dark lines represent foliation directions.

amphibolite (SPI1338), whereas in the diorite gneiss (SPI1311) an increasing trend from 0.52-0.56 pfu in the core to 0.54-0.58 pfu in the rim is observed (Tab. 6.2). In melt-absent amphibolite (430643), amphibole grains yield $(Na+K)_A$ values of 0.62-0.64 pfu in the rim and 0.64-0.68 pfu in the core, whereas diorite gneiss (475768) exhibit $(Na+K)_A$ of 0.52-0.62 pfu in the rim and 0.60-0.68 pfu in the core (Tab. 6.2). In the melt-present samples biotite grains are magnesio-biotite in composition with Mg# values of 0.51-0.58 and Ti content per formula unit (pfu) fall within 0.41 and 0.53 pfu (Fig. 6.6b; Tab. 6.2). In melt-absent amphibolite (430643), biotite grains are ferrobiotite in composition with Mg# varying between 0.38-0.39, and the Ti content ranges between 0.56-0.61 p.f.u (Fig. 6.6b; Tab. 6.2). Biotite in melt-absent diorite gneiss (475768) have the lowest Mg# (varying between 0.46-0.47), and the lowest Ti content (ranges between 0.26-0.28 p.f.u) (Fig. 6.6b; Tab. 6.2). The plagioclase grains in melt-present amphibolite (SPI1338) have an albite content

[Na/(Na+Ca)] varying between 48-55% with minor orthoclase (~1.5-1.7 mol%) (Fig. 6.6c; Tab. 6.2). In the melt-present diorite gneiss (SPI1311) and melt-absent samples (430643 and 475768), albite content [Na/(Na+Ca)] in the plagioclase are very similar and vary between 65-80% (Fig. 6.6c; Tab. 6.2). Plagioclase grains in all the studied samples do not show any chemical zoning between the core and rim compositions. In melt-present diorite gneiss (SPI1311) and melt-absent diorite gneiss (475768), K-feldspar have similar composition with orthoclase content [K/(K+Na+Ca)] of 92-97% (Fig. 6.6d).

6.4.5 Pressure-temperature estimates

Henry et al. (2005) proposed Ti-in-biotite geothermometer with the calibrated ranges of X_{Mg} = 0.275-1.000, and Ti = 0.04-0.60 pfu in biotite, for a temperature window of 480-800 °C. Biotite grains in all the studied samples fall within this range. Ti-in-biotite thermometer yields temperature estimates of 725±8°C, and 740±8°C for melt-present SPI1338 and SPI1311, respectively (Fig. 6.6e; Tab. 6.3). Similarly, melt-absent amphibolite (430643) records temperature of 741±3°C (Fig. 6.6e), while low Ti-biotite in melt-absent diorite gneiss (475768) yields a relatively low temperature of 636±5°C (Fig. 6.6e; Tab. 6.3). Ti-in-amphibole thermometer (Liao et al., 2021) is commonly applied for rocks in upper-amphibolite to granulite facies condition, and the thermometer is only temperature dependent with the presence of Ti-phases (rutile, ilmenite or titanite). Hence, this thermometer can be applied with confidence on all the studied rocks. Temperature values of 821±18°C for melt-present amphibolite (SPI1338), 789±10°C for melt-present diorite gneiss (SPI1311), 813±23°C for melt-absent amphibolite (430643), and 665±14°C for diorite gneiss (475768) are calculated using this thermometer (Fig. 6.6e; Tab. 6.3). Amphibole-plagioclase geothermometer yield temperatures ranging between 747-763°C at 0.2 GPa and 802-826°C at 1 GPa in melt-present amphibolite (SPI1338). Similarly, temperature values are measured for other samples (temperature estimates at 1 GPa are provided in Tab. 6.3). Pressure values in melt-present amphibolite (SPI1338) range between 0.10-0.22 at 500°C and 0.8-0.9 GPa at 950°C (pressure estimates at 950°C are provided in Tab. 6.3). Next, calculated pressure values are used in conjunction with temperature estimates to obtain intersections in the P-T space that yield pressure-temperature conditions of 770-805°C at 0.52-0.69 GPa and 665-680°C at 0.62-0.71 GPa for melt-present amphibolite (SPI1338) and diorite gneiss (SPI1311) (Fig. 6.7). Similarly, melt-absent amphibolite (430643) and diorite gneiss (475768) have P-T conditions of 685-750°C at 0.56-0.84 GPa, and 615°C at 0.66 GPa

	Amphibolite SPI1338				Diorite gneiss SPI1311				
Mineral	Amp	Amp	Plag	Bt	Amp	Amp	Plag	Kfs	Bt
Position	Core	Rim			Core	Rim			
SiO_2	40.61	41.06	55.82	35.42	43.55	43.86	62.13	64.02	36.64
TiO_2	2.04	2.07	0	4.13	1.52	1.55	0	0	4.56
Al_2O_3	12.35	12.31	27.79	15.31	10.01	10.23	23.88	18.78	15.41
FeO(tot)	19.82	19.49	0	19.97	16.74	16.75	0.09	0	16.72
MnO	0.18	0.19	0	0.1	0.44	0.45	0	0	0.11
MgO	7.74	7.93	0	10.68	10.37	10.54	0	0	11.24
CaO	11.49	11.39	9.78	0	11.27	11.51	5.01	0.03	0
Na_2O	1.42	1.38	6.06	0	1.3	1.4	8.58	0.51	0
K_2O	1.58	1.51	0.26	9.74	1.18	1.21	0.31	15.56	9.77
Total	97.23	97.33	99.71	95.35	96.38	97.49	99.98	98.91	94.47
No of O	24	24	8	22	24	24	8	8	22
Si	6.28	6.19	2.52	5.38	6.61	6.59	2.75	2.98	5.53
Ti	0.23	0.23	0	0.47	0.17	0.18	0	0	0.52
Al	2.23	2.32	1.48	2.74	1.79	1.81	1.25	1.03	2.74
Fe(tot)	2.47	2.49	0	2.54	2.12	2.07	0	0	2.11
Mn	0.03	0.03	0	0.01	0.06	0.06	0	0	0.01
Mg	1.86	1.81	0	2.42	2.35	2.36	0	0	2.53
Ca	1.86	1.89	0.47	0	1.83	1.85	0.24	0	0
Na	0.39	0.45	0.53	0	0.38	0.41	0.74	0.05	0
K	0.31	0.33	0.02	1.89	0.23	0.23	0.02	0.92	1.88
Total	15.65	15.71	5.02	15.45	15.54	15.55	5	4.99	15.31
Mg#	0.45	0.44	0	0	0.55	0.55	0	0	0.57
Ti	0.23	0.23	0	0.23	0.17	0.18	0	0	0.52
Ab			51.9				74.3	4.8	
Or			0.02				1.7	95	

	Amphibolite 430643				Diorite gneiss 475768				
Mineral	Amp	Amp	Plag	Bt	Amp	Amp	Plag	Kfs	Bt
Position	Core	Rim			Core	Rim			
SiO_2	40.88	39.84	59.5	34.62	42.00	43.46	62.86	65.04	36.21
TiO_2	2.04	1.61	0	4.79	0.87	0.63	0	0	2.35
Al_2O_3	11.67	12.92	25.25	14.06	10.4	10.24	23.08	18.47	14.95
FeO(tot)	22.31	22.06	0.11	24.02	20.63	20.07	0.05	0	21.51
MnO	0.44	0.42	0	0.16	0.43	0.41	0	0	0.25
MgO	6.51	5.97	0	7.72	7.75	8.03	0	0	9.66
CaO	11.2	11.36	7.23	0	11.26	11.72	4.42	0.01	0
Na_2O	1.54	1.28	7.82	0.01	1.58	1.12	9.43	0.53	0.1
K_2O	1.37	1.59	0.14	9.51	1.39	1.2	0.09	15.76	9.44
Total	97.96	97.05	100.05	94.89	96.31	96.88	99.93	99.81	94.47
No of O	24	24	8	22	24	24	8	8	22
Si	6.31	6.19	2.66	5.4	6.51	6.64	2.79	3	5.57
Ti	0.24	0.19	0	0.56	0.1	0.07	0	0	0.27
Al	2.12	2.37	1.33	2.58	1.9	1.85	1.21	1	2.71
Fe(tot)	2.88	2.87	0	3.13	2.67	2.57	0	0	2.77
Mn	0.06	0.06	0	0.02	0.06	0.04	0	0	0.03
Mg	1.5	1.38	0	1.79	1.79	1.83	0	0	2.22
Ca	1.85	1.89	0.35	0	1.87	1.92	0.21	0	0
Na	0.46	0.39	0.68	0	0.48	0.33	0.81	0.05	0.03
K	0.27	0.32	0.01	1.89	0.28	0.23	0.01	0.93	1.85
Total	15.69	15.66	5.03	15.37	15.66	15.48	5.03	4.98	15.45
Mg#	0.36	0.35		0.39	0.42	0.44			0.47
Ti	0.24	0.19		0.56	0.1	0.07			0.27
Ab			65.7				79	4.9	
Or			1.7				0.5	95.1	

Table 6.2 - Mineral chemistry data of amphibole (Amp), plagioclase (Plag), K-feldspar (Kfs), and biotite (Bt) for four studied samples. Modal proportions in the host are shown for each mineral. Compositions shown here are highlighted in Tab. Ap.2.3-Ap.2.3.Analyses were rejected for totals outside of 98.0-101.0% for feldspars and below 94% for hornblende and biotite.

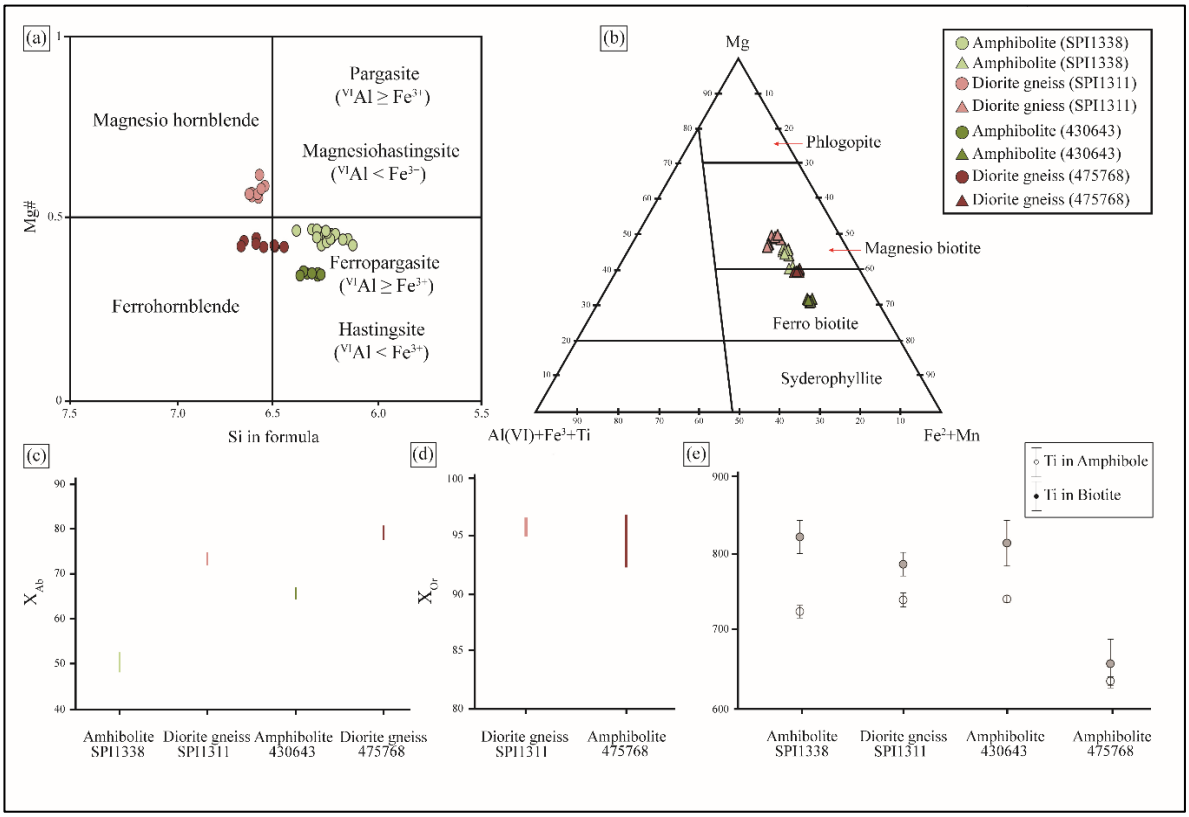

Figure 6.6 – Mineral major element compositions in the studied samples. (a) Mg# vs. Si in amphibole show very similar compositions across the studied samples. (b) Biotite end member plots (following Foster, 1960 and Sepidbar et al., 2017) exhibit homogeneous composition for melt-present amphibolite (SPI1338), diorite gneiss (SPI1311), and melt-absent diorite gneiss (475768). Melt-absent amphibolite (430643) has biotite with ferrobiotite composition. (c-d) Albite content in plagioclase and orthoclase content in K-feldspar in all the studied samples. X_{Ab} in plagioclase record variable compositions. (e) Ti-in-biotite (following Henry et al., 2005) for the studied samples yield average temperature estimates of 725°C, 740°C, 741°C and 636°C. Ti-in-amphibole (following Liao et al., 2021) thermometers exhibit temperature values of 821°C, 789°C, 813°C, and 665°C for melt-present amphibolite (SPI1338), diorite gneiss (SPI1311), melt-absent amphibolite (430643) and diorite gneiss (475768), respectively.

(Fig. 6.7). The low measured temperature is consistent with the lack of melt microstructures in these samples (Fig. 6.4). The P-T estimate confirms previous observation made by Piazolo (2002). Temperature estimates derived from amphibole-plagioclase thermometers are comparable to those derived from Ti-in-biotite thermometers, whereas Ti-in-amphibole thermometers produce slightly higher values (Tab. 6.3).

6.4.6 Quantitative orientation analysis using EBSD

Crystallographic preferred orientation (CPO)

Melt-present samples

In the melt-present amphibolite (SPI1338), amphibole CPO exhibits a girdle of poles to (100) and (010) planes oriented subnormal to the shear plane (XY-pole figure section), whereas the [001] axis shows a strong maximum parallel to the shear direction (X axis) (Fig. 6.8a). The amphibole M-index is 0.18. When the plagioclase CPO is considered alongside the amphibole, the maxima are extremely weaker with poles to (100) and (010) randomly oriented, and poles to (001) forming a very weak girdle normal to the shear direction (Fig. 6.8b). The plagioclase M-index is 0.21. Quartz grains do not exhibit any characteristic CPO as supported by close to zero M-index value of 0.13 (Fig. 6.8c). In the melt-present diorite gneiss (SPI1311), amphibole CPO exhibits very similar fabric to the amphibolite (SPI1338); with poles to (100) planes oriented normal to the shear plane, and the [001] axes forming girdle subparallel to the shear direction (Fig. 6.8d). However, compared to amphibolite SPI1338, poles to (100) planes show a stronger maximum close to the 'Z' direction and [001] form a relatively weaker girdle subparallel to the shear plane in the diorite gneiss

Geothermobarometry

Sample No.	T(L) (in °C)	T(H) (in °C)	T(HB) (in °C)	P(M) (in GPa)
Amphibolite (SPI1338)	821±18	725±8	802-826	0.8-0.9
Diorite gneiss (SPI1311)	789±10	740±8	636-698	1.1-1.3
Amphibolite (430643)	813±23	741±3	715-758	1.06
Diorite gneiss (475768)	665±14	636±5	636	12.4-12.6

Table 6.3 - P-T results of the studied samples calculated using conventional geothermobarometers. T(L): temperature estimates using Ti-in-amphibole thermometer following Liao et al. (2021); T(H): temperature estimates using Ti-in-biotite thermometer by Henry et al. (2005); T(HB): temperature estimates at 1 GPa using hornblende-plagioclase thermometer following Holland and Blundy (1994); P(M): pressure estimates at 950 °C using hornblende-plagioclase barometer following Molina et al. (2015).

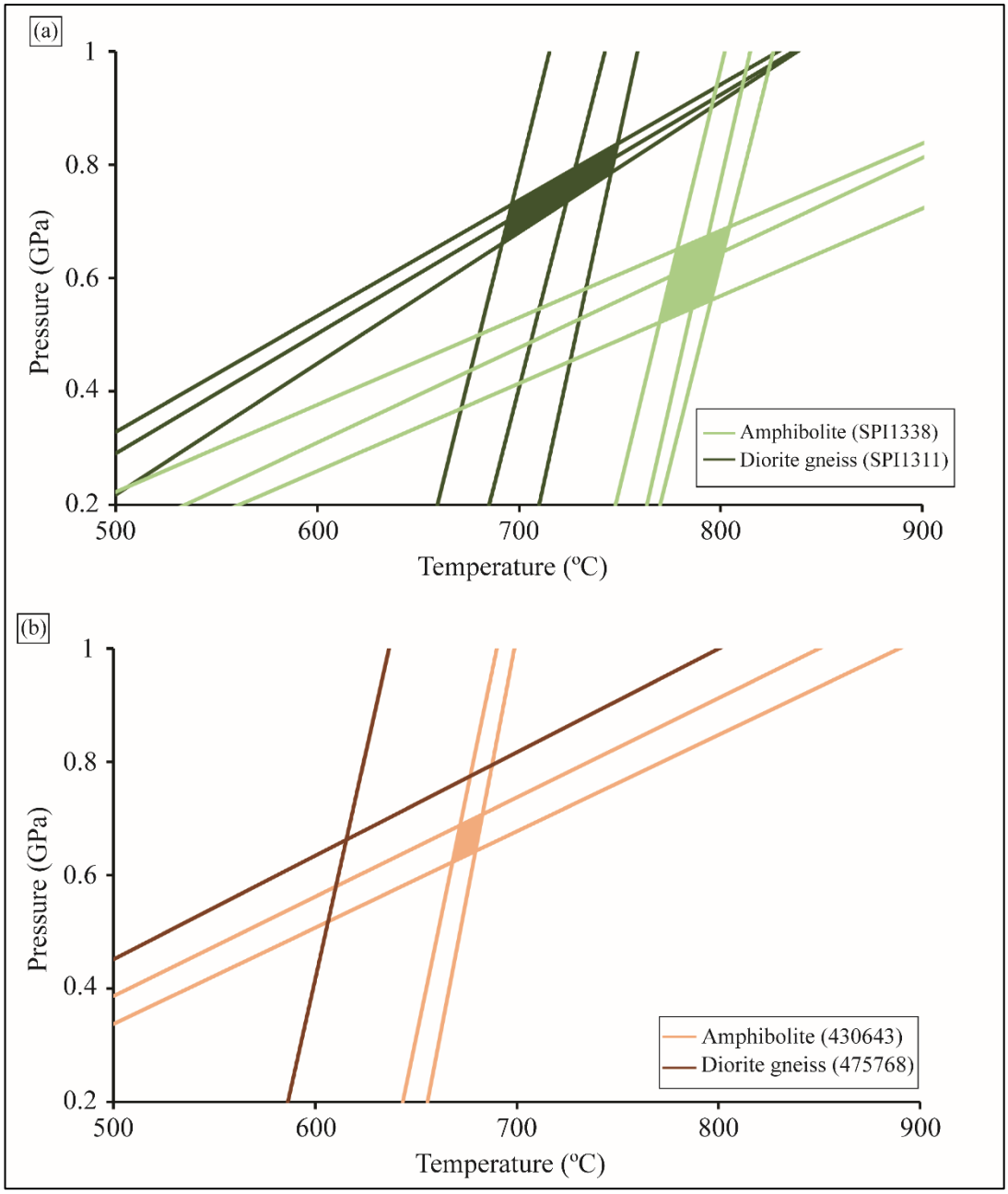

Figure 6.7 – Plagioclase-amphibole geothermobarometers reveal P-T ranges for the studied samples

SPI1311 (Fig. 6.8d). The amphibole M-index is 0.5. Similar to the amphibolite (SPI1338), plagioclase grains show disordered CPO, strongly dominated by few grain orientations (Fig. 6.8e). Quartz CPO is also very weak with poles to (0001) plane oriented close to the stretching direction while poles to (10-10) and (10-20) planes show a weak girdle normal to the shear plane (Fig. 6.8f). Quartz M-index is 0.4.

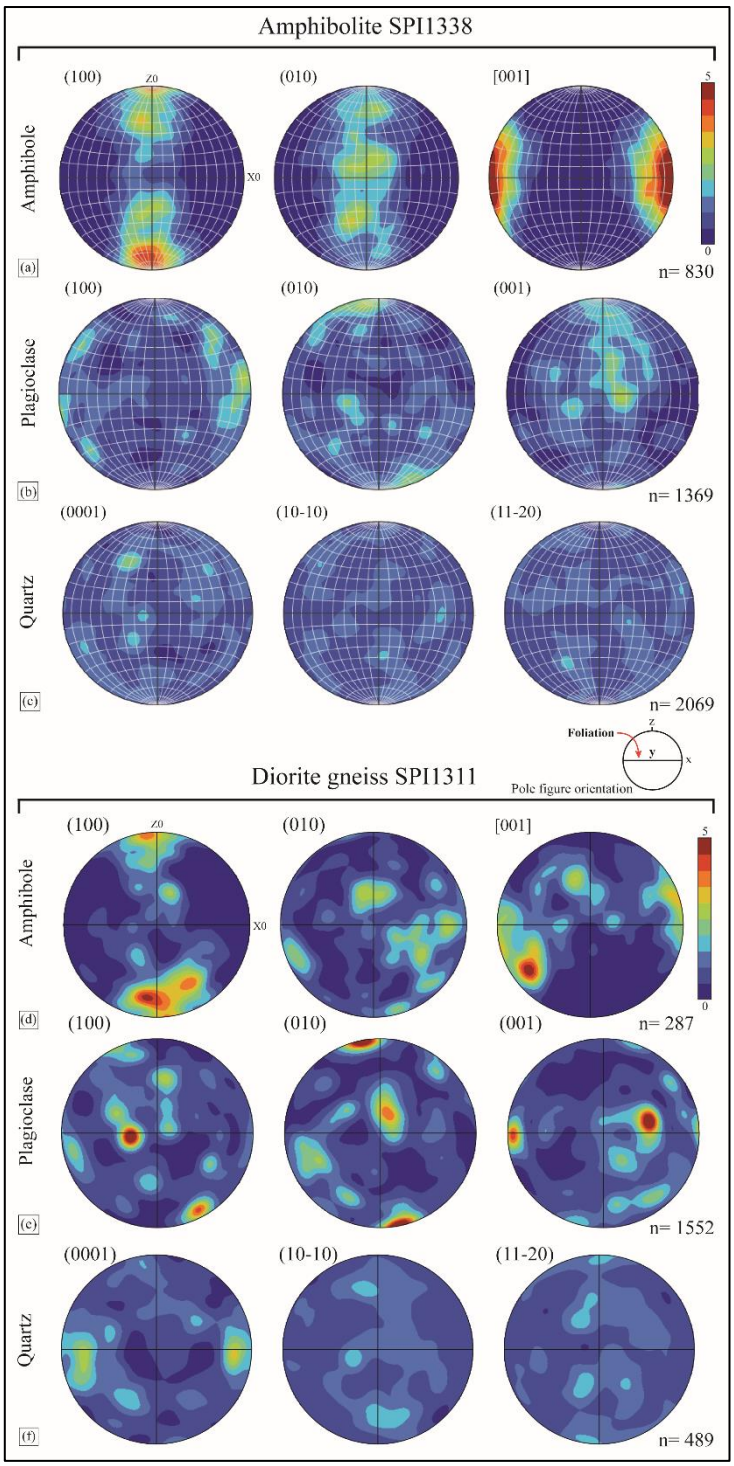

Figure 6.8 – Pole figure crystallographic orientations for melt present samples (one point per grain). Here, n is the number of grains analyzed.

Melt-absent samples

In the melt-absent amphibolite (430643) and diorite gneiss (475768), similar to the melt-present samples, amphibole show a strong CPO with (100) poles aligned normal to the

foliation (XY-pole figure section), and [001] axes aligned sub to the shear direction (X-direction) (Fig. 6.9a, d). The amphibole M-index is 0.2 and 0.5 in melt-absent amphibolite (430643) and diorite gneiss (475768), respectively. Similar to melt-present samples, the

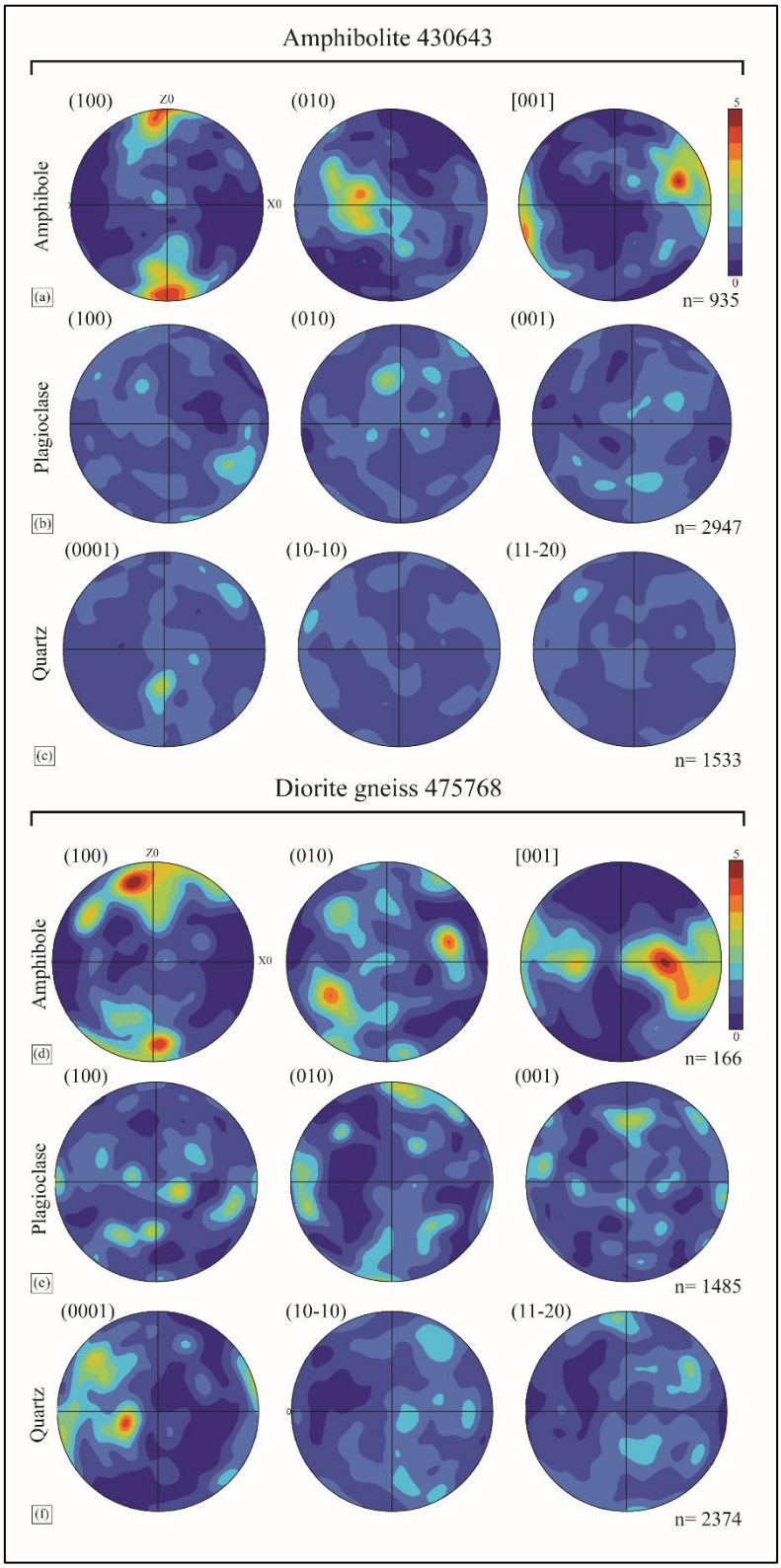

Figure 6.9 – Pole figures of crystallographic orientation (one point per grain) for melt-absent samples. Here, n is the number of grains analyzed.

plagioclase CPOs in melt-absent amphibolite (430643) and diorite gneiss (475768) are random with poles to (100), (010), and (001) randomly oriented (Fig. 6.9b, e). The plagioclase M-index is 0.1 and 0.4 in the melt-absent amphibolite (430643) and diorite gneiss (475768), respectively. Similarly, quartz grains also do not exhibit any characteristic CPO in both the samples (Fig. 6.9c, f). However, poles to (0001) form a weak girdle normal to the shear plane in the diorite gneiss (475768) (Fig. 6.9f). Quartz grains have M-index values of 0.4 and 0.1 in amphibolite (430643) and diorite gneiss (475768), respectively.

Inter- and intragrain characteristics

Melt-present samples

Misorientation angle distribution (MAD) of the studied samples (Fig. 6.10) display very low frequency of MAD at low misorientation angle for amphibole, plagioclase, and quartz grains in the melt-present SPI1338 (Fig. 6.10a-c). In comparison, relative frequencies of neighbour pair MADs for amphibole and quartz grains increase by six times in the diorite gneiss (SPI1311) even though plagioclase exhibit negligible values (Fig. 6.10f-h). Hence, dislocation creep is found to be active only in the amphibole and quartz grains in melt-present diorite gneiss (SPI1311). However, the misorientation axes-angle pair for amphibole subgrains (2-10°) record development of misorientation axes with a maximum around [010] and another weak clustering around <104> in the melt-present SPI1338 (Fig. 6.10d). In comparison, diorite gneiss SPI1311A exhibits [010] crystallographic direction and <214> as the dominant rotational axes for the small misorientation angle (i.e., 2-10°) in amphibole (Fig. 6.10j). Similarly, even though plagioclase do not show development of subgrain boundaries (Fig. 6.10b, g), the misorientation axes for plagioclase subgrains correspond to rotation around the twin axis [100] in both the samples, and an additional weak clustering close to [001] axis in diorite gneiss SPI1311. The misorientation axes for quartz subgrains are strongly oriented around [001] direction in both the samples (Fig. 6.10e, j). Maximum orientation spread of the constituent minerals reaches up to 20.5° in the diorite gneiss (SPI1311), whereas amphibolite (SPI1338) exhibits a maximum value of 16.5° (Fig. 6.10d, i). It should be noted that this includes very large grains (in the order of 2-3 mm). In the melt-present amphibolite (SPI1338) average mean orientation spread for plagioclase, amphibole, and quartz grains with 100 μm^2 grain area are 0.003°, 0.003°, and 0.006°, respectively. In the diorite gneiss (SPI1311), average mean orientation spread for grains with

100 µm^2 grain area exhibit ten times higher values of 0.02°, 0.106°, and 0.051°, for plagioclase, amphibole, and quartz, respectively (Tab. 6.1). Values of maximum orientation spread/area also exhibit very similar results with diorite gneiss having higher values than amphibolite (Tab. 6.1).

High resolution targeted EBSD maps in melt-present amphibolite (SPI1338) (Fig. 6.11), with misorientation profile ('A-B' profile in Fig. 6.11a), across a quartz grain, shows highest cumulative change in crystal orientation up to 4° associated with subgrain boundaries (Fig. 6.11b). All the other minerals show very little change (<1°) (Fig. 6.11a-b). This is also supported by GROD angle map of plagioclase where local misorientations increase only to 3-4° towards the edge of the grains and are mostly associated with twin boundaries (Fig. 6.11c). Amphibole show local misorientation of only ~1-2° in the GROD

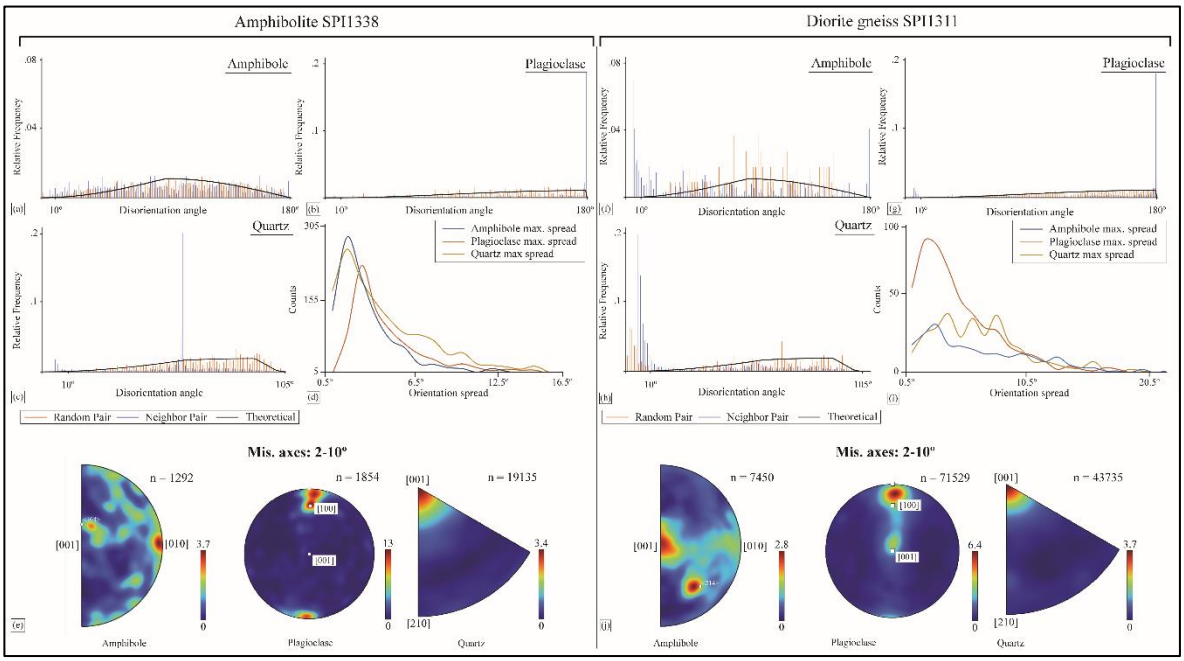

Figure 6.10 – Misorientation angle distribution (MAD) and misorientation axis-angle pair in the melt-present samples. MAD between neighbour pair (blue) and random pair (orange) of: amphibole (shown in 'a', and 'f'), plagioclase (shown in 'b', and 'g'), and quartz ('c', and 'h'). The uniform (black) curve corresponds to the theoretical misorientation distribution for randomly oriented grains. Note for the low angle interval (<10°), the MAD of amphibole grains has small values in the diorite gneiss (SPI1311). Amphibole and plagioclase lack MAD at the low-angle interval in the amphibolite (SPI1338). Maximum orientation spread of the constituent mineral are also provided (in 'd' and 'i'). ('e' and 'j') Plot of misorientation-axis data for low angle (2-10°) internal sub-grain boundaries shown in the crystallographic reference frame. Note that the misorientation axes of the amphibole grains in the amphibolite (SPI1338) and diorite gneiss (SPI1311) are oriented differently.

angle map (Fig. 6.11d). The GND density map also does not correspond to the local misorientation observed in GROD angle map for plagioclase and amphibole grains (Fig. 6.11e). GND density calculation from the large maps indicate the maximum GND density value of $0.05x10^{14}m^{-2}$ for both plagioclase and amphibole (Fig. AP6 – 3 in Appendix). Similar analyses with the diorite gneiss (SPI1311) exhibits highest cumulative change in crystal orientation varying between 2-8° in the plagioclase grains ('A-B' and 'C-D' profiles in Fig. 6.11f-g). This is also supported by the GROD angle map of plagioclase where areas with high-misorientation are observed and maximum local misorientation reach up to 12° (Fig. 611h). Thus, quartz grains in the amphibolite (SPI1338) and plagioclase grains in the diorite gneiss (SPI1311) exhibit a higher degree of orientation change, despite the absence of subgrain boundaries in the MAD analyses for these grains collectively (Fig. 6.10). Local subgrain boundaries are identified in the misorientation profiles (red arrows in Fig. 6.11g). The higher degree orientation change observed in the quartz grain of diorite gneiss (SPI1311), however, can be related to the development of subgrain boundaries inferred from the MAD analysis (Fig. 6.10h and observed locally in Fig. 6.11g). Misorientation profile across an amphibole grain in the diorite gneiss (SPI1311) also exhibits a slightly higher degree cumulative change of ~ 4° (profile 'G-H' in Fig. 6.11f-g) compared to the amphibolite (SPI1338), however, elsewhere the orientation change is <2° (profile 'I-J' in Fig. 6.11f-g). An increase in the misorientation values is also observed in the GROD angle map of amphibole grains (arrowed in Fig. 6.11i). Here, GND density map of plagioclase and amphibole represent well-preserved dislocation lines (Fig. 6.11j) indicating dislocation creep, this also corresponds well to the areas of high-misorientations displayed in the GROD angle map (arrowed in Fig. 6.11j). A higher GND density value of $0.1x10^{14}m^{-2}$ is observed for the constituent amphibole and plagioclase grains in this sample (Fig. AP6 – 3 in Appendix).

Melt-absent samples

Melt-absent amphibolite (430643) and diorite gneiss (475768) display similar high frequencies of neighbour pair MADs at low MAs of <10° for amphibole grains (Fig. 6.12a, f). The values are higher than observed in melt-present samples (Fig. 6.10). The misorientation axes-angle pairs for amphibole subgrains (2-10°) record [001] axis as the dominant misorientation axis in both the samples, while an additional [010] axis is observed in the diorite gneiss (475768) (Fig. 6.12e). Neighbour pair MADs at low misorientation

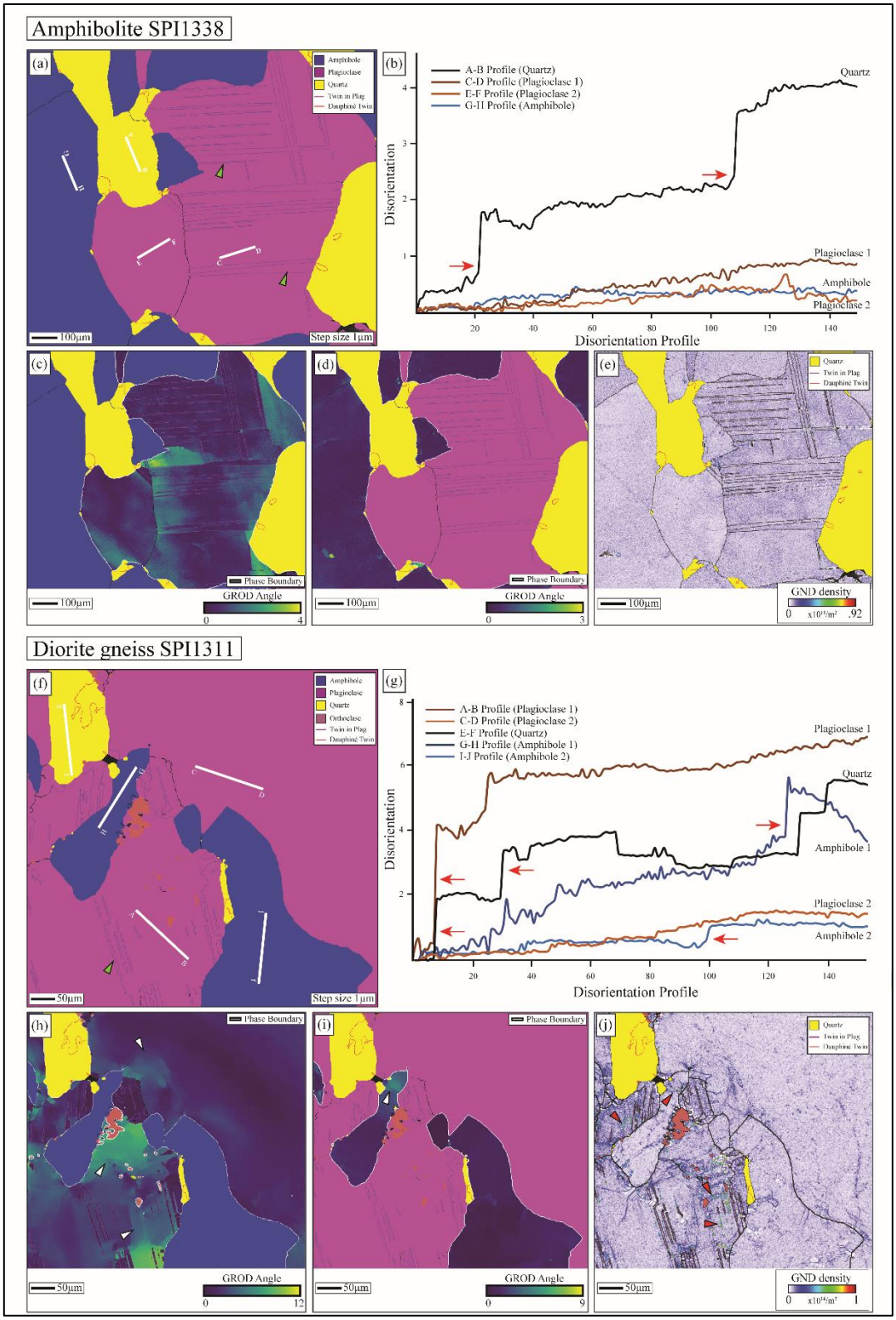

Figure 6.11 – Detailed quantitative orientation analysis of amphibole, plagioclase, and quartz grains in melt-present amphibolite (SPI1338) and diorite gneiss (SPI1311). (a, b, f, and g) Misorientation profiles of constant lengths (~150µm) exhibit cumulative changes in crystal orientations. Note, amphibole and plagioclase grains display minimal change in crystal orientation in SPI1338. In the diorite gneiss (SPI1311), for both amphibole and plagioclase, large cumulative changes of ~6-7° are observed. Green arrows indicate plagioclase twins. Red arrows mark the subgrain boundaries. (c, d) In amphibolite SPI1338, GROD maps reveal low misorientation in plagioclase and amphibole. (h, i)

The GROD values of plagioclase and amphibole in diorite gneiss SPI1311 are slightly higher (white arrows). (e, j) GND density maps of amphibole and plagioclase show similar values in both the samples. Amphibole and plagioclase in diorite gneiss (SPI1311) exhibit areas with highest GND densities (marked with red arrows) associated with regions of high GROD values.

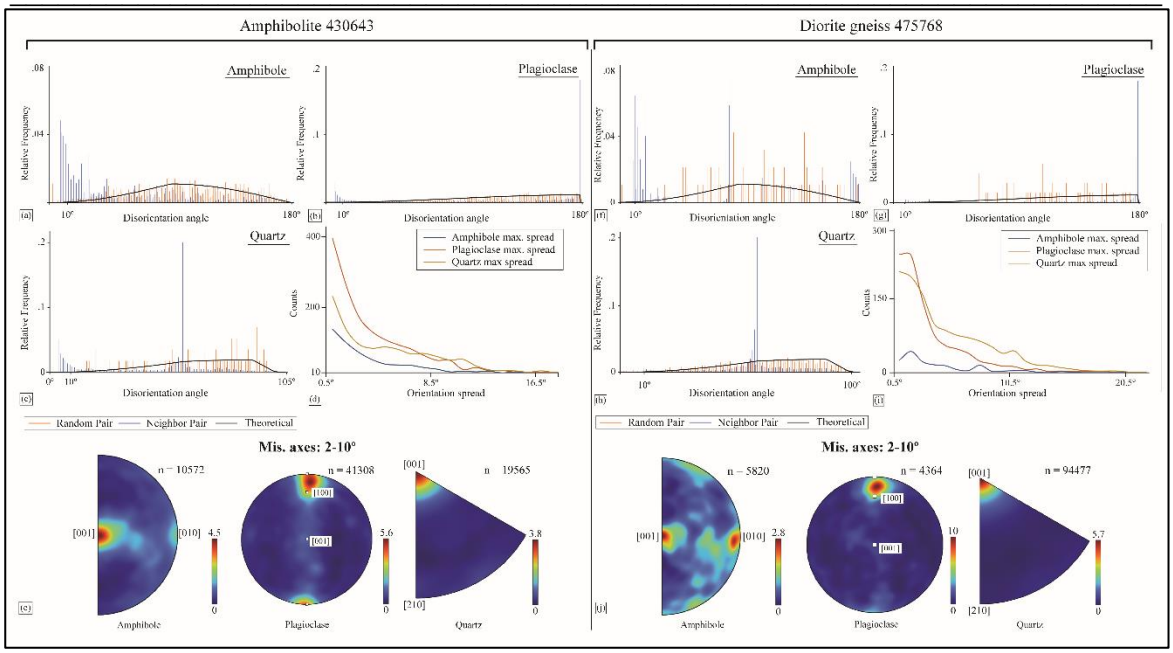

Figure 6.12 – Misorientation angle distribution (MAD) and misorientation axis-angle pair in the melt-absent samples. MAD between neighbour pair (blue) and random pair (orange) of: amphibole (shown in 'a', and 'f'), plagioclase (shown in 'b', and 'g'), and quartz ('c', and 'h'). The uniform (black) curve corresponds to the theoretical misorientation distribution for randomly oriented grains. Note for the low angle interval (<10°), the MAD of amphibole grains in the two samples is comparable and has minimal values. Plagioclase lack MAD for the low-angle interval. Maximum orientation spread of the constituent mineral are also provided (in 'd' and 'i'). ('e' and 'j') Plot of misorientation-axis data for low angle (2-10°) internal sub-grain boundaries shown in the crystallographic reference frame. Note the amphibole grains display both [001] and [010] as misorientation axes in the diorite gneiss (475768).

angles for plagioclase in both the melt-absent samples yield negligible values (Fig. 6.12b, g) comparable to the melt-present samples (Fig. 6.10). However, the misorientation axis-angle pairs yield development of misorientation axis close to twin axis [100] (Fig. 6.12e). Quartz grains in amphibolite (430643) record a relatively higher frequency of MAD at low MA (Fig. 6.12c, h) similar to the observation made in melt-present diorite gneiss (SPI1311) (Fig. 6.10). In comparison, relative frequency of neighbour pair MADs for quartz grains in the melt-absent diorite gneiss (475768) display negligible values (Fig. 6.12h). However, similar to melt-present amphibolite (SPI1338), [001] is found to be the dominant misorientation axis for quartz subgrains in both the samples (rotation measured for 2-10° low angle grain boundaries). Hence, MADs at low MA show only quartz grains in melt-

absent amphibolite (430643), and amphibole grains in both the melt-absent samples develop low angle subgrain boundaries similar to the observation made in melt-present diorite gneiss (SPI1311). Maximum orientation spread of all the minerals in amphibolite (430643) reach up to 16.5° (Fig. 6.10d), while mean orientation spread (normalized to 100 μm^2 grain area) are almost fifteen times higher than recorded in melt-present low-strain amphibolite (SPI1338) with values of 0.06°, 0.04°, and 0.07°, for anorthite, amphibole, and quartz grains respectively (Tab. 6.1). Melt-absent diorite gneiss (475768) exhibits maximum orientation spread for all the minerals reaching up to 20.5° (Fig. 6.12i). Average mean orientation spreads (normalized to 100 μm^2 grain area) for all the minerals are ~0.03°. Values of maximum orientation spread/area also exhibit very similar trends (Tab. 6.1). Misorientation profiles in melt-absent amphibolite (430643) exhibit highest cumulative change in crystal orientation in the plagioclase grains associated with subgrain boundaries ('C-D' and 'E-F' profiles in Fig. 6.13a-b). Changes in the crystal orientations are continuous (for 'E-F' profile) or have a step wise increase (for 'C-D' profile) but it does not correlate with the lack of substantial low-angle grain (subgrain) boundaries observed in the MAD analysis (Fig. 6.12b). Misorientation profile also records substantial change inside the amphibole grain ('G-H' profile with a maximum 4° cumulative change in Fig. 6.13a-b) and is perhaps associated with the subgrain boundaries observed in the MAD analysis (Fig. 6.12a, 6.13b). Hence, misorientation profiles in melt-absent amphibolite (430643) record higher degree change in crystal orientation compared to the melt-present amphibolite (SPI1338). The increased degree of internal deformation is also supported by high GROD angle map of plagioclase and amphibole where local misorientation reaches up to ~15° and 7°, respectively (white arrows in Fig. 6.13c-d). The GND density maps with plagioclase and amphibole correspond well to the local misorientations observed in GROD angle maps (Fig. 6.13e) and indicate deformation by dislocation creep. Similar to amphibolite (439643), melt-absent diorite gneiss (475768) also records a relatively higher degree cumulative changes in the plagioclase grains (Fig. 6.13f-g). However, plagioclase grains lack development of substantial subgrain boundaries as inferred from the MAD analysis (Fig. 6.12g). This is also similar to the observation made in the melt-present diorite gneiss SPI1311 (Fig. 6.10-6.11). Amphibole grains display zigzag profile with relatively smaller change in crystal orientation (Fig. 6.13f-g) compared to melt-present diorite gneiss (Fig. 6.11f-g). GROD angle of plagioclase grains exhibits higher degree misorientations (marked in Fig. 6.13h-i) and are associated with high GND density values (marked with red arrows in Fig. 6.13j). Hence, the

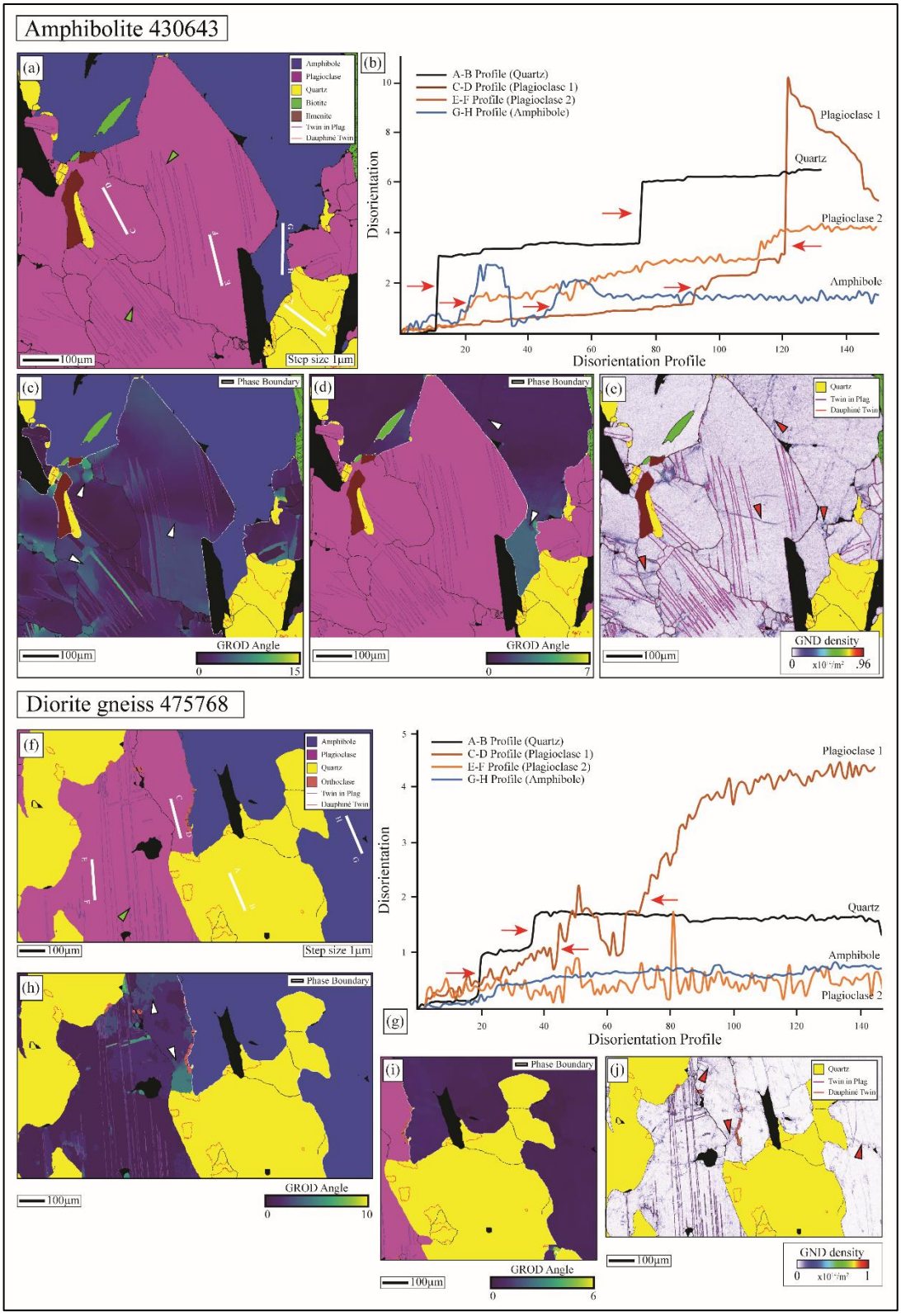

Figure 6.13 – Detailed quantitative orientation analysis of the amphibole, plagioclase, and quartz grains in melt-absent amphibolite (430643) and diorite gneiss (475768). In the amphibolite (430643): (a-b) misorientation profiles show cumulative changes in crystal orientations. Quartz and amphibole grains record relatively large change of ~4-6°. Plagioclase grains display continuous or step wise changes varying between 4-8°. (c, d) GROD maps yield lowest values for amphibole and plagioclase grains. Areas with high misorientations are marked in both plagioclase and amphibole. (e) GND density map corresponds well with the misorientations observed in GROD angle map (red

arrows). The diorite gneiss (475768) exhibits: (f) a negligible cumulative change in quartz and amphibole grains. Plagioclase grains have greater values than amphibole and quartz. (h-j) GROD angle maps yield higher degree misorientation for plagioclase (white arrows) associated with high GND densities (red arrows). Red arrows in the misorientation profiles display subgrain boundaries.

---

internal misorientations of plagioclase grains are similar in both melt-absent diorite gneiss (475768) and melt-present diorite gneiss (SPI1311), even though both the samples lack substantial development of plagioclase low-angle grain boundaries. In contrary, the amphibole grains record higher degree change in crystal orientation in the melt-present diorite gneiss (SPI1311) even though both the samples exhibit similar frequency of low-angle grain boundaries observed from the MAD analysis.

6.5 Discussion

6.5.1 Melt present versus melt absent microstructural signatures: A summary

The studied samples (Fig. 6.1-6.2) are subdivided into melt-present vs. melt-absent based on the field observations of undeformed quartzofeldspathic materials oriented along the foliation planes of amphibolite (SPI1338) and diorite gneiss (SPI1311). The other two samples lack any such felsic vein (430643 and 475768). Evidence of former melt-presence in amphibolite (SPI1338) and diorite gneiss (SPI1311) is also proved by the microstructural observations where anhedral, xeonomorphic quartz grains with cuspate grain boundaries and low-dihedral angle (LDA) dominate (Fig. 6.3-6.4). Moreover, the K-feldspar grains in diorite gneiss (SPI1311) are interstitial and primarily occur along irregular grain boundaries of biotite suggesting localized partial melting (Fig. 6.4). Previous studies from this area suggest syn-deformation melt movement (see Chapter 3 for details). Amphibolite (430643) and diorite gneiss (475768) lack any such microstructural evidence of former melt and rather display an overall granoblastic texture, typical of subsolidus rocks (Fig. 6.4). The local deformation features in quartz-plagioclase grains (i.e., undulose extinction and deformation twins) suggest that these rocks formed under the influence of external tectonic stresses.

The quartz grains in the melt-present diorite gneiss (SPI1311) are elongated with high aspect ratio (~3-4) and are parallel to the foliation (Fig. 6.1, 6.3). Similarly, diorite gneiss 475768 displays elongated ameboid quartz grains parallel to the foliation (Fig. 6.1,

6.4). Diorite gneiss (SPI1311) records some degree of post-melt deformation evidenced by the occurrence of small, recrystallized grains along the boundaries of elongated quartz grains (Fig. 6.4). In all the samples, amphibole grains are elongated (Tab. 6.1) with regular and/or cuspate grain boundaries while plagioclase grains are subhedral and exhibit straight and/or inundated grain boundaries. Amphibole grains in all the samples also display a strong shape preferred orientation (SPO) with the strongest SPO shown by the melt-absent diorite gneiss 475768 (Fig. 6.5). Plagioclase grains also have strong SPO, but weaker than the amphibole grains in all the studied samples (Fig. 6.5). Melt-present diorite gneiss (SPI1311) also exhibits some randomly oriented plagioclase grains. In the following section, Next, the plausible deformation mechanism operating in the examined samples and the influence of grain boundary melt network on the CPO-SPO patterns will be discussed.

6.5.2 Dislocation creep represents a minor deformation mechanism in the studied samples

The solid framework in all the studied samples does not record the strain observed in the field, this is indicated by no pronounced sample scale CPO of plagioclase-quartz grains (Fig. 6.8-6.9). In the amphibolite (SPI1338) it is consistent with a melt-present deformation where strain is accommodated by the melt phase and deformation ceases to exist once the melt solidifies. No samples scale CPO of quartz-plagioclase grains (Fig. 6.8b-c), a very weak frequency of neighbour pair MADs at low MAs (Fig. 6.10a-c), and minimal grain orientation spread (Fig. 6.10d, 6.11a-d) in the amphibolite (SPI1338) indicate lack of dislocation creep. Though individual quartz grain records relatively higher degree change in crystal orientation (up to 4° in Fig. 6.11a-b), the mean orientation spread (per 100μm^2 area) for all the other minerals is very little and only vary between 0.003-0.006° (also <1° change along misorientation profiles and low GROD angle map for plagioclase and amphibole, Fig. 6.11a-d). This suggests that the deformation observed in the quartz grains is local and growth-related (see Chapter 5) while plagioclase, and amphibole grains do not show any evidence of major dislocation creep. Lack of grain substructures and absence of high GND densities in the plagioclase-amphibole grains (Fig. 6.11e) also support this. In comparison to the melt-present amphibolite (SP1338), subgrain boundary development (Fig. 6.10f, h), a relatively higher degree change in crystal orientation (Fig. 6.11f-g), larger mean orientation spread (0.01-0.05° change per 100μm^2 area), and areas with high misorientations (Fig. 6.11h-i) in the diorite gneiss (SPI1311) indicate an increased activity of dislocation creep.

GND density map also displays high dislocation densities associated with high misorientation (Fig. 6.11j) and an overall increase in the GND density values relative to the amphibolite (Fig. AP6 – 3). Higher activity of dislocation creep is also inferred from the minor grain recrystallization along the grain boundaries of elongated quartz grains (Fig. AP6 – 1) giving rise to an increased quartz M-index value (Fig. 6.8f). A faint prism [c] slip system development can be observed from the quartz CPO pattern (Fig. 6.8f). However, no sample scale CPO of plagioclase grains (Fig. 6.8e) and a very weak frequency of neighbour pair MADs at low MA (i.e., little development of subgrain boundaries) (Fig. 6.10f) advocate for other active deformation mechanism instead of dislocation creep in the diorite gneiss (SPI1311). Similar observations can be made in melt-absent amphibolite (430643) and diorite gneiss (475768). Compared to the melt-present samples, both the melt-absent samples reveal an increased frequency of subgrain boundaries (Fig. 6.12a, f), relatively large mean orientation spread of 0.03-0.07° (per 100μm^2 area), and higher degree orientation change (Fig. 6.13a-b, e) for the amphibole grains indicating dislocation creep. However, amphibole grains in the diorite gneiss (475768) with very little change in crystal orientation (Fig. 6.13f-g, i) may suggest deformation by another mechanism(s). In addition, lack of sample scale CPO of plagioclase-quartz grains (Fig. 6.9b-c, e-f), and a very weak frequency of low-angle grain boundaries in plagioclase in the amphibolite (430643) and for both plagioclase-quartz in the diorite gneiss (475768) (Fig. 6.12) also indicate a different major deformation mechanism. However, an increase in the plagioclase local misorientations (from misorientation profiles and GROD) (Fig. 6.13a-c, f-h) in areas with high GND densities in both the melt-absent samples compared to their melt-present counterparts suggests increased activity of dislocation creep but it cannot produce a strong CPO. This contrasts with earlier research where solid-state dislocation creep produce characteristic CPOs in plagioclase (Berger and Stünitz, 1996). Hence, both the melt-present and melt-absent samples show very similar CPO, SPO patterns, orientation spread and indicate deformation mechanism other than dislocation creep to be active. Both the melt-absent samples (amphibolite 430643 and diorite gneiss 475768) and melt-present diorite gneiss (SPI1311) record an increased activity of dislocation creep compared to the melt-present amphibolite (SPI1338), where no evidence of dislocation creep is found.

6.5.3 Similar CPO patterns resulting from different dominant deformation mechanisms: Melt present grain boundary sliding versus melt absent, aqueous fluid present deformation via dissolution precipitation creep

CPO of minerals are traditionally interpreted as evidence of deformation by dislocation creep. The observed strong CPO of amphibole characterize (100) [001] slip system. Amphibole CPO with slip on the (100) plane with burgers vector [001] is in accordance with the experimentally defined slip systems from synthetic aggregates (Dollinger and Blacic, 1975). Naturally deformed amphibole with (100) [001] easy slip has been shown to occur under middle to upper amphibolite facies condition (~650-750 °C, 0.6-1 GPa) (e.g., Berger and Stünitz, 1996; Tatham et al., 2008; Getsinger et al., 2013). If the observed CPO patterns of amphiboles resulted from dislocation creep, the misorientation axis will be perpendicular to the slip direction (Llyod et al., 1997). In the melt-present amphibolite (SPI1338), misorientation axis-angle pair is somewhat consistent with the development of this rotation axis (Fig. 6.10e) but another rotation direction is also seen (Fig. 6.10e and girdle distribution of 010 poles in 6.8a). Additionally, misorientation angle distribution (MAD) (Fig. 6.10a-d) and intracrystalline deformation (Fig. 6.11a-e) indicate very little contribution of dislocation creep. Hence, dislocation creep giving rise to CPO pattern in the amphibole grains of melt-present amphibolite (SPI1338) cannot be justified. For the other melt-present sample, even though crystal plastic deformation in the amphibole grain is interpreted from the MAD analyses (Fig. 6.10f) and targeted high resolution EBSD map (Fig. 6.11, 6.13), the intracrystalline misorientations are only essentially accommodated around the [001] axis (and only to a lesser extent by the [010] axis) (Fig. 6.10j). Thus, majority of the misorientation is incompatible with the activation of (100) [001] slip system through dislocation creep, observed from the CPO geometrics of the studied amphiboles (Soret et al., 2019). Amphiboles are typically elongated in the c-axis, which is also the fastest growth direction. In the studied samples, this long axis direction [001] is aligned with the stretching direction within the foliation plane (Fig. 6.5a, c; Fig. 6.8a, d), thus it may indicate a growth fabric where the long axes of the amphibole grains grew preferentially within the shear plane. Similar inferences were made by Giuntoli et al. (2018) and by Stünitz et al. (2020). Given the extreme elastic anisotropy of amphiboles, it is likely that amphibole will have anisotropic growth rates. In the amphibolite (SPI1338), amphibole grains exhibit a strong girdle in (100) whereas in the other samples a maximum of (100) poles with a weak girdle subnormal to the shear direction is observed (Fig. 6.8a, d). It has been proposed that such girdles can form through cataclastic flows leading to a fine-grained matrix created by fracturing and comminution (Imon et al., 2004; Kim and Jung, 2019). Cataclastic flow is unlikely in these samples as: a. the confining pressure of 0.6-0.8

GPa (Fig. 6.7) will inhibit the frictional processes, b. the high strain domains record similar grain size of amphibole compared to its low strain counterparts (Tab 6.1), c. a strong correlation between small angle misorientation axes and crystallographic direction (Fig. 6.10e, j), and d. most of the strain will be accommodated by the melt-phases in the melt-present samples. Thus, presence of girdle, strong alignment of [001] axes parallel to the shear direction, and a strong SPO suggest a component of rigid body rotation around [001] in addition to preferential growth. Coincidence of crystallography and crystal shape produce the alignment of the [c] axis observed in the samples. Aspiroz et al. (2007) also studied similar naturally deformed amphibole with a lack of crystal plastic deformation and interpreted rigid body rotation as the dominant deformation mechanism. Hence, the mechanical rigid body rotation of the amphibole grains in the studied sample may have occurred in the melt-present samples where melt phase facilitates grain rotation or grains can be oriented during magmatic flow under deformation. High strain melt-present deformation facilitating grain rotation can also be inferred from the higher M-index value of amphibole CPO in the diorite gneiss (SPI1311). The high strain can be achieved by grain boundary sliding due to the presence of melt along the grain boundaries (Rosenberg, 2001; Walte et al., 2005). Rigid body rotation assisted by melt-present GBS forming a strong CPO pattern of the amphibole grains is also inferred by Stuart et al (2018).

In the melt-absent samples (430643 and 475768), amphibole grains display a relatively increased activity of dislocation creep from the MAD, GROD angle deviation, and GND density analyses (Fig. 6.12a, f; Fig. 6.13). However, a) lack of intense dynamic recrystallization (Fig. 6.4), b) no sample scale CPO of plagioclase-quartz grains (Fig. 6.8, 6.9), c) low frequency of subgrain boundaries in the plagioclase (Fig. 6.12), c) disparity between observed amphibole slip system and the misorientation axis for low-angle rotation (Fig. 6.9, 6.12), d. strong SPO of amphibole-plagioclase grains on the foliation plane (Fig. 6.5) suggest dislocation creep was not responsible for the observed strong CPO pattern of the amphibole. Due to lack of any weak layer in the matrix the rigid body rotation also cannot operate. Apart from the rigid body rotation, the strong SPO and CPO parallel to the lineation may also indicate oriented dissolution-precipitation creep (Berger and Stünitz, 1996). Lobate grain boundaries (Fig. 6.4) and amphibole with slightly different $(Na+K)_A$ from the core to rim (Tab. 6.2) reveal that dissolution and precipitation was responsible for the CPO patterns in the melt-absent samples. Although CPOs are not produced by diffusion creep, numerical modelling suggests that it is possible in minerals with anisotropic

dissolution and growth rates (Bons and den Brok, 2000; Stokes et al., 2012). A stronger SPO in the diorite gneiss (475768) may indicate more oriented growth of elongated amphibole grains accompanied by local pressure-dissolution during high strain deformation. However, fracture network structures in the amphibole grains for aqueous grain boundary fluid migration in the studied melt-absent amphibolites (430643 and 475768) have not been thoroughly investigated. Previous research indicates that the aligned amphibole in amphibolite (430643) formed along foliation planes as a result of a syntectonic fluid flux and associated metamorphism (Piazolo, 2002). The melt in the grain boundaries of amphibolite (SPI1338) and diorite gneiss (SPI1311) may also allow dissolution of ions from one location and overgrowths parallel to the extension direction and accompany the rigid body rotation. Amphibole deforming by dissolution-precipitation creep at geological strain rates and temperatures ranging from 500 to 750 °C is shown by Stokes et al. (2012). In the studied samples, Ti-in-amphibole and Ti-in biotite thermometers indicate crystallization temperatures varying between 740-810 °C, except in the diorite gneiss (475768) where a crystallization temperature of ~650 °C is observed (Fig. 6.6e; Tab. 6.3). A high deformation temperature is also inferred from the weak CPO pattern in the diorite gneiss (475768) (Fig. 6.9f). The metamorphic conditions are further corroborated by amphibole-plagioclase geothermobarometer (Fig. 6.7), which also indicate similar values. Thus, these P-T conditions observed in the studied rocks are also consistent with dissolution-precipitation creep.

Plagioclase grains in the studied samples, except in the melt-present amphibolite (SPI1338), record variable amount of dislocation creep but lack any sample scale CPO (Fig. 6.8, 6.9) or high-frequency of subgrain boundary development (Fig. 6.10g; Fig. 6.12b, g). Thus, it does not represent a characteristic fabric type of crystal plasticity. The average grain size of plagioclase decreases from the melt-present amphibolite (SPI1338) to diorite gneiss (SPI1311), but no evidence of dynamic recrystallization or grain fragmentations are found. In melt-present diorite gneiss (SPI1311), plagioclase grains are more albitic than in the amphibolite (SPI1338) (Fig. 6.6c), and the SPO pattern records differently oriented grains (Fig. 6.5d). This is due to an external melt influx (refer to Chapter 3 for more details) where melt-crystallized plagioclase grains are randomly oriented. The large offset in the SPO may have caused due to the rotation in the presence of deformation. Activity of GBS is thought to result in weak to little CPO or may weaken previously formed CPO (Bestmann and Prior, 2003; Svahnberg and Piazolo, 2010). Melt-assisted GBS is thus proposed for plagioclase

grains in the amphibolite (SPI1338) and diorite gneiss (SPI1311). The dissolution precipitation creep is the dominant deformation mechanism in the melt-absent samples, but unlike amphibole, there is no strong crystallographic control over plagioclase grain shape, resulting in a lack of CPO.

6.6 Conclusion

- Our observations suggest a strong amphibole fabric with similar CPO patterns in all the studied samples may form due to various deformation mechanisms. In the melt-present samples, rigid body rotation is the dominant deformation mechanism as evidenced by a strong correlation between grain aspect ratio, SPO and CPO strength. High aspect ratio of amphibole which coincides with its fast growth direction allowed preferential alignment of the long axes of amphibole grains parallel to the stretching direction. In the melt-absent samples, dissolution precipitation creep and oriented growth of amphibole parallel to the [001] axis form the CPO.

- Crystal plastic deformation observed in the amphibole and plagioclase grains in the studied samples have negligible effect in the overall deformation of these rocks. Hence it is not the dominant deformation mechanism. Misorientation axes are incompatible with the observed slip systems suggesting dislocation creep had minor contribution to the observed CPOs in amphibole and plagioclase.

Chapter 7

Discussion and synthesis

The main chapters of this thesis, Chapter 2 to Chapter 6, provide in-depth analyses of various physicochemical and rheological characteristics of a rock system influenced by melt migration. As the thesis developed, a set of tools were developed to help identify former melt presence at different scale in high grade rocks. The main contributions of this thesis are highlighted in this chapter, along with limitations and opportunities and an integrated discussion of the data and the insights gained for understanding the melt-rock interaction. Remaining gaps in our knowledge related to melt fluxing in low to mid crustal rocks are highlighted and future avenues of investigations discussed.

7.1 Techniques used to characterize volume of equilibration in heterogenous high-grade rock analysis – opportunities and pitfalls

Fluids can dissolve material, transport solutes, and precipitate new minerals during metamorphism (Philpotts and Ague, 2009; Yardley, 2009). Percolation of high viscous silicate melt can result in a variety of metasomatic reactions such as formation of rocks rich in pargasite and phlogopite (e.g., Tommasi et al., 2017; Stuart et al., 2018a, 2018b). All of this can result in open system behaviour and metasomatic changes within the whole-rock composition (Newton, 1990). Metamorphic segregation or differentiation also forms domains of different bulk compositions within an unbanded rock (Turner, 1941, Robin, 1979, Williams et al., 2000). Segregation occurs when minerals are physically or chemically moved into layers that concentrate similar minerals, resulting in alternating layers of light and dark minerals in gneisses (Robin, 1979). It is accountable for metamorphic and

structural characteristics including metamorphic layering, crenulation, spaced and slaty cleavage, quartz rods, mylonite banding, gneissic layering, and migmatite layering (Robin, 1979). Segregation or differentiation in migmatites is also caused by the physical and chemical movement of minerals (Turner, 1941; Robin, 1979). Partial melting, melt migration along grain boundaries, and melt accumulation form segregated zones of leucocratic and melanocratic rock during crystallization (Lindh and Wahlgren, 1985). Secondly, diffusion in solids, possibly enhanced by intergranular fluid, also contributes to the formation of composition domains (Lindh and Wahlgren, 1985). In the thesis, an alternative method, MapComp, is proposed to determine bulk composition for such rocks that show heterogeneous compositional domains (Fig. 2.1). Using a software package called XMapTools, microXRF X-ray elemental map and quantitative EMPA spot analyses are used for determining local bulk chemistry. Samples with varying degrees of heterogeneity are investigated to assess the reliability of this technique in comparison to traditional whole-rock XRF analyses (Fig. 2.2-2.5). The results show that the presented method is indeed a viable alternative to whole rock XRF for determining precise local bulk chemistry (Fig, 2.7; Tab. 2.2). We advise areas with with sides ~20 times the maximum grain size properly represent suitable areas for MapComp analyses. The advantage of this method over traditional whole rock XRF is its flexibility in selecting areas and determining local bulk chemistry of specific domains with ease. Moreover, compositions from millimetre-scale compositional domains cannot be determined using X-ray fluorescence (XRF). It has also been discovered that the whole rock chemistry determined using X-ray maps from EPMA and MapComp (i.e., micro XRF X-ray maps) yields extremely similar results (Fig. 2.10; Tab. 2.6). While bulk chemistry determination using EPMA X-ray maps has high running costs and can take a day to measure more than a couple of square centimetres, the MapComp approach has the advantage of being low cost and quick. Combining textural information and local bulk chemistry from quantitative micro XRF maps can reveal a key metamorphic event in the formation of small-scale inhomogeneities. However, this approach is only limited for rocks with grain size >15 µm and for elements with concentration >10 ppm. Also, the user must be well versed with operating XMapTools as proper pixel classification and internal standardization will only ensure reliable results. We observe a higher degree error for elements with low concentration in our studied rocks (such as Ti, Na, and K) (Tab. 2.4, 2.6). Therefore, care must be taken with minerals that are extremely sensitive to minute changes in Na_2O, K_2O, and TiO_2 weight percentages.

7.2 Geochemical studies of melt-rock interaction: implications in the regional geology of Akia terrane and Alanngua complex

Next, we present a case study where MapComp-derived bulk compositions are used to determine and differentiate conditions of metamorphism in the Akia terrane vs. Alanngua complex in the southwest Greenland (Chapter 3). In the studied amphibolites, Na_2O is only present in plagioclase grains and there is no discernible zoning pattern (Fig. 3.4-3.6); therefore, MapComp is confidently applied. Even though it is recommended for isochemical phase diagrams to use a specific fixed bulk rock chemistry in which the phases are in chemical equilibrium, for *Island I* amphibolite we observe that the bulk composition from the entire heterogeneous area and for the equilibriated domain is comparable, and both domains produce phase diagrams with remarkably similar large P-T fields. Even though garnet is only found along felsic veins, it was added to the equilibrium assemblage to better constrain the P-T condition (Fig. 3.8). This may explain why numerous previous studies may have utilized rocks with minute heterogeneous domains but still produced viable results and why, in general, whole rock XRF yields reliable bulk compositions despite the presence of millimeter-thick heterogeneous domains. Utilization of MapComp approach is rather suitable for *Island II* amphibolite, where large felsic vein (Zone 2, thickness in centimeters) will undoubtedly have a significant impact on the measured bulk composition, if included in the calculation. Consequently, phase diagrams using the MapComp bulk compositions for Island amphibolites yield medium- to high-pressure high temperature metamorphism of 760-812 °C at 0.61-0.76 GPa (Fig. 3.10). The peak P-T estimates document conditions above the solidus and are consistent with observations from the field (Fig. 3.2). In addition, the results confirm prior observations of granulite facies metamorphism at 820-850 °C and 0.8-1 GPa (Kirkland et al., 2018a). Even though the amphibolites on the mainland do not produce a precise P-T range, it can be concluded that MapComp analyses provide extremely reliable isochemical diagrams. Even though the results were unable to definitively indicate the existence or absence of a terrane boundary between the Akia terrane and Alanngua complex, they do suggest that both terranes underwent high-temperature metamorphism. The estimated temperature ranges are also consistent with conventional geothermometer readings (Fig. 3.7). A high temperature metamorphism and partial melting associated with ductile deformation also can be utilized to verify the bolide impact model of ≥3 Ga (Garde et al., 2012a, 2014; Keulen et al., 2015). All the samples studied here occur almost within

the central zone of the proposed Mesoarchean impact structure. In fact, the mainland amphibolites which also record high temperature metamorphism is collected < 5 kilometre away from the gneisses that were interpreted as Mesoarchean impact melts by Keulen et al. (2015). Hence, it is difficult to comprehend how the amphibolites underwent high temperature metamorphism in the presence of melt, and ductile deformation at a deep crustal level, while the surrounding rocks still preserve impact related features (planner deformation fabric, brittle fractures, cleavage, K-feldspar melting and other macrotextures as proposed by Garde et al., 2012a, 2014; Keulen et al., 2015). A similar interpretation was proposed by Kirkland et al. (2018a).

7.3 Diffuse porous flow – is it an important process in the lower and middle crust?

The differentiation of crust and mantle from a single reservoir explains heterogeneity in crustal structure and its composition (Brown and Rushmer, 2006). This differentiation is a direct indication that mass and heat transfer occurred within the Earth due to melt migration. However, the nature of melt migration, particularly the role of diffuse porous flow in the middle-lower crust, is yet to be fully understood. Due to the scarcity of data on porous melt flow in the crust, this thesis takes a bottom-up approach, focusing on identifying and characterizing examples of melt flux from natural samples. The field area studied in this Ph.D. provides a window into natural processes occurring in the ductile mid to lower crust, as well as evidence for the relationship between melting, melt migration, and deformation. The first step in determining the former presence of melt in shear zones is to make critical observations during field investigations. Based on the cross-cutting relationships of different veins (Fig. 4.2), the field relationships provide information on the relative timing of deformation. Observations of undeformed leucocratic veins within low- and high-strain zones, with or without high-temperature minerals in associated rocks, are reliable field indicators of the former presence of melt. The relationships between these features and deformation structures (shear bandings, open and closed fold types in Fig. 4.2) can be used to infer melt-present deformation. Additionally, these features can be utilized to identify strain variability within the crust (Fig. 4.3). Grain size reduction (forming a bimodal grain size), dynamic recrystallization-growth of finer grain fractions, undulose extinction in grains, and core-mantle structures are examples of typical microstructures that form during

solid-state deformation. These common microstructures, however, are rarely observed in the samples studied, and indicate that the samples formed during melt-present deformation in a shear zone. Microstructures suggesting the former presence of melt include a) interstitial grains with low dihedral angles, b) 'string of beads' texture, c) elongated mineral along grain boundaries interpreted to be melt films, d) spatially distant grains connected in 3D, e) the inclusion of micro granite melt pockets at grain triple junctions, and f) coexisting three mineral associations of quartz + plagioclase + K-feldspar (Fig. 4.4-4.6). In the lower crust of the Akia terrane, the low- and high-strain shear zones appear strongly different in the field, but there is a lack of microstructural evidence of deformation heterogeneity. Microstructural features such as narrow films, pools, corroded grain boundaries, polycrystalline intergrowth indicate presence of former melt. The minimum melt fraction calculated in the field and from microstructures varies greatly between low-strain and high-strain samples (Fig. 4.7), and both indicate a larger melt fraction than predicted by the P-T calculation. At the thin section scale, all observed samples have mineral compositions that are broadly homogeneous (Fig. 4.4-4.6). All these features suggest porous melt migration that reflects strain partitioning in the dioritic crust (Fig. 4.14). The degree of homogeneity is proportional to the time-integrated volume of melt flux, with more homogeneous mineral compositions in rocks indicate large volumes of melt fluxing (Fig. 4.9). A greater degree of melt fluxing increases the percentage of silica in high-strain samples, indicating that the rheology of the high-strain shear zones is weaker (Fig. 4.8). Due to the inherent complexity of crustal rocks and the vast variety of melt compositions present in the lower crust, the style of melt-rock reactions varies greatly, and consequently, rocks fluxed by porous melt flow may be overlooked. Additionally, identification of melt-rock interaction in the crust is challenging because the mineral assemblage and microstructure created are typical for lower crustal rocks. The strongly foliated fabric observed in the high-strain zones is formed by the self-organization of melt and solid phases. Deformation is partitioned into the melt phase and deformation ceased when the rock crossed the solidus and the melt crystallized. As a result, the solid components of the rock experienced little or no deformation, and few deformation microstructures are visible (Fig. 4.11-4.13). The elongated minerals (amphibole and biotite) rotated mechanically within the melt giving rise to a strong CPO pattern (4.11-4.12). Actively deforming melt bearing systems are complex because they are highly dynamic, where deformation leads to melt distribution and control the change in deformation mechanism (Vigneresse, 2004; Rutter et al., 2006). Understanding the rheology of melt bearing crust is also critical as it influences the tectonic evolution of orogenic belts.

Geophysical measurements show that several modern mountain belts, notably the Himalayan–Tibetan system, have melted crust underneath. Geological and geophysical evidence also suggests that melting has been occurring for approximately 30 million years, giving rise to a large melt accumulation zone. However, efficient melt extraction and migration during deformation is unlikely to occur when large melt volume of melt is present (i.e., >20%, RCMP threshold). When the melt volume is low (<10%), flow can occur laterally due to differential pressures within the deforming orogens. Larger volumes of melt promote buoyant vertical transport of magma and may form plutons in the upper crust. However, we see local melt segregation and vein formation here, where melt from grain boundaries is transported locally to dilatant sites (Fig. 4.2, 4.4, 4.6). But evidence of large-scale melt extraction/melt loss is limited (Fig. 4.2). In high strain zones, on the other hand, more veins form in response to increased melt influx (Fig. 4.3). Thus, the field evidence points to a melt-accumulation zone within the lower crust. This conclusion is supported by mineral phase equilibria modelling, which shows that these rocks would have produced only 2-3 vol% melt at the exposed level, implying that the higher melt% observed in the area (Fig. 4.7) was due to more extensive melting at deeper crustal levels. Phase equilibria modelling suggests peak pressure temperature condition of the studied section is 790-805°C, and <0.55 GPa (Fig. 4.10). Granulite facies metamorphism observed in nearby rocks indicates a similar P-T condition with temperatures ranging from 760 to 812 °C and pressures ranging from 0.61-0.76 GPa (Fig. 3.10; Kirkland et al., 2018a). However, there is a distinct difference between these rock types: while amphibolites undergo metasomatism, resulting in heterogeneous rocks with varying compositional domains (Fig. 3.3-3.5), dirotic gneiss does not (Fig. 4.4-4.6). This also suggests that the melt was very similar in composition to the diorite gneiss and that it was formed at a depth from the same source rock (Fig. 7.1a) and then moved upwards via the permeability network formed by the incipient melting of biotite (Fig. 7.1b; 4.14). Melt-pathways are recorded by variously arranged leucosomes, as seen on the outcrop. Leucosome is commonly found as foliation-parallel veins or as discordant veins and shear bands. These leucosomes defined a three-dimensional former melt-flow network which provided pathways for melt redistribution and accumulation (Brown et al. 1999; Brown2004). As long as the permeable network exists and the pores are not completely compacted, porous melt flow from the bottom will continue, eventually giving rise to the accumulation zone (Fig. 7.1c). When diffuse porous melt migration occurs in the presence of deformation, low- and high-strain shear zones formed, which also facilitate melt movement (Fig. 4.14). The ‘frozen-in’ melt microstructures

observed in amphibolites (Fig. 3.3-3.4) may also indicate that the melt influxed other rock types during its journey as long as the rock units were below the solidus, and the temperature was maintained for the melt to migrate. Melt accumulation in this mid-lower crustal region could be due to the presence of a rigid impermeable layer at the top and formed by the ductile-brittle transition or other factors. Widespread melting at depth and the formation of this accumulation zone may result in a high viscosity contrast, resulting in buoyant vertical transport of the entire crustal package (e.g., Lexa et al. 2011). The difference between melt retention and melt loss has important implications for crustal-scale rheology and tectonics. Because the effective viscosity of melt-bearing lithosphere is greatly influenced by temperature, composition, and, most importantly, melt distribution. Melt accumulation and retention zones, such as the one investigated here, are extremely weak and can function as a structural detachment horizon. The existence and consequences of a mechanically weak crustal layer in the current channel-flow model for the Himalayan orogen are being examined in detail (Harris, 2007). Connolly and Podladchikov (2007) and Connolly (2010) used numerical simulations and concluded that upward obstruction of fluid flow from a large volume can produce strongly channelled fluid flow where fluid migrates as fluid-filled porous waves in accordance with the pressure gradient.

7.4 Melt-present and melt-absent deformation – New tools of identification and lessons learnt

This thesis investigates new dimensions of several local-scale processes that occur during syn-deformational melt migration. In turn, the integrated effects of these processes can influence processes and tectonics on a regional scale. This thesis also makes extensive use of microstructures indicative of the former presence of melt as one of the critical features for identifying melt microstructures in the studied rocks (Chapter 2-6). Former melt presence is investigated in rocks ranging from granitoid with nearly 100% starting melt to a high-grade shear zone sample with less than 5% melt. Thus, the thesis validates the use of melt-microstructures by earlier researchers while exploring potential new related microstructures (Daczko et al., 2016; Stuart et al., 2018b; Meek et al., 2019; Daczko and Piazolo, 2022). All of these studies successfully employ field and optical microstructural characteristics to delineate the presence of melt. However, with the development of new techniques, it is now possible to go beyond optical characteristics. Most importantly, none of the previous works

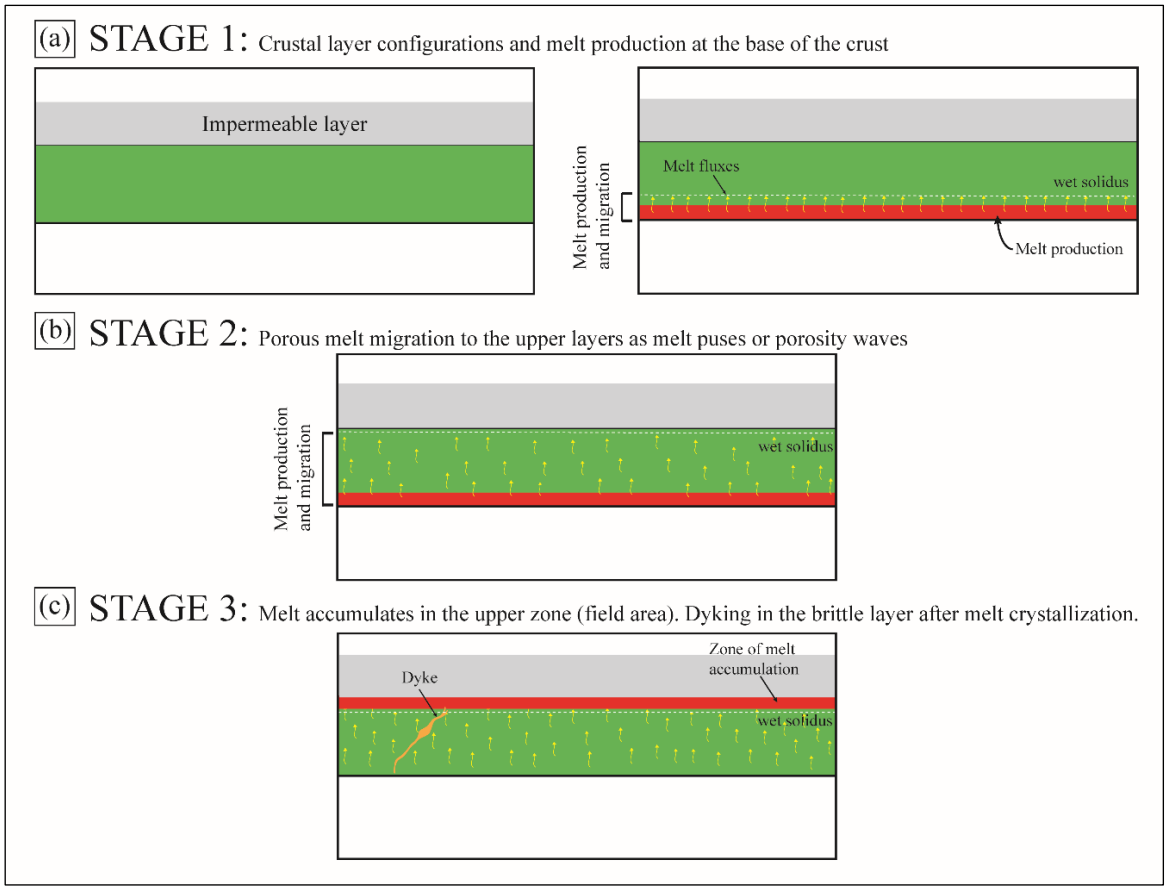

Figure 7.1 – Schematic diagram depicting the development of melt-accumulation zone in the middle-lower crustal section of Chapter 4. At stage 1: the dioritic crust melts at the bottom. Melt begins to escape and migrate upward from this zone. Stage 2: at the advanced stage, melt from the base of the crust migrates extensively upwards, fluxing the upper portion of the crust. Melt cannot escape due to the presence of an impermeable layer on top. Stage 3: almost all the melt migrated upward, forming a melt pool at the base of the impermeable layer. A later dyke cut across this layer as melt crystallization will make the crust stiffer. The whole package can migrate upward due to buoyancy.

---

demonstrated and differentiate internal crystallographic orientation characteristics of minerals in a subsolidus shear zone vs. a melt-present shear zone, which has been covered in this thesis. An identification scheme is provided to characterize grains pseudomorphing former melt, useful for rocks with very low melt fractions and/or high strain zones with cryptic melt signatures. Significant changes in crystal orientation, dauphiné twins, pronounced misorientation, and crystal substructures with oriented GNDs advocating the development of slip systems are typical of solid-state crystal plastic deformation (Law, 1990; Wilsdorf and Hansen, 1991; Hirth and Tullis, 1992; Stipp et al., 2002). However, we find that the deformation features within the quartz grains crystallised from the melt differ significantly from rocks that experienced solid-state deformation by dislocation creep

caused by large-scale tectonic stresses. We propose that quartz grains pseuodmorphing former melt are subjected to local stresses throughout a decreasing temperature window associated with rock cooling during and after melt crystallization in a confinement. Mineral growth in confined spaces occurs in other geological settings, such as vein initiation and growth (e.g., Fletcher and Merino, 2001), salt growth in pore spaces (e.g., Wellman and Wilson, 1965; Scherer 2004), and mineral growth due to CO_2 sequestration. Dynamic recrystallization during crystal plastic deformation and nucleation of new grains are well studied in geology, but how nucleation of new minerals can also induce plastic deformation is not well understood. Crystals in extrusive magma can deform plastically to accommodate strain when the critical resolved shear stress on favourably oriented lattice planes is exceeded (Kendrick et al., 2017). Crystal plasticity in intrusive silicic magma has never been quantified before. The quantitative data presented here are the first direct evidence of crystal plastic deformation in granite or migmatite. By analysing the sample scale CPO pattern of melt pseudomorphed quartz-plagioclase grains from the Pembroke granulites, we determine that the viscous strain partitioned completely in the melt during deformation, despite the small melt volume, as evidenced by no CPO patterns of the quartz and plagioclase grains (Fig. 5.9). This is also consistent with our other studies where melt phase between a network of rigid suspended particles has accommodated all the strain (Fig. 4.11-4.12, 6.8-6.9). It is likely that strain localizes to new melt pathways or other weaker portions of the crust upon crystallization and/or extraction of the melt, and hence the crystallised portion of the crust highly inhibited post-melt deformation. However, we observe development of amphibole CPO in all the melt-present samples (Fig. 4.11-4.12, 6.8-6.9). Numerous previous studies have suggested that amphibole CPO patterns are predominantly related to brittle deformation (e.g., Babaie and Tour, 1994; Allison and Tour, 1977; Kitamura, 2006). Ko and Jung (2015) conducted deformation experiments and identified four distinct fabric types of amphiboles (type-I to type-IV) based on differential stress within a temperature range of 490-700°C. Type-I CPO has (100) poles subnormal to the shear plane and [001] axes aligned parallel to the shear direction. In contrast, a type-2 pattern is formed by a cluster of (100) poles subnormal to the shear plane and (010) poles aligned subparallel to the shear direction. Type-3 pattern is a combination of type-1 and type-2, with (010) poles and [001] axes forming a girdle subparallel to the lineation. Unlike in other patterns, type-4 shows a girdle of (100) poles and [001] subparallel to the lineation. Naturally deformed amphiboles are also grouped according to this classification where type I CPO develop under low-strain conditions (Mainprice and Nicolas, 1989; Kitamura, 2006; Tatham et al., 2008). Type IV

CPO forms under high-strain conditions and/or in mylonitized shear zones in the middle crust (Imon et al., 2004; Lamarque et al., 2016; Tatham et al., 2008). Other studies have proposed that the amphibole CPOs are a response of crystal plastic deformation (Cao et al., 2010). It has been proposed that CPO strength produced by brittle deformation is weaker than CPO strength produced by plastically deformed amphiboles (Diaz et al., 2007; Cao et al., 2010; Ko and Jung, 2015). Brittle deformation results in the highest MUD values, implying shearing of amphibole parallel to the (100) plane, and both the (100) poles and the [001] axes simply rotate on the (100) plane.

In our study, we observed the formation of four distinct types of CPO patterns in low- and high-strain melt-present samples collected next to each other (Fig. 4.11-4.12). Amphibole CPO in melt-present amphibolite (SPI1338) does not conform to any of the CPO-types described above, whereas amphibole grains in melt-present diorite gneiss exhibit a combination of type III and type IV (Fig. 6.8). MUD values with the highest values are associated with both (100) poles and [001] axes (Fig. 6.8). In-depth orientation studies show no significant crystal plastic deformation in amphibole, with only a 2-4° change in crystal orientation (Fig. 6.11, 6.13), but porphyroclasts with core-mantle structures or bent cleavage planes are absent. A model involving grain rotation in the presence of melt giving rise to amphibole CPO is proposed for melt-present rocks. Quartz grains are melt-crystallized products and thus do not contain any CPO (Fig. 6.8c), whereas lack of CPO in plagioclase exemplify the influence of melt (Fig. 6.8b). These general characteristics are also shared by melt absent amphibolite and diorite gneiss (Fig. 6.8-6.9), which exhibits strong CPO patterns of amphibole grains but only a 2-4° change in crystal orientation. Though amphibole in melt-present diorite gneiss (SPI1311) and melt-absent samples (430643 and 475768) display change in crystal orientation, grain substructures, and development of ordered GND densities (Fig. 6.11, 6.13), they are local very local and do not contribute to the emergence of strong CPO patterns observed in amphibole. We infer a model with dissolution precipitation creep and anisotropic growth parallel to the [001] direction forming similar CPO and SPO patterns in melt-absent samples. Quartz and plagioclase have no preferred crystallographic growth direction and thus do not form a CPO. The absence of CPO in quartz and plagioclase grains also indicates absence of dislocation creep. Hence, while amphibole fabrics are typically consistent with deformation by dislocation creep, it may not be the major strain accommodating mechanism for amphiboles in the studied mid to lower crustal level. One reason dislocation creep dominates in experiments is that amphibole is deformed

as a single-phase material, and the high stresses used in these experiments force dislocation to operate. Type-I fabric is associated with low-stress conditions in the study of crustal anisotropy, whereas type-II fabric is associated with high-stress conditions (in collision and subduction zones) (Ko and Jung, 2015). However, the current study reveals that amphibole CPO is more complex, owing to the presence of melt. Strong CPOs can form in the presence of melt due to mechanical rotation. Thus melt-present zones can contribute to large seismic anisotropies in the crust. The strain rate of the deforming amphibolite in melt-absent samples is controlled by the rate of dissolution, mass transfer, and precipitation process through melt/fluid. Veveakis et al. (2014) discovered that a rock with a nonlinear, non-Newtonian rheology and interstitial melt under compression develops an instability that does not exist when the solid is Newtonian. This instability causes rapid melt segregation and can result in a network of regularly spaced sub-parallel leucosomes oriented perpendicular to the maximum compression axis. Here, we observe that the solid matrix behaves as Newtonian during syn-melt deformation. Furthermore, despite the high strength of individual phases (amphibole, pyroxene, and plagioclase), diffusion creep mechanisms (typically with low stress exponents) can be used to facilitate deformation in mid to lower crustal rocks at significantly lower stresses than dislocation creep. The procedures described here (Chapters 5 and 6) establish a direct link between mineral deformation mechanisms in the presence of melt. This may also represent an important if not typical deformation characteristics of melt crystallized and framework minerals in the lower crustal high-grade granulitic rocks.

Identifying former melt-presence within a deforming high-grade crust

Migmatitic complexes are crustal levels where migrating melt becomes trapped during ascent and crystallizes within the previously suprasolidus crust (now preserved as host migmatites). Thus, these complexes represent an intermediate process between the shallow anatectic front operating at the upper crustal level and deep crust melting. As these rocks preserve the superimposed effects of melting, melt segregation-migration, and melt loss, their study is inherently complicated. In the PhD thesis, the field scale and microstructural characteristics of such zones are examined in detail.

To identify such zones, researchers must first identify exposed field regions where the process of melt transport from the sites of generation to the sites of accumulation is

arrested. This is often indicated by estimates of pressure-temperature condition supporting suprasolidus condition of the rock unit (Chapter 3). Once such areas are identified several field criteria can be established to characterize syn-deformational melt movement:

(a) melt migration accompanied by deformation often produce continuous or discontinuous dyke like structures (Holness et al., 2005; Brown 2004; Weinberg and Regenauer-Lieb 2010), or hydrofractures where melt accumulate into an open gap due to dynamic fracturing. We also recognize local channelized melt movement in the field, where melt migrates from high-pressure zones to low-pressure dilatant sites created by syn-melt deformation (Fig. 4.2). Diffuse porous flow occurs at the microscale and progresses to channelized melt movement, which results in segregated leucosomes observed in the field (Etheridge et al., 2021). Foreign melt ingress during diffuse porous flow or melt segregation can cause rock heterogeneity (Fig. 3.2, 4.2).

(b) As observed in the field, strain in the suprasolidus condition causes shape preferred orientation of elongated crystals (Fig. 3.2, 4.2).

(c) strongly oriented thin, elongated felsic layers formed during active melt migration in the presence of deformation. They are often identified as zones of increased felsic proportion or compositional bands formed during melt-rock interaction (Fig. 4.3; Stuart et al., 2016, 2018). These felsic layers are frequently observed parallel to the host foliation, or they may exhibit strong offsets, pinch-swell structure, sheared or folded bands, axially oriented veins, and a high proportion of undeformed quartzofeldspathic minerals (Fig. 3.2 in Chapter 3; Fig. 4.2 in Chapter 4). These veins also contain peritectic minerals and coarser quartz +plagioclase ± K-feldspar grains crystallized from the melt.

(d) the presence of faults and shear zones as melt-transfer zones in suprasolidus and subsolidus rocks (Daczko and Piazolo, 2022; Hutton et al., 1992; Richards and Collins, 2004).

(e) In addition to the aforementioned criteria, melt-accumulation zones (as observed here) have the following characteristics: lack of preservation of peritectic minerals (peritectic minerals can back react and dissolve if enough melt is present) and absence of collapse of formerly melt-filled structures (Brown et al. 1999). Creation of low- and high-strain zones for effective melt transport and accumulation. Strain induced re-organization of felsic veins can cause strong bandings comparable to stromatitic migmatites (Haslová et al., 2008a; Závada et al., 2018). Melt accumulation resulted in the formation of mesocratic rock

devoid of melanosomes-leucosome banding. Melt accumulation is also identified by: a. the absence of broad mafic selvedges surrounding thin felsic domains, and b. the volume of melt in leucosomes> peritectic minerals.

Earlier works have proposed the possibility of a dynamic interaction between melt migration and deformation during diffuse porous melt flow (Stuart et al., 2018b; Meek et al., 2019; Piazolo et al., 2020). However, the detailed interplay process, and associated signatures, both at tectonic scale and local scale, were not addressed earlier. Similarly, diffuse porous melt migration resulting in a melt accumulation zone in the mid-lower crust had not previously been identified.

The former presence of melt in the field is easily confirmed by petrographic observations when the amount of melt in the representative samples is nearly 7 to 10 vol.%. The features include (also including the features identified during melt-accumulation in Chapter 3): A) grain scale heterogeneity caused by melt-rock interaction during fluxing of compositionally distinct melt or during melt segregation from the host rock (Fig. 2.2-2.5 in Chapter 2; Fig. 3.3 in Chapter 3; Fig. 4.4-4.6 in Chapter 4; Fig. 6.1 in Chapter 6), B) characteristics of melt pseudomorphs, such as elongated xenomorphic quartz grains with cuspate grain boundaries, low dihedral angles, strings of beads texture, quartz-plagioclase intergrowth, etc. (refer to Fig. 3.4 in Chapter 3; Fig. 4.4-4.6 in Chapter 4; Fig. 5.2-5.4 in Chapter 5; Fig. 6.3 in Chapter 6), C) absence of extensive dynamic recrystallization or core-mantle structures.

However, when the melt volume is extremely low <5 vol.%, these melt-microstructures are not always prevalent (Stuart et al., 2018; Daczko and Piazolo, 2022). Here, a set of criteria for recognizing melt-pseudomorphed grains are identified, even if their petrographic characteristics are obscure. These include: (A) lack of sample scale CPO of melt-crystallized grains (Fig. 4.11-4.12 in Chapter 4; Fig. 5.5, 5.7, 5.9 in Chapter 5;), (B) undulose extinction and formation of subgrain boundaries (Fig. 4.13 in Chapter 4; Fig. 5.5, 5.7, 5.9 in Chapter 5), (C) localized disorientation along the grain edges of melt-crystallized quartz (Fig. 5.5, 5.7, 5.9 in Chapter 5), (D) distinct substructure, with high GND densities at subgrain boundaries and the development of multiple slip systems (Fig. 5.6, 5.8, 5.10 in Chapter 5) relating to stresses involved during melt-crystallization in a confined space, (E) strong SPO pattern of the elongated matrix minerals such as amphibole and biotite (Fig. 3.4 in Chapter 3; Fig. 4.4-4.6, 4.10-4.11 in Chapter 4; Fig. 5.4 in Chapter 5; Fig. 6.5, 6.8 in

Chapter 6), and (F) very minute activity of dislocation creep in the host minerals as evidenced by no CPO of plagioclase grains and very minute distortions observed within the amphibole grains (Fig. 4.13 in Chapter 4; Fig. 6.10-6.11 in Chapter 6). Thus, the thesis validates the use of melt-microstructures by previous researchers (Daczko et al., 2016; Stuart et al., 2018b; Meek et al., 2019), but provides in-depth EBSD microstructural characteristics of melt crystallized grains that are consistent regardless of geodynamic environment or melt percentage.

Chapter 8

Conclusions and future work

8.1 Conclusions

The presence of melt in the middle to lower crust causes a significant decrease in strength, making it rheologically weak. This thesis sought to identify the mechanisms and processes at work during syn-deformation porous melt migration. The following conclusions have been drawn from this study:

1. Melt-rock interaction can cause grain scale heterogeneity. These rocks can be used to identify compositional domains, and the proposed MapComp method can be utilized to derive pressure-temperature conditions during melting and melt migration. However, the presented method is constrained by the spatial resolution of micro XRF data of 15 µm and trace element concentrations commonly in the order of 10 ppm.

2. Whole rock geochemical data (obtained by MapComp) of the melt-present rocks produce very reliable P-T estimates. The studied field area in the Akia terrane, SW Greenland, exhibits syn-deformational high-pressure, high-temperature granulitic facies metamorphism (760-812 °C at 0.61-0.76 GPa), which is consistent with previous estimates.

3. Lower crustal diorite gneiss in the Akia Terrane is identified to have experienced both in-situ partial melting and external melt fluxing during progressive deformation. An external melt of similar chemistry infiltrated this portion of the crust via porous flow along an interconnected grain boundary network. The melt migration

and organization are aided by deformation and create high strain domains, which further facilitate melt transportation and the formation of melt accumulation zone. Melt microstructures are readily identified and porous melt flow is evidenced by large volume of crystallized melt and grain scale microstructural and geochemical homogenization.

4. Melt crystallized quartz grains exhibit crystal bending and formation of subgrain boundaries with tilt and twist walls parallel to quartz basal and prism planes and a lack of sample scale CPO. These features are distinctive from quartz deformed under sub-solidus conditions. This provides us with a toolbox to identify melt microstructures in rocks with little evidence of diffuse porous flow.

5. The presence of melt along grain boundaries can absorb a significant amount of differential stress, as demonstrated by very minor dislocation creep of the deforming matrix. However, high aspect ratio of amphibole and biotite facilitate rigid body rotation as evidenced by a strong correlation between grain aspect ratio, SPO and CPO strength that allowed preferential alignment of the long axes of amphibole-biotite grains parallel to the stretching direction.

8.2 Remaining knowledge gap and scope of future research

The identification of rock fluxed by porous melt flow, as well as the microstructural and geochemical tools developed in this thesis for characterizing melt-rock interaction and identifying features attributed to syn-melt deformation, have been studied primarily in arc settings, but should be applied to other settings and must be tested against different rock compositions and mineral assemblages. Due to the recent discovery of this phenomenon in the crust, there are numerous possible future research directions. Based on this thesis and current literature, several new avenues of future research must be pursued in order to understand, recognize, and predict melt-related phenomena in the crust. Here, a selection of possible topics is provided:

8.2.1 MapComp bulk chemistry determination

During bulk chemistry determination, the MapComp analyses identified large scale errors for low-concentration elements. For better constraints, samples with complex zoning and more than one Na-rich phase should be investigated. Furthermore, the limit beyond which heterogeneity has pronounced influence on phase equilibria modelling must also be studied using a diverse set of samples with increasing heterogeneity.

8.2.2 Diffuse porous flow

In the thesis, we advocate for diffuse porous flow within the mid to lower crust. However, previous research on porous melt flow in the lower crust identified heavy replacement and hydration of rocks in high strain shear zones (Stuart et al., 2018a; Meek et al., 2019). There is no evidence of replacement microstructures during melt-rock interaction in this study. This is also due to the lack of any precursor rock with a pre-melt history. The true extent of porous flow can only be determined by studying the microstructural and geochemical changes in a variety of samples with pre-, syn-, and post-melt histories. Because the melt-rock reaction can change the composition of the rock undergoing melt fluxing, it can also change the composition of the fluxing melt. Here, the melt that fluxed through the diorite gneiss is preserved (type 1 to type 3 vein types in Chapter 4), and although the open-system nature of melt flux prevents constraining the true melt composition, further research along these lines is possible. Does migration by porous melt flow have a quantifiable impact on the composition of the melting fluid? And is the effect consistent? These can be tested in other field areas where outcrops preserve both fluxing melt and fluxed rocks, or through experimental techniques. Many locations have reported an association of large volumes of melt and large-scale shear zones. Therefore, it is possible to investigate whether porous melt flow is a viable mechanism of strain localization in the high-T crust, such as within the Himalayas (India), the North American Cordillera arc (United States), and other collisional orogens.

Additionally, this thesis focuses on porous melt flow through the dioritic root of the magmatic arc in Akia terrane. Is it possible, however, to detect porous melt flow within the surrounding metasedimentary basement rocks? What distinguishes the porous flow through various meta-sedimentary rocks from the examples examined in this thesis? Field evidence

also suggests that the melt–rock reaction in the metapelite and metapsammite unit is likely to differ substantially. Melt-enhanced nucleation may account for the presence of abundant garnet in metapelite samples close to the shear zone. This will also aid in the investigation of how porous melt flow can affect the rheological behaviour of a specific rock type.

8.2.3 Melt-rock interactions in an open system

Limitations of modelling open systems with thermodynamic isochemical phase diagrams manifests potential of experimental petrology to study melt-rock interaction and high-temperature kinematics. One of the outcomes of this thesis, such as chemical homogenization due to external melt fluxing, is a compelling prospect for further investigation using melt-rock reaction experiments. Additionally, a promising area for further investigation is how melt-rock interactions affect the zoning, REE patterns in specific minerals and geochronometers like zircon, monazite, and apatite. This has not been explored in this study, but the samples examined in this thesis would be excellent candidates for further study along these lines. This could be especially important for obtaining a P-T-D-t history of Akia terrane by studying the island and mainland amphibolites. Other mainland amphibolite samples must also be studied to better constrain the P-T condition of Akia terrane. A holistic approach combining pressure-temperature-deformation-isotopic responses with thermal, rheological, and kinematic condition of lower crustal melt-fluid pathways will attribute to the true nature of Archean geodynamics operative in the Akia terrane. This will have further implications in resolving conflicting models of tectenothermal history of Akia terrane.

8.2.4 Partial melt zones vs. diffuse porous flow

From this study, we understand little partial melting and deformation are prerequisites for the development of permeability during melt-fluxing. But how do migmatites formed entirely by partial melting differ from rocks formed by both diffuse porous flow and partial melting? Deformation of partially molten rocks causes melt segregation and extraction, but how does this mechanism differ from those observed in diffuse porous flow? Will the response of partially melt shear zones be similar to that seen in diffuse porous flow? Further research into the microstructures and crystallographic

responses of partial melt shear zones vs. shear zones with diffuse porous flow will help us understand the deformation processes at work, as well as the rheological implications.

8.2.5 Deformation microstructures

To further advance our understanding of syn-melt deformation textures outlined in this thesis, high temperature syn-melt deformation experiments should be conducted to understand the deformation conditions necessary for the formation of such microstructures Deformation experiments on natural and synthetic migmatite samples will significantly enhance our understanding in predicting shear zone and mid-lower crustal dynamics. Can experimental deformation studies using natural samples replicate the observed deformation microstructures of amphibole-plagioclase grains in the presence of melt?

High-grade metamorphic rocks and glacier ice deform based on the same nonlinear flow laws. Hence, Ice can be used as a good analogue to study deformation of crystalline rocks. The results of this research can also be applied to the deformation of rocks in the middle to lower crust, which will help us understand large-scale plate tectonic processes like mountain building, orogenic collapse, and escape tectonics (Kohlstedt et al., 2009; Brown et al., 2011; Jamieson et al., 2011). In order to understand the growth induced deformation in crystallizing grains, samples with prograde, retrograde and reaction products must be studied. Will extrusive rocks with a faster crystallization rate produce the same deformation microstructures seen here? The inherent distortion of crystal lattices can affect melt-crystallized zircon grains and thus geochronology.

Appendices

Appendix 2 – Supporting information for Chapter 2

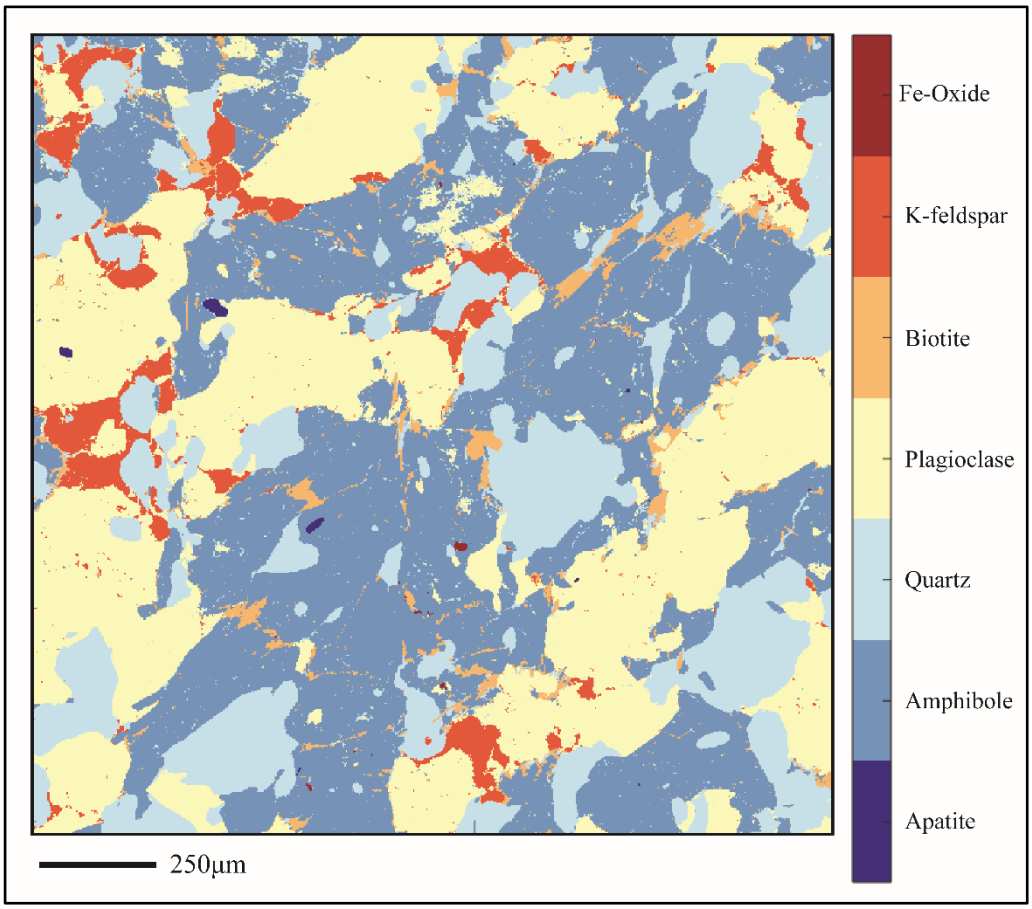

Figure AP2 – 1: EPMA major element map of 'Area I_2' within 'Domain I' in *Heterogeneous rock III: Diorite Gneiss* (SPI1321).

Appendix 3 – Supporting information for Chapter 3

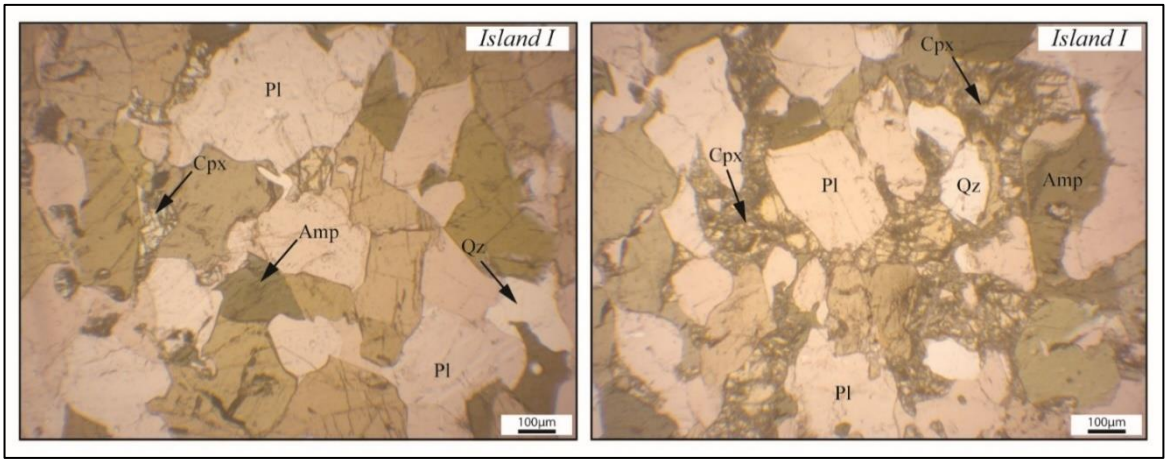

Figure AP3 – 1: Clinopyroxene grains in *Island I* show irregular grain boundaries and are corroded by surrounding amphibole gains.

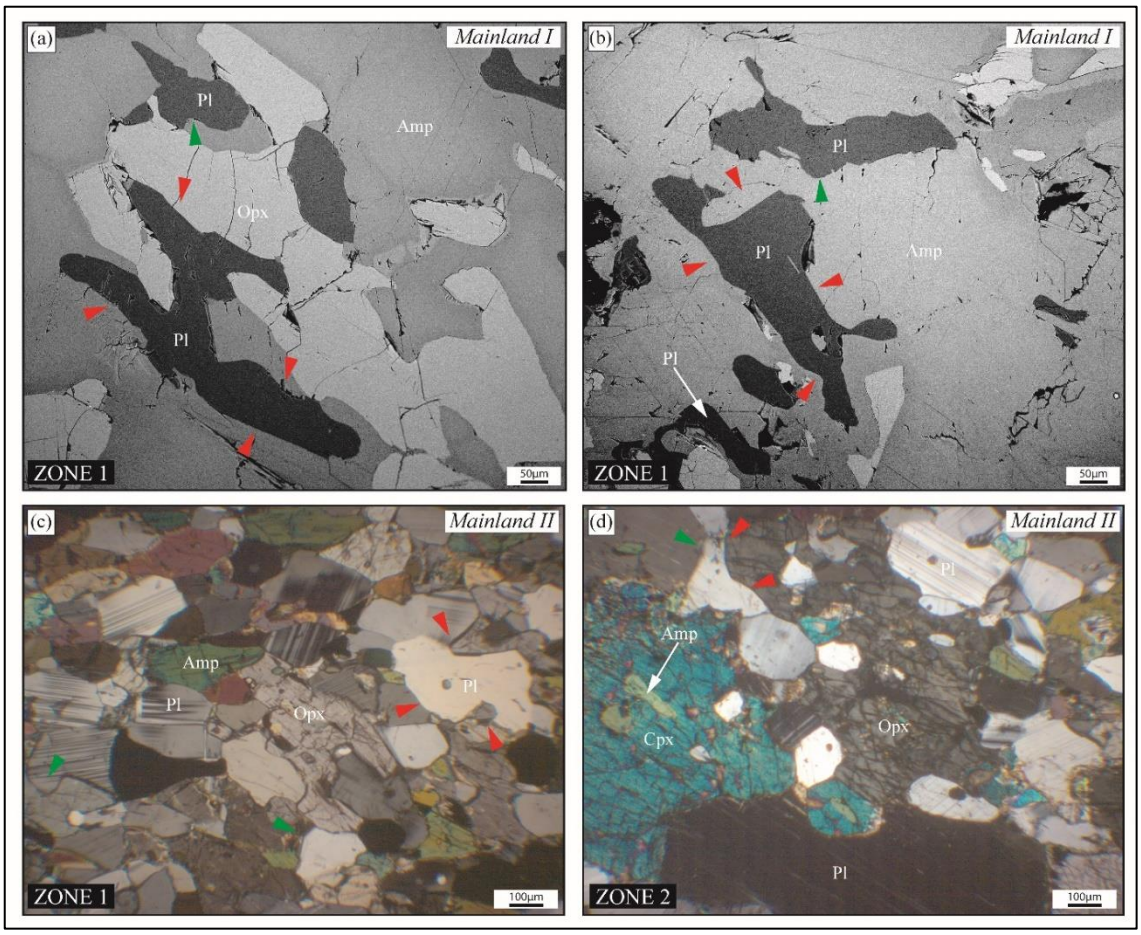

Figure AP3 – 2: Microstructures indicative of former melt presence in the *Mainland* amphibolites. (a-d) Plagioclase grains in *Mainland I* and *Mainland II* display irregular anhedral grains (red arrows) extended along grain boundaries of orthopyroxene, clinopyroxene and amphibole and/or have cuspate grain boundaries (green arrows) indicative of crystallization from melt.

Table AP3.1: Mineral chemistry data of Amphibole (Amp/Hbl). Felsic vein = 'Zone 2'.). Representative analyses shown in Tab. 3.2 are highlighted.

Sample	Textural Position	SiO_2	TiO_2	Al_2O_3	MnO	FeO	MgO	CaO	Na_2O	K_2O	Total
1338H19	Matrix	40.87	2.05	12.27	0.22	19.43	7.90	11.10	1.39	1.58	96.81
1338H26	Matrix	40.63	2.00	12.42	0.23	20.06	7.71	11.38	1.39	1.60	97.42
1338H25	Matrix	40.39	2.06	12.35	0.21	19.37	7.92	11.35	1.37	1.56	96.60
1338H24	Matrix	40.75	2.01	12.23	0.20	19.92	7.83	11.23	1.36	1.60	97.13
1338H23	Matrix	40.45	2.02	12.45	0.20	19.78	7.81	11.36	1.40	1.59	97.06
1338H22	Matrix	40.99	2.08	12.31	0.18	19.75	7.98	11.30	1.39	1.56	97.55
1338H10	Matrix	40.76	1.78	12.30	0.18	19.49	8.23	11.26	1.34	1.44	96.78
1338H11	Matrix	40.87	1.95	12.18	0.20	20.00	7.72	11.37	1.28	1.60	97.17
1338H12	Felsic vein	41.56	1.94	12.17	0.16	18.99	8.41	11.49	1.09	1.51	97.34
1338H1	Matrix	40.55	1.74	12.26	0.23	19.70	8.05	11.45	1.28	1.58	96.83
1338H3	Matrix	40.65	1.77	12.26	0.23	19.58	7.94	11.31	1.43	1.53	96.70
1338H14	Matrix	40.76	2.13	12.16	0.23	19.57	7.92	11.31	1.28	1.59	96.96
1338H15	Matrix	40.98	1.99	12.07	0.26	19.80	7.78	11.06	1.56	1.57	97.07
1338H16	Matrix	41.12	1.97	12.36	0.21	19.32	8.18	11.36	1.33	1.59	97.43
1338H17	**Matrix**	**40.43**	**1.96**	**12.84**	**0.23**	**19.45**	**7.92**	**11.50**	**1.50**	**1.69**	**97.52**
1338H14_1	Matrix	40.91	1.92	12.31	0.26	19.53	7.92	11.30	1.39	1.65	97.19
1338H14_2	Matrix	41.00	1.92	12.26	0.23	19.62	8.12	11.26	1.34	1.58	97.35
1338H14_3	Matrix	41.06	1.97	12.38	0.16	19.67	8.16	11.53	1.37	1.52	97.82
1338_H18	Matrix	40.54	1.79	12.27	0.20	19.52	7.84	11.29	1.32	1.64	96.43
1338H21	Matrix	40.55	1.83	12.71	0.22	19.71	7.82	11.51	1.37	1.63	97.35
1338H150_6	Near/inside felsic vein	41.33	1.75	12.14	0.20	18.60	8.57	11.48	1.41	1.56	97.04
1338H140_6	Near/inside felsic vein	41.28	2.24	12.28	0.19	18.44	8.10	11.48	1.29	1.66	96.96
1338H552_6	Near/inside felsic vein	39.91	1.81	12.93	0.18	19.97	7.49	11.31	1.46	1.65	96.71
1338H550_6	Near/inside felsic vein	40.79	2.01	12.34	0.14	18.47	8.37	11.28	1.34	1.55	96.30
1338H653_6	Near/inside felsic vein	41.05	2.07	11.73	0.14	19.23	8.35	11.12	1.34	1.59	96.62
1338H551_6	Near/inside felsic vein	41.09	1.79	12.28	0.17	19.41	8.19	11.26	1.34	1.56	97.09
1338H851_6	Near/inside felsic vein	40.76	1.84	12.08	0.18	19.53	8.05	11.08	1.31	1.58	96.41
1340H2	Rim (matrix)	41.44	1.64	12.54	0.20	17.79	9.18	11.56	1.30	1.25	96.92
1340H1	Rim (matrix)	40.55	1.64	13.75	0.22	17.66	8.71	11.37	1.34	1.31	96.55
1340H3	Core (matrix)	41.20	2.06	12.44	0.15	17.67	8.96	11.38	1.35	1.42	96.63
1340H4	Rim (matrix)	41.27	1.96	12.39	0.23	17.96	8.99	11.47	1.30	1.41	96.99
1340H6	Core (matrix)	41.14	1.73	13.07	0.17	17.56	8.94	11.37	1.28	1.29	96.56
1340H7	**Core (matrix)**	**41.13**	**1.68**	**13.20**	**0.19**	**17.89**	**8.81**	**11.38**	**1.28**	**1.22**	**96.77**
1340H8	(inclusion in grt in matrix)	40.79	2.09	12.78	0.16	17.62	8.92	11.44	1.36	1.28	96.45
1340H9	Rim (matrix)	41.11	1.92	12.98	0.20	17.62	8.61	11.53	1.26	1.40	96.63
1340H10	Core (matrix)	41.45	1.65	12.68	0.15	17.80	9.02	11.42	1.30	1.16	96.65
1340H11	Core (inclusion in grt in matrix)	41.57	2.18	12.47	0.08	16.18	9.85	11.57	1.26	1.49	96.66
1340H12	Rim (matrix)	40.72	1.82	13.28	0.15	17.91	8.76	11.45	1.29	1.27	96.65
1340H13	Core (matrix)	40.76	1.99	12.56	0.19	18.01	8.99	11.52	1.29	1.40	96.71
1340H19	Core (matrix)	41.53	1.72	12.74	0.15	17.07	9.55	11.50	1.23	1.23	96.72

1340H20	Rim (matrix)	43.11	1.84	12.65	0.20	16.92	9.10	11.55	1.16	1.36	97.89
1340H22	Rim (matrix)	42.43	1.72	12.15	0.16	17.52	9.35	11.24	1.35	1.21	97.13
1340H23	Core (matrix)	41.71	1.80	12.27	0.20	17.54	9.19	11.29	1.27	1.27	96.57
1340H26	Core (matrix)	42.16	1.66	12.83	0.19	17.05	9.41	11.57	1.24	1.24	97.37
1340H30	Core (felsic)	45.73	0.62	10.67	0.31	14.48	12.30	11.25	1.03	0.65	97.06
1340H31	Rim (felsic)	45.59	0.58	10.55	0.35	14.56	12.48	11.43	1.03	0.78	97.35
1340H32	**Core (felsic)**	**44.90**	**0.60**	**10.47**	**0.28**	**15.48**	**12.10**	**11.15**	**1.00**	**0.76**	**96.75**
1340H35	Rim (felsic)	44.55	0.57	11.76	0.33	14.81	11.52	11.52	1.05	0.84	96.98
1340H38	Core (felsic)	44.76	0.61	11.45	0.31	14.29	11.72	11.21	1.07	0.77	96.18
1340H18_7	Core (matrix)	41.28	1.65	12.50	0.14	17.42	9.45	11.19	1.29	1.18	96.10
1340H18_8	Rim (matrix)	40.74	1.95	12.46	0.19	17.58	9.04	11.21	1.31	1.23	95.71
1340H120_6	Rim (matrix)	41.36	1.73	12.53	0.17	17.32	9.23	11.28	1.20	1.33	96.16
1340H119_6	Core (matrix)	41.29	1.93	12.39	0.16	18.12	8.99	11.03	1.30	1.41	96.62
1340H121_6	Rim (matrix)	42.04	1.64	13.12	0.14	17.20	8.97	11.55	1.25	1.18	97.09
1341B_H6	Amp 1	42.42	1.76	11.44	0.27	16.44	10.19	11.69	1.31	1.48	97.04
1341B_H14	Amp 1	42.36	1.72	11.10	0.28	16.75	10.07	11.70	1.21	1.50	96.75
1341B_H27_1	Amp 1	42.35	1.80	11.19	0.28	17.14	9.73	11.67	1.24	1.62	97.08
1341B_H24_1	Amp 1	41.92	1.83	11.48	0.31	16.60	9.89	11.80	1.19	1.57	96.64
1341B_H24	Amp 1	42.08	1.81	11.37	0.27	16.83	9.81	11.63	1.25	1.52	96.63
1341B_H26	Amp 1	42.37	1.79	11.34	0.34	17.20	9.75	11.67	1.26	1.57	97.33
1341B_H_31_1	Amp 1	42.86	1.51	11.40	0.31	17.50	9.30	11.84	1.13	1.12	97.01
1341B_H31	Amp 1	42.49	1.77	11.45	0.31	16.83	9.74	11.71	1.16	1.62	97.14
1341B_H28	Amp 1	43.14	1.57	11.35	0.31	16.75	9.78	11.94	1.10	1.37	97.35
1341B_H29	Amp 1	42.61	1.72	11.23	0.30	17.15	9.72	11.63	1.17	1.55	97.12
1341B_H30	Amp 1	42.07	1.87	11.55	0.28	17.24	9.52	11.62	1.24	1.57	97.01
1341B_H30_1	**Amp 1**	**41.82**	**1.64**	**11.46**	**0.32**	**18.48**	**8.57**	**11.79**	**1.02**	**1.57**	**96.67**
1341B_H34	Amp 1	41.96	1.82	11.46	0.28	17.35	9.56	11.71	1.29	1.62	97.08
1341B_H34_1	Amp 1	42.17	1.84	11.15	0.28	17.50	9.66	11.71	1.19	1.60	97.16
1341B_H36	Amp 1	42.03	1.88	11.26	0.22	17.35	9.66	11.73	1.13	1.65	96.97
1341B_H37	Amp 1	42.09	1.89	11.36	0.21	17.52	9.51	11.65	1.29	1.63	97.20
1341B_H41	Amp 2	49.20	0.51	6.45	0.35	13.47	13.64	12.22	0.71	0.45	97.01
1341B_H40	Amp 2	42.36	1.71	11.28	0.32	18.19	9.05	11.72	1.38	0.93	96.96
1341B_H42	**Amp 2**	**48.50**	**0.35**	**7.19**	**0.31**	**14.39**	**13.10**	**12.29**	**0.78**	**0.57**	**97.49**
1341B_H39	Amp 2	41.94	1.63	11.65	0.31	18.27	8.91	11.80	1.32	1.29	97.15
1341B_H40_1	Amp 2	42.48	1.50	11.15	0.34	18.25	9.24	11.76	1.21	1.28	97.30
1341B_H46	Amp 2	50.38	0.23	5.64	0.35	13.37	13.91	12.48	0.51	0.37	97.25
1341B_H49	Amp 1	42.16	1.42	11.61	0.31	18.34	8.92	11.84	1.26	1.23	97.11
1341B_H43	Amp 2	42.31	1.80	11.46	0.28	17.89	9.10	11.76	1.12	1.57	97.34
1341B_H44	Amp 2	41.75	2.06	11.60	0.29	18.14	8.82	11.75	1.27	1.64	97.38
1341B_H50	Amp 2	48.95	0.53	7.01	0.34	13.80	13.53	12.03	0.67	0.55	97.43
1399AH6_20	Core	46.59	0.63	8.39	0.11	8.17	16.21	11.64	1.62	0.72	94.10
1399AH6_12	Core	47.77	0.62	7.46	0.09	7.88	16.65	11.75	1.49	0.74	94.47
1399AH10_3	Rim	52.33	0.21	4.61	0.13	6.97	18.75	11.84	0.94	0.33	96.11
1399AH18_8	Core	48.29	0.64	7.60	0.10	7.69	17.25	12.05	1.44	0.73	95.79
1399AH72_7	Core	50.65	0.24	6.03	0.14	7.68	18.34	11.60	1.10	0.33	96.13
1399A_H6_12	Core	49.10	0.53	7.10	0.11	7.95	17.56	11.74	1.37	0.66	96.11
1399A_H6_13	Core	48.20	0.40	8.01	0.13	7.97	17.20	11.68	1.45	0.50	95.54
1399A_H6_14	Rim (Adjacent to Cpx)	55.01	0.08	2.01	0.12	5.84	20.12	12.27	0.44	0.09	95.99
1399A_H6_15	Rim (Adj to Cpx)	54.83	0.11	2.11	0.14	5.99	20.24	12.39	0.40	0.09	96.30
1399A_H6_17	Core	47.10	0.59	7.99	0.11	8.12	16.95	11.82	1.48	0.69	94.85
1399A_H6_20	Core	48.22	0.47	7.37	0.14	7.99	17.32	11.81	1.31	0.50	95.14
1399A_H6_19	Core	49.07	0.50	6.99	0.12	7.63	17.53	12.07	1.32	0.64	95.87
1399A_H3	Core (Adj to Opx)	48.51	0.71	7.30	0.13	8.11	17.07	11.83	1.42	0.76	95.84
1399A_H2	Core (Adj to Cpx)	47.59	0.57	7.75	0.11	8.29	16.64	12.06	1.40	0.60	95.02
1399A_H4	Core	54.06	0.10	2.03	0.14	6.01	20.03	12.53	0.41	0.12	95.44

1399A_H8	Inclusion within Opx	47.14	0.70	8.34	0.10	8.14	17.03	11.53	1.66	0.67	95.32
1399A_H10	Core	48.53	0.62	7.02	0.10	7.99	17.46	11.93	1.35	0.58	95.57
1399A_H10_1	Core	48.48	0.64	6.96	0.10	7.74	17.38	11.88	1.40	0.70	95.28
1399A_H15	Rim	51.32	0.29	4.32	0.09	6.82	18.94	12.45	0.86	0.31	95.41
1399A_H34	**Core**	**48.75**	**0.66**	**6.71**	**0.16**	**7.71**	**17.72**	**11.49**	**1.41**	**0.45**	**95.06**
1399A_H33	**Rim**	**55.25**	**0.12**	**1.90**	**0.14**	**5.46**	**21.06**	**12.08**	**0.40**	**0.07**	**96.48**
1399A_H32	Rim	51.09	0.31	5.63	0.10	7.26	18.61	11.65	1.04	0.41	96.10
1399A_H31	Core	48.06	0.64	7.31	0.12	8.14	17.65	11.61	1.41	0.69	95.63
1399A_H27	Core	48.10	0.59	7.78	0.12	8.02	17.09	11.77	1.44	0.72	95.63
1399A_H39	Core	47.59	0.68	7.67	0.14	8.87	16.54	11.85	1.47	0.74	95.55
1399A_H40	Rim	55.04	0.11	1.44	0.11	6.06	20.46	12.27	0.35	0.10	95.95
1399A_H41	Rim	56.44	0.05	0.76	0.12	5.71	21.02	12.23	0.21	0.04	96.58
1399A_H57	Rim	53.93	0.17	2.60	0.12	6.61	19.36	12.49	0.53	0.11	95.92
1399A_H56	Core	49.07	0.61	6.73	0.10	8.28	17.30	12.13	1.24	0.68	96.14
1399A_H53	Rim	53.00	0.25	3.46	0.11	6.73	19.16	12.41	0.62	0.23	95.96
1399A_H52	Core	47.71	0.68	7.87	0.09	8.67	16.47	12.17	1.43	0.84	95.93
1399A_H55	Rim	54.23	0.19	2.59	0.12	6.21	19.77	12.63	0.47	0.17	96.37
1399A_H54	Core	47.80	0.58	7.26	0.13	8.41	16.90	12.11	1.31	0.73	95.23
1399A_H46	Core(inclusion in opx)	52.31	0.13	4.06	0.10	7.23	18.37	12.51	0.69	0.15	95.55
1399A_H44	Core(inclusion in opx)	47.68	0.65	7.46	0.12	8.71	16.43	11.93	1.42	0.61	95.01
1399A_H52	Core	47.51	0.60	7.25	0.12	8.63	16.86	12.04	1.33	0.66	95.01
1399A_H52_1	Core	47.68	0.62	7.24	0.11	8.37	16.98	11.78	1.32	0.75	94.85
1399A_H48	Rim	54.52	0.08	1.98	0.09	6.18	19.89	12.33	0.43	0.13	95.63
1399A_H59	Rim	54.26	0.20	2.43	0.17	6.21	20.48	11.53	0.47	0.15	95.89
1399A_H62	Rim	55.79	0.10	1.55	0.07	5.21	20.74	12.76	0.33	0.10	96.65
1399A_H63	Rim	54.43	0.16	2.39	0.09	5.42	20.34	12.63	0.46	0.14	96.06
1399A_H66	Core	47.46	0.63	8.17	0.10	8.00	16.97	11.51	1.54	0.70	95.08
1399A_H69	Rim	55.53	0.12	1.69	0.09	5.40	20.74	12.72	0.35	0.10	96.74
1399A_H68	Rim	54.55	0.15	2.43	0.10	5.43	20.52	12.10	0.50	0.11	95.89
1399A_H71	Core	48.29	0.78	7.95	0.08	7.29	17.23	12.10	1.31	0.76	95.79
1399A_H70	Core	49.90	0.57	6.10	0.13	6.83	18.49	11.48	1.23	0.45	95.18
1399A_H75	Core	47.68	0.65	7.84	0.13	7.80	17.25	11.56	1.44	0.70	95.05
1399A_H76	Core	48.04	0.66	7.49	0.10	7.63	17.46	11.58	1.45	0.62	95.04
1399A_H77	Rim	53.15	0.22	3.37	0.14	5.93	20.27	11.86	0.70	0.20	95.85
1382_H1	**Matrix**	**43.75**	**1.16**	**11.66**	**0.13**	**14.18**	**11.91**	**11.98**	**1.22**	**1.17**	**97.16**
1382_H2	Matrix	45.42	1.11	10.24	0.18	14.44	12.85	11.79	1.42	0.74	98.19
1382_H4	Matrix	44.86	1.96	10.70	0.21	14.31	11.85	11.62	1.64	0.85	98.00
1382_H4_3	Matrix	44.72	1.77	11.09	0.19	14.14	12.15	11.51	1.57	0.90	98.03
1382_H4_2	Matrix	44.64	1.86	10.81	0.17	14.52	11.78	11.61	1.64	0.91	97.94
1382_H7	Matrix	44.63	1.73	10.81	0.17	14.66	11.78	11.76	1.62	0.86	98.04
1382_H5_2	Matrix	44.75	1.76	11.00	0.19	14.44	11.75	11.58	1.59	0.89	97.95
1382_H8	Matrix	45.29	1.41	10.30	0.20	14.20	12.43	11.69	1.52	0.72	97.76
1382_H8_1	Matrix	45.09	1.21	10.36	0.17	14.97	12.00	11.72	1.48	0.88	97.89
1382_H8_2	Matrix	44.64	1.82	10.90	0.21	14.43	11.73	11.65	1.51	0.91	97.79
1382_H10	Matrix	45.37	1.34	10.59	0.19	14.16	12.17	11.75	1.41	0.78	97.76
1382_H16_4	Matrix	44.83	1.43	10.94	0.17	14.44	12.00	11.64	1.48	0.82	97.76
1382_H16_3	Near/inside vein	45.01	1.51	10.82	0.17	14.72	12.05	11.55	1.44	0.86	98.13
1382_H16_9	Near/inside vein	44.63	1.70	10.90	0.15	14.56	11.77	11.60	1.46	0.89	97.66
1382_H16_1	Near/inside vein	44.73	1.49	10.77	0.14	14.46	11.87	11.62	1.50	0.88	97.45
1382_H16_2	Near/inside vein	44.55	1.56	10.85	0.19	14.73	11.97	11.62	1.63	0.91	98.01
1382_H16_7	Matrix	44.30	1.42	10.88	0.15	14.83	11.88	11.50	1.52	0.88	97.37
1382_H16_6	Matrix	44.68	1.47	10.99	0.23	14.69	11.77	11.62	1.52	0.89	97.87
1382_H16_5	Matrix	45.09	1.34	10.22	0.19	15.67	11.63	11.54	1.56	0.59	97.83

1382_H16	Matrix	44.93	1.52	10.68	0.21	14.68	11.87	11.51	1.44	0.85	97.70
1382_H11	Near/inside vein	44.60	1.29	10.74	0.20	15.64	11.54	11.61	1.60	0.68	97.89
1382H52	Matrix	42.46	1.97	10.67	0.16	14.26	10.30	11.25	1.43	0.81	93.31
1382H53	Matrix	43.42	1.30	10.92	0.17	14.20	11.81	11.45	1.35	0.85	95.47
1382H54	Matrix	11.68	0.24	4.07	0.04	71.82	3.66	2.48	0.44	0.19	94.61
1382H55	Matrix	42.91	1.83	11.10	0.19	14.43	11.15	11.12	1.57	0.84	95.13

Table AP3.2: Mineral chemistry data of Biotite (Bt). Felsic vein = 'Zone 2'. Representative analyses shown in Tab. 3.5 are highlighted.

	Position	SiO_2	TiO_2	Al_2O_3	FeO	MnO	MgO	CaO	Na_2O	K_2O	Total
1338B0	Matrix	35.80	3.64	15.70	19.22	0.08	11.33	0.00	0.08	9.79	95.64
1338B4	Matrix	35.71	3.94	15.12	19.67	0.00	11.20	0.00	0.04	9.67	95.35
1338B5	Matrix	35.30	4.60	14.78	20.58	0.09	9.82	0.04	0.00	9.56	94.86
1338B6	**Matrix**	**35.42**	**4.13**	**15.31**	**19.97**	**0.10**	**10.68**	**0.00**	**0.00**	**9.74**	**95.43**
1338B7	Matrix	35.32	3.86	15.46	19.60	0.06	11.12	0.00	0.00	9.91	95.33
1338B8	Matrix	35.57	4.19	15.22	19.85	0.00	10.67	0.04	0.04	9.82	95.40
1338B9	Matrix	35.15	3.74	15.55	19.56	0.07	11.12	0.08	0.04	9.50	94.88
1338B10	Matrix	35.48	4.09	15.92	19.06	0.07	11.01	0.00	0.03	9.64	95.36
1338B11	Matrix	35.71	4.03	15.69	19.04	0.00	11.13	0.00	0.00	9.76	95.44
1338B12	Matrix	36.13	3.81	15.31	18.87	0.09	11.26	0.00	0.05	9.54	95.18
1338B1	felsic vein (Grt inclusion)	35.61	3.74	15.52	19.21	0.00	11.02	0.05	0.10	9.63	95.00
1338B2	felsic vein (Grt inclusion)	35.22	3.49	16.29	19.54	0.06	10.92	0.00	0.06	9.70	95.28
1338B3	Matrix	35.27	4.01	15.59	20.42	0.06	9.76	0.03	0.04	9.57	94.79
1338B195	felsic vein (Grt inclusion)	35.21	3.55	18.02	22.03	0.04	6.48	0.13	0.08	8.38	93.92
1340B2	Matrix	35.84	3.88	16.37	16.07	0.05	12.53	0.00	0.00	9.95	94.76
1340B1	Matrix	35.83	3.92	16.10	16.89	0.06	12.41	0.00	0.00	9.89	95.10
1340B4	felsic vein (inclusion inGrt)	35.52	3.94	15.32	18.50	0.06	11.30	0.00	0.04	9.71	94.39
1340B5	**Matrix**	**35.55**	**3.76**	**15.72**	**18.29**	**0.00**	**11.33**	**0.00**	**0.05**	**9.61**	**94.32**
1340B6	Matrix	35.94	3.68	15.90	17.67	0.07	12.03	0.00	0.00	9.87	95.16
1340B8	Matrix	35.79	4.23	15.64	17.58	0.00	11.51	0.00	0.05	10.04	94.86
1340B9	Matrix	35.63	4.37	15.53	18.01	0.07	11.49	0.00	0.05	9.81	94.97
1340B10	Matrix (inclusion in Grt)	35.78	3.48	16.19	16.69	0.00	12.36	0.00	0.10	9.48	94.08
1340_B71	felsic vein (Grt inclusion)	37.63	0.12	19.07	11.34	0.06	16.20	0.00	0.08	9.58	94.09
1340_B72	felsic vein (Grt inclusion)	37.16	0.11	19.06	11.02	0.03	16.36	0.13	0.10	9.58	93.55
1340_B73	felsic vein (Grt inclusion)	37.06	0.29	18.97	12.17	0.05	15.96	0.07	0.11	9.46	94.13
1340B13	felsic vein	36.45	3.61	16.07	16.95	0.08	11.92	0.04	0.10	9.78	95.10
1340B16	felsic vein	37.14	2.41	16.07	14.84	0.10	14.34	0.00	0.05	9.72	94.73
1340B21	**felsic vein**	**36.67**	**2.19**	**16.70**	**15.51**	**0.00**	**13.50**	**0.00**	**0.07**	**9.61**	**94.34**
1340B20	felsic vein	37.06	2.63	16.08	14.92	0.06	14.21	0.00	0.07	9.95	95.11
1340B23	felsic vein	37.28	2.82	17.18	13.91	0.05	14.04	0.00	0.04	9.88	95.29
1340B24	felsic vein	37.18	2.52	16.48	13.97	0.07	14.53	0.00	0.12	9.86	94.82
1340B26	felsic vein	37.01	2.21	16.20	14.26	0.12	14.40	0.07	0.07	9.46	94.28
1399A_B3_1	Matrix	38.91	1.96	14.11	8.04	0.00	19.96	0.03	0.33	9.49	92.83
1399A_B3_3	Matrix	38.93	1.91	14.37	7.96	0.00	19.98	0.03	0.31	9.52	93.01
1399A_B1	Matrix	38.55	1.97	14.81	9.10	0.03	19.00	0.03	0.29	9.55	93.33
1399A_B6	Matrix	38.74	2.03	14.10	8.65	0.00	19.67	0.03	0.29	9.76	93.27
1399A_B5	Matrix	38.93	2.16	13.98	8.10	0.03	20.10	0.03	0.30	9.58	93.21
1399A_B8	Matrix	38.57	2.00	14.19	8.65	0.00	19.82	0.03	0.29	9.31	92.86
1399AB3	Matrix	39.09	1.93	14.31	7.99	0.03	20.10	0.00	0.30	9.46	93.21
1399AB3_2	Matrix	38.88	2.02	14.14	7.88	0.00	19.87	0.00	0.32	9.35	92.48
1399AB52	Matrix	38.58	1.97	14.48	8.91	0.00	19.62	0.00	0.30	9.51	93.37

1399AB51	Matrix	38.55	1.93	14.28	8.61	0.00	19.70	0.00	0.30	9.61	93.00
1399AB53	**Matrix**	**38.31**	**1.99**	**14.24**	**8.63**	**0.00**	**19.71**	**0.00**	**0.30**	**9.53**	**92.73**
1399AB58	Matrix	38.76	2.32	13.97	8.38	0.00	19.98	0.00	0.27	9.73	93.43
1399AB60	Matrix	38.58	2.35	13.82	8.66	0.00	19.69	0.03	0.33	9.59	93.09
1399AB59	Matrix	38.76	2.17	14.09	8.42	0.05	19.81	0.00	0.30	9.67	93.30
1399AB61	Matrix	38.96	2.24	14.06	8.14	0.03	19.90	0.00	0.27	9.75	93.37
1399AB54	Matrix	38.54	2.38	13.97	8.42	0.03	19.57	0.00	0.28	9.54	92.74
1399AB55	Matrix	38.80	2.32	14.02	8.30	0.00	19.65	0.00	0.30	9.47	92.89
1399AB56	Matrix	38.72	2.35	14.06	8.71	0.06	19.62	0.00	0.25	9.71	93.49
1399AB57	Matrix	38.50	2.51	14.02	8.76	0.00	19.10	0.00	0.34	9.44	92.69
1399AB51_4	Matrix	38.54	1.49	14.63	8.77	0.03	19.62	0.00	0.28	9.58	92.97

Table AP3.3: Mineral chemistry data of Garnet (Grt). Representative analyses shown in Tab. 3.4 are highlighted.

	Position	SiO_2	TiO_2	Al_2O_3	FeOT	MnO	MgO	CaO	Total
1338G1	Felsic-core	38.02	0.05	20.78	27.45	2.66	3.07	8.21	100.24
1338G2	Felsic-core	37.73	0.00	21.00	27.51	2.61	3.20	8.32	100.37
1338G2_1	Felsic-core	37.63	0.04	20.95	27.87	2.81	3.05	7.98	100.33
1338G1_1	Felsic-core	37.69	0.05	21.28	27.60	2.63	3.26	8.36	100.87
1338G7	Felsic-core	37.05	0.04	20.82	27.27	2.20	3.51	8.58	99.47
1338G8	Felsic-core	37.37	0.06	20.90	27.19	2.13	3.18	8.84	99.67
1338G94	Felsic-rim	37.92	0.05	20.93	27.38	2.45	3.47	7.89	100.09
1338G96	**Felsic-core**	**37.69**	**0.00**	**21.01**	**25.47**	**2.04**	**3.38**	**9.86**	**99.45**
1338G93	Felsic-core	37.83	0.05	21.21	26.34	2.13	3.52	9.03	100.11
1338G95	**Felsic-rim**	**37.72**	**0.00**	**20.87**	**27.57**	**2.55**	**3.35**	**7.83**	**99.89**
1338G97	Felsic-rim	37.59	0.00	21.00	27.66	2.37	3.49	7.77	99.88
1338G98	Felsic-core	37.76	0.03	21.14	26.01	2.01	3.59	9.44	99.98
1338G99	Felsic-core	37.74	0.04	20.95	26.49	2.03	3.54	8.80	99.59
1338G395	Felsic-rim	37.58	0.03	20.80	25.40	1.86	3.32	10.27	99.26
1338G295	Felsic-rim	37.74	0.04	20.69	26.16	2.07	3.45	9.09	99.24
1338G795	Felsic-core	37.96	0.04	20.82	26.58	2.11	3.48	8.93	99.92
1338G595	Felsic-core	37.99	0.04	21.06	26.49	2.04	3.59	9.08	100.29
1338G495	Felsic-core	37.25	0.06	20.61	26.92	2.28	3.41	8.64	99.17
1340G1	Matrix-rim	37.91	0.05	21.54	27.79	2.07	4.29	6.67	100.32
1340G2	Matrix-rim	38.06	0.04	21.41	27.12	1.92	4.13	7.43	100.11
1340G3	Matrix-core	37.58	0.06	21.67	26.99	1.79	4.31	7.83	100.23
1340G4	Matrix-core	37.74	0.03	21.37	27.39	1.96	4.53	7.28	100.30
1340G5	Matrix-core	37.90	0.05	21.43	27.00	1.81	4.23	8.10	100.52
1340G6	Matrix-core	38.08	0.00	21.57	26.60	1.54	4.66	7.79	100.24
1340G6_1	**Matrix-rim**	**37.89**	**0.00**	**21.18**	**28.63**	**2.28**	**4.02**	**6.39**	**100.39**
1340G7_3	Matrix-rim	38.07	0.00	21.41	27.93	1.89	4.31	6.86	100.47
1340G7_1	Matrix-rim	37.60	0.03	21.46	27.62	1.92	3.91	7.51	100.05
1340G7_2	Matrix-rim	38.03	0.04	21.36	28.03	2.06	4.05	7.12	100.69
1340G7	Matrix-rim	38.06	0.04	21.51	28.27	2.00	4.22	6.66	100.76
1340G8_1	**Matrix-core**	**37.78**	**0.00**	**21.27**	**27.10**	**1.67**	**4.43**	**7.78**	**100.03**
1340G8	Matrix-rim	37.46	0.03	21.09	26.81	1.80	4.60	7.11	98.90
1340G9	Matrix	37.78	0.00	21.41	26.17	1.70	4.77	7.66	99.49
1340G11_7	Matrix-rim	37.36	0.00	21.28	27.94	2.07	4.28	6.47	99.40
1340G11_8	Matrix-rim	37.26	0.00	21.40	27.64	1.93	4.18	7.05	99.46
1340G11_6	Matrix-core	37.52	0.03	21.52	26.43	1.54	4.74	7.95	99.73
1340G11_5	Matrix-rim	38.08	0.03	21.21	28.68	1.98	4.35	6.35	100.68
1340G10	Matrix-rim	37.98	0.05	21.19	28.09	1.97	4.46	6.94	100.68
1340G12	Matrix-rim	38.01	0.00	21.01	28.53	2.29	3.89	6.66	100.39

1340G13	Matrix-rim	38.45	0.00	21.41	27.24	1.88	4.31	7.22	100.51
1340G97	Matrix-rim	38.06	0.00	21.10	27.98	1.98	4.24	6.74	100.10
1340G95	Matrix-rim	38.18	0.03	21.08	28.44	2.01	4.06	6.47	100.27
1340G91	Matrix-rim	38.21	0.04	20.92	28.64	2.22	4.20	6.59	100.82
1340G92	Matrix-core	38.11	0.04	21.35	27.49	2.03	4.56	6.98	100.56
1340G14	Matrix-rim	37.68	0.04	21.32	28.72	2.43	3.88	6.19	100.26
1340G15	**Felsic-core**	**38.71**	**0.00**	**21.98**	**25.12**	**1.93**	**6.41**	**6.54**	**100.69**
1340G16	**Felsic-rim**	**38.25**	**0.00**	**21.70**	**27.45**	**2.71**	**4.58**	**6.07**	**100.76**
1340G17	Felsic-core	38.63	0.00	21.82	25.41	2.05	6.40	6.29	100.60
1340G21	Felsic-rim	38.14	0.04	21.49	28.11	2.78	3.89	6.21	100.66
1340G22	Felsic-rim	37.54	0.00	21.37	28.26	2.93	3.97	5.78	99.85
1340G23	Felsic-core	38.02	0.03	21.75	24.87	1.93	6.52	6.33	99.45
1340G74	Felsic-rim	37.92	0.03	21.36	27.46	3.36	4.63	5.45	100.21
1340_G71	Felsic-core	37.86	0.00	21.41	26.91	2.75	5.35	5.55	99.83
1340G75	Felsic-core	37.95	0.00	21.76	25.89	1.96	6.39	5.92	99.87

Table AP3.4: Mineral chemistry data of Orthopyroxene (Opx). Representative analyses shown in Tab. 3.4 are highlighted.

	Position	SiO_2	TiO_2	Al_2O_3	Cr_2O_3	FeOT	MnO	MgO	CaO	Na_2O	Total
1399A_O1	Matrix	53.82	0.04	0.39	0.05	18.34	0.48	25.55	0.22	0.03	98.92
1399A_O2	**Matrix**	**53.91**	**0.00**	**0.50**	**0.04**	**18.11**	**0.44**	**25.79**	**0.32**	**0.03**	**99.14**
1399A_O4	Matrix	53.57	0.04	0.60	0.06	18.40	0.48	25.47	0.28	0.03	98.92
1399A_O8	Matrix	54.01	0.07	0.48	0.03	18.49	0.50	25.44	0.35	0.03	99.40
1399A_O7	Matrix	53.61	0.03	0.55	0.10	18.08	0.48	25.69	0.34	0.03	98.90
1399A_O9	Matrix	53.95	0.03	0.37	0.06	18.13	0.46	26.12	0.16	0.03	99.31
1399A_O10	Matrix	53.43	0.03	0.48	0.09	18.29	0.53	26.03	0.21	0.03	99.11
1399A_O13	Matrix	53.32	0.03	0.57	0.09	18.15	0.48	25.71	0.23	0.03	98.61
1399A_O12	Matrix	53.17	0.05	0.67	0.08	18.23	0.49	25.76	0.37	0.03	98.85
1399A_O14	Matrix	53.67	0.05	0.57	0.08	18.21	0.49	25.74	0.43	0.03	99.27
1399A_O16	Matrix	53.33	0.06	0.75	0.06	18.47	0.45	25.70	0.46	0.03	99.31
1399A_O20	Matrix	53.61	0.03	0.49	0.09	18.94	0.52	25.46	0.26	0.04	99.44
1399A_O21	Matrix	53.39	0.03	0.53	0.09	18.14	0.50	25.60	0.32	0.03	98.63
1399A_O100	Matrix	54.89	0.07	0.91	0.13	14.35	0.38	22.97	1.43	0.23	95.36
1399AO2	Matrix	54.13	0.03	0.50	0.06	17.75	0.48	25.88	0.34	0.03	99.19
1399AO2_5	Matrix	49.22	0.68	5.69	0.23	9.15	0.15	19.66	5.11	0.40	90.28
1399AO7	Matrix	54.18	0.03	0.51	0.06	17.91	0.44	25.82	0.16	0.03	99.14
1399AO8	Matrix	54.38	0.03	0.51	0.07	18.17	0.46	25.50	0.47	0.03	99.62
1399AO10	Matrix	52.75	0.03	0.41	0.03	18.16	0.46	24.45	0.29	0.03	96.60
1399AO14	Matrix	54.11	0.04	0.62	0.04	18.33	0.47	25.25	0.32	0.03	99.21
1399AO16	Matrix	53.85	0.03	0.73	0.05	18.24	0.49	25.34	0.40	0.03	99.15
1399AO13_2	Matrix	54.04	0.03	0.65	0.07	17.92	0.50	25.42	0.38	0.03	99.04
1399AO13_1	Matrix	54.05	0.03	0.64	0.07	18.29	0.46	25.33	0.36	0.03	99.26
1399AO8_7	Matrix	54.13	0.03	0.53	0.06	17.49	0.46	25.86	0.47	0.03	99.05
1399AO8_6	Matrix	2.94	0.04	0.27	0.02	1.75	0.02	0.15	1.14	0.03	0.00
1399AO4_5	Matrix	52.60	0.03	0.59	0.09	16.83	0.35	21.11	0.23	0.04	91.86
1399AO4_4	Matrix	54.64	0.03	0.56	0.06	18.13	0.48	25.23	0.45	0.03	99.61
1399AO4_3	Matrix	53.70	0.03	0.29	0.03	18.45	0.50	25.31	0.23	0.03	98.57
1399AO4_2	Matrix	52.31	0.03	0.64	0.08	17.66	0.38	23.84	0.39	0.04	95.37
1382_O1_1	Matrix	52.42	0.07	1.19	0.00	25.73	0.83	19.83	0.42	0.00	100.49
1382_O1	Matrix	52.42	0.07	1.03	0.00	25.93	0.88	19.39	0.38	0.00	100.12
1382_O1_9	Matrix	52.70	0.04	1.24	0.00	26.11	0.87	19.69	0.33	0.00	100.98
1382_O1_8	Matrix	52.47	0.03	1.06	0.00	25.90	0.86	19.79	0.38	0.00	100.49
1382_O1_12	Matrix	53.06	0.08	1.10	0.00	25.18	0.83	20.13	0.40	0.00	100.78
1382_O1_11	Matrix	52.60	0.07	1.11	0.00	26.04	0.85	19.72	0.32	0.03	100.74

1382_O3_4	Matrix	52.82	0.03	1.14	0.00	26.02	0.91	19.84	0.32	0.00	101.07
1382_O3	Matrix	52.87	0.10	1.01	0.00	25.95	0.87	19.71	0.42	0.00	100.93
1382_O3_1	Matrix	52.35	0.09	1.24	0.00	25.78	0.80	19.47	0.46	0.00	100.20
1382_O4_1	Vein	52.63	0.11	0.89	0.00	26.13	0.86	19.77	0.42	0.00	100.82
1382_O4_6	Vein	52.41	0.07	1.01	0.05	25.96	0.91	19.55	0.36	0.00	100.33
1382_O4_5	Vein	52.54	0.07	0.86	0.07	26.15	0.78	19.61	0.36	0.00	100.44
1382_O4_2	Vein	52.66	0.04	0.94	0.00	26.40	0.87	19.26	0.39	0.02	100.59
1382_O4_3	Vein	52.79	0.14	0.79	0.00	26.16	0.83	19.64	0.32	0.00	100.68
1382_O5	Matrix	52.80	0.03	0.94	0.00	25.73	0.83	20.04	0.30	0.00	100.67
1382_O4	Matrix	52.54	0.06	1.27	0.00	26.26	0.82	19.65	0.44	0.00	101.04
1382_O5_1	Matrix	52.57	0.09	1.11	0.03	25.68	0.80	19.82	0.37	0.00	100.47
1382_O7	Vein	52.43	0.10	1.14	0.00	25.66	0.76	19.84	0.74	0.00	100.67
1382_O6	Matrix	52.42	0.11	1.31	0.00	25.93	0.84	19.46	0.56	0.00	100.63
1382_O8	Matrix	52.99	0.05	0.97	0.00	26.07	0.79	19.95	0.38	0.00	101.20
1382_O7_4	Vein	52.95	0.05	0.94	0.00	25.05	0.74	19.85	0.97	0.00	100.55
1382_O7_1	Vein	52.30	0.11	1.25	0.04	25.67	0.75	19.60	0.63	0.00	100.34
1382_O7_2	Vein	52.31	0.08	1.42	0.00	25.78	0.82	19.86	0.59	0.00	100.86
1382_O7_3	Vein	52.86	0.20	1.09	0.00	25.36	0.81	20.02	0.45	0.00	100.79
1382_O11	Matrix	52.85	0.11	1.24	0.00	25.95	0.81	19.81	0.48	0.00	101.25
1382_O10	Matrix	52.44	0.09	1.17	0.00	25.69	0.72	19.63	0.73	0.00	100.47
1382_O9	Matrix	52.74	0.25	1.01	0.00	25.80	0.75	19.77	0.62	0.00	100.95
1382_O11_1	Matrix	52.67	0.07	1.14	0.00	26.05	0.73	19.79	0.46	0.00	100.92
1382O28_3	Matrix	51.54	0.08	1.08	0.00	25.11	0.83	19.62	0.42	0.00	98.67
1382O29_3	**Matrix**	**52.49**	**0.00**	**1.10**	**0.00**	**25.33**	**0.85**	**20.14**	**0.37**	**0.00**	**1000.28**
1382O23_3	Matrix	50.06	0.03	1.44	0.00	25.72	0.81	18.77	0.31	0.00	97.13
1382O22_3	Matrix	51.38	0.06	1.13	0.00	25.26	0.77	19.53	0.46	0.04	98.63
1382O21_3	Matrix	51.39	0.05	1.16	0.00	25.17	0.81	19.58	0.39	0.00	98.54
1382O21_4	Matrix	51.27	0.06	1.27	0.00	25.66	0.89	19.33	0.40	0.00	98.89

Table AP3.5: Mineral chemistry data of Clinopyroxene (Cpx). Felsic vein = 'Zone 2'. Representative analyses shown in Tab. 3.4 are highlighted.

	Position	SiO_2	TiO_2	Al_2O_3	Cr_2O_3	FeOT	MnO	MgO	CaO	Na_2O	Total
1338_C3	Matrix	50.03	0.23	2.59	0.03	12.82	0.30	10.27	21.72	0.43	98.42
1338_C4	**Matrix**	**51.16**	**0.17**	**2.05**	**0.00**	**12.66**	**0.41**	**10.67**	**22.25**	**0.39**	**99.76**
1338_C5	Matrix	50.79	0.23	2.58	0.00	13.24	0.41	10.45	21.78	0.53	100.01
1338_C6	Matrix	50.89	0.23	2.49	0.00	12.93	0.36	10.62	21.98	0.43	99.92
1338_C7	Matrix	50.48	0.22	2.78	0.00	12.84	0.35	10.40	22.20	0.53	99.79
1338_C8	Matrix	50.53	0.22	2.69	0.00	12.89	0.44	10.53	21.87	0.43	99.59
1341B_C1	Matrix	51.93	0.20	2.07	0.07	10.11	0.53	12.31	22.44	0.53	100.19
1341B_C2	Matrix	51.49	0.21	2.50	0.07	10.74	0.43	11.91	22.10	0.57	100.02
1341B_C3	**Matrix**	**52.20**	**0.15**	**1.97**	**0.07**	**10.17**	**0.43**	**12.20**	**22.25**	**0.47**	**99.91**
1341B_C4	Matrix	51.14	0.24	2.68	0.04	10.88	0.46	11.70	22.07	0.64	99.86
1341B_C5	Matrix	52.05	0.22	2.23	0.07	10.47	0.45	12.06	22.31	0.54	100.40
1341B_C8	Matrix	51.56	0.25	2.45	0.10	10.93	0.49	11.79	21.90	0.61	100.09
1341B_C6	Matrix	51.28	0.23	2.31	0.09	10.71	0.40	12.02	22.20	0.54	99.78
1341B_C8_1	Matrix	51.97	0.20	2.09	0.09	10.57	0.43	12.05	22.33	0.55	100.30
1341B_C8_6	Matrix	52.01	0.21	2.33	0.07	10.78	0.47	11.86	22.01	0.60	100.34
1341B_C14	Matrix	51.68	0.18	2.07	0.09	10.46	0.46	12.04	22.58	0.54	100.10
1341B_C15_1	Matrix	50.89	0.22	2.45	0.10	10.63	0.44	11.64	22.39	0.52	99.28
1341B_C15	Matrix	50.97	0.31	2.69	0.08	10.85	0.45	11.48	22.01	0.62	99.46
1341B_C17	Matrix	50.79	0.27	2.63	0.05	10.98	0.39	11.49	22.11	0.60	99.31
1341B_C17_1	Matrix	50.92	0.28	2.52	0.07	10.91	0.46	11.61	22.00	0.54	99.32
1341B_C19	Matrix	52.02	0.23	1.91	0.06	10.24	0.42	12.02	22.81	0.50	100.20
1341B_C21	Matrix	50.74	0.25	2.49	0.08	10.82	0.42	11.59	22.30	0.55	99.25
1341B_C23	Vein	51.42	0.14	1.67	0.00	10.95	0.43	11.64	22.79	0.45	99.49
1341B_C24	Vein	53.38	0.05	0.67	0.07	9.35	0.37	12.47	23.70	0.33	100.38

1341B_C27	Vein	52.96	0.04	0.59	0.03	8.91	0.39	12.57	24.04	0.26	99.79
1341B_C28	Vein	52.50	0.17	1.48	0.04	9.84	0.42	11.99	23.15	0.41	100.00
1341B_C22	Vein	53.35	0.06	0.72	0.05	9.33	0.45	12.62	23.48	0.23	100.29
1341B_C32	Vein	52.06	0.14	1.57	0.08	10.56	0.51	11.94	22.99	0.43	100.29
1341B_C31	Vein	52.38	0.11	1.32	0.05	10.17	0.40	12.09	23.16	0.37	100.05
1399A_C1	Matrix	53.53	0.04	1.14	0.17	5.07	0.19	15.52	23.30	0.57	99.53
1399A_C2	Matrix	53.55	0.07	1.42	0.21	5.57	0.17	15.72	22.39	0.59	99.68
1399A_C1_1	Matrix	53.32	0.05	1.23	0.22	4.99	0.20	15.29	23.15	0.61	99.06
1399A_C26	Matrix	53.66	0.06	0.84	0.18	4.64	0.15	15.42	23.80	0.52	99.27
1399A_C15	Matrix	53.07	0.05	1.27	0.26	5.21	0.13	15.37	22.49	0.64	98.49
1399A_C30	Matrix	53.43	0.05	1.02	0.27	4.44	0.11	15.65	23.58	0.48	99.03
1399A_C32	Matrix	53.57	0.05	1.14	0.28	4.63	0.15	15.40	23.29	0.53	99.04
1399A_C31	Matrix	53.49	0.05	1.14	0.17	4.66	0.14	15.43	23.45	0.58	99.12
1399AC28	Matrix	53.46	0.05	1.25	0.21	5.38	0.16	15.38	22.93	0.57	99.38
1399AC31	Matrix	53.42	0.07	1.29	0.17	5.50	0.19	15.61	22.65	0.59	99.50
1399AC29	**Matrix**	**53.75**	**0.00**	**0.80**	**0.23**	**4.88**	**0.13**	**15.61**	**23.71**	**0.54**	**99.65**
1399AC30	Matrix	53.44	0.07	1.37	0.23	5.46	0.19	15.39	22.28	0.57	99.00
1399AC33	Matrix	53.41	0.07	1.19	0.19	4.99	0.18	15.40	23.25	0.50	99.17
1399AC32	Matrix	53.24	0.05	1.31	0.18	5.45	0.17	15.12	22.64	0.59	98.75
1399AC62	Matrix	53.47	0.04	1.18	0.20	4.96	0.17	15.60	23.38	0.53	99.53
1399AC35	Matrix	53.60	0.04	1.25	0.18	5.29	0.16	15.45	22.52	0.56	99.05
1399AC34	Matrix	53.56	0.05	1.29	0.20	5.46	0.19	15.57	22.48	0.53	99.32
1399AC36	Matrix	54.08	0.04	0.52	0.18	4.49	0.13	15.72	23.86	0.35	99.36
1399AC37	Matrix	52.88	0.07	1.40	0.21	5.43	0.15	15.32	22.60	0.62	98.67
1382_C3_1	Matrix	52.64	0.27	2.22	0.03	10.54	0.33	13.15	21.62	0.49	101.30
1382_C3_2	Matrix	52.33	0.24	2.21	0.03	10.38	0.34	13.01	21.75	0.47	100.76
1382_C3_4	Matrix	52.71	0.27	2.18	0.05	9.23	0.31	13.37	22.73	0.46	101.31
1382_C3_5	Matrix	52.36	0.24	2.26	0.05	11.04	0.37	13.18	20.40	0.45	100.34
1382_C3_6	Matrix	51.83	0.25	2.13	0.04	10.09	0.32	13.08	21.66	0.46	99.86
1382_C3_7	Matrix	52.36	0.28	2.30	0.03	9.56	0.34	12.96	21.91	0.47	100.22
1382_C3_8	Matrix	52.76	0.26	2.19	0.04	9.92	0.30	13.22	21.99	0.51	101.19
1382_C3_9	Matrix	52.85	0.29	2.26	0.03	10.24	0.39	13.03	21.30	0.45	100.84
1382_C6	Matrix	52.31	0.26	2.28	0.03	9.81	0.32	12.82	22.13	0.47	100.44
1382_C5	Matrix	52.53	0.28	2.23	0.06	9.96	0.36	13.25	21.65	0.47	100.78
1382_C4	Matrix	53.14	0.19	1.83	0.03	8.77	0.32	13.27	22.75	0.41	100.71
1382_C11_1	Vein	52.52	0.23	2.09	0.05	8.52	0.31	13.25	22.53	0.52	100.03
1382_C11	Vein	52.74	0.27	2.17	0.05	9.17	0.31	12.96	22.27	0.51	100.45
1382_C12_1	Matrix	53.51	0.20	1.63	0.03	8.67	0.27	13.42	22.67	0.45	100.86
1382_C12	Matrix	52.51	0.25	2.25	0.04	9.54	0.33	12.80	22.20	0.48	100.40
1382_C13	Vein	52.66	0.28	2.23	0.04	9.58	0.34	13.03	22.23	0.49	100.87
1382_C14	Vein	53.30	0.23	1.94	0.06	8.50	0.31	13.16	22.62	0.49	100.62
1382_C13_1	Vein	53.01	0.26	2.24	0.03	10.31	0.32	13.27	21.44	0.44	101.31
1382_C15	Vein	52.90	0.28	2.14	0.03	9.99	0.30	13.04	21.91	0.39	100.98
1382_C16	Vein	53.12	0.23	2.13	0.03	9.66	0.29	13.42	21.66	0.49	101.04
1382_C16_1	Vein	53.15	0.27	2.01	0.06	9.03	0.33	13.23	22.43	0.50	101.02
1382C45	Matrix	51.33	0.25	2.27	0.04	9.76	0.32	12.53	22.31	0.50	99.30
1382C38	Matrix	51.16	0.28	2.27	0.03	10.30	0.31	12.86	21.40	0.48	99.09
1382C39	**Matrix**	**52.44**	**0.00**	**1.52**	**0.05**	**8.57**	**0.29**	**13.49**	**23.01**	**0.41**	**99.77**

Table AP3.6: Mineral chemistry data of Plagioclase (Plag). Felsic vein = 'Zone 2'. Representative analyses shown in Tab. 3.3 are highlighted.

	Position	SiO_2	Al_2O_3	CaO	Na_2O	K_2O	Total
1338P9	Matrix-rim	54.70	28.65	10.04	5.63	0.24	99.26
1338P9_1	Matrix-rim	55.28	28.24	10.16	5.75	0.23	99.66
1338P8	**Matrix-core**	**55.82**	**27.79**	**9.78**	**6.06**	**0.26**	**99.71**
1338P7	Matrix-rim	55.45	28.22	10.08	5.71	0.21	99.67
1338P16_1	Matrix-core	55.54	27.94	9.93	5.98	0.18	99.57
1338P18	Matrix-core	54.85	28.16	10.07	5.89	0.16	99.13
1338P17	Matrix-rim	54.92	28.29	10.27	5.48	0.16	99.12
1338P17_1	Matrix-core	55.74	27.71	9.65	6.07	0.23	99.40
1338P22	Matrix-rim	54.27	28.39	10.36	5.76	0.12	98.90
1338P22_1	Matrix-core	54.89	28.01	10.31	5.90	0.14	99.25
1338P25	Matrix-rim	54.64	28.17	10.34	5.62	0.16	98.93
1338P26	Matrix-rim	55.16	28.20	10.12	5.92	0.14	99.54
1338P27	Matrix-core	55.35	28.01	10.05	5.96	0.12	99.49
1338P11	Matrix-core	54.85	28.00	10.28	5.74	0.15	99.02
1338P10	Matrix-core	53.55	28.80	11.03	5.25	0.08	98.71
1338P5	Matrix-rim	54.47	28.05	9.99	5.85	0.17	98.53
1338P6	Matrix-core	54.96	27.43	9.80	5.91	0.12	98.22
1338Q1	Matrix-core	55.19	28.26	10.18	6.00	0.15	99.78
1338P220	Matrix-core	54.10	28.40	10.51	5.47	0.10	98.58
1338P218	Matrix-core	54.05	28.35	10.42	5.66	0.10	98.58
1338P219	Matrix-core	54.24	28.40	10.40	5.69	0.10	98.83
1338P221	Matrix-core	54.25	28.38	10.29	5.80	0.08	98.80
1338P521	Matrix-core	59.82	24.61	6.00	8.26	0.09	98.78
1340P1	**Matrix-core**	**46.56**	**33.94**	**17.12**	**2.01**	**0.03**	**99.66**
1340P4	Matrix-rim	46.57	33.81	16.84	1.91	0.07	99.20
1340P4_1	Matrix-rim	46.55	33.77	16.95	2.03	0.03	99.33
1340P7	Matrix-rim	47.35	33.23	16.01	2.30	0.05	98.94
1340P8	Matrix (intergrown with qtz)	47.14	33.49	16.23	2.26	0.11	99.23
1340P9	Matrix-core	47.36	33.34	16.18	2.41	0.05	99.34
1340P10	**Matrix-rim (inclusion inside Grt)**	**58.82**	**25.81**	**7.26**	**7.60**	**0.08**	**99.57**
1340P11	Matrix-core	56.35	26.98	8.90	6.72	0.09	99.04
1340P12	Matrix-rim	47.41	33.40	16.19	2.46	0.04	99.50
1340P13	Matrix-core	47.27	33.22	16.21	2.38	0.05	99.13
1340P17	Felsic-core	46.58	33.46	16.03	2.29	0.07	98.43
1340P18	Felsic-core	47.02	33.51	16.26	2.35	0.07	99.21
1340P26	Matrix-core	47.90	33.40	16.25	2.34	0.04	99.93
1340P25	Matrix-rim	48.47	32.98	16.11	2.57	0.06	100.19
1340P27	Felsic-core	49.96	31.62	14.80	3.22	0.05	99.65
1340P28	Felsic-core	51.91	30.68	13.41	4.11	0.05	100.16
1340P29	**Felsic-rim**	**52.91**	**29.85**	**12.37**	**4.71**	**0.07**	**99.91**
1340P31	Felsic-core	52.67	30.13	12.63	4.45	0.09	99.97
1340P30	Felsic-core	52.47	30.49	13.21	4.21	0.08	100.46
1340P36	Felsic boundary-core	54.80	28.91	11.17	5.39	0.08	100.35
1340P37	Felsic boundary-core	54.36	28.91	11.24	5.27	0.07	99.85
1340P38	Felsic boundary-core	51.96	30.66	13.36	4.21	0.07	100.26
1340P39	Felsic boundary-core	50.95	31.54	14.30	3.64	0.06	100.49
1340P40	Felsic boundary-core	53.68	29.39	11.75	4.98	0.11	99.91
1340P83	Felsic boundary-core	48.61	32.08	14.60	3.25	0.06	98.60
1340P84	Felsic-core	51.20	30.50	12.46	4.33	0.09	98.58
1340P118	Matrix-core	47.01	33.26	15.71	2.42	0.03	98.43
1340P218	Matrix-rim	46.28	33.84	16.80	1.94	0.02	98.88
1340P219	Matrix-rim	47.16	33.60	16.26	2.29	0.04	99.35

1340P217	Matrix-rim	47.27	33.50	16.19	2.29	0.03	99.28
1341B_P5	Matrix-rim	57.14	26.66	8.66	6.60	0.22	99.28
1341B_P4	Matrix-core	57.95	26.39	8.20	6.72	0.28	99.54
1341B_P7	Matrix-core	57.26	26.59	8.65	6.61	0.24	99.35
1341B_P8	Matrix-core	57.85	26.42	8.49	6.75	0.22	99.73
1341B_P10	Matrix-rim	57.23	26.71	8.60	6.51	0.26	99.31
1341B_P11	Matrix-rim	57.40	26.68	8.51	6.67	0.34	99.60
1341B_P16_1	**Matrix-rim**	**57.66**	**26.56**	**8.60**	**6.76**	**0.24**	**99.82**
1341B_P25	Matrix-core	57.17	26.67	8.58	6.64	0.25	99.31
1341B_P24	Matrix-core	57.16	26.70	8.69	6.64	0.22	99.41
1341B_P26	Matrix-core	57.13	26.53	8.48	6.62	0.24	99.00
1341B_P22_1	Matrix-rim	56.89	26.76	8.88	6.35	0.51	99.39
1341B_P22	Matrix-core	57.39	26.32	8.40	6.39	0.44	98.94
1341B_P28	Vein-core	57.51	26.83	9.03	6.39	0.16	99.92
1341B_P31	Vein-core	57.51	26.90	8.96	6.38	0.14	99.89
1341B_P30	Vein-core	57.37	26.76	8.72	6.55	0.14	99.54
1341B_P29	Vein-core	57.65	26.76	8.93	6.49	0.13	99.96
1341B_P32	Matrix-core	57.34	26.91	8.82	6.51	0.18	99.76
1341B_P32_1	Vein-rim	57.36	26.96	9.09	6.53	0.17	100.11
1341B_P34	Matrix-core	57.53	26.64	8.82	6.48	0.14	99.61
1341B_P35	Matrix-core	57.51	26.90	8.95	6.64	0.13	100.13
1341B_P33	Vein-rim	57.18	26.64	8.77	6.56	0.19	99.34
1399A_P1	**Matrix-rim**	**60.63**	**24.38**	**5.60**	**8.60**	**0.19**	**99.40**
1399A_P1_8	Matrix-core	60.14	24.45	5.70	8.43	0.07	98.79
1399A_P8	Matrix-core	60.52	23.88	5.13	8.60	0.09	98.22
1399A_P09	Matrix-core	60.43	24.21	5.37	8.82	0.05	98.88
1399A_P12	Matrix-rim	60.58	24.14	5.20	8.75	0.07	98.74
1399A_P15	Matrix-core	60.32	24.11	5.24	8.91	0.04	98.62
1399A_P14	Matrix-core	61.03	23.96	5.11	8.85	0.05	99.00
1399A_P16	Matrix-rim	60.39	24.20	5.09	8.72	0.04	98.44
1399A_P94	Matrix-core	59.66	24.13	5.56	8.36	0.11	97.82
1399A_P22	Matrix-core	60.45	24.01	5.25	8.72	0.03	98.46
1399A_P21	Matrix-core	60.36	23.77	5.08	8.59	0.05	97.85
1399A_P20	Matrix-core	60.54	23.87	5.20	8.70	0.03	98.34
1399AP10	Matrix-core	60.52	24.25	5.33	8.59	0.08	98.77
1399AP88	Matrix-core	60.77	24.27	5.31	8.64	0.08	99.07
1399AP89	Matrix-core	60.89	23.74	5.31	8.59	0.03	98.56
1399AP38_8	Matrix-core	60.75	24.16	5.33	8.38	0.07	98.69
1399AP39_9	Matrix-core	60.37	22.36	5.78	7.64	0.07	96.22
1399AP48_8	Matrix-core	60.80	24.20	5.36	8.51	0.03	98.90
1399AP8_7	Matrix-core	60.99	24.01	5.43	8.43	0.11	98.97
1399AP8_9	Matrix-core	60.55	24.15	5.24	8.52	0.08	98.54
1399AP79	Matrix-core	60.66	23.99	5.26	8.56	0.09	98.56
1382_P1	Matrix-core	56.48	28.06	10.28	5.86	0.17	100.85
1382_P1_1	Matrix-rim	56.05	28.15	10.32	5.74	0.14	100.40
1382_P2_1	Matrix-rim	56.27	28.21	10.28	5.73	0.16	100.65
1382_P2_2	Matrix-core	56.47	27.76	10.18	5.72	0.20	100.33
1382_P6	Matrix-rim	56.24	28.04	10.15	5.73	0.17	100.33
1382_P7	**Matrix-core**	**55.77**	**28.35**	**10.37**	**5.56**	**0.16**	**100.21**
1382_P5	Matrix-core	56.53	27.98	10.08	5.77	0.20	100.56
1382_P4_1	Matrix-rim	56.21	28.04	10.18	5.63	0.21	100.27
1382_P4	Matrix-core	56.19	28.06	10.18	5.74	0.18	100.35
1382_P9_6	Matrix-rim	56.19	27.58	10.10	5.82	0.23	99.92
1382_P9_8	Matrix-core	55.64	27.91	10.16	5.79	0.19	99.69
1382_P10	Vein-core	56.35	27.95	10.17	5.77	0.12	100.36
1382_P9_1	Matrix-core	56.43	27.76	10.20	5.98	0.09	100.46
1382_P25	Matrix-core	56.39	28.08	10.16	5.87	0.13	100.63
1382_P25_2	Matrix-core	56.23	28.10	10.03	5.74	0.10	100.20
1382_P31	Matrix-core	56.09	27.87	10.31	5.86	0.17	100.30
1382_P30	Vein-core	56.37	27.88	10.13	5.82	0.15	100.35

1382_P388	Vein-core	56.12	27.92	10.03	5.78	0.15	100.00
1382_P29	Matrix-core	56.37	27.99	10.16	5.87	0.17	100.56
1382_P28	Matrix-core	56.26	28.13	10.20	5.74	0.21	100.54
1382_P32	Matrix-core	56.42	27.70	10.20	5.80	0.15	100.27
1382P46	Matrix-core	54.93	28.26	10.41	5.60	0.12	99.32
1382P45	Matrix-core	54.66	28.17	10.12	5.72	0.16	98.83
1382P47	Matrix-core	54.18	28.53	10.72	5.43	0.15	99.01

Table AP3.7: Results from Ti-in-amphibole geothermometer. Here, b is coefficient with a value of 1.52

	Ti-Amp	log10Ti	b-log(Ti-Amp)	T(in K)	T(deg C)	Avg. Temp.	Avg. dev.
1338_H6	0.186	-0.73	2.25	1066.44	793.44	821	17
1338H19	0.187	-0.73	2.25	1067.54	794.54		
1338H26	0.19	-0.72	2.24	1070.83	797.83		
1338H25	0.182	-0.74	2.26	1061.98	788.98		
1338H24	0.177	-0.75	2.27	1056.33	783.33		
1338H23	0.195	-0.71	2.23	1076.25	803.25		
1338H22	0.246	-0.61	2.13	1127.26	854.26		
1338H8_2	0.208	-0.68	2.20	1089.95	816.95		
1338H8_3	0.211	-0.68	2.20	1093.04	820.04		
1338H10	0.201	-0.70	2.22	1082.64	809.64		
1338H11	0.258	-0.59	2.11	1138.31	865.31		
1338H12	0.201	-0.70	2.22	1082.64	809.64		
1338H31	0.21	-0.68	2.20	1092.01	819.01		
1338H13	0.233	-0.63	2.15	1114.91	841.91		
1338H1	0.24	-0.62	2.14	1121.61	848.61		
1338H3	0.206	-0.69	2.21	1087.88	814.88		
1338H5	0.213	-0.67	2.19	1095.08	822.08		
1338_H7	0.187	-0.73	2.25	1067.54	794.54		
1338H7_1	0.19	-0.72	2.24	1070.83	797.83		
1338H7_2	0.182	-0.74	2.26	1061.98	788.98		
1338H7_3	0.177	-0.75	2.27	1056.33	783.33		
1338H6_2	0.195	-0.71	2.23	1076.25	803.25		
1338H14	0.246	-0.61	2.13	1127.26	854.26		
1338H15	0.23	-0.64	2.16	1112.00	839.00		
1338H16	0.226	-0.65	2.17	1108.09	835.09		
1338H17	0.226	-0.65	2.17	1108.09	835.09		
1338H14_1	0.222	-0.65	2.17	1104.14	831.14		
1338H14_2	0.221	-0.66	2.18	1103.14	830.14		
1338H14_3	0.225	-0.65	2.17	1107.10	834.10		
1338_H18	0.208	-0.68	2.20	1089.95	816.95		
1338H21	0.211	-0.68	2.20	1093.04	820.04		
1338H150_6	0.201	-0.70	2.22	1082.64	809.64		
1338H550_6	0.233	-0.63	2.15	1114.91	841.91		
1338H653_6	0.24	-0.62	2.14	1121.61	848.61		
1338H551_6	0.206	-0.69	2.21	1087.88	814.88		
1338H851_6	0.213	-0.67	2.19	1095.08	822.08		
1340H2	0.187	-0.73	2.25	1067.54	794.54	Avg. T	Avg. dev
1340H1	0.188	-0.73	2.25	1068.64	795.64	813	16
1340H3	0.237	-0.63	2.15	1118.75	845.75		
1340H4	0.224	-0.65	2.17	1106.12	833.12		
1340H5	0.192	-0.72	2.24	1073.01	800.01		

1340H6	0.198	-0.70	2.22	1079.46	806.46		
1340H7	0.214	-0.67	2.19	1096.10	823.10		
1340H8	0.24	-0.62	2.14	1121.61	848.61		
1340H9	0.221	-0.66	2.18	1103.14	830.14		
1340H10	0.189	-0.72	2.24	1069.74	796.74		
1340H11	0.249	-0.60	2.12	1130.05	857.05		
1340H15	0.22	-0.66	2.18	1102.14	829.14		
1340H16	0.175	-0.76	2.28	1054.04	781.04		
130H17	0.187	-0.73	2.25	1067.54	794.54		
1340H18_6	0.195	-0.71	2.23	1076.25	803.25		
1340H18	0.213	-0.67	2.19	1095.08	822.08		
1340H19	0.195	-0.71	2.23	1076.25	803.25		
1340H20	0.207	-0.68	2.20	1088.91	815.91		
1340H22	0.195	-0.71	2.23	1076.25	803.25		
1340H23	0.206	-0.69	2.21	1087.88	814.88		
1340H119_6	0.221	-0.66	2.18	1103.14	830.14		
1340H121_6	0.186	-0.73	2.25	1066.44	793.44		
1382_H1	0.171	-0.77	2.29	1049.41	776.41	Avg. T	Avg. dev.
1382_H2	0.148	-0.83	2.35	1021.39	748.39	748	18
1382_H4	0.158	-0.80	2.32	1033.88	760.88		
1382_H4_3	0.166	-0.78	2.30	1043.53	770.53		
1382_H4_2	0.189	-0.72	2.24	1069.74	796.74		
1382_H4_4	0.165	-0.78	2.30	1042.34	769.34		
1382_H4_5	0.173	-0.76	2.28	1051.73	778.73		
1382_H4_8	0.159	-0.80	2.32	1035.11	762.11		
1382_H4_7	0.163	-0.79	2.31	1039.95	766.95		
1382_H5	0.149	-0.83	2.35	1022.66	749.66		
1382_H7	0.168	-0.77	2.29	1045.89	772.89		
1382_H5_2	0.144	-0.84	2.36	1016.24	743.24		
1382_H16_9	0.14	-0.85	2.37	1011.01	738.01		
1382_H16_1	0.161	-0.79	2.31	1037.54	764.54		
1382_H16_2	0.151	-0.82	2.34	1025.19	752.19		
1382_H16_7	0.121	-0.92	2.44	984.73	711.73		
1382_H16_6	0.146	-0.84	2.36	1018.83	745.83		
1382_H16_5	0.148	-0.83	2.35	1021.39	748.39		
1382_H16_19	0.119	-0.92	2.44	981.81	708.81		
1382_H16_20	0.124	-0.91	2.43	989.05	716.05		
1382_H16	0.142	-0.85	2.37	1013.64	740.64		
1382_H11	0.133	-0.88	2.40	1001.61	728.61		

Table AP3.8: Results from Ti-in-biotite geothermometer

	'a', 'b', and 'c' are surface fit coefficients							
Sample	a	b	c	Ti	X(Mg)	T(C)	Avg. T	Avg. dev
1338	-2.3594	4.6482E-09	-1.7283	0.413133	0.539	716.74	725	6
1338	-2.3594	4.6482E-09	-1.7283	0.44939	0.530	726.36		
1338	-2.3594	4.6482E-09	-1.7283	0.530139	0.486	740.23		
1338	-2.3594	4.6482E-09	-1.7283	0.471883	0.514	729.90		
1338	-2.3594	4.6482E-09	-1.7283	0.441235	0.529	723.74		
1338	-2.3594	4.6482E-09	-1.7283	0.478626	0.516	732.00		
1338	-2.3594	4.6482E-09	-1.7283	0.428801	0.530	719.99		
1338	-2.3594	4.6482E-09	-1.7283	0.465042	0.534	731.58		
1338	-2.3594	4.6482E-09	-1.7283	0.457778	0.537	730.09		
1338	-2.3594	4.6482E-09	-1.7283	0.433077	0.542	723.74		
1338	-2.3594	4.6482E-09	-1.7283	0.427267	0.532	719.95		
1338	-2.3594	4.6482E-09	-1.7283	0.398172	0.525	708.94		
1338	-2.3594	4.6482E-09	-1.7283	0.46168	0.486	722.13		
1340	-2.3594	4.6482E-09	-1.7283	0.438833	0.607	740.13	733	13
1340	-2.3594	4.6482E-09	-1.7283	0.442873	0.593	737.89		
1340	-2.3594	4.6482E-09	-1.7283	0.45214	0.548	730.65		
1340	-2.3594	4.6482E-09	-1.7283	0.430658	0.551	724.91		
1340	-2.3594	4.6482E-09	-1.7283	0.416887	0.574	725.67		
1340	-2.3594	4.6482E-09	-1.7283	0.48117	0.565	742.26		
1340	-2.3594	4.6482E-09	-1.7283	0.497269	0.558	745.12		
1340	-2.3594	4.6482E-09	-1.7283	0.396053	0.595	723.65		
1340 (FELSIC VEIN)	-2.3594	4.6482E-09	-1.7283	0.407214	0.582	724.36	686	16
1340 (FELSIC VEIN)	-2.3594	4.6482E-09	-1.7283	0.269732	0.657	687.28		
1340 (FELSIC VEIN)	-2.3594	4.6482E-09	-1.7283	0.265537	0.658	685.36		
1340 (FELSIC VEIN)	-2.3594	4.6482E-09	-1.7283	0.220646	0.648	652.83		
1340 (FELSIC VEIN)	-2.3594	4.6482E-09	-1.7283	0.246411	0.633	665.47		
1340 (FELSIC VEIN)	-2.3594	4.6482E-09	-1.7283	0.293719	0.659	700.55		
1340 (FELSIC VEIN)	-2.3594	4.6482E-09	-1.7283	0.293713	0.654	698.67		
1340 (FELSIC VEIN)	-2.3594	4.6482E-09	-1.7283	0.311928	0.667	711.34		
1340 (FELSIC VEIN)	-2.3594	4.6482E-09	-1.7283	0.280756	0.673	698.64		
1340 (FELSIC VEIN)	-2.3594	4.6482E-09	-1.7283	0.247654	0.667	677.78		

Appendix 4 – Supporting information for Chapter 4

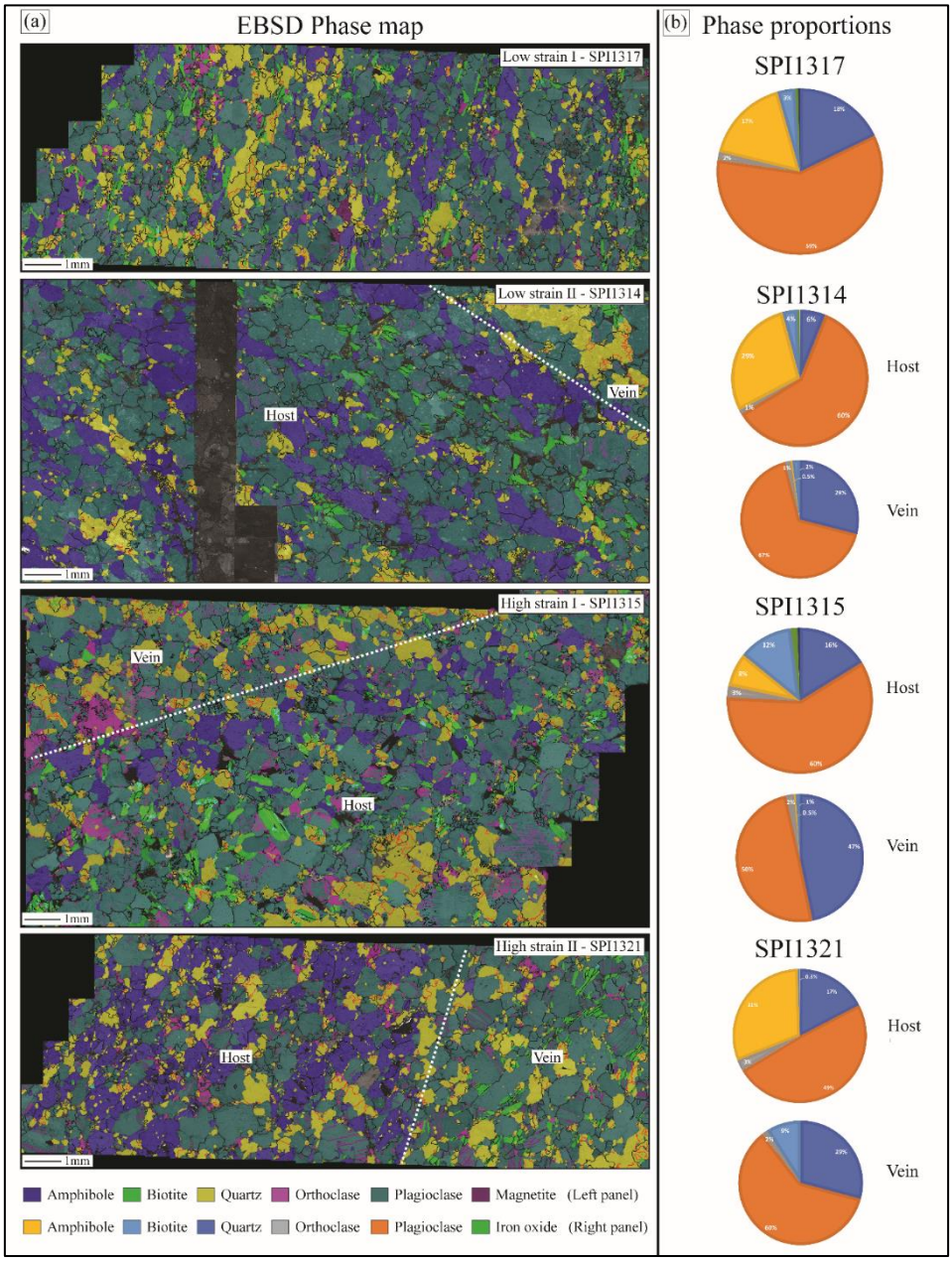

Figure AP4 – 1: EBSD phase maps and mineral modes of the studied samples. Left panel: EBSD colour coded phase map; step size = 10µm. Host and vein are marked. Right panel: modal% of minerals in the host and vein.

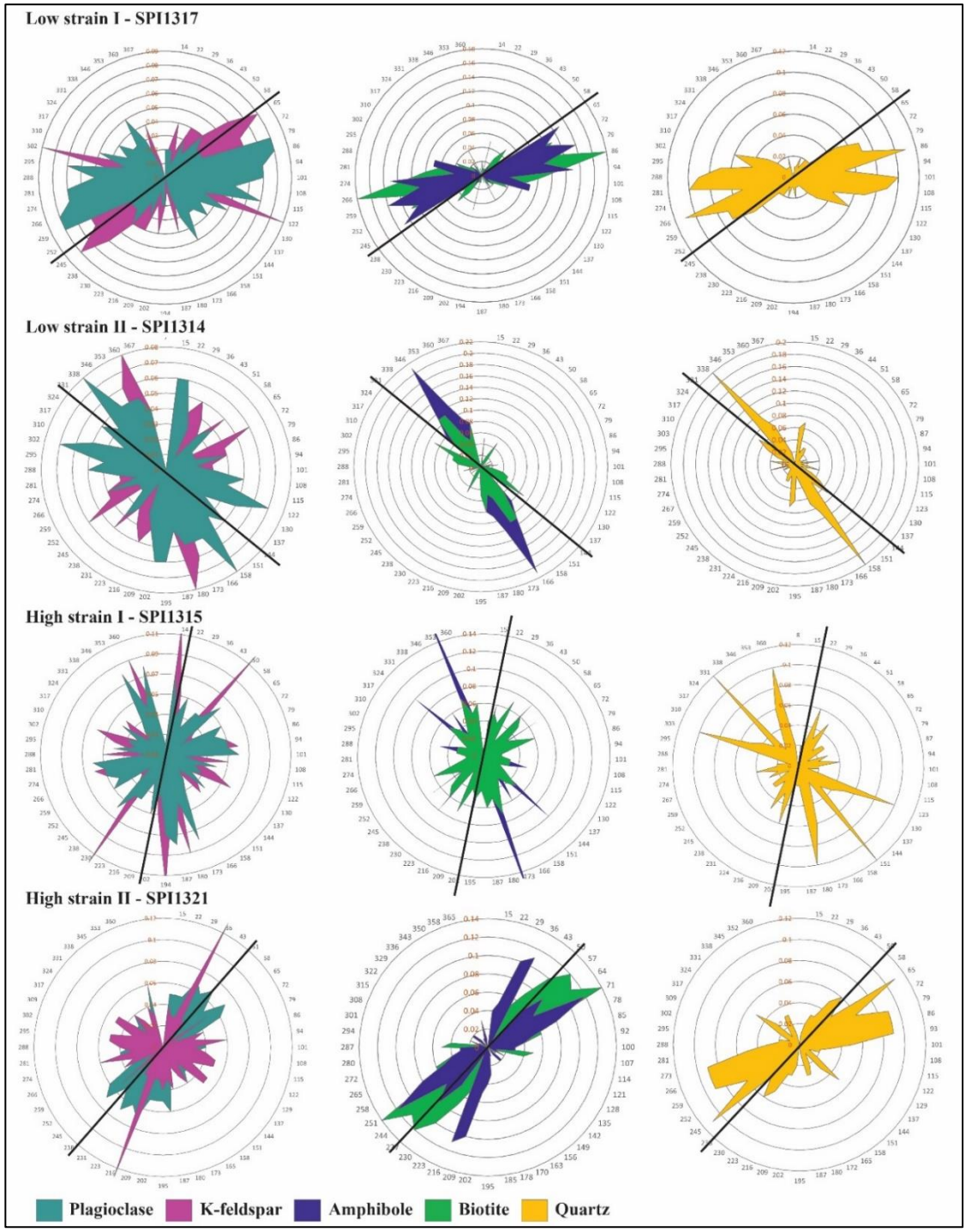

Figure AP4 – 2: Plot of grain shape preferred orientation (SPO) of constituent minerals for individual rock types. Dark line represents foliation direction.

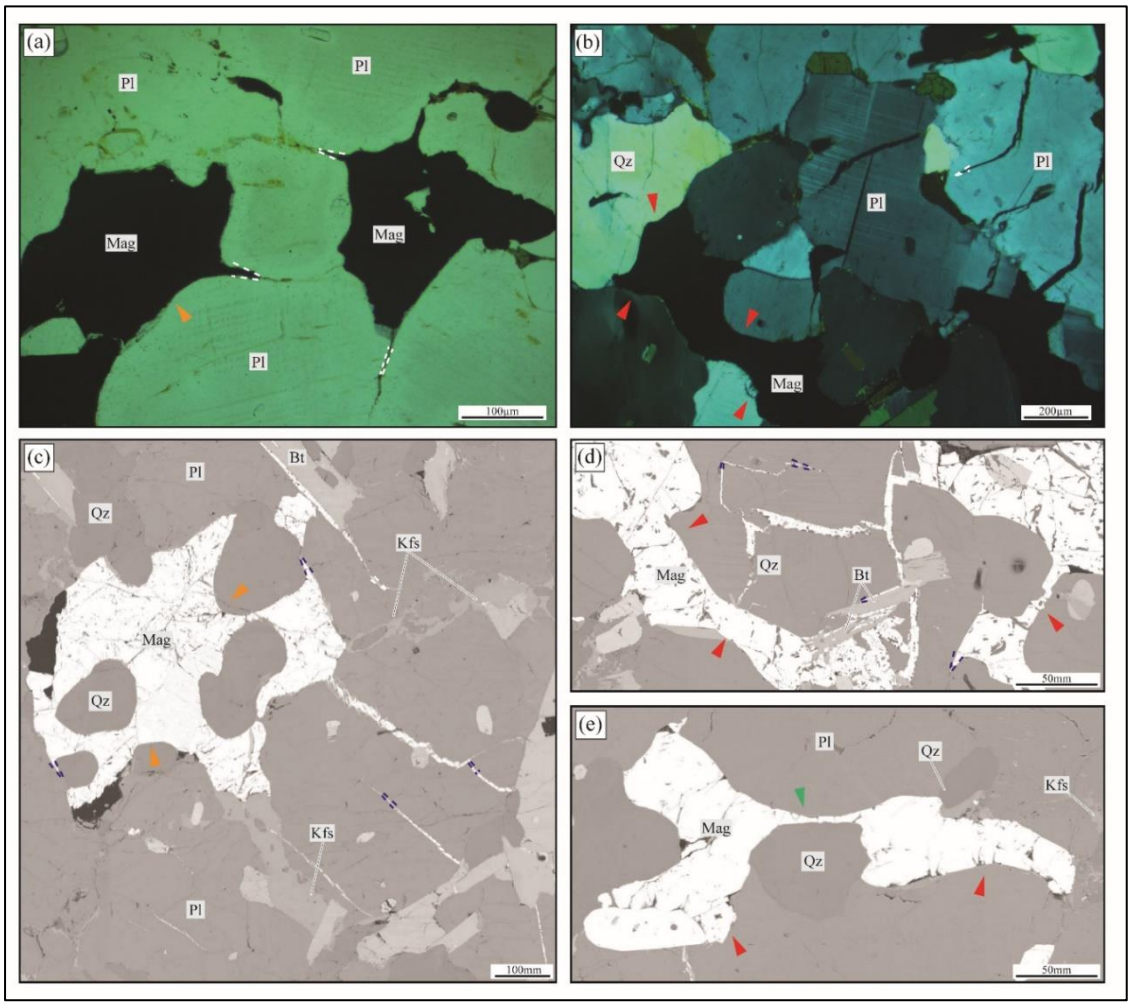

Figure AP4 – 3: Photomicrographs show microstructural features of magnetite grains in low strain II - SPI1314 and high strain I - SPI1315. (a-e) PPL, XPL and BSE images show anhedral grains (red arrows), cuspate grain boundaries (orange arrows). The grains are interstitial and exhibit low dihedral angle (some below <10°).

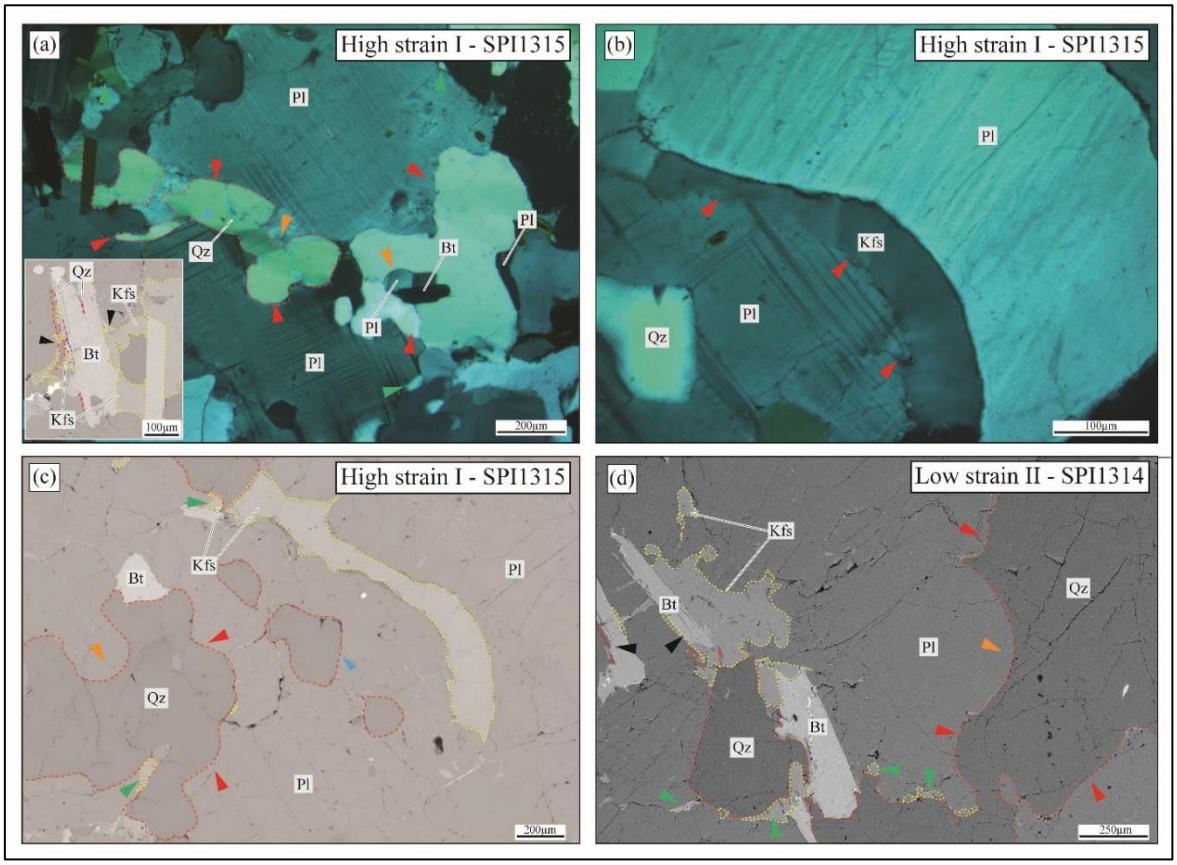

Figure AP4 – 4: Photomicrographs show distinct microstructural features of former melt presence in veins of low strain II - SPI1314 and high strain I - SPI1315. (a-d) XPL and BSE images show anhedral grains (red arrows), cuspate grain boundaries (orange arrows), interstitial grains (green arrows) along grain boundaries of other minerals, and low dihedral angles of the interstitial quartz and K-feldspar grains. Biotite grains with disequilibrium texture show local melting. Small quartz and K-feldspar grains are along the biotite grain boundaries like that observed in the host. Mineral abbreviations are after Whitney and Evans (2010).

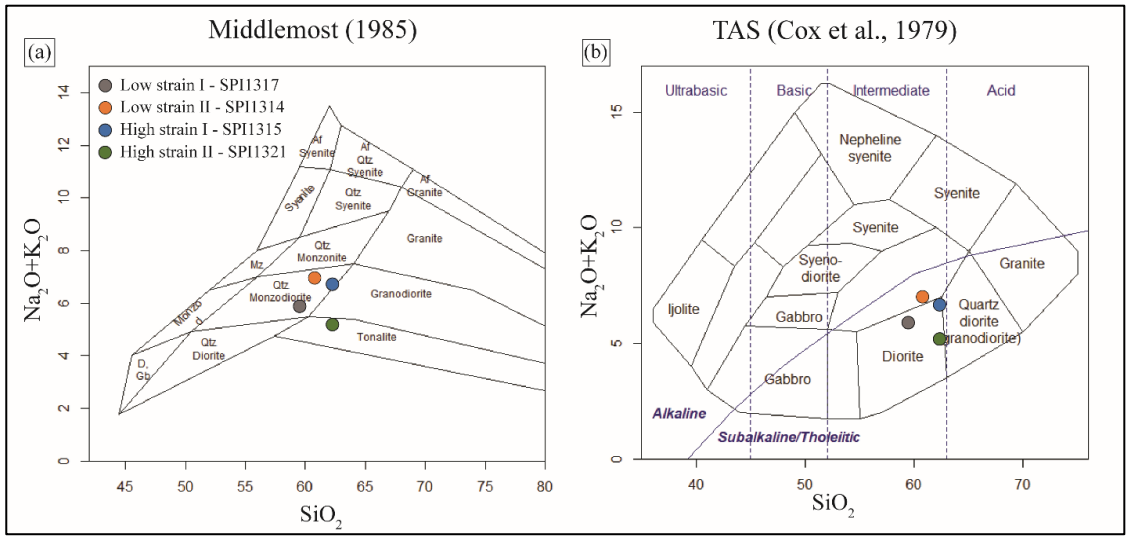

Figure AP4 – 5: Total alkali (Na_2O+K_2O) versus silica (SiO_2) classification diagrams (a) after Middlemost (1985) and (b) boundaries of Cox et al. (1979)

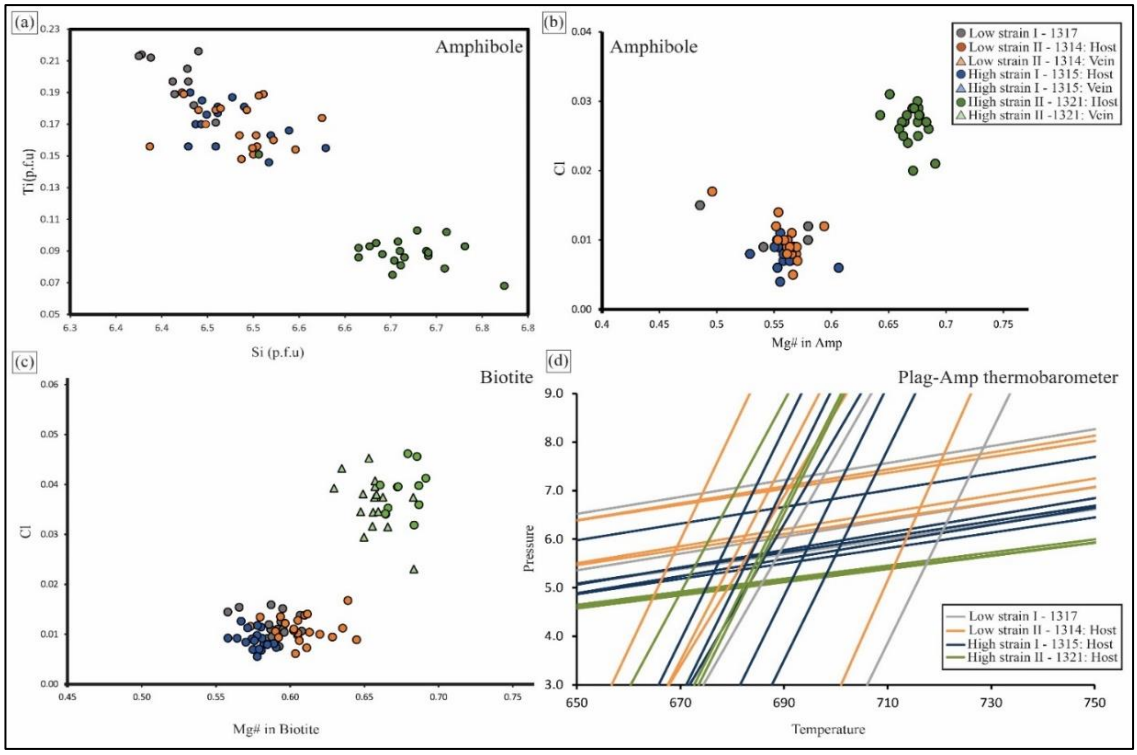

Figure AP4 – 6: Geochemical and conventional geothermobarometric plots. (a) Ti vs Si in amphibole display low Ti content in the high strain II - SPI1321. (b-c) Cl wt% vs Mg# in hornblende and biotite showing distinct clusters in high strain II – SPI1321. (d) Plagioclase-amphibole geothermobarometer show P-T range of all the studied samples.

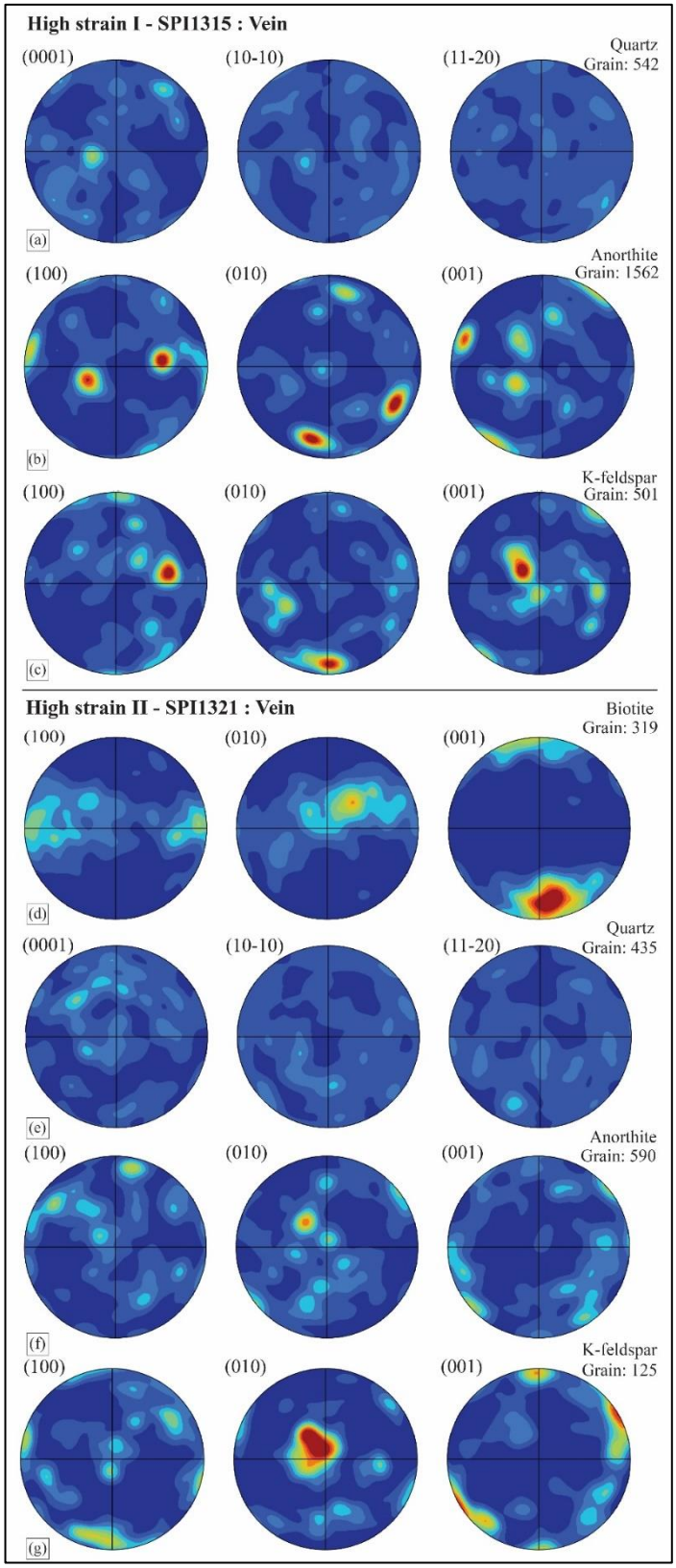

Figure AP4 – 7: CPO Pole figures (one point per grain) of constituent mineral grains from the veins of studied samples. (a, e) quartz, (b, f) plagioclase, and (c, g) K-feldspar in high-strain I - SPI1315: vein and high strain II - SPI1321: vein. (d) Biotite CPO in high strain II - SPI1321: vein.

Table AP4.1: Mineral chemistry data of plagioclase (Plag).). Representative analyses shown in Tab. 4.3 are highlighted.

Textural position	Sample	SiO_2	Al_2O_3	CaO	Na_2O	K_2O	BaO	Total
Large-Core	**1317P2**	**60.43**	**24.53**	**5.84**	**8.30**	**0.25**	**0.00**	**99.35**
Small-Core	1317P5_4	59.95	24.49	6.04	8.11	0.24	0.00	98.83
Small-Core	1317P3	59.50	25.06	6.38	8.04	0.14	0.06	99.18
Small-Core	1317P5	59.92	24.93	6.26	8.08	0.16	0.00	99.35
Large-Core	1317P22	59.62	24.69	6.26	8.03	0.20	0.00	98.80
Large-Rim	1317P6	59.55	24.77	6.24	8.09	0.16	0.00	98.81
Large-Core	1317P7	58.75	24.84	6.04	7.97	0.17	0.00	97.77
Small-Core	1317P12	58.74	24.76	6.22	7.68	0.17	0.00	97.57
Large-Core	1317P15	60.19	24.62	5.80	8.26	0.25	0.00	99.12
Medium-Core	1317P16	60.15	24.48	5.96	8.19	0.11	0.00	98.89
Large-Core	1317P25	60.04	24.57	5.96	8.18	0.20	0.00	98.95
Small-Core	1317P27	59.25	25.10	6.48	8.09	0.20	0.06	99.17
Small-Core	1317P31	59.88	25.11	6.46	7.92	0.19	0.00	99.56
Large-Core	1317P32	60.57	24.43	5.88	8.41	0.20	0.00	99.49
Large-Rim	1317P37	59.95	25.20	6.51	7.92	0.09	0.00	99.67
Small-Core	1317P38	58.14	24.72	6.49	7.56	0.16	0.00	97.07
Large-Core	1317P38	60.04	24.78	6.21	7.93	0.22	0.00	99.18
Large-Core	1317P47	59.92	24.41	5.88	8.18	0.21	0.00	98.60
Large-Core	1317_PL51_2	61.51	24.48	6.24	8.20	0.23	0.03	100.69
Large-Rim	1317_PL51_3	61.20	24.98	6.45	8.09	0.14	0.00	100.86
Large-Rim	1317_PL51_4	60.39	24.66	6.42	8.10	0.19	0.03	99.79
Small-Rim	1317_PL49	61.00	24.29	6.56	7.91	0.18	0.03	99.97
Large-Rim	1317_PL49_1	60.96	24.64	6.51	7.84	0.18	0.01	100.14
Large-Rim	1317_PL51	61.06	25.22	6.39	8.27	0.17	0.01	101.11
Large-Core	1317_PL51_1	61.73	24.14	5.95	8.44	0.24	0.06	100.57
Large-Core	1317_PL50	61.63	24.45	6.52	8.12	0.14	0.00	100.86
Small-Rim	1317_PL50_1	61.54	24.13	4.44	8.45	0.41	0.01	98.99
Large-Core	1317_PL50_2	61.60	24.61	6.11	8.19	0.27	0.01	100.80
Large-Core	1317_PL51_2	61.51	24.48	6.24	8.20	0.23	0.03	100.69
Small-Rim	1317_PL51_3	61.20	24.98	6.45	8.09	0.14	0.00	100.86
Small-Rim	1317_PL51_4	60.39	24.66	6.42	8.10	0.19	0.03	99.79
Small-Rim	1317_PL49	61.00	24.29	6.56	7.91	0.18	0.03	99.97
Large-Core	1317_PL49_1	60.96	24.64	6.51	7.84	0.18	0.01	100.14
Large-Core	1317_PL51	61.06	25.22	6.39	8.27	0.17	0.01	101.11
Large-Core	1317_PL51_1	61.73	24.14	5.95	8.44	0.24	0.06	100.57
Small-Core	1317_PL50	61.63	24.45	6.52	8.12	0.14	0.00	100.86
Small-Rim	1317_PL50_1	61.54	24.13	4.44	8.45	0.41	0.01	98.99
Large-Core	1317_PL50_2	61.60	24.61	6.11	8.19	0.27	0.01	100.80
Host	1314_p37	60.78	23.78	5.43	8.65	0.15	0.01	98.80
Host	1314_p38	61.11	24.10	5.67	8.56	0.17	0.01	99.62

Host	**1314_p42**	**61.39**	**24.35**	**5.59**	**8.34**	**0.15**	**0.04**	**99.86**
Host	1314_p43	61.77	23.92	5.41	8.57	0.18	0.03	99.88
Host	1314_p1	61.39	23.92	5.46	8.63	0.12	0.01	99.53
Host	1314_p2	62.22	23.80	5.19	8.79	0.30	0.02	100.32
Host	1314_p3	61.25	24.43	5.83	8.44	0.13	0.00	100.08
Host	1314_p4	61.61	23.84	5.54	8.48	0.14	0.01	99.62
Vein-core	1314_p5	61.83	23.87	5.44	8.61	0.21	0.01	99.97
Vein-rim	1314_p5_1	60.75	24.40	5.85	8.52	0.10	0.00	99.62
Host	1314_p2_2	62.05	24.04	5.21	8.68	0.22	0.00	100.20
Host	1314_p2_3	62.27	23.63	5.11	8.81	0.21	0.06	100.09
Host	1314_p7	61.86	23.95	5.21	8.50	0.23	0.01	99.76
Host	1314_p6	61.82	24.01	5.28	8.62	0.19	0.04	99.96
Host	1314_p8	61.67	24.34	5.53	8.74	0.21	0.03	100.52
Host	1314_p9	61.97	24.08	5.33	8.70	0.24	0.03	100.36
Host	1314_p10	59.57	25.31	6.92	7.80	0.11	0.00	99.71
Host	1314_p11	62.42	24.01	5.08	8.80	0.22	0.00	100.53
Host	1314_p12	59.00	25.38	6.90	7.82	0.19	0.05	99.34
Vein-core	1314_p13	61.58	24.44	5.51	8.61	0.19	0.04	100.37
Vein-rim	1314_p13_1	61.53	24.71	5.83	8.35	0.13	0.00	100.55
Vein-core	1314_p16	61.94	23.97	5.52	8.68	0.16	0.06	100.34
Vein-rim	1314_p16_1	61.84	24.09	5.42	8.60	0.13	0.03	100.11
Host	1314_p17	61.96	24.03	5.18	8.51	0.20	0.02	99.90
Host	1314_p18	61.82	23.93	5.47	8.67	0.20	0.06	100.15
Host	1314_p19	61.68	24.34	5.62	8.55	0.18	0.00	100.37
Host	1314_p20	61.56	24.18	5.43	8.60	0.27	0.03	100.07
Host	1314_p21	62.19	24.07	5.18	8.82	0.22	0.03	100.51
Host	1314_p22	58.77	23.86	5.89	8.59	0.24	0.00	97.35
Host	1314_p23	61.47	24.47	5.74	8.49	0.21	0.00	100.38
Host	1314_p19	62.03	23.75	5.12	8.82	0.27	0.00	99.99
Host	1314_p19_1	61.38	23.82	5.55	8.68	0.31	0.00	99.74
Host	1314_p30	61.70	23.91	5.52	8.45	0.26	0.02	99.86
Host	1314_p22	62.07	24.09	5.33	8.51	0.22	0.00	100.22
Host	1314_p40	101.31	0.00	0.00	0.00	0.01	0.00	101.32
Host-Rim	1314_PL24	62.63	24.02	5.51	8.52	0.15	0.02	100.86
Host-Rim	1314_PL22	61.93	23.99	5.69	8.50	0.16	0.00	100.27
Host-Rim	1314_PL23	61.91	23.99	5.58	8.49	0.22	0.03	100.23
Host-Rim	1314_PL26	61.55	23.64	5.59	8.31	0.23	0.00	99.33
Host-Core	1314_PL28_4	62.07	23.53	5.23	8.69	0.23	0.06	99.83
Intergrowth	1314_PL27	61.44	24.10	5.82	8.31	0.16	0.00	99.83
Host-Core	1314_PL28_2	61.22	24.36	5.77	8.17	0.10	0.01	99.62
Host-Core	1314_PL28_3	62.02	24.09	5.79	8.55	0.13	0.00	100.57
Host-Core	1314_PL28_1	61.38	23.78	5.43	8.63	0.15	0.00	99.36
Host-Rim	1314_PL28	62.92	24.20	5.60	8.44	0.11	0.00	101.26
Host-Rim	1314_PL30	62.24	24.01	5.65	8.31	0.23	0.00	100.43
Host-Rim	1314_PL29	62.31	24.86	3.13	4.20	0.10	0.00	94.60
Recrystallized	1314_PL29_1	61.90	23.71	5.60	8.52	0.22	0.01	99.95
Intergrowth	1314_PL29_2	61.82	23.83	5.60	8.65	0.12	0.03	100.04
Intergrowth	1314_PL29_3	60.63	23.86	5.57	8.35	0.14	0.02	98.58

Host-Rim	1314_PL34	60.42	24.20	5.64	8.44	0.23	0.01	98.93
Host-Rim	1314_PL35	61.69	23.74	5.39	8.62	0.17	0.04	99.65
Host-Rim	1314_PL31	60.10	23.56	5.60	8.26	0.21	0.05	97.79
Host-Rim	1314_PL32	61.31	23.61	5.54	8.61	0.18	0.00	99.26
Host-Rim	1314_PL32_1	59.52	23.76	5.91	8.28	0.20	0.02	97.68
	1315_p24	62.35	24.25	5.30	8.65	0.20	0.01	100.76
	1315_P24_1	61.88	24.57	5.57	8.37	0.11	0.03	100.53
Inside vein	1315_p25	62.23	24.11	5.22	8.83	0.25	0.03	100.67
	1315_p25_1	61.81	24.21	5.44	8.70	0.19	0.05	100.40
Rim	1315_PL3_1	60.78	23.30	5.38	8.49	0.26	0.05	98.28
Rim	1315_PL5	62.49	23.48	5.36	8.63	0.28	0.00	100.23
Core	1315_PL6	62.20	23.56	5.22	8.49	0.29	0.03	99.80
Rim	1315_PL7	61.60	24.28	5.63	8.44	0.22	0.00	100.16
Rim	1315_PL3	61.94	24.02	5.57	8.49	0.29	0.01	100.31
Rim	1315_PL2	61.79	23.68	5.62	8.45	0.18	0.01	99.73
Core	1315_PL1	61.28	23.48	5.34	8.47	0.26	0.01	98.83
Core	1315_PL8	62.46	23.52	5.18	8.65	0.23	0.03	100.06
	1315_PL10_2	61.96	24.22	6.02	8.15	0.26	0.00	100.61
	1315_PL10	61.36	23.91	5.58	8.47	0.18	0.00	99.51
Rim	1315_PL9	61.40	24.06	5.87	8.41	0.15	0.00	99.89
Core	1315_PL12	61.96	23.95	5.47	8.41	0.26	0.02	100.07
Core	1315_PL11	62.15	24.09	5.74	8.53	0.25	0.04	100.80
Core	1315_PL13	61.74	24.01	5.59	8.39	0.16	0.00	99.90
Core	1315_PL13_1	61.99	23.81	5.55	8.38	0.22	0.01	99.97
Core	1315_PL11_1	62.40	23.44	5.12	8.71	0.29	0.02	99.99
Rim	1315_PL16	61.27	23.21	5.58	8.37	0.16	0.00	98.59
Core	1315_PL18	61.86	24.04	5.60	8.54	0.24	0.00	100.28
Rim	1315_PL17	61.18	23.94	5.71	8.35	0.20	0.04	99.44
Rim	1315_PL14_1	61.50	23.81	5.55	8.34	0.31	0.04	99.54
Core	1315_PL14	61.94	23.90	5.34	8.59	0.31	0.00	100.08
Rim	1315_PL16	61.30	24.00	5.60	8.22	0.25	0.00	99.37
Core	1315_PL16_1	62.18	23.81	5.29	8.59	0.31	0.10	100.27
Host	1315_p1	61.61	23.58	5.10	8.67	0.29	0.00	99.25
Vein-core	1315_p2	61.60	24.21	5.42	8.69	0.19	0.02	100.13
Vein-rim	1315_p3	61.24	24.56	5.79	8.50	0.10	0.00	100.19
Host	1315_p4	61.87	24.02	5.23	8.48	0.28	0.03	99.91
Host	1315_p4_1	61.73	24.02	5.35	8.44	0.25	0.07	99.85
Host	1315_p5	61.23	24.32	5.86	8.43	0.22	0.01	100.07
Host	**1315_p6**	**61.60**	**24.12**	**5.35**	**8.60**	**0.26**	**0.00**	**99.93**
Vein-core	1315_p7	61.79	23.97	5.28	8.50	0.23	0.02	99.79
Vein-rim	1315_p7_4	61.70	24.12	5.47	8.55	0.30	0.00	100.14
Host	1315_p15	61.54	23.84	5.32	8.68	0.21	0.01	99.60
Host	1315_p16	61.61	24.35	5.44	8.38	0.14	0.05	99.97
Host	1315_p17	61.04	24.37	5.76	8.44	0.22	0.00	99.83
Host	1315_p18	61.56	24.02	5.48	8.60	0.22	0.00	99.88
Host	1315_p19	61.35	23.92	5.31	8.58	0.36	0.02	99.54
Host	1315_p20	61.86	24.02	5.43	8.57	0.26	0.00	100.14
Host	1315_p21	61.52	23.63	5.33	8.62	0.27	0.05	99.42

Host	1315_p22	61.43	23.78	5.31	8.37	0.17	0.02	99.08
Host	1315_p23	61.50	24.15	5.53	8.44	0.15	0.00	99.77
Large-Core	1321_p1	61.45	24.41	5.80	8.41	0.26	0.03	100.36
Large-Rim	1321_p2	61.24	24.24	5.70	8.29	0.24	0.02	99.73
Small-Core	1321_p3	61.56	24.38	5.70	8.28	0.15	0.04	100.11
Small-Rim	1321_p4	61.37	24.47	5.85	8.45	0.16	0.02	100.32
Host	**12321_p5**	**61.08**	**24.39**	**5.75**	**8.27**	**0.42**	**0.00**	**99.91**
Large-Rim with Kfs	1321_p6	61.45	24.49	5.76	8.63	0.13	0.01	100.47
Large-rim (away from Kfs)	1321_p7	61.54	24.34	5.71	8.54	0.14	0.01	100.28
Small	1321_p9	60.37	24.34	5.99	8.06	0.55	0.00	99.31
Small	1321_p10	60.58	25.27	6.38	7.97	0.10	0.02	100.32
Large-Core	1321_p11	61.11	24.49	5.74	8.27	0.28	0.03	99.92
Medium	1321_p12	61.46	24.29	5.69	8.41	0.24	0.00	100.09
Small	1321_p13	61.21	24.30	5.87	8.46	0.12	0.01	99.98
Large	1321_p14	61.57	24.31	5.67	8.27	0.26	0.02	100.10
Large	1321_p15	61.59	24.26	5.60	8.46	0.18	0.03	100.12
	1321_p16	60.73	24.47	6.14	8.20	0.15	0.00	99.69
Large-Core	1321_p17	61.41	24.33	5.76	8.42	0.17	0.00	100.09
Large-Rim	1321_p17_1	60.89	24.64	6.01	8.18	0.12	0.01	99.85
Mid size-Core	1321_p19	61.58	24.33	5.83	8.51	0.27	0.01	100.53
Mid size-Core	1321_p19_1	61.42	24.47	5.76	8.46	0.18	0.02	100.30
Inclusion in Hbl	1321_p21	61.15	24.67	5.91	8.48	0.09	0.00	100.30
Small size-Core	1321_p22	61.08	24.49	5.89	8.47	0.18	0.00	100.11
Small size-Core	1321_p24	60.97	24.49	5.78	8.47	0.17	0.03	99.90
Mid size-Core	1321_p25	61.62	24.47	5.71	8.61	0.15	0.06	100.62
Mid size-Core	1321_p25_1	61.21	24.25	5.78	8.37	0.14	0.01	99.76
Small size-Core	1321_p26	61.23	24.54	5.80	8.47	0.16	0.01	100.21
Small size-Rim	1321_p27	61.51	24.53	5.89	8.66	0.20	0.01	100.80
Small size-Core	1321_p27_1	61.59	24.58	5.68	8.60	0.12	0.00	100.57
Large size-Core	1321_p28	61.93	24.18	5.53	8.64	0.25	0.01	100.53
Large size-Rim	1321_p28_1	60.78	24.67	5.99	8.53	0.18	0.03	100.18
Large	1321_p29	61.39	24.32	5.67	8.65	0.25	0.02	100.30
Small	1321_p30	61.28	24.58	5.76	8.50	0.18	0.00	100.30
Small-Rim	1321_p31	61.20	24.36	5.92	8.52	0.17	0.02	100.19
	1321_p33	61.32	24.65	5.93	8.38	0.13	0.00	100.41
Inclusion Hbl	1321_p34	61.60	24.64	5.93	8.55	0.14	0.04	100.90

<u>Table AP4.2</u>: Mineral chemistry data of K-feldspar (Kfs). Representative analyses shown in Tab. 4.3 are highlighted.

	SiO_2	Al_2O_3	CaO	Na_2O	K_2O	BaO	Total
1317K15_3	62.54	18.85	0.00	0.51	15.45	1.80	99.15
1317K15_4	61.26	18.62	0.27	0.27	15.50	0.71	96.63
1317k2	62.67	18.79	0.00	0.77	15.19	1.68	99.10
1317K12	62.82	18.82	0.00	0.79	15.23	1.79	99.45

1317K17	62.83	18.86	0.00	0.72	15.46	1.48	99.35
1317K37	**62.66**	**18.87**	**0.00**	**0.69**	**15.14**	**1.96**	**99.32**
1317K89	62.71	18.94	0.00	1.09	14.82	1.83	99.39
1317_KL59_1	64.10	18.59	0.06	0.68	15.14	1.46	100.04
1317_KL59	62.81	18.23	0.09	0.48	15.56	1.33	98.51
1317_KL47	62.88	18.41	0.09	0.54	15.01	1.98	98.90
1317_KL60	63.48	18.66	0.08	0.59	15.05	1.74	99.60
1317_KL35	63.10	18.31	0.12	0.52	15.63	0.73	98.42
1317_KL44	65.18	18.55	0.08	0.71	15.29	0.86	100.67
1317_KL36_1	63.42	18.60	0.05	0.47	15.20	1.76	99.51
1317_KL36	63.12	18.57	0.18	0.40	15.56	1.36	99.19
1317_KL37	63.37	18.64	0.22	0.60	15.28	1.59	99.70
1317_KL37_1	64.27	18.79	0.11	0.48	15.77	1.41	100.82
1314_k30	63.43	18.75	0.00	0.69	15.23	1.47	99.57
1314_k322	63.84	19.00	0.00	0.56	15.41	1.49	100.30
1314_k31	64.48	18.96	0.01	0.75	15.33	1.47	101.01
1314_k32	**63.79**	**18.83**	**0.01**	**0.60**	**15.49**	**1.27**	**100.00**
1314_k1	63.56	18.92	0.00	0.80	15.12	1.71	100.11
1314_k2	63.99	18.80	0.00	0.83	14.89	1.73	100.24
1314_k4	63.96	18.81	0.00	0.66	15.25	1.34	100.02
1314_k5	64.30	18.85	0.00	0.52	15.19	1.63	100.49
1314_k6	64.11	18.89	0.01	0.58	15.74	1.67	101.00
1314_k7	**63.82**	**19.03**	**0.02**	**0.78**	**14.85**	**1.78**	**100.28**
1314_k7_1	64.13	18.87	0.10	0.64	15.69	0.83	100.26
1314_k7_8	64.21	18.88	0.17	0.73	15.24	1.15	100.38
1314_k8	63.56	19.54	0.04	0.42	14.98	2.62	101.16
1314_k9	63.63	18.81	0.00	0.52	15.46	1.61	100.03
1314_k10	63.84	19.10	0.20	0.91	14.94	1.11	100.10
1314_k10	64.65	18.77	0.00	0.49	15.76	1.04	100.70
1314_k11	63.55	18.76	0.00	0.62	15.49	1.77	100.19
1314_k13_1	64.29	18.82	0.00	0.51	15.78	1.11	100.51
1314_k13_4	64.46	18.59	0.00	0.50	15.87	0.88	100.30
1314_k12	63.71	18.72	0.00	0.74	15.11	1.84	100.12
1314_k15	64.02	18.93	0.01	0.57	15.42	1.58	100.53
1314_k16	63.87	18.71	0.00	0.82	14.91	1.90	100.21
1314_k17_1	64.46	18.62	0.00	0.55	15.76	0.82	100.22
1314_k17	64.09	18.94	0.00	0.85	14.90	1.72	100.50
1314_k17_2	63.86	18.73	0.00	0.65	15.36	1.65	100.25
1314_k18	63.71	18.76	0.02	0.46	15.81	1.08	99.83
1314_k17_5	64.11	18.93	0.00	0.77	15.07	1.50	100.38
1314_k17_6	64.01	19.07	0.00	0.72	15.48	1.34	100.62
1314_k17_7	63.69	18.72	0.00	0.61	15.46	1.38	99.86
1314_k17_8	64.17	18.77	0.00	0.54	15.79	0.99	100.27
1314_k17_9	64.03	18.97	0.00	0.47	15.79	1.12	100.38
1314_k17_10	63.94	18.92	0.00	0.52	15.48	1.31	100.17
1314_KL27	62.94	18.73	0.01	0.76	14.82	1.69	98.96
1314_KL27_1	63.50	18.70	0.00	0.69	15.04	1.61	99.54
1314_KL26	63.48	18.53	0.03	0.64	15.39	1.53	99.59

1314_KL29	63.23	18.66	0.03	0.63	15.20	1.79	99.54
1314_KL22	63.63	18.63	0.00	0.80	15.12	1.64	99.83
1314_KL23	64.17	18.44	0.02	0.68	15.11	1.54	99.96
1314_KL21	62.59	18.41	0.03	0.64	15.09	1.46	98.23
1314_KL24	63.85	18.59	0.00	1.06	14.47	1.63	99.61
1314_KL25	64.73	18.41	0.01	0.87	15.69	0.33	100.03
1314_KL26	63.21	18.42	0.05	0.80	14.97	1.30	98.76
1314_KL26_1	62.62	18.48	0.02	0.70	14.91	1.55	98.29
1315_k1	64.17	18.95	0.00	0.78	15.24	1.36	100.50
1315_k2	65.13	18.61	0.00	0.91	15.39	0.36	100.40
1315_k3	64.45	18.69	0.00	0.69	15.62	0.85	100.31
1315_k4	64.61	18.63	0.00	0.68	15.71	0.80	100.43
1315_k5	63.98	18.82	0.00	0.67	15.34	1.42	100.23
1315_k7	63.92	19.10	0.00	0.47	15.64	1.68	100.81
1315_k8	63.73	18.97	0.04	0.37	15.75	1.47	100.33
1315_k9	64.42	18.47	0.00	0.31	16.19	0.16	99.54
1315_k10	63.65	18.70	0.03	0.39	15.69	1.26	99.73
1315_k11	63.80	18.76	0.00	0.50	15.56	1.70	100.32
1315_k12	**64.14**	**18.71**	**0.04**	**0.62**	**15.51**	**0.82**	**99.84**
1315_k13	64.06	18.71	0.00	0.64	15.29	1.53	100.23
1315_k14	63.68	18.90	0.00	0.63	15.29	1.62	100.12
1315_k15	63.70	18.72	0.00	0.66	15.44	1.61	100.13
1315_k17	63.10	18.45	0.00	0.51	15.60	1.10	98.76
1315_k16	64.33	18.80	0.00	0.61	15.58	0.85	100.17
1315_k18	63.85	19.10	0.00	0.77	15.45	1.53	100.70
1315_k18_1	**64.10**	**19.11**	**0.01**	**0.48**	**15.68**	**1.43**	**100.82**
1315_k20	63.92	19.03	0.00	0.63	15.33	1.53	100.44
1315_KL8	64.05	18.68	0.03	0.62	15.67	1.63	100.68
1315_KL9	63.00	18.73	0.06	0.59	15.38	1.48	99.24
1315_KL9_1	63.67	18.67	0.03	0.53	15.19	1.62	99.71
1315_KL4	64.09	18.33	0.02	0.88	15.54	0.12	98.99
1315_KL6	62.94	18.29	0.10	0.40	15.37	1.20	98.30
1315_KL5	62.85	18.71	0.06	0.46	15.55	1.36	98.99
1315_KL4_1	63.89	18.63	0.03	0.67	15.14	1.61	99.96
1315_KL1	65.30	18.41	0.02	0.76	15.12	1.49	101.11
1315_KL1_1	63.78	18.79	0.04	0.78	15.16	1.62	100.16
1315_KL2	63.76	18.16	0.07	0.49	15.69	1.09	99.25
1315_k17	63.10	18.45	0.00	0.51	15.60	1.10	98.76
1315_k16	64.33	18.80	0.00	0.61	15.58	0.85	100.17
1315_k18	63.85	19.10	0.00	0.77	15.45	1.53	100.70
1315_k18_1	64.10	19.11	0.01	0.48	15.68	1.43	100.82
1315_k20	63.92	19.03	0.00	0.63	15.33	1.53	100.44
1321_k2	64.24	18.80	0.00	0.72	15.45	1.20	100.41
1321_k3	64.42	18.96	0.00	0.61	15.55	1.24	100.78
1321_k5	64.14	18.91	0.00	0.81	15.48	1.27	100.61
1321k6	64.06	18.97	0.00	0.78	15.37	1.23	100.41
1231_k8	65.37	18.73	0.00	0.52	16.13	0.10	100.86

1321_k9	65.27	18.51	0.00	0.43	16.43	0.06	100.70
1321_k10	65.40	18.51	0.04	0.48	16.14	0.07	100.63
1321_k12	64.45	18.76	0.01	0.75	15.41	1.12	100.50
1321_k13	63.80	18.91	0.07	0.77	15.32	1.02	99.88
1321_k15	64.53	18.90	0.01	1.02	15.09	1.15	100.70
1321_k16	64.24	18.70	0.00	0.57	15.72	1.28	100.51
1321_k17	64.11	18.65	0.00	0.72	15.45	1.12	100.05
1321_k19	64.05	18.67	0.14	0.51	15.62	0.52	99.51
1321_k20	63.79	19.17	0.01	0.70	15.40	0.83	99.90
1321_k25	64.44	18.86	0.00	1.07	15.02	0.98	100.37
1321_k26	64.31	19.05	0.00	0.89	15.41	0.99	100.64
1321_k28	64.67	18.84	0.00	0.79	15.55	0.88	100.73
1321_k29	64.52	18.85	0.00	0.65	15.86	0.82	100.70
1321_k30	64.17	18.76	0.00	0.89	15.54	0.81	100.17
1321_k30_1	64.29	18.84	0.00	0.93	15.35	0.98	100.39
1321_k32	64.50	18.82	0.00	0.67	15.92	0.66	100.57
1321_k33	64.81	18.76	0.02	0.54	15.87	0.85	100.86
1321_k34	64.34	18.84	0.00	0.47	16.11	0.81	100.58
1321_k31	64.53	18.76	0.00	0.56	16.01	0.67	100.54
1321_k31_1	65.38	18.78	0.00	0.55	16.06	0.54	101.31
1321_k35	64.69	18.86	0.00	0.77	15.55	0.83	100.70
1321_k36	64.43	18.80	0.00	0.62	16.14	0.79	100.79
1321_k36_1	64.94	18.95	0.00	0.71	15.63	0.77	101.00
1321_k37	64.45	18.83	0.00	0.77	15.77	0.90	100.72
1321_k38	64.22	18.93	0.00	0.75	15.40	1.06	100.35
1321_k39	64.52	18.79	0.00	0.62	15.86	0.86	100.65

Table AP4.3: Mineral chemistry data of Amphibole (Amp). Representative analyses shown in Tab. 4.3 are highlighted.

Analysis	SiO_2	TiO_2	Al_2O_3	Cr_2O_3	MnO	FeO	MgO	CaO	Na_2O	K_2O	F	Cl	Sum
1317H4	42.13	1.65	10.73	0.00	0.32	17.28	9.98	11.81	1.29	1.39	0.00	0.06	96.64
1317H2	**42.14**	**1.88**	**10.99**	**0.00**	**0.38**	**17.85**	**9.12**	**11.70**	**1.44**	**1.44**	**0.00**	**0.05**	**96.99**
1317H6	41.75	1.86	11.08	0.10	0.35	16.01	10.46	11.30	1.32	1.34	0.00	0.04	95.60
1317H1	42.84	1.51	10.70	0.03	0.36	16.51	10.62	11.72	1.20	1.29	0.00	0.06	96.83
1317H3	41.82	1.86	10.80	0.03	0.36	17.23	10.12	11.27	1.38	1.37	0.00	0.05	96.29
1317H10	42.03	1.72	10.89	0.05	0.41	17.08	9.84	11.65	1.35	1.43	0.00	0.03	96.48
1317H11_5	42.16	1.86	11.06	0.03	0.37	17.24	9.95	11.54	1.32	1.48	0.00	0.05	97.07
1317H18	42.32	1.59	11.01	0.00	0.39	17.42	9.69	11.59	1.33	1.46	0.00	0.04	96.84
1317H20	42.26	1.79	10.73	0.06	0.39	17.17	9.96	11.51	1.42	1.50	0.00	0.04	96.83

1317H17_3	42.21	1.72	10.79	0.04	0.38	17.13	9.93	11.54	1.33	1.39	0.00	0.06	96.52
1317_HL52	42.87	1.58	10.82	0.04	0.38	16.99	9.83	11.90	1.21	1.40	0.06	0.04	97.10
1317_HL44	42.93	1.93	10.59	0.04	0.34	17.06	10.11	11.65	1.37	1.37	0.05	0.05	97.49
1317_HL45	43.29	1.69	10.44	0.01	0.30	16.79	10.02	11.70	1.26	1.30	0.08	0.05	96.93
1317_HL31	42.10	1.63	10.63	0.07	0.47	17.25	10.03	11.84	1.35	1.27	0.10	0.04	96.79
1317_HL32	43.14	1.55	10.69	0.12	0.40	16.94	9.91	12.04	1.16	1.31	0.03	0.04	97.33
1317_HL33	43.04	2.02	10.71	0.00	0.30	16.60	10.18	12.22	1.05	1.42	0.04	0.03	97.62
1317_HL33_1	42.26	1.64	10.35	0.07	0.38	17.45	9.83	11.87	1.37	1.32	0.08	0.03	96.67
1317_HL31_2	42.77	1.85	10.57	0.07	0.43	16.80	10.04	11.74	1.34	1.38	0.08	0.03	97.10
1317_HL31_3	43.14	1.75	10.71	0.05	0.37	16.46	10.08	11.88	1.10	1.43	0.02	0.05	97.03
1317_HL31_4	43.18	1.68	10.57	0.00	0.36	16.18	10.48	12.01	1.20	1.31	0.06	0.05	97.08
1314_h32	42.37	1.49	10.14	0.04	0.42	17.42	10.32	11.55	1.42	1.31	0.00	0.04	96.51
1314_h1	42.95	1.66	10.14	0.04	0.41	16.39	10.66	11.58	1.39	1.28	0.00	0.03	96.53
1314_h2	**42.62**	**1.56**	**10.17**	**0.02**	**0.42**	**16.84**	**10.38**	**11.50**	**1.38**	**1.28**	**0.00**	**0.03**	**96.20**
1314_h3	42.84	1.36	10.21	0.05	0.46	16.78	10.49	11.55	1.44	1.27	0.00	0.04	96.49
1314_h4	41.97	1.65	10.50	0.09	0.45	16.92	10.21	11.30	1.60	1.36	0.00	0.05	96.11
1314_h5	42.15	1.37	11.12	0.05	0.38	16.08	10.77	11.61	1.37	1.40	0.00	0.05	96.34
1314_h6	42.86	1.58	10.52	0.04	0.44	16.97	10.52	11.47	1.48	1.32	0.00	0.03	97.23
1314_h7	42.69	1.58	10.38	0.08	0.50	16.79	10.47	11.54	1.44	1.27	0.00	0.02	96.76
1314_h9	42.85	1.30	10.26	0.04	0.45	17.28	10.43	11.39	1.44	1.25	0.00	0.03	96.73
1314_h10	42.95	1.32	10.51	0.07	0.43	17.03	10.30	11.44	1.25	1.35	0.00	0.04	96.69
1314_h12	43.18	1.66	10.40	0.10	0.45	16.46	10.60	11.52	1.36	1.27	0.00	0.04	97.03
1314_h13	42.33	1.66	10.49	0.06	0.47	17.47	10.17	11.31	1.54	1.35	0.00	0.05	96.89
1314_h14	42.57	1.58	10.39	0.06	0.46	17.03	10.50	11.53	1.64	1.31	0.00	0.04	97.11
1314_h17	42.79	1.43	10.30	0.06	0.44	16.77	10.55	11.53	1.39	1.31	0.00	0.03	96.60
1314_h17_1	39.26	0.49	14.51	0.00	0.47	18.60	8.04	11.59	1.27	1.79	0.00	0.06	96.10
1314_h17_2	42.67	1.35	10.32	0.06	0.40	16.74	10.38	11.53	1.24	1.23	0.00	0.03	95.96
1314_h17_3	42.88	1.43	10.33	0.09	0.44	16.82	10.36	11.60	1.24	1.28	0.00	0.03	96.50
1314_h20	43.13	1.41	10.37	0.05	0.52	16.79	10.40	11.41	1.46	1.25	0.00	0.04	96.82
1314_h21	43.06	1.35	10.19	0.05	0.43	16.79	10.55	11.20	1.48	1.29	0.00	0.04	96.43
1314_HL16	43.23	1.74	10.10	0.13	0.45	16.08	10.33	11.75	1.27	1.30	0.17	0.05	96.59
1314_HL15	43.23	1.45	10.34	0.01	0.41	16.71	9.96	11.42	1.38	1.23	0.18	0.05	96.38

1314_HL14	43.13	1.50	10.12	0.02	0.47	16.66	10.34	11.60	1.31	1.26	0.14	0.04	96.60
1314_HL14_1	42.80	1.72	10.18	0.10	0.45	16.52	10.19	11.59	1.44	1.30	0.14	0.03	96.46
1314_HL10	43.28	1.55	10.39	0.01	0.44	16.29	10.55	12.12	1.19	1.21	0.08	0.03	97.16
1314_HL11_1	43.50	1.86	10.16	0.06	0.35	16.30	10.04	11.76	1.21	1.31	0.11	0.04	96.68
1314_HL10_1	43.10	1.39	10.24	0.04	0.43	17.09	10.11	12.00	1.29	1.27	0.07	0.02	97.05
1315_h11	42.92	1.33	10.77	0.00	0.39	16.38	10.43	11.46	1.27	1.28	0.00	0.03	96.25
1315_h12	42.65	1.50	10.63	0.04	0.40	17.37	10.32	11.46	1.43	1.42	0.00	0.03	97.25
1315_h13	43.50	1.29	9.93	0.00	0.45	16.90	11.12	11.48	1.29	1.10	0.00	0.02	97.09
1315_h14	42.72	1.56	10.48	0.00	0.38	17.35	10.28	11.46	1.44	1.38	0.00	0.03	97.07
1315_h15	42.66	1.58	10.53	0.04	0.43	17.39	10.03	11.23	1.46	1.40	0.00	0.03	96.78
1315_h15_1	42.50	1.49	10.88	0.00	0.34	17.30	10.07	11.39	1.35	1.34	0.00	0.03	96.70
1315_h17	42.77	1.59	10.60	0.00	0.40	17.37	10.24	11.29	1.37	1.37	0.00	0.01	97.02
1315_HL10	43.05	1.38	10.09	0.03	0.36	16.86	10.18	11.76	1.39	1.30	0.08	0.03	96.52
1315_HL8	42.89	1.57	9.95	0.04	0.40	17.54	10.17	11.42	1.50	1.33	0.10	0.02	96.94
1315_HL9	42.89	1.38	10.17	0.01	0.40	17.33	10.24	11.73	1.49	1.29	0.22	0.04	97.17
1315_HL7	42.96	1.34	10.39	0.02	0.38	17.15	10.25	11.56	1.36	1.30	0.12	0.02	96.85
1315_HL10	42.79	1.45	9.97	0.01	0.41	16.81	10.55	11.57	1.29	1.25	0.17	0.02	96.28
1315_HL6	43.05	1.62	10.33	0.00	0.41	17.23	9.90	11.90	1.36	1.20	0.16	0.02	97.19
1315_HL4	43.24	1.10	11.37	0.00	0.33	16.54	9.98	12.32	1.36	1.29	0.09	0.02	97.65
1315_HL5	43.05	1.38	9.95	0.00	0.36	17.28	10.01	11.46	1.40	1.28	0.24	0.03	96.43
1315_HL2	41.23	2.30	11.56	0.00	0.31	16.44	9.06	12.27	1.34	1.34	0.22	0.03	96.09
1315_h1	43.12	1.45	9.92	0.02	0.40	16.90	10.54	11.55	1.38	1.21	0.00	0.03	96.53
1315_h2	42.27	1.66	10.30	0.00	0.38	17.11	10.45	11.43	1.51	1.36	0.00	0.03	96.50
1315_h3	42.48	1.54	10.37	0.01	0.40	17.68	10.17	11.25	1.39	1.36	0.00	0.04	96.69
1315_h4	42.92	1.43	10.16	0.00	0.39	16.90	10.47	11.41	1.28	1.32	0.00	0.04	96.31
1315_h5	42.03	1.36	10.53	0.00	0.40	17.40	10.10	11.36	1.49	1.41	0.00	0.04	96.11
1315_h7	**42.64**	**1.63**	**10.08**	**0.00**	**0.37**	**17.14**	**10.50**	**11.34**	**1.49**	**1.30**	**0.00**	**0.03**	**96.53**
1315_h8	42.54	1.37	10.17	0.03	0.43	17.54	10.28	11.66	1.43	1.29	0.00	0.03	96.76
1315_h9	42.35	1.61	10.40	0.02	0.40	17.16	10.31	11.36	1.62	1.33	0.00	0.04	96.60
1315_h10	43.38	1.36	10.01	0.00	0.36	16.46	10.56	11.73	1.21	1.29	0.00	0.03	96.38
1321_h1	44.47	0.91	9.33	0.09	0.34	13.92	12.56	11.78	1.22	1.07	0.00	0.11	95.79
1321_h2	45.70	0.61	9.31	0.01	0.29	14.00	12.70	11.95	1.00	0.94	0.00	0.10	96.61

1321_h3	45.25	0.83	9.15	0.07	0.32	13.39	13.12	11.84	1.19	1.00	0.00	0.10	96.27
1321_h4	**44.84**	**0.78**	**9.24**	**0.09**	**0.32**	**13.96**	**12.82**	**11.87**	**1.22**	**1.01**	**0.00**	**0.10**	**96.25**
1321_h6	45.26	0.83	9.65	0.04	0.35	14.34	12.75	11.55	1.19	1.03	0.00	0.11	97.10
1321_h7	44.47	0.82	9.98	0.10	0.40	14.13	12.61	11.55	1.30	1.08	0.00	0.11	96.55
1321_h8	44.70	0.83	9.93	0.11	0.41	14.41	12.55	11.52	1.45	1.11	0.00	0.11	97.13
1321_h8_1	44.97	0.81	9.84	0.11	0.35	14.18	12.34	11.72	1.21	1.04	0.00	0.12	96.69
1321_h9	44.63	0.85	9.84	0.05	0.30	14.69	12.38	11.67	1.21	1.08	0.00	0.10	96.80
1321_h11	45.00	0.86	9.89	0.12	0.38	14.12	12.68	11.48	1.35	1.13	0.00	0.11	97.14
1321_h12	44.75	0.77	9.43	0.04	0.37	14.27	12.83	11.41	1.34	0.99	0.00	0.11	96.31
1321_h13	44.68	0.79	9.57	0.12	0.37	14.19	12.81	11.64	1.39	1.04	0.00	0.11	96.70
1321_h15	44.91	0.72	9.74	0.03	0.39	14.16	12.70	11.77	1.28	1.07	0.00	0.11	96.88
1321_h16	44.81	0.78	9.97	0.10	0.38	14.62	12.65	11.50	1.29	1.07	0.00	0.12	97.29
1321_h17	46.87	0.62	8.51	0.05	0.33	13.84	13.16	11.81	1.08	0.83	0.00	0.08	97.18
1321_h14	45.07	0.71	10.09	0.10	0.39	14.28	12.02	11.67	1.06	1.00	0.00	0.11	96.50
1321_h18	45.18	0.80	9.74	0.04	0.32	14.05	12.76	11.49	1.16	1.09	0.00	0.12	96.75
1321_h19	44.93	0.67	9.81	0.06	0.34	14.02	12.87	11.73	1.15	0.96	0.00	0.08	96.64
1321_h20	44.78	0.75	9.72	0.09	0.41	14.23	12.71	11.39	1.42	1.08	0.00	0.11	96.70
1321_h20_1	45.15	0.81	9.91	0.17	0.32	13.86	12.80	11.89	1.16	1.03	0.00	0.11	97.21
1321_h22	45.26	0.91	9.57	0.08	0.34	14.21	12.56	11.57	1.15	0.98	0.00	0.10	96.73

Table AP4.4: Mineral chemistry data of Biotite (Bt). Representative analyses shown in Tab. 4.3 are highlighted.

		SiO_2	TiO_2	Al_2O_3	Cr_2O_3	FeO	MnO	MgO	CaO	Na_2O	K_2O	Total
Host	1317B1	35.85	3.21	15.51	0.00	17.25	0.27	12.61	0.00	0.00	9.89	94.62
Host	1317B3	41.31	3.05	14.38	0.00	15.95	0.21	10.49	0.08	0.05	8.36	93.93
Host	1317B14	36.40	3.13	15.80	0.03	16.42	0.26	12.84	0.00	0.04	9.84	94.79
Host	1317B15	36.15	3.13	15.95	0.00	16.76	0.16	12.30	0.00	0.04	9.99	94.50
Host	1317B16	35.92	3.60	16.11	0.00	16.83	0.20	12.48	0.00	0.03	9.44	94.65
Host	1317B18	36.55	3.59	15.69	0.00	17.07	0.23	12.12	0.00	0.00	9.87	95.14
Host	1317B17	45.22	1.68	18.32	0.07	10.75	0.18	6.85	5.45	2.33	3.38	94.28
Host	1317B23	36.28	3.66	15.83	0.04	16.86	0.21	12.09	0.00	0.00	9.76	94.77
Host	1317B21	36.12	3.76	15.72	0.00	16.69	0.24	12.39	0.00	0.05	9.75	94.75
Host	1317B12_6	37.07	3.07	15.52	0.05	15.73	0.24	12.25	0.05	0.04	9.67	93.74
Host	1317B21_5	35.92	3.58	15.62	0.00	17.07	0.23	12.28	0.06	0.00	9.41	94.19
Host	**1317B34**	**36.26**	**3.64**	**15.89**	**0.06**	**16.19**	**0.23**	**12.06**	**0.00**	**0.00**	**9.94**	**94.30**
Host	1317B32	36.36	3.85	15.90	0.04	16.39	0.15	12.09	0.00	0.00	9.98	94.80
Host	1317B28	36.26	3.66	15.62	0.00	16.80	0.24	11.99	0.00	0.03	9.79	94.42

Host	1317B48	36.06	3.67	15.57	0.03	17.02	0.18	12.22	0.00	0.03	9.65	94.48
Host	1317_BL73_1	36.92	3.47	15.57	0.06	16.29	0.19	12.05	0.13	0.03	9.55	94.37
Host	1317_BL73	36.92	3.48	15.06	0.01	16.34	0.20	11.83	0.09	0.05	9.54	93.70
Host	1317_BL73_2	36.79	4.17	15.57	0.02	16.62	0.25	12.10	0.03	-0.02	9.69	95.38
Host	1317_BL77	36.83	2.94	15.31	0.02	16.37	0.22	12.65	0.23	0.01	9.51	94.23
Host	1317_BL39	37.33	2.44	15.39	0.05	16.05	0.16	13.17	0.35	0.10	9.57	94.73
Host	1317_BL41	36.46	3.17	15.41	0.03	16.64	0.24	12.37	0.11	0.07	9.50	94.12
Host	1317_BL42	36.53	2.92	14.71	0.04	16.98	0.22	12.66	0.04	-0.01	9.69	93.92
Host	1317_BL51_3	36.37	3.77	15.01	0.07	16.75	0.19	11.65	0.13	0.04	9.41	93.54
Host	1317_BL51	36.33	3.93	15.13	0.08	16.63	0.24	11.69	0.08	0.05	9.63	93.92
Host	1317_BL51_1	36.77	3.52	15.61	0.01	16.81	0.17	12.18	0.10	0.07	9.60	95.02
Host	1317_BL39	36.69	2.37	15.34	0.05	15.69	0.23	12.98	0.37	0.10	9.45	93.42
Vein	1314_b33	36.40	3.76	14.93	0.06	17.37	0.18	12.10	0.00	0.01	9.84	94.69
Vein	1314_b43	34.10	2.80	15.61	0.00	18.17	0.49	12.98	0.20	0.01	7.60	92.00
Host	1314_b1	36.17	3.63	14.80	0.03	17.87	0.24	12.12	0.00	0.02	9.64	94.55
Host	1314_b2	36.09	1.91	15.43	0.04	16.08	0.27	14.36	0.02	0.02	9.36	93.63
Host	1314_b3	36.58	2.78	15.26	0.00	15.90	0.25	13.58	0.00	0.06	9.75	94.19
Host	1314_b4	36.63	2.97	14.94	0.07	15.74	0.28	13.85	0.03	0.05	9.77	94.36
Host	**1314_b5_1**	**36.38**	**3.23**	**15.35**	**0.07**	**16.61**	**0.24**	**12.85**	**0.00**	**0.02**	**9.88**	**94.66**
Host	1314_b5	35.98	2.44	16.39	0.01	15.99	0.25	13.17	0.03	0.03	9.87	94.20
Host	1314_b6	36.46	3.20	15.20	0.04	16.32	0.24	13.05	0.02	0.05	9.79	94.40
Host	1314_b7	36.66	3.44	15.49	0.08	16.94	0.26	12.31	0.00	0.02	9.75	94.98
Host	1314_b7_1	35.58	2.86	16.02	0.01	16.55	0.27	12.72	0.03	0.02	9.88	93.95
Host	1314_b7_2	36.23	2.93	14.96	0.04	16.83	0.28	13.02	0.03	0.01	9.65	94.02
Host	1314_b8	36.73	3.88	15.30	0.01	16.51	0.24	12.10	0.01	0.05	9.83	94.69
Host	1314_b9	36.46	3.69	15.69	0.07	16.10	0.21	12.51	0.00	0.00	9.80	94.55
Host	1314_b10	36.32	3.92	15.75	0.08	15.88	0.23	12.29	0.03	0.00	9.90	94.43
Host	1314_b11	36.39	2.75	15.16	0.10	15.44	0.24	14.15	0.07	0.01	9.52	93.86
Host	1314_b12	36.78	3.40	15.35	0.06	15.92	0.22	12.56	0.00	0.00	9.85	94.18
Host	1314_b14	36.23	3.32	15.32	0.08	16.25	0.22	12.92	0.00	0.02	9.75	94.15
Host	1314_b15	36.42	3.68	15.62	0.06	16.20	0.19	12.39	0.02	0.02	9.71	94.35
Host	1314_b16	36.51	3.76	15.69	0.08	16.50	0.21	12.16	0.02	0.02	9.92	94.91
Host	1314_b17	36.52	3.93	15.63	0.06	16.31	0.21	12.18	0.00	0.03	9.56	94.47
Host	1314_b18	36.34	3.67	15.61	0.07	16.21	0.22	12.40	0.00	0.06	9.74	94.34
Host	1314_b19	36.56	3.33	15.31	0.06	16.29	0.23	12.93	0.04	0.03	9.70	94.49
Vein	1314_BL11	36.10	4.06	16.01	0.04	17.41	0.14	10.90	0.06	0.07	9.45	94.40
Vein	1314_BL10	36.80	3.79	15.34	0.02	16.70	0.22	11.89	0.12	0.07	9.38	94.55
Vein	1314_BL10_1	36.56	3.97	14.93	0.05	16.32	0.23	11.92	0.02	0.05	9.46	93.68
Vein	1314_BL15	36.67	3.59	15.13	0.06	16.96	0.13	11.87	0.05	0.05	9.59	94.27
Vein	1314_BL14	36.40	3.60	14.87	0.04	17.03	0.19	12.11	0.06	0.07	9.79	94.32
Vein	1314_BL13	36.92	4.13	15.11	0.07	16.44	0.16	11.37	0.19	0.09	9.38	94.08
Host	1314_BL15_1	36.89	3.66	14.72	0.02	16.78	0.22	12.37	0.09	0.04	9.26	94.25
Host	1314_BL15_2	36.29	3.87	14.94	0.11	16.50	0.17	12.24	0.02	0.02	9.58	93.95
Host	1315_b1	36.12	3.83	15.15	0.00	17.00	0.19	12.38	0.01	0.02	9.58	94.30
Host	1315_b2	36.24	4.12	15.08	0.00	17.00	0.21	12.30	0.00	0.04	9.80	94.81
Host	1315_b3	36.09	3.65	14.69	0.01	17.68	0.22	12.44	0.00	0.01	9.87	94.69
Host	1315_b4	36.38	3.94	14.59	0.02	17.62	0.21	12.34	0.00	0.05	9.63	94.82
Host	1315_b5	36.27	3.93	15.19	0.02	17.24	0.19	12.04	0.00	0.07	9.75	94.74
Host	1315_b5_2	36.10	3.83	15.22	0.01	17.25	0.21	11.91	0.00	0.04	9.81	94.41
Host	1315_b6	36.47	3.94	15.33	0.00	17.18	0.20	11.99	0.00	0.03	9.84	95.00
Host	1315_b7	35.93	4.10	14.74	0.00	18.34	0.19	11.69	0.00	0.05	9.70	94.77
Host	1315_b8	36.19	3.85	15.13	0.00	17.59	0.19	12.16	0.01	0.05	9.64	94.85
Host	1315_b9	36.12	4.06	14.99	0.00	17.79	0.24	12.21	0.00	0.06	9.86	95.35
Host	1315_b11	36.32	3.56	14.90	0.03	17.48	0.20	12.42	0.02	0.02	9.63	94.59
Host	1315_b12	36.25	4.02	15.02	0.00	17.49	0.21	11.91	0.03	0.03	9.54	94.52
Host	**1315_b12_1**	**36.19**	**3.96**	**14.87**	**0.01**	**17.63**	**0.19**	**12.18**	**0.02**	**0.04**	**9.79**	**94.90**
Host	135_b13	35.82	3.92	14.86	0.02	17.49	0.18	11.99	0.01	0.00	9.72	94.04
Host	1315_b15	36.41	3.93	14.80	0.00	18.02	0.21	11.78	0.00	0.00	9.83	95.01
Host	1315_b16	36.00	4.01	14.91	0.00	17.74	0.18	11.88	0.00	0.03	9.55	94.32
Host	1315_b17	36.09	3.98	15.32	0.02	17.05	0.21	11.92	0.01	0.02	9.68	94.33

Host	1315_b18	36.18	3.99	15.23	0.02	17.97	0.20	12.27	0.02	0.03	9.78	95.70
Host	1315_b19	36.06	3.68	15.43	0.00	17.55	0.20	12.19	0.00	0.00	9.91	95.04
Host	1315_b20	36.00	4.42	15.29	0.00	17.50	0.17	11.78	0.00	0.00	9.98	95.17
Host	1315_b21	35.91	4.19	15.30	0.00	17.66	0.14	11.67	0.02	0.03	9.63	94.59
Vein	1315_BL13	36.08	4.02	14.84	0.00	18.55	0.23	11.00	0.06	0.08	9.18	94.19
Vein	1315_BL2	36.53	3.64	14.94	0.02	16.67	0.22	12.48	0.05	0.06	9.54	94.30
Vein	1315_BL1	36.25	4.13	14.53	0.00	17.61	0.17	11.54	0.04	-0.01	9.56	94.00
Vein	1315_BL6	36.44	4.04	14.60	0.04	17.39	0.23	11.51	0.04	0.04	9.38	93.89
Vein	1315_BL6_1	36.59	3.96	14.71	0.01	17.03	0.20	11.65	0.05	0.01	9.58	93.97
Vein	1315_BL6_2	36.74	4.14	14.62	0.01	17.50	0.19	11.85	0.03	0.04	9.60	94.87
Vein	1315_BL7	36.17	3.60	14.55	0.00	18.05	0.20	11.50	0.08	0.09	9.62	94.01
Host	1315_BL8	36.14	3.97	14.55	0.00	17.45	0.17	11.75	0.03	0.05	9.64	93.87
Host	1315_BL8_1	36.66	4.09	14.53	0.04	17.55	0.18	11.58	0.05	0.03	9.44	94.34
Host	1315_BL9	36.12	3.87	14.43	-0.02	17.55	0.18	11.75	0.05	0.05	9.31	93.49
Vein	1321_b1	37.37	3.36	16.08	0.04	14.05	0.13	13.35	0.01	0.04	10.04	94.60
Vein	1321_b2	37.62	2.23	15.75	0.00	14.39	0.13	14.47	0.00	0.04	9.94	94.66
Vein	1321_b3	37.35	2.51	15.28	0.03	14.83	0.14	14.24	0.00	0.03	9.90	94.40
Vein	1321_b1_1	37.13	2.61	15.63	0.03	14.36	0.16	13.82	0.00	0.00	10.00	93.84
Vein	1321_b4	36.46	2.55	16.51	0.06	14.63	0.14	13.70	0.03	0.02	9.82	94.00
Vein	1321_b5	37.38	3.27	17.01	0.02	15.63	0.01	11.41	0.00	0.03	9.88	94.80
Vein	1321_b5_1	36.04	2.81	16.71	0.04	16.03	0.03	11.94	0.00	0.03	9.74	93.54
Vein	1321_b6	37.26	2.67	15.15	0.09	14.25	0.15	14.12	0.00	0.05	9.88	93.73
Vein	1321_b7	37.22	2.74	15.41	0.06	14.52	0.15	14.05	0.00	0.01	9.99	94.27
Vein	1321_b8	37.00	2.59	14.88	0.06	14.95	0.11	13.96	0.00	0.00	9.87	93.53
Host	1321_b9	36.83	1.01	15.79	0.02	14.13	0.17	15.39	0.15	0.00	9.76	93.32
Host	**1321_b10**	**37.19**	**3.32**	**15.55**	**0.04**	**15.18**	**0.15**	**13.32**	**0.00**	**0.01**	**9.87**	**94.76**
Vein	1321_b10_1	36.95	2.93	15.55	0.03	14.52	0.14	14.03	0.00	0.00	10.12	94.39
Vein	1321_b11	37.13	2.50	15.57	0.03	15.15	0.10	14.05	0.03	0.00	9.66	94.32
Vein	1321_b11_1	36.84	2.68	15.43	0.02	15.62	0.14	13.40	0.00	0.05	9.86	94.16
Vein	1321_b11_5	47.58	2.08	13.49	0.05	12.84	0.12	11.26	0.02	0.00	8.24	95.76
Vein	1321_b12	36.80	0.73	16.41	0.08	14.09	0.10	15.32	0.03	0.05	9.88	93.60
Vein	1321_b13	45.06	0.90	9.22	0.06	13.80	0.32	13.05	11.61	1.26	1.00	96.35
Vein	1321_b14	46.73	0.58	8.28	0.07	13.28	0.33	13.76	11.99	1.00	0.83	96.90
Vein	1321_b14_1	63.39	0.02	18.63	0.01	0.15	0.00	0.01	0.00	0.63	15.42	98.26
Vein	1321_b13_1	36.94	2.68	15.41	0.02	14.46	0.18	14.06	0.03	0.02	9.70	93.62
Vein	1321_b13_2	36.93	2.80	15.22	0.02	14.42	0.16	13.96	0.00	0.02	9.89	93.54
Vein	1321_b13_3	36.99	2.64	15.51	0.01	14.53	0.17	14.20	0.02	0.04	9.88	94.10
Host	1321_b15	36.88	1.77	16.47	0.11	14.34	0.18	14.85	0.03	0.07	10.08	94.90
Host	1321_b18	37.45	1.33	16.95	0.10	13.65	0.13	15.11	0.03	0.04	9.90	94.80
Host	1321_b19	37.20	1.62	17.11	0.14	13.13	0.12	14.85	0.02	0.08	9.88	94.28
Host	1321_b20	36.91	1.39	15.30	0.05	15.42	0.23	15.15	0.00	0.02	10.12	94.71
Host	1321_b21	36.81	2.19	15.22	0.13	14.65	0.23	15.20	0.01	0.04	9.65	94.25
Host	1321_b22	35.46	2.51	15.13	0.12	14.29	0.29	15.72	0.04	0.03	8.46	92.19
Host	1321_b23	36.78	0.62	16.17	0.08	15.25	0.17	15.35	0.07	0.09	9.26	93.94
Host	1321_b24	37.07	0.63	16.68	0.06	15.03	0.17	15.02	0.00	0.00	9.95	94.71
Host	1321_b24_1	37.31	0.99	16.57	0.02	14.06	0.25	15.33	0.05	0.05	9.70	94.42
Host	1321_b25	36.70	0.82	16.95	0.07	14.07	0.17	15.04	0.01	0.06	10.02	94.05
Host	1321_b27	37.35	0.93	16.65	0.07	13.97	0.18	15.46	0.06	0.10	9.30	94.20
Host	1321_b26	36.86	1.79	16.45	0.07	14.30	0.20	14.27	0.01	0.00	9.82	93.87

Table AP4.5: Results from Ti-in-amphibole geothermometer. Here, b is coefficient with a value of 1.52

	b	Ti-Amp	Log(Ti-Amp)	b-log(Ti-Amp)	T(in K)	T(deg C)	Avg.	Avg. deviation
1317H4	1.52	0.19	-0.72	2.24	1069.74	796.74	803	16
1317H2	1.52	0.22	-0.67	2.19	1098.12	825.12		
1317H6	1.52	0.21	-0.67	2.19	1096.10	823.10		
1317H1	1.52	0.17	-0.77	2.29	1049.41	776.41		
1317H3	1.52	0.21	-0.67	2.19	1095.08	822.08		
1317H10	1.52	0.20	-0.71	2.23	1078.39	805.39		
1317H11_5	1.52	0.21	-0.67	2.19	1094.06	821.06		
1317H18	1.52	0.18	-0.74	2.26	1061.98	788.98		
1317H18_6	1.52	0.15	-0.84	2.36	1018.83	745.83		
1317H20	1.52	0.21	-0.69	2.21	1086.84	813.84		
1317H17_3	1.52	0.20	-0.71	2.23	1078.39	805.39		
1317_HL52	1.52	0.18	-0.74	2.26	1059.73	786.73		
1317_HL44	1.52	0.22	-0.66	2.18	1102.14	829.14		
1317_HL45	1.52	0.19	-0.71	2.23	1074.09	801.09		
1317_HL31	1.52	0.19	-0.73	2.25	1067.54	794.54		
1317_HL32	1.52	0.18	-0.75	2.27	1055.18	782.18		
1317_HL33	1.52	0.23	-0.64	2.16	1111.03	838.03		
1317_HL33_1	1.52	0.19	-0.72	2.24	1069.74	796.74		
1317_HL31_2	1.52	0.21	-0.68	2.20	1093.04	820.04		
1317_HL31_3	1.52	0.20	-0.70	2.22	1080.52	807.52		
1317_HL31_4	1.52	0.19	-0.72	2.24	1071.92	798.92		
1314_h32	1.52	0.17	-0.77	2.29	1048.24	775.24	771	22
1314_h1	1.52	0.19	-0.72	2.24	1069.74	796.74		
1314_h2	1.52	0.18	-0.75	2.27	1058.60	785.60		
1314_h3	1.52	0.16	-0.81	2.33	1031.43	758.43		
1314_h4	1.52	0.19	-0.72	2.24	1070.83	797.83		
1314_h5	1.52	0.16	-0.81	2.33	1031.43	758.43		
1314_h6	1.52	0.18	-0.75	2.27	1058.60	785.60		
1314_h7	1.52	0.18	-0.74	2.26	1059.73	786.73		
1314_h9	1.52	0.15	-0.83	2.35	1021.39	748.39		
1314_h10	1.52	0.15	-0.82	2.34	1025.19	752.19		
1314_h12	1.52	0.19	-0.73	2.25	1068.64	795.64		
1314_h13	1.52	0.19	-0.72	2.24	1069.74	796.74		
1314_h14	1.52	0.18	-0.75	2.27	1058.60	785.60		
1314_h17	1.52	0.16	-0.79	2.31	1039.95	766.95		
1314_h17_1	1.52	0.06	-1.24	2.76	868.27	595.27		
1314_h17_2	1.52	0.16	-0.81	2.33	1030.19	757.19		
1314_h17_3	1.52	0.16	-0.79	2.31	1039.95	766.95		
1314_h20	1.52	0.16	-0.80	2.32	1036.32	763.32		
1314_h21	1.52	0.15	-0.81	2.33	1028.95	755.95		
1314_h22	1.52	0.17	-0.76	2.28	1052.89	779.89		
1314_HL16	1.52	0.20	-0.70	2.22	1080.52	807.52		
1314_HL15	1.52	0.17	-0.78	2.30	1044.71	771.71		
1314_HL14	1.52	0.17	-0.76	2.28	1050.57	777.57		
1314_HL14_1	1.52	0.20	-0.71	2.23	1078.39	805.39		
1314_HL10	1.52	0.18	-0.75	2.27	1055.18	782.18		
1314_HL11_1	1.52	0.21	-0.67	2.19	1095.08	822.08		
1314_HL10_1	1.52	0.16	-0.80	2.32	1033.88	760.88		
1315_h1	1.52	0.17	-0.78	2.30	1043.53	770.53	775	13
1315_h2	1.52	0.19	-0.72	2.24	1070.83	797.83		

1315_h3	1.52	0.18	-0.75	2.27	1055.18	782.18		
1315_h4	1.52	0.16	-0.79	2.31	1039.95	766.95		
1315_h5	1.52	0.16	-0.81	2.33	1031.43	758.43		
1315_h7	1.52	0.19	-0.73	2.25	1067.54	794.54		
1315_h8	1.52	0.16	-0.81	2.33	1031.43	758.43		
1315_h9	1.52	0.19	-0.73	2.25	1065.33	792.33		
1315_h10	1.52	0.16	-0.81	2.33	1030.19	757.19		
1315_h11	1.52	0.17	-0.77	2.29	1048.24	775.24		
1315_h12	1.52	0.15	-0.84	2.36	1018.83	745.83		
1315_h13	1.52	0.18	-0.75	2.27	1056.33	783.33		
1315_h14	1.52	0.18	-0.74	2.26	1060.86	787.86		
1315_h15	1.52	0.17	-0.77	2.29	1048.24	775.24		
1315_h15_1	1.52	0.18	-0.74	2.26	1060.86	787.86		
1321_h1	1.52	0.10	-0.99	2.51	957.26	684.26	661	17
1321_h2	1.52	0.07	-1.17	2.69	893.03	620.03		
1321_h3	1.52	0.09	-1.03	2.55	940.62	667.62		
1321_h4	1.52	0.09	-1.06	2.58	930.06	657.06		
1321_h6	1.52	0.09	-1.04	2.56	938.89	665.89		
1321_h7	1.52	0.09	-1.03	2.55	940.62	667.62		
1321_h8	1.52	0.09	-1.05	2.57	935.40	662.40		
1321_h8_1	1.52	0.10	-1.02	2.54	944.04	671.04		
1321_h9	1.52	0.10	-1.02	2.54	945.73	672.73		
1321_h11	1.52	0.09	-1.07	2.59	928.25	655.25		
1321_h12	1.52	0.09	-1.06	2.58	931.85	658.85		
1321_h13	1.52	0.08	-1.09	2.61	919.01	646.01		
1321_h15	1.52	0.09	-1.07	2.59	928.25	655.25		
1321_h16	1.52	0.07	-1.17	2.69	893.03	620.03		
1321_h17	1.52	0.08	-1.10	2.62	915.20	642.20		
1321_h14	1.52	0.09	-1.05	2.57	933.63	660.63		
1321_h18	1.52	0.08	-1.12	2.64	907.39	634.39		
1321_h19	1.52	0.08	-1.08	2.60	924.60	651.60		
1321_h20	1.52	0.09	-1.05	2.57	935.40	662.40		
1321_h20_1	1.52	0.10	-0.99	2.51	955.64	682.64		
1321_h22	1.52	0.15	-0.82	2.34	1025.19	752.19		

Table AP4.6: Results from Ti-in-biotite geothermometer

	‘a’, ‘b’, and ‘c’ are surface fit coefficients							
	a	b	c	Ti	$X_{(Mg)}$	T(C)	Average T	Avg. Dev.
1317	-2.36	4.6482E-09	-1.73	0.37	0.59	712.06	712	20
1317	-2.36	4.6482E-09	-1.73	0.34	0.57	695.12		
1317	-2.36	4.6482E-09	-1.73	0.35	0.61	711.69		
1317	-2.36	4.6482E-09	-1.73	0.36	0.59	708.46		
1317	-2.36	4.6482E-09	-1.73	0.41	0.59	727.61		
1317	-2.36	4.6482E-09	-1.73	0.41	0.58	724.32		
1317	-2.36	4.6482E-09	-1.73	0.18	0.56	582.16		
1317	-2.36	4.6482E-09	-1.73	0.41	0.59	727.87		
1317	-2.36	4.6482E-09	-1.73	0.43	0.60	733.47		
1317	-2.36	4.6482E-09	-1.73	0.35	0.61	709.49		
1317	-2.36	4.6482E-09	-1.73	0.41	0.59	725.98		
1317	-2.36	4.6482E-09	-1.73	0.41	0.60	729.79		
1317	-2.36	4.6482E-09	-1.73	0.44	0.59	735.92		
1317	-2.36	4.6482E-09	-1.73	0.42	0.59	728.14		
1317	-2.36	4.6482E-09	-1.73	0.42	0.59	728.85		
1314	-2.36	4.6482E-09	-1.73	0.43	0.58	730.38	717	16

1314	-2.36	4.6482E-09	-1.73	0.41	0.57	724.69		
1314	-2.36	4.6482E-09	-1.73	0.22	0.64	647.65		
1314	-2.36	4.6482E-09	-1.73	0.32	0.63	701.37		
1314-vein	-2.36	4.6482E-09	-1.73	0.34	0.64	712.46		
1314	-2.36	4.6482E-09	-1.73	0.37	0.61	715.79		
1314-vein	-2.36	4.6482E-09	-1.73	0.28	0.62	679.76		
1314	-2.36	4.6482E-09	-1.73	0.36	0.61	716.73		
1314	-2.36	4.6482E-09	-1.73	0.39	0.59	720.04		
1314	-2.36	4.6482E-09	-1.73	0.33	0.60	699.51		
1314	-2.36	4.6482E-09	-1.73	0.33	0.61	703.24		
1314	-2.36	4.6482E-09	-1.73	0.44	0.59	736.70		
1314	-2.36	4.6482E-09	-1.73	0.42	0.61	733.52		
1314	-2.36	4.6482E-09	-1.73	0.44	0.61	741.29		
1314	-2.36	4.6482E-09	-1.73	0.31	0.64	704.87		
1314	-2.36	4.6482E-09	-1.73	0.39	0.61	724.01		
1314	-2.36	4.6482E-09	-1.73	0.38	0.61	721.71		
1314	-2.36	4.6482E-09	-1.73	0.42	0.60	732.53		
1314	-2.36	4.6482E-09	-1.73	0.42	0.59	732.70		
1314	-2.36	4.6482E-09	-1.73	0.44	0.60	739.40		
1314	-2.36	4.6482E-09	-1.73	0.42	0.60	732.28		
1314	-2.36	4.6482E-09	-1.73	0.38	0.61	721.38		
1315	-2.36	4.6482E-09	-1.73	0.44	0.59	735.50	736	4
1315	-2.36	4.6482E-09	-1.73	0.47	0.59	743.97		
1315	-2.36	4.6482E-09	-1.73	0.42	0.58	727.42		
1315	-2.36	4.6482E-09	-1.73	0.45	0.58	736.70		
1315	-2.36	4.6482E-09	-1.73	0.45	0.58	736.12		
1315	-2.36	4.6482E-09	-1.73	0.44	0.58	732.68		
1315	-2.36	4.6482E-09	-1.73	0.47	0.56	737.45		
1315	-2.36	4.6482E-09	-1.73	0.44	0.58	732.87		
1315	-2.36	4.6482E-09	-1.73	0.41	0.58	724.33		
1315	-2.36	4.6482E-09	-1.73	0.46	0.57	737.97		
1315	-2.36	4.6482E-09	-1.73	0.45	0.58	736.63		
1315	-2.36	4.6482E-09	-1.73	0.45	0.58	736.06		
1315	-2.36	4.6482E-09	-1.73	0.45	0.56	732.64		
1315	-2.36	4.6482E-09	-1.73	0.46	0.57	737.26		
1315	-2.36	4.6482E-09	-1.73	0.45	0.58	738.24		
1315	-2.36	4.6482E-09	-1.73	0.45	0.57	735.98		
1315	-2.36	4.6482E-09	-1.73	0.42	0.58	727.06		
1315	-2.36	4.6482E-09	-1.73	0.50	0.57	748.89		
1315	-2.36	4.6482E-09	-1.73	0.48	0.57	741.80		
1321-Vein	-2.36	4.6482E-09	-1.73	0.38	0.65	732.45	704	10
1321-Vein	-2.36	4.6482E-09	-1.73	0.25	0.67	678.65		
1321-Vein	-2.36	4.6482E-09	-1.73	0.28	0.66	693.69		
1321-Vein	-2.36	4.6482E-09	-1.73	0.30	0.66	700.16		
1321-Vein	-2.36	4.6482E-09	-1.73	0.29	0.65	694.70		
1321-Vein	-2.36	4.6482E-09	-1.73	0.37	0.59	712.19		
1321-Vein	-2.36	4.6482E-09	-1.73	0.32	0.60	694.62		
1321-Vein	-2.36	4.6482E-09	-1.73	0.30	0.66	705.60		
1321-Vein	-2.36	4.6482E-09	-1.73	0.31	0.66	706.94		
1321-Vein	-2.36	4.6482E-09	-1.73	0.29	0.65	697.82		
1321-Vein	-2.36	4.6482E-09	-1.73	0.37	0.63	726.13		
1321-Vein	-2.36	4.6482E-09	-1.73	0.33	0.66	716.15		
1321-Vein	-2.36	4.6482E-09	-1.73	0.28	0.65	690.66		
1321-Vein	-2.36	4.6482E-09	-1.73	0.30	0.63	696.17		
1321-Vein	-2.36	4.6482E-09	-1.73	0.30	0.66	704.99		
1321-Vein	-2.36	4.6482E-09	-1.73	0.32	0.66	711.09		
1321-Vein	-2.36	4.6482E-09	-1.73	0.30	0.66	702.66		
1321-Host	-2.36	4.6482E-09	-1.73	0.20	0.67	643.99	603	59
1321-Host	-2.36	4.6482E-09	-1.73	0.15	0.69	597.00		
1321-Host	-2.36	4.6482E-09	-1.73	0.18	0.69	636.46		

1321-Host-2.36	4.6482E-09	-1.73	0.16	0.66	595.83
1321-Host-2.36	4.6482E-09	-1.73	0.25	0.67	679.57
1321-Host-2.36	4.6482E-09	-1.73	0.29	0.69	706.60
1321-Host-2.36	4.6482E-09	-1.73	0.11	0.68	531.09
1321-Host-2.36	4.6482E-09	-1.73	0.09	0.68	478.14
1321-Host-2.36	4.6482E-09	-1.73	0.10	0.69	517.71
1321-Host-2.36	4.6482E-09	-1.73	0.20	0.66	644.11

Appendix 5 – Supporting information for Chapter 5

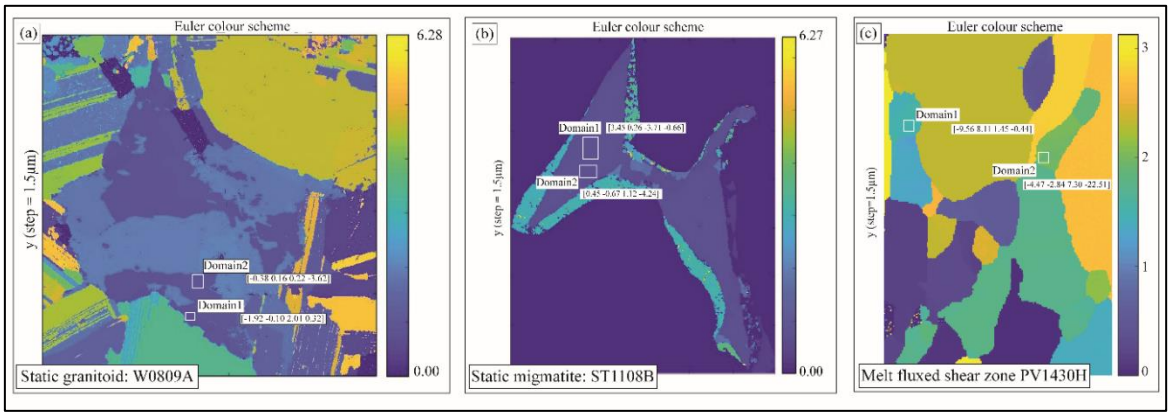

Figure AP5 – 1: WBV colour-coded magnitude map over the whole area. The studied domains are marked, as shown in Fig. 5.6a, 5.8a, 5.10a. Two 'Domains' are shown with weighted burgers vector (WBV) values parallel to the crystal axes of quartz (Tab. 5.3).

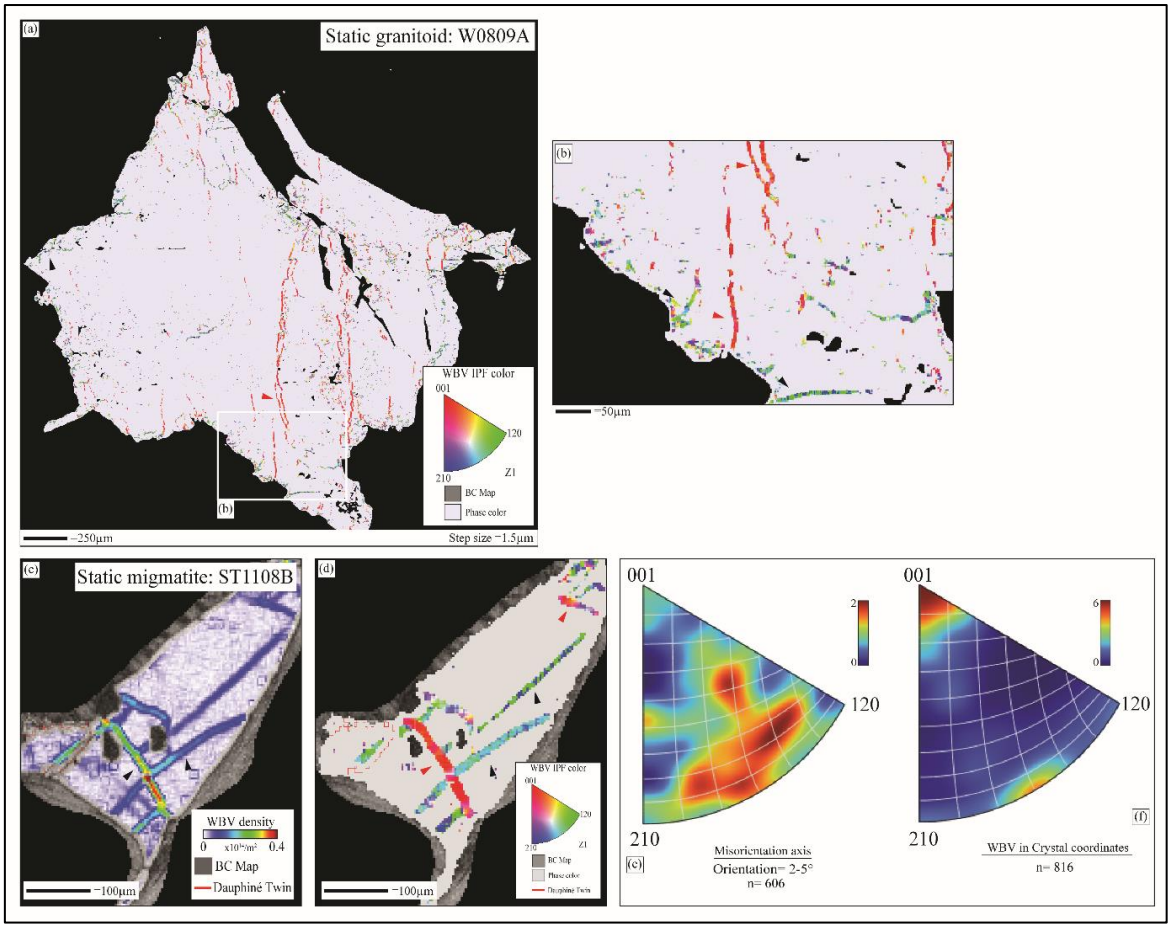

Figure AP5 – 2: Burgers vectors with different orientations along quartz substructures suggest the activation of two or more slip systems in melt-crystallized grains. (a-b) WBV IPF map of the studied quartz grain (as shown in Fig. 5.6a) shows WBVs close to the grain edges are parallel to <a> direction, whereas elongated, subparallel substructures extended inside the quartz grains have WBVs parallel to [c]. (c-d) WBV magnitude map of a quartz grain from ST1108B showing high GND densities along elongated subgrain boundaries (black arrows in 'c'). Subgrain boundaries parallel to the grain edges have WBVs oriented in <a> direction (black arrows in 'd') whereas other subgrain boundaries have WBVs parallel to [c] or mixed WBVs parallel to <c+a> (red arrows in 'd'). (e) Misorientation axis-angle pair show activation of different rotation axis and WBV IPF records clusters close to [c] and <a> axis denoting the same.

AP.5 Modelling stress relationships in quartz crystallizing within a confined space

Model set-up

To explain the stress values inferred from the studied samples, numerical modelling is performed to measure the magnitude and distribution of local stress in a material resembling granite. To calculate the stress values within the quartz, we use COMSOL, a multiphysics software based on the finite element method that simulates each of the three mentioned scenarios. Under stress, these models assume that both quartz and feldspar behave as linear-elastic materials. We employ a grain scale geometry wherein a single quartz grain is surrounded by plagioclase grains to simulate the interstitial geometry observed in one of the studied samples (yellow box in Fig. 5.3c, AP5 – 1). The inner region of interest is embedded in a large box (0.3mm by 0.3mm, Fig. AP5 – 3) to eliminate boundary effects and focus on the microscale. Complex microstructures (in this case, contacts between qtz-plag) are modelled at a higher resolution than the larger geometry, which is modelled at a lower resolution. We employ triangular mesh for both the quartz and plagioclase grains to better aid the numerical accuracy and stability of the simulation (Fig. AP5 – 3). The mesh resolution is high in the region of interest (Fig. AP5 – 3). Confining pressure is simulated by setting up compressional stresses (4, 6, and 11kbar in magnitude) on all the sides of the outer geometry (at 90° to the boundaries) to accurately model different crystallization depths of our studied samples (Tab. 5.1). For each scenario, first the specific set-up of the model is explained in detail and then the results are provided. Tab. AP5.1 lists the input values of elastic constants for α-quartz (low-quartz) and plagioclase feldspar (for simplistic reason, An_{100} is chosen).

AP.5.1 Scenario A: Stress generation inside an interstitial quartz grain due to the interplay between confining stress and force of crystallization

In this model, the force of crystallization acts radially outward from all sides of the studied crystal grain and "pushes against" the confining pressure acting on the sides of the outer geometry. From the observation of isolated interstitial quartz grain geometry (Fig. 5.2-5.4), it is inferred that the growth rate was significantly higher than the rate of nucleation. A supersaturation value of 1.1 is assumed for quartz crystallization (i.e., the melt is 10% supersaturated with silica is assumed; Norie et al., 2010). The partial molar volume of quartz is 22.68 cm^3 mol^{-1} (Tab. AP5.1) which renders a maximum value of FOC (eqn. 3 in section 5.5.4). Effects of having three different confining pressures (4, 6 and 11 kbar) are also modelled. For each model run, stresses within the central quartz grain are monitored as the grain starts to crystallize at 750°C. At 750°C (1023K) the FOC value is 35.77 MPa while it decreases to 20 MPa as temperature decreases down to 300°C (573K) (following eqn. 3). The maximum stress inside the quartz grain is 270 MPa at a FOC of 20 MPa and confining pressure of 4 kbar (400 MPa), concentrating at the pointed ends of the two grain contacts (Fig. AP5 – 4). The grain experiences a relatively homogeneous tensile stress of 230-240MPa elsewhere. For a confining pressure of 6 kbar and 11 kbar, the maximum differential stress is 420MPa and 800MPa, respectively (Fig. AP5 – 4; Tab. AP5.2). With a FOC value of 35.77 MPa, the accumulated stress inside the quartz grain is 255 MPa, 410 MPa and 780 MPa for 4 kbar, 6 kbar and 11 kbar confining pressures, respectively (Tab. AP5.2). This suggests that the accumulated differential stress inside the body is primarily regulated by the outside confining stress and FOC has a negligible effect.

AP.5.2 Scenario B: Stress generation inside a small quartz grain due to a far field tectonic deformation

In this scenario, we investigate melt crystallization at varying confining pressures, accompanied by tectonic stress acting under common geological strain rates of the ductile regime (Tab. AP5.1). The strain rates range from 10^{-9} to 10^{-14} with 10^{-1} interval. To model this scenario viscous flow laws of both quartz and feldspar are used.

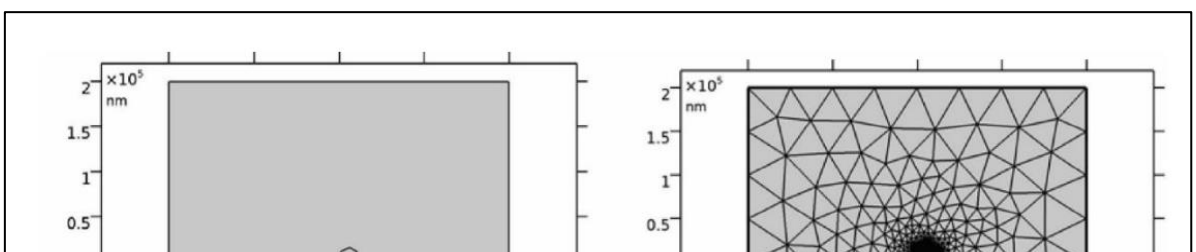

Feldspar flow law (dislocation creep for wet feldspar) (Rybacki and Dresen, 2000)

$$A\sigma^n d^{-m} \exp(-\frac{Q}{RT}) = \text{ë}$$

The input parameters are provided in Tab. AP5.1.

For the quartz flow law, we use the following equation, and the input parameters are provided in Tab. AP5.1.

$$\frac{\mu b D_l}{kT} . \left(\frac{\sigma}{\mu}\right)^n . e^{-\frac{H_L}{RT}} = \text{ë}$$

The models are set to run for 10^4 seconds, which resulted in strain amounts of 10^{-5}, 10^{-6}, 10^{-7}, 10^{-8} ,10^{-9}, 10^{-10} for the six different scenarios. This low finite strain is chosen, as microstructural observations suggest very little shape modification of the melt crystallized grains (optical photomicrographs in Fig. 5.2, 5.3, and Fig. 5.4 BSE results). In general, the accumulated stress is seen to be concentrated along the boundary between the input geometry of quartz and the surrounding plagioclase grains (Fig. AP5 – 5). Within this range of effective strain, the accumulated stress is in the order of 10^{-12} MPa at 10^{-10} s^{-1} strain rate to 10^{-15} MPa at 10^{-12} s^{-1} (Fig. AP5 – 5). At relatively higher strain rate values of 10^{-9} to 10^{-10} s^{-1}, a non-uniform distribution of stress is seen. The stresses at these strain rates are found in the order of 10^{-16} to 10^{-17} MPa (Tab. AP5.2).

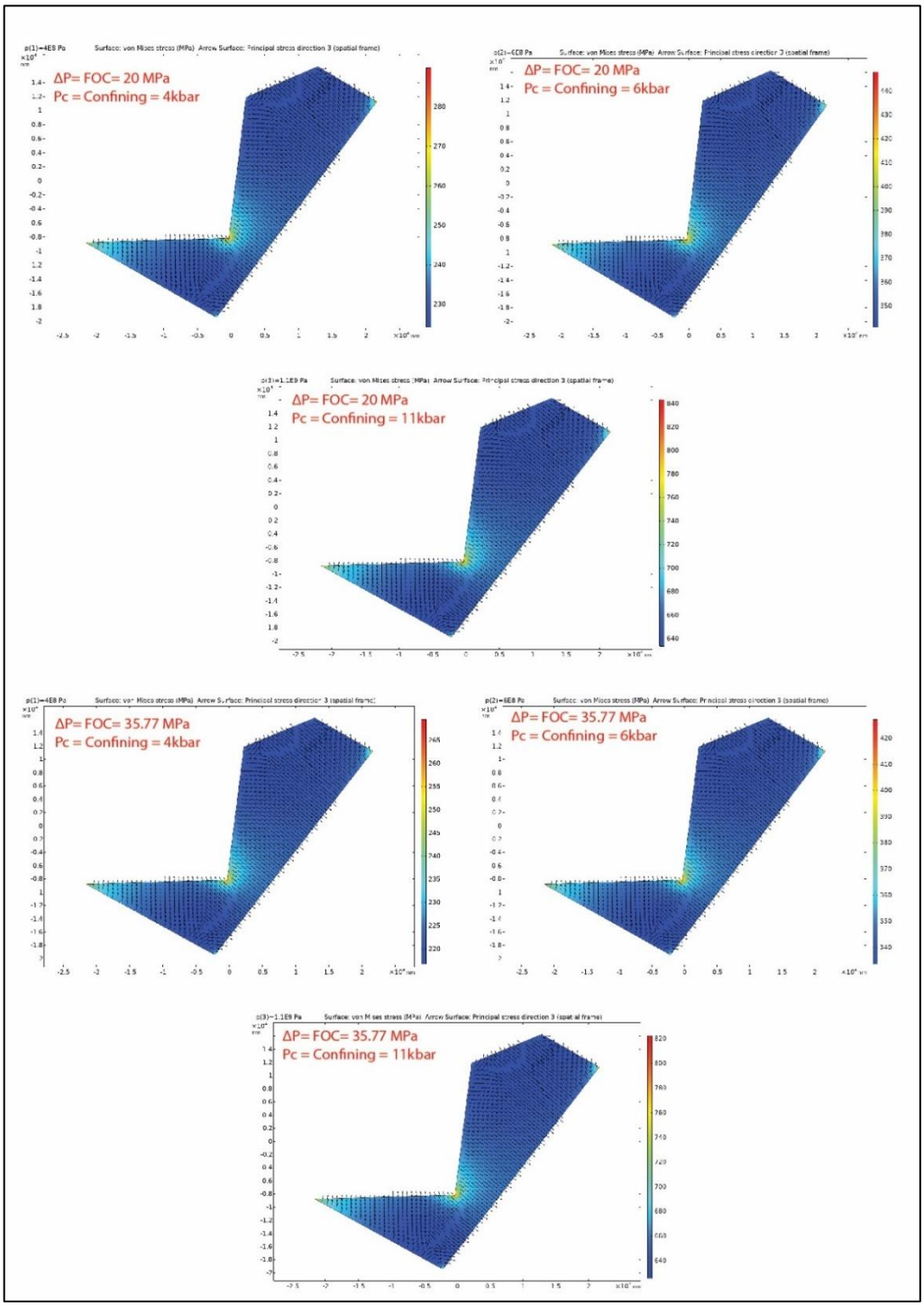

Figure AP5 – 4: Differential stress inside the quartz grain with force of crystallization (FOC) values of 20 MPa and 35.77 MPa, respectively.

Parameters/settings	Value	Unit	Comments/examples of relevant literature
Bulk modulus (K) of α-quartz	38.3	GPa	Pabst and Gregorová, 2013
Shear modulus (G) of α-quartz	44.1	GPa	
Poisson ratio of α-quartz	0.084	_	
Density α-quartz	2650	Kg/m^3	
Bulk modulus (K_{VRH}) of An_{100}	80.5	GPa	Pabst et al., 2015
Shear modulus (G_{VRH}) of An_{100}	38.3	GPa	
Density of An_{100}	2770	Kg/m^3	
Poisson ratio of An_{100}	0.295	_	
Geological strain rate	10^{-13} to 10^{-20}	s^{-1}	Heard, 1976; Pfiffner and Ramsey, 1982; Fagereng and Biggs, 2018 Kreemer et al., 2014
Confining stress at the outer box	400, 600 & 1100	MPa	In the studied samples melt crystallization occurred between 400-1100 MPa (Section 5.3; Craven et al., 2012, 2013; Jessop et al., 2019; Wang et al., 2014, 2019; Stuart et al., 2016)
Partial molar volume (from 25° to 750°C) – Scenario A	22.68 to 23.70	cm^3mol^{-1}	Dorogokupets, 1995
Ideal Gas constant (R)	8.314	$J\ mol^{-1}K^{-1}$	After Rybacki and Dresen, 2000
Input parameters for Feldspar flow law (Scenario B)			
Shear strain rate (ë)	10^{-9} to10^{-14}	S^{-1}	Variable strain rates are examined
Grain size (d)	_	µm	No grain size dependence, for details Frost and Ashby, 1982; Rybacki and Dresen, 2000
Material constant (A)	398	Mpa^{-n} $µm^m/s$	After Rybacki and Dresen, 2000
Stress exponent (n)	3	_	After Rybacki and Dresen, 2000
Activation energy (Q)	356	kj/mol	For wet plag after Rybacki and Dresen, 2000
Temperature (T)	573-1023	K	A variable temperature range is examined
Input parameters for Quartz flow law (Scenario B)			
Shear strain rate (ë)	10^{-9} to10^{-14}	S^{-1}	Variable strain rates are examined
Exponential number (e)	2.718	_	
Stress exponent (n)	3	_	

Shear modulus (μ)	$42x10^9$	N/m^2 (Pa)	
Burgers vector (b)	$5x10^{-10}$	m	corresponding to <a> slip
Diffusion constant (D_l)	2.9×10^{-5}	m^2s^{-1}	
Boltzmann constant	1.3862×10^{-23}	$J\ mol^{-1}\ K^{-1}$	
Molar activation enthalpy for self-diffusion (H_l)	$243x10^3$	$Jmol^{-1}$	
Temperature (T)	573-1023	K	A variable temperature range is examined
Input parameters for Scenario C			
Change in elastic constants (C_{ij}) of quartz with pressure	0.7% per 1kbar	-	Kimizuka et al., 2007; Dong et al., 2015; Ohno et al., 2006; Angel, 1992. In our studied samples a little change in confining pressure (4 to11kbar) impart no significant changes in these parameters. The values are kept constant with varying P and T.
Change in bulk modulus (K) of quartz with pressure	1% per 1kbar	-	
Change in bulk modulus (K) of plagioclase (An_{100}) with pressure	0.4% per 1kbar	-	
Change in elastic constants (C_{ij}) of An_{100} with pressure	Unidentifiable (due to scarcity of data)	-	
Change in elastic constants (C_{ij}) of quartz with temperature	15% softening; E, G, and K varies according to the Fig. AP5 – 6 and greatly influenced by α-β transition	Gpa/°C	Gregorová, 2013 Peng and Redfern, 2013

Table AP5.1: Input parameters for Scenario A-C.

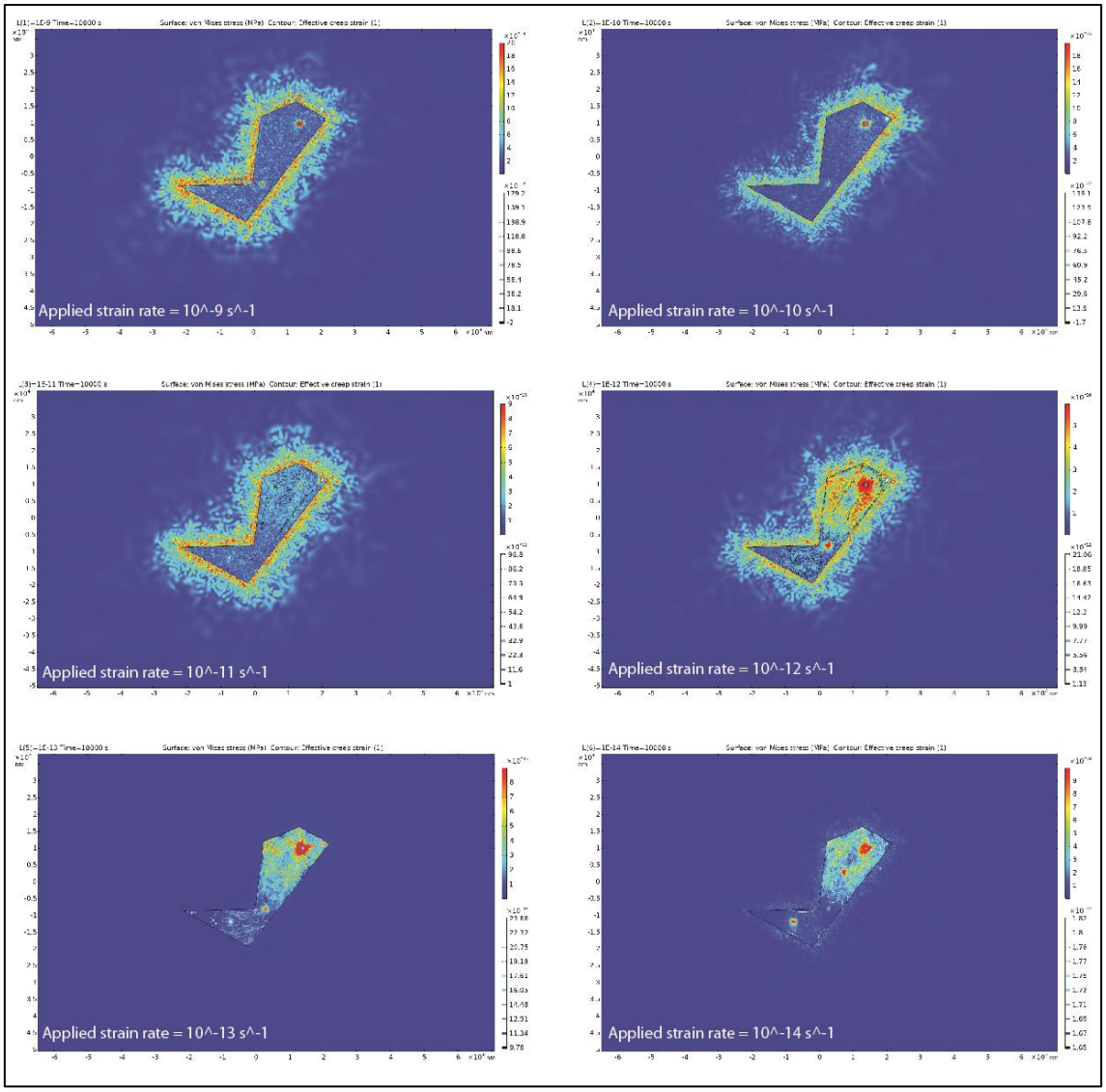

Figure AP5 – 5: Differential stress inside the quartz grain under variable strain rates. All the models are set to run for 10^4 seconds.

AP.5.3 Scenario C: Generation of stress inside an interstitial quartz grain due to differential volume changes between quartz and feldspar during cooling

We use a linear-elastic model to monitor stress concentration as confining pressure decreases from 4, 6, or 11 kbar while temperature decreases from 750 °C. The liquidus temperature of granitic melt is assumed to be at 750°C, and the lower limit of dislocation generation and movement during low stress deformation is 300°C (Hobbs et al. 1986; Dunlap et al., 1997; Stipp et al., 2002). Since rate of cooling/exhumation has no effect on the elastic responses of quartz-plagioclase, they are not included in the model. We

compare results in terms of absolute stress values as well as spatial distribution of stresses within the inner geometry. Change in elastic parameters of quartz with change in temperature, is shown in Fig. AP5 – 6, and Tab. AP5.1.

At 4 Kbar and 750°C, the maximum stress inside the quartz grain is 340 MPa, with a uniform average stress distribution of 220 MPa. At this confining pressure, cooling to 0°C reduces the maximum stress inside the body to 259 MPa, but a high stress amount of 250 MPa is seen to be uniformly distributed. Hence, a resultant differential stress amount of 30-80 MPa is found (Fig. AP5 – 7). Thus, cooling down of granitic melt from 750°C to 0°C at 4 kbar leads to an accumulation of maximum differential stress of ~80 MPa. At 8 kbar and 750°C, the average stress value inside the quartz grain is 320 MPa, whereas the maximum stress is 450 MPa. At this confining pressure, the maximum stress is 390 MPa after cooling to 0°C (Fig. AP5 – 7). Hence cooling of a granitic melt at this pressure develops differential stress of ~ 60-70 MPa. Likewise, a granitic melt cooling at 750°C and at 11kbar develops differential stress of ~100 MPa (Fig. AP5 – 7). The cooling is seen to have caused a volumetric contraction of the quartz grain, as shown by the black outline of the previous input geometry (Fig. AP5 – 7). However, this is impossible to identify in the microstructure. Hence cooling at different confining pressures can produce differential stress of ~80 MPa at 4kbar and ~100 MPa at 11kbar, Tab. AP5.2). Cooling down to 300°C will produce even lesser stress amount than observed here. Considering both the effect of change in confining pressure and temperature, an ascent of a quartz-feldspar microstructure (with a starting temperature of 750°C) from 6kbar to 2kbar (i.e., a 4 kbar change in confining pressure) can accumulate differential stress of 80 MPa (Tab. AP5.2) as it rises through the crust and cools down. Note, the range of the accumulated stress inside the quartz grain is higher at high temperature and very low in low temperature.

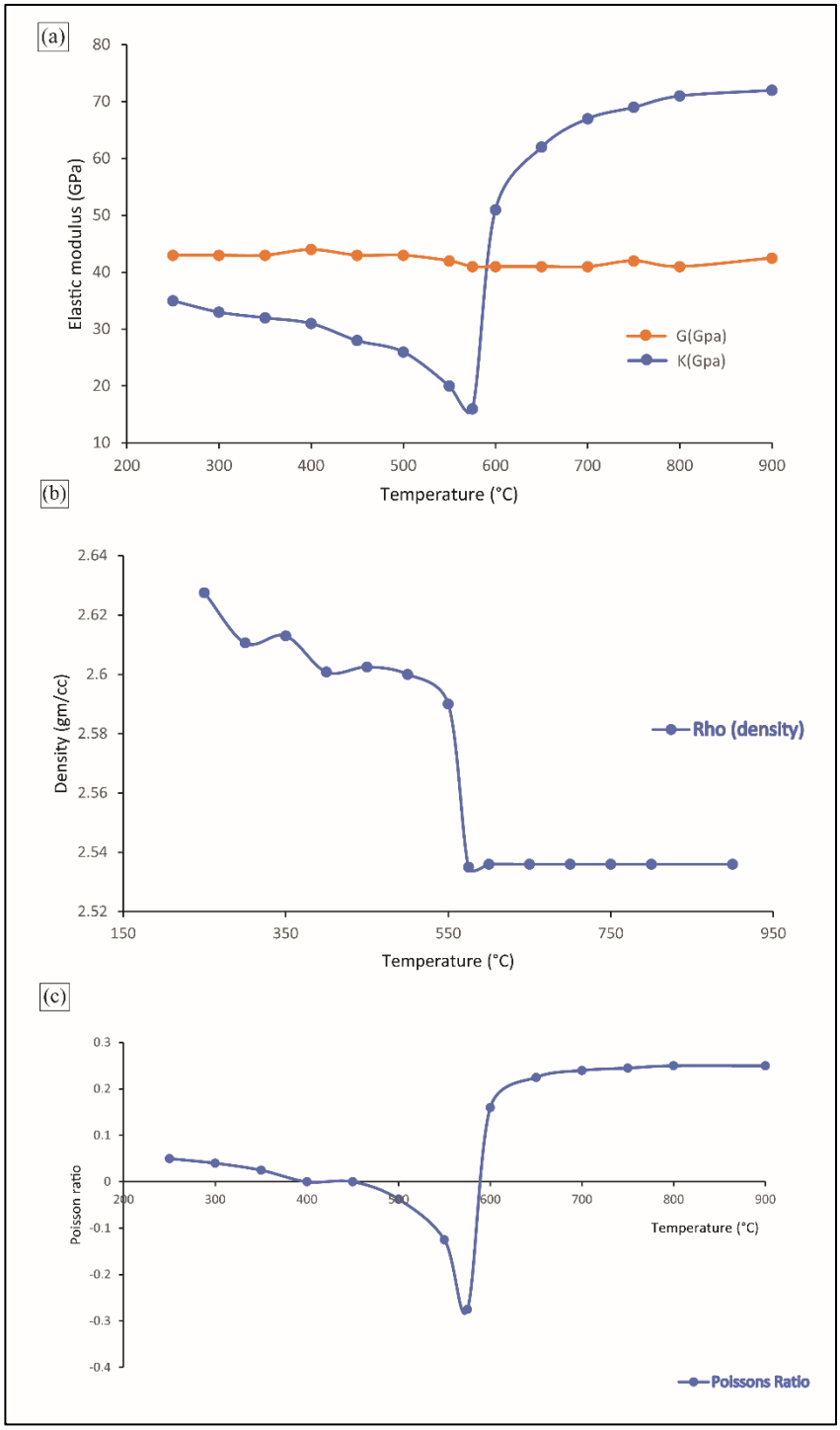

Figure AP5 – 6: Temperature dependence of elastic moduli (G and K), density, and possion ratio of quartz

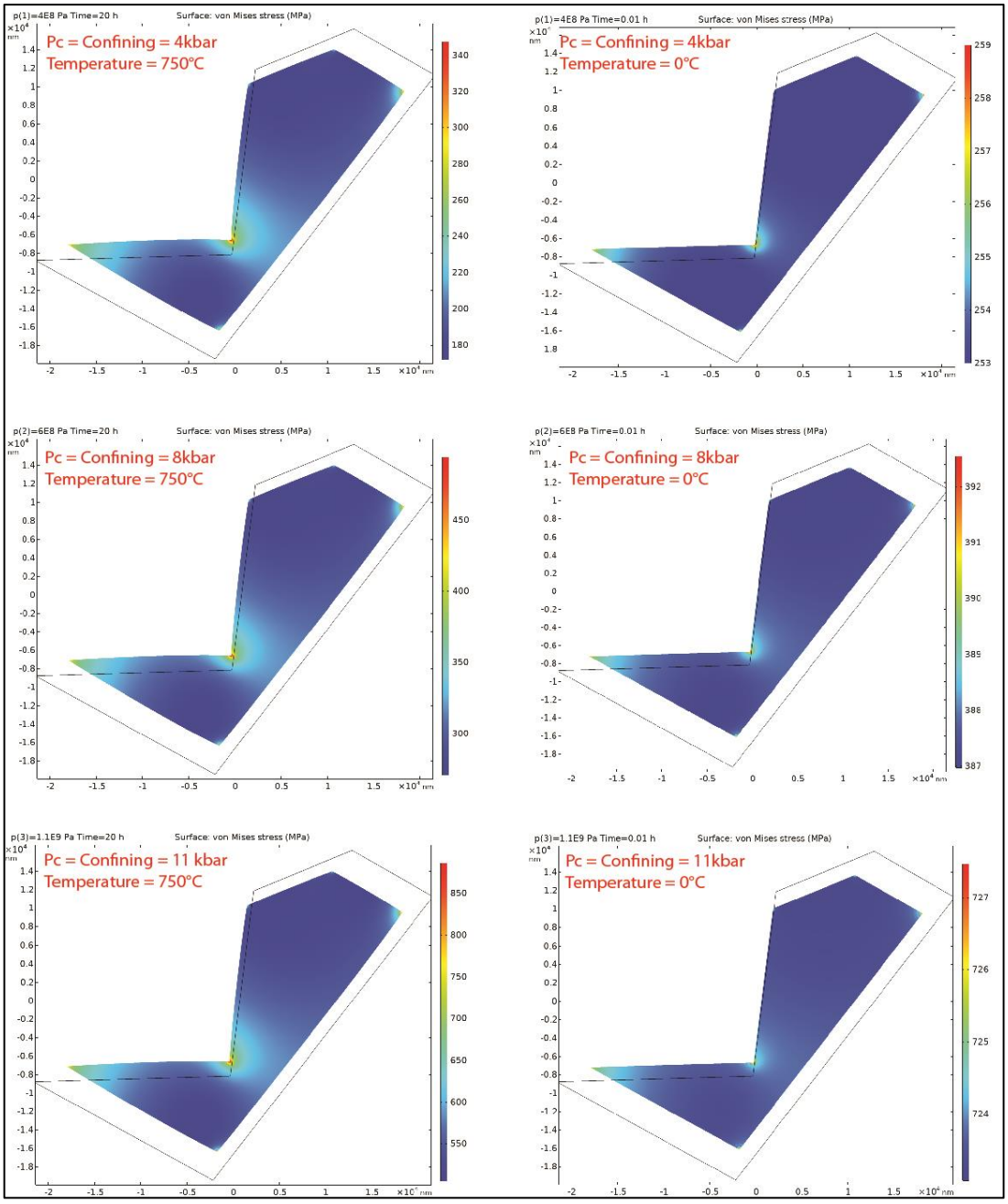

Figure AP5 – 7: Differential stress inside the quartz grain due to change in pressure-temperature during exhumation

Scenarios investigated	Controlling Parameters	Accumulated stress amount
Scenario A	FOC ~ 20 MPa	At 4 kbar 270 MPa
		At 6 kbar 420 MPa
		At 11 kbar 800 MPa
	FOC ~ 35.77 MPa	At 4 kbar 255 MPa
		At 6 kbar 410 MPa
		At 11 kbar 780 MPa
Scenario B	At 10^{-14} s^{-1} strain rate	At 4 kbar 10^{-17} MPa
	At 10^{-11} s^{-1} strain rate	At 4 kbar 10^{-14} MPa
	At 10^{-9} s^{-1} strain rate	At 4 kbar 10^{-12} MPa
Scenario C	Change in P_c – 4kbar and temperature from 750°C to 0°C	~80 MPa
	Change in P_c – 6kbar and temperature from 750°C to 0°C	~60-70 MPa
	Change in P_c – 11kbar and temperature from 750°C to 0°C	~100 MPa

Table AP5.2: **Development of stresses inside quartz grain under different scenarios**

Appendix 6 – Supporting information for Chapter 6

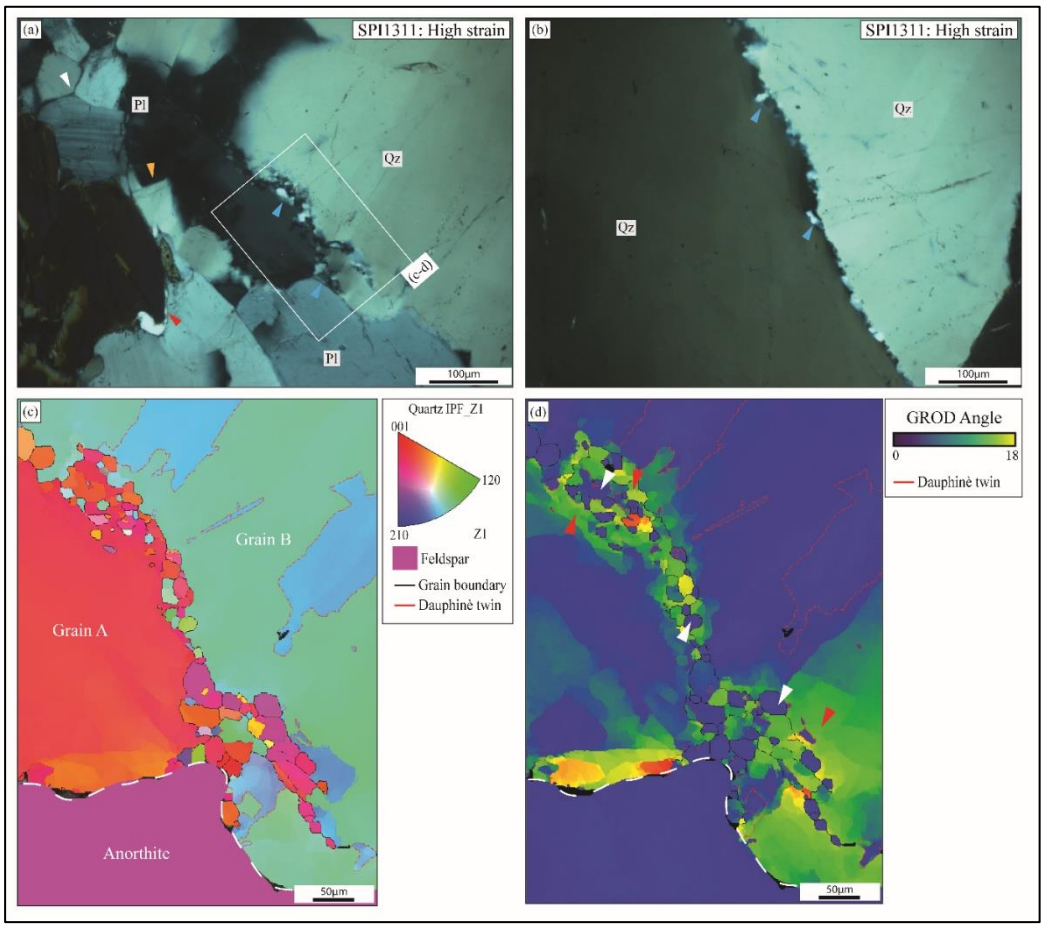

Figure AP6 – 1: Local solid state deformation features (dynamic recrystallization) in the melt-present diorite gneiss (SPI1311). (a) Newly formed bulges and fine-grained recrystallized quartz grains extending into another grain (marked with white rectangle). Features of former melt are preserved as elongated melt films (red arrow) and partial straight faceted grain (yellow arrow) in the surrounding areas. Solid state ~120° triple junctions are also found. (b) Recrystallized quartz grains are extremely well aligned parallel to the long axis of these elongated quartz grains. (c) IPF colouring indicates that the recrystalized grains have a similar crystal orientation (close to the [001] axis) and are related to their parent grain (Grain A). Grain B exhibits the formation of dauphiné twins near the recrystallized grain fractions. (d) Recrystallized grains have minimal GROD angle deviation (white arrows) in comparison to the surrounding parent grains (red arrows), which have a greater degree of internal distortion and a greater GROD angle.

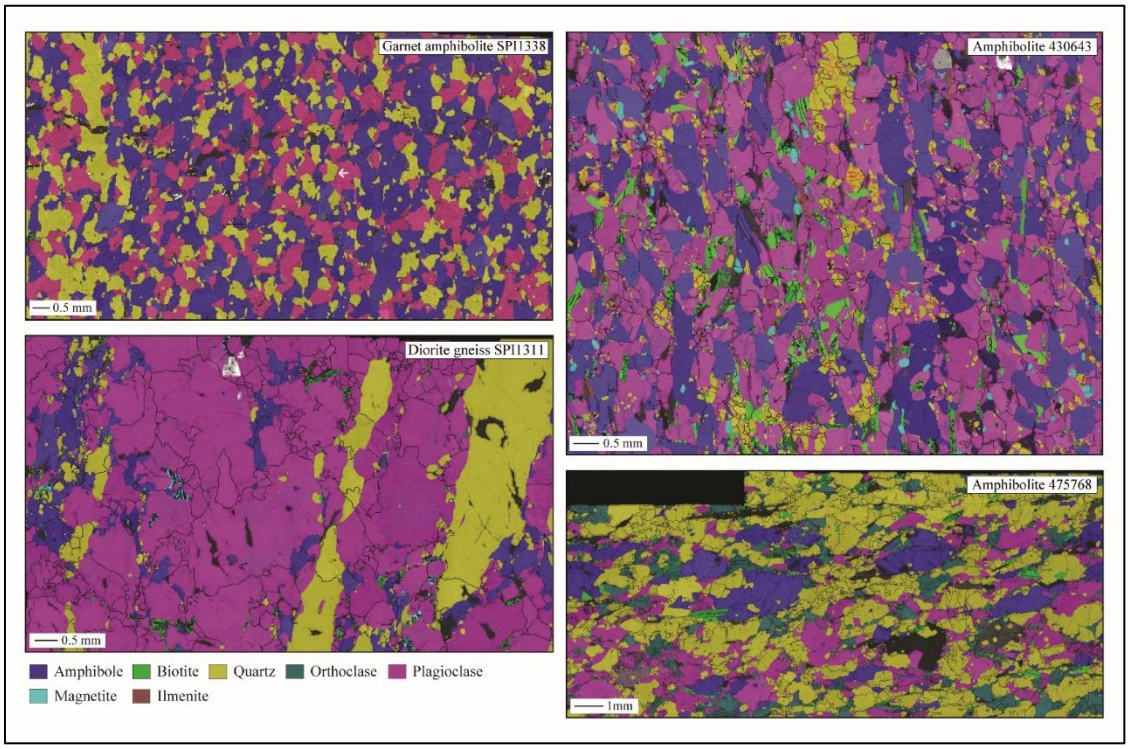

Figure AP6 – 2: EBSD phase map of the studied samples.

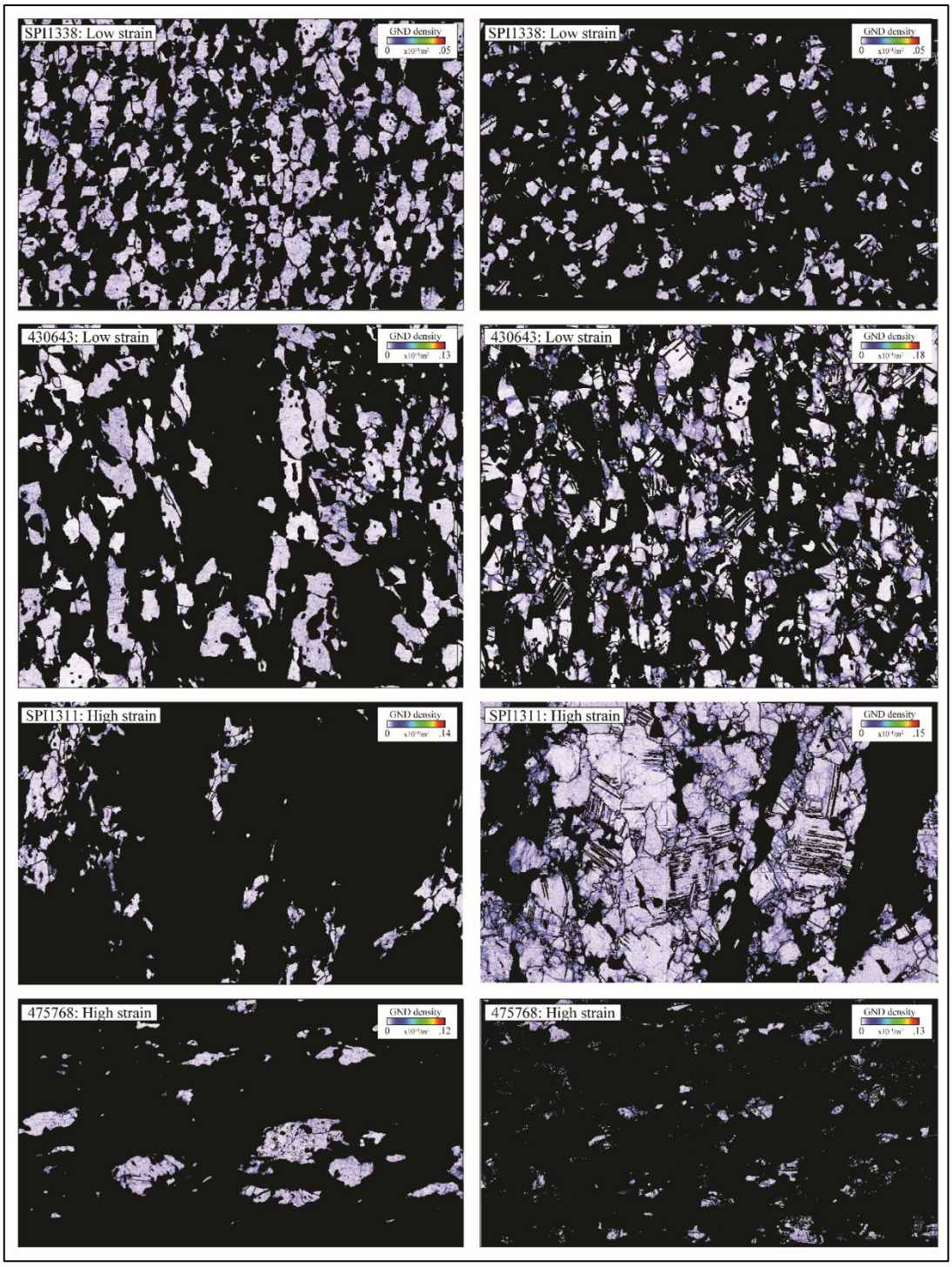

Figure AP6 – 3: GND density maps show very similar values for amphibole and plagioclase grains in the studied samples

References

Abbott, D., Burgess, L., Longhi, J. and Smith, W.H., 1994. An empirical thermal history of the Earth's upper mantle. *Journal of Geophysical Research: Solid Earth*, *99*(B7), pp.13835-13850.

Aharonov, E., Whitehead, J.A., Kelemen, P.B. and Spiegelman, M., 1995. Channeling instability of upwelling melt in the mantle. *Journal of Geophysical Research: Solid Earth*, *100*(B10), pp.20433-20450.

Allaart, J.H. and Jensen, S.B., 1979. Completion of 1: 500 000 reconnaissance mapping in the Precambrian of the Evighedsfjord—Søndre Strømfjord—Itivdleq region, southern West Greenland. *Rapport Grønlands Geologiske Undersøgelse*, *95*, pp.72-76.

Albee, A.L., 1965. A petrogenetic grid for the Fe-Mg silicates of pelitic schists. *American Journal of Science*, *263*(6), pp.512-536.

Allibone, A.H. and Norris, R.J., 1992. Segregation of leucogranite microplutons during syn-anatectic deformation: an example from the Taylor Valley, Antarctica. *Journal of Metamorphic Geology*, *10*(4), pp.589-600.

Allibone, A.H., Milan, L.A., Daczko, N.R. and Turnbull, I.M., 2009. Granulite facies thermal aureoles and metastable amphibolite facies assemblages adjacent to the Western Fiordland Orthogneiss in southwest Fiordland, New Zealand. *Journal of Metamorphic Geology*, *27*(5), pp.349-369.

Allison, I. and Tour, T.E.L., 1977. Brittle deformation of hornblende in a mylonite: a direct geometrical analogue of ductile deformation by translation gliding. *Canadian Journal of Earth Sciences*, *14*(8), pp.1953-1958.

Angel, R.J., 2004. Equations of state of plagioclase feldspars. *Contributions to Mineralogy and Petrology*, *146*(4), pp.506-512.

Arndt, N.T., 2013. The formation and evolution of the continental crust. *Geochemical Perspectives*, *2*(3), pp.405-405.

Arnold, J.W.S.H., Jacoby, W.R., Schmeling, H. and Schott, B., 2001. Continental collision and the dynamic and thermal evolution of the Variscan orogenic crustal root—numerical models. *Journal of Geodynamics*, *31*(3), pp.273-291.

Aspiroz, M.D., Lloyd, G.E. and Fernández, C., 2007. Development of lattice preferred orientation in clinoamphiboles deformed under low-pressure metamorphic conditions. A SEM/EBSD study of metabasites from the Aracena metamorphic belt (SW Spain). *Journal of Structural Geology*, *29*(4), pp.629-645.

Austrheim, H., 1987. Eclogitization of lower crustal granulites by fluid migration through shear zones. *Earth and Planetary Science Letters*, *81*(2-3), pp.221-232.

Austrheim, H., Erambert, M. and Engvik, A.K., 1997. Processing of crust in the root of the Caledonian continental collision zone: the role of eclogitization. *Tectonophysics*, *273*(1-2), pp.129-153.

Babaie, H.A. and La Tour, T.E., 1994. Semibrittle and cataclastic deformation of hornblende-quartz rocks in a ductile shear zone. *Tectonophysics*, *229*(1-2), pp.19-30.

Baratoux, L., Schulmann, K., Ulrich, S. and Lexa, O., 2005. Contrasting microstructures and deformation mechanisms in metagabbro mylonites contemporaneously deformed under different temperatures (c. 650 C and c. 750 C). *Geological Society, London, Special Publications*, *243*(1), pp.97-125.

Beaumont, C., Jamieson, R.A., Nguyen, M.H. and Lee, B., 2001. Himalayan tectonics explained by extrusion of a low-viscosity crustal channel coupled to focused surface denudation. *Nature*, *414*(6865), pp.738-742.

Beaumont, C., Nguyen, M.H., Jamieson, R.A. and Ellis, S., 2006. Crustal flow modes in large hot orogens. *Geological Society, London, Special Publications*, *268*(1), pp.91-145.

Bestmann, M. and Prior, D.J., 2003. Intragranular dynamic recrystallization in naturally deformed calcite marble: diffusion accommodated grain boundary sliding as a result of subgrain rotation recrystallization. *Journal of Structural Geology*, *25*(10), pp.1597-1613.

Berger, A. and Stünitz, H., 1996. Deformation mechanisms and reaction of hornblende: examples from the Bergell tonalite (Central Alps). *Tectonophysics*, *257*(2-4), pp.149-174.

Berger, A. and Kalt, A., 1999. Structures and melt fractions as indicators of rheology in cordierite-bearing migmatites of the Bayerische Wald (Variscan Belt, Germany). *Journal of Petrology*, *40*(11), pp.1699-1719.

Bestmann, M. and Prior, D.J., 2003. Intragranular dynamic recrystallization in naturally deformed calcite marble: diffusion accommodated grain boundary sliding as a result of subgrain rotation recrystallization. *Journal of Structural Geology*, *25*(10), pp.1597-1613.

Bhadra, S. and Bhattacharya, A., 2007. The barometer tremolite+ tschermakite+ 2 albite= 2 pargasite+ 8 quartz: Constraints from experimental data at unit silica activity, with application to garnet-free natural assemblages. *American Mineralogist*, *92*(4), pp.491-502.

Bird, J.E., Mukherjee, A.K. and Dorn, J.E., 1969. Correlations between high-temperature creep behavior and structure.

Binns, R.A., 1966. Granitic intrusions and regional metamorphic rocks of Permian age from the Wongwibinda district, northeastern New South Wales. In *Journal and Proceedings of the Royal Society of New South Wales* (Vol. 99, pp. 5-36).

Blacic, J.D., 1975. Plastic-deformati on mechanisms in quartz: the effect of water. *Tectonophysics*, *27*(3), pp.271-294.

Bleeker, W., 2003. The late Archean record: a puzzle in ca. 35 pieces. *Lithos*, *71*(2-4), pp.99-134.

Blumenfeld, P., Mainprice, D. and Bouchez, J.L., 1986. C-slip in quartz from subsolidus deformed granite. *Tectonophysics*, *127*(1-2), pp.97-115.

Bons, P.D. and den Brok, B., 2000. Crystallographic preferred orientation development by dissolution–precipitation creep. *Journal of Structural Geology*, *22*(11-12), pp.1713-1722.

Bons, P.D., Arnold, J., Elburg, M.A., Kalda, J., Soesoo, A. and van Milligen, B.P., 2004. Melt extraction and accumulation from partially molten rocks. *Lithos*, *78*(1-2), pp.25-42.

Bouchez, J.L. and Pecher, A., 1981. The Himalayan Main Central Thrust pile and its quartz-rich tectonites in central Nepal. *Tectonophysics*, *78*(1-4), pp.23-50.

Bouchez, J.L., Mainprice, D.H., Trepied, L. and Doukhan, J.C., 1984. Secondary lineation in a high-T quartzite (Galicia, Spain): an explanation for an abnormal fabric. *Journal of Structural Geology*, *6*(1-2), pp.159-165.

Bowen, N.L., 1913. The melting phenomena of the plagioclase feldspars. *American Journal of Science*, *4*(210), pp.577-599.

Bowen, N.L., 1940. Progressive metamorphism of siliceous limestone and dolomite. *The Journal of Geology*, *48*(3), pp.225-274.

Bridgwater, D. and Collerson, K.D., 1976. The major petrological and geochemical characters of the 3,600 my Uivak gneisses from Labrador. *Contributions to Mineralogy and Petrology*, *54*(1), pp.43-59.

Brouwer, F.M. and Engi, M., 2005. Staurolite and other aluminous phases in alpine eclogite from the central Swiss Alps: Analysis of domain evolution. *The Canadian Mineralogist*, *43*(1), pp.105-128.

Brown, M., 1973. The definition of metatexis, diatexis and migmatite. *Proceedings of the Geologists' Association*, *84*, pp.371-IN2.

Brown, M., 1994. The generation, segregation, ascent and emplacement of granite magma: the migmatite-to-crustally-derived granite connection in thickened orogens. *Earth-Science Reviews*, *36*(1-2), pp.83-130.

Brown, M., Averkin, Y.A., McLellan, E.L. and Sawyer, E.W., 1995. Melt segregation in migmatites. *Journal of Geophysical Research: Solid Earth*, *100*(B8), pp.15655-15679.

Brown, M. and Rushmer, T., 1997. The role of deformation in the movement of granitic melt: views from the laboratory and the field. *Deformation-enhanced fluid transport in the Earth's crust and mantle*, *8*, pp.111-144.

Brown, M. and Rushmer, T. eds., 2006. *Evolution and differentiation of the continental crust*. Cambridge University Press.

Brown, M. and Solar, G.S., 1998. Shear-zone systems and melts: feedback relations and self-organization in orogenic belts. *Journal of structural geology*, *20*(2-3), pp.211-227.

Brown, M. and Solar, G.S., 1999. The mechanism of ascent and emplacement of granite magma during transpression: a syntectonic granite paradigm. *Tectonophysics*, *312*(1), pp.1-33.

Brown, M., 2001. Crustal melting and granite magmatism: key issues. Physics and Chemistry of the Earth, Part A: Solid Earth and Geodesy, 26(4-5), pp.201-212.

Brown, M., 2001. Orogeny, migmatites and leucogranites: a review. *Journal of Earth System Science*, *110*(4), pp.313-336.

Brown, M., 2004. The mechanism of melt extraction from lower continental crust of orogens. *Earth and Environmental Science Transactions of the Royal Society of Edinburgh*, *95*(1-2), pp.35-48.

Brown, R., 2006. *Evolution and differentiation of the continental crust*. Cambridge University Press.

Brown, M., 2007. Crustal melting and melt extraction, ascent and emplacement in orogens: mechanisms and consequences. *Journal of the Geological society*, *164*(4), pp.709-730.

Brown, M., 2010. Melting of the continental crust during orogenesis: the thermal, rheological, and compositional consequences of melt transport from lower to upper continental crust. *Canadian Journal of Earth Sciences*, *47*(5), pp.655-694.

Brown, M., Korhonen, F.J. and Siddoway, C.S., 2011. Organizing melt flow through the crust. *Elements*, *7*(4), pp.261-266.

Brown, M., 2012. Introduction to a virtual special issue on crustal melting. *Journal of Metamorphic Geology*, *30*(5), pp.453-456.

Bruhn, D., Groebner, N. and Kohlstedt, D.L., 2000. An interconnected network of core-forming melts produced by shear deformation. *Nature*, *403*(6772), pp.883-886.

Buczynski, C. and Chafetz, H.S., 1987. Siliciclastic grain breakage and displacement due to carbonate crystal growth: an example from the Lueders Formation (Permian) of north-central Texas, USA. *Sedimentology*, *34*(5), pp.837-843.

Burg, J.P. and Vanderhaeghe, O., 1993. Structures and way-up criteria in migmatites, with application to the Velay dome (French Massif Central). *Journal of Structural Geology*, *15*(11), pp.1293-1301.

Cesare, B., Ferrero, S., Salvioli-Mariani, E., Pedron, D. and Cavallo, A., 2009. "Nanogranite" and glassy inclusions: The anatectic melt in migmatites and granulites. *Geology*, *37*(7), pp.627-630.

Carmichael, D.M., 1969. On the mechanism of prograde metamorphic reactions in quartz-bearing pelitic rocks. *Contributions to Mineralogy and Petrology*, *20*(3), pp.244-267.

Cartwright, I. and Barnicoat, A.C., 2003. Geochemical and stable isotope resetting in shear zones from Täschalp: constraints on fluid flow during exhumation in the Western Alps. *Journal of Metamorphic Geology*, *21*(2), pp.143-161.

Carson, C.J., 1999. Calculated mineral equilibria for eclogites in CaO-Na_2O-FeO-MgO-Al_2O_3-SiO_2-H_2O: application to the Pouebo Terrane, Pam Peninsula, New Caledonia. *Jour. Metam. Geol.*, 17, pp.9-24.

Cashman, K.V., Sparks, R.S.J. and Blundy, J.D., 2017. Vertically extensive and unstable magmatic systems: a unified view of igneous processes. *Science*, *355*(6331), p.eaag3055.

Cao, S., Liu, J. and Leiss, B., 2010. Orientation-related deformation mechanisms of naturally deformed amphibole in amphibolite mylonites from the Diancang Shan, SW Yunnan, China. *Journal of structural geology*, *32*(5), pp.606-622.

Christie, J.M. and Ord, A., 1980. Flow stress from microstructures of mylonites: example and current assessment. *Journal of Geophysical Research: Solid Earth*, *85*(B11), pp.6253-6262.

Clemens, J.D., 1989. The importance of residual source material (restite) in granite petrogenesis: a comment. *Journal of Petrology*, *30*(5), pp.1313-1316.

Clemens, J.D. and Mawer, C.K., 1992. Granitic magma transport by fracture propagation. *Tectonophysics*, *204*(3-4), pp.339-360.

Clemens, J.D., Droop, G.T. and Stevens, G., 1997. High-grade metamorphism, dehydration and crustal melting: a reinvestigation based on new experiments in the silica-saturated portion of the system KAlO 2–MgO–SiO 2–H 2 O–CO 2 at P≤ 1.5 GPa. *Contributions to Mineralogy and Petrology*, *129*(4), pp.308-325.

Clemens, J.D. and Holness, M.B., 2000. Textural evolution and partial melting of arkose in a contact aureole: a case study and implications. *Visual Geosciences*, *5*(4), pp.1-14.

Connolly, J.A.D., 1990. Multivariable phase diagrams; an algorithm based on generalized thermodynamics. *American Journal of Science*, *290*(6), pp.666-718.

Connelly, J.N. and Mengel, F.C., 2000. Evolution of Archean components in the paleoproterozoic Nagssugtoqidian orogen, west Greenland. *Geological Society of America Bulletin*, *112*(5), pp.747-763.

Connolly, J.A., 2005. Computation of phase equilibria by linear programming: a tool for geodynamic modeling and its application to subduction zone decarbonation. *Earth and Planetary Science Letters*, *236*(1-2), pp.524-541.

Connolly, J.A.D. and Podladchikov, Y.Y., 2007. Decompaction weakening and channeling instability in ductile porous media: Implications for asthenospheric melt segregation. *Journal of Geophysical Research: Solid Earth*, *112*(B10).

Connolly, J.A., 2010. The mechanics of metamorphic fluid expulsion. *Elements*, *6*(3), pp.165-172.

Correns, C.W., 1949. Growth and dissolution of crystals under linear pressure. *Discussions of the Faraday society*, *5*, pp.267-271.

Collins, W.J. and Sawyer, E.W., 1996. Pervasive granitoid magma transfer through the lower–middle crust during non-coaxial compressional deformation. *Journal of Metamorphic Geology*, *14*(5), pp.565-579.

Collier, M.L. and Kelemen, P.B., 2010. The case for reactive crystallization at mid-ocean ridges. *Journal of Petrology*, *51*(9), pp.1913-1940.

Coogan, L.A., Saunders, A.D., Kempton, P.D. and Norry, M.J., 2000. Evidence from oceanic gabbros for porous melt migration within a crystal mush beneath the Mid-Atlantic Ridge. *Geochemistry, Geophysics, Geosystems*, *1*(9).

Cooper, R.F. and Kohlstedt, D.L., 1979. Dislocation recovery in naturally deformed quartz. *Eos Trans. AGU*, *60*, p.370.

Craven, S.J., Daczko, N.R. and Halpin, J.A., 2012. Thermal gradient and timing of high-T–low-P metamorphism in the Wongwibinda Metamorphic Complex, southern New England Orogen, Australia. *Journal of Metamorphic Geology*, *30*(1), pp.3-20.

Daczko, N.R., Clarke, G.L. and Klepeis, K.A., 2001. Transformation of two-pyroxene hornblende granulite to garnet granulite involving simultaneous melting and fracturing of the lower crust, Fiordland, New Zealand. *Journal of Metamorphic Geology*, *19*(5), pp.549-562.

Daczko, N.R., Klepeis, K.A. and Clarke, G.L., 2001. Evidence of Early Cretaceous collisional-style orogenesis in northern Fiordland, New Zealand and its effects on the evolution of the lower crust. *Journal of Structural Geology*, *23*(4), pp.693-713.

Daczko, N.R., Piazolo, S., Meek, U., Stuart, C.A. and Elliott, V., 2016. Hornblendite delineates zones of mass transfer through the lower crust. *Scientific reports*, *6*, p.31369.

Daczko, N.R. and Piazolo, S., 2022. Recognition of melferite–A rock formed in syn-deformational high-strain melt-transfer zones through sub-solidus rocks: A review and synthesis of microstructural criteria. *Lithos*, p.106850.

Danis, C.R., Daczko, N.R., Lackie, M.A. and Craven, S.J., 2010. Retrograde metamorphism of the Wongwibinda Complex, New England Fold Belt and the implications of 2.5 D subsurface geophysical structure for the metamorphic history. *Australian Journal of Earth Sciences*, *57*(3), pp.357-375.

Davidson, C., Hollister, L.S. and Schmid, S.M., 1992. Role of melt in the formation of a deep-crustal compressive shear zone: The MaClaren Glacier Metamorphic Belt, south central Alaska. *Tectonics*, *11*(2), pp.348-359.

de Capitani, C. and Petrakakis, K., 2010. The computation of equilibrium assemblage diagrams with Theriak/Domino software. *American mineralogist*, *95*(7), pp.1006-1016.

Dey, J., Piazolo, S., Daczko, N., 2018. The recognition of quartz grown from a melt during static and dynamic conditions. *Master of Research, Thesis*. Macquarie University, Australia.

Dell'angelo, L.N. and Tullis, J., 1989. Fabric development in experimentally sheared quartzites. *Tectonophysics*, *169*(1-3), pp.1-21.

Dick, H.J.B., 1989. Abyssal peridotites, very slow spreading ridges and ocean ridge magmatism. Geological Society, London, Special Publications, 42(1), pp.71-105.

Dijkstra, A.H., Drury, M.R. and Frijhoff, R.M., 2002. Microstructures and lattice fabrics in the Hilti mantle section (Oman Ophiolite): evidence for shear localization and melt weakening in the crust–mantle transition zone?. *Journal of Geophysical Research: Solid Earth*, *107*(B11), pp.ETG-2.

Dijkstra, A.H., Barth, M.G., Drury, M.R., Mason, P.R. and Vissers, R.L., 2003. Diffuse porous melt flow and melt-rock reaction in the mantle lithosphere at a slow-spreading ridge: A structural petrology and LA-ICP-MS study of the Othris Peridotite Massif (Greece). *Geochemistry, Geophysics, Geosystems*, *4*(8).

Dingwell, D.B., Romano, C. and Hess, K.U., 1996. The effect of water on the viscosity of a haplogranitic melt under PTX conditions relevant to silicic volcanism. *Contributions to Mineralogy and Petrology*, *124*(1), pp.19-28.

D'lemos, R.S., Brown, M. and Strachan, R.A., 1992. Granite magma generation, ascent and emplacement within a transpressional orogen. *Journal of the Geological Society*, *149*(4), pp.487-490.

Dollinger, G. and Blacic, J.D., 1975. Deformation mechanisms in experimentally and naturally deformed amphiboles. *Earth and Planetary Science Letters*, *26*(3), pp.409-416.

Drury, M.R. and Urai, J.L., 1990. Deformation-related recrystallization processes. *Tectonophysics*, *172*(3-4), pp.235-253.

Dutta, D., Misra, S. and Mainprice, D., 2021. Syn-Shearing Deformation Mechanisms of Minerals in Partially Molten Metapelites. *Geophysical Research Letters*, *48*(22), p.e2021GL094667.

Dyck, B., Reno, B.L. and Kokfelt, T.F., 2015. The Majorqaq Belt: A record of Neoarchaean orogenesis during final assembly of the North Atlantic Craton, southern West Greenland. *Lithos*, *220*, pp.253-271.

Etheridge, M.A., Daczko, N.R., Chapman, T. and Stuart, C.A., 2021. Mechanisms of melt extraction during lower crustal partial melting. *Journal of Metamorphic Geology*, *39*(1), pp.57-75.

Evans, K.A., Powell, R. and Holland, T.J.B., 2010. Internally consistent data for sulphur-bearing phases and application to the construction of pseudosections for mafic greenschist facies rocks in Na2O–CaO–K2O–FeO–MgO–Al2O3–SiO2–CO2–O–S–H2O. *Journal of Metamorphic Geology*, *28*(6), pp.667-687.

Evans, K.A. and Bickle, M.J., 2005. An investigation of the relationship between bulk composition, inferred reaction progress and fluid-flow parameters for layered micaceous carbonates from Maine, USA. *Journal of metamorphic geology*, *23*(3), pp.181-197.

Faul, U.H., 2001. Melt retention and segregation beneath mid-ocean ridges. *Nature*, *410*(6831), p.920.

Flatt, R.J., Steiger, M. and Scherer, G.W., 2007. A commented translation of the paper by CW Correns and W. Steinborn on crystallization pressure. *Environmental geology*, *52*(2), pp.187-203.

Fletcher, R.C. and Merino, E., 2001. Mineral growth in rocks: kinetic-rheological models of replacement, vein formation, and syntectonic crystallization. *Geochimica et Cosmochimica Acta*, *65*(21), pp.3733-3748.

Folk, R.L., 1964. Some aspects of recrystallization of ancient limestones. *AAPG Bulletin*, *48*(4), pp.525-525.

Fossen, H. and Cavalcante, G.C.G., 2017. Shear zones–A review. *Earth-Science Reviews*, *171*, pp.434-455.

Friend, C.R.L., Nutman, A.P. and McGregor, V.R., 1988. Late Archaean terrane accretion in the Godthåb region, southern West Greenland. *Nature*, *335*(6190), pp.535-538.

Friend, C.R.L., Nutman, A.P., Baadsgaard, H., Kinny, P.D. and McGregor, V.R., 1996. Timing of late Archaean terrane assembly, crustal thickening and granite emplacement in the Nuuk region, southern West Greenland. *Earth and Planetary Science Letters*, *142*(3-4), pp.353-365.

Friend, C.R.L. and Nutman, A.P., 1994. Two Archaean granulite-facies metamorphic events in the Nuuk-Maniitsoq region, southern West Greenland: correlation with the Saglek block, Labrador. *Journal of the Geological Society*, *151*(3), pp.421-424.

Friend, C.R. and Nutman, A.P., 2005. New pieces to the Archaean terrane jigsaw puzzle in the Nuuk region, southern West Greenland: steps in transforming a simple insight into a complex regional tectonothermal model. *Journal of the Geological Society*, *162*(1), pp.147-162.

Friedrich, A.M., Hodges, K.V., Bowring, S.A. and Martin, M.W., 1999. Geochronological constraints on the magmatic, metamorphic and thermal evolution of the Connemara Caledonides, western Ireland. *Journal of the Geological Society*, *156*(6), pp.1217-1230.

Garbutt, J.M. and Teyssier, C., 1991. Prism< c> slip in the quartzites of the Oakhurst Mylonite Belt, California. *Journal of structural geology*, *13*(6), pp.657-666.

Garde, A.A., 2007. A mid-Archaean island arc complex in the eastern Akia terrane, Godthåbsfjord, southern West Greenland. *Journal of the Geological Society*, *164*(3), pp.565-579.

Garde, A.A., 1990. Thermal granulite-facies metamorphism with diffuse retrogression in Archaean orthogneisses, Fiskefjord, southern West Greenland. *Journal of Metamorphic Geology*, *8*(6), pp.663-682.

Garde, A.A., 1997. Accretion and evolution of an Archaean high-grade grey gneiss-amphibolite complex: the Fiskefjord area, southern West Greenland.

Garde, A.A., Friend, C.R., Nutman, A.P. and Marker, M., 2000. Rapid maturation and stabilisation of middle Archaean continental crust: the Akia terrane, southern West Greenland. *Bulletin of the Geological Society of Denmark*, *47*, pp.1-27.

Garde, A.A., 2007. A mid-Archaean island arc complex in the eastern Akia terrane, Godthåbsfjord, southern West Greenland. *Journal of the Geological Society*, *164*(3), pp.565-579.

Garde, A.A., McDonald, I., Dyck, B. and Keulen, N., 2012. Searching for giant, ancient impact structures on Earth: the Mesoarchaean Maniitsoq structure, West Greenland. *Earth and Planetary Science Letters*, *337*, pp.197-210.

Garde, A.A., McDonald, I., Dyck, B. and Keulen, N., 2012. Searching for giant, ancient impact structures on Earth: the Mesoarchaean Maniitsoq structure, West Greenland. *Earth and Planetary Science Letters*, *337*, pp.197-210.

Garde, A.A., Keulen, N., McDonald, I. and Brendan, D., 2013. Reply on" Searching for giant, ancient impact structures on Earth: The Mesoarchaean Maniitsoq structure, West Greenland" by Garde et al.[Earth Planet. Sci. Lett. 337-338 (2012) 197-210]. *Earth and Planetary Science Letters*, *369*, pp.336-343.

Garde, A.A., Dyck, B., Esbensen, K.H., Johansson, L. and Möller, C., 2014. The Finnefjeld domain, Maniitsoq structure, West Greenland: Differential rheological features and mechanical homogenisation in response to impacting?. *Precambrian Research*, *255*, pp.791-808.

Gardiner, N.J., Kirkland, C.L., Hollis, J., Szilas, K., Steenfelt, A., Yakymchuk, C. and Heide-Jørgensen, H., 2019. Building mesoarchaean crust upon Eoarchaean roots: the Akia terrane, West Greenland. *Contributions to Mineralogy and Petrology*, *174*(3), pp.1-19.

Getsinger, A., Rushmer, T., Jackson, M.D. and Baker, D., 2009. Generating high Mg-numbers and chemical diversity in tonalite–trondhjemite–granodiorite (TTG) magmas during melting and melt segregation in the continental crust. *Journal of Petrology*, *50*(10), pp.1935-1954.

Getsinger, A.J., Hirth, G., Stünitz, H. and Goergen, E.T., 2013. Influence of water on rheology and strain localization in the lower continental crust. *Geochemistry, Geophysics, Geosystems*, *14*(7), pp.2247-2264.

Giuntoli, F., Menegon, L. and Warren, C.J., 2018. Replacement reactions and deformation by dissolution and precipitation processes in amphibolites. *Journal of Metamorphic Geology*, *36*(9), pp.1263-1286.

Glikson, A.Y., 2005. Geochemical and isotopic signatures of Archaean to Palaeoproterozoic extraterrestrial impact ejecta/fallout units. *Australian Journal of Earth Sciences*, *52*(4-5), pp.785-798.

Gratier, J.P., Frery, E., Deschamps, P., Røyne, A., Renard, F., Dysthe, D., Ellouz-Zimmerman, N. and Hamelin, B., 2012. How travertine veins grow from top to bottom and lift the rocks above them: The effect of crystallization force. *Geology*, *40*(11), pp.1015-1018.

Green, E.C.R., White, R.W., Diener, J.F.A., Powell, R., Holland, T.J.B. and Palin, R.M., 2016. Activity–composition relations for the calculation of partial melting equilibria in metabasic rocks. *Journal of metamorphic Geology*, *34*(9), pp.845-869.

Greenfield, J.E., Clarke, G.L., Bland, M. and Clark, D.J., 1996. In-situ migmatite and hybrid diatexite at Mt Stafford, central Australia. *Journal of Metamorphic Geology*, *14*(4), pp.413-426.

Gregorová, E., Černý, M., Pabst, W., Esposito, L., Zanelli, C., Hamáček, J. and Kutzendörfer, J., 2015. Temperature dependence of Young′ s modulus of silica refractories. *Ceramics International*, *41*(1), pp.1129-1138.

Groebner, N. and Kohlstedt, D.L., 2006. Deformation-induced metal melt networks in silicates: Implications for core–mantle interactions in planetary bodies. *Earth and Planetary Science Letters*, *245*(3-4), pp.571-580.

Hacker, B.R. and Christie, J.M., 1990. Brittle/ductile and plastic/cataclastic transitions in experimentally deformed and metamorphosed amphibolite. *The Brittle-Ductile Transition in Rocks*, *56*, pp.127-147.

Hacker, B.R., Andersen, T.B., Johnston, S., Kylander-Clark, A.R., Peterman, E.M., Walsh, E.O. and Young, D., 2010. High-temperature deformation during continental-margin subduction & exhumation: The ultrahigh-pressure Western Gneiss Region of Norway. *Tectonophysics*, *480*(1-4), pp.149-171.

Hall, R.P. and Hughes, D.J., 1987. Noritic dykes of southern West Greenland: early Proterozoic boninitic magmatism. *Contributions to Mineralogy and Petrology*, *97*(2), pp.169-182.

Handy, M.R., Mulch, A., Rosenau, M. and Rosenberg, C.L., 2001. The role of fault zones and melts as agents of weakening, hardening and differentiation of the continental crust: a synthesis. *Geological Society, London, Special Publications*, *186*(1), pp.305-332.

Hasalova, P., Schulmann, K., Lexa, O., Štípská, P., Hrouda, F., Ulrich, S., Haloda, J. and Týcová, P., 2008a. Origin of migmatites by deformation-enhanced melt infiltration of orthogneiss: A new model based on quantitative microstructural analysis. *Journal of Metamorphic Geology*, *26*(1), pp.29-53.

Hasalova, P., Štípská, P., Powell, R., Schulmann, K., Janoušek, V. and Lexa, O., 2008b. Transforming mylonitic metagranite by open-system interactions during melt flow. *Journal of Metamorphic Geology*, *26*(1), pp.55-80.

Healy, B., Collins, W.J. and Richards, S.W., 2004. A hybrid origin for Lachlan S-type granites: the Murrumbidgee Batholith example. *Lithos*, *78*(1-2), pp.197-216.

Harte, B., Hunter, R.H. and Kinny, P.D., 1993. Melt geometry, movement and crystallization, in relation to mantle dykes, veins and metasomatism. *Philosophical Transactions of the Royal Society of London. Series A: Physical and Engineering Sciences*, *342*(1663), pp.1-21.

Harris, A.L., Haselock, P.J., Kennedy, M.J. and Mendum, J.R., 1994. The Dalradian Supergroup in Scotland, Shetland and Ireland. 33-53 in Gibbons, WE and Harris, AL. *A revised correlation of Precambrian rocks in the British Isles. Special Report of the Geological Society, London*, (22).

Harris, N., 2007. Channel flow and the Himalayan–Tibetan orogen: a critical review. *Journal of the Geological Society*, *164*(3), pp.511-523.

Hasalová, P., Schulmann, K., Lexa, O., Štípská, P., Hrouda, F., Ulrich, S., Haloda, J. and Týcová, P., 2008. Origin of migmatites by deformation-enhanced melt infiltration of orthogneiss: A new model based on quantitative microstructural analysis. *Journal of Metamorphic Geology*, *26*(1), pp.29-53.

Hasalová, P., Janoušek, V., Schulmann, K., Štípská, P. and Erban, V., 2008b. From orthogneiss to migmatite: geochemical assessment of the melt infiltration model in the Gföhl Unit (Moldanubian Zone, Bohemian Massif). *Lithos*, *102*(3-4), pp.508-537.

Heidelbach, F., Post, A. and Tullis, J., 2000. Crystallographic preferred orientation in albite samples deformed experimentally by dislocation and solution precipitation creep. *Journal of Structural Geology*, *22*(11-12), pp.1649-1661.

Henry, D.J., Guidotti, C.V. and Thomson, J.A., 2005. The Ti-saturation surface for low-to-medium pressure metapelitic biotites: Implications for geothermometry and Ti-substitution mechanisms. *American Mineralogist*, *90*(2-3), pp.316-328.

Hippertt, J.F., 1994. Microstructures and c-axis fabrics indicative of quartz dissolution in sheared quartzites and phyllonites. *Tectonophysics*, *229*(3-4), pp.141-163.

Hirth, G. and Tullis, J.A.N., 1992. Dislocation creep regimes in quartz aggregates. *Journal of structural geology*, *14*(2), pp.145-159.

Hobbs, B.E., 1968. Recrystallization of single crystals of quartz. *Tectonophysics*, *6*(5), pp.353-401.

Hobbs, B.E., Ord, A. and Teyssier, C., 1986. Earthquakes in the ductile regime?. *Pure and Applied Geophysics*, *124*(1), pp.309-336.

Holland, T. and Blundy, J., 1994. Non-ideal interactions in calcic amphiboles and their bearing on amphibole-plagioclase thermometry. *Contributions to mineralogy and petrology*, *116*(4), pp.433-447.

Holland, T. and Powell, R., 2003. Activity–composition relations for phases in petrological calculations: an asymmetric multicomponent formulation. *Contributions to Mineralogy and Petrology*, *145*(4), pp.492-501.

Holland, T.J.B. and Powell, R., 2011. An improved and extended internally consistent thermodynamic dataset for phases of petrological interest, involving a new equation of state for solids. *Journal of metamorphic Geology*, *29*(3), pp.333-383.

Hollister, L.S. and Crawford, M.L., 1986. Melt-enhanced deformation: A major tectonic process. *Geology*, *14*(7), pp.558-561.

Hollister, L.S., 1993. The role of melt in the uplift and exhumation of orogenic belts. *Chemical Geology*, *108*(1-4), pp.31-48.

Hollis, J.A., Clarke, G.L., Klepeis, K.A., Daczko, N.R. and Ireland, T.R., 2004. The regional significance of Cretaceous magmatism and metamorphism in Fiordland, New Zealand, from U–Pb zircon geochronology. *Journal of Metamorphic Geology*, *22*(7), pp.607-627.

Holness, M.B. and Clemens, J.D., 1999. Partial melting of the Appin Quartzite driven by fracture-controlled H 2 O infiltration in the aureole of the Ballachulish Igneous Complex, Scottish Highlands. *Contributions to Mineralogy and Petrology*, *136*(1-2), pp.154-168.

Holness, M.B., Cheadle, M.J. and McKenzie, D.A.N., 2005. On the use of changes in dihedral angle to decode late-stage textural evolution in cumulates. *Journal of Petrology*, *46*(8), pp.1565-1583.

Holness, M.B., Tegner, C., Nielsen, T.F., Stripp, G. and Morse, S.A., 2007. A textural record of solidification and cooling in the Skaergaard intrusion, East Greenland. *Journal of Petrology*, *48*(12), pp.2359-2377.

Holness, M.B., 2008. Decoding migmatite microstructures. Insights from a petrostructural study of the Finero peridotites, southern Alps. *Earth and Planetary Science Letters*, *477*, pp.59-72.

Holness, M.B. and Sawyer, E.W., 2008. On the pseudomorphing of melt-filled pores during the crystallization of migmatites. *Journal of Petrology*, *49*(7), pp.1343-1363.

Holness, M.B. and Vernon, R.H., 2015. The influence of interfacial energies on igneous microstructures. In *Layered intrusions* (pp. 183-228). Springer, Dordrecht.

Holness, M.B., Clemens, J.D. and Vernon, R.H., 2018. How deceptive are microstructures in granitic rocks? Answers from integrated physical theory, phase equilibrium, and direct observations. *Contributions to Mineralogy and Petrology*, *173*(8), p.62.

Holtzman, B.K., Groebner, N.J., Zimmerman, M.E., Ginsberg, S.B. and Kohlstedt, D.L., 2003. Stress-driven melt segregation in partially molten rocks. *Geochemistry, Geophysics, Geosystems*, *4*(5).

Holtzman, B.K., Kohlstedt, D.L., Zimmerman, M.E., Daines, M.J. and Phipps Morgan, J., 2003, April. Deformation-driven melt segregation and organization in the mantle. In *EGS-AGU-EUG Joint Assembly* (p. 11249).

Holyoke III, C.W. and Tullis, J., 2006. Mechanisms of weak phase interconnection and the effects of phase strength contrast on fabric development. *Journal of Structural Geology*, *28*(4), pp.621-640.

Holyoke III, C.W. and Tullis, J., 2006. Formation and maintenance of shear zones. *Geology*, *34*(2), pp.105-108.

Hutton, D.H., 1992. Granite sheeted complexes: evidence for the dyking ascent mechanism. *Earth and Environmental Science Transactions of the Royal Society of Edinburgh*, *83*(1-2), pp.377-382.

Imon, R., Okudaira, T. and Kanagawa, K., 2004. Development of shape-and lattice-preferred orientations of amphibole grains during initial cataclastic deformation and subsequent deformation by dissolution–precipitation creep in amphibolites from the Ryoke metamorphic belt, SW Japan. *Journal of Structural Geology*, *26*(5), pp.793-805.

Indares, A., White, R.W. and Powell, R., 2008. Phase equilibria modelling of kyanite-bearing anatectic paragneisses from the central Grenville Province. *Journal of Metamorphic Geology*, *26*(8), pp.815-836.

Jackson, M.D., Valvatne, P.H. and Blunt, M.J., 2003. Prediction of wettability variation and its impact on flow using pore-to reservoir-scale simulations. *Journal of Petroleum Science and Engineering*, *39*(3-4), pp.231-246.

Jackson, M.D., Cheadle, M.J. and Atherton, M.P., 2003. Quantitative modeling of granitic melt generation and segregation in the continental crust. *Journal of Geophysical Research: Solid Earth*, *108*(B7).

Jackson, M.D., Gallagher, K., Petford, N. and Cheadle, M.J., 2005. Towards a coupled physical and chemical model for tonalite–trondhjemite–granodiorite magma formation. *Lithos*, *79*(1-2), pp.43-60.

Jamtveit, B., Bucher-Nurminen, K. and Austrheim, H., 1990. Fluid controlled eclogitization of granulites in deep crustal shear zones, Bergen arcs, Western Norway. *Contributions to Mineralogy and Petrology*, *104*(2), pp.184-193.

Jamtveit, B., Putnis, C.V. and Malthe-Sørenssen, A., 2009. Reaction induced fracturing during replacement processes. *Contributions to Mineralogy and Petrology*, *157*(1), pp.127-133.

Jamieson, R.A. and Beaumont, C., 2013. On the origin of orogens. *Bulletin*, *125*(11-12), pp.1671-1702.

Jessell, M.W., 1987. Grain-boundary migration microstructures in a naturally deformed quartzite. *Journal of Structural Geology*, *9*(8), pp.1007-1014.

Jessop, K., Daczko, N.R. and Piazolo, S., 2019. Tectonic cycles of the New England Orogen, eastern Australia: a review. *Australian Journal of Earth Sciences*, *66*(4), pp.459-496.

Ji, S., Shao, T., Michibayashi, K., Oya, S., Satsukawa, T., Wang, Q., Zhao, W. and Salisbury, M.H., 2015. Magnitude and symmetry of seismic anisotropy in mica-and amphibole-bearing metamorphic

rocks and implications for tectonic interpretation of seismic data from the southeast Tibetan Plateau. *Journal of Geophysical Research: Solid Earth*, *120*(9), pp.6404-6430.

Johnson, T.E., White, R.W. and Powell, R., 2008. Partial melting of metagreywacke: a calculated mineral equilibria study. *Journal of Metamorphic Geology*, *26*(8), pp.837-853.

Jull, M., Kelemen, P.B. and Sims, K., 2002. Consequences of diffuse and channelled porous melt migration on uranium series disequilibria. *Geochimica et Cosmochimica Acta*, *66*(23), pp.4133-4148.

Kalsbeek, F. and Nutman, A.P., 1996. Anatomy of the Early Proterozoic Nagssugtoqidian orogen, West Greenland, explored by reconnaissance SHRIMP U-Pb zircon dating. *Geology*, *24*(6), pp.515-518.

Kelemen, P.B. and Dick, H.J., 1995. Focused melt flow and localized deformation in the upper mantle: Juxtaposition of replacive dunite and ductile shear zones in the Josephine peridotite, SW Oregon. *Journal of Geophysical Research: Solid Earth*, *100*(B1), pp.423-438.

Kelemen, P.B., Hirth, G., Shimizu, N., Spiegelman, M. and Dick, H.J., 1997. A review of melt migration processes in the adiabatically upwelling mantle beneath oceanic spreading ridges. Philosophical Transactions of the Royal Society of London. Series A: Mathematical, Physical and Engineering Sciences, 355(1723), pp.283-318.

Kelemen, P.B., Shimizu, N. and Salters, V.J., 1995. Extraction of mid-ocean-ridge basalt from the upwelling mantle by focused flow of melt in dunite channels. *Nature*, *375*(6534), p.747.

Kelsey, D.E. and Hand, M., 2015. On ultrahigh temperature crustal metamorphism: phase equilibria, trace element thermometry, bulk composition, heat sources, timescales and tectonic settings. *Geoscience Frontiers*, *6*(3), pp.311-356.

Kendrick, J.E., Lavallée, Y., Mariani, E., Dingwell, D.B., Wheeler, J. and Varley, N.R., 2017. Crystal plasticity as an indicator of the viscous-brittle transition in magmas. *Nature communications*, *8*(1), pp.1-12.

Keulen, N., Garde, A.A. and Jørgart, T., 2015. Shock melting of K-feldspar and interlacing with cataclastically deformed plagioclase in granitic rocks at Toqqusap Nunaa, southern West Greenland: implications for the genesis of the Maniitsoq structure. *Tectonophysics*, *662*, pp.328-344.

Kim, J. and Jung, H., 2019. New crystal preferred orientation of amphibole experimentally found in simple shear. *Geophysical Research Letters*, *46*(22), pp.12996-13005.

Kimizuka, H., Ogata, S., Li, J. and Shibutani, Y., 2007. Complete set of elastic constants of α-quartz at high pressure: a first-principles study. *Physical Review B*, *75*(5), p.054109.

Kirkland, C.L., Yakymchuk, C., Hollis, J., Heide-Jørgensen, H. and Danišík, M., 2018a. Mesoarchean exhumation of the Akia terrane and a common Neoarchean tectonothermal history for West Greenland. *Precambrian Research*, *314*, pp.129-144.

Kitamura, S., 2006. A preliminary report of the tephrochronological study of the eruptive history of Coatepeque Caldera, El Salvador, Central America.

Ko, B. and Jung, H., 2015. Crystal preferred orientation of an amphibole experimentally deformed by simple shear. *Nature communications*, *6*(1), pp.1-10.

Kohlstedt, D.L., 1992. Structure, rheology and permeability of partially molten rocks at low melt fractions. *Mantle flow and melt generation at mid-ocean ridges*, *71*, pp.103-121.

Kohn, M.J. and Spear, F.S., 1991. Error propagation for barometers: 2. Application to rocks. *American Mineralogist*, *76*(1-2), pp.138-147.

Kruhl, J.H., 1996. Prism-and basal-plane parallel subgrain boundaries in quartz: A microstructural geothermobarometer. *Journal of metamorphic Geology*, *14*(5), pp.581-589.

Kuhlmann-Wilsdorf, D. and Hansen, N., 1991. Geometrically necessary, incidental and subgrain boundaries. *Scripta metallurgica et materialia*, *25*(7), pp.1557-1562.

Lamarque, G., Bascou, J., Maurice, C., Cottin, J.Y., Riel, N. and Ménot, R.P., 2016. Microstructures, deformation mechanisms and seismic properties of a Palaeoproterozoic shear zone: The Mertz shear zone, East-Antarctica. *Tectonophysics*, *680*, pp.174-191.

Laporte, D. and Watson, E.B., 1995. Experimental and theoretical constraints on melt distribution in crustal sources: the effect of crystalline anisotropy on melt interconnectivity. *Chemical Geology*, *124*(3-4), pp.161-184.

Laporte, D., 1994. Wetting behavior of partial melts during crustal anatexis: the distribution of hydrous silicic melts in polycrystalline aggregates of quartz. *Contributions to Mineralogy and Petrology*, *116*(4), pp.486-499.

Laporte, D. and Provost, A., 2000. The grain-scale distribution of silicate, carbonate and metallosulfide partial melts: a review of theory and experiments. *Physics and chemistry of partially molten rocks*, pp.93-140.

Lamarque, G., Bascou, J., Maurice, C., Cottin, J.Y., Riel, N. and Ménot, R.P., 2016. Microstructures, deformation mechanisms and seismic properties of a Palaeoproterozoic shear zone: The Mertz shear zone, East-Antarctica. *Tectonophysics*, *680*, pp.174-191.

Lanari, P. and Engi, M., 2017. Local bulk composition effects on metamorphic mineral assemblages. *Reviews in mineralogy and geochemistry*, *83*(1), pp.55-102.

Lanari, P., Vidal, O. and Engi, M., 2013, April. XMapTools: a MATLAB©-based program for petrology (treatment of X-ray images, chemical and thermobarometric studies). In *EGU General Assembly Conference Abstracts* (pp. EGU2013-7030).

Lanari, P., Vidal, O., De Andrade, V., Dubacq, B., Lewin, E., Grosch, E.G. and Schwartz, S., 2014a. XMapTools: A MATLAB©-based program for electron microprobe X-ray image processing and geothermobarometry. *Computers & Geosciences*, *62*, pp.227-240.

Lanari, P., Wagner, T. and Vidal, O., 2014b. A thermodynamic model for di-trioctahedral chlorite from experimental and natural data in the system MgO–FeO–Al2O3–SiO2–H2O: applications to P–T sections and geothermometry. *Contributions to Mineralogy and Petrology*, *167*(2), pp.1-19.

Lanari, P., Wagner, T. and Vidal, O., 2014b. A thermodynamic model for di-trioctahedral chlorite from experimental and natural data in the system MgO–FeO–Al2O3–SiO2–H2O: applications to P–T sections and geothermometry. *Contributions to Mineralogy and Petrology*, *167*(2), pp.1-19.

Law, R.D., 1986. Relationships between strain and quartz crystallographic fabrics in the Roche Maurice quartzites of Plougastel, western Brittany. *Journal of Structural Geology*, *8*(5), pp.493-515.

Law, R.D., 1990. Crystallographic fabrics: a selective review of their applications to research in structural geology. *Geological Society, London, Special Publications*, *54*(1), pp.335-352.

Law, R.D., 2014. Deformation thermometry based on quartz c-axis fabrics and recrystallization microstructures: A review. *Journal of structural Geology*, *66*, pp.129-161.

Lee, A.L., Torvela, T., Lloyd, G.E. and Walker, A.M., 2018. Melt organisation and strain partitioning in the lower crust. *Journal of Structural Geology*, *113*, pp.188-199.

Leake, B.E., 1989. The metagabbros, orthogneisses and paragneisses of the Connemara complex, western Ireland. *Journal of the Geological Society*, *146*(4), pp.575-596.

Lexa, O., Schulmann, K., Janoušek, V., Štípská, P., Guy, A. and Racek, M., 2011. Heat sources and trigger mechanisms of exhumation of HP granulites in Variscan orogenic root. *Journal of Metamorphic Geology*, *29*(1), pp.79-102.

Levine, J.S., Mosher, S. and Siddoway, C.S., 2013. Relationship between syndeformational partial melting and crustal-scale magmatism and tectonism across the Wet Mountains, central Colorado. *Lithosphere*, *5*(5), pp.456-476.

Lloyd, G.E., Farmer, A.B. and Mainprice, D., 1997. Misorientation analysis and the formation and orientation of subgrain and grain boundaries. *Tectonophysics*, *279*(1-4), pp.55-78.

Lloyd, G.E., Law, R.D. and Schmid, S.M., 1987. A spherical electron channelling pattern map for use in quartz petrofabric analysis: correction and verification. *Journal of structural geology*, *9*(2), pp.251-253.

Lloyd, G.E., Ferguson, C.C. and Law, R.D., 1987. Discriminatory petrofabric analysis of quartz rocks using SEM electron channelling. *Tectonophysics*, *135*(1-3), pp.243-249.

Lloyd, G.E. and Freeman, B., 1994. Dynamic recrystallization of quartz under greenschist conditions. *Journal of Structural Geology*, *16*(6), pp.867-881.

Liao, Y., Wei, C. and Rehman, H.U., 2021. Titanium in calcium amphibole: Behavior and thermometry. *American Mineralogist*, *106*(2), pp.180-191.

Lindh, A. and WAHLGREN, C.H., 1985. migmatite formation at subsolidus conditions–an alternative to anatexis. *Journal of Metamorphic Geology*, *3*(1), pp.1-12.

Llorens, M.G., Gomez-Rivas, E., Ganzhorn, A.C., Griera, A., Steinbach, F., Roessiger, J., Labrousse, L., Walte, N.P., Weikusat, I. and Bons, P.D., 2019. The effect of dynamic recrystallisation on the rheology and microstructures of partially molten rocks. *Journal of Structural Geology*, *118*, pp.224-235.

Lowe, D.R., 1994. Accretionary history of the Archean Barberton greenstone belt (3.55-3.22 Ga), southern Africa. *Geology*, *22*(12), pp.1099-1102.

Lundstrom, C., 2000. Models of U-series disequilibria generation in MORB: the effects of two scales of melt porosity. *Physics of the Earth and Planetary Interiors*, *121*(3-4), pp.189-204.

Mahan, K.H., Williams, M.L., Flowers, R.M., Jercinovic, M.J., Baldwin, J.A. and Bowring, S.A., 2006. Geochronological constraints on the Legs Lake shear zone with implications for regional exhumation of lower continental crust, western Churchill Province, Canadian Shield. *Contributions to Mineralogy and Petrology*, *152*(2), pp.223-242.

Mainprice, D. and Nicolas, A., 1989. Development of shape and lattice preferred orientations: application to the seismic anisotropy of the lower crust. *Journal of Structural Geology*, *11*(1-2), pp.175-189.

Maliva, R.G. and Siever, R., 1988. Diagenetic replacement controlled by force of crystallization. *Geology*, *16*(8), pp.688-691.

Maliva, R.G. and Siever, R., 1988. Diagenetic replacement controlled by force of crystallization. *Geology*, *16*(8), pp.688-691.

Marchildon, N. and Brown, M., 2002. Grain-scale melt distribution in two contact aureole rocks: Implications for controls on melt localization and deformation. *Journal of Metamorphic Geology*, *20*(4), pp.381-396.

Marker, M. and Garde, A.A., 1988. Border relations between the amphibolite facies Finnefjeld gneiss complex and granulite facies grey gneisses in the Fiskefjord area, southern West Greenland.

Marsh, B.D., 1982. On the mechanics of igneous diapirism, stoping, and zone melting. *American Journal of Science*, *282*(6), pp.808-855.

McCormick, J.W. and JW, M., 1977. TRANSMISSION ELECTRON MICROSCOPY OF EXPERIMENTALLY DEFORMED SYNTHIC QUARTZ.

McGregor, V.R., Friend, C.R.L. and Nutman, A.P., 1991. The late Archaean mobile belt through Godthåbsfjord, southern West Greenland: a continent-continent collision zone. *Bulletin of the Geological Society of Denmark*, *39*(3-4), pp.179-197.

McKenzie, D.A.N., 1984. The generation and compaction of partially molten rock. *Journal of petrology*, *25*(3), pp.713-765.

McLellan, E., 1984. Deformational behaviour of migmatites and problems of structural analysis in migmatite terrains. *Geological Magazine*, *121*(4), pp.339-345.

McLellan, E.L., 1988. Migmatite structures in the Central Gneiss Complex, Boca de Quadra, Alaska. *Journal of Metamorphic Geology*, *6*(4), pp.517-542.

McLellan, E.L., 1989. Sequential formation of subsolidus and anatectic migmatites in response to thermal evolution, eastern Scotland. *The Journal of Geology*, *97*(2), pp.165-182.

Meek, U., Piazolo, S. and Daczko, N.R., 2019. The field and microstructural signatures of deformation-assisted melt transfer: Insights from magmatic arc lower crust, New Zealand. *Journal of Metamorphic Geology*.

Mehnert, K.R. and Schneider, G., 1973. Initial melting at grain boundaries of quartz and feldspar in gneisses and granulites. *Neues Jahrbuch für Mineralogie-Monatshefte*, pp.165-183.

Menegon, L., Piazolo, S. and Pennacchioni, G., 2011. The effect of Dauphiné twinning on plastic strain in quartz. *Contributions to Mineralogy and Petrology*, *161*(4), pp.635-652.

Milord, I., Sawyer, E.W. and Brown, M., 2001. Formation of diatexite migmatite and granite magma during anatexis of semi-pelitic metasedimentary rocks: an example from St. Malo, France. *Journal of Petrology*, *42*(3), pp.487-505.

Misra, S., Burlini, L. and Burg, J.P., 2009. Strain localization and melt segregation in deforming metapelites. *Physics of the Earth and Planetary Interiors*, *177*(3-4), pp.173-179.

Mogk, D.W., 1992. Ductile shearing and migmatization at mid-crustal levels in an Archaean high-grade gneiss belt, northern Gallatin Range, Montana, USA. *Journal of Metamorphic Geology*, *10*(3), pp.427-438.

Molina, J.F., Moreno, J.A., Castro, A., Rodríguez, C. and Fershtater, G.B., 2015. Calcic amphibole thermobarometry in metamorphic and igneous rocks: New calibrations based on plagioclase/amphibole Al-Si partitioning and amphibole/liquid Mg partitioning. *Lithos*, *232*, pp.286-305.

Muller, N., Qi, R., Mackie, E., Pruess, K. and Blunt, M.J., 2009. CO2 injection impairment due to halite precipitation. *Energy procedia*, *1*(1), pp.3507-3514.

Nelson, K.D., Zhao, W., Brown, L.D., Kuo, J., Che, J., Liu, X., Klemperer, S.L., Makovsky, Y., Meissner, R.J.J.M., Mechie, J. and Kind, R., 1996. Partially molten middle crust beneath southern Tibet: synthesis of project INDEPTH results. *Science*, *274*(5293), pp.1684-1688.

Nicolas, A. and Poirier, J.P., 1976. Crystalline plasticity and solid state flow in metamorphic rocks.

Nilsson, M.K., Söderlund, U., Ernst, R.E., Hamilton, M.A., Scherstén, A. and Armitage, P.E., 2010. Precise U–Pb baddeleyite ages of mafic dykes and intrusions in southern West Greenland and implications for a possible reconstruction with the Superior craton. *Precambrian Research*, *183*(3), pp.399-415.

Noiriel, C., Renard, F., Doan, M.L. and Gratier, J.P., 2010. Intense fracturing and fracture sealing induced by mineral growth in porous rocks. *Chemical Geology*, *269*(3-4), pp.197-209.

Norris, C.A., Danyushevsky, L., Olin, P. and West, N.R., 2021. Elimination of aliasing in LA-ICP-MS by alignment of laser and mass spectrometer. *Journal of Analytical Atomic Spectrometry*, *36*(4), pp.733-739.

Nutman, A.P. and Friend, C.R., 2007. Adjacent terranes with ca. 2715 and 2650 Ma high-pressure metamorphic assemblages in the Nuuk region of the North Atlantic Craton, southern West Greenland: Complexities of Neoarchaean collisional orogeny. *Precambrian Research*, *155*(3-4), pp.159-203.

Ohno, I., Harada, K. and Yoshitomi, C., 2006. Temperature variation of elastic constants of quartz across the α-β transition. *Physics and Chemistry of Minerals*, *33*(1), pp.1-9.

Okudaira, T., Takeshita, T., Hara, I. and Ando, J.I., 1995. A new estimate of the conditions for transition from basal< a> to prism [c] slip in naturally deformed quartz. *Tectonophysics*, *250*(1-3), pp.31-46.

Ostapenko, G.T. and Yaroshenko, N.S., 1975. Excess pressure upon solid-phases arising during hydration reaction (experimental-data on hydration of semihydrous gypsum and lime). *GEOKHIMIYA*, (1), pp.102-111.

Palin, R.M., Searle, M.P., Waters, D.J., Horstwood, M.S.A. and Parrish, R.R., 2012. Combined thermobarometry and geochronology of peraluminous metapelites from the Karakoram metamorphic complex, North Pakistan; New insight into the tectonothermal evolution of the Baltoro and Hunza Valley regions. *Journal of Metamorphic Geology*, *30*(8), pp.793-820.

Palin, R.M., Searle, M.P., Waters, D.J., Parrish, R.R., Roberts, N.M.W., Horstwood, M.S.A., Yeh, M.W., Chung, S.L. and Anh, T.T., 2013. A geochronological and petrological study of anatectic paragneiss and associated granite dykes from the D ay N ui C on V oi metamorphic core complex, N orth V ietnam: constraints on the timing of metamorphism within the R ed R iver shear zone. *Journal of Metamorphic Geology*, *31*(4), pp.359-387.

Palin, R.M., White, R.W., Green, E.C., Diener, J.F., Powell, R. and Holland, T.J., 2016. High-grade metamorphism and partial melting of basic and intermediate rocks. *Journal of Metamorphic Geology*, *34*(9), pp.871-892.

Park, A.F., 1983. Lit-par-lit migmatite fabrics in a metagabbro-anorthosite complex, Sygnefjell, Jotunheim, South Norway. In *Geochemical group of the mineralogical society. Meeting*.

Parsons, R.A., Nimmo, F., Hustoft, J.W., Holtzman, B.K. and Kohlstedt, D.L., 2008. An experimental and numerical study of surface tension-driven melt flow. *Earth and Planetary Science Letters*, *267*(3-4), pp.548-557.

Passchier, C.W. and Trouw, R.A., 2005. *Microtectonics*. Springer Science & Business Media.

Paterson, S.R., Vernon, R.H. and Tobisch, O.T., 1989. A review of criteria for the identification of magmatic and tectonic foliations in granitoids. *Journal of structural geology*, *11*(3), pp.349-363.

Pawley, M.J., Preiss, W.V., Dutch, R.A. and Reid, A.J., 2013. *A User's Guide to Migmatites*. Department for Manufacturing, Innovation, Trade, Resources and Energy.

Petford, N., 1996. Dykes or diapirs?. *Earth and Environmental Science Transactions of the Royal Society of Edinburgh*, *87*(1-2), pp.105-114.

Philpotts, A. and Ague, J., 2009. *Principles of igneous and metamorphic petrology*. Cambridge University Press.

Piazolo, S., Bons, P.D., Jessell, M.W., Evans, L. and Passchier, C.W., 2002. Dominance of microstructural processes and their effect on microstructural development: insights from numerical modelling of dynamic recrystallization. *Geological Society, London, Special Publications*, *200*(1), pp.149-170.

Piazolo, S., 2002. Overview of the metamorphic evolution of tonalitic gneisses and metasedimentary sequences from the Kangaatsiaq, Lersletten and Sydostbugten area–first comparison to adjacent areas. In *Workshop on Nagssugtoqidian and Rinkian geology, West Greenland. Danmarks og Grønlands Geologiske Undersøgelse Rapport* (Vol. 9, pp. 32-33).

Piazolo, S., Alsop, G.I., Nielsen, B.M. and Van Gool, J.A.M., 2004. The application of GIS to unravel patterns of deformation in high grade terrains: a case study of indentor tectonics from west Greenland. *Geological Society, London, Special Publications*, *224*(1), pp.63-78.

Piazolo, S., Prior, D.J. and Holness, M.D., 2005. The use of combined cathodoluminescence and EBSD analysis: a case study investigating grain boundary migration mechanisms in quartz. *Journal of Microscopy*, *217*(2), pp.152-161.

Piazolo, S., Bestmann, M., Prior, D.J. and Spiers, C.J., 2006. Temperature dependent grain boundary migration in deformed-then-annealed material: observations from experimentally deformed synthetic rocksalt. *Tectonophysics*, *427*(1-4), pp.55-71.

Piazolo, S., Montagnat, M. and Blackford, J.R., 2008. Sub-structure characterization of experimentally and naturally deformed ice using cryo-EBSD. *Journal of Microscopy*, *230*(3), pp.509-519.

Piazolo, S. and Jaconelli, P., 2014. Sillimanite deformation mechanisms within a Grt-Sil-Bt gneiss: effect of pre-deformation grain orientations and characteristics on mechanism, slip-system activation and rheology. *Geological Society, London, Special Publications*, *394*(1), pp.189-213.

Piazolo, S., Daczko, N.R., Silva, D. and Raimondo, T., 2020. Melt-present shear zones enable intracontinental orogenesis. *Geology*, *48*(7), pp.643-648.

Pickering-Witter, J. and Johnston, A.D., 2000. The effects of variable bulk composition on the melting systematics of fertile peridotitic assemblages. *Contributions to Mineralogy and Petrology*, *140*(2), pp.190-211.

Poirier, J.P. and Guillopé, M., 1979. Deformation induced recrystallization of minerals. *Bulletin de Mineralogie*, *102*(2), pp.67-74.

Powell, R., 1978. The thermodynamics of pyroxene geotherms. *Philosophical Transactions of the Royal Society of London. Series A, Mathematical and Physical Sciences*, *288*(1355), pp.457-469.

Powell, R., Holland, T.J.B.H. and Worley, B., 1998. Calculating phase diagrams involving solid solutions via non-linear equations, with examples using THERMOCALC. *Journal of metamorphic Geology*, *16*(4), pp.577-588.

Prior, D.J., Wheeler, J., Peruzzo, L., Spiess, R. and Storey, C., 2002. Some garnet microstructures: an illustration of the potential of orientation maps and misorientation analysis in microstructural studies. *Journal of Structural Geology*, *24*(6-7), pp.999-1011.

Putnis, A., 2009. Mineral replacement reactions. *Reviews in mineralogy and geochemistry*, *70*(1), pp.87-124.

Putnis, A. and Austrheim, H., 2010. Fluid-induced processes: metasomatism and metamorphism. *Geofluids*, *10*(1-2), pp.254-269.

Rampone, E., Piccardo, G.B., Vannucci, R. and Bottazzi, P., 1997. Chemistry and origin of trapped melts in ophioiitic peridotites. *Geochimica et Cosmochimica Acta*, *61*(21), pp.4557-4569.

Rampone, E., Hofmann, A.W. and Raczek, I., 2009. Isotopic equilibrium between mantle peridotite and melt: evidence from the Corsica ophiolite. *Earth and Planetary Science Letters*, *288*(3-4), pp.601-610.

Ranalli, G. and Fischer, B., 1984. Diffusion creep, dislocation creep, and mantle rheology. *Physics of the earth and planetary interiors*, *34*(1-2), pp.77-84.

Reiners, P.W., 1998. Reactive melt transport in the mantle and geochemical signatures of mantle-derived magmas. *Journal of Petrology*, *39*(5), pp.1039-1061.

Robin, P.Y.F., 1979. Theory of metamorphic segregation and related processes. *Geochimica et Cosmochimica Acta*, *43*(10), pp.1587-1600.

Rosenberg, C.L. and Handy, M.R., 2000. Syntectonic melt pathways during simple shearing of a partially molten rock analogue (Norcamphor-Benzamide). *Journal of Geophysical Research: Solid Earth*, *105*(B2), pp.3135-3149.

Rosenberg, C.L. and Riller, U., 2000. Partial-melt topology in statically and dynamically recrystallized granite. *Geology*, *28*(1), pp.7-10.

Rosenberg, C.L. and Handy, M.R., 2001. Mechanisms and orientation of melt segregation paths during pure shearing of a partially molten rock analog (norcamphor–benzamide). *Journal of Structural Geology*, *23*(12), pp.1917-1932.

Rutter, E.H., Brodie, K.H. and Irving, D.H., 2006. Flow of synthetic, wet, partially molten "granite" under undrained conditions: an experimental study. *Journal of Geophysical Research: Solid Earth*, *111*(B6).

Rubatto, D., Hermann, J. and Buick, I.S., 2006. Temperature and bulk composition control on the growth of monazite and zircon during low-pressure anatexis (Mount Stafford, central Australia). *Journal of Petrology*, *47*(10), pp.1973-1996.

Rybacki, E. and Dresen, G., 2004. Deformation mechanism maps for feldspar rocks. *Tectonophysics*, *382*(3-4), pp.173-187.

Sawyer, E.W., 1991. Disequilibrium melting and the rate of melt–residuum separation during migmatization of mafic rocks from the Grenville Front, Quebec. *Journal of Petrology*, *32*(4), pp.701-738.

Sawyer, E.W., 1998. Formation and evolution of granite magmas during crustal reworking: the significance of diatexites. *Journal of Petrology*, *39*(6), pp.1147-1167.

Sawyer, E.W., 1994. Melt segregation in the continental crust. *Geology*, *22*(11), pp.1019-1022.

Sawyer, E.W., Dombrowski, C. and Collins, W.J., 1999. Movement of melt during synchronous regional deformation and granulite-facies anatexis, an example from the Wuluma Hills, central Australia. *Geological Society, London, Special Publications*, *168*(1), pp.221-237.

Sawyer, E.W., 2001. Melt segregation in the continental crust: distribution and movement of melt in anatectic rocks. *Journal of metamorphic Geology*, *19*(3), pp.291-309.

Sawyer, E.W., 2008. *Atlas of migmatites* (Vol. 9). NRC Research press.

Scott, D.R. and Stevenson, D.J., 1986. Magma ascent by porous flow. *Journal of Geophysical Research: Solid Earth*, *91*(B9), pp.9283-9296.

Scherer, G.W., 2004. Stress from crystallization of salt. *Cement and concrete research*, *34*(9), pp.1613-1624.

Schilling, F.R., Partzsch, G.M., Brasse, H. and Schwarz, G., 1997. Partial melting below the magmatic arc in the central Andes deduced from geoelectromagnetic field experiments and laboratory data. *Physics of the Earth and Planetary Interiors*, *103*(1-2), pp.17-31.

Schott, B. and Schmeling, H., 1998. Delamination and detachment of a lithospheric root. *Tectonophysics*, *296*(3-4), pp.225-247.

Scott, D.R. and Stevenson, D.J., 1986. Magma ascent by porous flow. Journal of Geophysical Research: Solid Earth, 91(B9), pp.9283-9296.

Sederholm, J.J., 1923. *On Migmatites and Associated Pre-Cambrian Rocks of Southwestern Finland: Pt. I. The Pellinge Region* (No. 58). US Government Printing Office.

Sen, G. and Leeman, W.P., 1991. Iron-rich lherzolitic xenoliths from Oahu: origin and implications for Hawaiian magma sources. *Earth and Planetary Science Letters*, *102*(1), pp.45-57.

Sen, G., 1988. Petrogenesis of spinel lherzolite and pyroxenite suite xenoliths from the Koolau shield, Oahu, Hawaii: implications for petrology of the post-eruptive lithosphere beneath Oahu. *Contributions to Mineralogy and Petrology*, *100*(1), pp.61-91.

Shao, Y., Piazolo, S., Liu, Y., Lee, A.L., Jin, W., Li, W., Liang, C. and Wen, Q., 2021. Deformation Behavior and Inferred Seismic Properties of Tonalitic Migmatites at the Time of Pre-melting, Partial Melting, and Post-Solidification. *Geochemistry, Geophysics, Geosystems*, *22*(2), p.e2020GC009202.Sizova, E., Gerya, T., Stüwe, K. and Brown, M., 2015. Generation of felsic crust in the Archean: a geodynamic modeling perspective. *Precambrian Research*, *271*, pp.198-224.

Skemer, P., Katayama, I., Jiang, Z. and Karato, S.I., 2005. The misorientation index: Development of a new method for calculating the strength of lattice-preferred orientation. *Tectonophysics*, *411*(1-4), pp.157-167.

Sleep, N.H., 1988. Tapping of melt by veins and dikes. *Journal of Geophysical Research: Solid Earth*, *93*(B9), pp.10255-10272.

Smith, D.J., 2014. Clinopyroxene precursors to amphibole sponge in arc crust. *Nature Communications*, *5*, p.4329.

Soret, M., Agard, P., Ildefonse, B., Dubacq, B., Prigent, C. and Rosenberg, C., 2019. Deformation mechanisms in mafic amphibolites and granulites: record from the Semail metamorphic sole during subduction infancy. *Solid Earth*, *10*(5), pp.1733-1755.

Solano, J.M.S., Jackson, M.D., Sparks, R.S.J., Blundy, J.D. and Annen, C., 2012. Melt segregation in deep crustal hot zones: a mechanism for chemical differentiation, crustal assimilation and the formation of evolved magmas. *Journal of Petrology*, *53*(10), pp.1999-2026.

Spiegelman, M. and Kenyon, P., 1992. The requirements for chemical disequilibrium during magma migration. *Earth and Planetary Science Letters*, *109*(3-4), pp.611-620.

Spear, F.S., Kohn, M.J. and Paetzold, S., 1995. Petrology of the regional sillimanite zone, west-central New Hampshire, USA, with implications for the development of inverted isograds. *American Mineralogist*, *80*(3-4), pp.361-376.

Stallard, A. and Shelley, D., 1995. Quartz c-axes parallel to stretching directions in very low-grade metamorphic rocks. *Tectonophysics*, *249*(1-2), pp.31-40.

Steenfelt, A., Hollis, J., Kirkland, C.L., Sandrin, A., Gardiner, N.J., Olierook, H.K., Szilas, K., Waterton, P. and Yakymchuk, C., 2021. The Mesoarchaean Akia terrane, West Greenland, revisited: New insights based on spatial integration of geophysics, field observation, geochemistry and geochronology. *Precambrian Research*, *352*, p.105958.

Stevens, G., Clemens, J.D. and Droop, G.T., 1997. Melt production during granulite-facies anatexis: experimental data from "primitive" metasedimentary protoliths. *Contributions to Mineralogy and Petrology*, *128*(4), pp.352-370.

Stevenson, D.J., 1989. Spontaneous small-scale melt segregation in partial melts undergoing deformation. *Geophysical Research Letters*, *16*(9), pp.1067-1070.

Stipp, M., Stünitz, H., Heilbronner, R. and Schmid, S.M., 2002. Dynamic recrystallization of quartz: correlation between natural and experimental conditions. *Geological Society, London, Special Publications*, *200*(1), pp.171-190.

Stokes, M.R., Wintsch, R.P. and Southworth, C.S., 2012. Deformation of amphibolites via dissolution–precipitation creep in the middle and lower crust. *Journal of Metamorphic Geology*, *30*(7), pp.723-737.

Stolper, E., 1980. A phase diagram for mid-ocean ridge basalts: preliminary results and implications for petrogenesis. *Contributions to Mineralogy and Petrology*, *74*(1), pp.13-27.

STREIT*, J.E. and COX*, S.F., 1998. Fluid infiltration and volume change during mid-crustal mylonitization of Proterozoic granite, King Island, Tasmania. *Journal of Metamorphic Geology*, *16*(2), pp.197-212.

Stuart, C.A., Piazolo, S. and Daczko, N.R., 2018. The recognition of former melt flux through high-strain zones. *Journal of Metamorphic Geology*, *36*(8), pp.1049-1069.

Stuart, C.A., Meek, U., Daczko, N.R., Piazolo, S. and Huang, J.X., 2018. Chemical signatures of melt–rock interaction in the root of a magmatic arc. *Journal of Petrology*, *59*(2), pp.321-340.

Stuart, C.A., Daczko, N.R. and Piazolo, S., 2017. Local partial melting of the lower crust triggered by hydration through melt–rock interaction: an example from Fiordland, New Zealand. *Journal of Metamorphic Geology*, *35*(2), pp.213-230.

Stuart, C.A., Piazolo, S. and Daczko, N.R., 2016. Mass transfer in the lower crust: Evidence for incipient melt assisted flow along grain boundaries in the deep arc granulites of F iordland, N ew Z ealand. *Geochemistry, Geophysics, Geosystems*, *17*(9), pp.3733-3753.

Stünitz, H., Neufeld, K., Heilbronner, R., Finstad, A.K., Konopásek, J. and Mackenzie, J.R., 2020. Transformation weakening: diffusion creep in eclogites as a result of interaction of mineral reactions and deformation. *Journal of Structural Geology*, *139*, p.104129.

Stünitz, H. and Gerald, J.F., 1993. Deformation of granitoids at low metamorphic grade. II: Granular flow in albite-rich mylonites. *Tectonophysics*, *221*(3-4), pp.299-324.

Szilas, K., Hoffmann, J.E., Schulz, T., Hansmeier, C., Polat, A., Viehmann, S., Kasper, H.U. and Münker, C., 2016. Combined bulk-rock Hf-and Nd-isotope compositions of Mesoarchaean metavolcanic rocks from the Ivisaartoq Supracrustal Belt, SW Greenland: Deviations from the mantle array caused by crustal recycling. *Geochemistry*, *76*(4), pp.543-554.

Svahnberg, H. and Piazolo, S., 2010. The initiation of strain localisation in plagioclase-rich rocks: Insights from detailed microstructural analyses. *Journal of Structural Geology*, *32*(10), pp.1404-1416.

Szilas, K., Tusch, J., Hoffmann, J.E., Garde, A.A. and Münker, C., 2017. Hafnium isotope constraints on the origin of Mesoarchaean andesites in southern West Greenland, North Atlantic craton. *Geological Society, London, Special Publications*, *449*(1), pp.19-38.

Tanner, P.W.G. and Shackleton, R.M., 1979. Structure and stratigraphy of the Dalradian rocks of the Bennabeola area, Connemara, Eire. *Geological Society, London, Special Publications*, *8*(1), pp.243-256.

Tartarotti, P., Susini, S., Nimis, P. and Ottolini, L., 2002. Melt migration in the upper mantle along the Romanche Fracture Zone (Equatorial Atlantic). Lithos, 63(3-4), pp.125-149.

Tatham, D.J., Lloyd, G.E., Butler, R.W.H. and Casey, M., 2008. Amphibole and lower crustal seismic properties. *Earth and Planetary Science Letters*, *267*(1-2), pp.118-128.

Taylor, S.R. and McLennan, S.M., 1995. The geochemical evolution of the continental crust. *Reviews of Geophysics*, *33*(2), pp.241-265.

Teyssier, C. and Whitney, D.L., 2002. Gneiss domes and orogeny. *Geology*, *30*(12), pp.1139-1142.

Tinkham, D.K., Zuluaga, C.A. and Stowell, H.H., 2001. Metapelite phase equilibria modeling in MnNCKFMASH: the effect of variable Al2O3 and MgO/(MgO+ FeO) on mineral stability. *Geological Materials Research*, *3*(1), pp.1-42.

Tinkham, D.K. and Ghent, E.D., 2005. Estimating PT conditions of garnet growth with isochemical phase-diagram sections and the problem of effective bulk-composition. *The Canadian Mineralogist*, *43*(1), pp.35-50.

Tommasi, A., Vauchez, A., Femandes, L.A. and Porcher, C.C., 1994. Magma-assisted strain localization in an orogen-parallel transcurrent shear zone of southern Brazil. *Tectonics*, *13*(2), pp.421-437.

Tommasi, A., Langone, A., Padrón-Navarta, J.A., Zanetti, A. and Vauchez, A., 2017. Hydrous melts weaken the mantle, crystallization of pargasite and phlogopite does not: Insights from a petrostructural study of the Finero peridotites, southern Alps. *Earth and Planetary Science Letters*, *477*, pp.59-72.

Toy, V.G., Prior, D.J. and Norris, R.J., 2008. Quartz fabrics in the Alpine Fault mylonites: Influence of pre-existing preferred orientations on fabric development during progressive uplift. *Journal of Structural Geology*, *30*(5), pp.602-621.

Tucker, R.D., Robinson, P., Solli, A., Gee, D.G., Thorsnes, T., Krogh, T.E., Nordgulen, Ø. and Bickford, M.E., 2004. Thrusting and extension in the Scandian hinterland, Norway: New U-Pb ages and tectonostratigraphic evidence. *American Journal of Science*, *304*(6), pp.477-532.

Turcotte, D.L. and Ahern, J.L., 1978. A porous flow model for magma migration in the asthenosphere. *Journal of Geophysical Research: Solid Earth*, *83*(B2), pp.767-772.

Turner, F.J., 1941. The development of pseudo-stratification by metamorphic differentiation in the schists of Otago, New Zealand. *American Journal of Science*, *239*(1), pp.1-16.

Twiss, R.J., 1977. Theory and applicability of a recrystallized grain size paleopiezometer. In *Stress in the Earth* (pp. 227-244). Birkhäuser, Basel.

van Gool, J.A., Connelly, J.N., Marker, M. and Mengel, F.C., 2002. The Nagssugtoqidian Orogen of West Greenland: tectonic evolution and regional correlations from a West Greenland perspective. *Canadian Journal of Earth Sciences*, *39*(5), pp.665-686.

Vance, J.A., 1969, On synneusis: Contributions to Mineralogy and Petrology, v. 24, p. 7–29, doi: 10.1007/BF00398750.

Vance, D. and Mahar, E., 1998. Pressure-temperature paths from PT pseudosections and zoned garnets: potential, limitations and examples from the Zanskar Himalaya, NW India. *Contributions to Mineralogy and Petrology*, *132*(3), pp.225-245.

Vanderhaeghe, O., 2009. Migmatites, granites and orogeny: Flow modes of partially-molten rocks and magmas associated with melt/solid segregation in orogenic belts. *Tectonophysics*, *477*(3-4), pp.119-134.

Vernon, R.H. and Paterson, S.R., 2008. How late are K-feldspar megacrysts in granites?. *Lithos*, *104*(1-4), pp.327-336.

Vernon, R.H. and Clarke, G.L., 2008. Principles of metamorphic petrology. Ed.

Vernon, R.H., 2010. Granites really are magmatic: Using microstructural evidence to refute some obstinate hypotheses. *Journal of the Virtual Explorer*, *35*, pp.1-36.

Vernon, R.H., 2011. Microstructures of melt-bearing regional metamorphic rocks. *Geological Society of America Memoirs*, *207*, pp.1-11.

Veveakis, E., Regenauer-Lieb, K. and Weinberg, R.F., 2014. Ductile compaction of partially molten rocks: the effect of non-linear viscous rheology on instability and segregation. *Geophysical Journal International*, *200*(1), pp.519-523.

Vigneresse, J.L., 2004. A new paradigm for granite generation. *Earth and Environmental Science Transactions of the Royal Society of Edinburgh*, *95*(1-2), pp.11-22.

Walte, N.P., Bons, P.D., Passchier, C.W. and Koehn, D., 2003. Disequilibrium melt distribution during static recrystallization. *Geology*, *31*(11), pp.1009-1012.

Walte, N.P., Bons, P.D. and Passchier, C.W., 2005. Deformation of melt-bearing systems—insight from in situ grain-scale analogue experiments. *Journal of Structural Geology*, *27*(9), pp.1666-1679.

Wellings, S.A., 1998. Timing of deformation associated with the syn-tectonic Dawros–Currywongaun–Doughruagh Complex, NW Connemara, western Ireland. *Journal of the Geological Society*, *155*(1), pp.25-37.

Weinberg, R.F. and Searle, M.P., 1998. The Pangong Injection Complex, Indian Karakoram: a case of pervasive granite flowthrough hot viscous crust. *Journal of the Geological Society*, *155*(5), pp.883-891.

Weinberg, R.F. and Podladchikov, Y., 1994. Diapiric ascent of magmas through power law crust and mantle. *Journal of Geophysical Research: Solid Earth*, *99*(B5), pp.9543-9559.

Weinberg, R.F., 1997. Diapir-driven crustal convection: decompression melting, renewal of the magma source and the origin of nested plutons. *Tectonophysics*, *271*(3-4), pp.217-229.

Weinberg, R.F., 1999. Mesoscale pervasive felsic magma migration: alternatives to dyking. *Lithos*, *46*(3), pp.393-410.

Weinberg, R.F. and Regenauer-Lieb, K., 2010. Ductile fractures and magma migration from source. *Geology*, *38*(4), pp.363-366.

Weinberg, R.F. and Hasalová, P., 2015. Water-fluxed melting of the continental crust: A review. *Lithos*, *212*, pp.158-188.

Wenk, H.R., Monteiro, P.J. and Shomglin, K., 2008. Relationship between aggregate microstructure and mortar expansion. A case study of deformed granitic rocks from the Santa Rosa mylonite zone. *Journal of materials science*, *43*(4), pp.1278-1285.

Wenk, H.R. and Christie, J.M., 1991. Comments on the interpretation of deformation textures in rocks. *Journal of Structural Geology*, *13*(10), pp.1091-1110.

Wellman, H.W. and Wilson, A.T., 1965. Salt weathering, a neglected geological erosive agent in coastal and arid environments. *Nature*, *205*(4976), p.1097.

White, S., 1977. Geological significance of recovery and recrystallization processes in quartz. *Tectonophysics*, *39*(1-3), pp.143-170.

White, S.H., Burrows, S.E., Carreras, J., Shaw, N.D. and Humphreys, F.J., 1980. On mylonites in ductile shear zones. *Journal of Structural Geology*, *2*(1-2), pp.175-187.

Wheeler, J., Prior, D., Jiang, Z., Spiess, R. and Trimby, P., 2001. The petrological significance of misorientations between grains. *Contributions to mineralogy and petrology*, *141*(1), pp.109-124.

Wheeler, J., Mariani, E., Piazolo, S., Prior, D.J., Trimby, P. and Drury, M.R., 2009. The weighted Burgers vector: a new quantity for constraining dislocation densities and types using electron backscatter diffraction on 2D sections through crystalline materials. *Journal of microscopy*, *233*(3), pp.482-494.

White, R.W., Powell, R. and Halpin, J.A., 2004. Spatially-focussed melt formation in aluminous metapelites from Broken Hill, Australia. *Journal of Metamorphic Geology*, *22*(9), pp.825-845.

White, R.W., Powell, R. and Baldwin, J.A., 2008. Calculated phase equilibria involving chemical potentials to investigate the textural evolution of metamorphic rocks. *Journal of Metamorphic Geology*, *26*(2), pp.181-198.

White, R.W., Powell, R.O.G.E.R., Holland, T.J.B., Johnson, T.E. and Green, E.C.R., 2014. New mineral activity–composition relations for thermodynamic calculations in metapelitic systems. *Journal of Metamorphic Geology*, *32*(3), pp.261-286.

Whitney, D.L. and Evans, B.W., 2010. Abbreviations for names of rock-forming minerals. *American mineralogist*, *95*(1), pp.185-187.

Wimmenauer, W. and Bryhni, I., 2007. A systematic nomenclature for metamorphic rocks: 6 Migmatites and related rocks. *A proposal on behalf of the IUGS Subcommission on the Systematics of Metamorphic Rocks, Web version of*, *1*, p.5.

Wilson, C.J.L., 1975. Preferred orientation in quartz ribbon mylonites. *Geological Society of America Bulletin*, *86*(7), pp.968-974.

Williams, M.L., Melis, E.A., Kope, C.F. and Hanmer, S., 2000. Microstructural tectonometamorphic processes and the development of gneissic layering: a mechanism for metamorphic segregation. *Journal of Metamorphic Geology*, *18*(1), pp.41-58.

Windley, B.F. and Garde, A.A., 2009. Arc-generated blocks with crustal sections in the North Atlantic craton of West Greenland: crustal growth in the Archean with modern analogues. *Earth-Science Reviews*, *93*(1-2), pp.1-30.

Wang, B., Liu, H., Shu, L., Jahn, B.M., Chung, S.L., Zhai, Y. and Liu, D., 2014. Early Neoproterozoic crustal evolution in northern Yili Block: insights from migmatite, orthogneiss and leucogranite of the Wenquan metamorphic complex in the NW Chinese Tianshan. *Precambrian Research*, *242*, pp.58-81.

Yakymchuk, C., 2017. Behaviour of apatite during partial melting of metapelites and consequences for prograde suprasolidus monazite growth. *Lithos*, *274*, pp.412-426.

Yakymchuk, C., Kirkland, C.L., Hollis, J.A., Kendrick, J., Gardiner, N.J. and Szilas, K., 2020. Mesoarchean partial melting of mafic crust and tonalite production during high-T–low-P stagnant tectonism, Akia Terrane, West Greenland. *Precambrian Research*, *339*, p.105615.

Yardley, B.W.D., Barber, J.P. and Gray, J.R., 1987. The metamorphism of the Dalradian rocks of western Ireland and its relation to tectonic setting. *Philosophical Transactions of the Royal Society of London. Series A, Mathematical and Physical Sciences*, *321*(1557), pp.243-270.

Yardley, B.W., 2009. The role of water in the evolution of the continental crust. *Journal of the Geological Society*, *166*(4), pp.585-600.

Yi, K., Bennett, V.C., Nutman, A.P. and Lee, S.R., 2014. Tracing Archaean terranes under Greenland's Icecap: U–Th–Pb–Hf isotopic study of zircons from melt-water rivers in the Isua area. *Precambrian Research*, *255*, pp.900-921.

Závada, P., Schulmann, K., Konopásek, J., Ulrich, S. and Lexa, O., 2007. Extreme ductility of feldspar aggregates—Melt-enhanced grain boundary sliding and creep failure: Rheological implications for felsic lower crust. *Journal of Geophysical Research: Solid Earth*, *112*(B10).

Závada, P., Schulmann, K., Racek, M., Hasalová, P., Jeřábek, P., Weinberg, R.F., Štípská, P. and Roberts, A., 2018. Role of strain localization and melt flow on exhumation of deeply subducted continental crust. *Lithosphere*, *10*(2), pp.217-238.

Zen, E.A., 1966. *Construction of pressure-temperature diagrams for multicomponent systems after the method of Schreinemakers: A geometric approach* (Vol. 1225). US Government Printing Office.

Zhu, W., Gaetani, G.A., Fusseis, F., Montési, L.G. and De Carlo, F., 2011. Microtomography of partially molten rocks: three-dimensional melt distribution in mantle peridotite. *Science*, *332*(6025), pp.88-91.